NOVA SCHOOL OF SCIENCE & TECHNOLOGY

DEPARTMENT OF CHEMISTRY

SUPRAMOLECULAR STRATEGIES FOR THE SENSING AND TRANSPORT OF PEPTIDES: FROM DISCRETE TO BIOMIMETIC SYSTEMS

JOANA MAFALDA NUNES PAULO SILVA MARTINS

Master in Biochemistry

DOCTORATE IN CHEMISTRY

NOVA University Lisbon
September, 2025

DEPARTMENT OF
CHEMISTRY

SUPRAMOLECULAR STRATEGIES FOR THE SENSING AND TRANSPORT OF PEPTIDES: FROM DISCRETE TO BIOMIMETIC SYSTEMS

JOANA MAFALDA NUNES PAULO SILVA MARTINS

Master in Biochemistry

Adviser: Nuno Miguel Jesuíno Basílio
Assistant Professor, NOVA School of Science and Technology, NOVA University of Lisbon

Co-adviser: João Carlos dos Santos Silva e Pereira de Lima
Full Professor, NOVA School of Science and Technology, NOVA University of Lisbon

Examination Committee

Rapporteurs: Maria João Pedrosa Ferreira Moreno Silvestre
Associated Professor, University of Coimbra

Fábio Monteiro Fernandes
Assistant Professor, Instituto Superior Técnico, University of Lisbon

Adviser: Nuno Miguel Jesuíno Basílio
Assistant Professor, NOVA School of Science and Technology, NOVA University of Lisbon

Members: Maria Alexandra Núncio de Carvalho Ramos Fernandes
Full Professor, NOVA School of Science and Technology, NOVA University of Lisbon

Artur Jorge Carneiro Moro
Assistant Professor, NOVA School of Science and Technology, NOVA University of Lisbon

Carina Alexandra Marques Esteves
Auxiliary Researcher, NOVA School of Science and Technology, NOVA University of Lisbon

Pedro Miguel Veríssimo Mateus
Auxiliary Researcher, Instituto de Tecnologia Química e Biológica António Xavier, NOVA University of Lisbon

DOCTORATE IN CHEMISTRY

NOVA University Lisbon
September, 2025

Supramolecular Strategies for the Sensing and Transport of Peptides: From Discrete to Biomimetic Systems

This document was created with the (pdf/Xe/Lua)LaTeX processor and the NOVAthesis template (v7.3.3) [1].

Acknowledgements

Se resumir quatro anos de trabalho em pouco mais de 300 páginas já é uma tarefa hercúlea, arranjar palavras para agradecer àqueles que estiveram comigo enquanto passei por ansiedades, felicidades, tristezas e aventuras e que contribuíram para cá chegar, inteira e com a sanidade mental (mais ou menos) intacta é praticamente impossível, mas vou dar o meu melhor.

Primeiro que tudo, tenho de agradecer às pessoas que mais influenciaram e ajudaram ao meu trabalho chegar onde chegou, os meus orientadores, Professores Nuno Basílio e João C. Lima. Ao Professor Nuno Basílio que sempre acompanhou o meu trabalho de perto, com entusiasmo e ideias, mesmo quando eu me sentia desmotivada e frustrada, que sempre me incentivou a ter um papel de maior responsabilidade e me ajudou a tornar-me na profissional que sou hoje; ao Professor João C. Lima, sempre disposto a dar uma nova perspetiva e ajudar a pensar de outra forma sobre qualquer assunto e a levar o trabalho um pouco mais além. Obrigada aos dois por confiarem em mim e nas minhas capacidades mesmo quando eu própria não o fazia.

Obrigada ao CHARM (Cultural Heritage and Responsive Materials) Research Group, que me recebeu durante estes últimos 6 anos de braços abertos, por me ter ajudado a construir tanto o meu espírito crítico como sentido prático e pela companhia nos melhores e piores dias de laboratório.

Agradeço também às instituições de acolhimento e financiamento que tornaram este trabalho possível. Ao Departamento de Química da Faculdade de Ciências e Tecnologia da Universidade NOVA de Lisboa (FCT NOVA) e ao Laboratório Associado para a Química Verde (LAQV-REQUIMTE), que me deram todas as condições necessárias para poder desenvolver o meu trabalho e à Fundação para a Ciência e Tecnologia pelo suporte financeiro providenciado pela bolsa de doutoramento que me foi atribuída (2021.06296.BD) e pelos projetos em que me inseri durante estes anos. À União Europeia e aos fundos do programa de financiamento Horizon 2020 que permitiram a estadia em Boston no laboratório do Professor Timothy M. Swager, pelo projeto VIT (101008237). A todos os membros dos serviços de gestão, secretariado e apoio técnico da faculdade e do LAQV - a vossa ajuda é imensurável e quase sempre passa despercebida para quem só vê o produto final.

Uma vez que a ciência é um processo colaborativo, tenho muito a agradecer a todos os que participaram e contribuíram para esta tese, quer do CHARM quer aos nossos colaboradores dentro da FCT NOVA. Obrigada a todos aqueles que participaram nos projetos, MSc. Beatriz Raimundo, MSc. Hanieh Mahmoodi, MSc. Daniel Miranda, que contribuíram diretamente para alguns dos resultados apresentados ou que trabalharam paralelamente em otimização de condições e na síntese de compostos. Aos colaboradores de outros laboratórios, em particular ao grupo Structural and Molecular Biology Research Group, do UCIBIO, FCT NOVA - à Professora Ana Sofia Ferreira, Dra. Filipa Marcelo e à Dra. Ana Sofia Grosso, por me ajudarem a dar um passo para fora da minha área de conforto.

Thank you to all our international collaborators, from Santiago de Compostela, Bordeaux, Santiago do Chile and Boston. To Professor Javier Montengro, Dr. Alicia Rioboo, MSc. Lucía Mendéz-Goméz and MSc. Yeray Folgar-Cameán, who welcomed me so warmly in Santiago de Compostela, at CIQUS, and for all the contributions that led to such interesting and successful work. To MSc. Kevin Droguett for the time spent in our lab and the all the hard work helping us furthering the work in membranes. To Dr. Nathan D. McClenaghan for the help providing us with the Blue-Box samples and in trying to uncover the curious structures that this receptor makes by crystallography studies. And finally to Professor Timothy M. Swager and Dr. Georgios Toupalas, from the Swager Lab, MIT, Boston, for welcoming me during my three month stay across the ocean, for allowing me to learn immensely for such a short time, for the amazing opportunity to work in their lab and at one of the top institutions in the world, and for letting me explore different ways to look and do science, that will definitely shape the way I look at my work. Thank you to the Montenegro lab and especially to Lucía for all the help, for stopping her work and helping me for almost two full weeks, for the wonderful company and for helping me train my galego. Moitas grazas! Thank you as well to all of the Swager Lab, in particular to Professor Tim, Georgios, Brian, Collette, Rina, Ashton, Maryam, Chi, Jesús, Benedikt, Michael, Abdusalom, Haosheng, Molly, Jennifer and all the others for welcoming me in the crazy world of research in America and for being more than ready to help when I most needed it. In particular, to Georgios Toupalas who helped me immensely, kept me company on the crazy long days and put up with me and my questions during the three months at MIT. Go lobsters!

Thank you to my fellow PhD student, friend and house-mate Tobi for all the after-work venting, all the summer and fall evenings on the porch and for making Coolidge Corner a home away from home. You made Boston that much more incredible, and I will be forever grateful. Can't wait to see you achieve great things!

Agradeço a todos os fotoquímicos, aos que ainda cá estão e aos que já andam noutras aventuras. Aos Professores António J. Parola, Fernando Pina e César Laia pelos debates científicos, pelo apoio e pelas diversas histórias e perspectivas sobre todos os assuntos e mais alguns. Aos investigadores, colegas e amigos: Alberto, Alfonso, Ambrósio, Ana, Artur, Catarina, Clara, Cláudia, Diogo, Francisco, Hanieh, João, Lúcia, Maria, Micael, Miriam, Rita, Sandra, Tiago, Vanessa, Vitor e ao Zé, pela companhia e bons momentos dentro e fora do laboratório.

Um obrigada especial ao André Seco, Liliana Gomes, Beatriz Raimundo e às fotoquímicas honorárias Alexandra Borges e Sofia Pires - por praias, bares de Aveiro, aventuras no Porto e em águas internacionais, quando me lembro dos momentos mais felizes e mais marcantes destes últimos 6 anos, eram vocês que estavam lá ao meu lado. Não há palavras para vos agradecer.

À família que se escolhe: Catarina e Laura que me aturam literalmente desde que eu me lembro, ao Xico que eu não vejo vezes suficientes, mas está sempre lá, à Catarina e ao Tiago, futuros vizinhos e companheiros de aventuras, ao Miguel, Muri, Philip, João Cruz, André e Fátima, Ricardo e Gabriela, e a todos os outros que são demasiados para listar aqui, obrigada pela vossa paciência e compreensão, pelos desabafos, pelo apoio, distrações e por todas as aventuras.

Obrigada ao Jorge e à Teresa pelo apoio incondicional nestes últimos anos e por me incentivarem a ir à aventura apesar das minhas inseguranças e ansiedades. É um orgulho fazer parte da pandilha!

Um enorme obrigada à minha família: os meus pais e o meu irmão, João, e Carolina. Por todos estes anos de apoio, pela ajuda do dia-a-dia que parece simples, mas é insubstituível, pelas piadas e macacadas, pelo incentivo em continuar, mas acima de tudo por estarem lá para mim independentemente do caminho que eu decidir seguir.

Por fim, ao André. Presenciaste todas as cabeçadas, todos os momentos em que a vontade de desistir era imensa, todos os momentos de fraqueza, todas as incertezas e inseguranças, todas as ansiedades, e mesmo assim puxaste-me para cima quando mais precisava e deste-me a força que precisava para estar aqui neste momento a escrever estas palavras, mais leve e orgulhosa do meu percurso do que estaria doutra maneira. Obrigada por tudo.

"What you're looking at matters, but not as much as how you're looking or who you're looking with."

— John Green, The Anthropocene Reviewed: Essays on a Human-Centered Planet

Abstract

Supramolecular chemistry has had a great relevance in the development of new assays in biological applications and in understanding the forces and mechanisms that drive the complex biochemical processes in cells. This field hinges on the exploration of the non-covalent interaction, prevalent in nature, and takes advantage of the reversibility of this type of linkage to create stimuli-responsive, self-assembled synthetic systems. This can take the form of binary discrete systems or reach high degrees of complexity with capacity to mimic some biological functions. These can be used in applications that benefit from the reversible nature of these systems, e.g. continuous monitoring of biological targets and stimuli-responsive drug-delivery. Macrocycles are a class of molecules that is often used in these applications due to their inherent affinity towards relevant biological targets and, in some cases, their ease of functionalization to design novel specificity.

This dissertation explores supramolecular systems based on macrocyclic receptors, going from simple host-guest interactions to biomimetic systems with actuators integrated into more complex structures. The first receptors explored were *p*-sulfonatocalix[4]arene (SC4) and Stoddart's Blue-Box (BB) in order to evaluate their binding properties to different peptide families. These were then applied in different sensing systems: monofunctionalized SC4 were applied in discrete and aggregation-based strategies for the ratiometric sensing of biologically relevant targets; BB and cucurbit[7]uril (CB7) were used in heteroternary host:dye:host complexes that successfully differentiate between different pharmacological agents known to accumulate in aqueous environments. Finally, different monofunctionalized SC4 were used in conjunction with synthetic and biological membranes: a light-activated counterion activator for the transmembranar transport of polycationic peptides was developed, based on a photoactive azobenzene moiety in its tail, which enabled the transport of this highly hydrophilic cargo across synthetic and cell membranes controlled with UV and green light; and a pyrene functionalized SC4 that allowed membrane anchored sensing and elucidation of the types of structures that these peptide-SC4 present in membrane.

Keywords: host-guest, biomimetic, sensing, transmembranar transport

Resumo

A química supramolecular tem mostrado grande relevância no desenvolvimento de ensaios para aplicações biológicas e na elucidação de diversos mecanismos por trás de processos bioquímicos em células. Esta área basea-se em explorar a interação não-covalente, prevalente na natureza, para criar sistemas sintéticos que apresentam a reversibilidade, resposta a estímulos e capacidade de auto-montagem que este tipo de ligação providencia. Estes sistemas podem ir desde sistemas binários discretos até a alta especificidade que é capaz de mimetizar algumas funções biológicas e vêm aplicação em áreas que benificiam desta reversibilidade, como a monitorização de sistemas biológicos e a entrega de fármacos controlada por diferentes estímulos. Macrociclos são uma classe de moléculas que é frequentemente usada para estas aplicações devido às suas afinidades inerentes para alvos biológicos e, em alguns casos, pela possibilidade de modular esta especificidade.

Esta dissertação explora sistemas supramoleculares baseados em receptores macrocíclicos, desde as mais simples interações hospedeiro-hóspede, até à sua integração sistemas auto-organizados complexos. Os primeiros recetores testados foram o *p*-sulfonatocalix[4]areno (SC4) e a "Blue-Box" de Stoddart (BB) de modo a avaliar a sua capacidade de complexação de diferentes famílias de péptidos. Estes foram posteriormente aplicados em diferentes sistemas de deteção: SC4 monofuncionalizados foram aplicados na deteção de alvos biorelevantes usando estratégias com sistemas discretos e baseados em agregação. A BB e o recetor cucurbit[7]urilo (CB7) foram usados em sistemas hóspede:indicador:hóspede para a diferenciação de diferentes tipos de fármacos encontrados como contaminantes em meios aquáticos. Finalmente, SC4 monofuncionalizados também foram aplicados em sistemas com membranas sintéticas e biológicas: um transportador controlado por luz para o transporte de péptidos policatiónicos, baseado em activação por contraião, permitiu a passagem destes analitos hidrofílicos através de membranas sintéticas e celulares, controlado por luz UV e luz verde; um SC4 funcionalizado com pireno para deteção de analitos com um recetor ancorado numa membrana e para elucidação do tipo de estrutura que estes complexos SC4-péptido apresentam em membrana.

Palavras-chave: hospedeiro-hóspede, biomimético, deteção, transporte transmembranar

Contents

List of Figures

List of Tables

Listings

Acronyms

α-CD	α-cyclodextrin *(p. 15)*
β-CD	β-cyclodextrin *(pp. 15, 29)*
γ-CD	γ-cyclodextrin *(pp. 15, 16)*
ACh	Acetylcholine *(p. 194)*
Arg	Arginine *(pp. 41, 44, 45, 195)*
ArgOMe	Arginine-o-methylesther *(pp. 85, 86, 89, 134, 234, 238, 239)*
Asp	Aspartate *(pp. 38, 165)*
ATP	adenosine triphosphate *(pp. 20, 102)*
BB	Stoddart's Blue-Box *(pp. 5, 10, 11, 36–40, 47, 55–67, 69, 111–113, 132, 133, 165–168, 199–202, 204, 206, 208–213, 279, 280, 283, 298)*
BDT	benzene-1,2-dithiol *(pp. 114, 115)*
C343	Coumarin 343 *(p. 112)*
CAC	Critical Aggregation Concentration *(pp. 52, 76–81, 83, 134, 219, 223)*
CB6	cucurbit[6]uril *(pp. 13–15, 33, 34)*
CB7	cucurbit[7]uril *(pp. 13–15, 17–19, 24, 31, 33, 34, 47, 55–66, 69–72, 113, 126–129, 132, 133, 196–218, 279, 280, 283, 298)*
CB8	cucurbit[8]uril *(pp. 13, 14, 17–19, 24)*
CBn	Cucurbit[n]urils *(pp. 13–15, 19, 36, 69)*
CF	5,6-carboxyfluorescein *(pp. 99–101, 106, 108, 129, 133, 247–255)*
CL	Chemiluminescence *(pp. 87, 88, 114, 135, 238)*
CMC	Critical Micelle Concentration *(pp. 78, 79, 83–85)*
COSY	Correlated Spectroscopy *(pp. 60, 61, 130, 201–208, 267, 269, 271–273)*
CT	charge-transfer *(pp. 10, 11, 38–40, 165, 166, 210)*
Cys	Cystamine *(pp. 70, 214–216)*
DABCO	1,4-Diazabicyclo[2.2.2]octane *(p. 88)*

DAPI	4′,6-diamidino-2-phenylindole *(pp. 91, 109, 136, 264–266)*
DBU	2,3,4,6,7,8,9,10-octahydropyrimido[1,2-a]azepine *(pp. 88, 238)*
DLS	Dynamic Light Scattering *(pp. 79, 97, 103, 118, 129)*
DM-DABCO	1,4-dimethyl-1,4-Diazabicyclo[2.2.2]octane *(pp. 50, 51, 55, 188–193, 195)*
DMEM	Dulbecco's Modified Eagle Medium *(pp. 135–137, 257)*
DMSO	dimethyl sulfoxide *(pp. 95, 122, 137)*
DNA	deoxyribonucleic acid *(pp. 3, 9, 12, 17, 24, 114)*
DPH	1,6-diphenylhexatriene *(pp. 87, 89, 91, 135, 239)*
DR	Ditopic Receptor *(pp. 68, 69, 72)*
EC_{50}	Effective Concentration at 50% of maximum effect *(pp. 29, 99–101, 106, 108, 133, 248, 251)*
EDC	1-Ethyl-3-(3-dimethylaminopropyl)carbodiimide *(p. 72)*
ESI-MS	Electrospray Ionization-Mass Spectrometry *(pp. 69–71, 126, 127, 214–216)*
Et-DASPI	*Trans*-4-[4-(diethylamino)styryl]-1-methylpyridinium iodide *(pp. 56–61, 63–66, 125, 126, 196–199, 205, 206, 209, 211)*
EYPC	Egg Yolk Phosphatidylcholine *(pp. 97, 99–101, 103–109, 129, 135, 247, 248, 251–253, 258–265)*
FBS	fetal bovine serum *(pp. 135, 136)*
FRET	Förster Ressonance Energy Transfer *(pp. 23, 113)*
GC5A	*p*-Guanidiniumcalix[5]arene *(p. 9)*
Glu	Glutamate *(pp. 38, 165)*
Gly	Glycine *(pp. 44, 182)*
GUV	Giant Unilamellar Vesicles *(pp. 106–110, 115, 129, 135, 136, 264, 265)*
HMBC	Heteronuclear Multiple Bond Correlation *(pp. 268, 270)*
HOMO	Highest Occupied Molecular Orbital *(pp. 21, 40)*
HR-MS	High Resolution-Mass Spectrometry *(pp. 76, 119, 121, 122, 124, 129)*
HSQC	Heteronuclear Single Quantum Correlation *(pp. 44, 50, 53, 130, 171, 172, 174, 175, 177, 178, 180, 192, 193, 269, 271)*
IC_{50}	half maximal inhibitory concentration *(p. 101)*
IDA	Indicator Displacement Assay *(pp. 21–24, 28, 29, 36, 41–43, 45, 47–49, 54, 55, 62, 65, 76, 79, 98, 103–106, 111, 112, 170, 183, 190, 220, 262, 263, 277)*
ITC	Isothermal Titration Calorimetry *(pp. 38–41, 43, 45, 46, 54, 58, 59, 64, 79, 118, 132, 167, 168, 184, 185, 195, 198, 199)*

Jd-DASPI *Trans*-4-[2-(2,3,6,7-Tetrahydro-1H,5H-benzo[ij]quinolizin-9-yl)-ethenyl]-1-methylpyridinium iodide *(pp. 56, 58, 59, 61–67, 125, 126, 196–200, 202, 207–209, 212, 213)*

LCG Lucigenin *(pp. 42, 43, 45, 47–50, 52, 54, 76, 77, 79, 80, 96–98, 104–106, 113, 114, 170, 183, 189, 190, 220, 224, 225, 244–246, 259, 262, 263, 275)*

LUMO Lowest Unoccupied Molecular Orbital *(p. 40)*

LUV Large Unilamellar Vesicles *(pp. 97, 99–101, 103–108, 129, 131, 133, 247, 248, 251–255, 258–263)*

Lys Lysine *(p. 41)*

mCPBA *meta*-chloroperoxybenzoic acid *(pp. 87, 89–91, 135, 239)*

Me-DASPI *Trans*-4-[4-(dimethylamino)styryl]-1-methylpyridinium iodide *(pp. 56, 58, 59, 63–66, 125, 196–201, 203, 204, 210, 212, 213)*

MTT 3-(4,5-Dimethylthiazol-2-yl)-2,5-Diphenyltetrazolium Bromide *(pp. 101, 257)*

Nan Nandrolone *(pp. 62–64)*

NHS n-hydroxysuccinimide *(p. 34)*

NIR near-infrared *(pp. 18, 19)*

NMR Nuclear Magnetic Resonance *(pp. 14, 40–43, 45, 46, 49, 51, 53, 59–61, 69, 71, 72, 76, 79, 95, 97, 111, 117, 119–122, 124–126, 128–131, 169, 171–181, 183, 192–194, 201–208, 217, 218, 241, 267–275)*

NOE Nuclear Overhauser Effect *(p. 44)*

Npx Naproxen *(pp. 62–64)*

O-DCB o-dichlorobenzene *(pp. 84, 85, 87, 88, 91, 129, 130, 134, 135, 231, 234–239)*

O/W Oil in Water *(pp. 83–87, 90, 114, 129, 134, 231, 234–238)*

PB phosphate buffer *(pp. 76, 86, 98, 105–109, 129, 130, 223, 235, 262–265)*

PBS phosphate buffer saline *(pp. 29, 135, 136)*

PCA Principal Component Analysis *(pp. 24, 81, 82, 113, 133, 230, 283, 308)*

PET Photoinduced Electron Transfer *(pp. 21, 36, 48, 49, 52, 55, 113)*

PFAS perfluorinated alkyl substances *(pp. 8, 12, 24)*

Phe Phenylalanine *(pp. 10, 14, 38, 40, 112, 165, 167)*

PPh3 Triphenylphosphine *(p. 88)*

PSS Photostationary State *(pp. 95, 97, 241)*

RNA ribonucleic acid *(pp. 26, 33)*

ROESY Rotating Frame Nuclear Overhauser Effect Spectroscopy *(pp. 44, 60, 61, 130, 172, 173, 175, 176, 178, 179, 181, 201–208, 268, 270, 272–274)*

SC4	*p*-Sulfonatocalix[4]arene *(pp. 6–8, 24, 31, 33, 35–37, 41–49, 51, 52, 69–73, 75–81, 85, 93, 95, 97, 98, 111–115, 118–120, 130, 170, 172, 173, 175–181, 183–185, 194, 231–234, 245)*
SC6	*p*-Sulfonatocalix[6]arene *(pp. 24, 33, 35, 231–234)*
SC8	*p*-Sulfonatocalix[8]arene *(pp. 24, 33, 35, 84, 231–234)*
SuFEx	Sulfur(VI) Fluoride Exchange *(pp. 114, 115)*
TAMRA-R$_8$	carboxytetramethylrhodamine-labeled R$_8$ peptide *(pp. 101, 102, 135, 136, 256, 257)*
TBAF	tetrabutylammonium fluoride *(pp. 87, 88)*
TCPO	bis(2,4,6-trichlorophenyl)oxalate *(pp. 87, 89, 134, 238)*
TE	Transport Efficiency *(pp. 99, 100)*
TES	triethylsilane *(pp. 87–89, 238)*
TFPN	3,4,5,6-tetrafluorophthalonitrile *(p. 115)*
TOCSY	Total Correlation Spectroscopy *(pp. 44, 130, 171, 173, 174, 176, 177, 179, 180)*
Trp	Tryptophan *(pp. 10, 37–41, 210)*
TS	transition states *(pp. 32, 34)*
Tyr	Tyrosine *(pp. 10, 38, 40, 165, 167)*
UV-vis	UV-Visible *(pp. 38–40, 57–60, 63–66, 95, 97, 117, 133, 165, 166, 199, 200, 209, 210, 212, 213, 241, 283)*

Symbols

ε molar extinction coefficient *(p. 132)*

γ surface tension *(pp. 84–86)*

λ wavelength *(pp. 29, 38, 39, 59, 76, 95, 107, 109, 117, 165, 166, 196, 230, 238, 264–266)*

Φ quantum yield *(p. 95)*

δ chemical shift *(pp. 42, 182)*

1

Introduction

Supramolecular chemistry is the field of chemistry that goes "beyond molecular chemistry" and studies the interactions molecules can establish and the associations and constructs that can come from these interactions.[2]

Although the coining of the term "supramolecular chemistry" is attributed to 1987 Nobel Prize winner Jean-Marie Lehn and to the advances brought on by his and fellow laureates Donald J. Cram and Charles J. Pedersen's work, it could be said that the fundaments for this field go back much further in time, to the discovery of intermolecular forces.[2–5] These are the driving forces for the formation of different non-covalent bonds and understanding them is essential for studying how molecules interact and assemble, allowing for successful programming of their function from the first steps of molecular design. Supramolecular chemistry often draws inspiration from the interactions found in nature, which enable interconnectivity and cooperativity between molecules in biological systems. These novel synthetic systems present ample application in the biomedical field, as is the case with pharmacological applications, seeing as their biomimetic properties can be used in aiding their interaction with biological systems, increasing the compatibility and efficiency of the desired effect. Biological inspiration also has a significant role in the creation of novel responsive materials and introducing alternative strategies in other adjacent fields like supramolecular electronics.[6–8]

While nature has had billions of years for the optimization of these highly-complex supramolecular assemblies and is constantly evolving, chemists have had a relatively short window of time to try to achieve a fraction of this functionality. Nonetheless, advances in the development of responsive systems and materials have already greatly contributed to our quality of life in this short interval. In the health sciences, it enabled the development of sensors for different disease biomarkers and contaminants, the development of more stable and biocompatible vaccines, responsive materials for medical use, etc.[9–15]

Despite these remarkable advances, challenges remain in the development of more efficient systems - design of receptors for different guests is essential for targeted action, not only in sensing, but also in the transport or pharmacological activity of drugs and therapeutic agents. While arrays of different components can work in tandem for the differentiation of biomarkers, distinction between similar analytes remains difficult. This is particularly true for the development of orthogonal receptors for peptides and proteins, which, although made out of a limited number of monomers, exceed the several thousands of variations across the human proteome.[16,17]

Several macrocyclic receptors have shown high binding affinities and high selectivity for different families of guests, including peptides and proteins, and their modular use aids further distinction.[9,18–20] This thesis explores the design of novel supramolecular systems based on these preexisting receptors, such as calixarenes and cucurbiturils. It addresses both discrete assemblies (of two or more molecules) and more complex structures that incorporate multiple interacting elements, aiming to create platforms for fundamental and applied research. The main two objectives are the deeper understanding of interactions between several different macrocyclic molecules and respective guests, and their use in carefully designed selective sensing and transport systems for peptides and other biorelevant targets. These include applications in distinction between different length polycationic peptides, through several sensing mechanisms, as well as the photocontrolled transport of this same hydrophilic cargo across synthetic and cellular membranes.

1.1 The Supermolecule: molecular recognition in host:guest chemistry

Supramolecular chemistry focuses on the interaction between different molecules and the responsive dynamic systems that can be achieved by taking advantage of the non-covalent bonds that these building blocks can establish. These assemblies can go from a few molecules interacting, forming discrete complexes, as will be explored in this Section - the supermolecules - to polymolecular associations that can self-assemble spontaneously or under different stimuli, to form microscopic structures or larger materials, found in Section 1.2 - the supramolecular assemblies (Figure 1.1).[6]

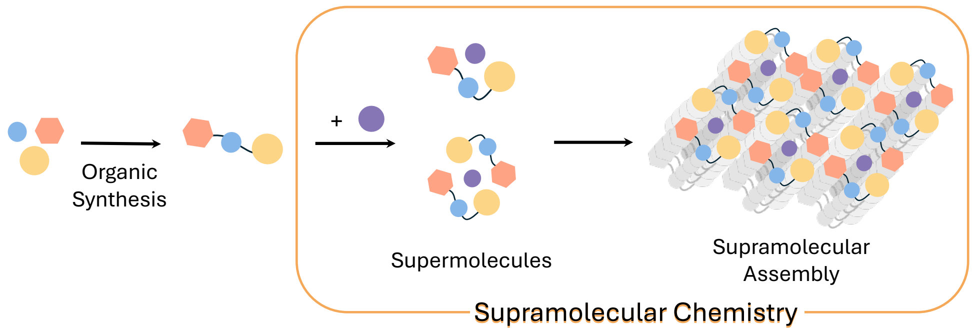

Figure 1.1: Organic synthesis takes several building blocks and uses the covalent linkage to produce new molecules, while supramolecular chemistry takes different molecules and uses the non-covalent bond for the formation of discrete systems - supramolecules - or to further the self-assembly process and form the larger supramolecular assemblies. Adapted from Lehn (1995).[6]

1.1.1 Non-Covalent Interactions

The driving force behind any of these molecular assemblies, independent of complexity, is the non-covalent bond. These interactions are driven by intermolecular forces originating from the physical properties of a given molecule and the solvent effects which it is submitted to, that allow the establishment of weak reversible bonds between molecules.[21] The forces behind intermolecular interactions that can be seen in nature, in enzyme-substrate or receptor-neurotransmitter interactions, in the formation of the phospholipidic membrane, are the same that allow the interactions between any molecules: hydrogen bonds, ionic interactions, London dispersion forces, van der Waals interactions, π-stacking, cation-π interactions, to name a few (see Figure 1.2).[21,22]

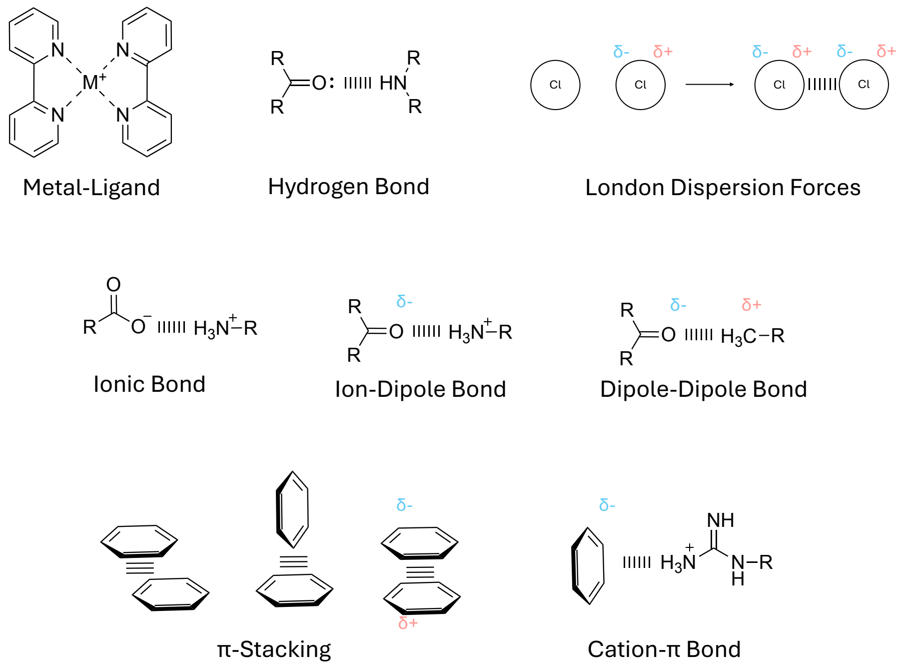

Figure 1.2: Schematization of main non-covalent interactions that can occur between molecules: metal-ligand interactions, hydrogen bonds, the London dispersion forces, ionic bond, ion-dipole bond, dipole-dipole bond, π-stacking and cation-π bond.

When compared to covalent bonds, the non-covalent counterpart are remarkably lower in energy. The hydrogen bond has a typical energy of 20 kJ/mol while the C-H covalent bond averages at $\approx$ 430 kJ/mol. Although weaker than covalent interactions, these can achieve high energies for a given intermolecular interface through a summation effect, where several interactions and effects contribute in a cooperative manner for the binding.[21–23] While this additive effect of these interactions allows the formation of strong associations, these remain weak enough to provide the flexibility and reversibility necessary for responsive systems. In biological systems, metabolic regulation, deoxyribonucleic acid (DNA) accessability and consequent gene expression, protein folding, among many other processes are dependent on both the formation and breaking of non-covalent bonds for their correct operation. It also allows for molecules to be used several times for the same function, minimizing energetic expenses of the cell on synthesis of new molecules.[24,25] Moreover, two molecules that present complementary sites, as well as compatible size and shape so as to allow their optimal approximation, should also present high selectivity when compared to their binding to other molecules. The complementarity and cooperativity effects work together to allow highly-specific interactions to occur, e.g. antibody-antigen recognition.[2,22,24,25]

1.1.2 Host:Guest Chemistry

The weaker nature of non-covalent bonds make these more susceptible to the entropic penalty of structural reorganization that might be needed for the binding process, as well as the loss of degrees of freedom of both molecules after binding. A way to reduce this penalty is the use of cyclic synthetic receptors that present a pre-organized binding site that does not require additional rearranging.[3,6,22]

The macrocyclic species can act as a receptor (or host) for specific molecules with complementary size and arrangement of binding moieties (the guests). Host-guest chemistry is the field of study that focuses on these interactions and the development of innovative macrocyclic receptors to uncover novel selectivities and functionality, taking advantage of the high binding affinities that come with having these preorganized pockets.[3,26]

In polar solvents, particularly in water due to its ability to act both as hydrogen bond donor and acceptor, solvation of the host and guest is often prevalent, reducing considerably the binding strength of the host-guest complexes. Nonetheless, to achieve successful biomimetic systems, the synthetic hosts need to be soluble in this medium and be able to efficiently interact with their guests in water as well as having binding energies high enough to overcome the penalty of desolvation of both molecules.[27,28]

One way to achieve this is using the classical hydrophobic effect - hydrophobic molecules are not able to establish interactions with water molecules, and there is a need to leave a cavity within water structure for these to localize. The formation of one cavity for several hydrophobic solutes is more advantageous entropically than leaving several cavities in the solvent interaction network, leading hydrophobic molecules to associate when in aqueous solution.[28,29] Macrocyclic receptors are able to achieve binding in water by presenting relatively hydrophobic cavities with polar or charged groups at their portals, making use of the hydrophobic effect and adding the hydrosoluble moieties for both additional binding sites for the guests and for macrocycle solubility. This structure enables these water-soluble receptors to reach affinity constant values in the realm of picomolar or below, comparable to the biotin-avidin affinity (10^{13} - 10^{15} M^{-1}).[27,30–32]

Some examples of water-soluble macrocyclic receptors are the cyclophanes - calixarenes, pillararenes, cavitands -, cucurbiturils and cyclodextrins (Figure 1.3).[32] The next sections go into the properties of some of these hosts, with a greater focus on biological target recognition and for the receptors used during the course of this thesis. More complex applications and structures achieved in recent years will be explored in Sections 1.2 and

1.3.

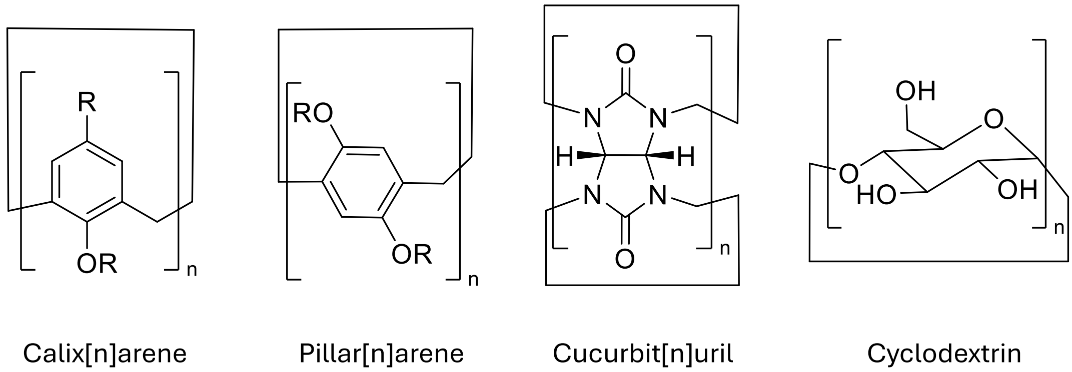

Figure 1.3: General chemical structure of some examples of water-soluble macrocyclic hosts: calix[n]arene, pillar[n]arene, cucurbit[n]uril and cyclodextrin.

1.1.3 Cyclophanes

Cyclophanes are macrocycles composed of aromatic units connected together by bridge moieties. These can take many shapes and, so, provide different properties in terms of size, flexibility, functionality and guest recognition. Furthermore, these often present portals that are easy to decorate with different substituents to fit the needed specificity for the target guests in a multivalent manner. Their highly aromatic cavities present both a hydrophobic pocket to drive binding through hydrophobic effect but also present distinct electronic distributions that can provide adequate binding sites for both electron-rich and electron-deficient guests, depending on the aromatic ring substituents added.[27,32–37]

The most prominent examples of cyclophane hosts are calixarenes, cavitands, pillararenes and the particular case of cyclobis(paraquat-p-phenylene), more commonly known as Stoddart's Blue-Box (BB).

1.1.3.1 Calixarenes

Calixarenes are cyclophanes bridged by methylene groups in the *meta* position, that present a calix-like shape, with distinct lower and upper-rims, that result from the condensation of phenols with formaldehyde.[38] While the initially synthesized calixarenes were not water soluble, *para*-substituted calixarenes with charged and hydrophilic moieties were quickly obtained thereafter.[39,40]

While these can be synthesized with 4 to 8 or more units (n=4-8, Figure 1.3), the smaller, less flexible calix[4]arene and calix[5]arene are the ones that provide higher affinity and specificity towards different guests.[41] Larger calixarenes, due to their flexibility, resemble more closely their acyclic counterparts. Due to the flatter conformations these adopt in aqueous solutions, these calixarenes lack some of the advantages of a preorganized binding cavity that the smaller hosts provide. Nonetheless, the increased flexibility allows them to have conformational adaptation, or "induced fit", necessary for binding to larger or multiple guests and see application due to this differentiating factor.[35,42]

The smaller calixarenes, composed of 4 units, if functionalized with small substituents, can adopt four distinct conformations: cone, partial cone and 1,2- and 1,3-alternate conformations (Figure 1.4).[41,42] Cone conformation is often the more stable of the four, due to stabilization by hydrogen bonding between the lower-rim hydroxyl groups, although varying the substitutions on both rims can lead to different preferential conformations. Cone conformation is usually the ideal one for obtaining higher affinity and specificity of the binding process, due to overall binding site orientation. Substitution with different functional groups in both upper and lower rim can help lock the calixarene into this conformation, reducing the energetic loss if conformational rearrangement is needed.[41,43] Nonetheless, the remaining conformations also present characteristic selectivity and affinity for specific guests.[44]

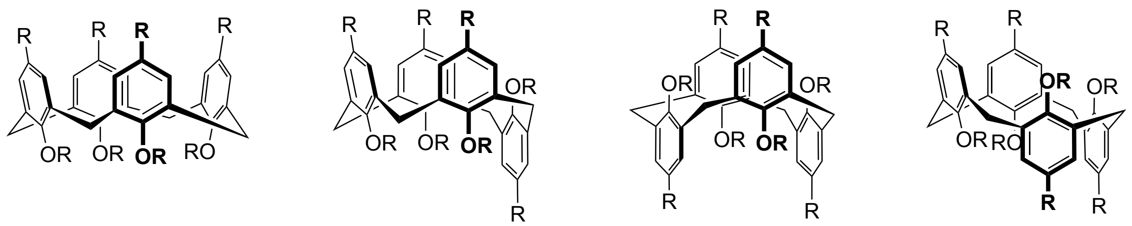

Figure 1.4: Calix[4]arene structure and possible conformations it can assume in aqueous solution.

Water-soluble calixarenes can bind a variety of molecules from smaller ions like alkali-metal cations, to larger biorelevant molecules like peptides and proteins. The substituents added for increased solubility also uncover different binding specificities, with the use of positively and negatively charged or neutral hydrophilic groups.

In the family of negatively charged calixarenes, *p*-Sulfonatocalix[4]arene (SC4) is of particular interest due to its high affinity towards several cations, including environmental contaminants like heavy metals and herbicides, neurotransmitters, biogenic amines, cationic amino acid residues and several dyes, with concomitant variation of the optical properties of the latter.[44–51] Its portal remains negatively charged at physiological and acidic pH, due to the low pK_a of the sulfonate groups, making it a versatile platform for different applications (pK_a of benzenesulfonic acids usually falls below 0, while p-hydroxybenzoic acid has a pK_a of 4.6).[52,53] This moiety added to the electron-rich aromatic panels allow the establishment of several ionic and cation-π interactions, as well as taking advantage of the hydrophobic effect for increased affinity for cationic guests with additional hydrophobic regions.[42,54]

SC4 binds alkali-metal and metal cations with relatively low affinities in the case of mono-cationic species and reaches mM affinities for di-cationic species (Figure 1.5 A).[45] Affinity and specificity for some guests can be increased by functionalization of SC4 with moieties like crown-ethers. Locking of the host in 1,3-alternate conformation, with addition of crown-6-ether substitutions, has shown to increase selectivity for ceasium (Figure 1.5 B).[44]

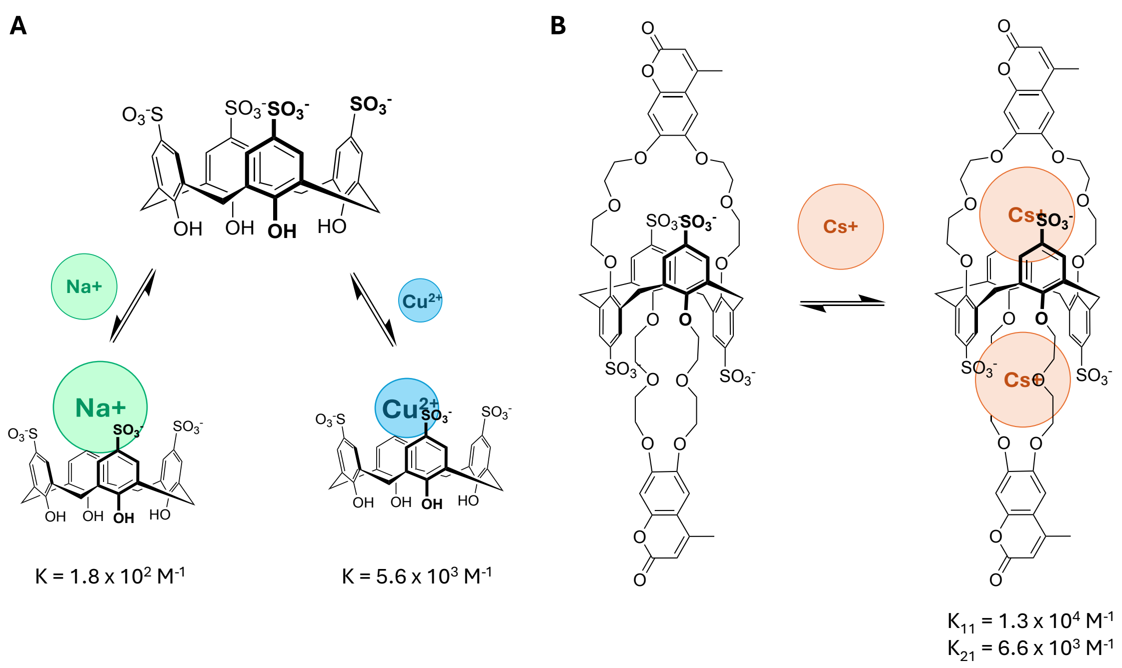

Figure 1.5: **A.** SC4 binding to mono-cation Na^+ and di-cation Cu^{2+} and respective affinity constants and **B.** SC4-bis(crown-6-ether), synthesized by Valeur and coworkers, binding to Cs^+ and respective affinities for binding of the first and second cesium cations.[44,45] Ionic radius of cations not to scale.

SC4 ability to bind biologically relevant molecules like acetylcholine, choline, as well as the basic amino acids arginine and lysine was unveiled early on.[46,47] Further investigation showed a particular specificity for neurotransmitters and methylated amino acid counterparts, especially for lysine. This difference is caused both by the higher energy necessary for desolvation of the unmethylated amino acids when compared to the modified ones, as well as by the deeper insertion of methylated side-chains in the cavity and additional contribution of CH-π interactions between methyl and aromatic moieties of the host for stabilization of the complex (Figure 1.6 A).[47,55–58] Preferential binding to unmethylated arginine when compared to lysine is most likely due to the ability of guanidinium moiety to establish both cation-π and π-π interactions with SC4 aromatic units (Figure 1.6 B).[47,55]

Furthermore, the binding to these targets has a multivalent nature that is clearly unveiled when investigating the affinity of SC4 towards cationic peptides. The affinity towards both di and tripeptides with lysine and arginine residues leads to one and two orders of magnitude of increase, respectively, when compared to the amino acid.[59] Larger polyarginines and polylysines reach affinities in the nM range or lower for this host, although detection methods for differently charged peptides remain limited.[60,61]

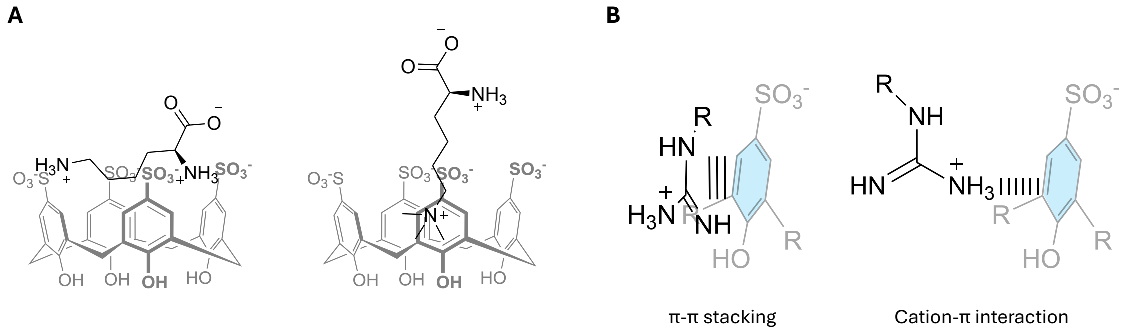

Figure 1.6: **A.** Proposed binding for lysine and trimethylated-lysine to SC4. **B.** Interactions that the guanidinium moiety can make with the aromatic rings of SC4.

This can be further extended to protein recognition, where binding can be both topological, at cationic regions of proteins, in specific residues or even in clefts or pockets in proteins, where additional hydrogen bonds and hydrophobic effect aid in the stabilization of such complexes (crystallographic structure of SC4 binding to cytochrome *c* shown in Figure 1.7 A). The use of calixarenes with larger molecules is possible and has a role in protein modulation, camouflage, dimerization and sensing.[35,62,63] A deeper look into the application of these molecules with proteins can be found in Section 1.3.3.

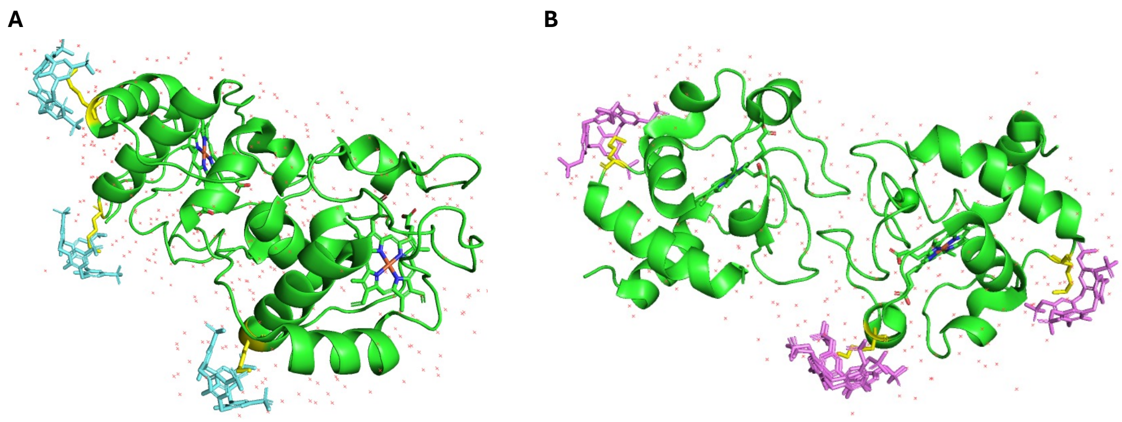

Figure 1.7: Crystalographic structures of cytochrome *c* complex with **A.** *p*-sulfonatocalix[4]arene, SC4, shown in blue, (PDB: 3TYI) and **B.** methylphosphonato-calix[4]arene, shown in pink (PDB: 5NCV), with the residue each host is binding shown in yellow.[35]

Other negatively charged calixarenes include those with phosphonate substituents in the upper rim, which can achieve effective recognition of proteins with cationic regions both for sensing and co-crystallization applications (Figure 1.7 B).[35,64,65]

Calixarenes modified with cationic groups in the same position also represent an important group of hosts for the detection of various relavant molecules, from phosphates and polyphospates to environmental contaminants like perfluorinated alkyl substances

(PFAS).[66–69] The most studied of the cationic calixarenes are the ones presenting ammonium, trimethylammonium and guanidinium substituents (Figure 1.8). *p*-Guanidinium-calix[5]arene (GC5A) has shown particular recognition properties in water, with its ability to selectively bind to important biomarkers (e.g. lysophosphatidic acid, adenosine triphosphate, phenylpyruvic acid) with almost nM affinities (Figure 1.8).[67,68]

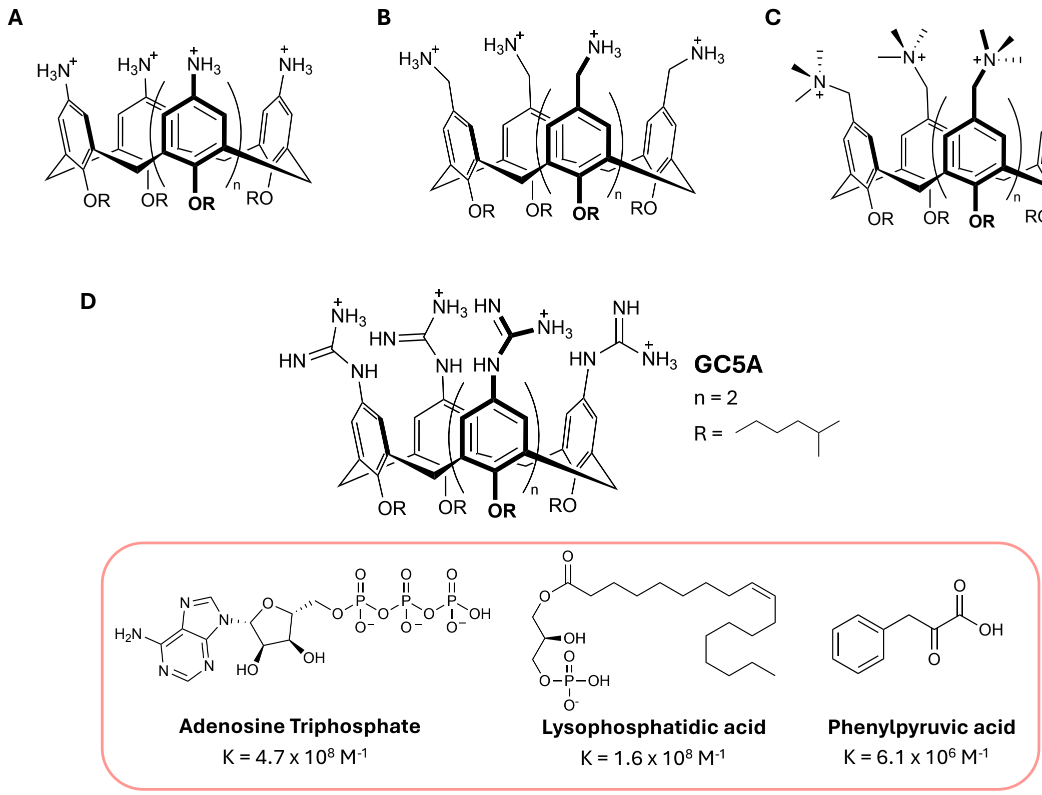

Figure 1.8: Structures of the most relevant cationic calixarenes substituted in the upper rim with **A.** and **B.** with ammonium, **C.** trimethylammonium and **D.** guanidinium groups, with the example of GC5A and respective guests with the corresponding 1 to 1 binding affinities below.[67,68]

Substitution of calixarenes with zwitterionic and neutral hydrophilic moieties can be effective as well. Some examples include the work by Casnati, Ungaro and coworkers, where they modified calixarenes with zwitterionic amino acid residues or dendrimeric hydrophilic structures, uncovering new specificities and properties. Argininocalix[4]arenes, similarly to *p*-guanidiniumcalixarenes, bind DNA and can lead to its condensation for facilitation of its transport across phospholipidic membranes, while functionalization with zwitterionic amino acids improves the recognition of Gram-negative bacteria.[70,71]

Many complex structures can be obtained using calixarene as a platform and it would take a comprehensive review to cover the extent of water-soluble hosts that can be obtained. A final and recent example of calixarene modification for addition of both functionality and more efficient binding to more hydrophobic guests is the azocalixarenes developed by Guo's Lab.[72] This work is based on previously obtained azocalixarenes, however it presents charged groups that can modulate its affinity. Sulfonate substituted azocalixarenes reach μM affinity towards drugs like doxorubicin while the azocalixarene with trimethylammonium groups can reach nM affinities for hydrocortisone.[73–75]

1.1.3.2 Stoddart's Blue-Box

Stoddart's Blue-Box (BB), or cyclobis(paraquat-p-phenylene), is a cyclophane composed of two paraquat units, bound together in a face-to-face structure by two phenylene units, making it, in contrast with the other examples presented herein, a highly electron-deficient but shallow cavity, optimal for binding of small electronegative guests (Figure 1.9 A). The synthesis of BB as a PF_6^- salt was first reported in 1988 by Williams *et al.* for application as a receptor for rotaxanes and catenanes.[34] This receptor was shown to bind electron-rich aromatic molecules, as its design first intended, with concurrent appearance of a red-shifted absorption band, concordant with the formation of stabilized charge-transfer (CT) states upon complexation and overlap of the molecular orbitals of both species (Figure 1.9 B).

Furthermore, the water-soluble tetrachloride salt species was also reported to bind to several biomolecules, including the aromatic amino acids Tryptophan (Trp), Phenylalanine (Phe) and Tyrosine (Tyr) in aqueous solutions, although its specificity showed to be limited, showing mM affinities towards tryptophan and neurotransmitters like serotonin and norepinephrine.[76,77] Its affinity in water toward naphthalene units, however, is able to reach the μM range as shown by the water-soluble naphthalene guest presented in Figure 1.9 C.[78]

The affinity to the latter moiety and similar electron donors has become a way to control the assembly of this molecule in more complex structures. Its affinity can be modulated by reduction of the BB to its diradicalar species, which presents distinct binding affinity towards these guests, or by displacement with other higher affinity receptors or addition of other stimuli-responsive moieties in the guest.[33,79] This control is particularly relevant for its application in rotaxanes, pseudorotaxanes and molecularly interlocked molecules, that hinge on this controlled variation of host location for the oriented movement of its molecular components.[33,78]

1.1.3.3 Pillararenes and cavitands

Other two common types of cyclophanes used for molecular recognition in biological and biomimetic applications are the pillararenes and cavitands. Both present similarities to calixarenes, with methylene bridges connecting the aromatic units. However, pillararenes are synthesized by connecting its 1,4-dimethoxybenzene units by methylene bridges in positions 2 and 5, originating barrel-like receptors with identical upper and lower rim.[80,81] Cavitands on the other hand are resorcinarene-based macrocycles and present both methylene bridges in distinct positions in relation to the hydroxyl groups but can also present additional linkages in the phenol moieties, often with added aromatic panels

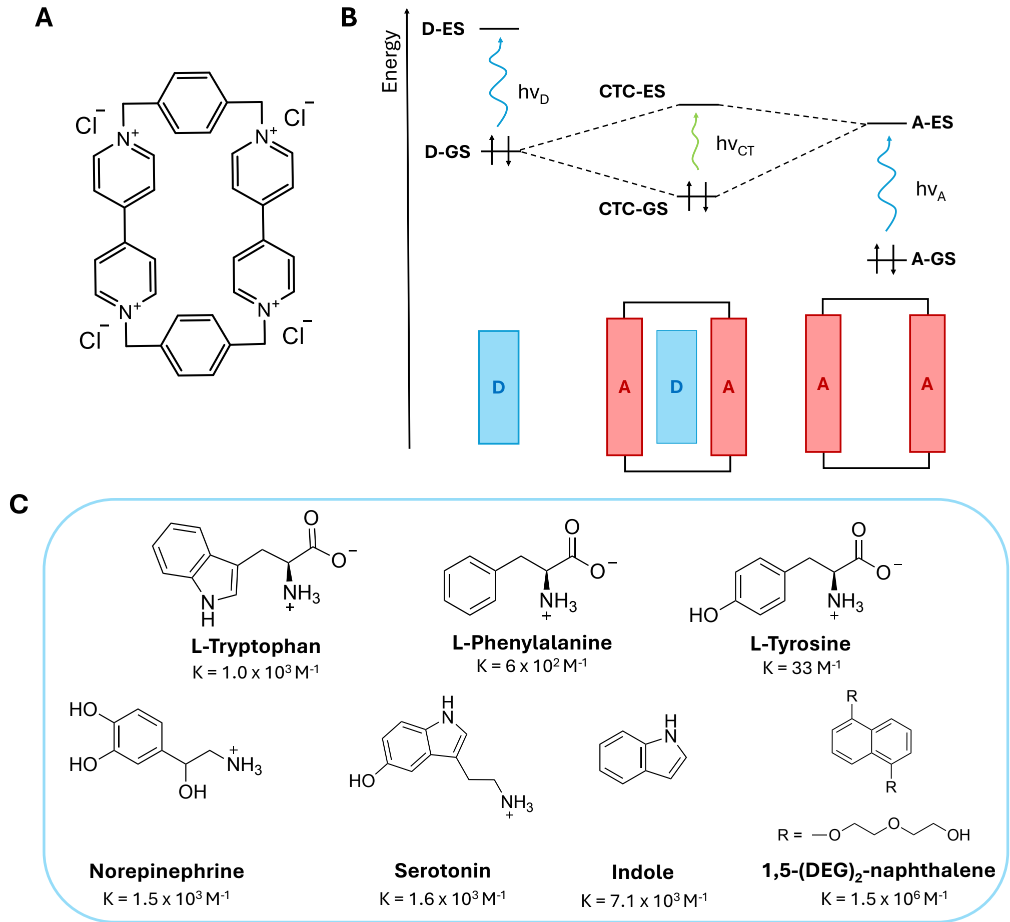

Figure 1.9: **A.** Chemical structure of the BB receptor. **B.** Diagram of the ground (GS) and excited states (ES) of the different species envolved in the charge-transfer phenomenon. The blue arrows represent the normal absorption for the receptor BB, represented as A, and the electron donor guest, represented as D, and the green arrow the red-shifted absorbance associated with the CT complex (CTC) and respective states that are created by interaction of orbitals between donor and acceptor. **C.** Biological relevant guests and synthetic naphthalene guest of the receptor BB and respective affinity constants of the 1 to 1 complexes.

in the upper rim, creating a more elongated cavity (deep cavitands). Neither are capable of inversion like calixarenes, although they can present other structural dynamics of note (Figure 1.10).[82–84]

Pillararenes, being a more recently obtained macrocycle, have been explored with different functional groups and in most cases were found to present similar guests to those of calixarenes, like choline, acetylcholine and basic amino acids for anionic variants and phosphates and sulphonates for cationic ones.[85–87]

Cavitands on the other hand, have been a known platform in supramolecular chemistry for longer, leading to a great variety in structure and properties. These go from shallower cavitands, as is the case of the tetraphosphonate cavitands which present high selectivity towards methylated amino acids, to deep cavitands, that present an extended hydrophobic binding cavity, with several sites for hydrogen bonding. These are able to bind a great variety of guests due to the great diversity of sites of interaction and type of bonds that they can establish, e.g. hydrogen bonds, hydrophobic effect, π-π and cation-π interactions.[83,84,88,89] Additional functional groups can be added both in the upper or lower rim of these hosts. Substitutions in the upper rim can include charged moieties, like phosphonate, carboxylate and ammonium substituents, which provide ionic interactions towards cavitand's guests, or addition of hydrogen bond donors/acceptors, like amide substituents.[30,88] Substitution in the lower rim can also provide useful functionality including increased amphiphilicity or even recognition sites for other guests, being even able to act in an allosteric manner and control host conformation (Figure 1.10 B).[90] All of these different functionalities make these hosts capable of binding different drugs and pharmacological agents, pollutants like PFAS and other fluorinated organic molecules, biomolecules from neurotransmitters and other small molecules to proteins and DNA.[18,90–94]

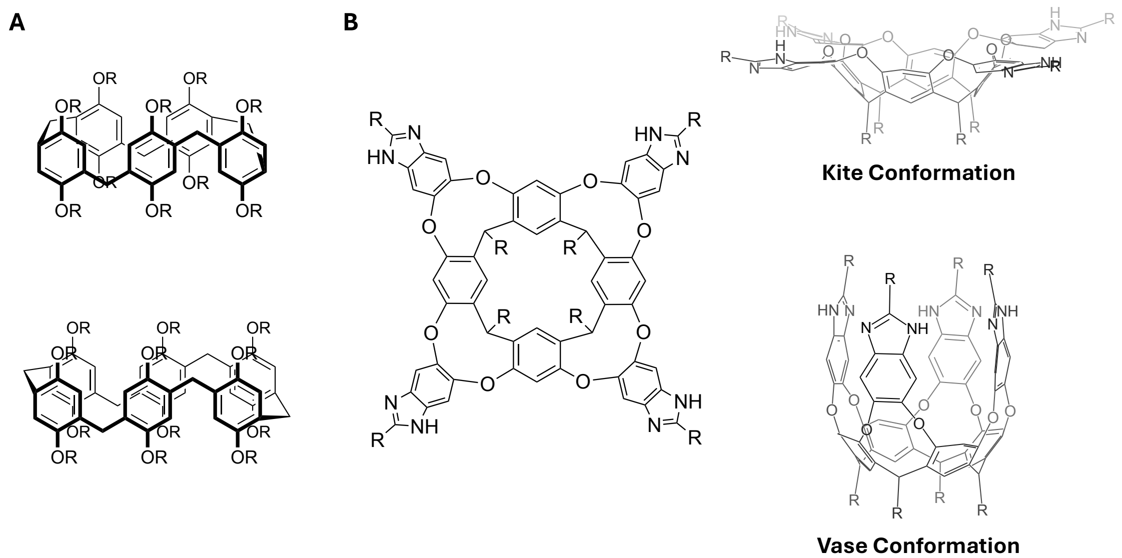

Figure 1.10: Structures of macrocycles **A.** pillararene, with 5 and 6 units, and **B.** cavitands, with the example of deep cavitands and its two distinct conformations.[83,84]

1.1.4 Cucurbiturils

Cucurbit[n]urils (CBn) are rigid macrocycles composed of glycouril units, that are unsoluble in organic solvents and present relatively low solubility in water. CBn are named after their shape, due to their close similarity to pumpkins, which belong to the *Cucurbitaceae* family (Figure 1.11 A). This family of molecules presents remarkable properties without further modification and have been extensively studied and employed in a myriad of applications. The synthesis of the first CBn was done in 1905 by Behrend *et al.* by condensation of glycouril with formaldehyde in acidic conditions, although it was only identified as a macrocyclic molecule of 6 units, cucurbit[6]uril (CB6), much later.[95,96]

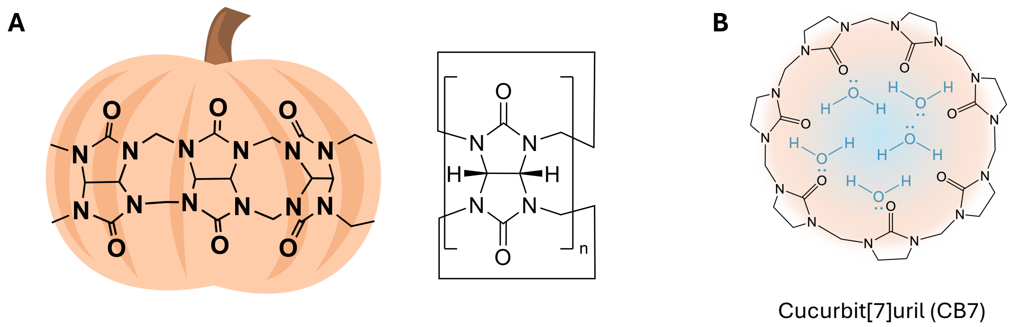

Figure 1.11: **A.** Shape comparison of CBn with pumpkins and general structure of these hosts and **B.** top-down view of the host with 7 units, CB7, with "high energy" water molecules in its cavity.

The size, rigidity and hydrophobic nature of the pocket, with its electronegative portals are what provides cucurbiturils their particular characteristics. In aqueous medium, several water molecules can reside inside the CBn pocket, with the total number increasing with the size of the cavity (Figure 1.11 B). These, however, do not present enough space to efficiently establish the hydrogen bonds that are prevalent in bulk solvent, neither are they able to establish these bonds with the hydrophobic cavity, which is enthalpically unfavourable.[28,29] These, often called "high-energy", water molecules create an additional enthalpic driving force that, in addition to the ion-dipole interactions that these hosts can establish, are responsible for some of the binding events reaching ΔH values close to -100 kJ/mol and affinities below the nM range.[28,97]

Given these characteristics, these hosts form high affinity complexes with organic molecules presenting ammonium groups, in particular diammonium organic molecules that present size and volume compatibility with the CBn cavity, maximizing the previously mentioned effects. The enthalpic effect of the "high-energy" water molecules is maximized for the hosts of 7 and 8 units, cucurbit[7]uril (CB7) and cucurbit[8]uril (CB8). The former can bind its guests with affinities up to 10^{17} M^{-1}, while the later reach 10^{12} M^{-1} affinities, presenting comparable or higher affinities than the ones observed in biological systems.[97–100]

In terms of their biological targets, these hosts present naturally high affinities towards hydrophobic amino acids, in particular phenylalanine (Phe) when this residue is located near or in the N-terminal, due to the added ammonium moiety. CB7 is a particularly good match for this amino acid residue, presenting μM affinities towards small peptides like Phe-Gly and Phe-Gly-Gly as well as for the N-terminal of Insulin, while CB8, with its larger cavity, can bind two peptides with N-terminal Phe. The larger cavity of CB8 also provides it with the ability of binding small peptide sequences in 1 to 1 binding ratios, in particular ones with a N-terminal methionine residue (Figure 1.12), with inclusion of two residues inside its cavity and a third one interacting in the outside and portal regions of this host.[101]

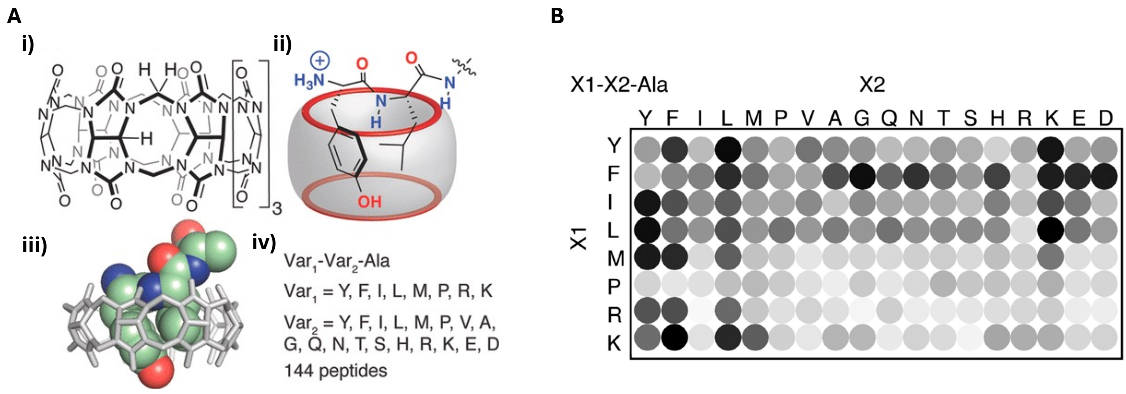

Figure 1.12: **A.** i) Chemical structure of cucurbit[8]uril (CB8). ii) Schematization of the complex of CB8 and the peptide YLA and iii) respective semiempirical model of the CB8-YLA complex based on 2D-Nuclear Magnetic Resonance (NMR) data. iv) Peptide library screened in the study by Hirani *et al.*. **B.** Fluorescence assay for the binding of CB8 to the library of 144 peptides of sequence Var1-Var2-Ala. The density of each circle correlates to the average degree of fluorescence enhancement observed upon adding 200 μM peptide to 40 μM CB8 complex with the dye Tetramethyl Benzobis(imidazolium) (MBBI) at room temperature in 10 mM sodium phosphate, pH 7.0. Reproduced with permission from J. Am. Chem. Soc. 2018, 140, 38, 12263–12269. Copyright 2018 American Chemical Society.[101]

Other notable selectivities of the unmodified CBn towards biological relevant guests include CB6 affinity towards biogenic amines, in particular spermine (10^{10} M^{-1}) and spermidine (10^8 M^{-1}), and CB7 and CB8 presenting selective binding towards abuse drugs and pharmacological agents, as is the case of steroidal drugs and hormones, with the smaller host presenting selectivity towards nandrolone (10^7 M^{-1}) and the larger one for vecuronium, pancoronium and testosterone ($> 10^7$ M^{-1}).[102–105] The smaller cucurbituril, CB5, presents a small binding pocket and is only capable of complexing inorganic cations at its carbonyl portals, reaching μM affinities towards Ba^{2+} and decreasing sharply for larger cations.[106]

Furthermore, the low toxicity of CBns and their affinities speak to their utility in drug delivery and controlled drug release and other potential biological applications.[103,107]

Cucurbit[n]urils, unlike previously mentioned hosts, are not easily functionalized and are more often used in supramolecular strategies to add or modulate its recognition properties or responsivity to stimuli. Nonetheless, some strategies have been developed for the functionalization of this host or further structural changes. Functionalization can be done by hydroxylation of the glycouril unit in the CBn structure, or by modifying the glycouril unit prior to host synthesis.[108,109] During the cyclization process it is also possible to introduce more complex structural variability, including inverted glycouril units and altogether different units, as can be seen in Figure 1.13, with these different units providing a series of different properties to the CBn.[110–112] Functionalization with methyl groups appears to improve solubility of these hosts, while monofunctionalization examples are often employed to obtain hosts with conjugated responsive units.[113,114] The CB6 receptor with the two aromatic panels and functionalized glycouril units both improves solubility and changes the selectivity of this host towards nitroaromatics, amino acids and neurotransmitters.[111]

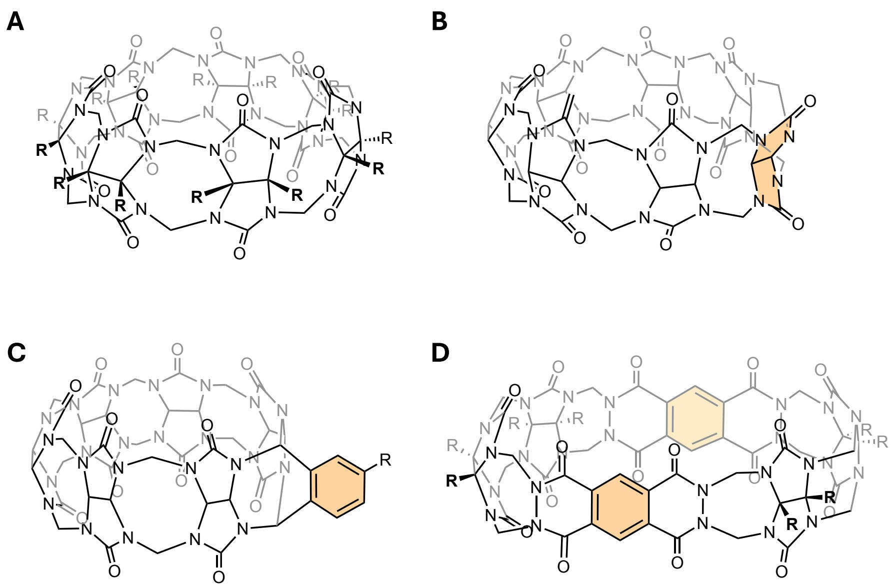

Figure 1.13: Structure of different CBn homologues: **A.** fully functionalized CB7 with different R groups; **B.** inverted-CB7 (iCB7); **C.** CB6 with a functionalized benzene unit and **D.** a CB6 host with two face-to-face aromatic panels and substituted glycouril units.[108–112]

1.1.5 Cyclodextrins, Other Macrocycles and Acyclic Examples

A myriad of other examples can be found in the realm of supramolecular receptors. Some of these, like cyclodextrins, follow the same principle of the macrocylic structure with an hydrophobic pocket, while others use acyclic structures and provide them only enough flexibility to still adapt to a wider variety of structures while maintaining the advantages of a preorganized binding site.[115–117]

Cyclodextrins are macrocyclic oligosaccharides that present hydrophobic cavities of variable size, with the most commonly used variants being α-cyclodextrin (α-CD), β-cyclodextrin (β-CD) and γ-cyclodextrin (γ-CD) with 6, 7 and 8 units, respectively. These present mM affinity towards a variety of neutral molecules, which include the amino acids valine, alanine and glycine and small to medium size drugs like chlorpromazine.[32,115,118,119] Further modifications to the structure can provide it with affinities falling below the μM range (Figure 1.14 A). This is the case of suggamadex (Bridion™), a functionalized γ-CD which can bind steroidal drugs, like rocuronium, and is used as a sequestering agent to reverse the guests' anesthetic effects.[120] Several other cyclodextrins have been applied in pharmacological formulations as well due to their lack of toxicity and ability to solubilize and increase the bioavailability of several drugs.[121,122]

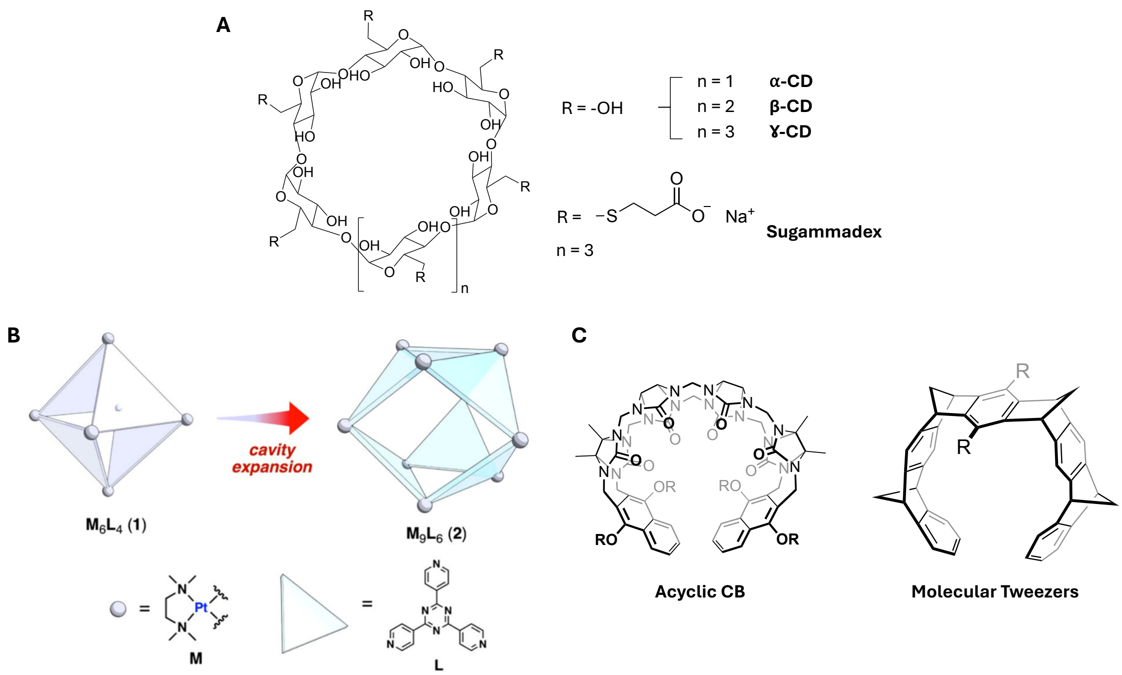

Figure 1.14: Structure of different supramolecular receptors: **A.** cyclodextrins (CD), with examples of α, β and γ-CD and the commercially available Sugammadex; **B.** Fujita's organometallic cages composed of Pt^{+} and organic ligands, which, depending on the size of the cage can include different target guests; and **C.** an acyclic cucurbituril and molecular tweezer presenting semi-rigid binding pockets. B reproduced with permission from J. Am. Chem. Soc. 2024, 146, 47, 32311–32316. Copyright 2024 American Chemical Society.[116,117,120,123]

Fujita's organometallic cages take a different approach of creating a binding pocket and preorganized structure from those seen so far. They take advantage of the metal-ligand interaction to create different binding pockets by varying the coordination sites in the ligand and using different metals, like paladium and platinum, and variable ligand to metal ratios.[123,124] Most of these establish π-π and CH-π interactions with their guests but selectivities also depend on the size of the cage, with smaller cages being able to selectively bind small peptides with aromatic residues at specific sites and perfluorinated contaminants, while larger ones (Figure 1.14 B) can bind to larger drugs like rifampicin, which represents a broad scope of possible guests.[123,125,126]

The prevalent preorganization concept observed here is what allows many of these interactions to happen. The host however, can be preorganized, without the need for a cyclic or completely enclosed structure. Both acyclic counterparts of some of these molecules or other novel structures can have cleft-like binding sites which are preorganized but present enough flexibility for certain induced-fit interactions to be able to happen. This is the case of acyclic cucurbiturils which, due to the rigidity of the glycouril oligomer, present a well defined hydrophobic pocket (Figure 1.14 C) which can equal the nM affinities observed for CB7 and CB8 for rocuronium and vecuronium, due to retained enthalpy-driven binding that is typical of the cyclic hosts.[116] Additionally, these present a higher affinity for a variety of amino acids, making them a broader spectrum host for these biological targets.[127] Other acyclic examples are the molecular tweezers, open semi-rigid torus-shaped molecules, often composed of different aromatic moieties, that can have varied structures and functinalities, leading to highly distintc affinities. The example presented in Figure 1.14 C is often functionalized with anionic groups, adding ionic binding sites for the already electronegative aromatic cavity, leading to these presenting high affinity and selectivity towards cationic amino acids and these same residues in proteins.[117,128]

1.2 Supramolecular Assemblies: the role of self-assembly and chemical programming

Molecular recognition is not only essential for discrete host-guest interactions but for understanding how different combinations of molecules are going to assemble in solution as well. This can take many forms and come from unintended side-effects when studying molecules for other applications. However, this capacity, although sometimes difficult to predict, can be introduced in the molecular design *a priori*. This approach where these properties are pre-programmed into the molecule and uses them as building blocks for constructing more complex systems, denominated as a "bottom-up" approach, is the guiding principle for self-assembly and prevalent in this field.[6,129]

The transduction of the information built into molecules to structural micro- and macroscopic effects and functional variation is a key element in biological systems, being responsible for the correct folding of proteins, the compartmentalization provided by phospholipidic membranes, the ability of DNA to code genetic information through the different sequencing of 4 different monomers, among other key functions.[130]

Although complex assemblies present in biological systems are still not completely understood, supramolecular chemistry is continuously working to achieve similar levels of complexity and chemical programming.[6,7,129] It aims at mimicking some of these concepts both in synthetic and biological engineered systems, which can be achieved through careful synthesis of molecules with sites of noncovalent interaction with other elements in mind. This design can target the assembly of simpler structures like that of host capsules and dimers, ternary and quaternary assemblies, rotaxanes and pseudorotaxanes, to the more complex supramolecular polymers, vesicles and nanoparticles.[14,131–134] In this section, examples of different levels of self-assembly in supramolecular chemistry will be included, with a focus on the responsive systems and the diverse stimuli these can respond to, as well as chemical programmed systems and how we can extract information from these systems.

1.2.1 Introducing responsiveness

One of the great advantages of the approach of supramolecular chemistry is that the non-covalent bonds that allow these assemblies to form are labile. This allows for variations in the system and distinct stimuli of different natures to influence the assembly of these systems, leading to detectable and programmable changes. This stimuli can be the sudden increase in concentration of one of the species, redox reactions, temperature and pH fluctuations or even light, which can influence the structure or binding properties of the molecules in the supramolecular assembly. All of these offer different advantages and can be used in several applications.[135–141]

In pharmaceutical applications, one of the goals of developing novel drugs and formulations is improving their specificity and decreasing undesired and deleterious side effects. Controlled drug release can be designed in order to take advantage of all of the mentioned stimuli individually or even depend on the presence of several at the same time, to achieve this goal. This is particularly important in cancer therapy, where different types of cancer cells present elevated concentration of certain biomarkers, decreased pH, decreased oxygen levels and consequent high reductive potential, etc, which can be exploited for controlled drug release in such conditions.[75,142]

The combination of different stimuli with light is particularly interesting due to the properties of light as a stimulus, due to the capacity for remote control of the system with little to no chemical waste production, with the added benefit of high spatiotemporal precision.[143] One way to employ this is the use of photoswitches in different conditions as light-controlled competitors for a host-drug complex - photoconversion between two competitor species can lead to the binding of the higher affinity form of the photoswitch to the host cavity and consequent light-activated release of the desired cargo.[137–139]

The work by Pischel and Basílio shows how light and pH can be simultaneously used for controlled release of drugs, using a simple host-guest-competitor system. In this example, a chalcone/flavylium photoswitch takes advantage of the differential affinity of these two species towards CB7, where this host can be bound to the drug memantine (K = 2.5×10^4 M^{-1}) in the presence of the chalcone (K = 4×10^2 M^{-1}) and releasing the drug from the cavity of CB7 when pH is decreased below 4 and upon UV-light irradiation, due to formation of the better competitor flavylium ion (K = 9×10^5 M^{-1}) (Figure 1.15 A).[137]

More recently, this has been applied with the larger CB8 and different photoswitches (Figure 1.15 B), including diarylethene derivatives with the ability to switch with NIR and visible light. Infrared photoswitches are ideal due to the improved tissue penetration of

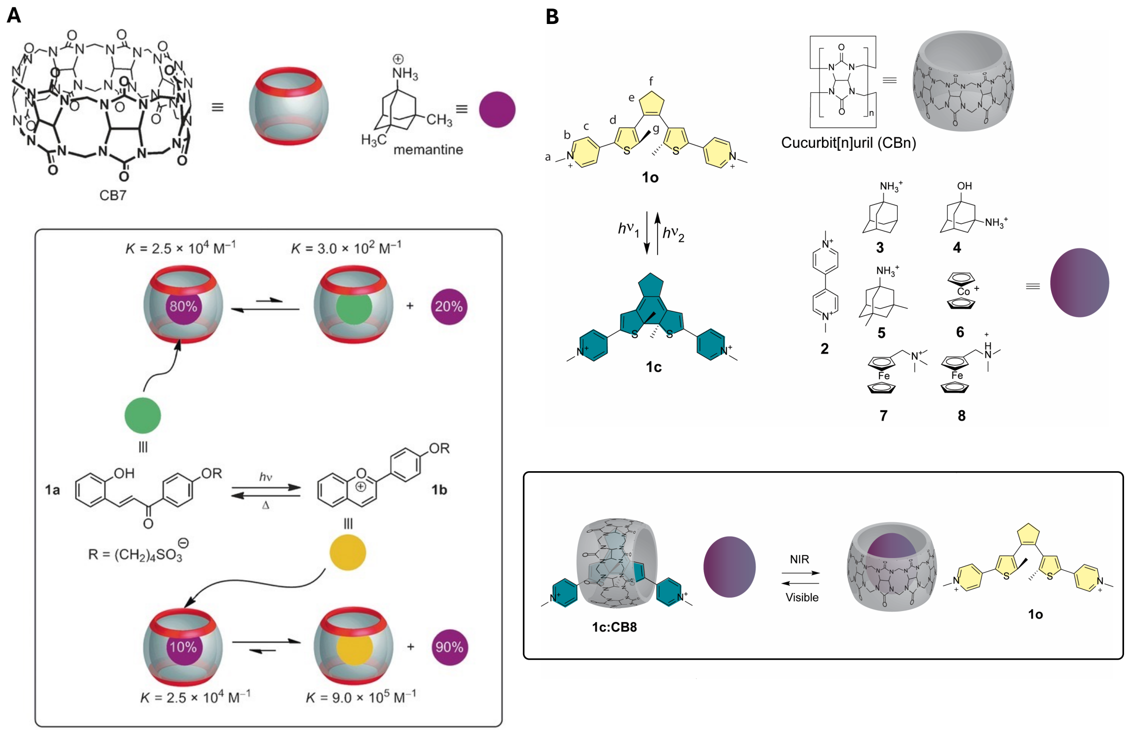

Figure 1.15: **A.** Coupling of a flavylium photoswitch with a memantine-CB7 host-guest equilibrium for the phototriggered release of the drug (memantine). Reproduced with permission from Chem. Eur. J. 2016, 22, 15208. Copyright 2016 Wiley-VCH GmbH. **B.** Photocontrolled complexation and release of high-affinity guest molecules from CB8 using near-infrared (NIR)-visible light responsive diarylethene derivatives. Reproduced with permission from Chem. Eur. J. 2019, 25, 3477. Copyright 2019 Wiley-VCH GmbH.[137,138]

this range of light (Figure 1.15 B).[138,139]

Calixarenes or calixarene-guest complexes can be used in order to create stimuli-responsive systems as well. This can be achieved through similar designs as those described for CBn but it is also possible to use the self-assembly of amphiphilic hosts or complexes into micelles and vesicles as a drug delivery mechanism.

Within the field of cancer targeted therapies, the work by Guo's Lab showcases the ability to target these high reductive potential environments by stimuli-responsive calixarenes. Azocalixarenes, previously addressed in Section 1.1.3.1, are an example of a group of molecules that can act as a targeted transporter for release of drugs and sensors in these environments through the reduction of the azo-linkage and formation of an aminocalixarene that presents markedly different binding properties.[72,75]

On the other hand, calixarene is often used in self-assembly based approaches for the preparation of micelle and vesicle-like structures. This comes not only from its versatility as a host but also from the optimal shape and flexibility that its cone conformation presents, adapting easily to these curved surfaces. Furthermore, functionalization with charged groups in one rim and hydrophobic chains in the other allow locking of the smaller calixarene in this optimal conformation, with the polar region in contact with aqueous solution, while the hydrophobic tail is what composes the inner compartment in micelles, or the interior of bilayers in vesicles. The variety of structures that can be achieved by altering the calixarene and its guests can allow the encapsulation of drugs in the hydrophobic inner compartment of micelles, or the encapsulation in aqueous milieu in vesicles. Stimuli like light, pH and presence of specific biomarkers can act as triggers for the dissassembly of these structures and induce drug release.[131,140,144]

Chemical control over locomotion is another example of a process that is highly dependent on the presence of different stimuli. This movement is achieved in biological systems by using different molecular machines, as is the case of the actin-myosin complex, which achieves unidirectional movement when adenosine triphosphate (ATP) is present to initiate the dissociation/association and myosin conformational change cycle that enables movement.[145] Synthetic molecular machines work in a similar fashion, where different stimuli are needed in order to have controlled and directional movement. One example of this is the first iteration of Feringa's molecular motor, which uses a combination of light and thermal inputs in order for the rotation of the molecule to be unidirectional, upon different isomerization steps.[141] Other structures introduce the self-assembly of different macrocycles into an axle - rotaxanes and pseudorotaxanes - and different axles and hosts can be used in order to take advantage of different stimuli to control the macrocycles' movement across the axle.[136,146]

Other complex responsive materials can also be developed with this stimuli-responsive behaviour. One other field where these concepts are often applied is in the development of supramolecular responsive materials and hydrogels for biological applications. These show the possibility to take changes on the molecular level and see their effects on macroscopic properties of the materials, with controlled responses through different types of stimuli, much like the previous examples.[14,147,148]

Some of these examples present increasingly biomimetic behaviour and some of the more complex systems are addressed in further detail in Section 1.3.

1.2.2 The age of information: supramolecular sensing systems

Another facet of self-assembled systems is in the chemical programming but also in the extraction of information from the molecular interplay resulting from their interaction with biological systems. This information can be gathered from a supramolecular system by coupling the recognition of a target molecule or an alteration of the interactions being established with some type of readout mechanism. This can give feedback on the state of a supramolecular assembly after a given stimulus, or can be used as a way to sense a variation in the environment where the supramolecular system is inserted, be it concentration of a biomarker, temperature, humidity, etc.[10] These mechanisms are often optical, due to the accessibility of spectroscopic techniques and, in some cases, due to the ability to detect changes with the naked eye. Because macrocyclic hosts and their guests are often optically silent, it is necessary to combine them either with chromophores or fluorophores that bind their cavity with concurrent optical response or modify the macrocycles themselves to present this responsive unit in their structure.[10,149] A mixture of the two strategies can have successful applications as well.

Several mechanisms can be used to provide this optical response. Receptors with responsive units covalently linked to them often rely on intramolecular photophysical mechanisms like Photoinduced Electron Transfer (PET) in order to have an optical variation upon binding. PET-based fluorescence indicators prensent a donor-linker-acceptor structure where electron transfer from donor to acceptor leads to a deactivation of the radiative relaxation mechanism (Figure 1.16 A). When there is binding in the donor moiety, changes in molecular orbital stabilities will block the PET process and lead to a turn-on fluorescence response.[150,151]

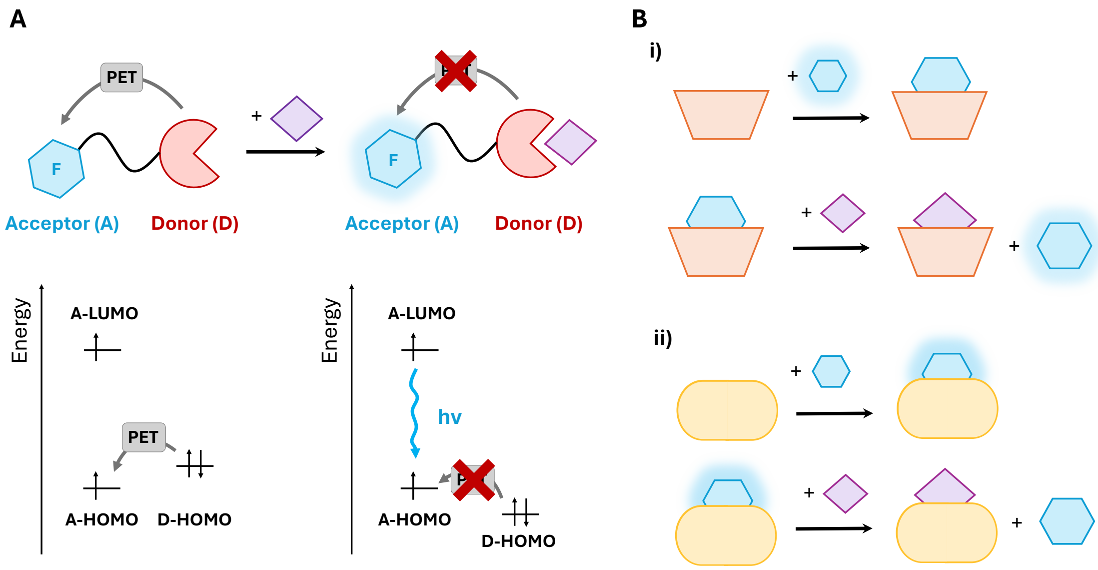

Figure 1.16: Schematization of a covalent and non-covalent strategy for sensing. **A.** Photoinduced Electron Transfer (PET) based indicators, presenting a donor-linker-acceptor structure, often are not emissive due to the PET process. Binding of an analyte that stabilizes the Highest Occupied Molecular Orbital (HOMO) of the Donor moiety leads to inactivation of PET and allows the radiative relaxation to happen. **B.** Indicator Displacement Assay (IDA) with different hosts, presenting different effects on the dye. i) Schematization of an IDA where the dye becomes quenched when included in the cavity and its displacement leads to a turn-on signal. ii) Schematization of an IDA where the dye suffers an enhancement of its emission when enclosed in the cavity, leading to a turn-off signal upon its displacement.[150,152]

Non-covalent strategies on the other hand regularly rely on the inclusion of an indicator into a macrocyclic cavity. Fluorophores present high variability of optical properties depending on the environment in which they are inserted. In aqueous solution, inclusion in a cavity that is generally hydrophobic leads to significant change in the microenvironment of the dye, leading to the necessary signal variation. Other factors like rigidification of the indicator or charge-transfer with the host can also lead to changes in the optical properties of the indicator.[51] Once the host-indicator complexes are established, these can be used in competitive assays, where the consequent release of these indicators when the target analyte binds to the cavity is the readout mechanism - this type of assay is also known as Indicator Displacement Assay (IDA) (Figure 1.16 B). The simplicity of this type of assay and the ability to have libraries of indicators that bind with different affinities towards the studied host, has led to the IDA becoming one of the most used readout mechanisms in host-guest chemistry.[149,152]

Readout mechanisms using both covalent and non-covalent strategies have specific advantages and are employed in different applications. While receptors with covalently-linked indicators see a greater application for cell imaging, due to the ability to maintain optical variation to stimuli at lower concentration, in array-like applications it is often advantageous to expend a higher synthetic effort in the development of different receptors with novel selectivities and using the imense library of available dyes as possible reporters with variable affinities.[114,149,153]

Several groups have developed different dye-conjugated cucurbiturils for live-cell imaging of distinct organelles and biomolecules, all of them seemingly maintaining a low cytotoxicity, while allowing detection at rather low concentrations of sensor.[114,153]

The IDA has seen application in a myriad of systems, with a variety of different host-indicator combinations. This methodology has been applied for quantitative and qualitative analysis of binding of hosts to varied guest families, from environmental contaminants, biomarkers, food safety analysis, etc.[19,48,99,154,155] These can also be used to monitor enzymatic reactions, in label-free tandem assays, with different host-dye complexes reporting distinct enzymatic reactions concomitantly, taking advantage of the distinct affinities of the different hosts towards reagents and products of the enzymatic reactions being studied.[156] IDA-based monitoring in live-cell imaging has also been successfully applied for the monitoring of neurotransmitters in cellular environments, however the concentration of host and indicator needed are often much higher than for covalently-linked reporters, in order for the complexes to be assembled in physiological conditions.[157]

Some examples use both of these strategies for creation of intramolecular IDA which can both increase signal to noise ratio and decrease the concentration of dye needed for application in live cells, while also improving selectivity.[158,159] Work by Jolliffe and coworkers presented an example of an intramolecular IDA sensor based on a peptidic structure, for phosphatidylserine detection in cells. The structure of the sensors presents two zinc(II) dipicolylamine receptor moieties and a coumarin-based dye, all linked covalently to the flexible peptidic backbone. The coumarin moiety remains quenched in the absence of the analyte due to an intramolecular charge transfer complex it can establish with the zinc(II) dipicolylamine receptor closest to it. When displaced by the guest phosphatidylserine, which presents an extra binding site towards the remaining zinc(II) dipicolylamine moiety, the dye regains its emission and this can be detected in a time-dependant manner in cell imaging assays (Figure 1.17).[159]

While these remain relatively simple in terms of number of elements contributing to

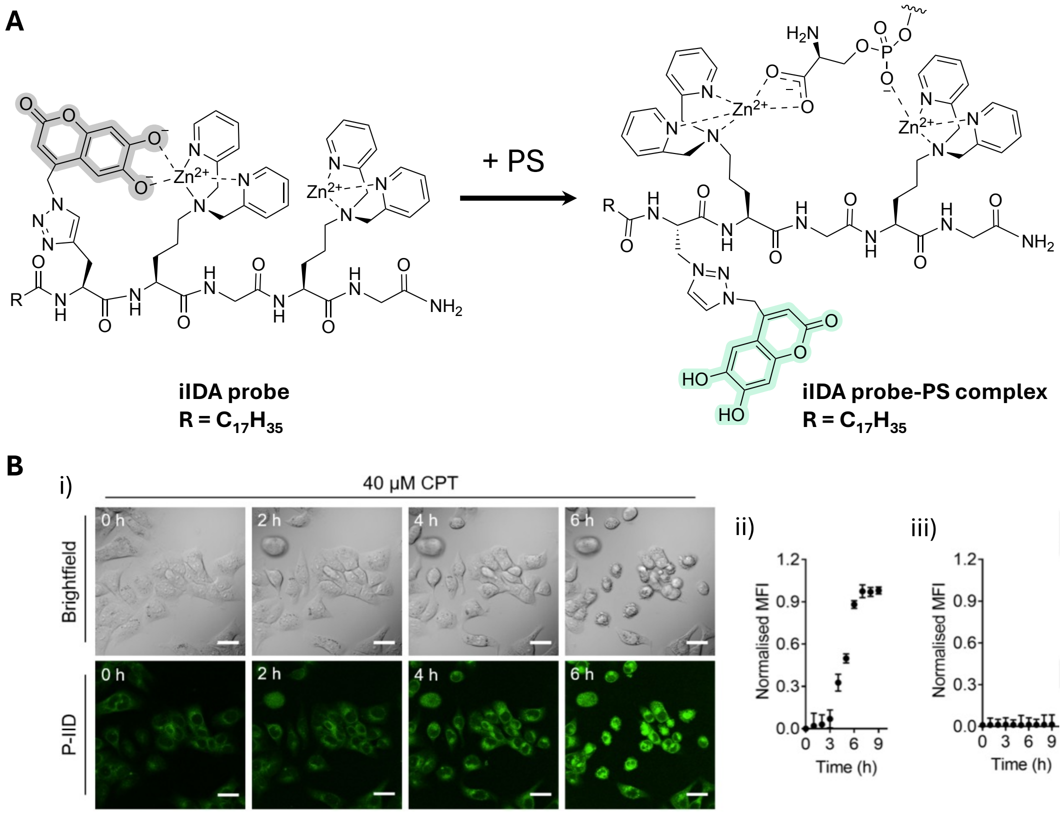

Figure 1.17: A. Chemical structure of the intramolecular IDA (iIDA) probe developed by Jolliffe and coworkers and proposed binding mechanism with phosphatidylserine (PS). B. i) Time-lapse imaging of a single field of HCC-1806 cells simultaneously treated with an apoptosis-inducing agent resulting in elevated levels of PS (40 μM) and stained with the iIDA probe (15 μM) over the course of 6 h (5% CO_2 at 37 °C). ii) Quantification of the change in the mean fluorescence intensity (MFI) over the total imaging time of 9 h. iii) Change in MFI when untreated HCC-1806 cells were incubated with iIDA probe (15 μM) for 9 h. Scale bar represents 30 μm. Reproduced with permission from Angew. Chem. Int. Ed. 2019, 58, 3087. Copyright 2019 Wiley-VCH GmbH.[159]

the system, further complexity and self-assembly of different interacting elements can be helpful in order to extract a higher quantity of information from the analyte samples. This is increasingly important in the analysis of complex samples, as is the case of biofluids, contaminated samples with environmental pollutants or illicit drugs, which present a great variety of analytes, from proteins, glycosaminoglycans, drugs, contaminants, among others.[160] Some strategies use more than one dye in order to have a ratiometric response while others use array-like strategies to extract analyte fingerprints for their detection.[161–165]

Ratiometric probes use photophysical phenomena like Förster Ressonance Energy Transfer (FRET) and formation of excimers and exciplexes to avoid interferance of environmental factors and probe concentration variations, on the optical readout mechanism, improving signal-to-noise ratios and, in the case of FRET, allowing distance measurement between the two indicators used, providing important structural information.[161–163]

Array strategies often use mixtures of different hosts and dyes in combinatorial libraries, creating differential sensing systems based on the simple yet efficient IDA, that aim at imititating the detection strategy of the olfactory system. The non-covalent nature of the interactions allows the adaptation of the library to different analyte inputs, with different hosts yielding distinct molar fractions of complexes with the analytes and indicators present in the samples and, consequently, different optical responses.[164,165] This differential sensing yields unique fingerprints depending on the analytes present in the samples, even if some of its elements present unknown structures. Furthermore, with the advent of data analysis methodologies and higher computational power, the capacity to rapidly analyze large quantities of data has increased and become more acessible, going from linear dimensionality reduction methodologies like Principal Component Analysis (PCA) and Linear Discriminant Analysis (LDA) to complex artificial neural networks. This evolution has allowed the concurrent development of differential sensing systems with increasing amount of data being extracted and analyzed.[164]

Examples of these methodologies include the use of different hosts and indicators at fixed concentrations for different competitive responses upon sample analysis. Several groups have employed this methodology both for direct analysis of samples or for monitoring alterations in a given sample. Hof and coworkers have employed this strategy with different calixarenes - *p*-sulfonatocalix[4]arene, SC4, *p*-Sulfonatocalix[6]arene (SC6) and *p*-Sulfonatocalix[8]arene (SC8) - and two distinct indicators to distinguish different lysine methylation patterns in peptides with great success.[166] More recent examples by the same group use different strategies for differentiation of a higher amount of analytes. Such is the case of the Dimer Dyes, where the detection hinges on the dimerization-dependant optical response of modified calixarene reporters, that is applicable even in high salt concentrations. These have been successfully applied both for protein differentiation, with the use of three different calixarenes modified with indicator moieties, and for illicit drugs and adulterants differentiation when used in arrays with the hosts CB7 and CB8 (Figure 1.18).[9,167]

Hooley's and Dalcanale's group have also achieved successful distinction of different post-translational modification patterns in peptides and proteins and monitorization of the correspondant enzymatic reactions, differentiation of DNA G-quadruplex structures and the detection of different PFAS, using various cavitands and indicators at fixed concentrations.[90,91,168,169]

Guo and coworkers employ a slightly different strategy, which uses the variation of host fractions and pH in the arrays as if these were novel groups of receptors, seeing as different starting conditions lead to different end points in terms of complex fractions and, consequently, optical response, improving the differentiation capacity of a system with a more limited number of receptors and indicators (Figure 1.19). This was applied successfully both for differentiation of proteins in complex mixtures, but also for product quality and composition distinction in honey sample analysis.[170]

The variety of systems that exist is fast-growing and increasingly more efficient in the extraction of information from different samples. This has improved both disease

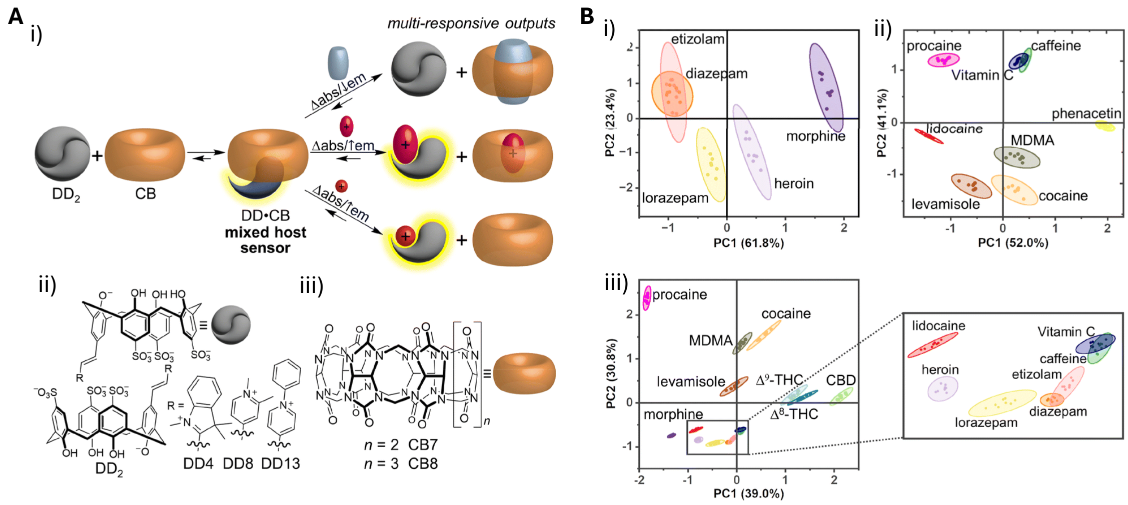

Figure 1.18: **A.** i) DimerDye complexation with cucurbit[n]uril forms a mixed host chemosensor. ii) DimerDye host chemosensors DD4, DD8, and DD13, and iii) cucurbit[n]uril hosts CB7 and CB8. **B.** PCA analysis of i) central nervous system depressants, neutral benzodiazepines and cationic opiates using DD8-CB8, DD13-CB8 and DD13-CB7, ii) of anesthetics, amphetamine and other common adulterants, using DD4-CB8, DD13-CB8, and DD13-CB7, and iii) all tested drugs and adulterants, using all host combinations. Sample set (n = 8) enclosed by 95% confidence ellipses. Samples contain DD, CBn and drug at 10.5, 21 an 105 μM, respectively, in NaH_2PO_4/Na_2HPO_4 (8.4 mM, pH 7.4) in H_2O with 2% MeOH. Reproduced with permission from Chem. Sci., 2024,15, 12388-12397. Copyright 2024 Royal Society of Chemistry.[167]

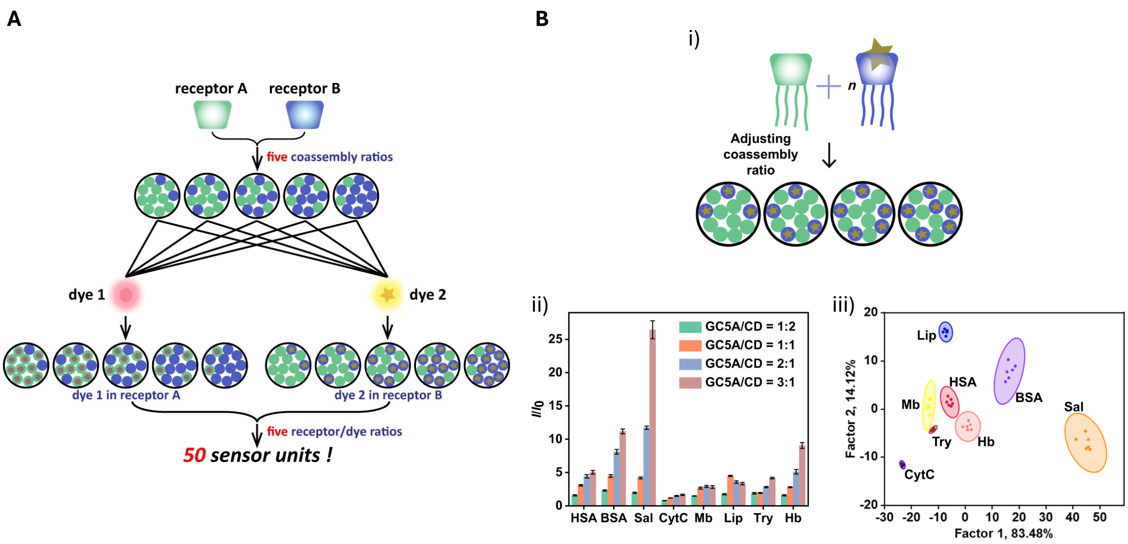

Figure 1.19: **A.** Formation of 50 sensor units utilizing two receptors and two dyes. **B.** i) Schematic diagram of sensor array 3, SA3, used for recognition of a mixture of proteins ([dye] = 1 μM). ii) Fluorescence response patterns of SA3 with different host ratios, relative to dye concentration, of amphiphilic guanidiniumcalix[4]arene and cyclodextrin, against various proteins (23.8 μg/mL for each protein). iii) Canonical score plot for the two factors of simplified fluorescence response patterns obtained from LDA with 95% confidence ellipses (n = 6). Reproduced with permission from Nat Commun 13, 4293 (2022). Copyright 2022 Springer Nature.[170]

diagnosis ability, detection of contaminants in environmental analysis, improving food safety, detection of drugs and adulterants, among other advances, showing the importance of the continuous improvement of such sensing strategies.

1.3 Biomimetic systems

From early on, it was clear that much of the inspiration for supramolecular systems is in the complex interplay of molecular elements that is found in nature.[2–4] Throughout the years, the great distance between biological systems and supramolecular synthetic ones has become marginally smaller, with the urge to imitate the former driving researchers to clarify how these work and leading to small steps towards increasingly more complex supramolecular assemblies.[7,28,171]

Different strategies have been used for development of biomimetic systems, with a focus on different natural properties. One of these was the confinement or anchorage of these synthetic molecules in compartments like micelles, liposomes and polymerosomes. The application of lipid-based compartments has become an important step towards the development of biomimetic systems because of the key role that compartmentalization plays in nature. These allow the separation of cell/organism functions between markedly distinct enclosed environments, which allow cell digestion, energetic metabolism, protection of cellular components, etc.[172] Liposomes in particular are a clear synthetic counterpart to the cellular membrane's phospholipidic bilayer (example of a cell membrane in Figure 1.20) and have made a great impact in the development of more biocompatible and stable therapeutic agents, especially in the development of vaccines, which often include cargo that is particularly susceptible to degradation, like ribonucleic acid (RNA).[13,173,174]

The exploration of different energy regimes has also been a point of interest in supramolecular chemistry. The out-of-equilibrium nature of biological systems leads to the necessity for consistent energy (and matter) inputs but also provides it with unique properties. Most supramolecular biomimetic systems still work by reaching the thermodynamically stable state and anything beyond that remains a challenge. Nonetheless, great effort is being made to obtain more examples of systems that are kinetically trapped or in these out-of-equilibrium states (Figure 1.21).[7,175–177]

This section will dive into examples of how supramolecular synthetic systems can both interplay with biomolecules, cells and cell-like structures to elucidate biological processes but also to achieve novel synthetic therapeutic agents, bio-inspired catalysts and materials. This includes a closer look into previously mentioned examples that have been used in combination with different synthetic and biological elements, including confinement into lipid compartments, showing works that explore in the same system many of the concepts described herein.[60,156,157]

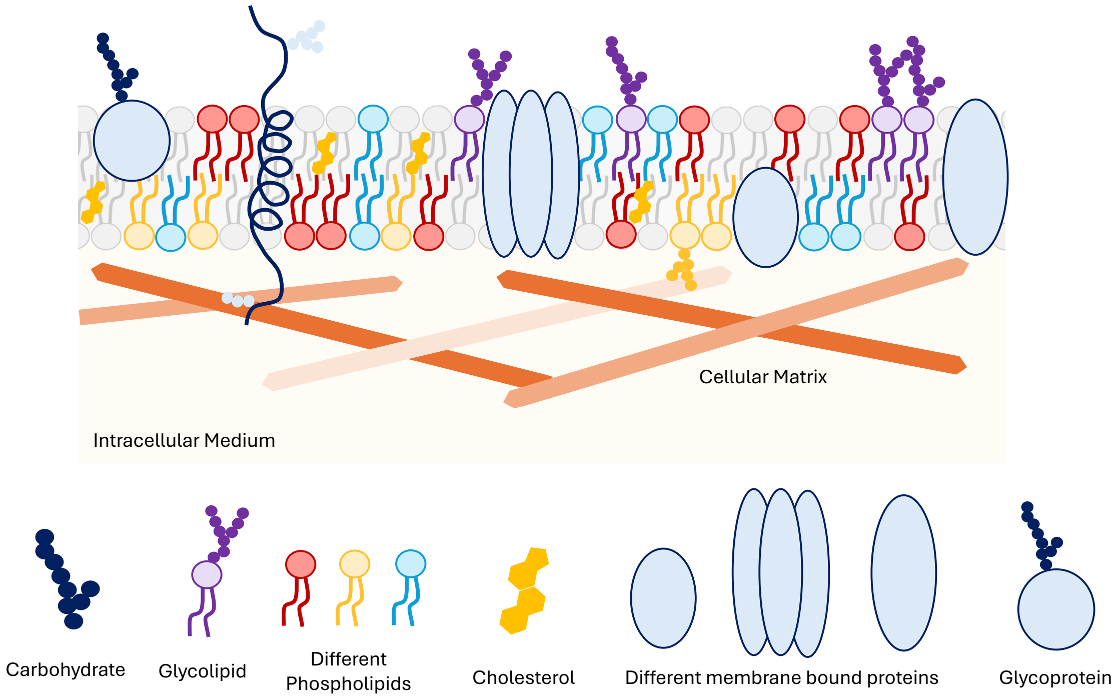

Figure 1.20: Schematization of a cell membrane with examples of the different molecular elements that contribute to its physical properties and functionality. Adapted from Chem. Rev. 2016,116,4, 2023–2078.[7]

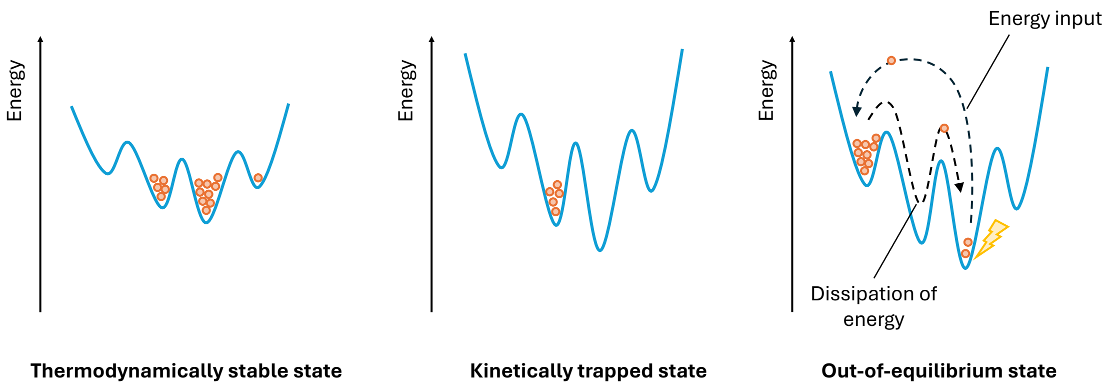

Figure 1.21: Thermodynamic regimes of a chemical system, from left to right: thermodynamically stable state where the system evolves to the minimum of energy; kinetically trapped state, where the system fall into a local minimum of energy, often in cases where the activation energy to reach the thermodynamic minimum is high; and out-of-equilibrium systems where an input of energy takes the system to a higher energy state that eventually dissipates its energy and ends up in the thermodynamic minimum if no further energy is inputed. Adapted with permission from Nature Nanotech. 2015, 10, 111–119. Copyright 2015 Springer Nature.[175]

1.3.1 Across the phospholipidic membrane: supramolecular transporters and sensors

Compartimentalization of biological processes, as mentioned above, is essential for the maintenance of homeostasis and for the cellular environments to remain in their out-of-equilibrium state. Compartments are necessary to establish and maintain chemical gradients that allow important biochemical mechanisms, like oxidative phosphorylation and photosynthesis. They also allow the separation of different biochemical pathways while maintaining the communication between them, leading to the existance of different tissues with distinct functions. This is only possible due to the presence of the complex semipermeable phospholipidic membrane (see Figure 1.20). Transport across the phospholipidic membrane is highly controlled through selective channels, transporter proteins or endocytosis and often requires energetic input.[172]

Supramolecular chemistry has yielded a plethora of examples of novel systems that are reliant on the concept of compartmentalization, either in facilitating the crossing of these barriers to improve drug delivery or to use vesicles as vectors and platforms for the creation of multifunctional systems.[7,175]

In some of the most simple examples, amphiphilic supramolecular receptors can be anchored in membranes simply by exploiting the hydrophobic effect. The hydrophobic moiety of these molecules tends to partition into the apolar membrane interior and the charged moiety tends to remain in the aqueous interface, either in the interior or exterior of the vesicles. The sensing system explored by Zhong, Hooley and coworkers (previously mentioned in Section 1.2.2) uses this simple strategy for the anchoring of amphiphilic cavitands in cellular membranes and the implementation of an IDA in live cells (Figure 1.22). These small receptors show the capacity to retain two different styrylpyridinium indicators in the periphery of the cellular membrane, that would accumulate in mithocondria and nuclei in the absence of the amphiphilic host. Despite being much simpler than the majority of biological receptors, the cavitands were used for successful detection of different signalling molecules (Figure 1.22 shows the ability to selectively detect choline over betaine) that were added to the cell cultures, with clear displacement of the membrane bound indicators, resulting either in dye accumulation at the previous mentioned organelles or even complete elimination from the cells.[157]

Other examples that show the versatility of biomimetic supramolecular systems is in the development of transporters, where strategies go from discrete supramolecular assemblies to complex out-of-equilibrium systems. Counterion activation is one of the simpler strategies for transport across membranes, consisting on the association of amphiphilic molecules (the counterion activators) to the target hydrophilic cargo to create complexes that become more membrane-permeable. These complexes are then able to directly translocate through the membrane, avoiding energy-dependant pathways and eventual entrapment of the cargo in endosomes.[178] Amphiphilic calixarenes have been found to be remarkably efficient counterion activators, with some of these receptors presenting

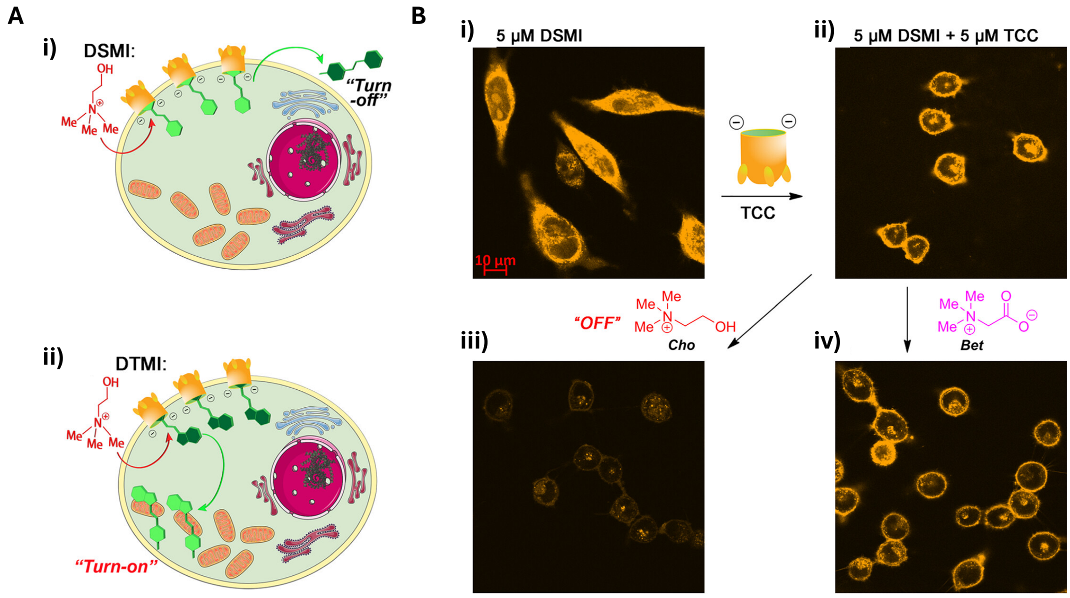

Figure 1.22: Schematization of the IDA assays in cell with the cavitand TCC and styrylpyridinium dyes, DSMI and DTMI, system. **A.** Representations of the i) "turn-on" and ii) "turn-off" IDA processes with the two different dyes tested. **B.** IDA sensing example with TCC-DSMI. DSMI channel fluorescence images (λ_{exc} = 488 nm and window of detection between 570-632 nm) of live HeLa cells treated by i) 5 μM DSMI for 1 h, ii) TCC-DSMI (pre-mix, 5 μM each) then phosphate buffer saline (PBS) for 1 h, iii) TCC-DSMI (pre-mix, 5 μM each) then 50 mM Choline for 1 h, and iv) TCC-DSMI (pre-mix, 5 μM each) then 50 mM betaine for 1 h. Adapted with permission from ACS Sens. 2023, 8, 8, 3195–3204. Copyright 2015 American Chemical Society.[157]

Effective Concentration at 50% of maximum effect (EC_{50}) in the nM range.[37,179–182]

Out-of-equilibrium transporter systems often rely on stimuli to serve as both an energy input, driving the system towards a higher energy state, and provide dynamic control over the structure/polarity of the transporters. The development of stimulus-responsive membrane carriers commonly uses light as a stimulus to drive this transport, often hinging on photoisomerization of moieties in the transporter as the driving force for either activation or blocking of transport.[146] This has mainly been applied for the selective transport of small ions across membranes through different structures of transporters, including channels (Figure 1.23 A), mobile transporters (Figure 1.23 B) and anchored transporters (Figure 1.23 C).[146,183–185]

Synthetic channels can control the flow of a select group of small molecules across membranes through different strategies. The presented example achieves this with an amphiphilic β-CD gated pore, that presents a photoactive azobenzene moiety as the gate (Figure 1.23 A). The system shows slightly higher rates of transport for small cations when azobenzene is in its *trans* configuration and enclosed in the β-CD cavity, without particular selectivity between Li^+, Na^+ and K^+, and showed decreased rate of cation transport and marked increase of anion transport when the azobenzene moiety is in its *cis* configuration and outside the host cavity and the channel is effectively unblocked.[183]

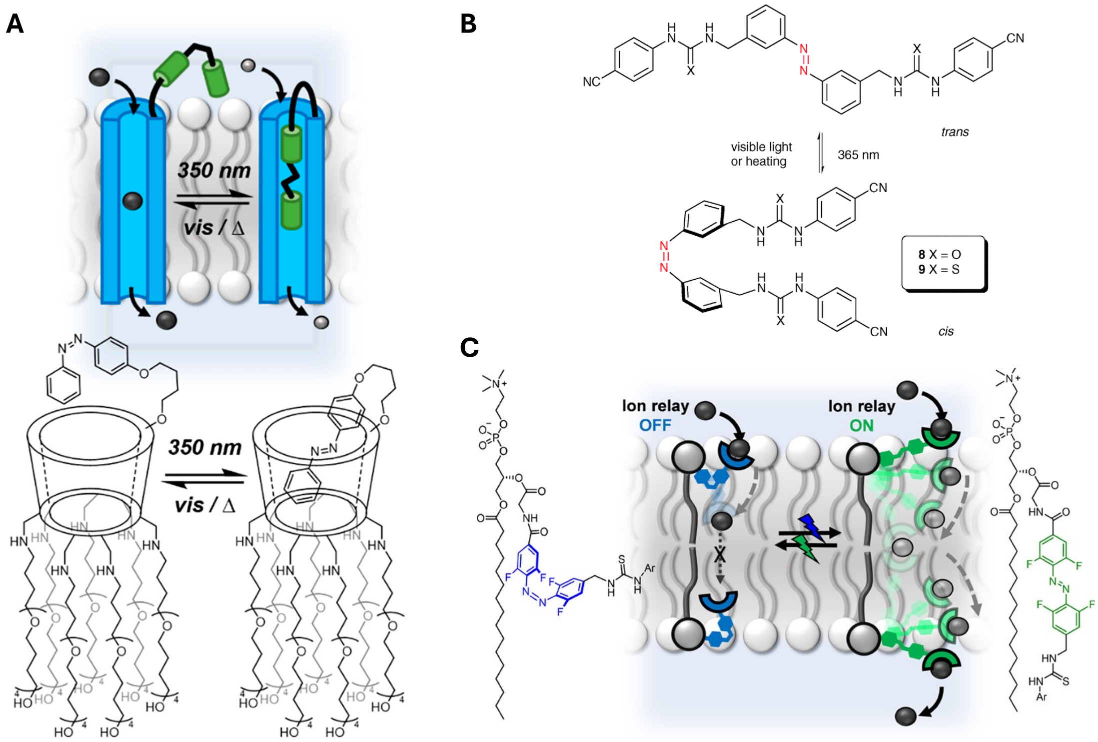

Figure 1.23: **A.** Reversible photocontrol of channel pore size controls ion channel selectivity. Photoswitching of azobenzene moiety of β-cyclodextrin-based channel via pseudorotaxane formation controls its ion selectivity. Reproduced with permission from J. Am. Chem. Soc. 2023, 145, 50, 27167–27184, original in Org. Lett. 2008, 10, 17, 3693–3696. Copyright 2023 American Chemical Society.[146,183] **B.** Photoswitchable mobile carrier based on bis-(thio)urea azobenzene. Adapted with permission from Chem. Commun., 2014,50, 15305-15308. Copyright 2014 Royal Society of Chemistry.[184] **C.** Schematic representation of tetrafluoroazobenzene thiourea photoswitchable relay transporter by Langton and coworkers and its activity as a membrane anchored transporter. Adapted with permission from J. Am. Chem. Soc. 2022, 144, 23, 10455–10461. Copyright 2022 American Chemical Society.[185]

The mobile photoresponsive shuttles are often membrane soluble species that present binding sites towards the target cargo. The light-controlled transport can be done through either distinct affinities of different isomers of the transporter towards its cargo or through changes in structure/shape, flexibility and dipolar moment, that can influence membrane permeability and mobility. The example shown in Figure 1.23 B uses the azobenzene moiety as the photoactive unit of the molecule as well. The *trans* isomer of this species presents a linear conformation and irradiation with UV-light originates the bent *cis* isomer, which aligns the NH moieties in an ideal orientation for Cl^- binding, resulting in 10 times superior binding affinities in comparison with the linear species. This change in affinity is mirrored by the transport capacity of this system with the *cis* species presenting considerably higher efficiency than that of the *trans*.[184]

The final design strategy presented for photoactive transporters is the use of membrane anchored molecules. Langton and coworkers have done extensive work in this field and have developed a relay tranporter based on a phospholipid with one of the hydrophobic tails modified with the photoactive tetrafluoroazobenzene unit and an anion complexation site.[185] Once again, the transport ability hinges on the structural changes induced by light - when in the *cis* conformation the receptor unit does not reach far enough into the interior of membrane to allow the passage of the anions into the inner leaflet, not allowing release in the inner milleau, while when irradiated with green light, the elongated *trans* conformation is obtained, with the ability to extend across the membrane and pass towards the transporters in the inner leaflets of the vesicle (Figure 1.23 C). This mechanism requires the presence of the transporter in both inner and outer leaflets and appears to be related to the tail flexibility in the membrane, with little to no transport even for the *trans* isomer when cholesterol is added and the membrane becomes less fluid.

For many of these approaches, however, the mechanisms of action behind these transporters remain unclear and further work needs to be done in uncovering how these constructs influence membrane structure, dynamics and permeability. Furthermore the application of photocontrolled transporters for larger hydrophilic cargo remains limited.

Other systems aim at joining several of these processes in the same biomimetic construct. An example that joins membrane-bound transporters with a encapsulated sensing system is exemplefied by the recent work of Jiang *et al*.[132] Label-free tandem enzymatic assays have been explored by this group both in solution and encapsulated in liposomes, to monitor both confined enzymatic reactions and transport across membranes by protein channels and amphiphilic counterion activators.[60,156] In their 2025 work they have developed a cascade of processes that uses all of these concepts in a protocell design, that encloses the label-free tandem enzymatic assays inside a vesicle and controls the input of the substrate through different membrane transport mechanisms (example shown in Figure 1.24). The system was explored with both different transport mechanisms and different host-indicator complexes, SC4-Lucigenin and CB7-Berberine, allowing the monitoring of transport and enzymatic conversion of distinct substrates. This not only increases the selectivity of the system, through three distinct "selection" mechanisms - transport, enzymatic reaction and host-guest complexation -, but also allows the study of encapsulated enzymatic processes and their interaction and dependency on transport of substrate into the compartment itself, by concomitant evaluation of the kinetics of the fast transport process and the slower enzymatic reaction.[132]

Despite the progress brought forth by the work shown in this section and other more complex systems, getting close to the complexity of biological systems still remains a challenge and the obtention of synthetic cell-like systems is a goal that the scientific community is continuously striving towards.

1.3.2 The synthetic enzymes: supramolecular systems as catalysts

Another area in which supramolecular assemblies can imitate biological processes is in catalysis, with small macrocycles being able to mimic some of the functions of enzyme

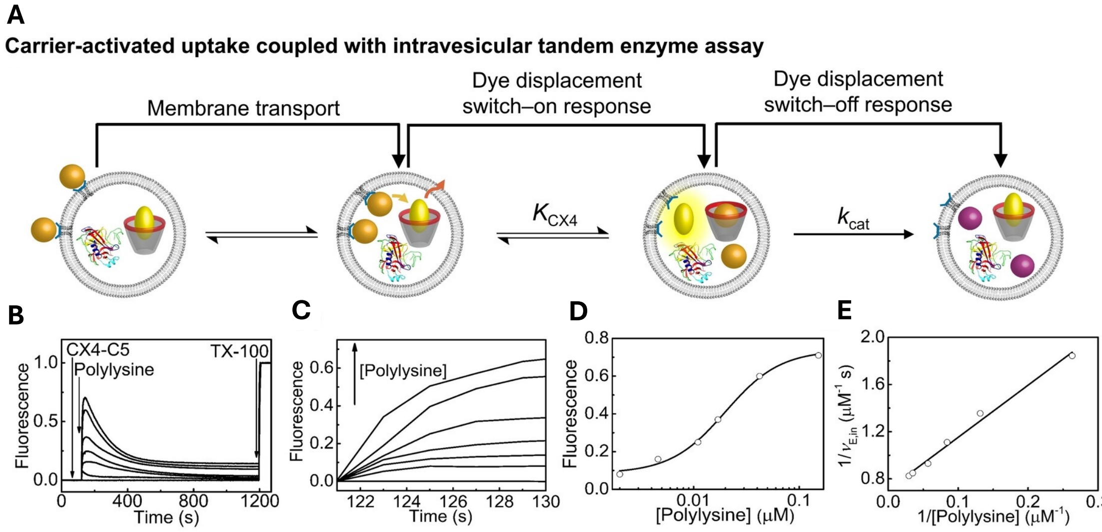

Figure 1.24: **A.** A substrate is translocated by the amphiphilic carrier, SC4-C5, into liposomes containing co-encapsulated SC4-LCG reporter pair as well as the enzyme trypsin. The substrate rapidly displaces the LCG from SC4 (switch-on fluorescence response) and the slower enzymatic cleavage of the substrate to a low-affinity product occurs, reforming the LCG-SC4 complex (switch-off fluorescence response). **B.** Experimental fluorescence traces corresponding to transport of polylysine (0-0.15 μM) into SC4/LCG +trypsin-loaded liposomes (SC4 at 550 μM, LCG at 500 μM, trypsin at 5.7 U/L, SC4-C5 at 1 μM) in 10 mM NaH_2PO_4 buffer, pH 7.0, 25°C. **C.** The initial membrane transport rate increases with polylysine concentration. **D.** Resulting Hill plot for SC4-C5. **E.** Linear dependence of the initial rates of the intravesicular enzymatic reaction on (calculated) internal polylysine concentration. Adapted with permission from Angew. Chem. Int. Ed. 2025, 64, e202425157. Copyright 2015 Wiley-VCH GmbH.[132]

substrate binding sites.[186–191] This enzyme-mimic function relates to the properties of these synthetic pockets. Several effects can come into play for these small receptors, including the preorientation of substrates in an ideal manner inside the pocket, stabilization of intermediate species or transition states (TS) allowing faster rates of reaction or even co-location of reactants in the pocket effectivelly increasing the chances of these to come into contact.[186–191] Additionally, it is known that pK_a shifts of ligands in protein binding pockets is essential for reactivity modulation, allowing enzymatic activity to happen accordingly.[192–194] The same properties are often observed for these much simpler macrocyclic receptors, where the high shifts of pK_a are driven by preferential stabilization of one of the species of the acid-base equilibrium over the other, either by hydrophobic effect or by electrostatic stabilization of the charged group (Figure 1.25).[193,194] These synthetic pK_a modulators have proven to be valuable in improving the bioavailability of several pharmacological agents, either by improved solubility, stabilization of the active form, protection against deprotonation/protonation dependant degradation pathways, among other effects.[194]

Several hosts are used for catalysis of different reactions, however both cucurbiturils and calixarenes see further application due to their advantageous properties.

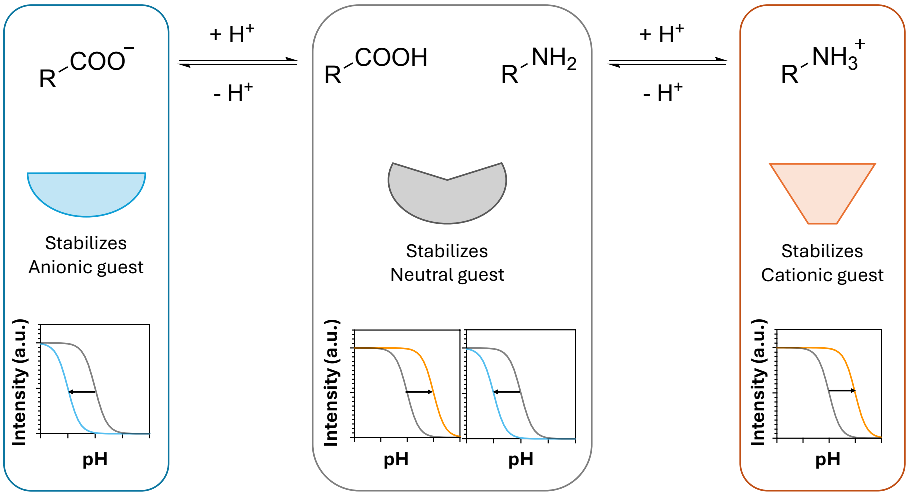

Figure 1.25: Schematization of pK_a shift by stabilization of one of the species by a supramolecular host, with examples of a carboxylate and primary amine functional groups.

p-Sulfonatocalixarenes can lead to catalytic effect through the simultaneous complexation of both reactant and metal ligands, through interactions with the negative portals. The aromatic panels of the calixarene can also play an important role acting as weak bases or nucleophiles. Basílio *et al.* have shown both these effects in the Ni^{2+}-catalyzed hydrolysis of 2,4-dinitrophenyl picolinate by SC4, SC6 and SC8, with the smaller two hosts improving reaction rates through the complexation of both reactant and metal ion and SC8 showing the contribution of the phenolate as a weak base in reaction rate enhancement.[188] Calixarenes have also proven to be versatile platforms for construction of synthetic enzymes, through careful functionalization of the upper rim to add the necessary catalytic and activating units. This is the case of the use of these hosts as synthetic RNases, through functionalization with copper (II) and zinc (II) complexes and guanidinium moieties, joining the catalytic effect of the former with stabilization/activating capacity of the latter. Furthermore, different sites of functionalization can lead to distinct preferential RNA cleavage sites, showing the ability to modulate the specificity of the catalysis process through host design.[187,195]

Cucurbiturils provide the sites for metal complexation, at their carbonyl portals, much like calixarenes, but their rigid structure often leads to improved orientation of enclosed reactants and, in some cases, selective stabilization of intermediates and transition states.[189–191,196–199] This is the case of the ability of both CB6 and CB7 to catalyze click reactions in water.[197] The reaction between azides and acetylenes in the vincity of ammonium groups was the first reported to happen inside the cucurbituril cavity (Figure 1.26 A). This reaction appears to occur mainly due to the improved orientation of reagents and their co-location near one another, leading to improved reaction rates up to 10 000 fold without the need to add metallic catalysts.[197,198] More recently, this system has been applied for the successful CB6-assisted click-cycloaddition of conjugates to proteins under mild, metal-free, conditions (Figure 1.26 B).[199] A recent work by Colaço *et al.* showed an example of the capacity for transition state stabilization of cucurbiturils, for the studied diazocine photoswitch (Figure 1.26 C i)). In this system the *Z* state is thermodynamically favourable over the *E* state, and CB7 is capable of catalyze the thermal conversion from *E* to *Z* species, through stabilization of the transition state (Figure 1.26 C ii)) with consequent release of the product.[191]

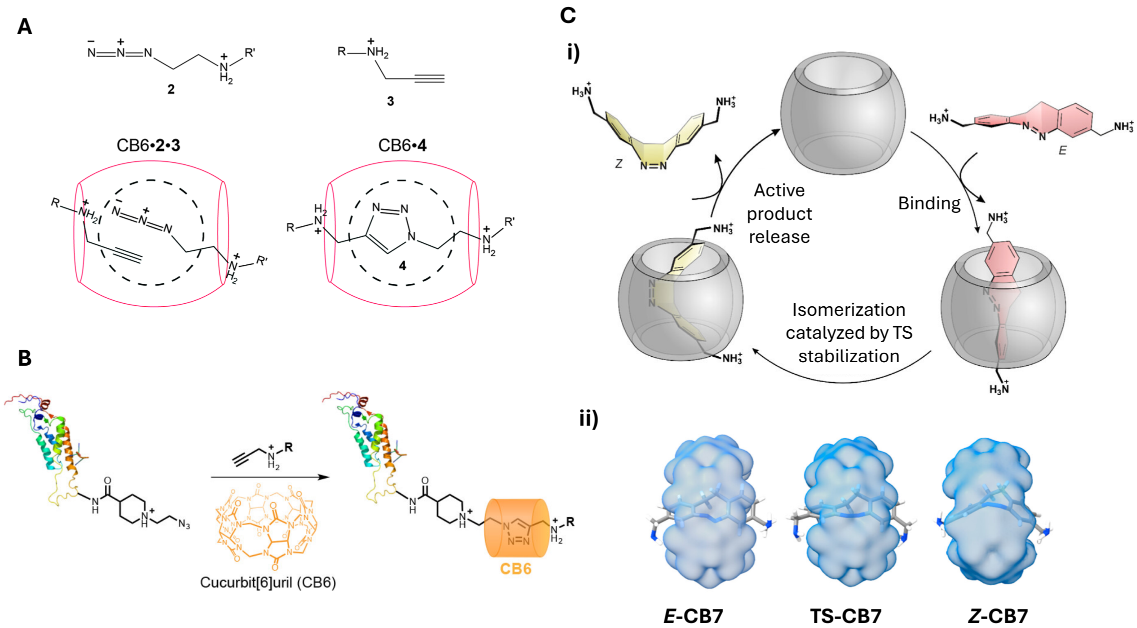

Figure 1.26: Examples of CB6 and CB7 as a catalysts, through reagent orientation and transition state stabilization. **A.** Click reaction of azide (2) and alkyne (3) to form a [1,2,3]-triazole (4) catalyzed by CB6. Adapted with permission from Chem. Soc. Rev., 2015,44, 394-418. Copyright 2015 Royal Society of Chemistry.[196] **B.** A protein bioconjugation strategy using CB6 click chemistry. An azidoethylpiperidine can be installed via n-hydroxysuccinimide (NHS) ester chemistry, providing a functional handle for subsequent modification via the CB6 click reaction. Adapted with permission from J. Am. Chem. Soc. 2017, 139, 28, 9691–9697. Copyright 2017 American Chemical Society.[199] **C.** i) Proposed catalytic cycle for the isomerization *E* $\longrightarrow$ *Z*-diazocine by supramolecular catalysis inside CB7. ii) Structures of the *E* isomer, the transition state (TS), and the *Z* isomer of the diazocine bound inside CB7. Geometries are optimized at the pbe/def2-SVP, D4 level of density functional theory. Slender structures of the *E* isomer and the TS fit well into the cavity of CB7, the bent *Z* isomer does not. Adapted with permission from J. Am. Chem. Soc. 2025, 147, 1, 734–745. Copyright 2025 American Chemical Society.[191]

1.3.3 Protein-Supramolecular non-covalent bioconjugates

A final example for synthetic supramolecular systems that aim at mimetizing biological systems is their application in combination with biomacrolecules. The marriage of biological and synthetic elements can take advantage of the imense functionalities provided by proteins, while modulation of its function can be achieved through small receptors and supramolecular scaffolds.[200]

The interactions that result from these assemblies have helped to clarify the nature of some protein-protein interactions (PPI) and can unveal novel targets for disease therapeutics. Acyclic supramolecular receptors have been found to be efficient in the modulation of biological interfaces, both by enhancement of the these interactions between biomacromolecules but also inhibiting the action of certain proteins by competing for their binding sites. This is the case of the molecular tweezers introduced by Schrader, which were found to stabilize an intrinsicly disordered protein-protein interface, between the protein 14-3-3 and the small peptide Cdc25CpS216, increasing the complex stability when compared to other studied PPI.[201] More recently, the use of a conjugated molecular tweezer with a peptidic guest for this same protein was employed as a PPI inhibitor and shows great potential for the design of novel therapeutic agents based on supramolecular and bioengineering solutions.[202]

Calixarenes have been used extensively as aids in co-crystallization of proteins, acting as "supramolecular glues", and can lead to the formation of complex frameworks with both biological and synthetic supramolecular components. The work by Peter B. Crowley and coworkers shows the versitality of different calixarenes as glues, showing that while the smaller calixarene of 4 units tends to encapsulate only one residue, the larger sulphonated calix[6]arene and calix[8]arene (SC6 and SC8) are capable of adapting more fully to the topology of proteins, and encapsulating different residues, even non-cationic ones (the example of SC8 binding to a pentameric lectin can be observed in Figure 1.27). These have successfully been used for encapsulation of proteins, formation of oligomers and highly hydrated porous frameworks.[35,203,204] Additionally, the same group has shown that non-covalent protein PEGylation can also be achieved through a functionalized SC4, with potential to increase protein half-life *in vivo* for therapeutic applications.[205]

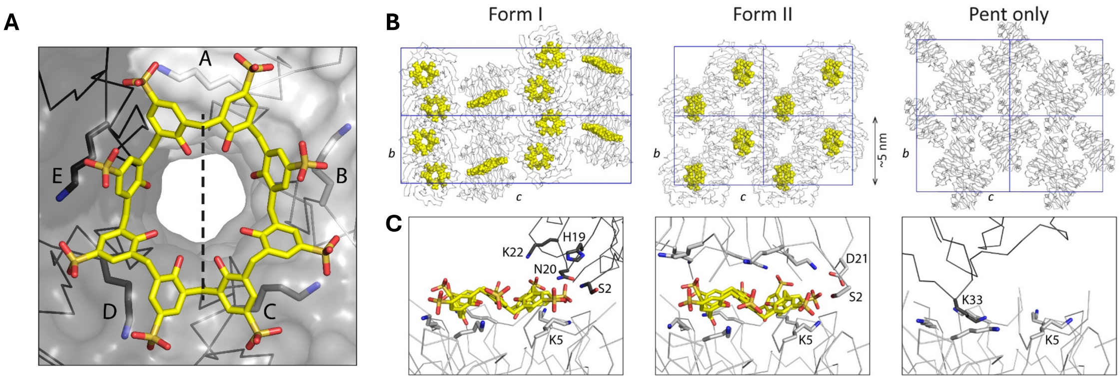

Figure 1.27: **A.** Crystalographic structure of SC8 binding pocket in pentameric lectin (subunits A-E). **B.** Packing of the crystal for the different forms of lectin-SC8 complex and lectin only, with the protein represented in grey and SC8 in yellow. **C.** Details of the binding sites with the relevant side chains shown as sticks. Adapted with permission from Biomacromolecules 2024, 25, 2, 1303–1309. Copyright 2024 American Chemical Society.[203]

Cucurbiturils have proven to be useful tools for the assembly of both natural occurring and engineered proteins into dimers, tetramers and other complex assemblies.[206,207] It is possible to add recognition moieties, e.g. N-terminal FGG-tags, to provide CBn anchoring sites for the binding of two or more proteins into complex structures in a controlled fashion. This can be used to modulate the function of different proteins, increasing the stability of these assemblies and creating novel bio-inspired therapeutic agents.[206] More complex structures can also be obtained, both by addition of CBn binding sites and by using naturally occurring binding sites. This includes the use of cucurbiturils as "supramolecular glues" as well, which can lead to the creation of complex layered crystalline structures, with variable flexibilities depending on the proteic elements with which these are cocristalyzed.[207,208]

1.4 Outlook

Clear advances have been achieved throughout the last decades, with supramolecular chemistry becoming a increasingly useful tool in biological applications. Nonetheless, in several fields, it is still necessary to continue to uncover how different molecular elements interplay and how we can effectively use them.

This thesis explores several of the fields presented in this introduction with a focus on the interaction of macrocyclic molecules with peptides and other relevant biological targets. The chapter structure follows the same structure as the introduction, going from simple recognition between hosts and their targets and incrementally increasing the complexity of the systems studied, for the development of sensors and transporters for different peptidic targets, ending with examples of biomimetic systems.

The following chapter (Chapter 2) of this dissertation studies two different cyclophane receptors, *p*-sulfonatocalix[4]arene (SC4) and Stoddart's Blue Box (BB) and their properties in terms of selectivity and affinity for different families of peptides. Chapter 3 applies these hosts in more complex assemblies, in both binary and heteroternary assemblies, using different macrocycles and dyes. A modified SC4 sensor is applied in the sensing of small model molecules, using both a competitive PET sensing strategy and the structural adaptability of SC4 in an IDA system. Additionally, a family of CB7-Dye-BB heteroternary complexes is presented and the ability of this system is explored for sensing of different drugs and peptides with orthogonal binding sites. Initial steps towards development of ditopic receptors presenting two macrocyclic moieties are presented as well at the end of this chapter. Chapter 4 explores systems that hinge on self-assembly (and disassembly) in both ordered and disordered structures as distinct sensing mechanisms. These strategies focus on the aggregation behaviour and changes of properties of the bound and unbound receptors to provide a higher capacity to distinguish very similar peptide targets. The last chapter (Chapter 5) explores the insertion of the more discrete systems in phospholipidic membranes, studying the capacity of these designs both as light-responsive transporters of hydrophilic peptides and as probes for the transport mechanism and for biomarker sensing at the membrane surface.

2

Characterization and Recognition properties of cyclophane hosts

In order to reach well thought out, complex supramolecular assemblies, a fine understanding of all of its elements needs to be reached. While it is known that Stoddart's Blue-Box (BB) is a promiscuous receptor with mM affinities for some specific aromatic compounds, its study for the binding of peptides with aromatic and anionic residues remains lacking.[76,77] *p*-Sulfonatocalix[4]arene (SC4) has been found to reach nanomolar affinities towards polycations, but there is a need for further enlightenment into the stoichiometry of such complexes as well as if they present well-defined binding sites or of these are more dynamic systems.[60] The aim of this section is to go into these host:guest interactions in discrete systems with the aim to clarify their properties. With this characterization done, it opens the way for the application of these cyclophanes in more complex systems, as will be discussed in later chapters.

2.1 Blue-Box as a receptor for C-terminal aromatic residues

BB, as described in section 1.1.2, is not often used as a receptor outside its application in rotaxanes and supramolecular responsive materials. Despite its higher affinity towards Trp ($K_a = 1.1 \times 10^3 M^{-1}$, in 50 mM phosphate buffer pH 7), this receptor does not appear to have specificity towards this amino acid when compared to, for example, indole and norepinephrine ($K_a = 7.1{\times}10^3 M^{-1}$ and $K_a = 1.5{\times}10^3 M^{-1}$, respectively, in 0.3 M phosphate buffer pH 7).[76,77] However, in the context of a peptide, the positioning at N and C-terminal, or at other sites, can influence the binding properties of the guest. It is known that the aromatic carbons at the bipyridinium unit present an acidic character that allows the establishment of additional R-C-H$\cdots$O-R interactions, which, added to ionic ones with the C-terminal, need to be taken into account as well for the overall binding affinity.[33]

Thus, the binding of BB tetrachloride salt species with different peptides, that present these aromatic and negative residues, is presented in this section (Figure 2.1). To this end a small library of amino acids and peptides with these residues was put together to evaluate the influence of positioning of residues in the affinity towards this receptor: DL-Tryptophan (Trp), DL-Phenylalanine (Phe), L-Tyrosine (Tyr), L-Glutamate (Glu), L-Aspartate (Asp), WGGGG, GGWGG, GGGGW, GGGGY and GGGGF. The photophysical and thermodynamic characterization of these complexes was done by UV-Visible (UV-vis) spectroscopy and Isothermal Titration Calorimetry (ITC).

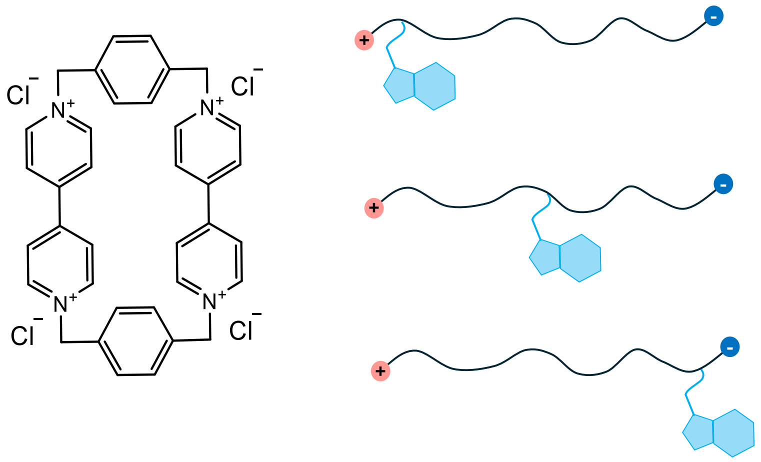

Figure 2.1: Chemical structure of the Blue-Box receptor and schematization of some of the target flexible peptides, presenting tryptophan residues at different sites.[209,210]

Initial studies were done by UV-vis spectroscopy in water at pH 7, by following the appearance of the Charge Transfer (CT) band upon titration of BB with each given analyte. For the aromatic amino acids, the characteristic CT bands were observed at distinct wavelengths for each guest, at lower energy, a behaviour typical for these types of complexes, with a increased red-shift the better the electron donor the guest (λ_{CT} is 415, 400 and below 400 nm for Trp, Tyr and Phe, respectively).[76] The respective affinity constants obtained from this data were concordant with previously reported values (Table 2.1 and Figure 2.2) and, while the appearance of the CT absorbance band cannot confirm the inclusion of the guests in the cavity, seeing as association in the outside face is also possible, it is a clear indication of a successful association.[209,210] On the other hand, negative, non-aromatic amino acids showed a general increase of baseline, without a clear CT band appearing, concordant with the aggregation of the BB-amino acid complex due to charge neutralization and no quantitative information could be obtained. ITC studies of the binding of aromatic amino acid to BB yielded comparable affinity constants, however, due to these being relatively low, the full thermodynamic parameters could not be accurately obtained for these smaller guests, due to the lack of initial plateau in the ITC isotherms (see Figure 2.3 A).

Titration of BB with the small peptide library also led to the appearance of CT bands at the same wavelength as the correspondant aromatic amino acid residue present. The appearance of this characteristic band indicates that the binding is occurring at the aromatic residue. While the affinity for GGWGG remains in the same order of magnitude as that of the aromatic amino acid, the peptide with this residue in both the N- and C-terminals,

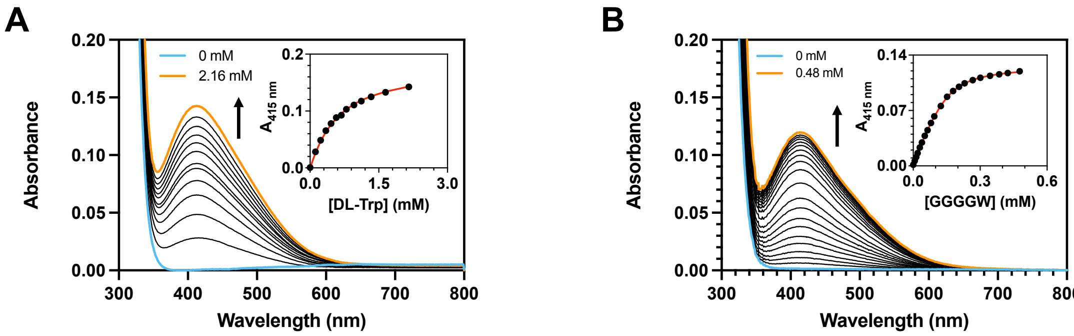

Figure 2.2: Direct titration of BB (0.2 mM) with **A.** DL-Trp and **B.** GGGGW, followed by UV-vis spectroscopy. In both cases the appearance of a CT band can be observed at λ = 415 nm.

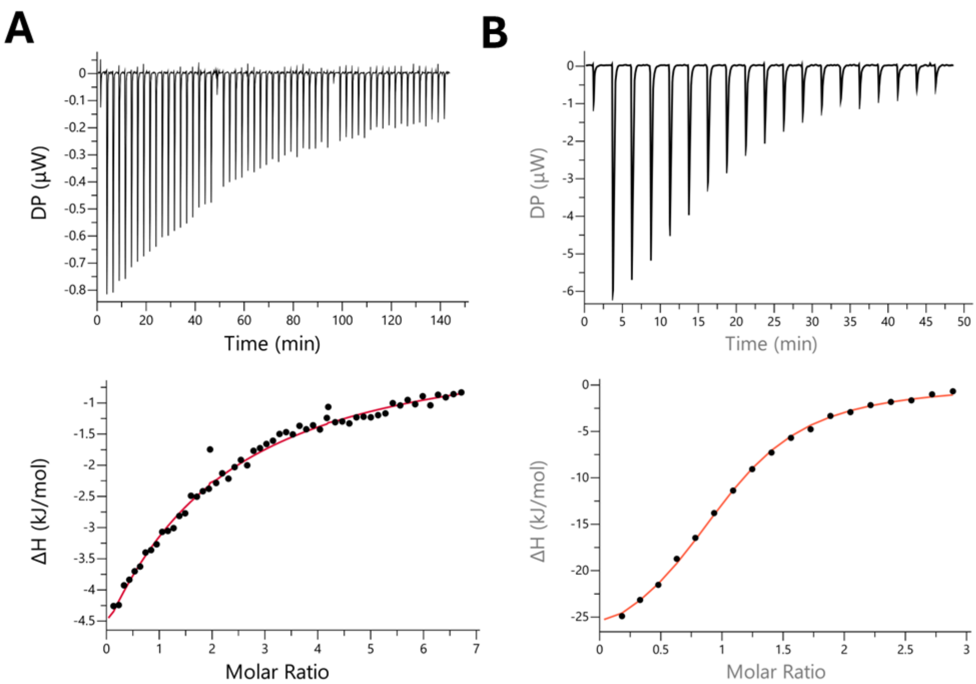

Figure 2.3: ITC isotherms of titration of **A.** BB (0.1 mM) with DL-Trp and **B.** GGGGW (0.1 mM) with BB, at 25°C. Number of sites obtained for the binding of BB to GGGGW was 1.07 ± 0.02, while number of sites was not obtained for DL-Trp due to lack of full isotherm curve.

Table 2.1: Affinity constants (K /M^{-1}) and thermodynamic parameters (ΔG, ΔH and -TΔS / $kJmol^{-1}$) calculated by direct titration followed by UV-vis and ITC. All experiments were carried out in water pH 7, at 25 °C.

Guest	**UV-vis**	**ITC**			
	K / M^{-1}	K / M^{-1}	ΔG / $kJmol^{-1}$	ΔH / $kJmol^{-1}$	$-T\Delta S$ / $kJmol^{-1}$
L-Tyr	-[a]	$3.6 \pm 0.1 \times 10^2$	-15.8 ± 0.3	-[b]	-[b]
DL-Phe	1.7×10^2	$< 1 \times 10^3$	-[c]	-[c]	-[c]
DL-Trp	2.0×10^3	$3.0 \pm 0.5 \times 10^3$	-19.9 ± 0.4	-[b]	-[b]
WGGGG	1.8×10^4	$1.3 \pm 0.1 \times 10^4$	-23.6 ± 0.1	-[b]	-[b]
GGWGG	4.2×10^3	$5.7 \pm 0.4 \times 10^3$	-21.5 ± 0.2	-[b]	-[b]
GGGGW	1.0×10^5	$7.1 \pm 0.4 \times 10^4$	-27.7 ± 0.1	-25.4 ± 0.4	-2.3 ± 0.5
GGGGY	1.2×10^4	$6.6 \pm 0.1 \times 10^3$	-21.8 ± 0.1	-[b]	-[b]
GGGGF	1.9×10^3	$7.5 \pm 1.0 \times 10^3$	-22.1 ± 0.3	-[b]	-[b]

Values for this parameter were not obtained due to [a] poor solubility of guest stock solution, [b] lack of initial plateau in ITC isotherms, due to low affinity constant and [c] low affinity of the guest towards BB.

WGGGG and GGGGW, present an increase in affinity for this host with a more significant increase for GGGGW. While the differences are not high enough to form a solid conclusion, it seems that the presence of the negative charge does contribute to a stronger binding, both for the peptides with Trp residues in C-terminal and for the ones with Tyr and Phe (Figure A.3), as well. The reason for the increased of affinity for WGGGG is not clear, yet it could be due to the flexibility of the glycine residues, which could allow the nearing of the anionic site to the receptor, where GGWGG would not have the glycine chain long enough to allow it. Further studies with peptides with longer chains could clarify this, e.g. GGGGWGGGG. Aditionally, structural studies by NMR could also help clarify if any significant conformational changes are occurring upon binding to BB or if other effects are at play.

Furthermore, much like what was observed for the amino acids, the study with the peptides with different aromatic residues at the C-terminal shows that the affinity increases with the increase of the electron donor capacity of each residue (with the ΔE between Lowest Unoccupied Molecular Orbital (LUMO) and HOMO being ≈ 5.2, 5.7 and 6.2 eV, for Trp, Tyr and Phe, respectively).[76,211,212]

For the peptide with tryptophan in the C-terminal, the affinity was high enough that the thermodynamic parameters could be obtained by ITC. These indicate that the binding has a greater enthalpic contribution, when compared to that of entropic effects. Considering the small size of BB's cavity, leading to a small number of water molecules present in the cavity, and the ready appearance of CT band, it indicates that the binding is mostly driven by the π-π donor-acceptor interactions and ionic ones between host and guest, much like previous studies with BB but, seemingly, with ionic interactions leading to increased affinities towards this host.[213,214] Unfortunately, the effect on thermodynamic parameters of the added electrostatic interaction in the C-terminal when compared to the increase observed for the peptide with Trp at the N-terminal could not be clarified due to the low affinities and low solubility of some of these guests.

Despite the small differences and inconclusive thermodynamic characterization this is valuable information for the effective design of novel and more complex systems, like the one discussed in Chapter 3.

2.2 SC4 as a receptor for cationic residues

This subsection was done in collaboration with MSc. Kevin Droguett from Universidad Pontificia de Santiago do Chile, who performed some of the competitive assays and ITC assays, as well as in collaboration with Dr. Filipa Marcelo, Dr. Ana Sofia Ferreira and Dr. Ana Sofia Grosso, from the Structural and Molecular Biology Research Group, at UCIBIO, FCT NOVA, who helped in the development of the quantification assay and further aquisition and interpretation of the NMR spectroscopy data.

SC4 derivatives offer an electron-rich aromatic binding pocket decorated by negatively charged sulfonate groups, which is particularly selective towards a series of relevant biological targets, including methylated Lysine (Lys) and Arginine (Arg) amino acids over their parent unmethylated counterparts. The utility of these receptors has been successfully demonstrated in various applications, as discussed in farther detail in the previous chapter.[47,55,56,59–61]

Albeit their only moderate affinity towards unmethylated lysine and arginine residues, SC4 derivatives and their larger cavity analogs selectively bind arginine- and lysine-rich peptide sequences with affinity constants reaching values higher than 10^9 M^{-1}.[47,60,215]

While it is known that binding of these receptors to its cationic guests is mostly driven by cation-π interactions, stoichiometry of the complexes and effect of multivalent binding on guests' structure is yet to be delved into. It is also unclear if there is any preferential binding site in these larger targets.

In this section of the work, the complexation of SC4 with different oligoarginines was evaluated by ITC, NMR and fluorescence spectroscopies. The library of oligoarginines selected was RRGG-NH_2, RRRG-NH_2, RRRR-NH_2, RRRRRR-NH_2 and RRRRRRRR-NH_2 (R_2G_2, R_3G, R_4, R_6 and R_8, respectively), in order to compare guests presenting one or more binding sites, as well as different affinities for the host.

2.2.1 Quantification of oligoarginines

Due to the hygroscopic nature of these peptides, difficulties in descerning stoichiometry led to inaccurate or often only apparent quantitative analysis of the complexes. To avoid this issue, the first objective of this work was to develop a simple and rapid quantification protocol for these oligoarginines. For that effect, two methods were used in tandem: ^{1}H-NMR and fluorescence spectroscopy. The initial quantification would be done by quantitative NMR and the concentration value would then be used to calibrate an IDA, using SC4 and a known indicator, in order to use this technique for calibration of stock concentrations in the future. The indicator chosen for the SC4 host was the dye Lucigenin (LCG), due to its stability, well reported binding to this host and high variation of its quantum yield between its free and bound states.

Quantification by ^{1}H-NMR spectroscopy was done by comparative method, with an internal reference added in a known concentration to a coaxial tube, as described in Section 7.5.3. The chosen reference was maleic acid due to its alkene protons being located in a region where no calixarene or peptide proton chemical shifts (δ) are expected to appear. Quantification was possible due to the consistently distinct chemical shift of one of oligoarginines α protons (H_α) from the remainder ones, which was attributed to the N-terminal H_α. ^{1}H-NMR spectra used for quantitive analysis can be found in Figure 2.4 for R_4 and in Figure A.5 for the remaining peptides. When accounting for the volume ratio between inner and outer NMR tubes (see Section 7.5.3), integration of both reference and H_α signals allowed the obtention of the relative concentration of the peptides in D_2O solution.

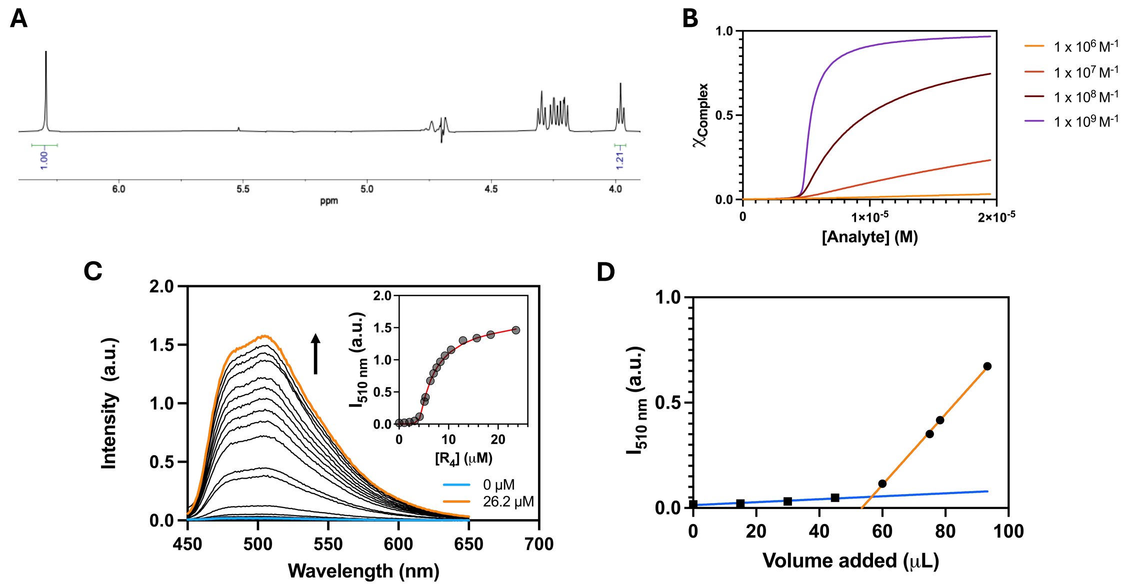

Figure 2.4: **A.** Cropped ^{1}H-NMR spectrum used for the quantification of R_4, by referencial method, using maleic acid as a reference (δ = 6.29 ppm, d_1 = 25 s) and one of R_4 H_α (δ = 3.98 ppm). **B.** Comparison of binding curves for the LCG-SC4 for guests going from μM to nM affinities. **C.** Indicator Displacement Assay of LCG (0.1 μM) from SC4 (3 μM) with R_4, followed by fluorescence spectroscopy (λ_{exc} = 369 nm).

The method chosen for routine quantification was the Indicator Displacement Assay (IDA) with the well characterized, high affinity SC4-LCG host-guest pair ($K_{SC4-LCG}$ = 8.1×10^7 M^{-1}, see Table 2.2). This competitive method allows the determination of non-emissive guests' concentration by a more accessible, less expensive technique. Due to the high affinity of these complexes, if an excess of host is present in the initial host-dye solution, the guest with an unknown concentration will first saturate this host, without displacement of the dye, not inducing an optical change (this is visually represented in Figure 2.4 B using the LCG-SC4 affinity and different SC4-guest affinities as examples). Once the free host is saturated, further addition of guest will displace the dye with a concurrent change in emission, which would give an indication of when, approximately, 1 equivalent of analyte to host has been added to the mixture.

Having confirmed the concentration of the peptide stock solutions by NMR quantification, these were used to obtain an accurate value of affinity and stoichiometry for the binding (Figure 2.4 C, for the peptide R_4 and Figure A.6 for the remaining peptides), with the affinity values presented in Table 2.2. At micromolar concentrations, the only peptides that appeared to present the 1:2 binding were the two with a higher amount of effective charges, R_6 and R_8.

With these factors now measured in a more accurate fashion, using quantified peptide solutions, quantification can be done of other stock solutions using the IDA method, with easily accessible equipment, by applying the values presented in Table 2.2 and fitting for peptide concentration.

Table 2.2: Affinity constants (K /M^{-1}) and thermodynamic parameters (ΔG, ΔH and -TΔS / kJmol^{-1}) calculated by direct titration followed by IDA and ITC. All experiments were carried out in phosphate buffer 5 mM at pH 7.4, at 25°C.

Guest	IDA		ITC			
	K_{11} / M^{-1}	K_{12}/ M^{-1}	K / M^{-1}	ΔG / kJmol^{-1}	ΔH / kJmol^{-1}	$-T\Delta S$ / kJmol^{-1}
LCG	8.1×10^7 [a]	- [b]	$(1.2 \pm 0.2) \times 10^8$	-46.1	-43.2 ± 0.2	-2.91
R_2G_2	5.8×10^6	- [b]	$(1.8 \pm 0.1) \times 10^6$	-35.7	-53.3 ± 0.3	17.7
R_3G	5.3×10^7	- [b]	$(7.7 \pm 1.4) \times 10^6$	-39.7	-50.3 ± 0.9	10.5
R_4	1.8×10^8	- [c]	$(3.0 \pm 0.6) \times 10^7$	-43.3	-45.6 ± 0.6	2.32
R_6	5.2×10^8	2.2×10^5	-	-	-	-
R_8	4.4×10^{10}	4.7×10^7	-	-	-	-

[a] Affinity value reported by our group in the same conditions.[215] [b] Appears to only present 1:1 binding. [c] 1:2 petide:calixarene complexes observed in NMR but the value of K_{12} is too low to be detected in the range of concentrations used.

2.2.2 Characterization of SC4-oligoarginine complexes

Having established a system for quantification of peptide solutions, the complexes were analysed by NMR spectroscopy and ITC.

To that effect, the binding of SC4 to two different peptides, R_2G_2 and R_4, was evaluated by titration of the peptides with SC4, followed by ^{1}H-NMR, in phosphate buffer 5 mM pH 7.4 in a 90%:10% H_2O:D_2O mixture.

Full characterization of both the free peptides and the complexes at different peptide-host ratios was done through the analysis of the 2D ^{1}H-Total Correlation Spectroscopy (TOCSY), ^{1}H-Rotating Frame Nuclear Overhauser Effect Spectroscopy (ROESY) and ^{1}H-^{13}C-Heteronuclear Single Quantum Correlation (HSQC) spectra, that can be found in their entirety in the Supplementary Information (Figures A.7 to A.27). This allowed the assignment of the peptide chemical shifts by analysing both the typical ^{13}C and ^{1}H shifts for the different arginines (Figure A.28), as well as by analyzing the full spin system in the TOCSY experiment and the through space interactions established between them in the ROESY experiment.[216,217] Performing the experiments in a 90%:10% H_2O:D_2O mixture allowed the confirmation of the N-terminal residues by the absence of H_{NH} chemical shift, due to increased proton exchange for deuterium. For R_2G_2, a through space interaction between an Arg and Glycine (Gly) residue allowed their identification and the distinction of Gly3 from the C-terminal Gly. In regards to R_4, Arg4 was identified by a Nuclear Overhauser Effect (NOE) signal between the amide proton between Arg3 and 4 and the amide at the C-terminal, while clarification between Arg2 and Arg3 was possible due to the through space interaction between Arg4 H_α shift and Arg3 NH proton.

When analysing the full titrations with SC4, it was observed that some of these arginine H_γ and H_δ suffer a significant upfield shift with increasing concentrations of the host, in both peptides. This is commonly observed upon guest inclusion into the calixarene cavity, due to the shielding effect of the hosts' aromatic rings. The lower shift, and even downfield shift of the remainder arginine protons suggests that these remain on the outside of the cavity, while those closer to the guanidinium group, in the side chain, are bound in the cavity. The guanidinium protons are only observable with excess calixarene so their complexation-induced chemical shift could not be evaluated. On the other hand, most of the nitrogen-bound protons suffer a sharpening of their signal when in the presence of excess of SC4, which could be indicative of decreased solvent exposure of these moieties, reducing the proton-deuterium exchange rates.

For both peptides, the predominant binding site seems to be Arg1 (Figure 2.5 C and Annex A.30), due to the corresponding protons suffering the largest complexation-induced chemical shift, concordant with encapsulation in the calixarene cavity. For both peptides, the chemical shifts associated with this residue have an initial change that appears to stabilize near the equivalence point. The remaining residues of R_2G_2 reach saturation with a small excess of calixarene, suggesting a 1 to 1 binding ratio for this complex. On the other hand, some R_4 proton chemical shifts continue to change after the equivalence point and up to at least 10 equivalents of SC4, in particular for Arg4. This suggests that there is a 2 to 1 binding ratio of receptor to peptide, with the initial binding of one calixarene to Arg1 and the second one binding predominantly to Arg4, which suffers a marked upfield shift only after the equivalence point. The binding sites in Arg1 and Arg4 are likely due to the tendency of the system to reduce repulsion between the two highly anionic hosts, leading to the two binding sites being at the terminal residues.

The binding curves obtained from the titration data discussed above, presented in

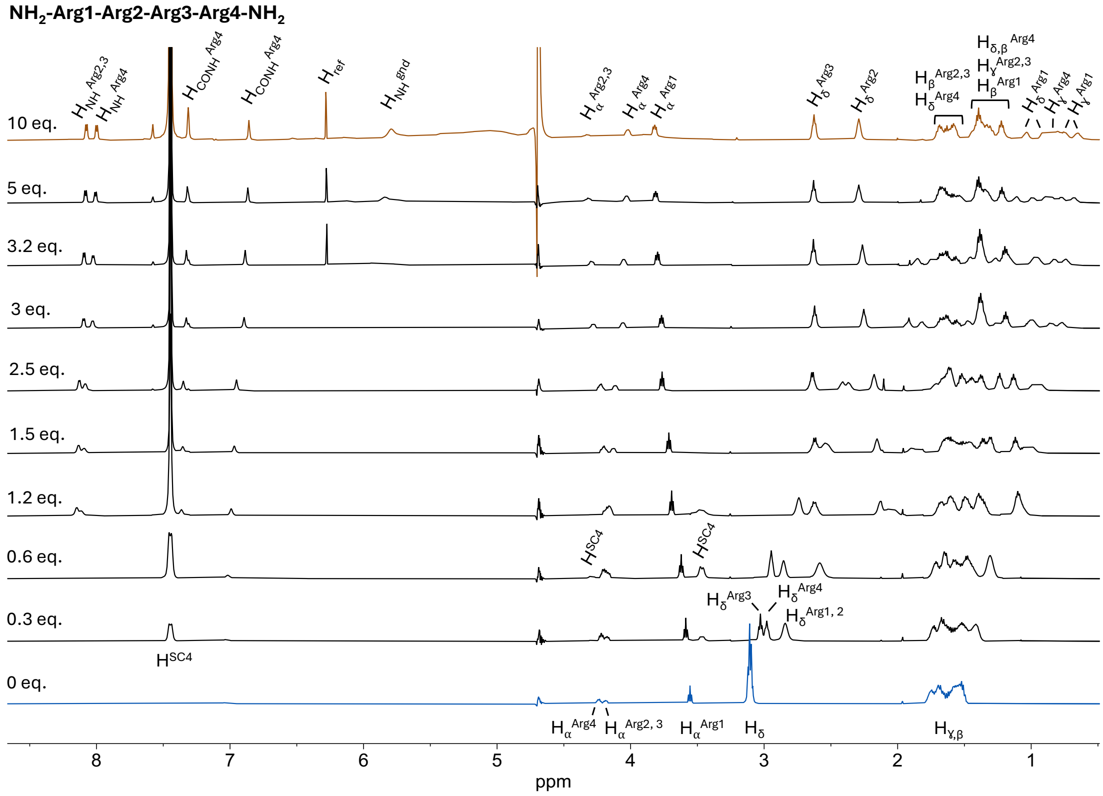

Figure 2.5: Titration of peptide R_4 (0.59 mM, quantified by LCG-SC4 IDA, Figure A.29) with SC4 followed by ^{1}H-NMR spectroscopy.

Figure 2.6, support this hypothesis. Because these chemical shifts are all dependent on the same binding processes, simultaneous fitting of all the curves yielded identical affinities for the same host:guest system (outliers were more prevalent in the case of the R_4 titrations due to the necessity to prepare solutions in batch above 1.5 equivalents, see methods in Chapter 7). Due to the high affinities of these complexes and high concentrations at which the NMR studies are done, the 1:1 affinities (K_{11}) obtained by this method are innacurate, reporting only that these values are above 1×10^5 M^{-1} for both peptides. However the binding of the second host unit to R_4 is supported by the presence of a second binding process which presents a lower affinity of $K_{12} = 7.4 \times 10^2$ M^{-1}.

The source of the changes observed for Arg2, with its signals first presenting a marked upfield shift, and a slight downfield shift when excess of SC4 is added, has not yet been clarified. It is tentatively suggested either a distribution of two populations when the 1 to 1 peptide-SC4 complex is predominant, with SC4 binding either Arg1 or Arg2 or, alternatively, the initial upfield shift being caused by Arg2 association to the host on the outside face of the calixarene, forming ionic and cation-π interactions with the aromatic panel. In both cases, the downfield shift at higher host concentration could be due to structural rearrangement of the peptide, both moving Arg2 away from the host.

Thermodynamic characterization by ITC is presented in Table 2.2. These studies show that the binding is mostly enthalpy driven, with the smaller peptide presenting a

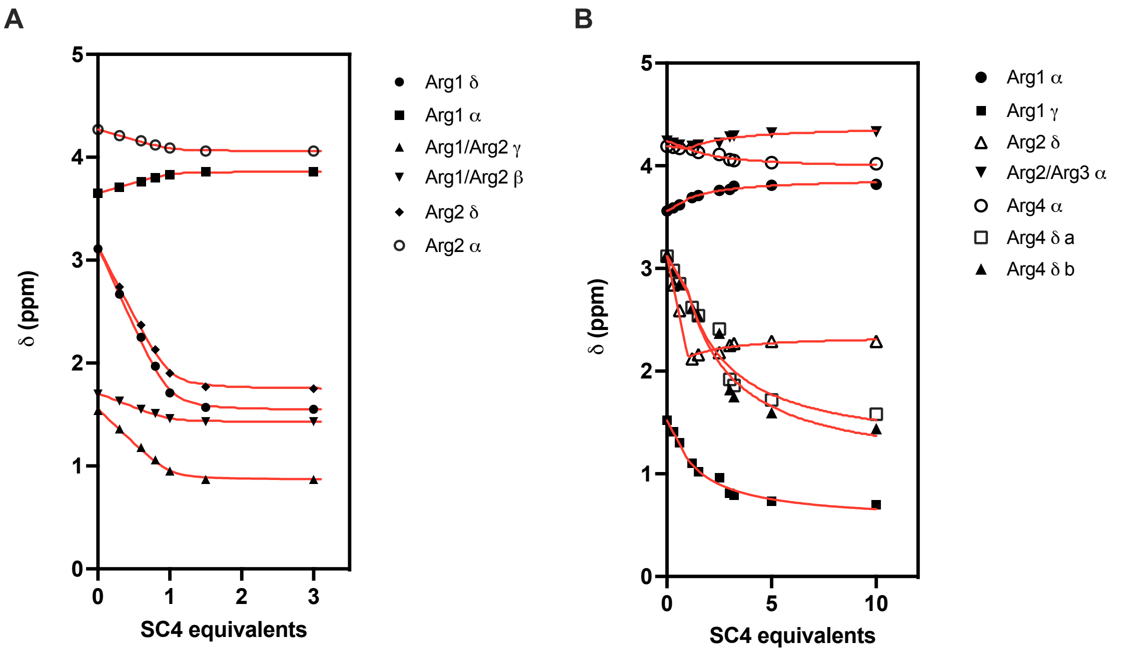

Figure 2.6: Chemical shift variation of **A.** R_2G_2 and **B.** R_4 at different equivalents of host SC4, followed by H^1-NMR. Assignment of chemical shifts presented was done using the 2D experiments mentioned, at different SC4 equivalents.

considerable entropy penalty to the binding. The isotherms obtained for R_6 and R_8 seem to indicate that the binding of two SC4 is occurring, by the equivalence point obtained for the titration of host with guest ($N \approx 0.6$ and $N \approx 0.5$, for R_6 and R_8, respectively). However, it was observed that these solutions become turbid near the charge neutralization point, and this aggregation process appears to be interfering with the ITC experiments, hindering the obtention of the thermodynamic parameters (Figure A.31 and A.32).

It is necessary to evaluate the binding of SC4 to the remaining peptides by NMR spectroscopy, in order to ascertain if more than one calixarene unit binds to the three arginine peptide, and if more than two units can bind to the larger peptides. However, the ones that were studied by this technique aided in the understanding of the preferential binding sites of the host in these polycationic molecules. Additionally, a quantification method was established to determine the stoichiometry of the complexes at μM concentrations. The next chapters will build on this new information and use the SC4 host to develop more complex and applied supramolecular systems.

3

Binary and Heteroternary Discrete Sensing Systems in Water

In the previous chapter, a higher complexity system was already employed in the competitive assay used for characterization of SC4:peptide complexes. When it comes to sensing of small molecules with either synthetic or biological hosts, IDA and other assays based on competition are the gold standard for both qualitative and quantitative evaluation of binding of spectroscopically silent guests. Furthermore, the notion of competitive systems is already prevalent in both biological systems as well as pharmacological applications. Competitive interactions between several different elements, be it biological components or pharmacological agents, aid in the control of metabolic pathways and of key proteins related to disease.[218] Competition goes hand-in-hand with cooperative interactions and allosteric control, being the key mechanisms that modulate protein function. These mechanisms also exist for synthetic, non-covalent systems and so, these can be tools in the development of biomimetic supramolecular systems.[219–221]

The first section of this chapter will go into the development of a ratiometric IDA based on the SC4-LCG system described in the previous chapter. The ratiometric component is added by use of a dye covalently linked to calixarene. The second system, uses the macrocycle cucurbit[7]uril (CB7) in conjunction with BB and a family of hemicyanine dyes, that can form heteroternary complexes that can be used in receptor displacement assays, with different photophysical responses depending on which of these receptors is being displaced. Both of these systems aim at exploring the versatility of all these receptors but also the potential of supramolecular strategies in sensing and differenciation of guests in water, by approaching the concepts of competition and cooperativity and using them to our advantage.

3.1 SC4-4Py-Lucigenin ratiometric indicator displacement assay

Indicator Displacement Assays (IDA), as exemplified in the previous chapter, see application for the detection of a myriad of molecules. The possibility to mix and match different hosts with different dyes to uncover novel specificities and optical responses provide the simple IDA with unexpected versatility.[19,48,99,149,152,154,155] Additionally the insertion of the dyes in the calixarene structure can add to this versitility when applying these strategies in array-like sensing platforms (see Figure 3.1 A and B).[27] Despite being powerful tools, akin to many other turn-off or turn-on strategies, these assays can be susceptible to interferences by environmental factors and are dependent on probe concentration, which can impede quantitative analysis or lead to misleading results in qualitative ones. One way to circunvent this is to use a ratiometric readout system. It is expected that, for a pair of dyes in the same system, the ratio of the two signals should be independent of probe concentration and their emission should be altered in a comparable manner when changes are introduced to the environment. This allows more accurate quantitative assays and alleviates the need for extensive controls in qualitative assays.[161–165]

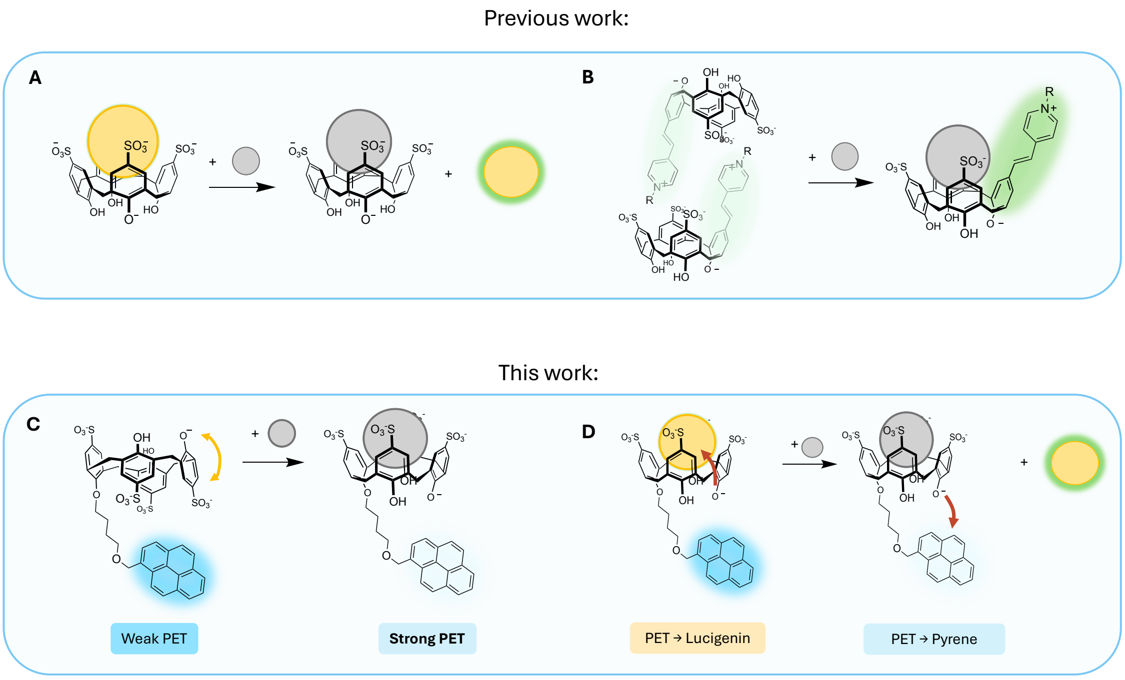

Figure 3.1: Schematization of sensing methods using calixarene hosts developed in previous work and the work presented in this chapter: **A.** typical IDA assay with calixarene and desired guest; **B.** Hof and coworkers DimerDye strategy using a calixarene modified with a fluorescent dye; **C.** PET modulated by conformational adaptation of calixarene and **D.** competitive PET strategy yielding a ratiometric signal, with the increase of lucigenin emission and quenching of pyrene emission upon guest binding.

Herein, a novel ratiometric indicator displacement assay is presented that explores both the modularity of IDAs and the ratiometric signal provided by the second reporter, covalently linked to the host. This strategy is based on the same SC4 receptor explored in Section 2.2, monosubstituted with an alkyl linker connecting it with a pyrene moiety (SC4-4Py, Figure 3.2). Lucigenin (LCG) is regularly used with this receptor, due to its high affinity towards SC4 and due to the almost complete quenching of its emission once bound, by photoinduced electron transfer (PET).[156] Additionally, SC4 aromatic moieties are rather flexible, both when unsubstituted or when the lower-rim substituents are smaller than propyl groups.[42] The sulfonate group on the other hand, is not able to transverse the inside of the cavity, which means this flexibility gives free rotation for the passage of the phenol group on the inside of the host, being able to shift from cone to inverted cone conformation in this manner.[41,42] While the monosubstituted site does not present said flexibility, the remainder of the molecule will have a dynamic structure of the receptor in the absence of an analyte, which can overall increase the distance between quencher and indicator, decreasing the expected quenching of the pyrene unit by PET from the phenolate at neutral pH. Locking of the conformation by analyte binding should draw the phenolate nearer to the pyrene unit and lead to increased quenching. This binary design should lead to two distinct emission signals which vary in different manners. Firstly, when LCG binds to the SC4-4Py receptor unit, the emission of LCG should decrease extensively while pyrene's emission, despite becoming locked in cone conformation, should not be overly affected, due to the indicator LCG being a better electron acceptor than pyrene, competing for the PET by the phenolate unit. When a competitor is added, LCG should be released from the binding pocket, regaining its emission, while the competing effect for the PET process should disappear, leading to the expected quenching of pyrene emission, as observed for the quenching originating from conformational rearrangement of the calixarene moiety (see Figure 3.1 C and D).

SC4-4Py was synthesized by direct monoalkylation of SC4 with 1-((4-bromobutoxy)-methyl)pyrene in basic media and isolated by reverse-phase chromatography (see Chapter 7.2.1, Figure 7.1). Despite its similarities with the parent host SC4, characterization of this novel sensor needed to be done, due to both its novel photophysical properties and to the eventual influence the monofunctionalization might have in its binding properties.

SC4-4Py presents comparable absorption and emission to that of other water soluble pyrenes. A quenching of the sensor emission was observed with increasing pH, which should correspond to the deprotonation of one of the phenol groups of the SC4 unit, with a pK_a of 5.6 (Figure 3.3). This quenching at pH values above the phenolate pK_a is a strong evidence that the mechanism involves an electron transfer from the phenolate to the excited pyrene. In the protonated form, phenol, either this mechanism is absent or is much less important.

SC4-4Py ^{1}H-NMR spectrum at neutral pH presents a broadening of the proton signals of the SC4 methylene bridges and aliphatic tail protons (Figure 3.5). This phenomenon is thought to be caused by decreased rate of conformational shift, due to stabilization of the deprotonated phenolate by formation of intramolecular hydrogen bonds, which is common for the calixarene unit.[222] The marked decrease of pK_a is also in line with the aditional stabilization of the phenolate form by an intramolecular hydrogen bond when compared to its monomer unit (phenolsulfonic acid, phenol moiety pK_a = 9.1), which corresponds to a high ΔG variation of 19.9 kJmol^{-1}.[223]

A family of known SC4 guests with biological interest, found in Figure 3.2, was chosen to evaluate the binding properties of SC4-4Py and to test this novel ratiometric IDA.

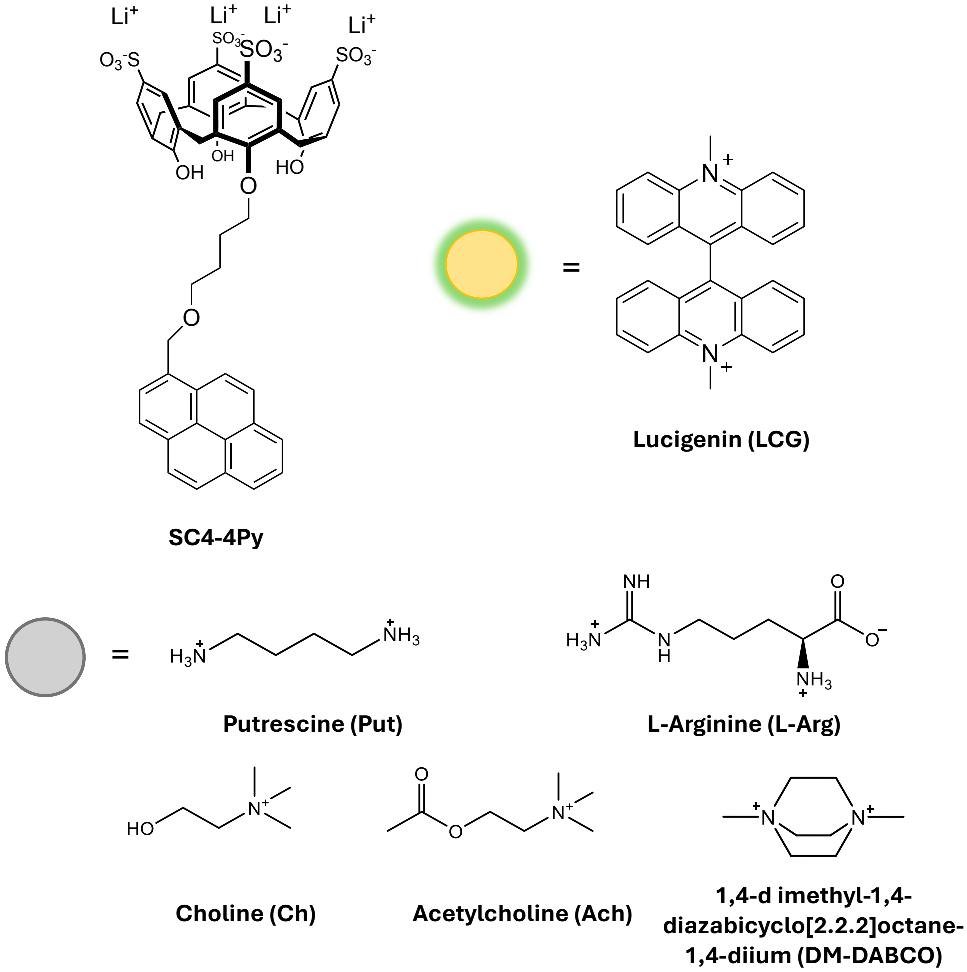

Figure 3.2: Structure and schematization of SC4-4Py and dye Lucigenin (LCG) and SC4-4Py and calixarene guests analyzed in this section.

Direct titration of SC4-4Py with Putrescine was done both at acidic and neutral pH to evaluate the extent of quenching of this sensor in the presence of a guest. Little to no quenching of pyrene emission was observed at acidic pH, below the phenolate pK_a, while at neutral pH, pyrene's emission was reduced to almost 60% of the initial value (Figure 3.3 B and C), despite the host being in an already partially quenched state. Quenching by the guest counterions was excluded by the lack of quenching of SC4-4Py emission by the sodium salts of I^- and Cl^- (Figure B.1). Furthermore, a sharpening of calixarene ^{1}H-NMR signals in the presence of both acetylcholine and the spherical, dicationic guest, 1,4-dimethyl-1,4-Diazabicyclo[2.2.2]octane (DM-DABCO), was also observed (Figure 3.5 B and B.10). This process is more marked for DM-DABCO possibly due to both better shape and size complementarity, but also due to its higher affinity for this host. The sharpening of calixarene ^{1}H-NMR signals could be related with the rigidification or locking of the calixarene conformation upon guest binding.

^{1}H-^{13}C-HSQC experiments support that the calixarene in the presence of guest is in its cone conformation, seeing as it presents the typical carbon chemical shifts observed

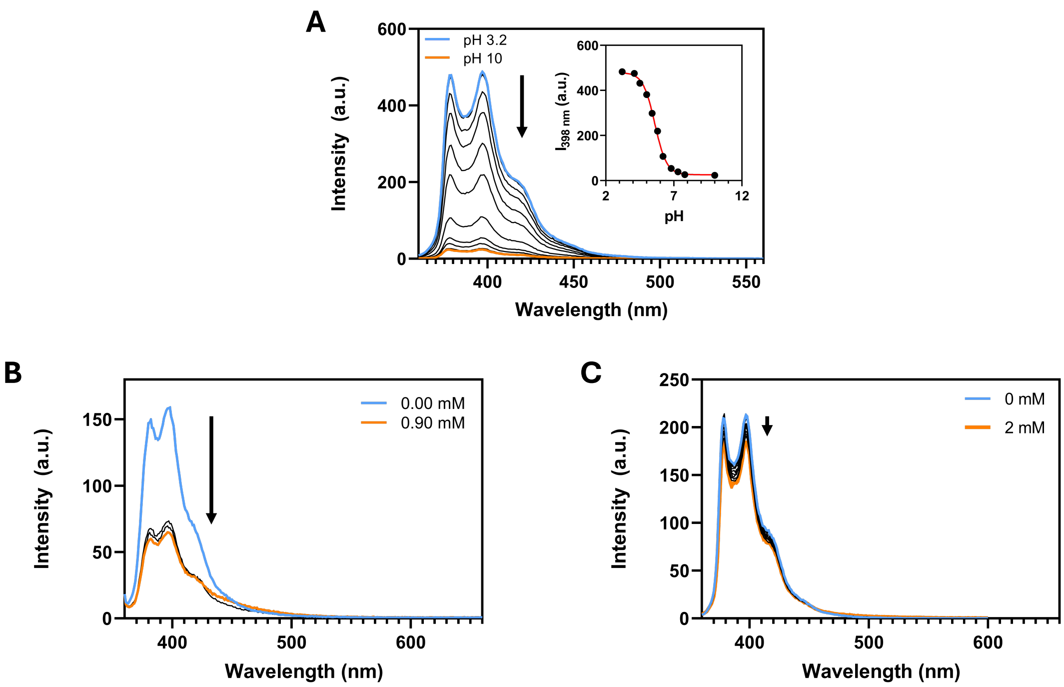

Figure 3.3: **A.** Fluorescence spectra of SC4-4Py at different pH in phosphate buffer 5 mM and respective pK_a fitting of the data, yielding a pK_a for deprotonation of one of the SC4-4Py's phenolate group. Direct titration of SC4-4Py (2 μM) by Putrescine at **B.** pH 7.4 and **C.** 3.4 in 5 mM phosphate buffer.

for this conformation, as well as the typical pattern of two sets of calixarene methylene-bridge doublets, caused by the equatorial and axial protons being in distinct environments (Figure 3.5 C, full HSQC spectra in Figure B.6). Due to signal broadening of SC4-4Py chemical shifts at pH 7, no conclusion could be drawn for the conformation of this receptor when free in solution. Nonetheless, it is suggested that the rigidity induced by guest binding overall decreases the distance between the quencher and pyrene, leading to an eficient through space electron transfer from the phenolate ion to pyrene, resulting in the quenching of its fluorescence (Figure 3.4).

NMR studies were also done at pH 3 in the absence and presence of the guest DM-DABCO (see Figures B.7, B.8 and B.9), in order to confirm the conformational changes. Remarkably, sharpening of calixarene signals was observed for both samples. Decreasing of pH for the free SC4-4Py should break the hydrogen bonds established at neutral pH and lead to a rapid interconversion between conformations, which falls out of the regime of intermediate exchange, leading to the sharpening observed.[224] This is further supported by slight sharpening of SC4-4Py signals when the temperature is decreased from 25 to 5 °C(Figure B.11). At pH 3, addition of DM-DABCO leads to shifts in calixarene signals, including the splitting of SC4 methylene bridge protons into two doublets. Despite the ^{1}H-NMR spectrum suggesting the partial cone configuration of the free SC4-4Py sensor at pH 3, due to two of the methylene protons being in the same overall chemical environment, the

^{1}H-^{13}C-HSQC spectrum of this same sample presents the carbon chemical shifts usually associated with the cone conformation (see Figure B.9). It is hypothesized that at pH 3 SC4-4Py is in a more open cone conformation, making the methylene bridge proton environment more similar between axial and equatorial positions, however no conclusive results were obtained in this regard.

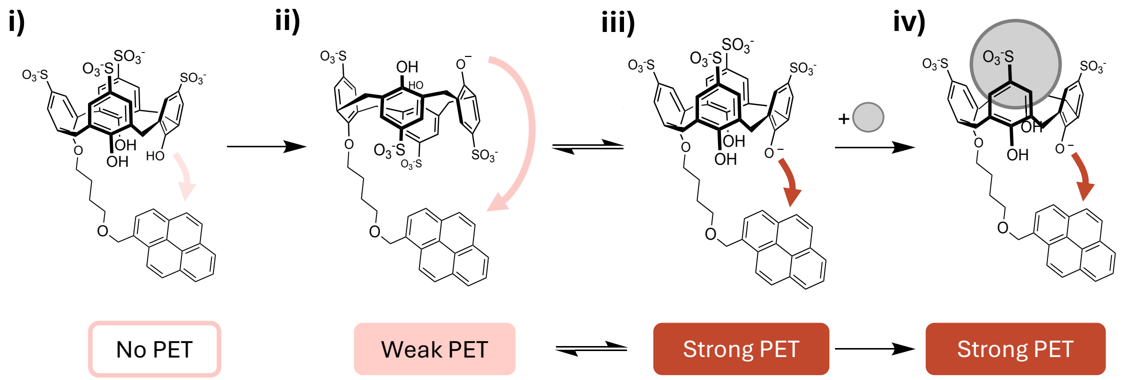

Figure 3.4: **A.** Schematization of the change in conformation dynamics proposed for SC4-4Py. i) Below phenolate pK_a, the calixarene remains flexible and the phenolate remains protonated, so little quenching is observed. It is expected that the calixarene changes between the conformation represented in ii) and iii), due to the formation of hydrogen bonds, where the phenolate is farther away from the pyrene unit and switches with a position where it is closer, respectively. iv) Binding of a guest leads to conformational blocking in the cone conformation, leading to the PET between phenolate and pyrene, resulting in further quenching of its emission.

After establishing the mechanism of sensing for the SC4-4Py, titration of LCG was done with the host, yielding almost complete quenching of LCG emission (Figure 3.6 A). The affinity obtained by fitting of the experimental data was of 1.7 x 10^7 M^{-1}, in the same order of magnitude as previously reported by our group for other mono-O-substituted calixarenes, showing that the monofunctionalization does not significantly affect the binding.[215]

Competitive assays were then performed with >90% SC4-4Py-LCG complex, with excitation at 340 nm and following both pyrene (360-400 nm) and lucigenin (450-600 nm) emission. Despite aggregates being observable at high concentrations of SC4-4Py and analyte, the displacement assays were maintained below Critical Aggregation Concentration (CAC) (Figure B.2). An initial quenching of SC4-4Py emission is observed, corresponding to the guest binding to the excess of host in solutions. Following this, LCG starts being displaced from the SC4 cavity and consequently suffers an enhancement of its emission. LCG emission seems to reach a lower plateau than expected, which is most likely due to the quenching by the counterions of the studied analytes (chloride, bromide and iodide anions, see Figure B.3 and Table B.1). The affinity constants obtained by fitting the ratio between LCG and SC4-4Py (I_{505nm}/I_{398nm}), while accounting for anion quenching of LCG emission (see Figures 3.6 and B.4), were in the same order of magnitude as other assays

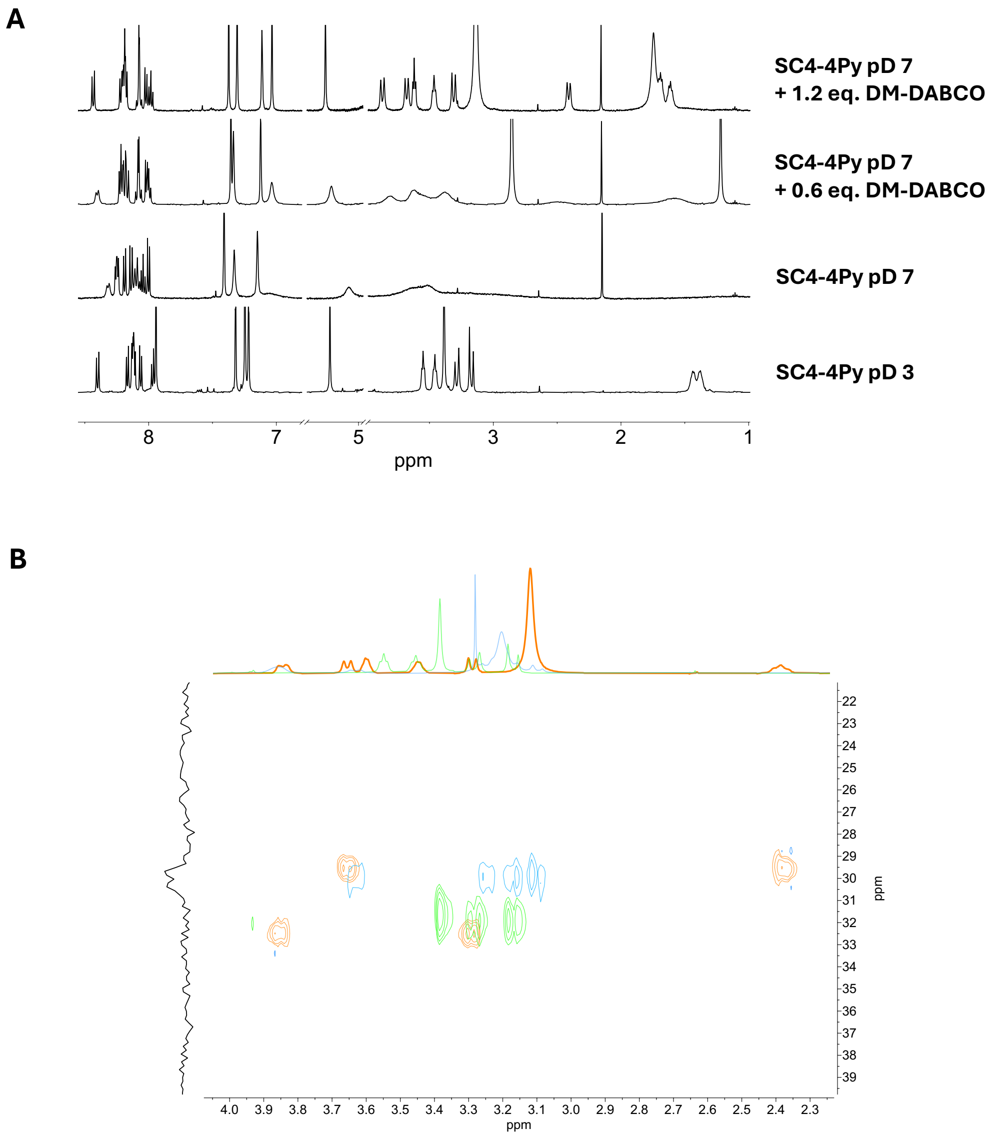

Figure 3.5: **A.** ^{1}H-NMR spectra of SC4-4Py at 0.5 mM, in the absence and presence of 0.6 and 1.2 equivalents of DM-DABCO at pD 7 and free SC4-4Py at pD 3. **B.** ^{1}H-^{13}C-HSQC of the SC4-4Py (0.5 mM) with 1.2 eq. of DM-DABCO pD 7 (orange), SC4-4Py (0.2 mM) with 1 eq. of DM-DABCO pD 3 (blue) and free SC4-4Py (0.5 mM) pD 3 (green). ^{13}C-NMR trace corresponds to the SC4-4Py-DM-DABCO sample at pD 3.

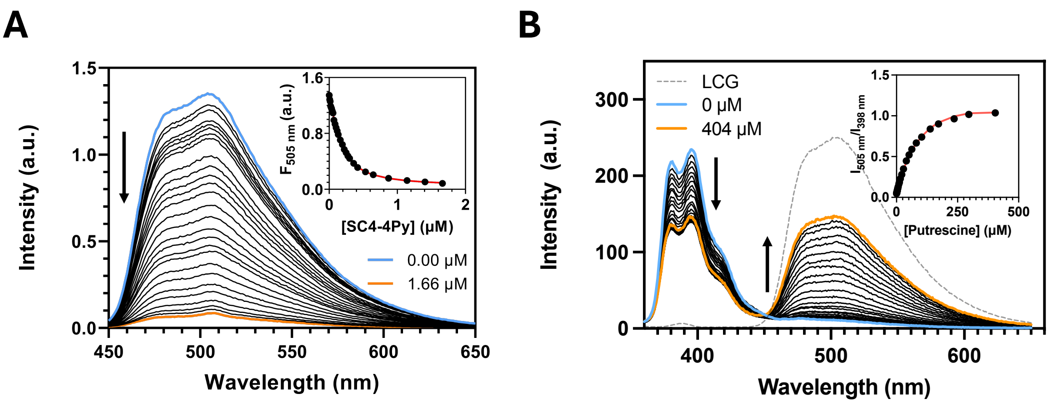

Figure 3.6: **A.** Direct titration of LCG, 0.19 μM, with SC4-4Py and **B.** displacement assay of Putrescine, done with LCG at 0.5 μM and SC4-4Py at 3 μM, followed by fluorescence spectroscopy. Fitting of the data found in inset was corrected for quenching of LCG emission.

previously reported in the literature, as well as those obtained by direct titration of SC4-4Py with the analytes (Table 3.1 and Figures B.5 and 3.6).

Table 3.1: Affinity constants (K / M^{-1}) of the several analytes, obtained by ratiometric IDA (rIDA), by fitting of the ratio between Lucigenin and SC4-4Py emission, by direct titration of the SC4-4Py sensor with the analytes, following the resulting quenching of pyrene emission, and full thermodynamic characterization by ITC, at 25°C.

Guest	**rIDA**	**Direct Titration**	**ITC**			
	K / M^{-1}	K / M^{-1}	K / M^{-1}	ΔG / $kJmol^{-1}$	ΔH / $kJmol^{-1}$	$-T\Delta S$ / $kJmol^{-1}$
L-Arginine	4.2×10^3	5.8×10^3	$(3.9 \pm 1.0) \times 10^3$	-20.5	-[a]	-[a]
Choline	2.0×10^4	3.9×10^4	$(1.4 \pm 0.3) \times 10^4$	-23.7	-[a]	-[a]
Acetylcholine	3.3×10^4	6.8×10^4	$(1.4 \pm 0.3) \times 10^4$	-23.6	-[a]	-[a]
Putrescine	1.6×10^5	2.7×10^5	$(1.1 \pm 0.6) \times 10^5$	-28.9	-13.9 ± 1.4	-15.9
DM-DABCO	5.9×10^6	1.1×10^7	$(2.9 \pm 0.7) \times 10^6$	-36.9	-18.3 ± 0.8	-18.6

[a] Values for this parameter were not obtained due to lack of initial plateau in ITC isotherms.

Thermodynamic characterization of the SC4-4Py binding events was performed by ITC and the fitting results can be found in Table 3.1, with respective isotherms in Figure B.12. The affinities obtained by this technique are in good agreement with the ones obtained by the competitive assays, with a higher degree of variation for those obtained only by direct titration of SC4-4Py, further supporting the accuracy of the rIDA as a more accurate quantitative technique. Due to aggregation of SC4-4Py, concentration could not be increased further, impeding the obtention of full isotherms for the lower affinity guests, lacking the initial plateau necessary to obtain the empirical value of ΔH. Titrations with putrescine and DM-DABCO seem to suggest however, that these binding events are both enthalpy and entropy driven, with equal contributions from establishment of non-covalent interactions but also from desolvation of both guest and host.[225] Although it is known that rigidification and loss of degrees of freedom in the calixarene happen, these are also highly charged species and it is common that there are a great number of solvent molecules present in the calixarene cavity. This appears to be enough of a contribution to overcome the entropy penalization.

While lucigenin's typical response to anions has shown to be a hindrance for this new assay, cross-technique analysis seems to suggest that this ratiometric competitive assay does present a higher accuracy than using solely turn-on or turn-off mechanisms. Ideally, a substitute for this dye could be found in order to eliminate the need for extra data correction, as was done in these examples. Nonetheless, despite not resolving the issue with quenching of lucigenin by guests counterions, the added complexity in calixarene conformations and consequent photophysical response to the aforementioned change aided in the correction for other factors. This shows the potential to further increase the robustness of the commonly used and ubiquitous IDA with carefully designed supramolecular systems with higher complexity. Furthermore, the presence of a PET mechanism dependant on host conformation opens new doors to the development of similar sensors with dyes that emit further in the visible range than pyrene.

3.2 Heteroternary host:guest:host orthogonal sensing of pharmacological agents and peptides

With competition-based sensing strategies still in mind, the exploration of other displacement assays with different host and guest molecules was the natural next step.

Although BB as a host offers some specificity for C-terminal aromatic amino acids, as discussed in Section 2.1, the interest for this macrocycle also comes from the types of assemblies it can form in the presence of other hosts and specific guest molecules. It was shown in the 2016 paper by Tootoonchi *et al.* that, when in the presence of CB7 and guests presenting binding sites for both hosts, these three molecules can assemble cooperatively into heteroternary and quaternary complexes (Figure 3.7). Despite the relatively low affinities between both hosts, and each of the hosts and the model guest (mM or below), the affinities of binding of CB7 to the preformed BB:guest complex, and vice-versa, fall well below the μM range.[133] The formation of the quaternary complex, by binding of a second CB7 unit, is also observed at μM affinities. This phenomenon is thought to be due to the model guest allowing the alignment of both hosts in such a way where several hydrogen bonds can form between CB7's electronegative portals and BB's charged nitrogen atoms.[133,226]

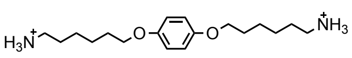

Model Guest, GH_2^{2+}

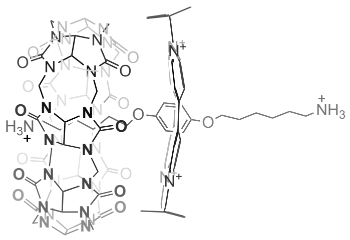

Ternary Complex, CB7-GH_2-BB

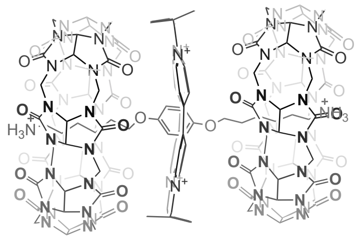

Quaternary Complex, $(CB7)_2$-GH_2-BB

Figure 3.7: Structure of the model guest reported by Kaifer's Lab and respective ternary and quaternary complexes it can form with BB and CB7.

This work leverages these hosts' capacity to self-assemble in heteroternary and quaternary complexes in a cooperative manner in order to develop a two host displacement system for different target analytes. This supramolecular assembly was explored with three different reporter guests, a family of merocyanine dyes, DASPI dyes (*Trans*-4-[4-(dimethylamino)styryl]-1-methylpyridinium iodide (Me-DASPI), *Trans*-4-[4-(diethylamino)styryl]-1-methylpyridinium iodide (Et-DASPI) and *Trans*-4-[2-(2,3,6,7-Tetrahydro-1H,5H-benzo-[ij]quinolizin-9-yl)-ethenyl]-1-methylpyridinium iodide (Jd-DASPI), Figure 3.8), known to bind CB7 with μM affinities. Binding to CB7 induces an enhancement of the emission of Me-DASPI, and, while binding to BB is not reported for these fluorophores, the paraquat moieties in BB are known electron acceptors, forming charge-transfer complexes with electron-rich guests, leading to quenching of the guest's emission.[78,227,228] These two distinct responses upon binding of each host should result in a distinct response depending on which we are displacing, as later schematized in Figure 3.12.

3.2.1 The CB7-DASPI-BB system

The DASPI dyes were chosen due to their ease of synthesis and easy modification at the aniline moiety, which should allow for modulation of host binding without too extensive synthetic routes (see Section 7.2.3). For that the Me-DASPI, Et-DASPI and Jd-DASPI were the chosen dyes, with, dimethyl, diethyl and julolidine moieties in the aniline group, to afford an increase in size at this site and see what influence this may have in the binding of both hosts..

In order to have a better understanding of the system and to know the optimal conditions to achieve the sucessful distinction between analytes that displace the two different hosts, the first objective was to obtain the affinity constants for the equilibriums that describe the CB7-Dye-BB system, as schematized in Figure 3.8. For this effect, characterization of the dye family, their 1 to 1 binding affinities towards each host and, finally, assembly of the more complex structures were evaluated.

The pK_a corresponding to the protonation of the nitrogen atom in the aniline moiety was found to vary between 2.5 and 4.5 for the free dyes (Table B.2 and Figures 3.9, B.13 and B.14).[229]

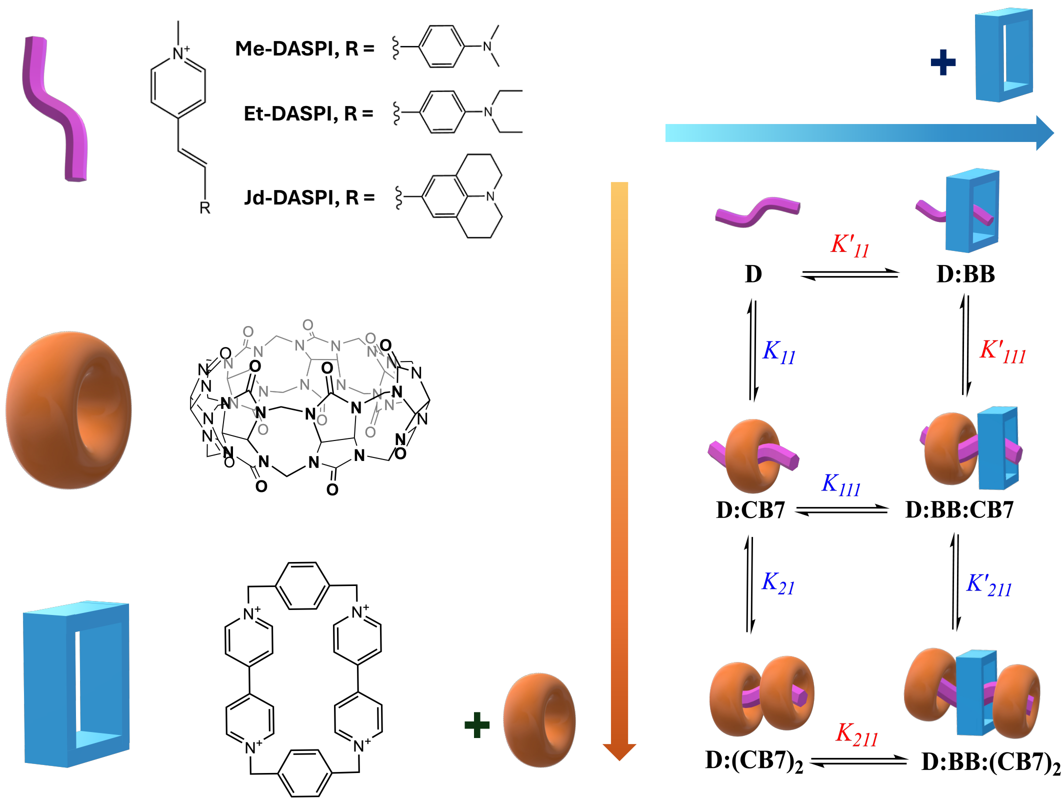

Figure 3.8: Structure of the family of DASPI dyes selected for this system and expected equilibrium between them and the hosts CB7 and BB, with the respective association constant for each binding event. The affinities identified will be used for characterization of the system and the remaining, in red, can be inferred from the ones obtained experimentally.

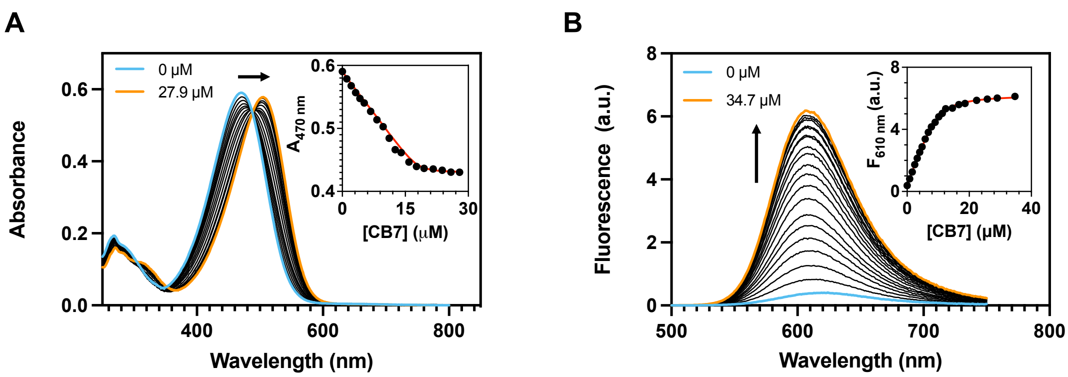

Figure 3.9: Titration of Et-DASPI with CB7 followed by **A.** and UV-vis and **B.** fluorescence spectroscopies (λ_{exc} = 486 nm) with dye concentration fixed at 18 and 9.8 μM, respectively. Fitting of the experimental data to each of the adequate models presented in Annex I can be found in inset. All experiments were done at pH 8.

Complexation of the dyes by both hosts was evaluated by UV-vis and fluorescence spectroscopies, as well as Isothermal Titration Calorimetry (ITC), in water. The pH of the samples was maintained above 8 in order to ensure that the main dye species in solution was the monoprotonated one, but not surpassing 9 to avoid BB degradation, with the exception of the titration of Me-DASPI with CB7. Affinity towards CB7 was higher than previously reported values for Me-DASPI (K_{11}^{lit} = 1.4 x 10^5 M^{-1}, compared to K_{11} = 3.0×10^6 M^{-1}, both at pH 10).[227] Affinity towards Et-DASPI remains in the same order or magnitude while Jd-DASPI decreases in one order of magnitude, when compared to the dye with methylaniline substitution (Table 3.2). Furthermore, the complexation of CB7 shifts the pK_a of Me-DASPI by almost 4 units, while for Jd-DASPI little change is observed (Table B.2 and Figures B.13 and B.14). This shift in pK_a can be explained by a higher affinity of CB7 towards the dicationic species, stabilizing it and consequently displacing its acid-base equilibrium. The small shift for Jd-DASPI can speak to the incapacity of CB7 to bind at the bulky julolidine moiety and lack of stabilization of the protonated species and/or to the overall hindrance for its protonation due to structural reasons.[230]

Table 3.2: Affinity constants (K / M^{-1}) of the several binding events for the CB7-DASPI-BB system, obtained by Fluorescence spectroscopy. The equilibriums described by each of the mentioned affinity constants can be found in Figure 3.8.

Dye	K_{11}	K_{21}	K_{111}	K_{211}
Me-DASPI	3.0×10^6	-	2.5×10^7	-
Et-DASPI	1.0×10^6	-	9.5×10^6	-
Jd-DASPI	3.0×10^5	1.5×10^3	3.0×10^3	1.0×10^5

Thermodynamic analysis of the binding of CB7 to the dyes gave a lower value of affinity for these binary complexes, however, these were not too distinct for Et and Jd-DASPI (Table 3.3 and Figure B.16). With the increase of the size of the group in the aniline, a decrease of enthalpic contributions is noted in concurrence with an increase of entropy of the binding. Considering the structures and properties of the dyes, it is thought that the binding of both Et-DASPI and Jd-DASPI to the host cavity is driven by hydrophobic effect more than the methyl substituted dye, which would be reflected as an entropic effect on the binding, while decrease in enthalpic contribution could be due to poorer size compatibility and less non-covalent interactions established.[231]

Fluorescence spectroscopy data of the Jd-DASPI titration with CB7 seems to indicate that another process beyond the 1:1 complexation is occurring, due to the lack of plateau after saturation of guest (Figure B.18). This is thought to correspond to the binding of a second CB7 unit and, although low, the obtained K_{21} for Jd-DASPI was included in the model for calculation purposes (Annex I).

Affinities of this family of dyes towards BB was analyzed by ITC, UV-vis and Fluorescence spectroscopies. Although ITC experiments seem to indicate that binding is present for at least Me-DASPI and Et-DASPI (both $K'_{11} \approx 1\times10^3$ M^{-1}, Figure B.16), the lack

Table 3.3: Thermodynamic parameters, ΔG, ΔH and -TΔS / kJmol^{-1} obtained by ITC for the binding of CB7 to the DASPI dyes, 11, measured in aqueous solution pH 8, at 25 °C.

Dye	**K_{11} / M^{-1}**	**No. sites**	**ΔG / kJmol^{-1}**	**ΔH / kJmol^{-1}**	**-TΔS / kJmol^{-1}**
Me-DASPI	$(4.8 \pm 0.7) \times 10^5$	1.05 ± 0.02	-32.4	-22.5 ± 0.9	-9.91
Et-DASPI	$(3.3 \pm 0.9) \times 10^5$	1.14 ± 0.04	-31.5	-15.0 ± 1.1	-16.5
Jd-DASPI	$(3.5 \pm 0.7) \times 10^5$	0.97 ± 0.03	-31.7	-15.9 ± 0.9	-15.7

of significant photophysical changes in UV-vis and Fluorescence spectroscopies might indicate that another exothermic process might be accounting for the variations observed by ITC. The value of $K'_{11} = 1 \times 10^3$ was used for following system characterization but it is necessary to perform further control experiments to confirm such affinity.

Despite the low affinity of BB towards these dyes, ternary complex formation was evaluated by UV-vis, Fluorescence and NMR spectroscopies as well as by ITC (Figures 3.10 and 3.11 and Table 3.4). A hypsochromic shift was observed in the UV-vis spectroscopy assays, for all the Dye-CB7 complexes, but these did not regain the characteristic spectra of the free dye upon addition of the second host, which is concordant with the formation of a new species. Additionally, the addition of BB at μM concentrations leads to an almost complete quenching of emission for both Me-DASPI and Et-DASPI and only a partial quenching for Jd-DASPI. The latter however maintains the maximum wavelength of emission that was observed for the Jd-DASPI:CB7 complex (λ_{max} (complex) = 640 nm and λ_{max}(free dye) = 658 nm). Binding affinities of BB to the preformed host:guest complex show an increase of at least 10 000 fold (Table 3.2 and Figures 3.10, B.19 and B.17), when compared to the assays in the absence of CB7, showing the importance of this second host being present for the formation of these high affinity, cooperative structures.

Table 3.4: Thermodynamic parameters, ΔG, ΔH and -TΔS / kJmol^{-1} obtained by ITC for the binding of BB to the pre-formed CB7-DASPI complex, 111, measured in aqueous solution pH 8, at 25 °C.

Dye	**K_{111} / M^{-1}**	**No. sites**	**ΔG / kJmol^{-1}**	**ΔH / kJmol^{-1}**	**-TΔS / kJmol^{-1}**
Me-DASPI	$(9.3 \pm 0.8) \times 10^6$	1.130 ± 0.004	-39.8	-36.1 ± 0.28	-3.76
Et-DASPI	$(7.2 \pm 1.2) \times 10^6$	1.23 ± 0.02	-39.2	-38.5 ± 1.0	-0.70
Jd-DASPI	$(1.3 \pm 0.2) \times 10^4$	1.00[a]	-23.5	-19.2 ± 2.1	-4.27

[a] Value fixed at 1.00 for the fitting of the data to the experimental values obtained.

^{1}H-NMR spectra of the free dye, Dye-CB7 and CB7-Dye-BB complex were obtained

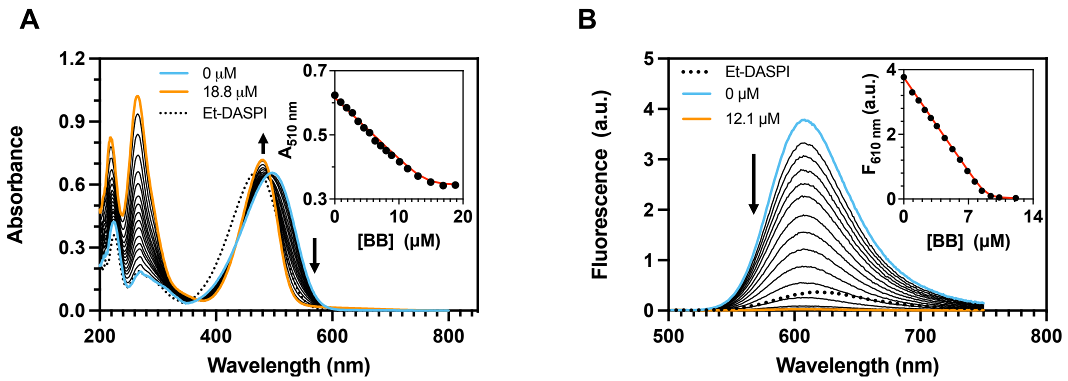

Figure 3.10: Titration of the Et-DASPI-CB7 complex with BB followed by **A.** UV-vis and **B.** fluorescence spectroscopies. The concentration of dye and CB7 were fixed at, respectively, 16.7 μM and 19.5 μM, for UV-vis spectroscopy studies and at 10 μM and 20 μM for fluorescence spectroscopy studies (λ_{exc} = 432 nm). Fitting of the experimental data to each of the adequate models presented in Annex I can be found in inset. All experiments were done at pH 8.

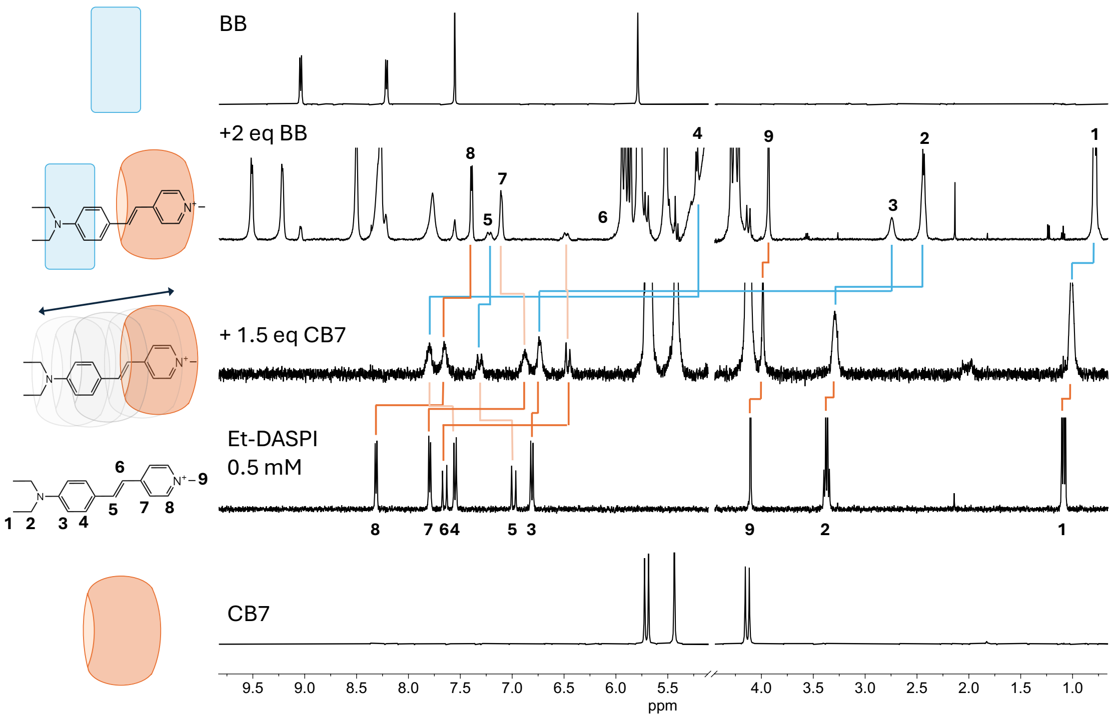

Figure 3.11: ^{1}H-NMR spectra of CB7, Et-DASPI, CB7-Et-DASPI and CB7-Et-DASPI-BB complexes and BB in D_2O pD 8 and respective expected structures based on the assigned Et-DASPI proton chemical shifts. Arrow on the CB7-Et-DASPI suggested structure represents the expected mobility of CB7 on the dye, due to the signal broadening at 1.5 and lower equivalents of host. Assignment of free dye was done by comparative method with previously reported ^{1}H-NMR spectrum and the 1:1 and 1:1:1 complex assignement was done by analysis of 2D experiments ^{1}H-Correlated Spectroscopy (COSY) and ^{1}H-ROESY, presented in the appendix.

and a structure is proposed based on the variations observed in the DASPI chemical shifts (the example of Et-DASPI is shown in Figure 3.11 and the remainder are presented in the Appendix Figures B.20 and B.21). Assignment of DASPI proton signals for all samples was possible by aquisition and analysis of 2D experiments (^{1}H-COSY and ^{1}H-ROESY presented in the Supplementary Information in Figures B.22 to B.33). Binding of CB7 to the dyes leads to an upfield shift of the pyridium proton shifts, while the aniline protons suffer a downfield shift or only a slight upfield one. The shifts observed and the broadening of these signals indicate that this host is in a dynamic structure, mobile across the dyes but with higher residence time on the charged pyridinium moieties, which become more shielded inside the CB7 cavity. Addition of 1 equivalent of BB to this mixture, leads to shifts of aniline protons in the order of 3 to 4 ppm, concordant with the localization of these protons in BB cavity, the region most affected by the ring current anisotropic effect. Furthermore, pyridinium proton signals are also shifted, suggesting a rearrangement of CB7 on the dye upon BB binding, but remaining in the charged region of the molecule. In the case of Jd-DASPI, due to the lower affinities, it is possible to see the slow exchange between the dye in the CB7 complex and in the ternary complex, while in the remaining cases 1 equivalent of BB is sufficient to fully saturate the previously formed complex. Splitting of the signals of BB and CB7 also indicate the presence of a slow exchange between the free species and complexes.

Beyond the confirmation of the presence of a ternary complex, formation of quaternary complexes with two CB7 units was hypothesized as well. It is possible that quaternary complexes can form, with some results seemingly accounting for the formation of more complex structures, but assays performed with Jd-DASPI-BB, with addition of an excess of CB7 led to aggregation of the final species so only tentative hypothesis can be extrapolated from the results (Figure B.34). Formation of quaternary complexes were included in the final fittings but did not alter the outcome for the Me and Et-DASPI systems. NMR studies confirm the presence of the ternary complexes for the three dyes but no quaternary complexes were observed (Figure 3.11). Crystallography studies of the complexes is underway but the initial estimations report only on the 1:1:1 complex as well.

3.2.2 The CB7-DASPI-BB displacement system for detection of pharmacological agents

With the widespread use of both prescription and over-the-counter drugs, questions about their environmental endpoint and impact arose in the scientific community and public discourse. Bioaccumulation of some drug classes has been recognized as a growing problem, with their detection in both soil and water, although the presence of these drugs has been more extensively studied in the latter.[232–234] One of the main classes of drugs found in aquatic environments are Non-Steroidal Anti-Inflammatory Drugs (NSAIDs), like Ibuprofen and Naproxen, due to their generalized use as over-the-counter medication.[235] Other classes of drugs found in aquatic environments are antidepressants, analgesics, antibiotics, steroids, among others.[232]

Due to the rising need to understand the impact of this environmental release of pharmaceuticals, there is also a need for efficient sensing strategies for several different types of drugs.

Cucurbit[*n*]urils (CBn), in particular CB7 and CB8, can bind drugs from hormones to analgesics with varying affinities, reaching the nM range.[103,105] Stoddart's Blue-Box (BB), or cyclobis(paraquat-p-phenylene), while it is a more promiscuous receptor, can bind aromatic moieties like naphthalene with micromolar affinities, so it is expected that this receptor would have similar affinity towards naproxen.[34,76] It is important to underline that CB7 and BB can also be of interest for sensing of peptide or protein-based drugs due to their orthogonal affinities towards N-terminal aromatic amino acids and C-terminal tryptophan residues, respectively, which will be discussed in the following subsection.[9,76]

After careful characterization of the ternary system with each of the three dyes, the ternary complex was used for the detection of the chosen drugs, Nandrolone (Nan) and Naproxen (Npx), as schematized below.

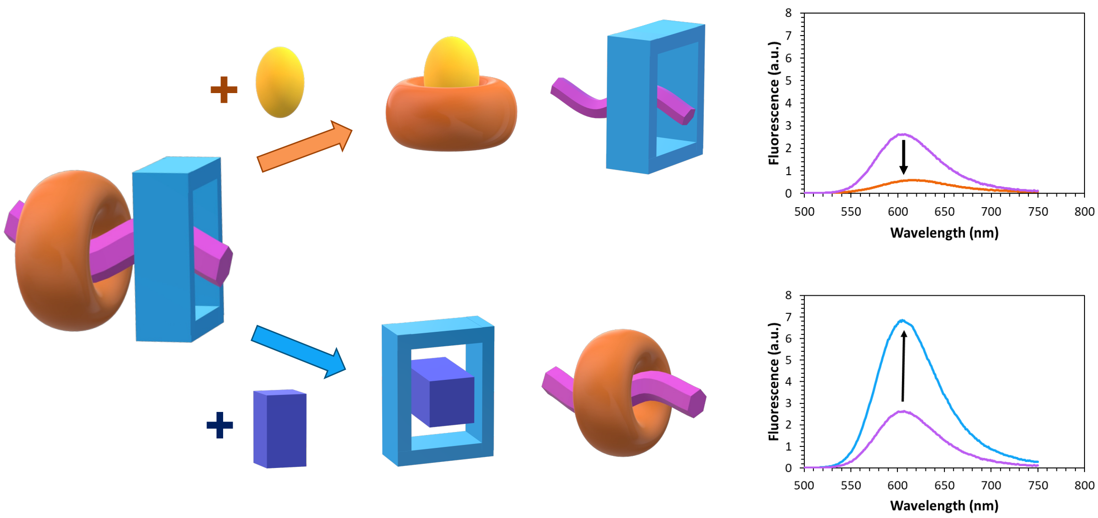

Figure 3.12: Schematization of the Host displacement assay with two distinct analytes. Competitors for the binding of CB7 will lead to a decrease in emission of the overall sample due to either the quenching effect of BB on the dye or the full disassembly of the complex and freeing of the dye (when working at μM concentrations). Competitors for BB will displace the host from the ternary complex and an enhancement of emission should be observed, correspondant to the 1:1 complex between CB7 and the dye.

Direct titration of the hosts with the chosen guests, as well as quantitative characterization by IDA (with the CB7-Jd-DASPI complex) showed selective binding of Npx by BB and Nan by CB7, as indicated by literature and each host binding properties (Figure 3.13 and B.36).

When applying the ternary complexes to the host displacement assays, an equilibrium of the species in solution was chosen so as to have the possibility for further enhancement of emission, when displacing BB from the complex, or quenching, when displacing CB7.

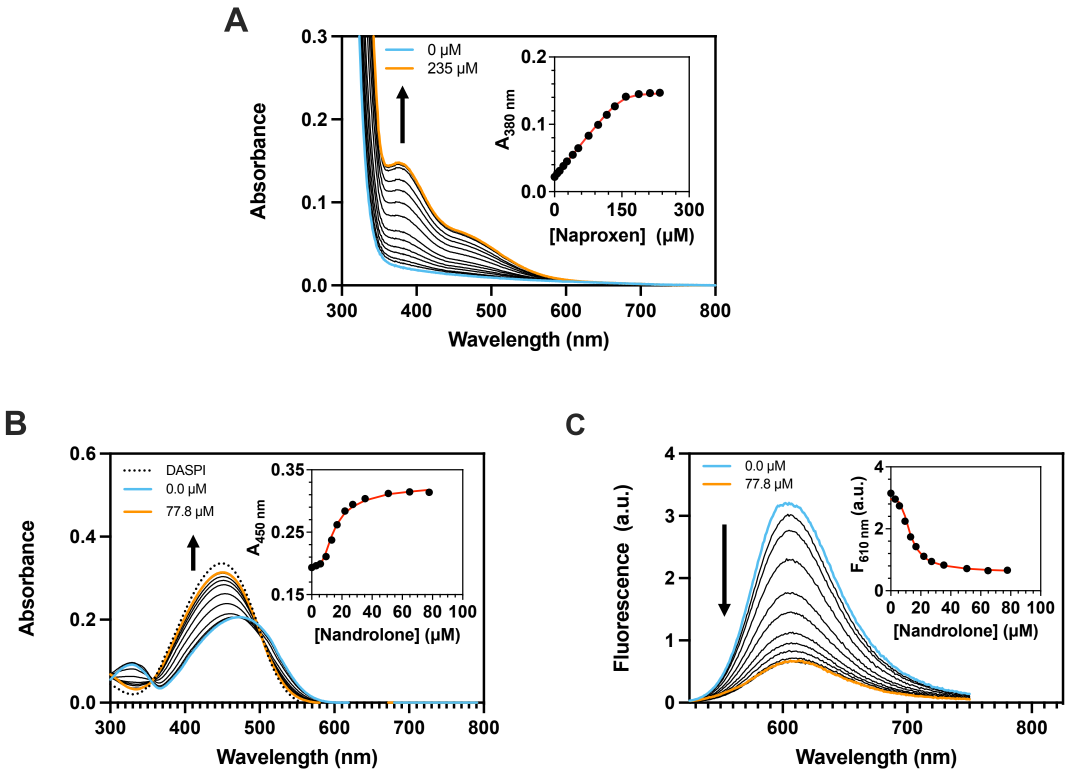

Figure 3.13: **A.** Direct titration of BB (150 μM) with Naproxen, followed by UV-vis spectroscopy and displacement of Me-DASPI (8 μM) from CB7 (15.5 μM) with the analyte Nandrolone followed by **B.** UV-vis and **C.** fluorescence spectroscopies (λ_{exc} = 468 nm), in aqueous solution pH 8.

The concentrations chosen were 8.6, 25 and 8 μM for Et-DASPI, CB7 and BB, in order to maximize the amount of ternary complex while still having this variation in emission, as schematized in Figure B.35.

The fluorescence response for each binding event, when Npx and Nan were added and BB and CB7 were respectively removed, occurred as expected (Figure 3.12), with the first event yielding an enhancement and the latter a quenching of emission of the dye. Quantitative analysis of the ternary systems with the different dyes in the presence of these dyes generally yielded comparable results with those obtained through other techniques and available in the literature. Both results with the Jd-DASPI ternary system and the guest nandrolone and Me-DASPI ternary system and the guest naproxen showed a slight decrease in the calculated CB7-Nan and BB-Npx affinities, respectively, when using the emission data for the fitting. Nonetheless, these variations are slight and appear to be within the error obtained when analyzing these binding events with other techniques.

Despite its complexity in terms of binding equilibria involved, this host displacement assay system can be applied for quantitative analysis, but most importantly, it shows the benifit of possible application in array-like detection methods, due to the presence of very distinct responses with the same system for different guests. This design can also be

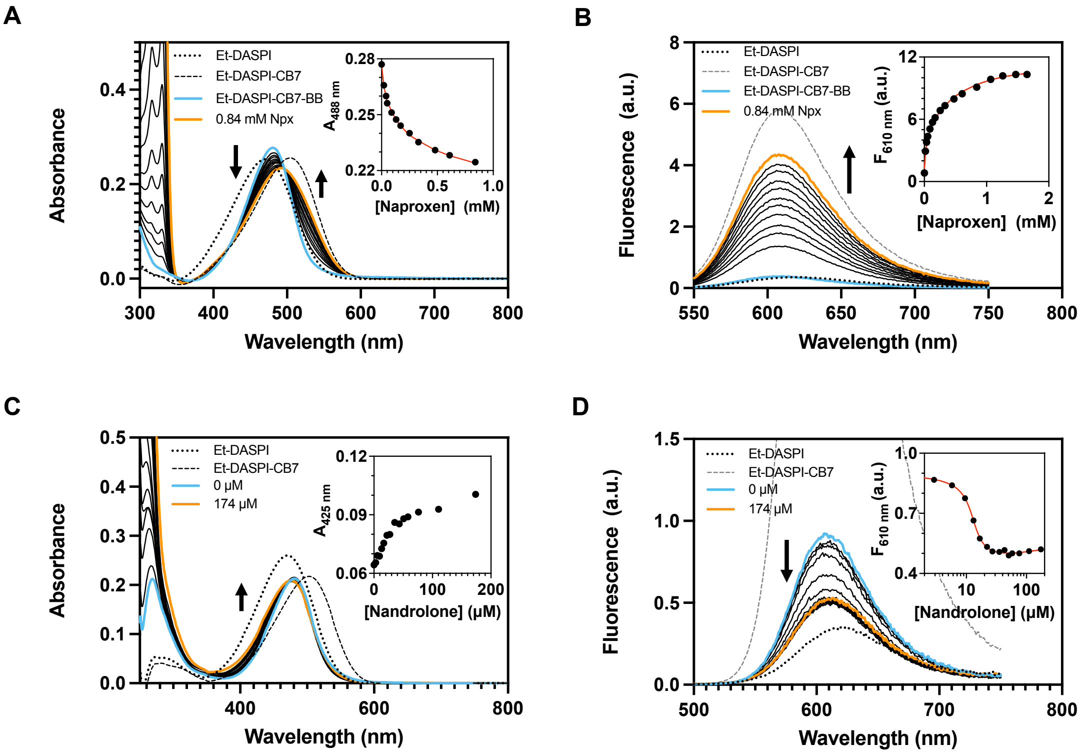

Figure 3.14: Host Displacement Assay with CB7-Et-DASPI-BB complex with two the two guests discussed in this section, **A.** and **B.** Naproxen and **C.** and **D.** Nandrolone, followed by **A.** and **C.** UV-vis and **B.** and **D.** fluorescence spectroscopy (λ_{exc} = 488 nm), with respective fitting of the data using the ternary complex model in the inset. CB7, BB and Et-DASPI concentration was fixed at 25, 8 and 8.6 μM for Naproxen displacements and at 20, 6 and 8.7 μM for Nandrolone displacements, respectively.

Table 3.5: Affinity constants (K / M^{-1}) of the several host-guest complexes between the two hosts, CB7 and BB, and the guests Nandrolone, Nan, and Naproxen, Npx, obtained by different techniques.

Technique	K_{Npx-BB}	$K_{Npx-CB7}$	K_{Nan-BB}	$K_{Nan-CB7}$
Direct titration	$> 5.0 \times 10^{5}$[a]	-	-	
ITC	2.2×10^{6}[c]	-	-	-
IDA	-	$< 1 \times 10^{3}$[b]	-	1.8×10^{7}[b], 4.2×10^{7}[a]
Host Displacement Assays:				
Me-DASPI	6.5×10^{5}[b]	$< 1 \times 10^{3}$[b]	$< 1 \times 10^{3}$[b]	1.5×10^{7}[b]
Et-DASPI	1.0×10^{6}[b]	-	$< 1 \times 10^{3}$[b]	1.0×10^{7}[b]
Jd-DASPI	1.0×10^{6}[b]	-	$< 1 \times 10^{3}$[b]	4.3×10^{6}[b], 1.5×10^{7}[a]

Affinities calculated using the herein developed host displacement assay, using [a] UV-vis and [b] fluorescence spectroscopy and [c] ITC data.

explored in the future with different dyes, aiming at adding a shift in emission or another novel response, with the aim to add the benefits of ratiometric measurements to a system with two distinct receptors.

3.2.3 CB7-DASPI-BB displacement system for detection of peptides

Due to their complementarity in terms of amino acid side-chain affinities, with CB7 and BB binding preferentially to the N-terminal and C-terminal aromatic residues respectively, it was important to explore the potential of the system in distinguishing peptides with binding sites for both hosts from those that present solely one of these binding sites. However, because BB presents low affinity towards all of the DASPI dyes, it is likely that both CB7 and BB are displaced once the first host is removed from the complex, independently of the guest presenting the adequate binding sites, due to the loss of the cooperative effect.

In order to evaluate if this ternary system presents the potential for orthogonal detection of peptides with the binding sites for both hosts despite the remarked disadvantages, two different peptides were selected to help distinguish these events: FGG, which should only lead to CB7 displacement from the complex, and FGGW, which presents binding sites for both hosts.

Binding to each of the hosts was evaluated for the chosen guests by direct titration and binary indicator displacement assay (IDA), using the CB7-Me-DASPI, which can be found in Figures B.37 and B.38, with respective affinities in Table 3.6. As expected, FGG binds only with low affinity to BB, but binds with sub micromolar affinities to CB7, while FGGW binds to both hosts with relatively high affinities. Of note is the fact that CB7 appears to be able to bind FGGW at the two distinct sites. Given its affinity towards FGG, it is expected that the higher affinity site, which is in the same order of magnitude, corresponds to the N-terminal. At μM concentrations, it is expected that CB7 binds preferencially to the N-terminal, leaving the C-terminal available for BB to bind to (Figure B.39). Nonetheless, when analysing data from the host displacement model, this capacity of CB7 to bind at both sites should be taken into account.

Capacity of the system to distinguish both of the selected guests was tested by UV-vis and fluorescence spectroscopy, presented in Figure 3.15, with respective affinities obtained presented in Table 3.6. Assays with FGG showed consistency to the results obtained with each host individually, with Jd-DASPI assays with both techniques and Et-DASPI UV-vis assays being the exceptions to this rule. Both assays yielded an affinity one order of magnitude lower than the one found in literature and the one obtained by other techniques in this work, speaking to other interferences in the optical response of the dyes.

When analysing the fluorescence assays done with FGGW, the results across dyes are more inconsistent and are highly dependant on the starting concentrations of the ternary complex species. Furthermore, the differences in signals between FGG and FGGW when in the presence of the same host:dye:host assembly presents comparable variations,

Table 3.6: Affinity constants (K / M^{-1}) of the several host-guest complexes that can be obtained with the CB7-dye-BB ternary system and the guests FGG and FGGW, obtained by different techniques.

Technique	K_{FGG-BB}	$K_{FGG-CB7}$	$K_{FGGW-BB}$	$K_{FGGW-CB7}$
Direct titration	2.8×10^2	-	1.5×10^5	-
IDA	-	8.8×10^7	-	5.0×10^{7} [i], 8.0×10^{5} [ii]
Host Displacement Assays:				
Me-DASPI	1.0×10^{3} [a],[b]	2.6×10^{7} [a], 8.6×10^{7} [b]	- [c]	- [c]
Et-DASPI	1.0×10^{2} [a], 1×10^{3} [b]	4.0×10^{7} [a], 3.3×10^{6} [b]	- [c]	- [c]
Jd-DASPI	1.0×10^{3} [a]	1.8×10^{6} [a]	- [c]	- [c]

Affinities calculated using the host displacement assay developed and presented herein, using both [a] fluorescence and [b] UV-vis spectroscopy data. [c] Fitting of the data provided more than a single adequate value of affinity constants and emission/absorbance of each species. For the hosts that bind at two different sites [i] corresponds to the K_{11} and [ii] to the K_{21}.

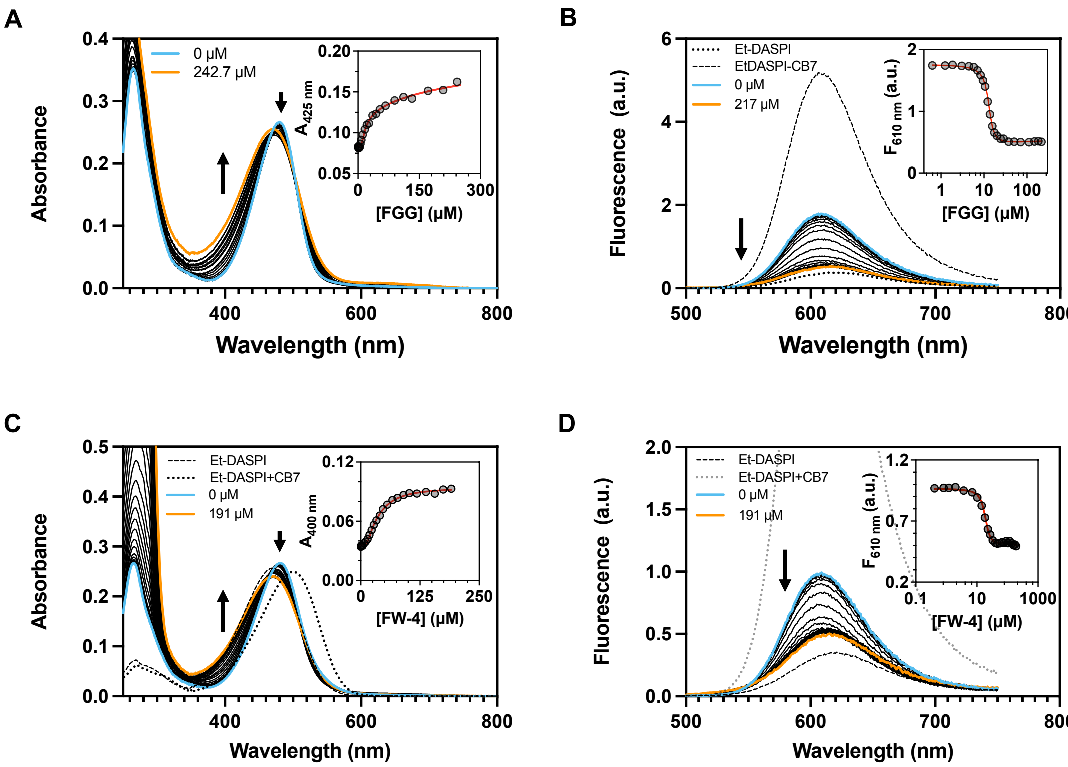

Figure 3.15: Host Displacement Assay with CB7-Et-DASPI-BB complex with two the two guests discussed in this section, FGG (followed by **A.** UV-vis and **B.** Fluorescence spectroscopy, λ_{exc} = 470 nm) and FGGW (followed by **C.** UV-vis and **D.** Fluorescence spectroscopy, λ_{exc} = 470 nm) and respective fitting of the data using the ternary complex model, can be found in the inset. CB7, BB and Et-DASPI concentration was fixed at 20, 6 and 8 μM for FGG displacements and at 25, 6 and 8 μM for FGGW displacements, respectively.

not allowing qualitative distinction. Factors associated with the model and optimization method are important to consider as well for quantitative analysis - parameters like the initial guesses and limits in which the model will search for an answer (bounds) influence the outcome in a large degree. When looking at the example presented in Figure 3.15, fittings with differently defined bounds led to almost equally acceptable fittings (Figure 3.16). While the fitting 1 is the one which presents emission values of the species most concordant with previous results, slight variations seem to have a high impact on the result of BB-FGGW affinity. The model uses least squares method for minimazion of the difference between experimental and calculated data - while a useful and efficient method, the minimization process could fall erroneously into local minimums of the overall model while overlooking the true minimum inside the restraints inputed. Additionally, when fitting too many variables at once, these types of models tend to fall into overfitting of the data in which some considered parameters are unecessary or might be overcompensating for errors in other parameters, leading to misleading results.[236] For systems like that of Jd-DASPI, where it is unclear if we do have quaternary complexes forming and where the different species final emission and absorbance is not known to begin with, it is difficult to get clear quantitative results. For those where both hosts bind, the addition of novel variables and lack of new optical signal lead to loss of information, that would be crucial to distinguish events.

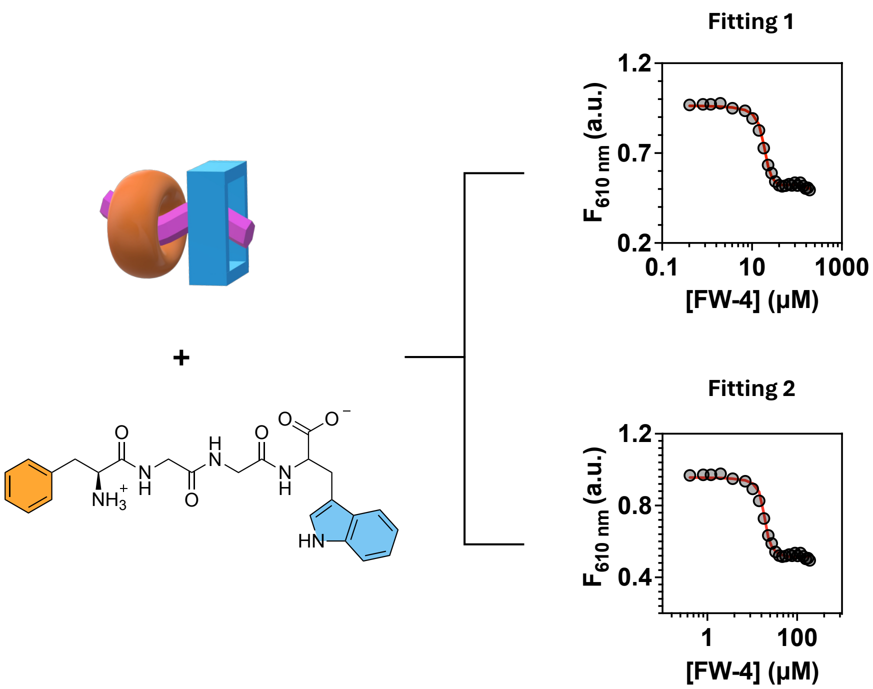

Figure 3.16: Example of two different fittings of the experimental data obtained from Et-DASPI host displacement assay with the peptide FGGW. Bounds for the fitting and results obtained are presented in Table 3.7.

These various factors, added to the low affinity of BB to the dyes studied, leads to the incapacity of the system to distinguish binding of FGG and FGGW to both hosts in an

Table 3.7: Affinity constants (K / M^{-1}) obtained for the same data set, presented in Figures 3.15 and 3.16 but obtained with different bounds for the model optimization, showing the ability for acceptable fittings with affinities several orders of magnitude different and small changes in the remaining parameters.

Parameters	**Fitting 1**		**Fitting 2**	
	Result	**Bounds**	**Result**	**Bounds**
$K_{FGGW-BB}$ / M^{-1}	1.7×10^5	$1 - 1 \times 10^6$	1.0	$1 - 5 \times 10^3$
$K_{FGGW-CB7}$ / M^{-1}	5.2×10^6	$1 \times 10^3 - 1 \times 10^9$	1.3×10^7	$1 \times 10^3 - 1 \times 10^9$
$F_{Et-DASPI}$	0.44	0 - 3	0.54	0 - 3
$F_{CB7-Et-DASPI}$	3.50	1 - 10	2.44	1 - 10
$F_{CB7-Et-DASPI-BB}$	0.02	0 - 1	0.41	0 - 1
$\sum(F_{calc} - F_{exp})^2$	0.0037		0.0080	

unequivocal manner.

In this section, it is possible to see that the increase of complexity does bring advantages, but can also increase the number of variables and problems that need to be accounted for. Increasing complexity without additional information (like the ratiometric signals observed in section 3.1) leads to models and optimizations falling in the realm of overfitting of data. Strategies to overcome the limitations observed here could fall both on the photophysical response of the system but also in the design of the system in itself. Several dyes were tested with these hosts, to test if they could form these ternary complexes but with a shift in emission, however most of them were unsucessful. Covalently linked receptors for orthogonal sensing were also explored and can be found in the following section.

Nonetheless, the supramolecular assembly of CB7-Dye-BB shows great promise for its applicability in qualitative array-like assays, with its ability to provide distinct signals using one system only. This assay in addition with other qualitative assays with different dyes and receptors could be sufficient to ensure speciation in cases like those of aqueous media contaminated with different pharmacological agents and is an avenue that will be explored in the future with this system.

3.3 Ditopic Receptors for Orthogonal Peptide Sensing

This section of the project was developed in the context of the project RATIOPEP - 2022.02538.PTDC, with some of the synthesis steps having been performed by MSc. Beatriz Raimundo, MSc. Daniel Miranda and MSc. Hanieh Mahmoodi.

A strategy that could improve problems like the ones faced in the previous section is the incorporation of single receptors in a covalently interconnected system, in the form of a novel Ditopic Receptor (DR). These receptors allow for increased affinity and selectivity of the separate elements, enabling selective detection of small sequences and hot-spots. When allied with tandem indicator displacement assays, the characteristic ratiometric signal will arise, showing the spectral signature of the complexed analyte, while also being self-corrected. These ditopic sensors could be able to distinguish between similar sequences which, in ordinary tandem assays and systems like the ones presented in Sections 3.1 and 3.2, would originate identical signals (Figure 3.17).

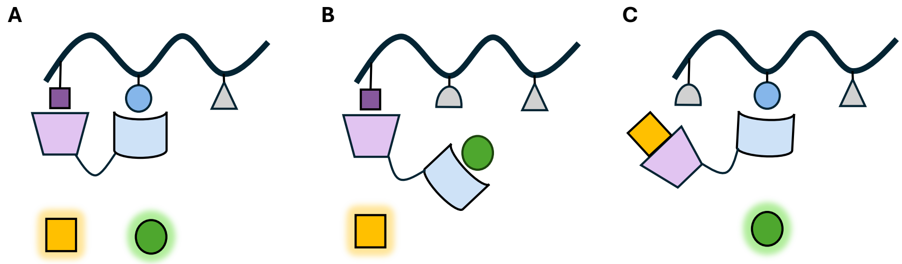

Figure 3.17: Ditopic Receptor indicator displacement assays schematization with **A.** a analyte that binds to both receptors and **B.** and **C.** with two analytes that bind selectively to one or the other receptor moieties

Ideally, more than one DR would be synthesized to evaluate how different specificities and affinities of the hosts, as well as distance between them and flexibility of the linker could influence both the photophysical response as well as quantitative measurements of the system. However, due to time constraints and difficulty and low yields of some of the synthesis steps, the focus of this section of the project started by tackling the monofunctionalization of CB7. Not only is this receptor particularly interesting due to its high affinities towards N-terminal aromatic amino acids and specific sequences, but its monofunctionalization is particularly challenging due to low yields and limited reactivity and solubility of CBn. Despite the potential shown by the CB7-dye-BB system, the other macrocycle initially selected was SC4, due to easier monofunctionalization and also considerably higher affinity constants for its targets.

The first step in the monofunctionalization of CB7 was the addition of a hydroxyl moiety on one of the seven glycouril units of this macrocycle (Figure 3.18). This oxidation reaction has previously been reported by two main strategies: the photolysis of hydrogen peroxide as a source of hydroxyl radicals and direct oxidation with a chemical oxidant.[109,237,238] The latter was chosen due to lack of adequate equipment for bulk photolysis of hydrogen peroxide and due to the low improvement in relation to chemical homolysis. Chemical oxidation was successful and separation of monohydroxyl-CB7 (CB7-OH, Figure 3.19) from CB7 and dihydroxyl-CB7 (CB7-$(OH)_2$) was achieved by reverse phase chromatography with the polymeric resin CHP20P. Monitorization of the presence of CB7 in each fraction was done by enhancement of berberine emission, a know dye that binds CB7 with high affinities.[51] Despite the characteristic distinguishing chemical shifts of the monohydroxy variant in relation to unsubstituted CB7 (Figure 3.19), it was previously reported that 1:1:1 proportions of CB7, CB7-OH and CB7-$(OH)_2$ yielded an almost inestinguishable ^{1}H-NMR spectrum from that of pure CB7-OH.[237] Because of this, the fractions containing detectable amounts of CB7 variants with berberine assay were analyzed by Electrospray

Ionization-Mass Spectrometry (ESI-MS) in the presence of guest Cystamine (Cys), in order to confirm the degree of hydroxylation of each fraction (m/z calculated for CB7-Cys was of 657.7, CB7-OH-Cys of 665.7 and CB7-OH_2-Cys of 673.7, see Chapter 7.2.4 Figures B.42 to B.45).

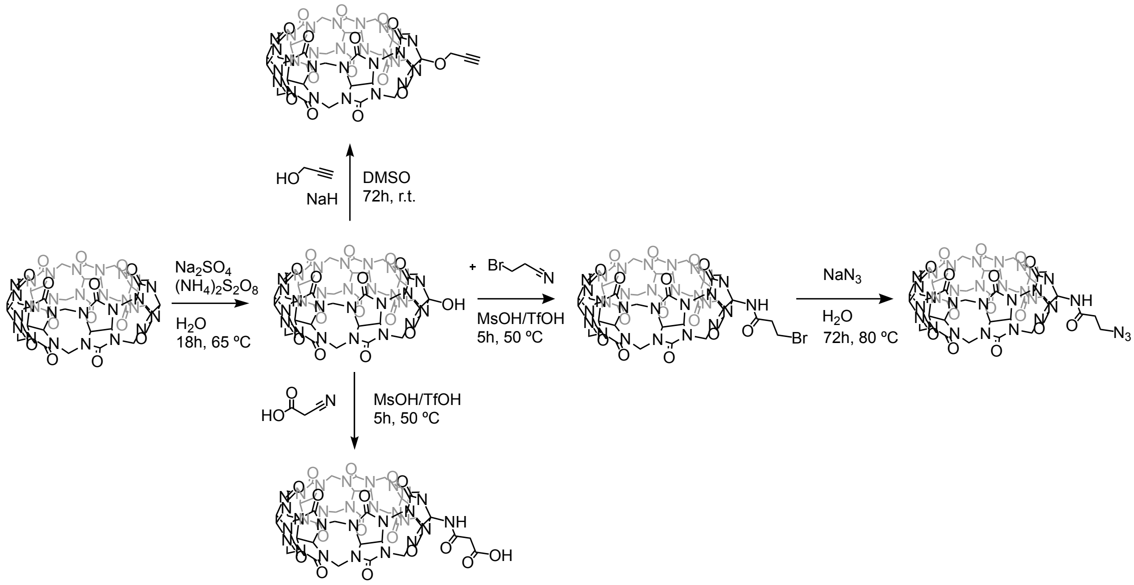

Figure 3.18: Reaction scheme of CB7 monofunctionalization strategies and respective conditions used.

After separation of CB7-OH from CB7 and CB7-$(OH)_2$, further functionalization was done by two different methods. The first hinged on the formation of the propargyl alkoxide and consequent substitution reaction on the C-OH of CB7, in order to add the alkyne for future click-reaction.[176] Although the reaction appeared to be successful by ESI-MS analysis (Figure B.46), it always originated a mixture of CB7-propargyl and CB7-OH that could not be purified successfully by the reported methodology, due to the increased solubility of both compounds in the presence of a high amount of salt, originated from the reaction of NaH with trace water in the CB7 cavity.

The second strategy was based on the formation of a carbocation in highly acidic conditions, as reported by Kim and coworkers.[239] This functionalization was tested with the list of substituents that can be found in Table B.3. Although different reactants were tried in order to add the alkyne moiety to CB7, e.g. propargyl alcohol and 5-hexynenitrile, these did not react in the conditions reported. It was hypothesized that these functional groups might have some steric hindrance in approaching the host molecule due to their bulkiness, limiting the type of substituents that could be used in this host. However, with smaller, already reported substituents, the reactions were successful: 3-bromopropionitrile and 2-cyanoacetic acid were used to obtain CB7 host with bromide (CB7-Br) and carboxylate (CB7-COOH) functional groups, to test different reaction mechanisms for covalent linkage to SC4 (Figure 3.18).

Consumption of CB7-OH and appearance of two triplet proton chemical shifts at 2.85

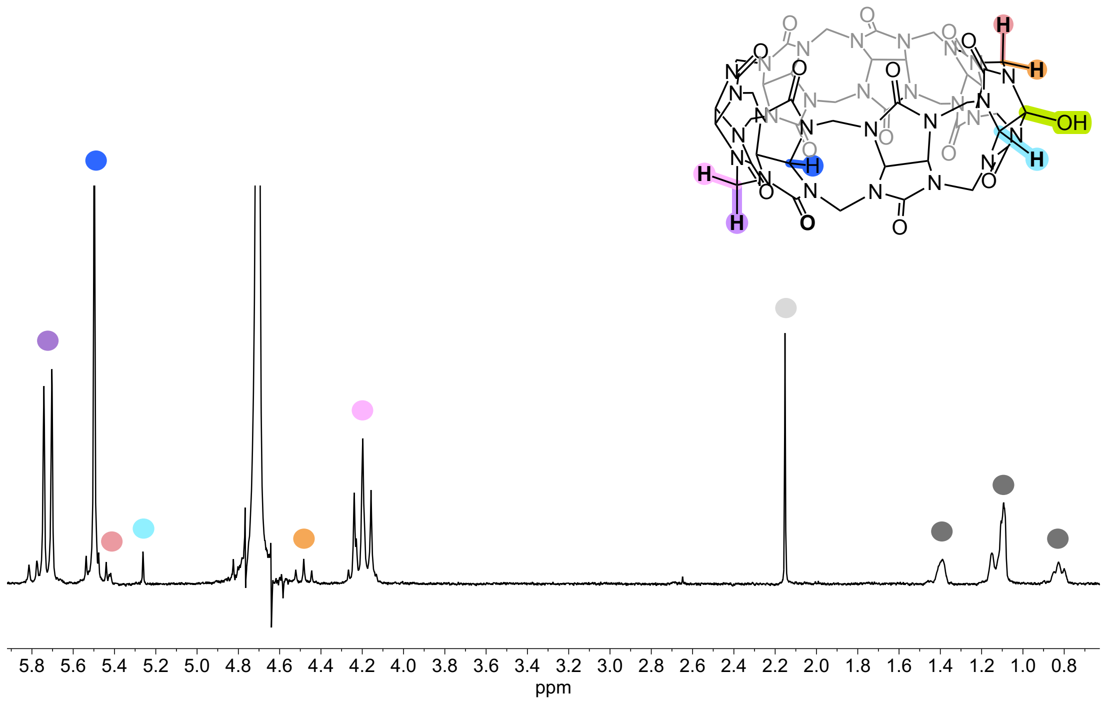

Figure 3.19: ^{1}H-NMR spectrum of a CB7-OH fraction with respective protons assigned, based on the paper by Ayhan *et al.*, as well as guest 1-adamantamine proton chemical shifts for the bound (dark grey) and free (light gray) species.[237] The proton chemical shift marked in pink was used as a reference for the integration of monofunctionalization protons for further reactions.

and 3.50 ppm, as reported in the literature, were the main evidences supporting the successfull synthesis of CB7-Br, as seen in Figure 3.20.[239] This compound was further reacted with sodium azide in water so as to prepare this macrocycle for a click reaction. This was done in an NMR tube in D_2O and it is observable by ^{1}H-NMR that the triplet signals that should correspond to the -CH_2- groups of the substituent (Figure 3.20, full spectra in Figure B.48) suffer a significant upfield shift after a few hours of reaction time. This test indicates the possibility of reaching the necessary reactants for a click reaction through this synthetic route could be a feasible option, by obtention of CB7-N_3. Isolation and ESI-MS analysis of these two products needs to be done, as well as 2D-NMR experiments, to fully confirm the conversion to this species. In addition to that, strategies for obtaining the calixarene derivative with the alkyne substitution are currently being explored, but the necessary final reactant has yet to be obtained.

CB7-OH reaction with 2-cyanoacetic acid appears to also have been successful, with the appearance of a singlet at 3.92 ppm, but trace amounts of CB7-OH were still detectable in ^{1}H-NMR spectrum of the reaction mixture after work-up (Figure B.49).

Simultaneously, MSc. Hanieh Mahmoodi, working under the project scope, obtained the monofunctionalized SC4 shown in the Figure 3.21. Having the amine group in

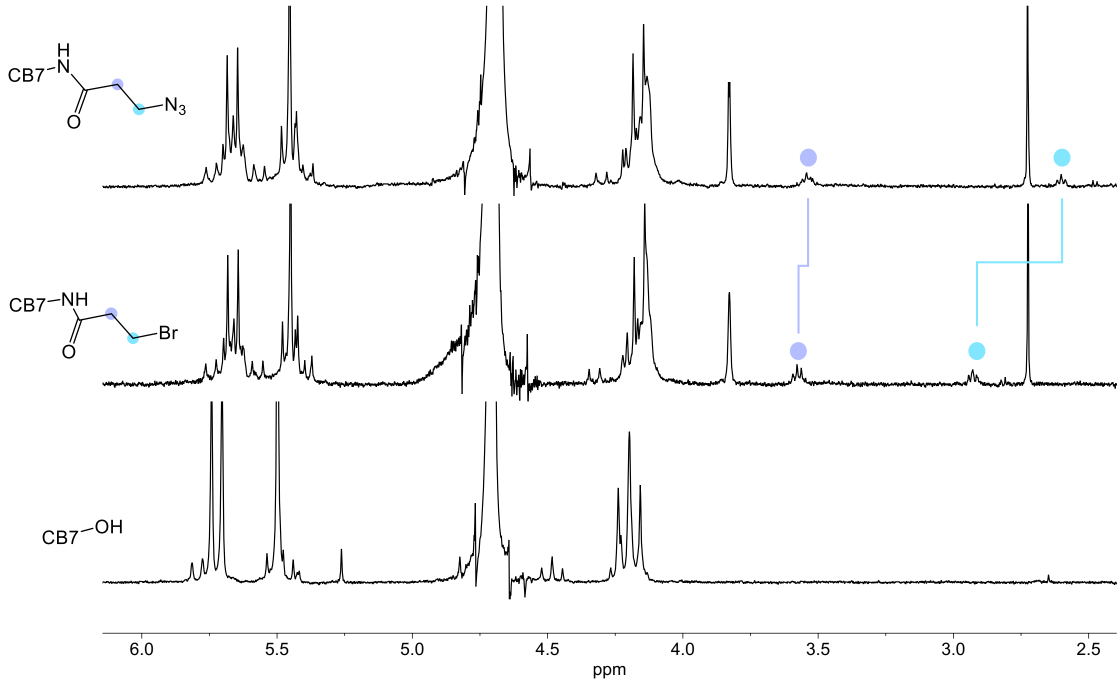

Figure 3.20: ^{1}H-NMR spectra of the products CB7-OH, CB7-Br and CB7-N_3 in D_2O in the presence of 1-adamantamine for CB7-OH and p-Xylylenediamine for the remaining two. Full spectra can be found in the Supplementary Information, Figure B.48.

SC4, it is possible to directly conjugate CB7-COOH with this group, by 1-Ethyl-3-(3-dimethylaminopropyl)carbodiimide (EDC) mediated conjugation, or further functionalize SC4-NH2 with a alkyne moiety for final DR synthesis with click reaction.

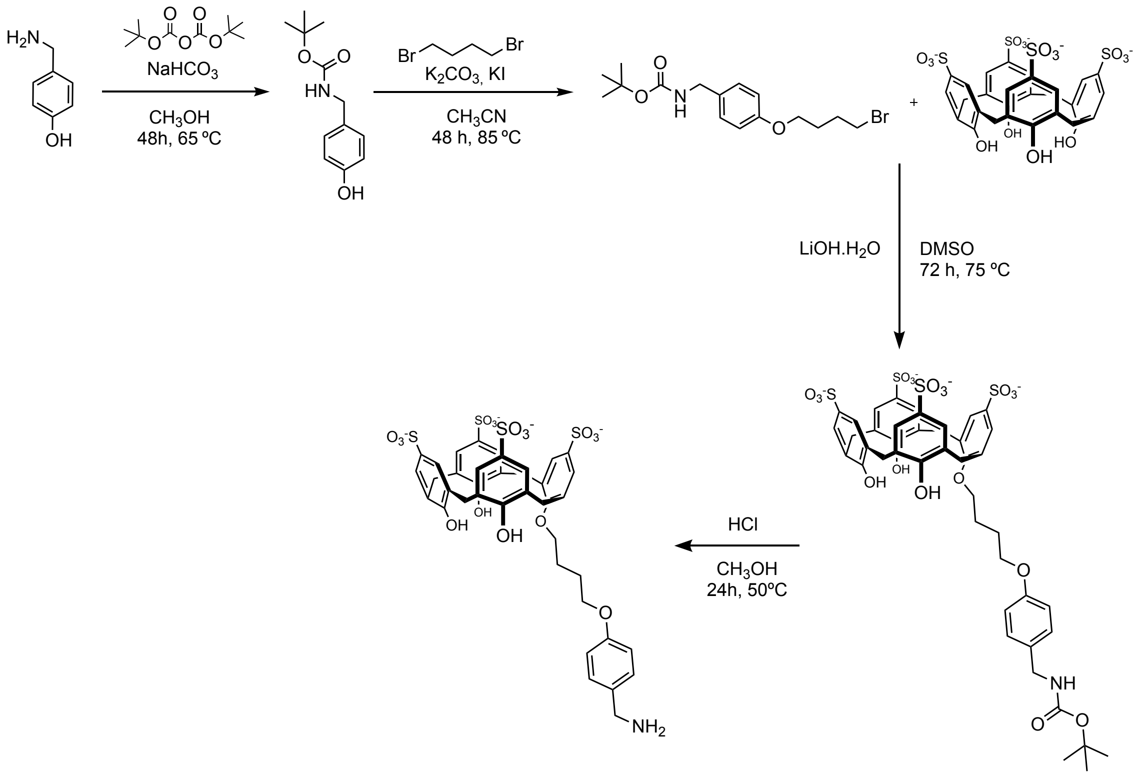

Figure 3.21: Reaction scheme of SC4 monofunctionalization and conditions used for each reaction step.

4

Self-Assembly-based strategies for peptide sensing

Another property inherent to both supramolecular and biological systems is the capacity of several different elements of a system to self-assemble into more complex structures. While this self-assembly process can be driven by strong non-covalent interactions between elements, the medium where this system is inserted is can be equally important. In the case of aqueous solutions, the driving force related to the hydrophobic effect can be as relevant for the overall binding of two molecules as other non-covalent interactions. These properties are behind many self-assembled structures like the formation of micelles, layers in interfaces and vesicles and respective membranes, formation of supramolecular polymers, channels, among others.[14,147,148] One of the greatest benefits of these self-assembly based systems is their responsiveness to stimuli, leading to either dissassembly or changes in the overall properties of the assembly in itself.

The concept of aggregation and aggregates is closely associated with the self-assembly of molecules, but its definition is not completely consensual - while aggregates can sometimes be referred as ordered assemblies, other sources use this term to refer to amorphous assemblies and, as such, distinguish them from the previously referenced ordered structures that can be achieved through self-assembly.[240,241] The word aggregation will be used according to the latter definition, where it refers to agglomerates of molecules without a clear or obvious structure.

In this section, seeing as SC4 has proven to be a versatile sensing platform, the host was once again explored, this time using the self-assembly mechanisms mentioned. Firstly the aggregation of the SC4-nPy family of sensors, based on the SC4-4Py sensor shown in Section 3.1, was explored for the ratiometric detection of high affinity polycationic guests. The second sensing mechanism explored was based on the self-assembly of O-substituted SC4 surfactants on interfaces between bulk aqueous phase and organic droplets. Due to their receptor functionality, their response in these emulsions was studied in the absence and in the presence of their specific guests.

4.1 SC4-nPy family as an aggregation-based ratiometric sensing array for polycations

While SC4-4Py has proven to be a useful host and reporter for ratiometric IDA in water, the presence of the pyrene moiety and the amphiphilic design led it to aggregate in the presence of highly charged guests above a given concentration. This aggregation presented the simultaneous appearance of an emission band consistent with the formation of pyrene excimers, appearing as an unstructured band above 400 nm.

Despite presenting a hindrance for the applicability of the SC4-4Py-LCG system for detection of highly charged guests, aggregation-based systems can have a great potential as an alternate detection mechanism. SC4 presents high affinities for polycations, going below nM affinities, however, much like encountered in Section 2.2, the distinction between polycations comprising closely spaced positively charged residues can be challenging. Different polycations displaying affinity constants below the μM range, in physiological conditions, can equally saturate the macrocyclic receptor, leaving no window of differentiation for these high affinity targets.

The SC4-nPy family of sensors was designed and synthesized with these challenges in mind. These use the same monofunctionalization-based design that has been previously used to exploit the photophysical properties of pyrene-based probes and the SC4 binding selectivity towards cationic targets to create a versatile aggregation-based sensing platform. Variation of the length of the alkylic linker (n = 4, 6 and 8) that connects the receptor to the indicator grants this library of amphiphilic sensors different aggregation capacities based on the substituent hydrophobicity. It is expected that, when free in aqueous medium these sensors present pyrene's monomer emission, λ_{em} < 400 nm, and, upon charge neutralization at the SC4 moiety, if above Critical Aggregation Concentration (CAC), the complex will aggregate and its emission shift to the expected excimer emission, λ_{em} > 400 nm, originating the desired ratiometric signal (Figure 4.1). This strategy allies the benefits of dual-signal sensing systems with an aggregation-based detection - modulation of aggregation capacity allows detection beyond the limits imposed by quick saturation of the host, enabling the sensing high affinity guests at μM concentrations and opening the door to the possible distinction of polycationic targets with different effective charges.

The desired SC4-nPy chemosensors were synthesized by direct monoalkylation of SC4 with the corresponding derivative in basic media, as described previously. The products were isolated by reverse phase column chromatography and identified by NMR spectroscopy and High Resolution-Mass Spectrometry (HR-MS).

The CAC of the SC4-nPy in the absence of target analytes was determined by front-face fluorescence spectroscopy measurements of the chemosensors in aqueous, buffered solutions (phosphate buffer (PB) ,5 mM pH 7.4). The three compounds present absorption and emission spectra concordant with that expected for the pyrene dye - in dilute conditions (< 10 μM) all three SC4-nPy present a strong emission at 370-400 nm with

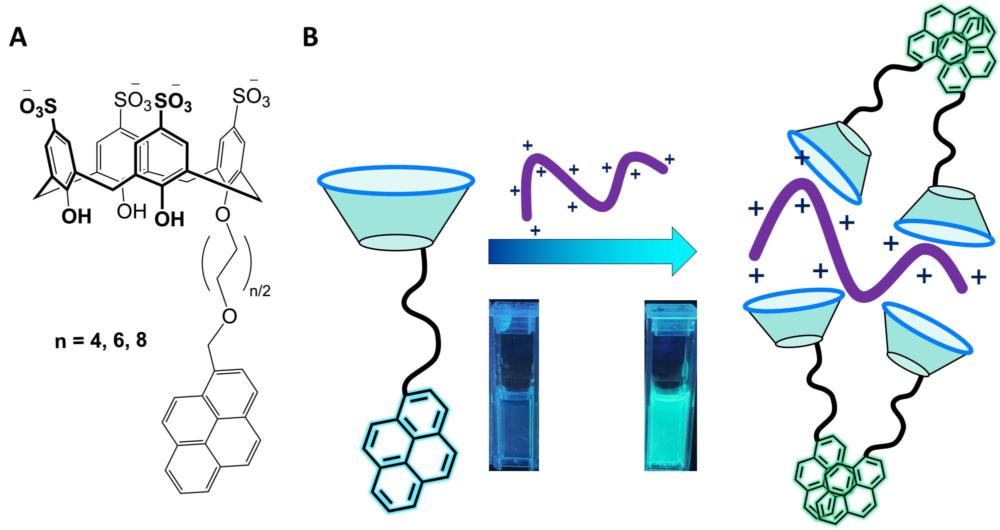

Figure 4.1: **A.** Structure of the molecular sensors SC4-nPy (n = 4, 6 and 8) and **B.** schematization of the mechanism that originates the desired ratiometric measurement.

vibrational resolution, which is consistent with the monomeric form of pyrene being the major species in solution; increasing the SC4-nPy concentration leads to appearance of a wide, structureless, excimer-like emission band centred at 498 nm, that, according to the excitation spectra monitored at 498 nm, can be assigned to the formation of emissive ground-state aggregates (Figure 4.2 A). Plotting the relative emission intensity at 498 nm against the concentration of SC4-nPy allows the determination of the CAC at the point where this emission band suddenly appears, defining the aggregation onset. As expected, the CAC decreases with the increase in the size of the alkyl chain linker, being 2 , 1 and 0.05 mM for SC4-4Py, SC4-6Py and SC4-8Py (Figure 4.2 B, C and D), respectively.

After these initial studies, the same small library of oligoarginine peptides used in Chapter 2 was used to test the ability of these chemosensors to differentiate between differently charged polycations: RRGG-NH_2, RRRG-NH_2, and the oligoarginines RRRR-NH_2, RRRRRR-NH_2 and RRRRRRRR-NH_2 (R_2G_2, R_3G, R_4, R_6 and R_8, respectively). The critical aggregation concentration of all the receptor-peptide complexes was estimated by fluorescence spectroscopy to determine the aggregation onset for each complex. Then, the affinity of the peptides towards the chemosensors was determined at sub-CAC concentrations by competitive assays using the lucigenin (LCG) dye as probe.

To ascertain if the binding properties of the calixarene moiety were maintained despite the monofunctionalization, the binding constants of the SC4-nPy chemosensors towards the LCG dye were obtained by direct titration experiments (Figure 4.4 A). As observed for other SCn derivatives, the addition of SC4-nPy to a LCG solution, leads to a considerable quenching of its fluorescence emission due to the formation of a host:guest complex with the SC4 receptor moiety. Fitting the titration data to 1:1 binding model allows the determination of the binding constants (Table 4.1). The LCG affinity towards the

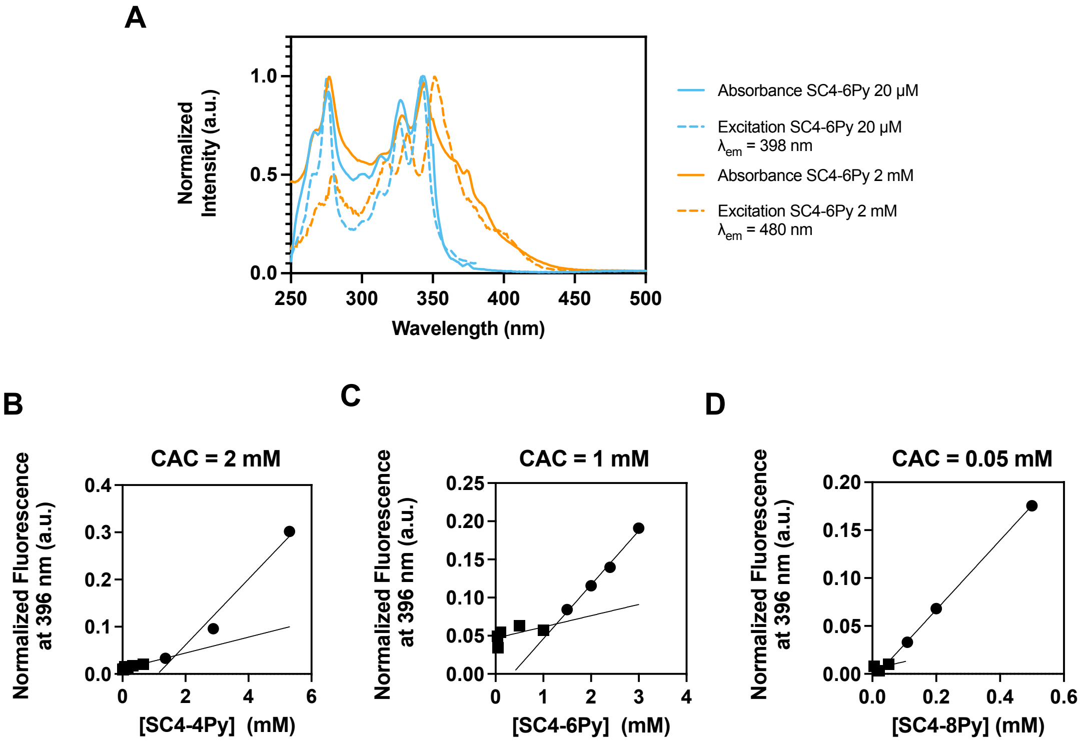

Figure 4.2: **A.** Excitation spectra (full line) and absorbance spectra (dashed line) of SC4-6Py at 20 μM (blue) and at 2 mM (orange) with the emission maximum fixed at 396 and 480 nm, respectively. Emission variation at 498 nm with increasing concentrations of SC4-nPy sensors **B.** SC4-4Py, **C.** SC4-6Py, **D.** SC4-8Py. The critical aggregation concentration is represented in each of the respective sensor plot.

monosubstituted SC4-nPy is relatively high (> 10^7 M^{-1}), independent of the size of the alkyl spacer, and, as observed for the monofunctionalized SC4 receptors reported in previous work, only slightly lower than that observed for the parent receptor SC4 (Table 4.1).

It was necessary to determine the extent of aggregation of SC4-nPy family in the presence of each element of the library in order to unveil the expected response of each sensor in relation to number of charges but also to indicate the limits of concentration at which displacement assays could be done. To this end the CAC of each receptor-peptide complex was estimated for a 1:2 ratio, by fluorescence spectroscopy (see Figure C.5 and Table C.1). Expectedly, the same trend found for the free sensors was observed for their complexes with the oligoarginines, with a consistent decrease in CAC with the increase of alkylic chain of the sensor. This is concordant with previous results, where increase in alkyl chain length linearly relates to the decrease of the logarithm of Critical Micelle Concentration (CMC) of both single chain amphiphiles and tetrameric species with the 4 unit calixarene, SC4, as the polar moiety (Figure 4.3 A).[242–245] This relation was also observed with the increase of guest effective charge, as shown for the three sensors up to the six residue oligoarginine (Figure 4.3 B). Although formation of micelles has been previously confirmed for fully substituted calixarenes, with alkyl chain susbtituents, it is not clear that the monofunctionalized species form this type of structure. In the absence of guest, some species can be detected below 10 nm but polydisperse large aggregates are the most prevalent structure. In the presence of peptide these appear to be polydisperse as well, without a clear distribution detectable by Dynamic Light Scattering (DLS) experiments (Figure C.6) and eventually precipitate out of solution. Despite precipitation occurring for the sensor-peptide complexes, the sensors present the expected distinct aggregation capacity and different responses with differently charged polycationic guests.

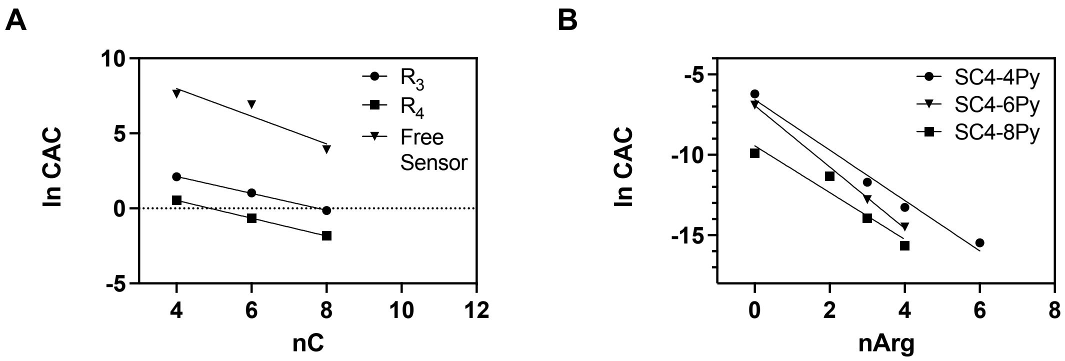

Figure 4.3: Variation of the natural logarithm of CAC (M) with **A.** the number of carbons in the alkyl chain of the sensors and **B.** the number of arginine residues in the oligoarginine guests. This relation presents the expected linearity often found for different surfactants when alkyl chain length is increased, leading to decreased CMC or CAC.

Once characterized, the receptor-lucigenin complexes were employed as reporter binding pairs in indicator displacement assays (IDA) for the determination of the binding constants of the SC4-nPy towards the selected library of peptides (Figure 4.4 B). Addition of R_4 to a solution containing the SC4-4Py-LCG complex leads to gradual recovery of the fluorescence intensity due to the release of the LCG dye from the calixarene cavity through competitive binding with R_4. The titration data can be fitted to a competitive binding model, allowing the determination of the binding affinity of the R_4 peptide towards the SC4-4Py chemosensor. These experiments were repeated for the other peptides and SC4-nPy chemosensors (see Figure 4.4 B and supplementary information, Figures C.7 to C.9), and the results (Table 4.1) show that the affinities of the arginine peptides toward the new SC4-nPy receptors are only slightly affected when compared with those observed with the parent SC4. The affinities of the different peptides for the SC4-nPy chemosensors show a consistent increase as the overall charge of the polycation is increased. Noteworthy, for peptides with 6 or more arginine residues, the aggregation onset falls below 50 nM, which is below the limit of detection for the dye and equipment setup. Thus, the affinities obtained were not under optimal displacement conditions and may still reflect contributions from aggregation, preventing accurate determination of binding constant values for the monofunctionalized chemosensors. Furthermore, the low concentrations at which aggregation is observed also limits the use of NMR spectroscopy and ITC to characterize the complexes, due to the interferance that aggregation processes has on these alternative techniques. Nonetheless, comparing these values with the ones obtained in Chapter 2, the affinity constants up to R_4 are consistent with the SC4 affinities towards the same oligoarginines, which indicate that the trend could be the same for these receptors, although not directly quantifiable.

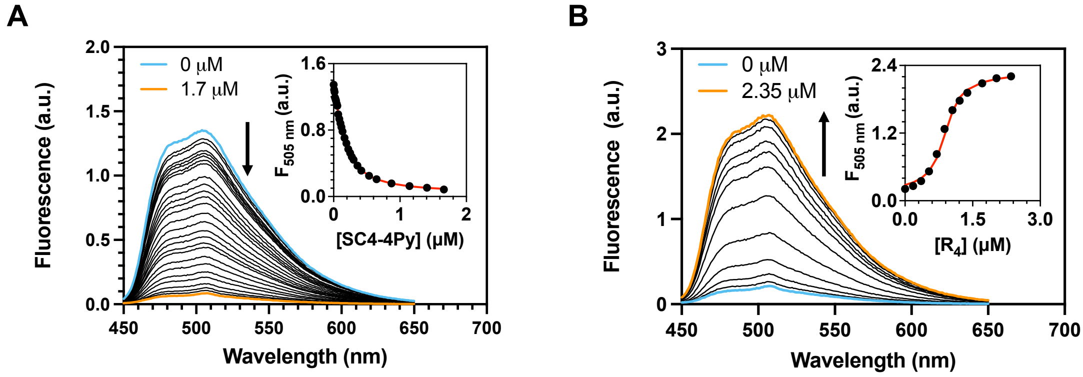

Figure 4.4: **A.** Fluorescence titration of LCG with SC4-4Py and **B.** indicator displacement assay with the SC4-4Py-LCG pair and the peptide R_4, followed by fluorescence spectroscopy (λ_{exc} = 369 nm). The concentration of the Lucigenin dye was fixed at 0.19 μM for the first assay and the concentrations of dye and SC4-4Py were fixed at 0.1 and 0.4 μM, respectively, for the competitive assay with R_4.

Table 4.1: Apparent affinity constants (K / M^{-1}) calculated by competitive dye displacement assays using lucigenin (LCG) as a fluorescence probe for the SC4 receptor and the SC4-nPy sensors, n = 4, 6, 8. All experiments were carried out in 5 mM phosphate buffer at pH 7.3.

Guest	**K / M^{-1}**		
	SC4-4Py	**SC4-6Py**	**SC4-8Py**
LCG[a]	1.2×10^7	1.6×10^7	1.1×10^7
R_2G_2	9.1×10^5	9.2×10^5	9.5×10^5
R_3G	9.1×10^6	4.4×10^6	3.1×10^6
R_4	4.3×10^7	3.2×10^7	3.7×10^7
R_6	$>1 \times 10^8$[b]	-[c]	-[c]
R_8	-[c]	-[c]	-[c]

[a] Affinity constant obtained by direct titration of LCG with the given receptor. [b] Only the lower limit of the K can be estimated because the titration curves display a sharp levelling-off at 1 equiv. of peptide, which is characteristic of very high binding affinity, precluding the accurate determination of the K under the experimental conditions. [c] No affinity constants were obtained due to the CAC being lower than the lower detection limit for the technique used.

After establishing that the SC4-nPy chemosensors retain the general binding properties of the parent SC4 receptor, direct fluorescence titrations were conducted by adding increasing concentrations of peptide to SC4-nPy at a fixed concentration, in batch. These experiments showed identical trends to those shown by the variations in CAC, with different oligoarginines showing distinct ability to trigger the aggregation process for each sensor. As can be observed from Figure C.11 A, the addition of R_2G_2 to a solution SC4-6Py leads to a moderate quenching of the pyrene emission. However, the hexarginine peptide R_6 clearly induces the aggregation of SC4-6Py as demonstrated by the decrease in the intensity of monomer emission and the concomitant appearance of a new and intense excimer-like emission band centered at, approximately, 480 nm. Considering that the complexation-induced aggregation of the SC4-nPy chemosensors can be expected to depend on their amphiphilic character (in line with CAC of the free compounds and complexes) and on the overall charge of the target peptides, the induced aggregation of the 3 chemosensors was screened for the different oligoarginines. As can be observed, the most hydrophobic compounds present a higher tendency to aggregate in the presence of a given peptide - for example, under the selected sensing assay conditions, SC4-4Py does not aggregate in the presence of R_3G, while SC4-6Py presents a small but measurable aggregate emission increase and SC4-8Py shows considerable aggregation induced by this peptide. Similarly, the aggregation of SC4-4Py is only observed for oligoarginines with 4 or more cationic residues, while SC4-6Py starts to aggregate with R_3G and SC4-8Py with the peptide with only two arginine residues. These observations indicate that a highly positively charged peptides leads not only to higher affinities but also more efficient charge neutralization of the SC4 moiety, which are thought to be the main mechanisms behind this aggregation phenomenon. For the larger polycations, under the chosen concentrations of sensor, it becomes challenging to distinguish the observed output, as both R_6 and R_8 lead to equally efficient aggregation of the chemosensors.

Taking advantage of the clear differences of CAC for these complexes with different peptides and sensors, the concentrations could be adjusted in order to allow the naked-eye visualization of the change in emission color. Visually, it is possible to clearly distinguish the presence of peptides with two arginines from the ones with more arginine residues. When analysing these results at lower concentrations by fluorescence spectroscopy and normalizing the values for the highest ratio for each sensor it is possible to further this visual distinction up to R_4, for the assay at 50 μM, while the larger peptides can only be distinguished by adjusting the sensor concentration to a lower value (1 μM).

A Principal Component Analysis (PCA) was conducted using both monomer and aggregate emission (λ = 376, 420 and 480 nm) and, taking advantage of the ratiometric measurement that this system allows, the complete distinction up to R_8 is possible at the concentration of 10 μM of peptide and 5 μM of the sensors. Similar analysis using only the quenching of monomer emission at different wavelengths yields less distinction for both large and small oligoarginines, as well as presenting a higher error for the triplicates of a given peptide (Figure C.16).

Although successful distinction was obtained in this proof of concept study, one of the main limitations of this work falls on the variability introduced by concentration variations. Ideally, a calibration curve should be performed for each of the guests with different number of charges, as well as other calibration assays, in order to use this array-like sensing assay in more complex samples as is the case of biological ones.

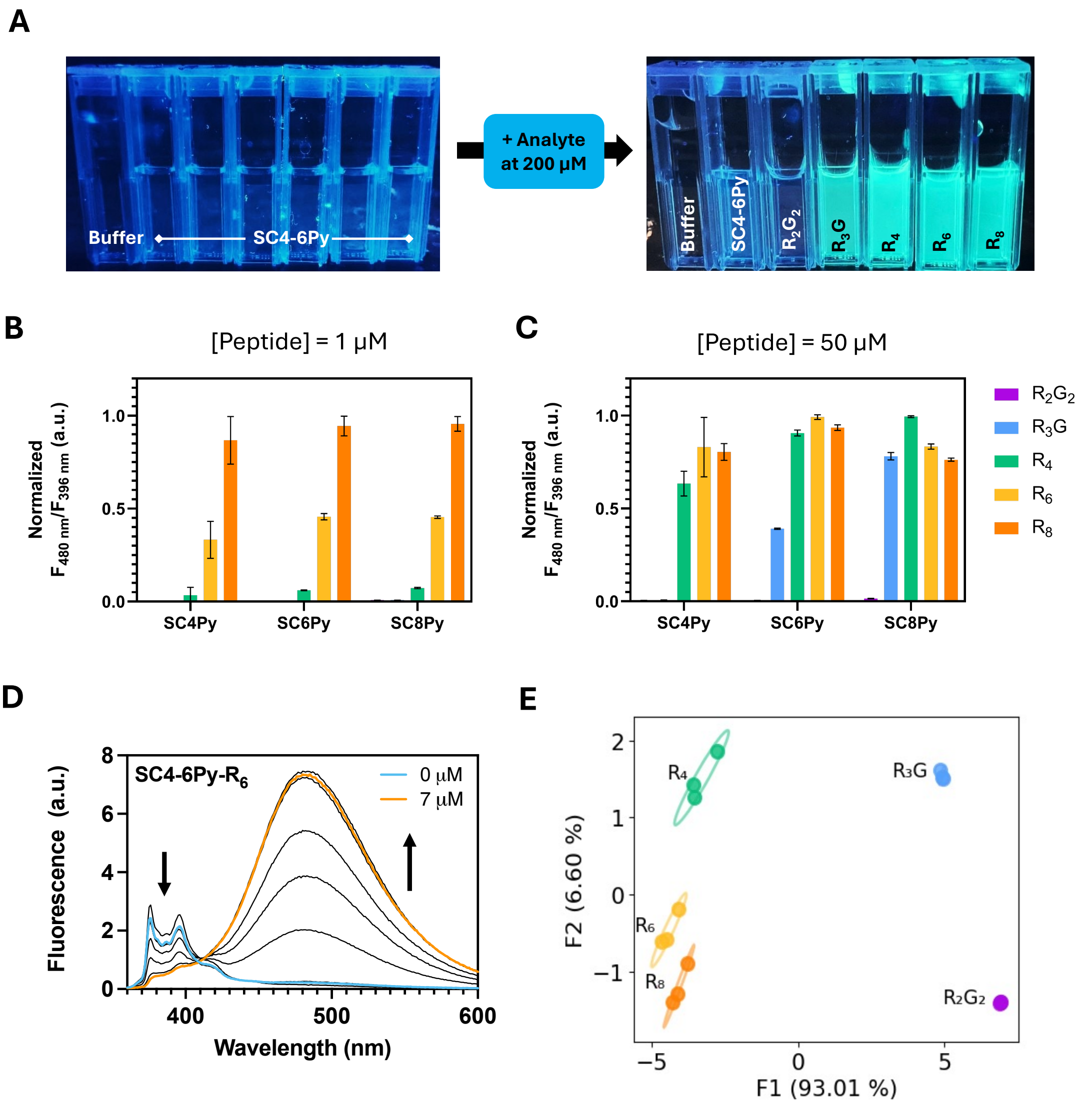

Figure 4.5: **A.** Visual array under fluorescent light (λ_{exc} = 366 nm) performed with the sensor SC4-6Py at 5 μM, before and after the addition of 200 μM of each of the peptides, with two negative controls, one with only phosphate buffer 5 mM and the other with only the sensor molecule. Bar plots of the fluorescence ratio at 480 and 396 nm of the SC4-nPy sensors (5 μM) are represented as well, with the values normalized for the highest ratio for the three sensors at the corresponding concentration of peptide. The peptide concentration used was **B.** 1 and **C.** 50 μM. **D.** Fluorescence titration of SC4-6Py (1 μM, λ_{exc} = 347 nm) with R_6 with the peptide concentration varying between 0 and 7 μM. **E.** Principal component analysis (PCA) of the emission of the three SC4-nPy sensors (5 μM) in the presence of 10 μM of each peptide. The data used consisted of emission at three different wavelengths (λ = 376, 420 and 480 nm) normalized at 396 nm, and using triplicate samples of each of the peptides. The ellipses correspond to 95% confidence intervals for each group of peptide samples, with R_2G_2 and R_3G not observable due to higher accuracy in the classification.

Despite its limitations, the use of the different CAC for the investigated chemosensor-peptide pairs and the use of this stimuli-responsive self-assembly-based system allowed detection beyond the limit of conventional affinity-based assays. This alternate strategy makes this a powerful prospective system for the successful differentiation between polycationic high affinity guests like this peptide family and, eventually, proteins with polycationic sequences or cationic patches on their surface.

4.2 *p*-Sulfonatocalix[4]arene based surfactants in coalescence-based sensing strategies

This section of work was developed in collaboration with Professor Timothy M. Swager and Dr. Georgios Toupalas, during a three month stay at the Swager Lab, Massachussets Institute for Technology, Cambridge, MA, in the scope of the European Horizon2020 project VIT ("Polymer engineering via molecular design: embedding electrical and optical properties into VITrimers", Grant agreement ID: 101008237).

Oil in Water (O/W) emulsions consist of an organic phase dispersed in an aqueous phase, stabilized by the presence of a surfactant in the interface between the two phases. These can be characterized as large supramolecular systems, seeing as they hinge on non-covalent interactions between different elements and solvents to self-assemble into spherical droplets, with the surfactant molecules at the interface between these (disperse phase) and bulk solvent (continuous phase). Their formation and overall characteristics are key in several fields, including surfactant chemistry, formulation development in pharmacological and cosmetic industries, and fuel industry.[246–248]

While more complex emulsions have been successfully employed for sensing and detection of both environmental and biological targets with great success, O/W emulsions, despite their ease of preparation, have yet to be fully explored for such purposes.[249,250] In this work, O/W emulsions were used as a platform for creating a sensing system. A family of surfactants based on calixarenes of different sizes was selected for their dual functionality, having the capacity to stabilize the interface and serve as receptors inserted into a confined platform. The family of molecules chosen for this was based on the previously characterized SCn moiety, but instead of the monofunctionalized species, fully O-substituted calixarenes were used, with varying length alkyl chains and variable calix-arene host size (SCn-mC, Figure 4.6). These oligomeric surfactants allow the stabilization of O/W emulsions due to their amphiphilic and multivalent nature, can presenting low CMCs, while also acting as receptors for cationic molecules.[39,242] The sensing mechanism is based on the expected alteration of the system properties caused by complexation: when binding of cationic guests occurs, there will be a charge neutralization in the calixarene polar head, leading to a dimished effect on the surface tension in comparison to the free surfactant, and consequently affect the stability of the emulsion or alter the morphology of the droplets.

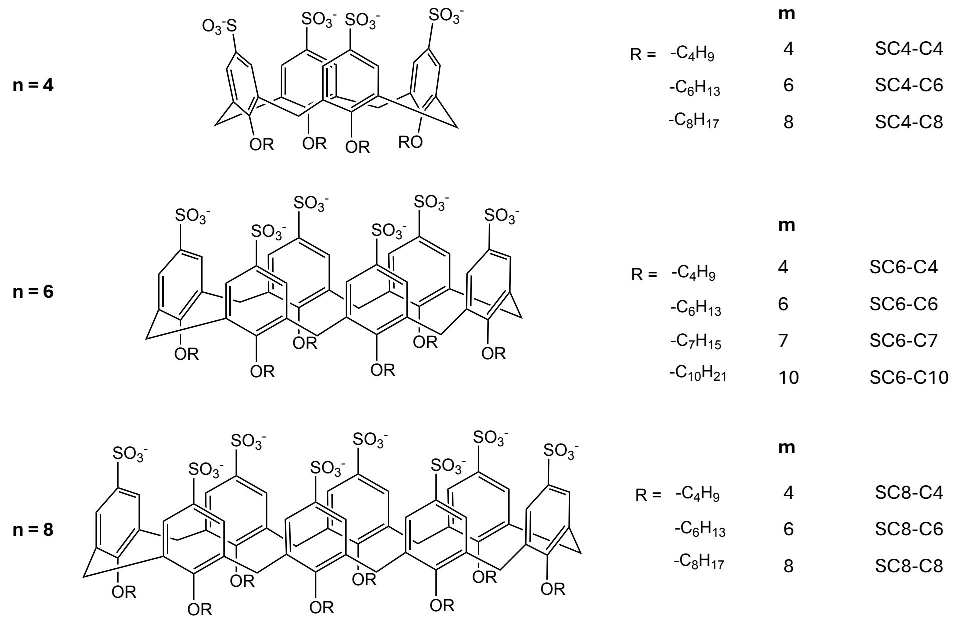

Figure 4.6: SCn-mC surfactant chemical structure and respective designation.

O/W emulsions were obtained by addition of a small aliquot of organic solvent to a solution of the given surfactant and vortexed for 5 to 10 seconds or until a stable dispersion was observed (see Chapter 7 for full methodology). While mixtures without any surfactant quickly separated in two distinct phases, droplets could be observed either on the top or in the bottom of the aqueous solution for surfactant samples, depending on the organic phase and after letting the dispersion settle, confirming that emulsions were successfully obtained. These initial studies with the polydisperse samples showed that these surfactants were particularly promising for the stabilization of o-dichlorobenzene (O-DCB) droplets in aqueous solution, when compared to results with diethylbenzene, where little to no droplet formation was observed (Figure C.17). Surfactant concentrations as low as 0.025 wt% successfully stabilized polydisperse emulsions of O-DCB in water, confirmed under optical microscope, up to 24 hours after droplet preparation (Figure 4.7 and Figures C.18, C.19, C.20 and C.21).

In order to compare the full library of surfactants and relate it to the capacity to stabilize droplet formation, surface tension, γ / mN m^{-1}, values were measured using the Contact Angle Apparatus, with the pendant drop method, for O-DCB droplets in 0.025 wt% aqueous surfactant solution. The CMCs could not be obtained for the full SCn-mC library due to time constraints, however, comparison at this fixed concentration, added to literature CMC values for the water-air interface, gave an indication of the most efficient of the surfactant molecules and the effect on surface tension. γ decreases with the increase of alkyl chain length at this concentration only up to the 7 carbon alkyl chain surfactants, with SC4-8C showing similar γ to those without surfactant. SC8, while it showed the ability to stabilize the droplets visually, in the conditions of the pendant drop assay no effect on solvent surface tension was observed, so no conclusions could be drawn. For

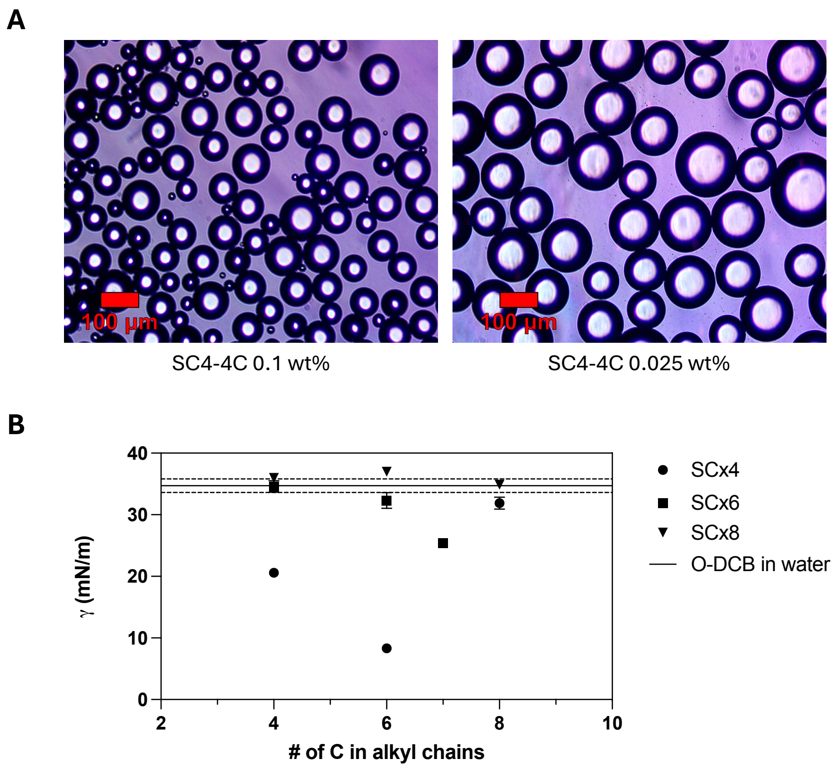

Figure 4.7: **A.** Optical microscope images of polydisperse emulsions of O-DCB in aqueous solution of SC4-4C surfactant at 0.1 and 0.025 wt%. **B.** O/W surface tension, γ / mN m^{-1} variation with calixarene host size and alkyl chain length of O-DCB droplets of the different surfactant solutions at 0.025 wt%. O-DCB value in water in the absence of surfactant presented as a black line with respective error as dashed lines.

full, adequate analysis, the CMC of all the species should be obtained, while accounting for the slow kinectics that these species present both for structural rearrangement and for exchange between the micelles formed at higher concentrations and interface between organic and aqueous phase.[39,242] Due to these time limitations and constraints of the system, SC4-4C was chosen to try to achieve a proof of concept for this O/W emulsion stability-based sensing mechanism.

Monodisperse droplets were made by microfluidic fabrication, by mixing the two phases in a microfluidic chip with 50 μm channels.[249,251] The concentration selected was 0.037 wt%, which corresponds to the necessary amount to cover the spherical O/W interface fully in a monolayer of the chosen calixarene surfactant, SC4-4C, calculated by approximate area of calixarene receptor in solution.[252] Addition of previously reported SC4 guests to these monodisperse emulsions, Arginine-o-methylesther (ArgOMe), and oligoarginines R_6 and R_8, leads to coalescence of the droplets. In Figure 4.8 the concentrations at which coalescence starts to be consistently observed are shown, corresponding to addition of 50, 5 and 1 μM for ArgOMe, R_6 and R_8, respectively, to a 0.037 wt% ($\approx$ 350 μM) SC4-4C solution.

Repetition of surface tension measurements by pendant drop method in the presence

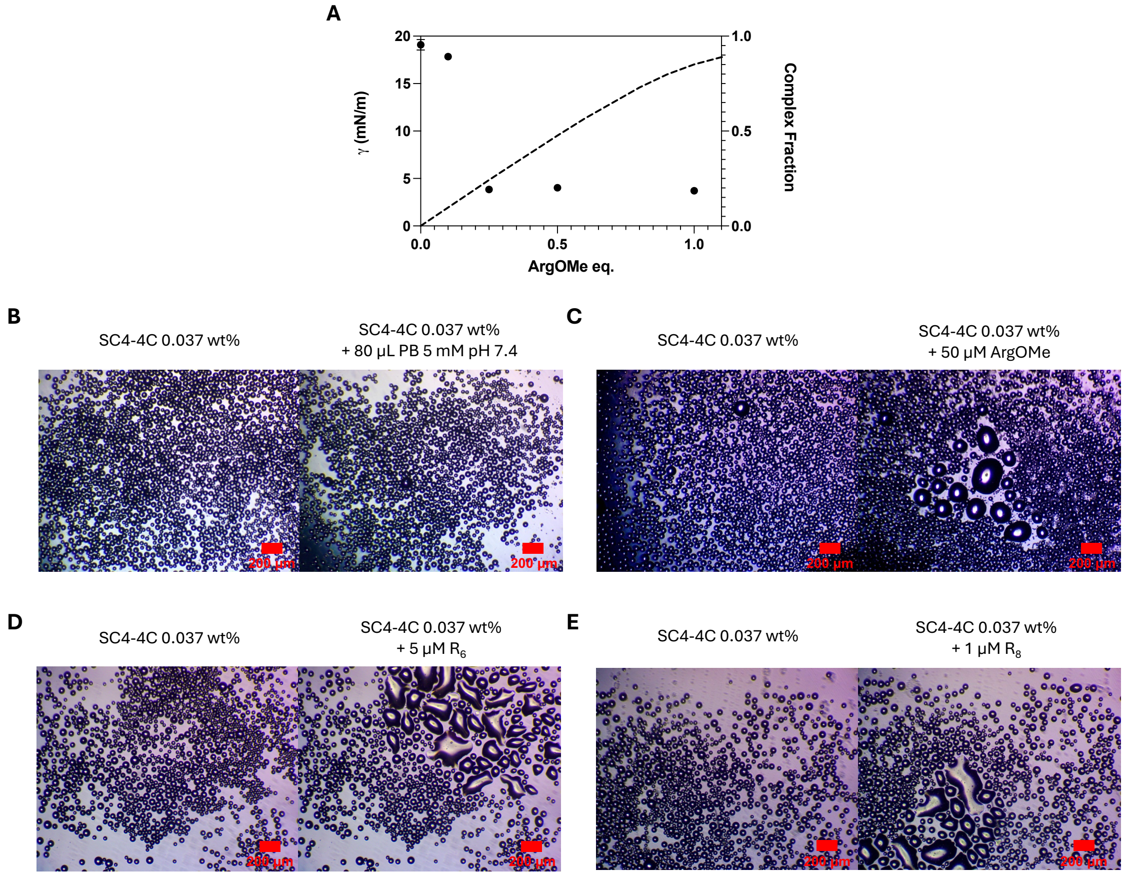

Figure 4.8: **A.** O/W surface tension, γ / mN m^{-1} variation of O-DCB in SC4-4C 0.035 wt% solution with increase of ArgOMe concentration, represented in equivalents to the surfactant concentration. Complex fraction at the given ratio of SC4-4C and ArgOMe represented as a dashed line with respective values in the secondary axis. Optical microscope images of monodisperse droplets of O-DCB in 0.037 wt% in SC4-4C solution before and after addition of **B.** 80 μL PB 5 mM pH 7.4, **C.** 50 μM ArgOMe, **D.** 5 μM R_6 and **E.** 1 μM R_8. Images shown corresponds to the concentrations were coalescence started to occurr consistently for triplicate analysis; for full array of concentrations tested, at different magnifications, see Figures C.22 to C.25.

of ArgOMe shows a marked decrease in surface tension well below saturation of the calixarene receptor. Additionally, an increased turbity of the calixarene-ArgOMe samples was observed with the increase of ArgOMe concentration, up to the charge neutralization point at 2 equivalents of this guest. Such effect seems to correlate with the interval of concentration at which droplet coalescence starts to be observed more consistently, with the drop in surface tension observed between 35 and 87.5 μM ArgOMe and the coalescence onset visually detected to be equal to or below 50 μM. Due to both of these factors, it is likely that the decrease in surface tension observed could be due to sedimentation during the pedant drop tensiometry assay, which is a known limitation of the method, leading to apparent surface tension decreases.[253] Considering these results, it was not possible to ascertain if the surface tension was influenced by the complexation, so the mechanism of coalescence could not be clarified, but alterations in the system appear to correlate between different experiments.

Given this consistent response and despite the visual response provided by droplet coalescence, a clearer and measureable readout mechanism was needed for a facile and efficient detection system. Several strategies were attempted based on turn-on fluorescence signals, all of them taking advantage of the capacity of droplets to act as microcontainers. If different species, not capable of partitioning into the aqueous medium, are added to distintc emulsion batches, we can have them separate, with mixing and, consequently, reacting only upon this triggered coalescence.

Chemiluminescence (CL) was initially tested as a readout mechanism, due to the high signal-to-noise ratios associated with the most common CL reactions. These are often triggered by the oxidation of an initial reagent into an unstable peroxide that will lead to a chemical excitation of a fluorescent aromatic hydrocarbon with low oxidation potential. The reaction used in this study was the peroxyoxalate reaction, where an oxalic phenylester reacts with hydrogen peroxide to originate 1,2-dioxetanedione, which is able to excite the aromatic hydrocarbon dyes.[254,255] The reaction was done with bis(2,4,6-trichlorophenyl)oxalate (TCPO) as the oxalate precursor and 9,10-(diphenylethynyl)anthracene as reporter. Even though CL was observed in organic phase both with H_2O_2 and triethylsilane (TES) protected peroxide (with addition of a catalyst for the deprotection, see Figure 4.9 A), in O-DCB-Water emulsions, no emission was visually observed or detected by fluorescence spectroscopy both before and after coalescence (Figure 4.9, Table 4.2 and Figure C.26). The most efficient catalyst for deprotection of $(TES)_2$-peroxide, tetrabutylammonium fluoride (TBAF), was likely binding to the calixarene moiety in the surfactants and interfering with the stability of the droplets, not allowing the formation of droplets in the first place. Other catalysts were used but their efficiency was limited in organic solvent so it is possible that the extent of CL was too low to be detectable in the droplets (see droplets obtained with different catalysts in Figure C.27). Additionally, there's the possibility that, in the O/W emulsion, the oxalate could partition to some extent into the aqueous phase and degrade in contact with water before the droplets with different contents were mixed and coalesced.[256]

With the poor success of CL-based turn-on fluorescence strategies, a turn-off mechanism was attempted based on the epoxidation reaction presented in Figure 4.10 A. Epoxidation of dyes like 1,6-diphenylhexatriene (DPH), with λ_{exc} = 350 nm and λ_{em} = 420 nm, leads to interruption of the π-system and consequently, change in absorption and emission properties of the fluorophore, leading to quenching or blue-shifted emission.[257,258]

This reaction was first evaluated in O-DCB, with *meta*-chloroperoxybenzoic acid (mCPBA), soluble in the organic medium, acting as oxidizer of DPH. DPH emission was quenched to approximately 60% after 1 hour after addition of mCPBA (Figure C.28). Monodisperse droplets were prepared at 0.037 wt% of SC4-4C, in two separate batches, with 0.1 mM of DPH and 5 mM of mCPBA in the organic phase, respectively. Fluorescence microscopy shows the presence of the dye in the DPH droplets and no emission in the

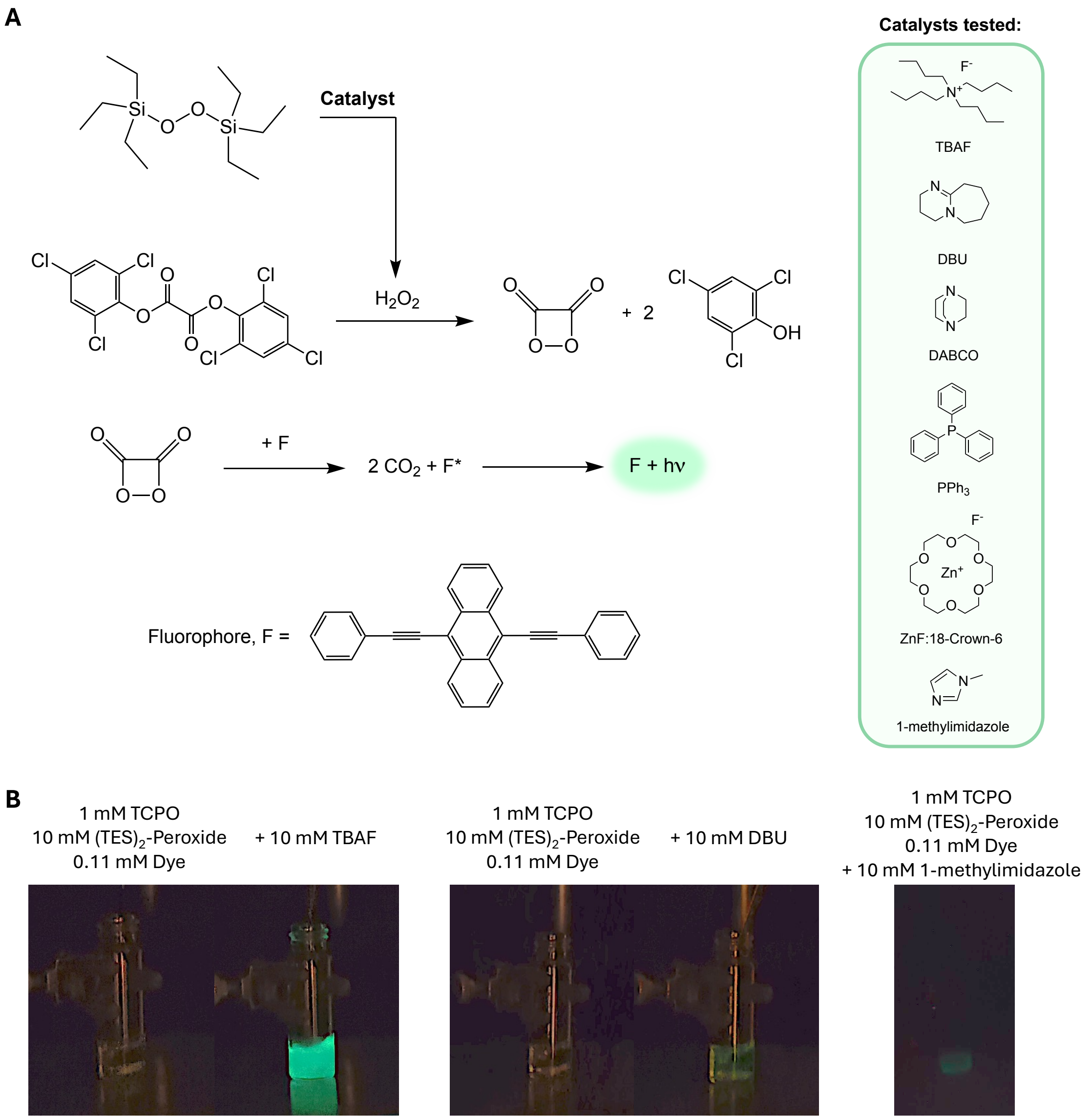

Figure 4.9: **A.** Strategy for chemiluminescent peroxalate reaction using TES-protected peroxide. Deprotection of the peroxide was used to generate H_2O_2 in the organic phase and catalysts tested for the deprotection reaction are presented on the right, from top to bottom: TBAF, 2,3,4,6,7,8,9,10-octahydropyrimido[1,2-a]azepine (DBU), 1,4-Diazabicyclo[2.2.2]octane (DABCO), Triphenylphosphine (PPh3), ZnF, ZnF:18-Crown-6 and 1-methylimidazole. **B.** CL visually detected in O-DCB phase with catalysts TBAF, DBU and 1-Methylimidazole.

Table 4.2: Results for the chemiluminescence assays with TES-protected peroxide and respective catalyst used for deprotection reaction and respective concentration. TCPO and fluorophore concentration were fixed at 1.7 mM and 0.11 mM, respectively.

Catalyst	[Catalyst]	CL in O-DCB	CL in droplets
TBAF	10 mM	✓	✗
DBU	10 mM	✓	✗
DABCO	10 mM	✗	✗
PPh3	10 mM	✗	✗
ZnF	Sat.	✗	✗
ZnF:18-Crown-6	Sat.	✗	✗
1-methylimidazole	10 mM	✓	✗

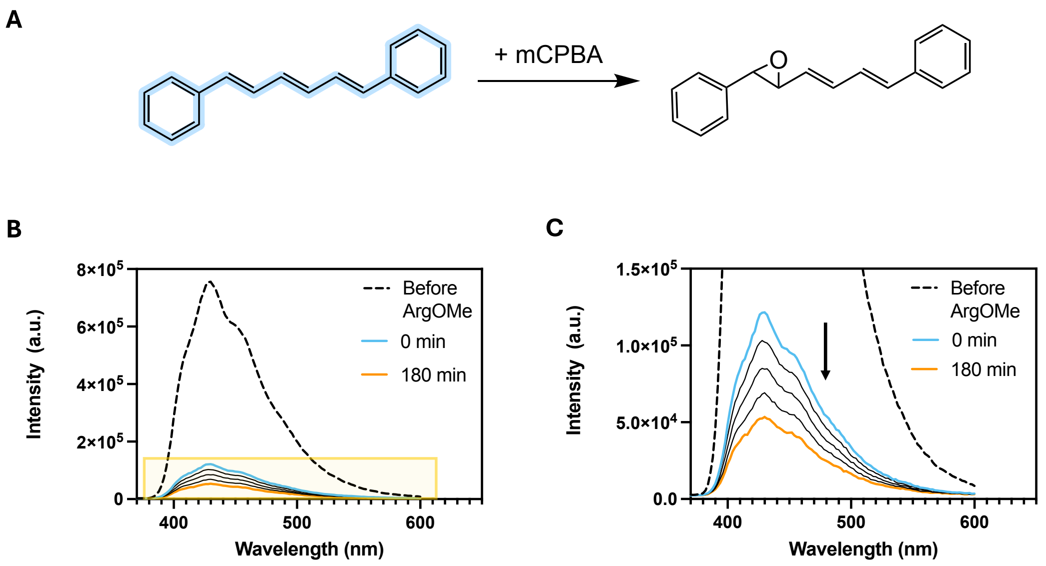

Figure 4.10: **A.** Epoxidation reaction with DPH and *meta*-chloroperoxybenzoic acid (mCPBA), with the site selected as example of where epoxidation can occurr. **B.** Emission spectra (λ_{exc} = 350 nm) of the mix of two different batches of polydisperse droplets in SC4-4C 0.037 wt%, with mCPBA and DPH in the organic phase, before and after the addition of ArgOMe, followed up to 180 minutes after addition of the guest. In **C.** the zoom in of the area highlighted in yellow in B is presented, for better visualization of the evolution of DPH emission after addition of an excess of guest.

mCPBA batch. Small aliquots (5 μL) of each batch were added to the same glass plate and checked for quenching of DPH emission without any guest present and in the presence of increasing concentrations of the 8 residue oligoarginine, R_8. The emission showed a sigmoidal dependence on the peptide concentration, with a marked decrease for samples where coalescence occurred (confirmed by microscopy studies). Control experiments were made to verify the source of this quenching - the same assay was performed only with DPH droplets and a similar trend could be observed. This reveals that the coalescence appears to be the main contributing factor for quenching of DPH emission, either by physical phenomenon (dispersion of emited light in droplets) or by oxidation from mixing with oxygen present in the aqueous phase.

A detection mechanism was successfully achieved, even though the mechanism of quenching could not be clarified, due to the time constraints of this project. Ideally, O/W emulsions with different organic solvents could still be tested with this family of surfactants, in order to control the partioning of the different reactants between phases and, eventually, lead to a successful turn-on detection method. Moreover, other chemiluminescence-based sensing strategies could be explored as well.

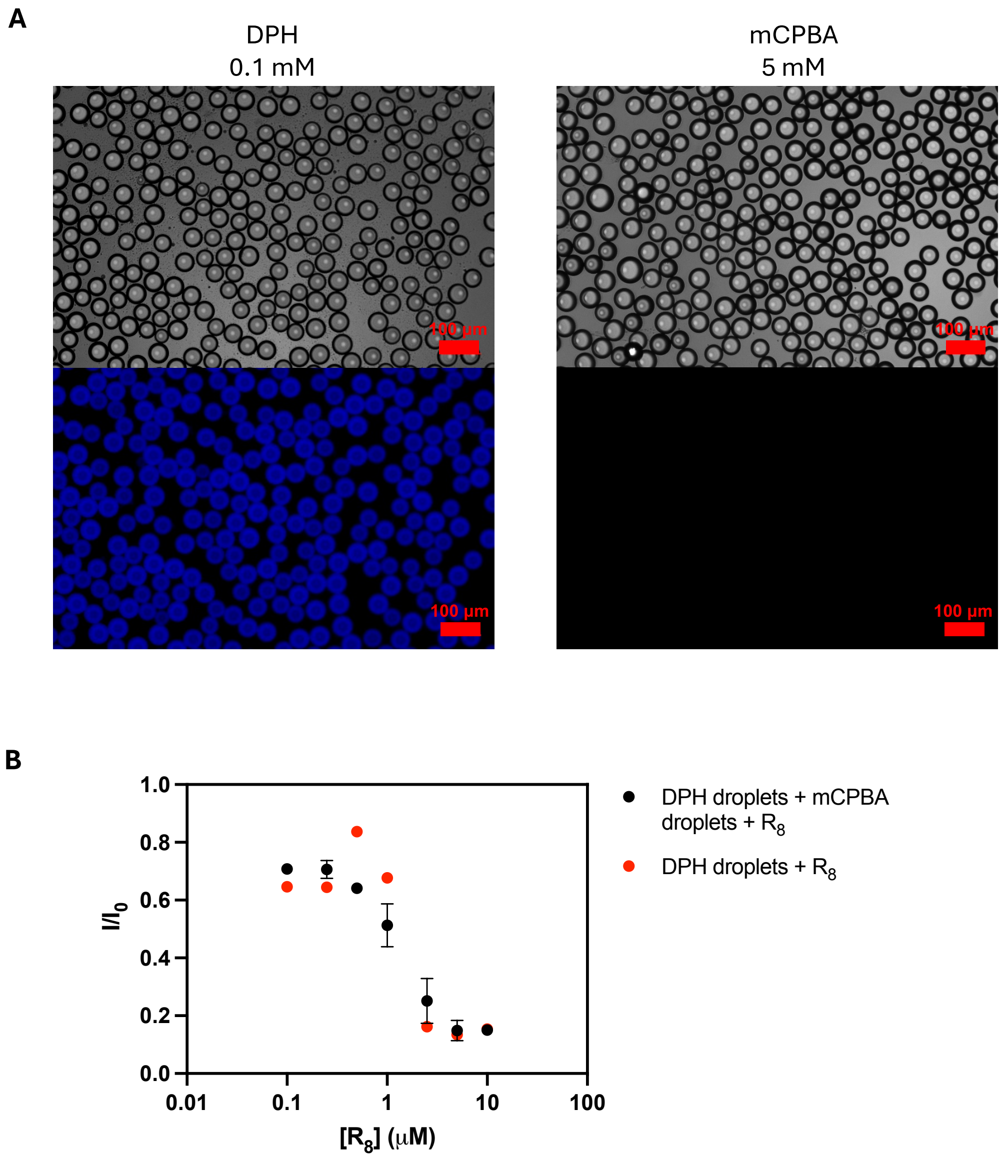

Figure 4.11: **A.** Fluorescence microscopy images of the two monodisperse batches of DPH 0.1 mM and mCPBA 5 mM in O-DCB droplets, prepared in SC4-4C 0.037 wt%. Top images correspond to the brightfield image and the bottom images correspond to the fluorescence microscopy ones, using the 4',6-diamidino-2-phenylindole (DAPI) channel for excitation and detection. Consistent emission is observed for the droplets with the dye DPH and no emission is observed for mCPBA droplets, as expected. **B.** Variation of emission ratio with the increase of peptide, R_8, concentration. The black circles represent the samples where 5 μL of each droplet batch were mixed before analyte addition and in red using only DPH droplets, which do not have triplicate measurements due to time limitations.

5

Mixed biomimetic systems based on host-guest chemistry and self-assembly

In biological environments, several factors contribute for the establishment of complex functional structures, from environmental stimuli to the diverse interactions that can be established between different biomolecules.[2,7,172] When we transpose this notion to biomimetic supramolecular systems, the same factors need to be taken into consideration when designing the system. When using a bottom-up approach, it is necessary to take advantage of each building-block capacity to self-assemble into complex structures, which can be aided by the incorporation of inclusion complexes, contributing to the stability of such structures or for addition of functionality or stimulus-responsiveness to the system.[7]

Liposomes, as previously mentioned in the Introduction (see Section 1), offer not only a way to compartimentalize function, much like observed for cellular membranes, but also aid in the stabilization and biocompatibility of encapsulated compounds. These can also serve as platforms for the study of different membrane-incorporated receptors, either for transport or sensing of a variety of target molecules.[7,13,173,174]

In this section, liposomes serve as a base not only for study of supramolecular receptors in a cell-like environment, but also as a platform for the development of novel sensing platforms and responsive transporters. In this chapter, a light-responsive transport system will be presented, which was based on the calixarene receptor, SC4, and a photoactive azobenzene moiety, studied in these artificial membranes and in cellular environment with very positive results.[215] Additionally, a sensing system based on the same receptor, but with the amphiphilic design described in Sections 3.1 and 4.1, was applied in the same liposomal platform, for the detection of polycationic cargo in biomimetic environments.

5.1 Light-Activated Transport of Polycationic Peptides

This work has been developed in collaboration with CIQUS, at the Santiago de Compostela University, Spain, and published in the Journal of the American Chemical Society in 2023.[215] Coauthors on this paper contributed on the synthesis of peptides (Dr. Alicia Rioboo) and SC4-Azo 2 (MSc. Beatriz Raimundo), as well as on the realization of some of the triplicates in the photophysical characterization and in the biological assays of cell microscopy, flow cytometry and cytotoxicity assays (PhD Student Yeray Folgar-Cameán). Most of this section corresponds to the reproduction of this publication with an added final comment regarding relevant work that has been developed since the publication of this work by other research groups.

Selective transport of ions, metabolites, and large biomolecules across lipid membranes is a fundamental process for the maintenance of cellular function and homeostasis in living organisms.[259] While small, moderately polar molecules can spontaneously cross cell membranes by passive diffusion, the translocation of hydrophilic substances with low permeability, including biologically relevant ions and large biomolecules, is generally accomplished through a variety of transport mechanisms involving stimulus-responsive membrane proteins. These biomolecular machines and active transporters are frequently claimed as a source of inspiration for the development of artificial supramolecular channels and carriers.[143,260–264] Synthetic transporters, usually designed as simplified prototypes of their biological counterparts, are useful biomimetic tools, not only to investigate membrane transport mechanisms and but for use as active pharmaceutical ingredients or drug-delivery systems as well.[134,143,261–268]

Stimulus-responsive artificial transporters displaying photomodulated activity are particularly appealing due to the advantages of using light as a stimulus. Photoactive systems allow remote application, a high degree of spatiotemporal precision, and, in most cases, no production of chemical waste.[136,143,269] Their utility for biological and pharmaceutical applications has led to the successful development of a considerable number of photoresponsive artificial channels and pores operating through different mechanisms.[143] However, independently of their functional mechanism, most photoresponsive transporting systems are designed to target small ions, while those directed to larger biomolecules remain unexplored.[184,185,270–277]

Among the different systems developed to transport large hydrophilic cargos across membranes, amphiphilic counterion activators have proven to provide efficient synthetic carriers using relatively simple and synthetically accessible molecules.[265,278] Counterion activation phenomena result from the binding of polyionic species with oppositely charged molecules, forming charge-neutralized complexes with higher membrane permeability.[265] Fundamental studies on counterion-activated membrane transport have been frequently carried out using cationic peptides as cargo molecules.[61,179,279–282] These investigations have made important contributions to elucidate the intriguing high membrane permeability of polycationic peptides, showing that their dynamic association with anionic molecules present in cell membranes (e.g., anionic lipids or glycosaminoglycans) plays an important role in their transport mechanism.[265,283] Systematic screenings have identified pyrene carboxylate amphiphiles as prime activators for the transport of poly- and oligoarginines across phosphatidylcholine lipid bilayers.[61,279] Amphiphilic sulfonatocalixarenes have also been shown to be highly efficient counterion activators for the membrane transport of cationic peptides.[180–182]

The excellent translocation activity of these anionic macrocyclic receptors was correlated with their binding affinity toward positively charged peptides and their membrane partitioning properties, with moderately amphiphilic receptors affording better activators.[180] Previous comprehensive structure-activity studies have reported that subtle variations on the electronic and structural nature of activators can lead to dramatic changes in their transport activity.[61,179,281,284] Consequently, the dynamic control of the structure/polarity of counterion activators offers a promising conceptual strategy to develop stimulus-responsive membrane carriers. We hypothesized that azobenzene photoswitches, which are known to experience significant conformational and polarity changes ($\Delta\mu \approx 3$ D) upon *E*-*Z* photoisomerization, would provide a rational design motif for the potential construction of new light-responsive membrane transporters.[285,286] In this work, we report the first synthesis of such photoswitchable counterion activators for the membrane translocation of hydrophilic peptide cargos. Our design relied on *p*-sulfonatocalix[4]arene-azobenzene conjugates (Figure 5.1 A), as anionic receptors with photomodulated amphiphilicity, which enables the light-triggered transport activation of cationic peptides across artificial lipid bilayers and inside living cells (Figure 5.1 B).

The synthesis of the photoresponsive counterion activators 1 and 2 was accomplished by direct monoalkylation of the SC4 macrocycle (the more organo-soluble lithium salt) with the respective azobenzene precursor in dimethyl sulfoxide (DMSO) (see Chapter 7).[287] The ^{1}H-NMR results of both compounds in CD_3OD (Figures 7.9 and 7.10) show two pairs of doublets for the four methylene bridges indicating that, in this solvent, 1 and 2 adopt the cone conformation.[288] In D_2O, the ^{1}H-NMR spectra of 1 and 2 (Figures 7.11 and 7.12) are substantially different from those observed in CD_3OD, showing broader resonances, which can be tentatively assigned to intermediate conformational and/or aggregation exchange dynamics on the NMR chemical shift timescale.[36]

The photochromic properties of 1 and 2 were investigated in diluted aqueous solution by UV-vis absorption spectroscopy and in CD_3OD by ^{1}H-NMR. Photochemical irradiation using a UV-light wavelength (λ_{irr}) of 366 nm led to quantitative conversion of the E isomers into the respective *Z*-forms, with the quantum yields (Φ) of photoconversion being $\Phi_1^{E\to Z} = 0.4$ and $\Phi_2^{E\to Z} = 0.4$ (see Figure 5.2 and Figure D.1).

On the other hand, irradiation of the *Z*-forms at $\lambda_{irr} = 500$ nm originates a Photostationary State (PSS) composed of 70 and 80% of *E*-1 ($\Phi_1^{Z\to E} = 0.6$) and *E*-2 ($\Phi_2^{Z\to E} = 0.5$), respectively (Figure 5.2 and Figure D.1). As generally observed for other azobenzene photoswitches, the *E* isomers can be quantitatively recovered in the dark through the thermal $Z \to E$ isomerization, with 1 and 2 presenting activation energies of 215 and 93 kJ/mol, respectively (Figures D.2 and D.3).[289] Despite the substantial difference in activation energies, both *Z*-1 and *Z*-2 are metastable species, presenting minimal thermal interconversion at room temperature during the time frame of our experiments, allowing for their use in binding studies and counterion activation assays without interferences from the thermal $Z \to E$ isomerization.

The binding affinity of the anionic calixarene activators toward cationic peptides was

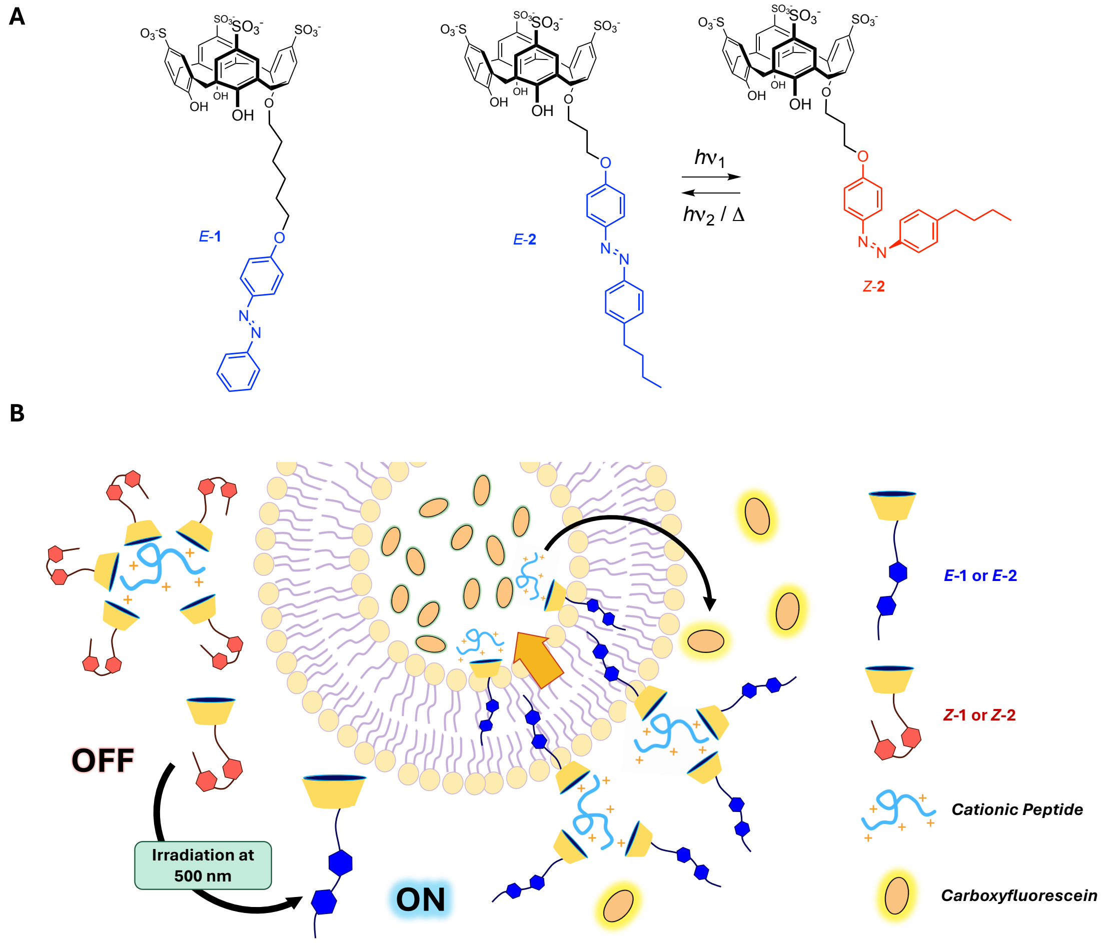

Figure 5.1: **A.** Molecular structure of the photoresponsive counterion activators investigated in this work, with the relevant *E*-*Z* photoisomerization illustrated with activator 2. Both compounds were synthesized as lithium salts. **B.** Schematic representation of the phototriggered transport of cationic peptides across phospholipidic membranes.

investigated using a small library of highly hydrophilic oligoarginines, from 3 to 8 residues. These peptides are not able to spontaneously transverse zwitterionic artificial membranes in vesicle assays, which allows the accurate evaluation of the calixarenes 1 and 2 as counterion activators without interferences from the transport of the peptide alone.[290–292] First, the formation of host-guest complexes between 1/2 and the selected peptides was verified by indicator displacement assays using LCG as the fluorescent indicator.[156] As previously reported for other sulfonatocalixarene derivatives, the formation of host-guest binding pairs between calixarenes 1/2 in the *E*- and *Z*-forms and LCG results in significant static fluorescence quenching (see Figure 5.3 A and Figure D.4).[156] Quantitative analysis of the fluorescence titration data using a 1:1 host:guest binding model allows the determination of the respective binding constants (K, M^{-1}) reported in Table 5.1. As can be observed, both 1/2 display high affinity for the LCG dye, on the 10^7 M^{-1} range, which seems to be independent of the nature and conformation of the azobenzene arm. Furthermore, the observed binding constants are only slightly smaller than the one

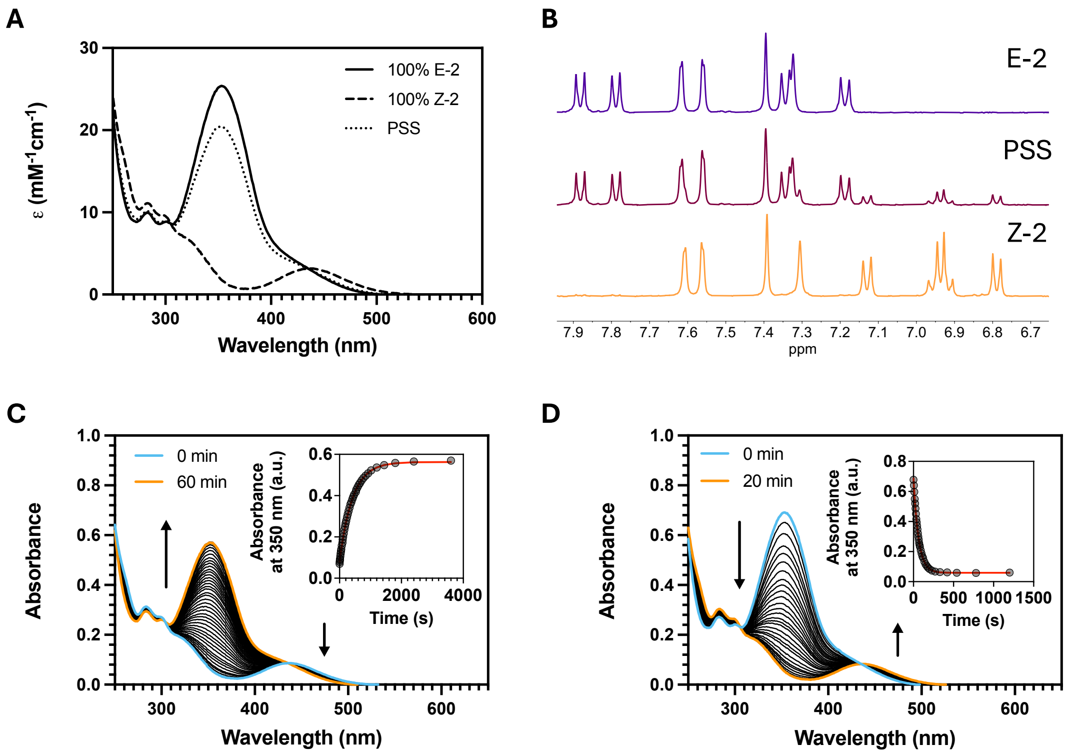

Figure 5.2: **A.** Absorbance spectra of both *E* and *Z* isomers of 2 and the photostationary state (PSS; 80:20 *E:Z*) obtained after irradiation at 500 nm. **B.** Partial ^{1}H-NMR (in CD_3OD) spectra of the aromatic region of 2 at the dark-adapted state (*E* isomer), PSS upon irradiation at 500 nm (*E:Z* 80:20) and at 366 nm (*Z* isomer). **C.** $Z \rightarrow E$ and **D.** $E \rightarrow Z$ photoisomerization of 2 followed by UV-vis spectroscopy upon irradiation at 500 and 366 nm.

observed for the parent SC4 receptor (K = 8.1 $\times 10^7$ M^{-1}, see Figure D.4), suggesting that these monofunctionalized receptors retain their recognition properties. The host:LCG binding pairs were then employed in the above-mentioned indicator displacement assays to investigate the binding affinity of oligoarginines toward 1 and 2 (see Figure 5.3 B and Figures D.6-D.9). The obtained results (see Table 5.1) show that both 1 and 2 display high affinity toward oligoarginines with binding constants that increase with the number of arginine residues (at least up to R_6), reaching the nM range for larger, highly positively charged peptides.

Having shown that 1 and 2 bind the target peptides with high affinities and that the binding does not show significant dependence on the *E/Z* conformation (see Table 5.1, R_3 and R_4), the next step was to evaluate their effectiveness as photoresponsive counterion activators, using Egg Yolk Phosphatidylcholine (EYPC) Large Unilamellar Vesicles (LUV) as model zwitterionic membranes. The slightly negative ζ-potential of EYPC-LUV shifts to more negative values with the addition of increasing concentrations of the anionic calixarene activators 1 and 2, suggesting that these amphiphilic species are embedded in the lipid membrane (Figure D.10). DLS control experiments also confirmed liposome integrity under the experimental conditions employed in the different membrane transport assays,

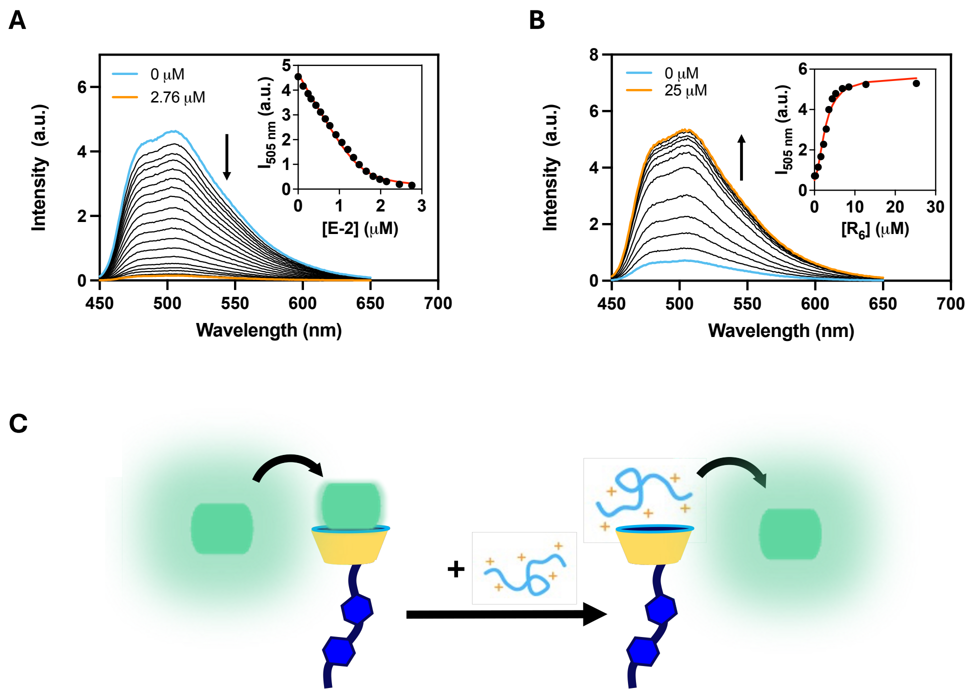

Figure 5.3: **A.** Direct titration of the lucigenin dye (LCG, 1.5 μM) with increasing concentrations of *E*-2 in water (5 mM PB, pH 7.3), followed by fluorescence spectroscopy (λ_{exc} = 369 nm). **B.** Indicator displacement titration of hexaarginine (R_6) using *E*-2:LCG as the reporter pair (5 mM phosphate buffer, pH 7.3), followed by fluorescence spectroscopy (λ_{exc} = 369 nm). LCG and *E*-2 concentrations were fixed at 4 and 4.3 μM, respectively. **C.** Schematization of the indicator displacement assay (IDA) illustrating the formation of the dye:*E*-2 complex and subsequent removal of LCG by the addition of peptides to the mixture, leading to the observed regaining of emission in B.

Table 5.1: Apparent affinity constants (K / M^{-1}) calculated by competitive indicator displacement assays using LCG as a fluorescence probe for the SC4 receptor and counterion activators 1 and 2.

Guest	**SC4**	***E*-1**	***Z*-1**	***E*-2**	***Z*-2**
LCG	$(8.1 \pm 0.9) \times 10^7$	$(2.5 \pm 0.7) \times 10^7$	$(2.3 \pm 0.4) \times 10^7$	$(2.6 \pm 0.7) \times 10^7$	$(3.4 \pm 0.8) \times 10^7$
R_3	$(5.5 \pm 0.3) \times 10^6$	$(2.6 \pm 0.8) \times 10^7$	$(2.4 \pm 0.6) \times 10^7$	$(4.1 \pm 0.2) \times 10^6$	$(3.6 \pm 0.3) \times 10^6$
R_4	$(2.7 \pm 0.4) \times 10^8$	$(3.9 \pm 0.3) \times 10^7$	$(3.2 \pm 0.7) \times 10^7$	$(1.2 \pm 0.6) \times 10^8$	$(7.8 \pm 1.3) \times 10^7$
R_6	$>1 \times 10^9$ [a]	$>5 \times 10^8$ [a]		$>5 \times 10^8$ [a]	
R_8	$>1 \times 10^9$ [a]	$>5 \times 10^8$ [a]		$>5 \times 10^8$ [a]	

[a] Only the lower limit of the K can be estimated because the titration curves display a sharp levelling-off at 1 equiv. of peptide, which is characteristic of very high binding affinity, precluding the accurate determination of the K under the experimental conditions.

which ruled out potential membrane disruption interferences (Figure D.10). Established dye efflux assays were performed using the 5,6-carboxyfluorescein (CF) dye encapsulated at self-quenching concentrations in egg yolk phosphatidylcholine large unilamellar vesicles (EYPC-LUV⊃CF).[61,179,279,292] In these experiments, the fractional release of trapped CF (or fractional transport activity, Y), triggered by the addition of counterion activators and peptides, is monitored by time-resolved fluorescence spectroscopy and calibrated by the addition of Triton X-100 (Figure D.11).

The studies were performed with both 1 and 2 in the *E* and *Z* configurations in the presence of fixed concentrations of liposome and cationic peptide. It should also be noted that in the absence of peptides, the addition of counterion activators does not affect the intensity of the fluorescence signal, discarding the leakage of the vesicle contents by 1 or 2 alone (Figure D.11). Likewise, the addition of peptides alone or nonbinding anionic peptides in the presence of calixarene activators also results in unmodified fluorescence signal, confirming that the formation of the calixarene-peptide complex is critical to activate the transport process. Transport activity was observed in the presence of peptides containing four, six, or eight arginine residues. Although complete sigmoidal dose-response curves could not be obtained for 1 and 2 in the presence of R_4 (see Figure D.12), the results show a higher efficiency of *E* isomers to translocate this peptide across the lipid membrane, supporting the hypothesis that these calixarene-based activators can be used in light-activated transport assays. In contrast to R_4, R_6 (Figure 5.4) and R_8 (Figure D.17) allow quantitative analysis of the resulting concentration-dependent transport activity plots by fitting these data to the Hill equation.[61,179,279,292] This approach retrieves the Y_{max} (i.e., maximal CF release relative to liposome lysis after the addition of Triton X-100) and EC_{50} (i.e., the effective counterion activator concentration required to reach $Y_{max}/2$) as the relevant parameters to measure the efficiency of the counterion activators. Because counterion activators with low EC_{50} do not necessarily display high Y_{max}, Matile and co-workers proposed an equation, $TE = Y_{max} \times pEC_{50}/f$, to evaluate the Transport Efficiency (TE) as a function of Y_{max} and the negative logarithm of the EC_{50} (pEC_{50}), with f = 20.6 being a scaling factor.[179]

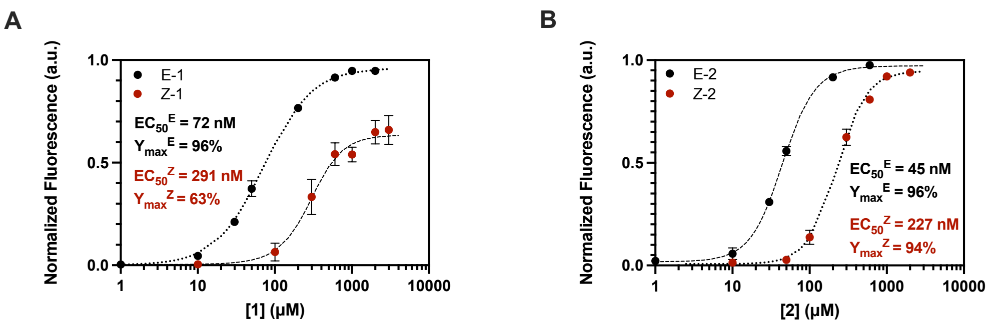

Figure 5.4: Concentration-dependent counterion transport activity obtained from CF efflux assays for **A.** *E*-1/*Z*-1 and **B.** *E*-2/*Z*-2 at a constant R_6 concentration (4 μM). The experimental data were fitted to the Hill equation (dotted and dashed lines).

The results summarized in Table 5.2 demonstrate that, in line with previous studies of anionic amphiphilic calixarenes, the monofunctionalized calixarenes 1 and 2 are highly efficient counterion activators. In all cases, the *E* isomers showed lower EC_{50} and generally higher Y_{max} values than their corresponding *Z* analogs.[180,181] This indicates that, although both *E* and *Z* calixarenes counterions can activate the transport of cationic peptides, the *E* isomer shows an enhanced membrane transport activation (by a factor of up to 5-fold in EC_{50}, Figure 5.4 and Table 5.2). Here, the counterion selectivity combined with the photoswitchable activation properties of 1 and 2 sets favorable conditions for the development of light-activated transporters for cationic peptides across phospholipid membranes.

Table 5.2: Counterion activation efficiency parameters of amphiphilic sulfonatocalixarenes 1 and 2 in the *E* and *Z* conformations for the R_6 and R_8 transport across egg yolk phosphatidylcholine large unilamellar vesicles (EYPC-LUV⊃CF)

Peptide	Activator	EC_{50} (nM)[a]	Y_{max} (%)[a]	TE [b]
R_6	*E*-1	72 ± 5	96 ± 1	19.4 ± 0.2
	Z-1	291 ± 32	63 ± 5	10.8 ± 0.8
	E-2	45 ± 2	96 ± 1	20.2 ± 0.2
	Z-2	227 ± 17	94 ± 2	16.6 ± 0.3
R_8	*E*-1	24 ± 2	91 ± 2	20.3 ± 0.4
	Z-1	99 ± 3	69 ± 2	13.3 ± 0.4
	E-2	11 ± 1	93 ± 2	22.2 ± 0.3
	Z-2	30 ± 4	94 ± 2	20.8 ± 0.4

[a] Obtained from the fitting of the Hill equation to the experimental dose-response data (e.g., data shown in Figure 5.4 and in the Supporting Information). [b] Calculated from TE = $Y_{max} \times pEC_{50}/f$, with $pEC_{50} = -\log EC_{50}$ (in mM) and f = 20.6. [c] All experiments were carried out in 5 mM phosphate buffer at pH 7.3, with a fixed concentration of peptides and EYPC-LUV⊃CF at 4 and 15 μM, respectively, for all experiments. Standard deviations were obtained from triplicate experiments (see the Appendix C).

CF-efflux assays, similar to those described above, were also performed to demonstrate photoinduced peptide transport across phospholipid membranes using calixarene-based counterion activators. To this aim, *Z*-1 and *Z*-2 were added to EYPC-LUV⊃CF dispersions at fixed concentrations to study the CF release upon in situ light stimulation. As illustrated in Figure 5.5, the addition of the peptide in the presence of *Z*-2 leads to a small increase in the CF fluorescence intensity, in agreement with the translocation of a residual fraction of R_6 across the lipid bilayer. Irradiation with 500 nm light promotes the conversion of *Z*-2 into *E*-2, a stronger counterion activator, leading to ca. 50% of extra dye released as a result of the light-triggered translocation of R_6 into the liposome (Figure 5.5 iii). These results were further confirmed by analogous experiments carried out with the 2-R_8, 1-R_6, and 1-R_8 activator-peptide pairs (see Figures D.20 and D.21).[1]

[1] The 2-R_8, 1-R_6, and 1-R_8 pairs lead to lower fractions of light-induced dye efflux, providing controls to rule other effects, such as light-induced vesicle rupture, that can be anticipated to be independent of the nature of the activator-peptide pair. There is no corresponding record for this reference.

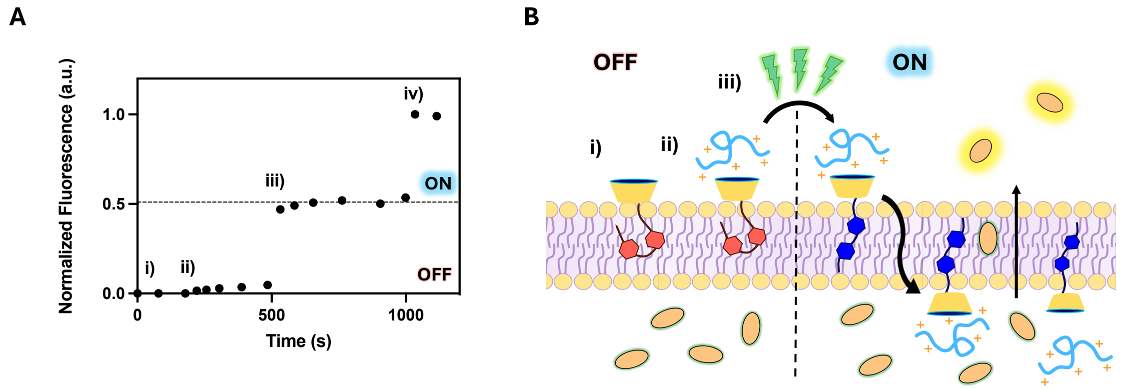

Figure 5.5: **A.** Light-modulated dye efflux assays performed with 4 μM R_6, 60 nM *Z*-2, and 15 μM EYPC-LUV⊃CF (50 mM CF inside the liposome, λ_{exc} = 490 nm) and **B.** schematization of each phase in the assay. (i) First, the activator *Z*-2 was added to a liposome solution (ii) followed by the addition of the peptide. (iii) The same sample was irradiated for 25 min at 500 nm, leading to a significant increase in CF release. (iv) Finally, in order to normalize the measurement for the maximum emission possible, the vesicles were lysed by addition of a small aliquot of Triton X-100.

Success in artificial vesicle assays encouraged us to conduct transport experiments of fluorescently labeled peptides in living cells (Figure 5.6). We first employed confocal fluorescence microscopy to evaluate counterion activator 2 for the intracellular transport of a carboxytetramethylrhodamine-labeled R_8 peptide (TAMRA-R_8) into the cytosol of HeLa cells. Cationic peptides usually remain trapped inside the endosomes when incubated with cells at low μM concentrations.[283,291] As expected, control experiments at a fixed TAMRA-R_8 low concentration (3 μM) and in the absence of calixarene activators confirmed an almost negligible cytosolic signal from the labeled peptide (Figure 5.6 B and Figure D.27). However, in agreement with vesicle assays, the *E* isomer of the counterion activator exhibited a significant increase of the intracellular delivery as compared to the less hydrophobic *Z* configuration (Figure 5.6 B). Confocal micrographs of cells incubated with TAMRA-R_8, in the presence of the E isomer of the calixarene activator 2, revealed a strong diffuse fluorescence signal in the cytosol, nucleus, and nucleolus of the cells (Figure 5.6 B). To validate and compare these results, flow cytometry quantification of peptide uptake was carried out in the presence of both *Z* and *E* isomers of the calixarene 2. The cytometry experiments validated the *E* isomer selective transport and indicated a four-fold intracellular delivery enhancement (Figure5.6 C and Figure D.28). Although the trend of activity of the two calixarene isomers was maintained in vesicles and cell assays, the observed variations on the EC_{50} values can be due to the different experimental conditions, membrane composition, and competing energy-dependent internalization pathways.[61,179,284,293] Additionally, the 3-(4,5-Dimethylthiazol-2-yl)-2,5-Diphenyltetrazolium Bromide (MTT) viability assay confirmed a low cellular toxicity for the counterion activators at the employed concentration regime (Figure D.29). The half maximal inhibitory concentration (IC_{50}) cytotoxicity values, of 16.88 μM for *E*-2 and of 19.16 μM for *Z*-2 (after 24 h of incubation), appeared 2-3 orders of magnitude higher than the nM activator concentrations, which were required for an efficient peptide cytosolic delivery with the trans isomer of the calixarene counterion activator (*E*-2). The anionic nature of the calixarene activator should prevent nondesired interactions with other components of the cell (glycosaminoglycans, anionic lipids, ATP, etc.). While parallel transport events of other charged biomolecules cannot be completely ruled out, those processes do not cause any limitation to cellular viability and efficient cargo transport (Figure D.29).

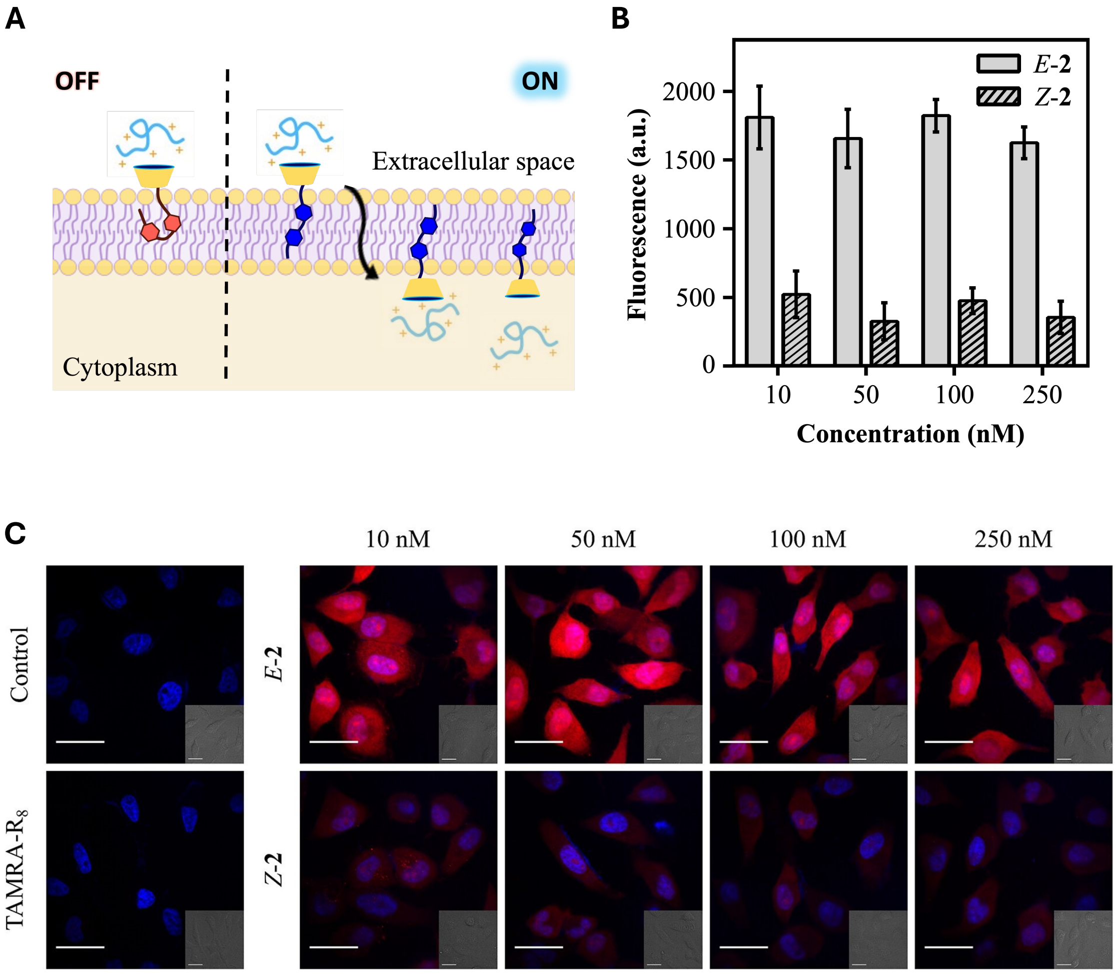

Figure 5.6: **A.** Schematic representation of oligoarginine intracellular delivery by both isomers of 2. **B.** Fluorescence intensity of HeLa cells incubated with 3 μM TAMRA-R_8 in the presence of different *E*-2/*Z*-2 concentrations, measured by flow cytometry. **C.** Confocal fluorescence microscopy images of the cellular uptake of 3 μM TAMRA-R_8 (in red) facilitated by *E*-2/*Z*-2. Hoechst stained nuclei can be seen in blue and differential interference contrast (DIC) images are presented as insets. Control experiments of TAMRA-R_8 in the absence of a calixarene activator are also included. Scale bars, 50 μm.

In conclusion, we introduce here the first photoswitchable amphiphilic counterion activators for the transport of cationic peptides across lipid membranes and inside cells. We have synthetized calixarene-based receptors monofunctionalized with an azobenzene unit that can be applied as photoresponsive counterions to gain control over the transport of cationic peptides across artificial lipid membranes and into the cytosol of living cells. Our design combines a high-affinity oligoarginine binding unit, based on a sulfonatocalixarene macrocyclic host decorated with azobenzene pendants, whose lipophilicity can be remotely controlled by light-induced interconversion between the more hydrophobic, extended *E* and the more polar, bent *Z* configuration. The transport efficiency of these light-sensitive counterion activators was significantly enhanced for the *E* azobenzene isomers, which allows their application as photomodulated carriers for hydrophilic cargos.

Since the publication of this work, several groups have been developing different photoactive transport systems, showing novel applications for such system, as well as trying to shed light on the mechanism of these markedly distinct transport efficiencies.[37,75,146,294–298] Wezenberg and coworkers have applied azobenzene photoactive units in the transport of Cl^- across phospholipic membranes using neutral transporters. While presenting distinct structures and showing a different trend than the 1 and 2 counterion activators, their work remarks upon the influence that different mobilities and partitioning into the membrane of *E* and *Z* isomers can also have on the transport mechanism, which could translate into the mechanism of the systems presented herein.[294]

5.2 Different sensing strategies anchored in phospholipic membranes

This subsection was done in collaboration with PhD Student Kevin Droguett from Universidad Pontificia de Santiago do Chile, who contributted with the photophysical studies of the SC4-nPy-LCG system in EYPC-LUVs. Microscopy studies were done in collaboration with Professor Javier Montenegro and PhD student Lucía Méndez-Gómez at the Montenegro Lab, CIQUS, Universidad de Santiago de Compostela, Spain.

SC4-nPy was shown to be a versatile sensing unit, with the application of SC4-4Py in a ratiometric IDA being able to detect smaller, monocationic or dicationic guests, and the full library of sensors, SC4-nPy, enabling the distinction of polycationic guests by their capacity to induce aggregation in the system. Due to the amphiphilic nature of these sensors, the alkyl pyrene moiety could act not only as reporter but also provide an anchor to insert this sensing system in phospholipidic membranes. Additionally, the anchoring of the pyrene moiety could act as a way to avoid aggregation when charge neutralization occurs and allow the use of the SC4-4Py-LCG displacement system for larger, polycationic guests (Figure 5.7).

The insertion of SC4-4Py in membranes was first evaluated by ζ-potential and fluorescence spectroscopy. Much like the SC4-Azo family of actuators, 1 and 2, addition of increasing SC4-4Py concentrations to an EYPC-LUV sample leads to the decrease of the ζ-potential of the vesicles, with overall maintenance of membrane integrity as evaluated by DLS (Figure 5.8 A). Additionally, pyrene is a known polarity probe, that presents variations in its emission vibrational profile depending on the polarity of the environment

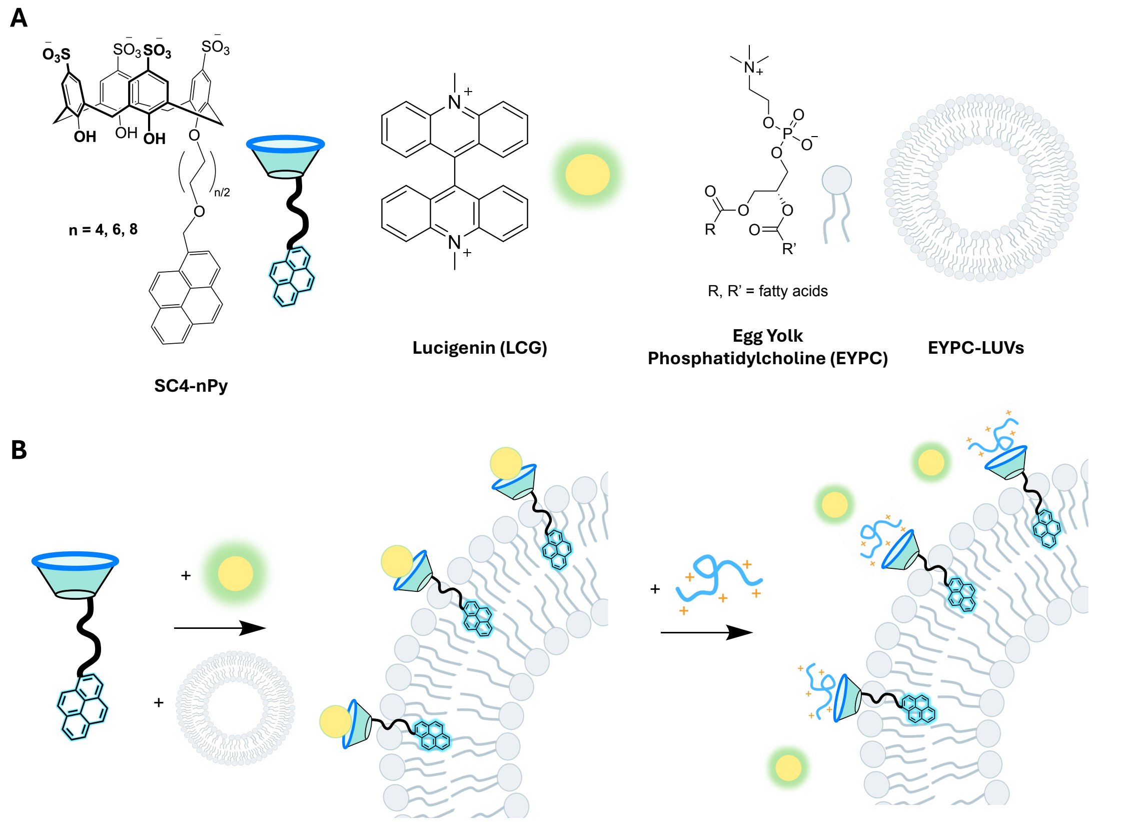

Figure 5.7: **A.** Elements of the membrane sensing system with SC4-4Py and LCG and the EYPC-LUVs. **B.** Schematization of the membrane anchored ratiometric indicator displacement assay (rIDA) for the detection of larger polycationic guests.

in which it is inserted.[299] The addition of LUV sample to all SC4-nPy sensors showed a decrease of the ratio between band I and band III emission (I_1/I_3), which is consistent with a decrease of polarity in the vicinity of pyrene. This decrease of I_1/I_3 added to the increase of emission intensity observed (Figure 5.8 B and Figures D.30 and D.31) and decrease of ζ-potential at the surface of the vesicles is consistent with the insertion of the pyrene tail in the more confined, less polar phospholipidic membrane of the EYPC-LUVs.

After evaluating the stability of SC4-nPy association to the liposomes (Figure D.31) and finding that these maintain the emission and I_1/I_3 ratio values consistent up to 1 to 2 hours after preparation, these samples were used to perform the titration of the sensors with LCG, to evaluate the affinity constant of this host-guest pair in these conditions (Figure 5.9 A). The affinities decrease one order of magnitude for the three sensors in the presence of EYPC-LUVs, showing that these might influence the binding of guests to the cavity, but not to an extensive degree.

The same oligoarginine library explored in section 4.1 was once again evaluated, both in the absence and, for those not displaying interferance from the aggregation process, in the presence of LCG. For the smaller peptides R_2G_2 and R_3G, all sensors showed a lack of aggregation in the presence of EYPC-LUV (Figures D.34 and D.35), unlike what is observed for SC4-6Py and SC4-8Py in buffer only (see Section 4.1). For R_4, no aggregation

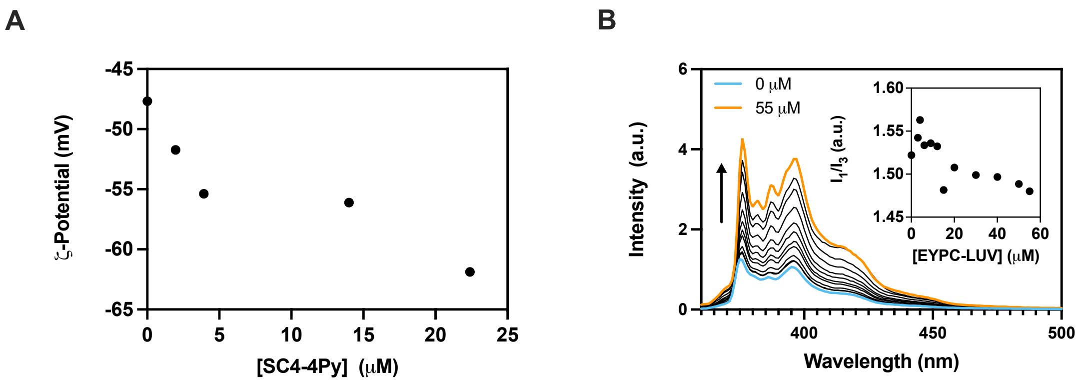

Figure 5.8: **A.** ζ-Potential of EYPC-LUVs (260 μM) before addition of SC4-4Py and at increasing concentrations of the sensor. **B.** Titration of SC4-4Py (5.75 μM) with EYPC-LUVs followed by fluorescence spectroscopy. The inset shows the variation of the ration between pyrene's emission band I (I_1, at 376 nm) and band III (I_3, at 386 nm). All studies were done in PB 5 mM pH 7.4.

is observed for the smaller sensor, SC4-4Py (Figure 5.9 B), allowing the use of this peptide in a membrane anchored IDA (Figure 5.9 C). The affinity constant values obtained with this method are presented in Table 5.3 and consistently present values one order of magnitude lower than those obtained in buffer only, much like what was observed for LCG direct titrations in the presence of LUVs. Despite this difference, relations between oligoarginine's affinities still remain consistent, with affinities increasing with the number of cationic residues and presenting identical values for the same guest across different sensors.

Table 5.3: Affinity constants (K / M^{-1}) calculated by indicator displacement assays in EYPC-LUV, using the dye LCG and SC4-nPy family of sensors in PB 5 mM pH 7.4, obtained by fluorescence spectroscopy.

Guest	SC4-4Py	SC4-6Py	SC4-8Py
LCG	3.1×10^6	2.1×10^6	1.4×10^6
R_2G_2	3.7×10^5	3.0×10^5	n.d.
R_3G	2.3×10^6	2.3×10^6	n.d.
R_4	4.4×10^7	-[a]	n.d.
R_6	-[a]	-[a]	n.d.
R_8	-[a]	-[a]	n.d.

[a] Affinity constants obtained displayed interferance from the aggregation process, even in the presence of EYPC-LUV.

Depite having avoided aggregation in rIDAs with the smaller oligoarginines, in the presence of SC4-6Py and SC4-8Py or for the larger oligoarginines, this process can still be observed by appearance of the pyrene excimer-like emission (Figure 5.10 A for R_6-SC4-6Py and remaining assays in Figures D.34 and D.35) when guest is added.

While an unintended interference for LCG-SC4-nPy rIDA, the appearence of this

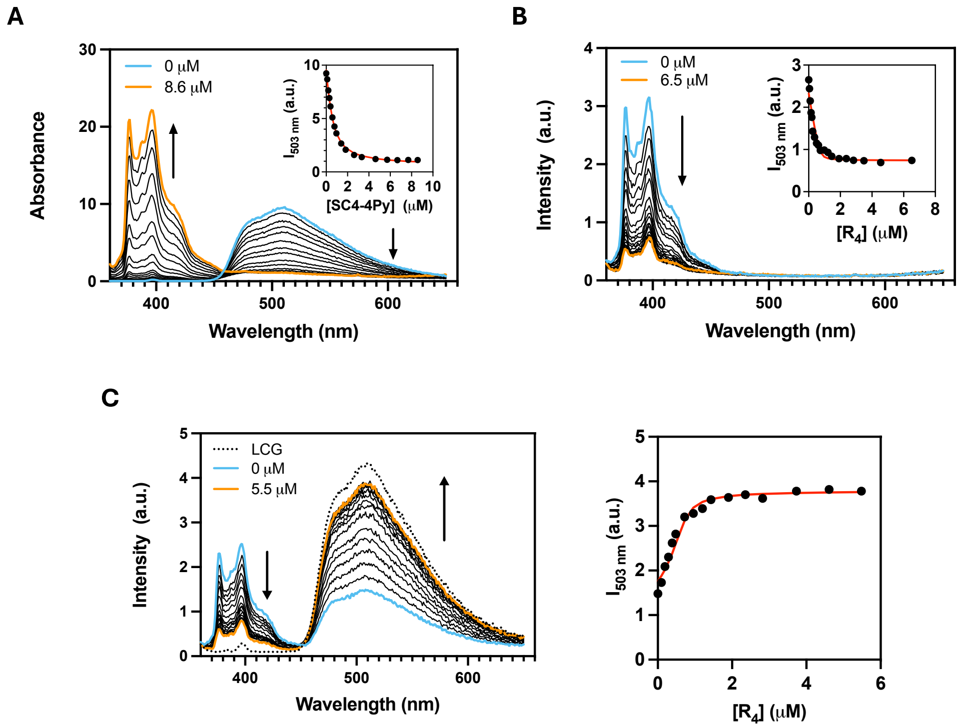

Figure 5.9: **A.** Titration of LCG (0.5 μM) with SC4-4Py in the presence of EYPC-LUV (200 μM) and **B.** titration of SC4-4Py (0.7 μM) incorporated into EYPC-LUV (7 μM) with the peptide R_4, followed by fluorescence spectroscopy (λ_{exc} = 340 nm). **C.** rIDA of the LCG-SC4-4Py pair (0.2 and 0.7 μM, respectively) inserted in EYPC-LUV (7 μM) with the guest R_4 and respective fitting of the experimental data. All studies were done in PB 5 mM pH 7.4.

excimer-like emission presented an opportunity to study what type of associations are present in mono-O-functionalized calixarene systems that could act as an emissive model for the SC4-Azo compounds. Despite the SC4-Azo counterion activators being chromophores, fluorescence provides a more robust signal in order to follow the mechanism involved in the transport process. With this in mind, the polycation transport capacity of SC4-4Py was studied in the presence of R_6 and this sensor was incorporated in Giant Unilamellar Vesicles (GUV) for observation by fluorescence microscopy.

Dye efflux assays with EYPC-LUV⊃CF show that SC4-4Py presents higher EC_{50} than that of any of the SC4-Azo activators (EC_{50} = 760 nM, see Figure 5.11 A). The reason for the difference between monofunctionalized calixarenes efficiency as transporters is not clear, but full study of the SC4-nPy library of sensors could help clarify these differences.

In order to confirm the location of the SC4-4Py sensor in vesicle solutions, as well as the type and location of aggregates formed in the presence of guest, larger vesicles, observable under microscope, needed to be obtained. EYPC-GUV were synthesized by the organic phase evaporation method (see section 7) leading to polydisperse samples. Fluorescence spectroscopy studies confirmed the enhancement of SC4-4Py emission and decrease of I_1/I_3 ratio when titrating the sensor with these larger vesicles (Figure 5.11

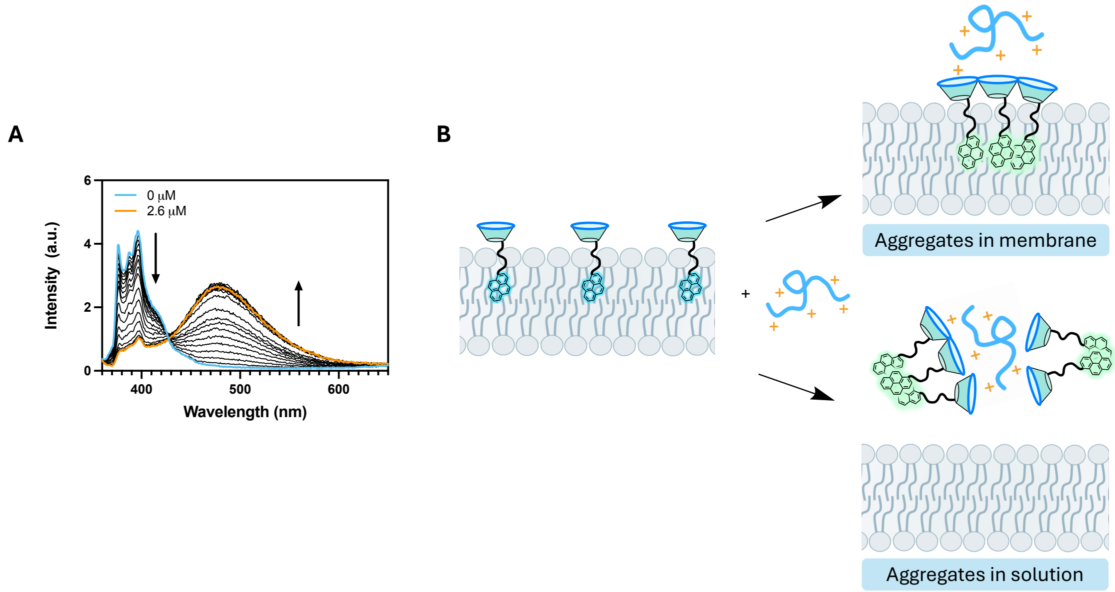

Figure 5.10: **A.** Titration of SC4-6Py incorporated into EYPC-LUV with the peptide R_6, in PB 5 mM pH 7.4, followed by fluorescence spectroscopy (λ_{exc} = 347 nm), and **B.** schematization of possible mechanisms involved with the aggregation process, with addition of guest causing rafting-like behaviour in the anchored sensor molecules or removing the sensor from the membrane leading to precipitates out of solution.

B). The aggregation phenomenon was observable as well in the presence of the guest R_6 (Figure 5.11 C).

Microscopy assays were initially done with the EYPC-GUV stock solution at 300 μM and direct addition of 30 μM SC4-4Py. Presence of the SC4-4Py sensor in the vesicle membrane was confirmed by the presence of blue emission associated with this structures, with little contribution of background fluorescence, as can be observed in Figure 5.12.

Addition of the guest peptide R_8 at 1 μM led to the appearance of aggregate-like emissive structures at the surface of the vesicles. Due to limitations related to the microscopy equipment excitation wavelength ($\lambda_{exc} \geqslant 400$ nm), no confocal images were obtained, so it was not clear if the emission was only originating in the external leaflet or if some of the calixarene partitions to the inside leaflet of the GUV phospholipidic membrane.

At 3 μM of R_8, more background precipitates start to be observed, concurrent with aggregates at the surface of vesicles, as well as EYPC-GUV agglutinated together by these same associations (Figure 5.13). Although assays were done with R_6 at concentrations in which aggregates could be observed by fluorescence spectroscopy, no such structures were observed (Figures D.38). Although no systematic studies were done, an increase of the size of the vesicles seems to occur with time (Figure D.40), however, this phenomenon and the different structures that appear with the passage of time needs to be further evaluated to establish a clear relation.

The SC4-nPy family of sensors showed to be a powerful tool not only as a sensor for specific guests, but also as a reporter for enlightning the mechanism of transport of

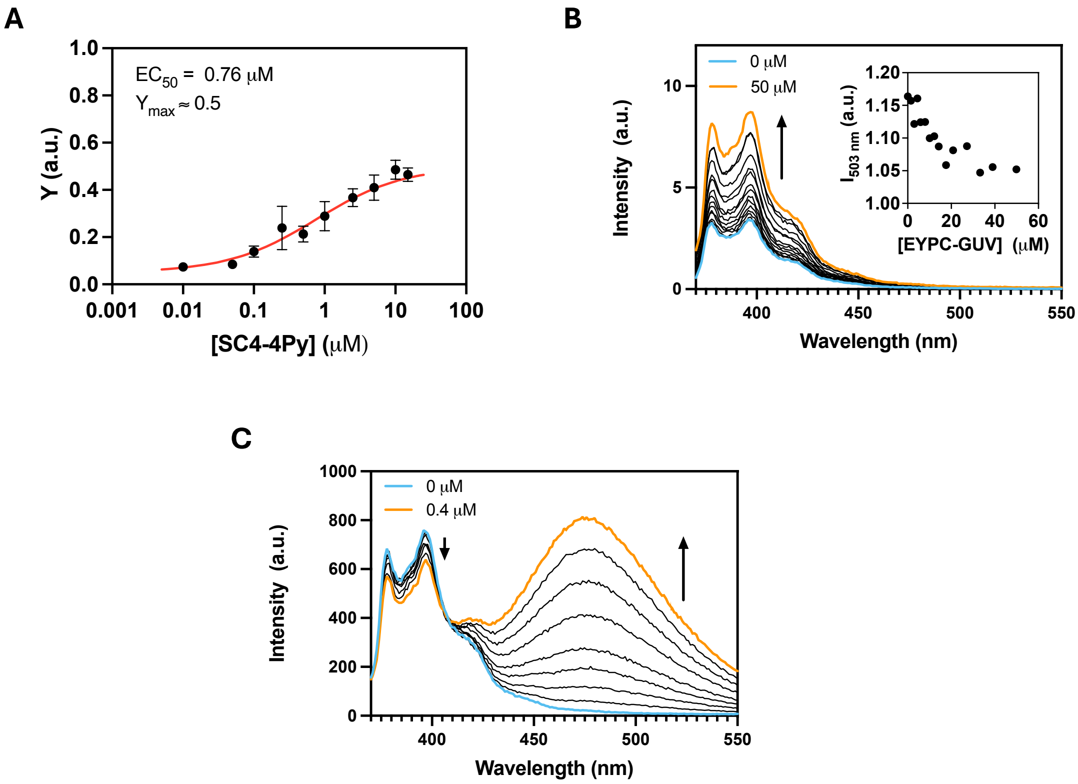

Figure 5.11: **A.** Concentration-dependent counterion transport activity obtained from CF efflux assays for SC4-4Py in EYPC-LUV⊃CF (21.8 μM), with the guest R_6 (4 μM). Respective EC_{50} and Y_{max} are presented in the figure. **B.** Titration of SC4-4Py (3 μM) with EYPC-GUV and **C.** titration of SC4-4Py (3 μM) in GUV membranes (30 μM) with the peptide R_6, both followed by fluorescence spectroscopy (λ_{exc} = 343 and 347 nm, respectively). All studies were done in PB 5 mM pH 7.4.

hydrophilic cargo with amphiphilic calixarenes, by counterion activation.

Moreover, incorporation of the sensor into the membranes was clearly confirmed. The preliminary microscopy results show as well that several different structures can be observed and might be related to the transport capacity of these amphiphilic calixarenes. It is possible that aggregation processes similar to the ones observed in this study, on the outside of the vesicles, hinders the transport process at higher concentrations and is the reason why a decrease of dye efflux is observed in certain assays, e.g. E-SC4-Azo compounds and R_4 above 1 μM. To confirm the relevance of these structures (Figure 5.13 B) concomitant dye efflux assays should be done at similar concentrations and conditions, as well as relating the appearance of the excimer-like emission with the efficiency of transport in the given concentrations. Understanding this mechanism can open up paths to enhancing the design of counterion activators and adding novel stimuli-responsive units without compromising on the efficiency of the transporter.

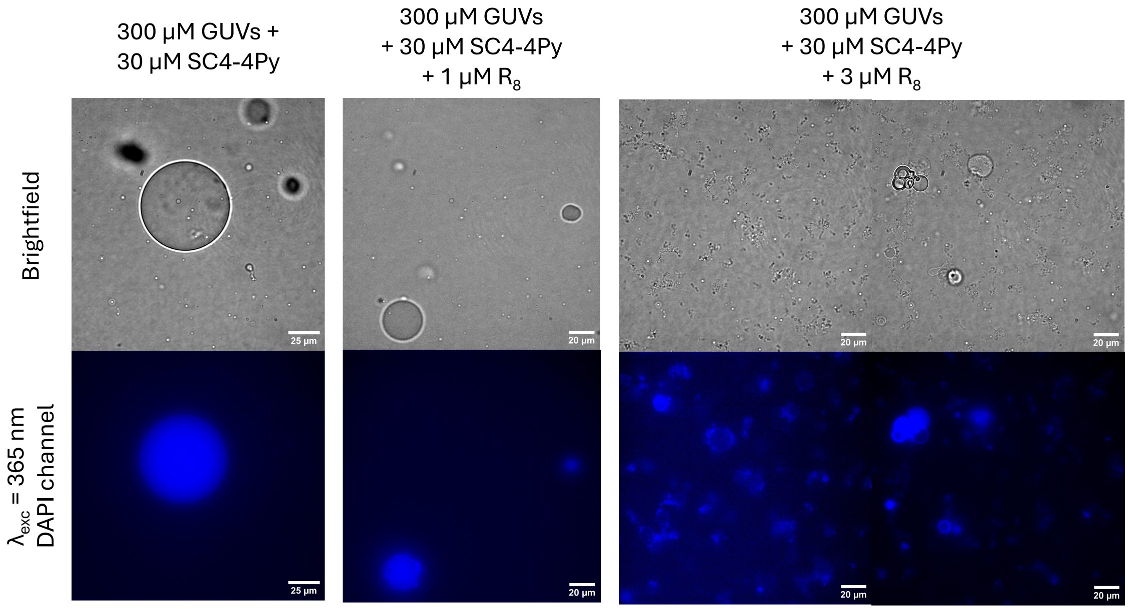

Figure 5.12: Fluorescence microscopy images of EYPC-GUV, in PB 5 mM pH 7.4, obtained in the confocal microscope in epifluorescence mode in the presence of only SC4-4Py and in the presence of the sensor and 1 and 3 μM of the peptide R_8, with the brighfield image and respective SC4-4Py emission (λ_{exc} = 365 nm) detected in the DAPI channel.

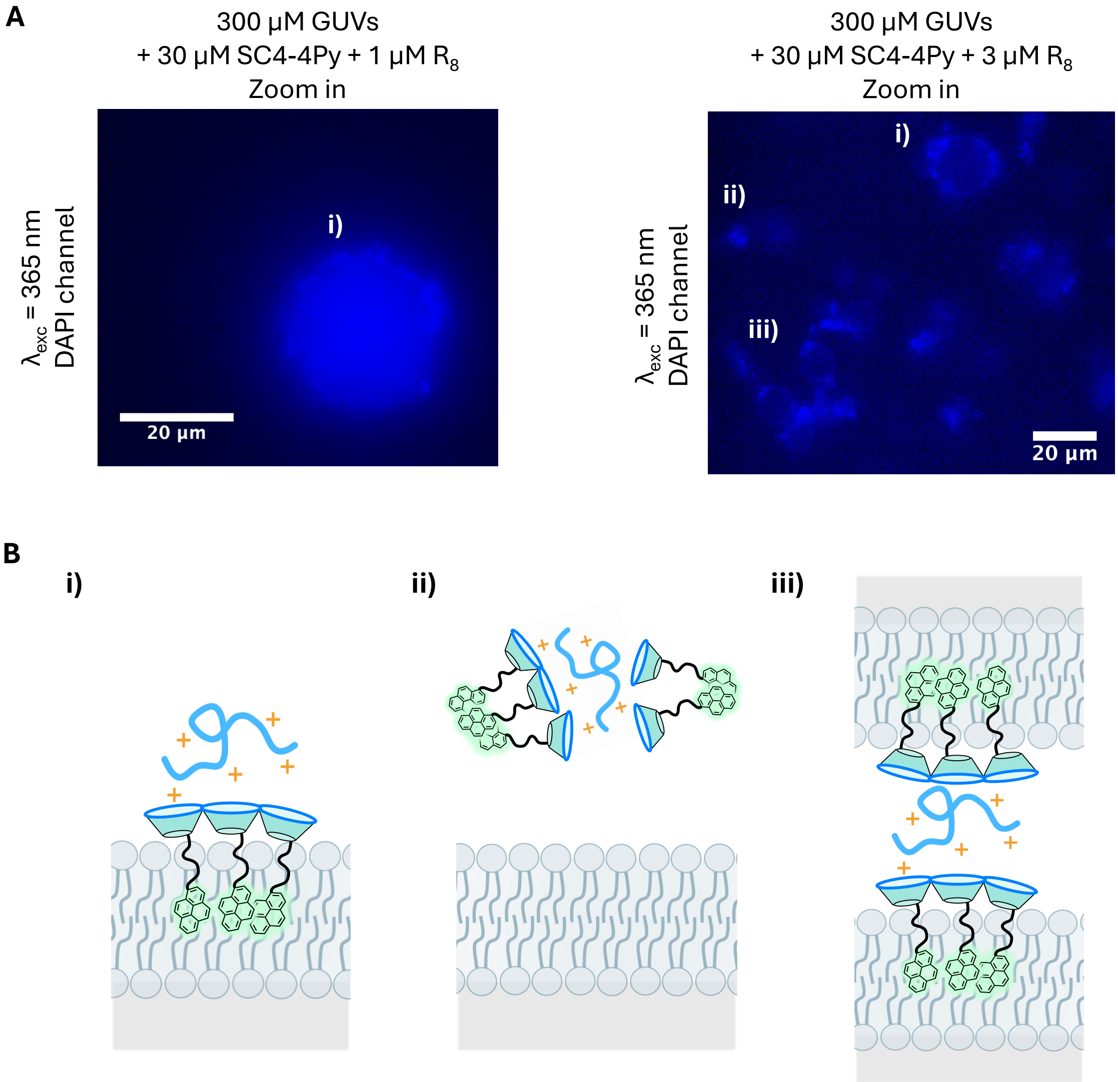

Figure 5.13: **A.** Zoom-in of the images presented in Figure 5.12, highlighting the different structures that are believed to be present. **B.** Schematization of the structures thought to be present in A: i) rafting-like behaviour, creating the irregular aggregate-like structure at the surface of the vesicles; ii) precipitates that extract the sensors from the membrane and iii) agglutination of vesicles driven by the host-guest multivalent complexes that form at the surface of the GUV.

6

General Conclusions and Future Perspectives

Despite its proven importance in the study of the ubiquitous non-covalent interactions in nature and their consequent application in a myriad of fields, supramolecular chemistry is still far from the hypercomplexity of biological systems and the ever elusive synthetic cells.[7,132,187,193] The work developed in this thesis has explored both applied and fundamental questions within this field, aimed at understanding both discrete macrocycle-biological target interactions, but also at inserting these systems in more complex, even biomimetic, systems, as is the case of transport across phospholipidic membranes and the membrane-anchored detection of analytes.

Firstly, discrete interactions of known macrocycles were studied with the aim of uncovering more information from previously known interactions, as well as novel specificities not previously considered for some known hosts.

Stoddart's Blue-Box (BB) interaction with peptides presenting aromatic residues at different sites was studied by spectroscopical techniques, unveiling 10 times increased affinity for peptides with tryptophan residue at the C-terminal, most likely due to the additional ionic interaction provided by the carboxylate group. The peptide with the tryptophan residue at the N-terminal presented higher affinity towards this host than the one with this residue in the middle of the peptide. Future structural analysis by NMR spectroscopy of these complexes might help understand this behaviour. Furthermore, influence of other types of residues and not just the positional dependency of the binding could unveil novel specificities for this host. The application of this host in competitive assays was also initially planned, in particular with the dye coumarin 343. Preliminary results showed that, despite its mM affinity towards BB (K = 5.1×10^3 M^{-1}, Figure 6.1), aggregation was observed even in IDA with aromatic amino acids, impeding the use of this technique. The possibility remains open for the use of another dye for this application, possibly based in the naphthalene moiety, which binds BB with μM affinities, allowing the use of lower concentrations and decreasing the likelyhood of aggregation occurring.[213]

p-Sulfonatocalix[4]arene (SC4) presents high binding affinities towards oligoarginines

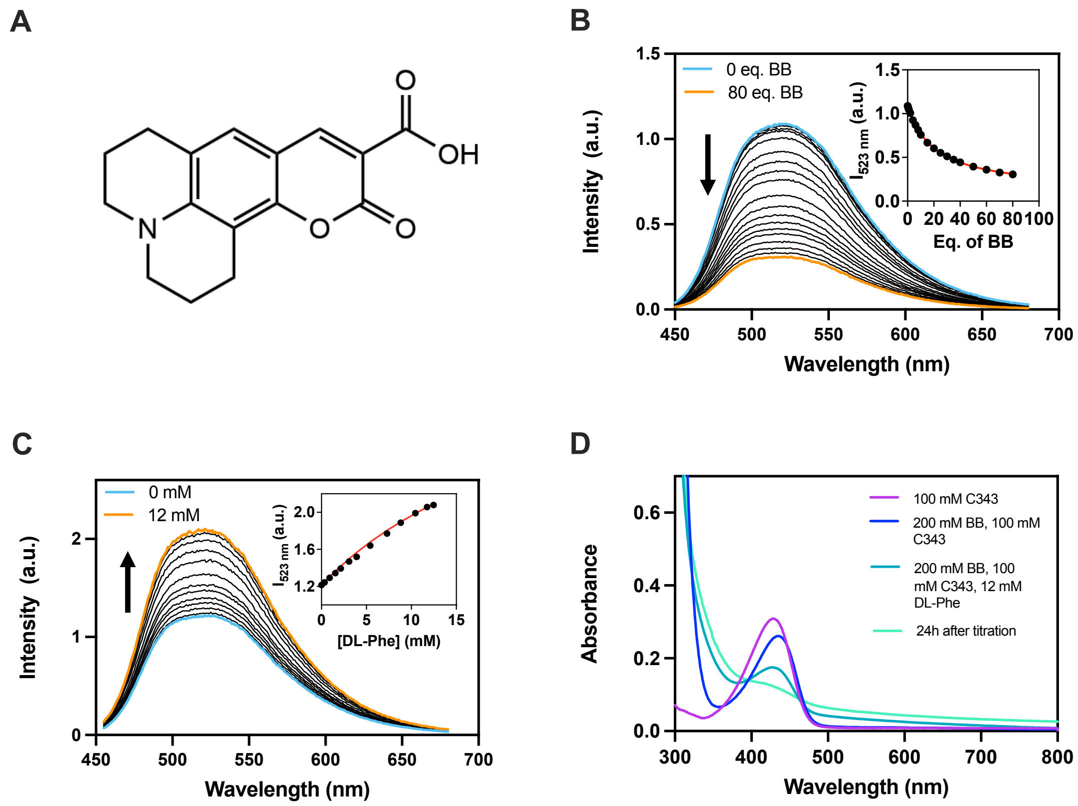

Figure 6.1: **A.** Chemical structure of the dye Coumarin 343 (C343). **B.** Direct titration of C343 (10 μM) with BB, followed by fluorescent spectroscopy (λ_{exc} = 440 nm). **C.** Indicator displacement assay (IDA) of C343 from BB (80 and 500 μM, respectively) with the analyte DL-Phe, followed by fluorescence spectroscopy. **D.** Absorption spectra of C343 after the addition of BB and after the addition of an excess of DL-Phe in the immediate and 24 hours after sample preparation.

despite its only moderate affinity towards the arginine and lysine amino acids. Analysis of the binding of this host was done by spectroscopical, structural and thermodynamic characterization techniques for two different oligoarginines with two and four arginine residues, R_2G_2 and R_4. SC4 showed a 1 to 1 binding ratio with the peptide R_2G_2, with preferential binding at the N-terminal. The presence of a second cationic residue and absence of the carboxylate moiety appears to contribute for the higher affinity for R_2G_2 when compared to the free amino acids. The binding of a second SC4 molecule can be observed for the 4 residue peptide, R_4, speaking to the capacity for multivalency of binding for these types of complexes. Despite presenting a low affinity for K_{21}, binding was found to occurr preferentially on the terminal residues. Further studies with the larger peptides need to be done to ascertain the number of hosts binding, however, the presented studies already reveal the multivalency of these complexes, with different hosts binding the same peptide, for those with four or more residues.

These receptors were then applied in the development of different sensing and transport systems. The first sensor was based on a ratiometric competitive assay, with binding-induced conformational rearrangement of the SC4 receptor and consequent quenching of the covalently bound dye. The evidence is strongly indicative of a competitive PET by the indicator used in the competitive assay, Lucigenin (LCG). Unlike other ratiometric strategies, this system allows for concomitant quenching of one dye's emission while the other becomes enhance, which is often difficult to achieve with FRET systems based on SC4 due to the quenching of indicator emission by this host, impeding efficient energy transfer between the two chosen dyes. Despite its success, future work is planned on improving the biological compatibility of this system, by both altering the covalently bound dye to one that presents emission in the visible range and also to improve is hydrophilicity, in order to improve receptor solubility and avoid interferance by aggregation with larger polycationic guests.

The second application was focused on the host BB and its use in tandem with the host cucurbit[7]uril, CB7. These hosts can self-assemble into ternary complexes in the presence of adequate guests, like the family of DASPI dyes used in this work, in a highly cooperative manner. The concentrations of the species can be adapted so as to, when a competitor for the different hosts is added, a turn-on or turn-off emission signal is obtained depending on the macrocycle displaced, making it able to distinguish between analytes with selective binding to each host. The host displacement assay was successfully applied for the sensing of two different pharmacological agents, naproxene and nandrolone, pharmacological contaminants known to accumulate in aqueous environments. The next step with this type of system, would be to obtain an heteroternary complex where the full dissassembly of the ternary complex would not be caused by CB7 removal, eventually leading to distinct optical signal between displacement of only one or both hosts. This would allow the orthogonal sensing of guests with binding sites for both hosts or even be applied in sensing of analytes in more complex samples. Section 3.3 explored this concept by the design of ditopic receptors based on SC4 and CB7. While different monofunctionalized variants of these hosts were obtained, the final ditopic receptors are yet to be synthesized and remain under development at the moment.

More complex strategies were then explored using calixarene once again as a platform for molecular recognition. The first strategy used an aggregation-based strategy for detection and differentiation of a family of oligoarginines. The SC4 host, much like in the first ratiometric assay, was covalently bound to a pyrene reporter, but the family of molecules was extended to present three sensors with different length alkylic linkers. These presented distinct aggregation capacities in the presence of differently charged guests, allowing the successful categorization of the analyzed cationic peptides by Principal Component Analysis (PCA). The successful distinction of peptides with differences only in the number of cationic residues present is very promising and it speaks to the potential of this system for application in different array-like sensing strategies for the differenciation of relevant proteins and peptides with cationic patches in more complex samples.

The second sensing strategy developed was based on the changes in the properties of amphiphilic SC4 surfactants when bound to cationic guests. Oil-in-water (O/W) emulsions were stabilized in the presence of these amphiphilic hosts and showed coalescence of the droplets once sufficient concentration of a guest was added, both for smaller guests like Arginine-o-methylester and the longer oligoarginines, R_6 and R_8. This visual response to the addition of a guest is a novel strategy for this types of systems and the possibility to add another optical readout mechanism to the emulsion samples was explored. Several turn-on strategies were tested, including pH probes and reactions with emissive products, among others, with poor success.[10,300] The main issues encountered were due to destabilization of the droplets when some of the reagents were added to the organic phase, as well as the partitioning of some of the species into the aqueous phase, inducing the emission response before coalescence occurred. Nonetheless, different strategies are still thought to have potential once successfully optimized: the use of a F^- releasing reaction to catalyze the chemiluminescence reaction, e.g. Sulfur(VI) Fluoride Exchange (SuFEx) reactions, could improve the CL yield in emulsions, or, alternatively, a similar reaction could be used with the formation of an emissive product in the organic phase. The reaction presented in Figure 6.2 was initially tested as a source of F^- ions for the CL reaction, however, the formation of a fluorescent product proved to be a more efficient strategy. When applied in droplets, however, this reaction was found to be inadequate due to interferance with droplet stabilization by the reagent benzene-1,2-dithiol (BDT). Due to time constraints on this project this path could not be yet optimized, nonentheless, the potential of emulsions as microcontainers for coalescence-induced readout mechanism is still one that deserves further exploration both with the SCn-mC family of surfactants as well as with other amphiphilic hosts and their respective targets.

Lastly, these same concepts were applied in biomimetic systems, with a particular focus on the light-responsive transport of large hydrophilic cargo across membranes and the application of previously mentioned sensing systems anchored in membranes. The use of SC4 monofunctionalized with an azobenzene photoactive unit provided a platform for efficient oligoarginine transport across artificial and cell membranes, achieving more than 50% increase in transport upon photoisomerization from the *Z* to *E* species. This marked difference in transport efficiency was also achieved in cells with effective concentrations remaining well below the cytotoxicity limit for these compounds. The mechanism that these counterion activators use to improve membrane transport remains unclear and further research into such mechanisms could help in the future development of even more efficient carriers for large hydrophilic cargo. Additionally, the modification of azobenzene with Cl moieties in the *ortho* positions could help shift the light used for irradiation to the red region, improving the applicability in biological systems. Furthermore, calixarenes modified with cationic moieties are currently being explored for controlled transport of DNA across membranes.

SC4-pyrene sensors were applied for ratiometric sensing of large cationic analytes, with the SC4-nPy-LCG system anchored in membrane, avoiding aggregate emission for the smaller peptides. For the larger peptides, aggregate emission was still present and analysis

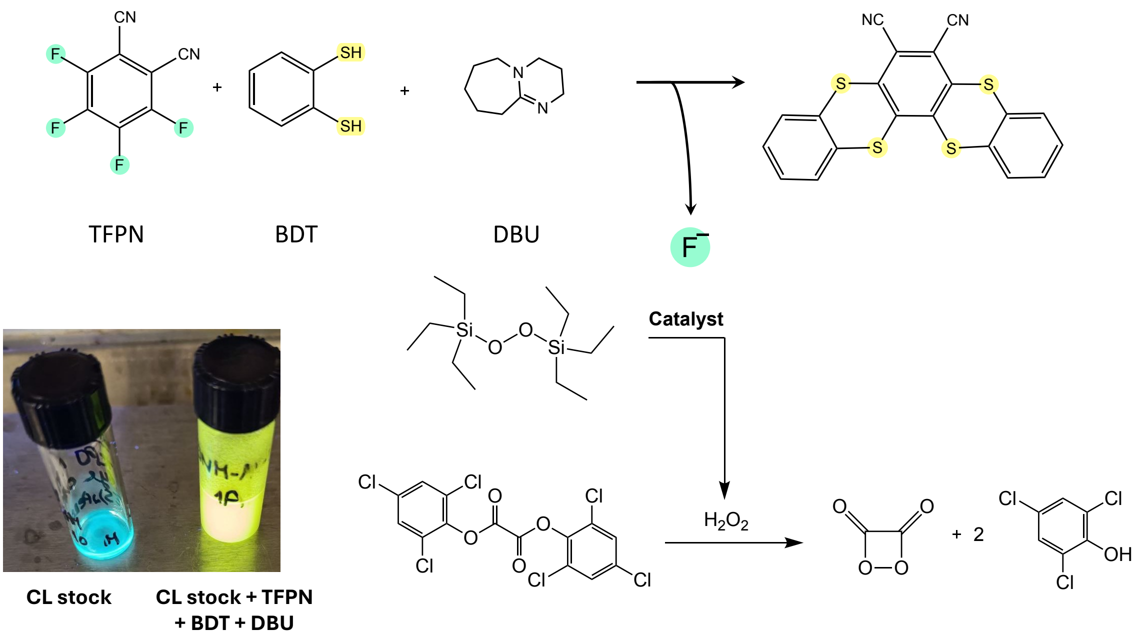

Figure 6.2: SuFEx reaction of 3,4,5,6-tetrafluorophthalonitrile (TFPN) and BDT and respective emissive product (yellow emission in the second flask) and effect of fluorine as a catalyst in the chemiluminescence reaction.

of these samples by fluorescence microscopy led to the clarification on the location of such amphiphilic SC4-guest complexes in Giant Unilamellar Vesicles (GUV). Preliminary studies showed a distribution of different structures at distinct concentrations and at different incubation times, which speaks to the great complexity that these systems can achieve and the need for further investigation into the dynamics of these complexes in membrane.

Several projects based on supramolecular chemistry concepts were explored herein with great success, both with application in sensing and transport of biologically relevant analytes. This thesis shows not only the versatility of the macrocyclic receptors, even without extended modification of their structure, but also opens the door for further investigation into these systems integrated in biological and biomimetic environments. Moreover, although not all of them were completely clarified, this research helped to uncover some of the mechanisms and complexity behind these small but powerful tools.

7

Materials and Methods

7.1 Reagents, Materials and Equipment

All experiments were done at room temperature, 25 °C, unless stated otherwise in the respective figure caption.

Commercially available reagents were used as received without further purification. Peptides R_4, R_6 and R_8 were synthesized by collaborators for the paper published in 2023 and remaining peptides were acquired from GeneCust with a purity superior to 95%.[215] All other compounds were synthesized and characterized as described below. Routine NMR experiments were run on a Bruker Avance III operating at 400 MHz (^{1}H) or 100 MHz (^{13}C), while quantification experiments, HSQC and peptide and respective calixarene complexes characterization were run either on Bruker NEO 500 or on Bruker Avance III 600 operating at 500 MHz (^{1}H) or 126 MHz (^{13}C) and 600 MHz (^{1}H) or 151 MHz (^{13}C), respectively.

UV-vis absorption spectra were recorded using a Varian Cary 100 Bio or a Varian Cary 5000 spectrophotometer in quartz or disposable plastic cuvettes with 10 mm optical path. Fluorescence spectra were recorded on a SPEX Fluorolog-3 Model FL3–22 or Varian Cary Eclipse spectrofluorimeter. In the case of emission measured in the microscopy glass supports, a HORIBA Jobin Yvon Fluorolog-3 spectrofluorometer (model FL-321) was used with the F-3000 Fiber Optic Mount.

All buffered solutions were prepared in 5 mM phosphate buffer pH 7.4 as measured with a Crison basic 20+ pH meter. For Sections 2.1 and 3.2 all solutions were prepared in water, at pH 7 and pH 8, respectively, unless stated otherwise in the respective Figures.

Continuous irradiations experiments done in Section 5.1 were conducted in a Spex Fluorolog-2 Model F111 spectrofluorometer equipped with a 150 W Xe lamp or in a custom photochemical reactor equipped with a 200 W Hg-Xe lamp and using bandpass or cut-off filters to isolate the desired wavelengths. The light flux (I_0) was determined using as actinometers, ferrioxalate in water for λ_{irr} = 365 nm ($I_0 = 3.2 \times 10^{-9}$ mol/s) and the diarylethene derivative 1,2-bis(2,4-dimethyl-5-phenyl-3-thienyl)perfluorocyclopentene in hexane for λ_{irr} = 500 nm ($I_0 = 9.1 \times 10^{-9}$ mol/s).

Confocal fluorescence microscopy images, obtained in Section 5.1, were taken with a Dragonfly spinning disc confocal microscope mounted on a Nikon Eclipse Ti-E and equipped with an Andor Zyla 4.2 PLUS sCMOS digital camera, and in Section 5.2 the same equipment was used in epifluorescence mode. Optical microscopy images, obtained in Section 4.2 were obtained in an inverted microscope equipped with an AmScope camera and fluorescence microscopy images were obtained on a Zeiss Axiovert 200 inverted widefield fluorescence microscope equipped with a Zeiss AxioCam HRc camera. All microscopy images were processed using ImageJ software (v1.52b).

Isothermal Titration Calorimetry (ITC) experiments were done on a MicroCal PEAQ-ITC by Malvern Panalytical, at 25 °C, and Dynamic Light Scattering (DLS) experiments were done on a Horiba nanoPartica SZ-100 series Nanoparticle Analyzer, with disposable plastic cells. ζ-potential measurements were done in the nanoparticle analyzer with carbon coated electrode ζ-potential disposable cells.

7.2 Synthesis Protocols

7.2.1 SC4-nPy Sensors

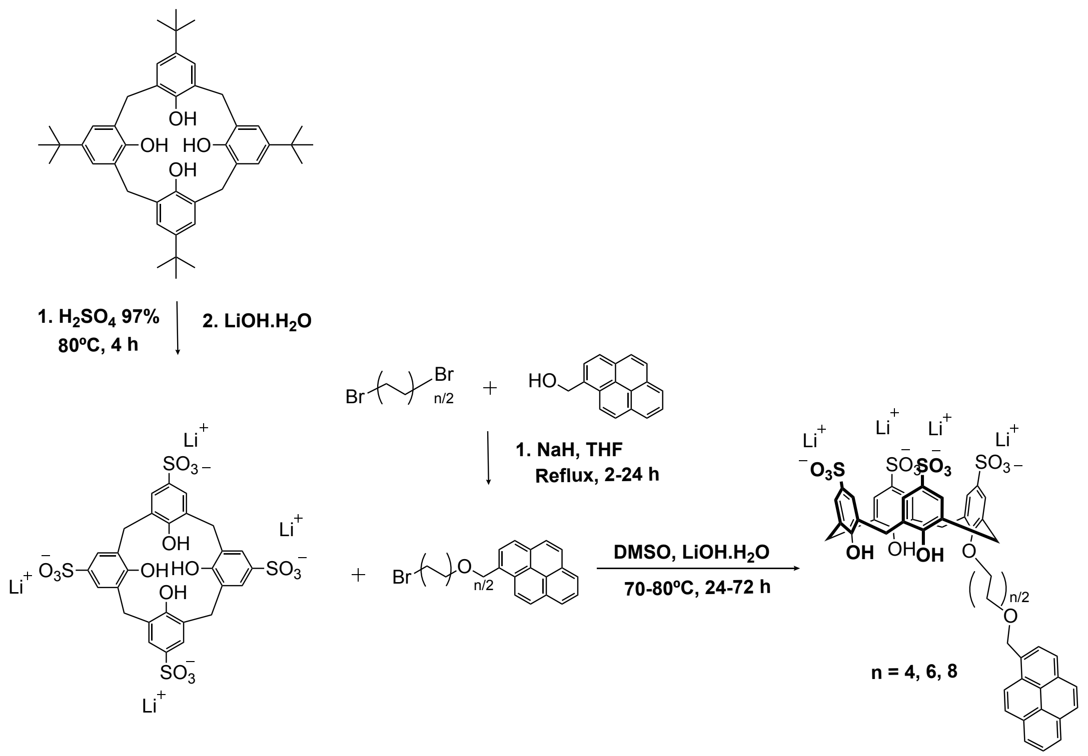

Figure 7.1: Reactional scheme for the synthesis of the SCnPy sensors.

The synthesis of the precursors, SC4 and bromo-alkyl functionalized pyrene, were performed according to previously reported protocols.[287,301]

1 eq of SC4, 0.75 eq of the respective bromoalkyl-oxymethylpyrene derivative and 3 eq. of $LiOH.H_2O$ were heated at 75 °C in dimethyl sulfoxide, under constant stirring, for

24h for SC4-4Py and SC4-6Py and for 48h for SC4-8Py. After the reaction mixture cooled to room temperature, it was neutralized with HCl and washed with diethyl ether and ethyl acetate to give an oily residue. The oily mixture was dissolved in a small amount of MeOH and precipitated with diethyl ether yielding a fine powder that was filtered and dried under vacuum. The SC4-nPy were isolated by reverse phase chromatography using a RP-18 stationary phase and a gradient of water-acetonitrile from 100:0 to 70:30 (v:v).

7.2.1.1 SC4-4Py

0.701 g (0.941 mmol) of SC4, 0.259 g (0.706 mmol) of 1-((4-bromobutyl)oxymethyl)pyrene and 0.118 g (2.823 mmol) of $LiOH.H_2O$ were used. The desired product (160 mg, 21% yield) was purified by reverse phase chromatography using a gradient of water:acetonitrile.

^{1}H-NMR (400 MHz, Methanol-d4) δ (ppm) 8.34 (d, J = 9.3 Hz, 1H, Py), 8.12 (t, J = 7.3 Hz, 2H, Py), 8.06 (d, J = 7.8 Hz, 1H, Py), 7.99 (s, 2H, Py), 7.97 (d, J = 7.5 Hz, 1H, Py), 7.92 (t, J = 7.6 Hz, 1H, Py), 7.50 (d, J = 1.9 Hz, 2H, Calix-Ar), 7.46 (d, J = 1.8 Hz, 2H, Calix-Ar), 7.27 (s, 2H, Calix-Ar), 7.17 (s, 2H, Calix-Ar), 5.20 (s, 2H, O-CH_2-Py), 4.45 (d, 2H, axial Calix-bridge), 4.23 (d, J = 12.8 Hz, 2H, axial Calix-bridge), 3.79 (t, 2H,), 3.73 (t, 2H), 3.25 (d, J = 13.2 Hz, equatorial Calix-bridge), 3.13 (d, J = 12.3 Hz, 2H, equatorial Calix-bridge), 1.89 (m, 4H, CH_2 alkyl chain).

^{13}C-NMR (101 MHz, Methanol-d4) δ (ppm) 161.08, 157.76, 156.93, 138.22, 134.68, 133.60, 133.12, 131.69, 131.35, 131.22, 130.85, 129.42, 129.24, 129.02, 127.94, 127.42, 127.12, 127.07, 126.49, 126.03, 125.97, 125.79, 125.58, 125.15, 124.86, 124.65, 124.42, 124.15, 123.32, 75.67, 71.06, 70.18, 33.27, 30.98, 26.52, 26.44.

HR-MS (ESI) m/z calcd for $C_{49}H_{38}Li_2O_{17}S_4$ [M^{2-}]: 520.0661; found: 520.0671.

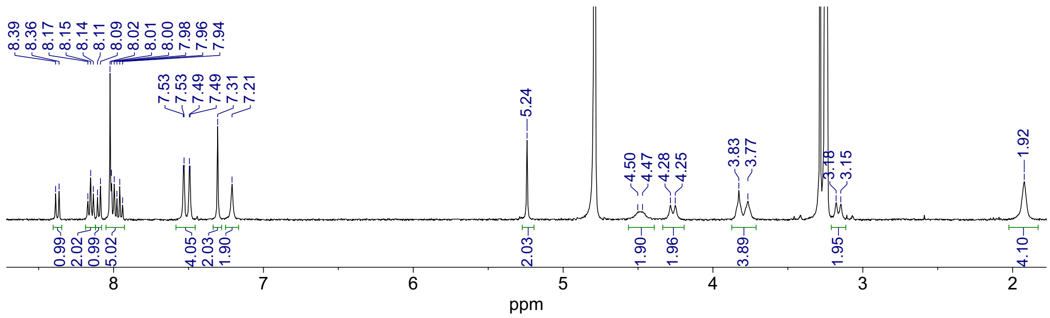

Figure 7.2: ^{1}H-NMR spectrum of SC4-4Py in methanol-d4. HDO peak observable at 4.79 ppm and methanol peak at 3.25 and 3.28 ppm.

7.2.1.2 SC4-6Py

1.49 g (2 mmol) of SC4, 0.49 g (1.5 mmol) of 1-((6-bromohexyl)oxymethyl)pyrene and 0.25 g (6 mmol) of $LiOH.H_2O$ were used. The desired product (189 mg, 11% yield) was purified by reverse phase chromatography using a gradient of water:acetonitrile.

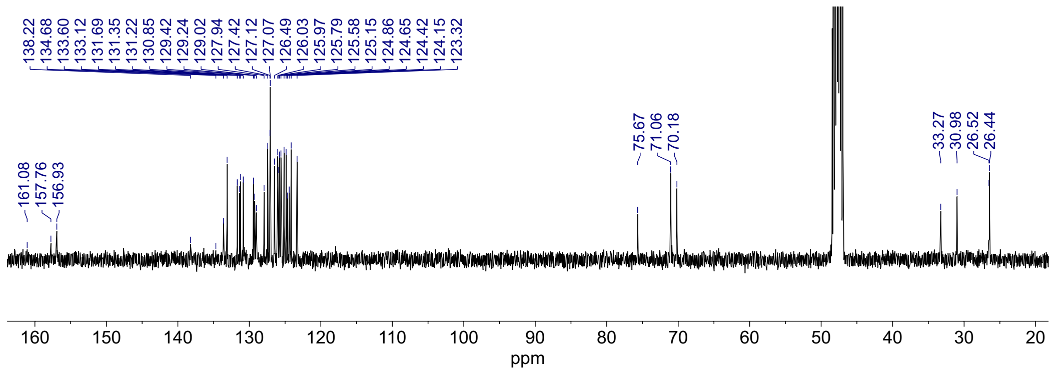

Figure 7.3: ^{13}C-NMR spectrum of SC4-4Py in methanol-d4.

^{1}H NMR (400 MHz, Methanol-d4) δ (ppm) 8.43 (d, J = 9.12 Hz, 1H, Py), 8.24 (t, J = 6.6 Hz, 2H, Py), 8.19 (dd, J = 4.3, 5.8 Hz, 2H, Py), 8.11 (s, 2H, Py), 8.05 (2H, Py), 7.63 (s, 2H, Calix-Ar), 7.57 (s, 2H, Calix-Ar), 7.39 (s, 2H, Calix-Ar), 7.29 (s, 2H, Calix-Ar), 5.24 (s, 2H, O-CH_2-Py), 4.54 (d, J = 12.4 Hz, 2H, axial Calix-bridge), 4.36 (t, J = 13.6 Hz, 2H, axial Calix-bridge), 3.72 (t, J = 6.2 Hz, 4H, O-CH_2-alkyl), 3.36 (d, J = 13.3 Hz, 2H, equatorial Calix-bridge), 3.24 (d, J = 12.5, 4H, equatorial Calix-bridge), 1.80 (J = 6.1 Hz, 2H, CH_2 alkyl chain), 1.73 (J = 6.2 Hz, 2H, CH_2 alkyl chain), 1.51 (4H, CH_2 alkyl chain).

^{13}C NMR (101 MHz, Methanol-d4) δ (ppm) 160.91, 157.71, 156.84, 138.24, 133.66, 133.09, 131.65, 131.36, 131.26, 130.83, 129.36, 129.19, 129.01, 127.93, 127.26, 127.08, 127.04, 126.47, 126.03, 125.96, 125.79, 125.58, 125.00, 124.92, 124.66, 124.45, 124.16, 123.30, 75.77, 71.00, 69.83, 33.24, 30.95, 29.52, 29.28, 25.74, 25.46.

HRMS (ESI) m/z calcd for $C_{51}H_{43}O_{17}S_4$ [M^{3-}]: 351.7133; found: 351.7134.

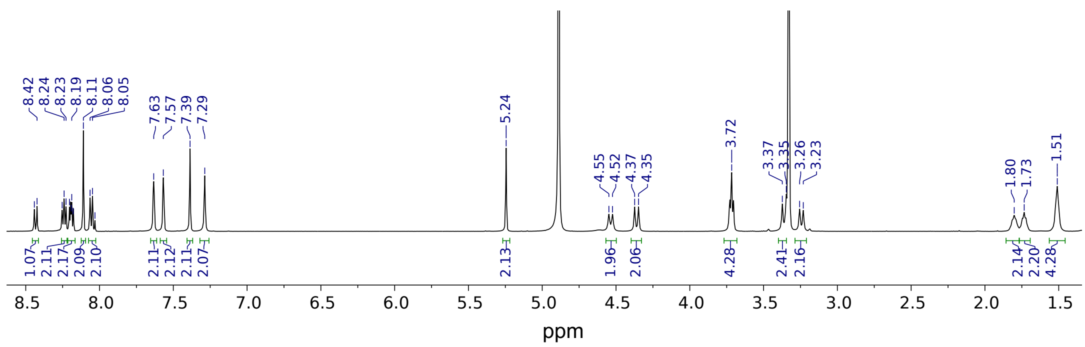

Figure 7.4: ^{1}H-NMR spectrum of SC4-6Py in methanol-d4. HDO peak observable at 4.89 ppm and methanol peak at 3.33 ppm.

7.2.1.3 SC4-8Py

392 mg (0.5 mmol) of SC4, 126 mg (0.3 mmol) of 1-((8-bromoctyl)oxymethyl)pyrene and 87 mg (1.8 mmol) of LiOH.H_2O were used. The desired product (97 mg, 17% yield) was purified by reverse phase chromatography using a gradient of water:acetonitrile.

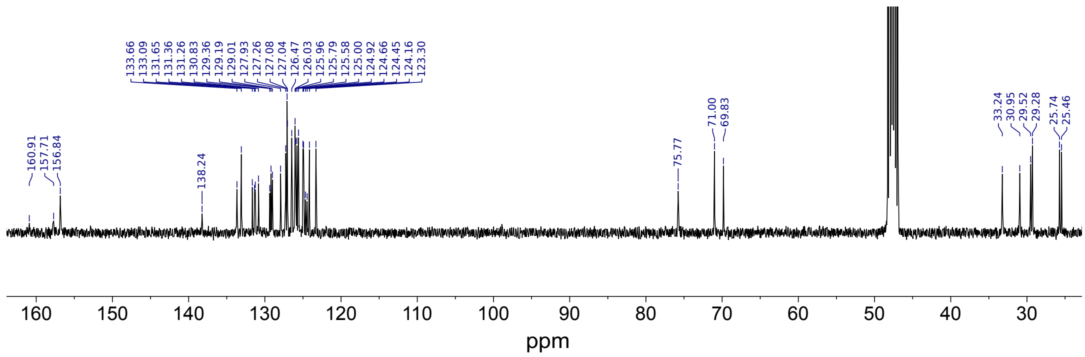

Figure 7.5: ^{13}C-NMR spectrum of SC4-6Py in methanol-d4.

^{1}H NMR (500 MHz, Methanol-d4) δ (ppm) 8.46 (d, J = 9.3 Hz, 1H, Py), 8.28 – 7.97 (m, 8H, Py), 7.69 (d, J = 2.2 Hz, 2H, Calix-Ar), 7.65 (d, J = 2.3 Hz, 2H, Calix-Ar), 7.52 (s, 2H, Calix-Ar), 7.42 (s, 2H, Calix-Ar), 5.24 (s, 2H, O-CH_2-Py), 4.23 (d, J = 19.1 Hz, 2H, axial Calix-bridge), 4.20 (d, J = 18.4 Hz, 2H, axial Calix-bridge), 3.82 (t, J = 6.5 Hz, 2H, O-CH_2-alkyl), 3.68 (t, J = 6.4 Hz, 2H, O-CH_2-alkyl), 3.55 (d, J = 13.7 Hz, 2H, equatorial Calix-bridge), 3.49 (d, J = 14.4 Hz, 2H, equatorial Calix-bridge), 1.79 (q, J = 13.6, 2H, alkyl chain CH_2), 1.69 (q, J = 13.4 Hz, 2H, alkyl chain CH_2), 1.55 (q, J = 15.9 Hz, 2H, alkyl chain CH_2), 1.36-1.26 (m, J = 13.6, 16.7 Hz, 4H, alkyl chain CH_2).

^{13}C NMR (101 MHz, Methanol-d4) δ (ppm) 153.95, 153.27, 150.34, 141.64, 137.64, 136.35, 133.08, 131.61, 131.41, 131.26, 130.83, 129.48, 127.24, 127.17, 127.12, 127.06, 127.05, 127.01, 126.82, 126.79, 126.63, 126.59, 125.82, 125.00, 124.92, 124.69, 124.44, 124.14, 123.46, 76.89, 71.10, 69.53, 31.02, 30.90, 29.46, 29.26, 28.81, 28.48, 25.54, 25.46.

HR-MS (ESI) m/z calculated for $C_{53}H_{48}O_{17}S_4$ [M^{2-}]: 520.0892; found: 542.0917.

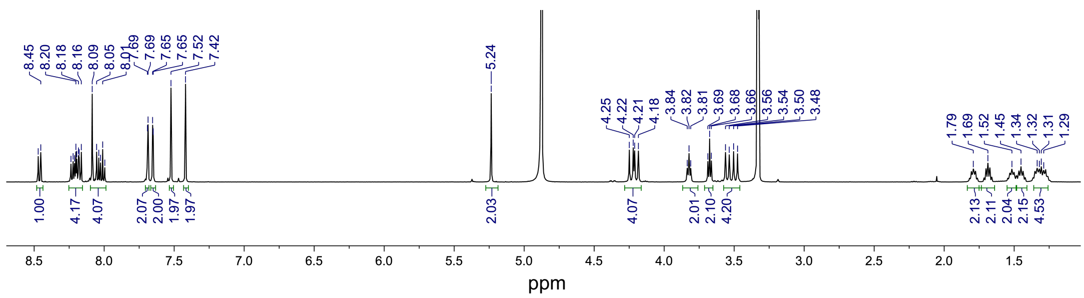

Figure 7.6: ^{1}H-NMR spectrum of SC4-8Py in methanol-d4. HDO peak observable at 4.89 ppm and methanol peak at 3.33 ppm.

7.2.2 SC4-Azo Counterion Activators

The synthesis of the precursors, SC4, 1.2, 2.1 and 2.2, were performed according to previously reported protocols.[287,302,303]

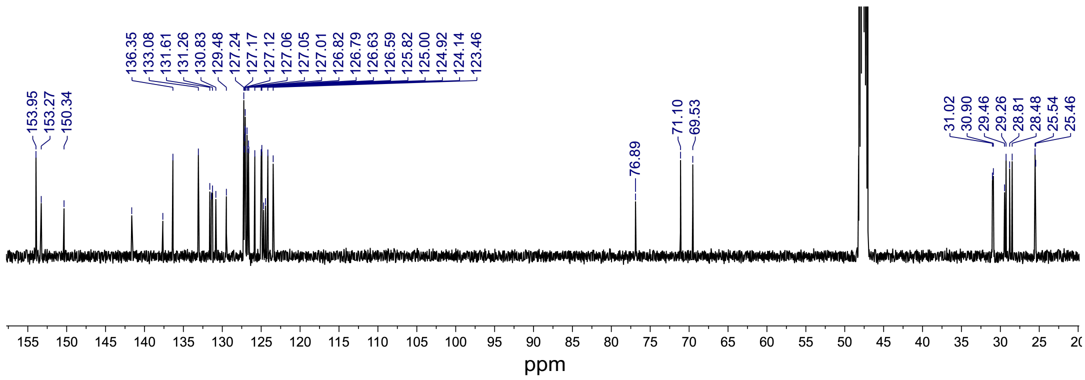

Figure 7.7: ^{13}C-NMR spectrum of SC4-8Py in methanol-d4.

7.2.2.1 SC4-Azo 1

1.48 g (2 mmol) of SC4, 0.54 g (1.5 mmol) of compound 1.2 and 0.25 g (6 mmol) of $LiOH.H_2O$ were heated at 72 °C in DMSO, under constant stirring, for 72h. After the reaction mixture cooled to room temperature, it was neutralized with HCl and precipitated two times, first with diethyl ether and then with ethyl acetate, in both cases not forming a precipitate but an oily mixture. The solvent was evaporated, the mixture was dissolved in methanol and precipitated with diethyl ether once again, this time forming a yellow precipitate that was filtered and dissolved in bi-distilled water. The different by-products were separated from the compound 1 by RP-18 chromatography with 1:9 (v:v) acetonitrile:water. The fraction with the final compound was evaporated and dried under vacuum, yielding a total of 95 mg of compound 1 (6% yield).

^{1}H NMR (400 MHz, Methanol-d4) δ (ppm) 7.88 (t, J = 8.9 Hz, 4H, H3 and H4), 7.62 (d, J = 2.2 Hz, 2H, H13), 7.55 (d, J = 2.3 Hz, 2H, H14), 7.52 (d, J = 7.8 Hz, 2H, H2), 7.46 (t, J = 8.4, 6.0 Hz, 1H, H1), 7.38 (s, 2H, H15), 7.29 (s, 2H, H12), 7.07 (d, J = 9.0 Hz, 2H, H5), 4.64 (d, J = 12.3 Hz, 2H, H16 axial), 4.36 (d, J = 13.2 Hz, 2H, H17 axial), 4.13 (t, J = 6.5 Hz, 2H, H6), 3.90 (t, J = 6.7 Hz, 2H, H11), 3.36 (d, J = 13.3 Hz, 2H, H17 equatorial), 3.33 (d, J = 12.4 Hz, 2H, H16 equatorial), 1.92 (dq, J = 13.3, 6.6 Hz, 4H, H7 and H10), 1.68 (dq, J = 17.3, 8.2 Hz, 4H, H8 and H9).

^{13}C NMR (101 MHz, Methanol-d4) δ (ppm) 162.06, 161.63, 158.03, 157.03, 152.77, 146.69, 138.12, 133.53, 133.21, 130.47, 130.09, 129.39, 129.21, 128.77, 128.04, 126.48, 126.02, 125.94, 125.52, 124.38, 122.09, 114.51, 75.76, 68.12, 33.39, 31.00, 29.56, 28.97, 25.78, 25.70.

HR-MS (ESI) m/z calculated for $C_{46}H_{42}N_2O_{17}S_4$ $[M^{4-} + 2H^+]^{2-}$: 511.0688; found, 511.0691.

7.2.2.2 SC4-Azo 2

1.48 g (2 mmol) of SC4, 0.563 g (1.5 mmol) of 2.2 and 0.25 g (6 mmol) of $LiOH.H_2O$ were dissolved in 10 ml of DMSO and were heated to 75 °Cunder constant stirring for 48 h. The reaction mixture was then precipitated two times with diethyl ether and once with ethyl acetate. The final precipitate was filtrated over vacuum, yielding a yellow

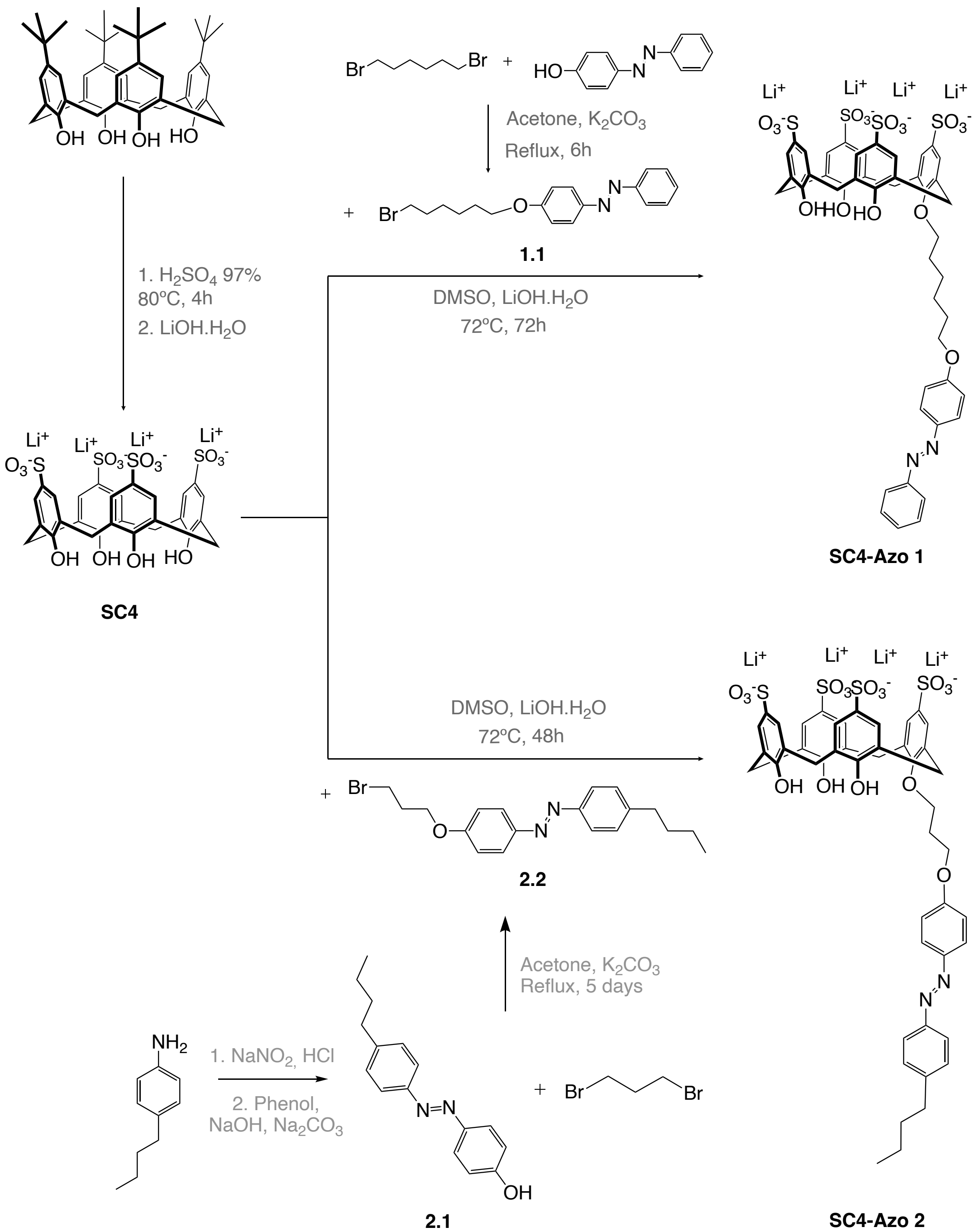

Figure 7.8: Reactional scheme for the synthesis of the SC4-Azo counterion activators, 1 and 2.

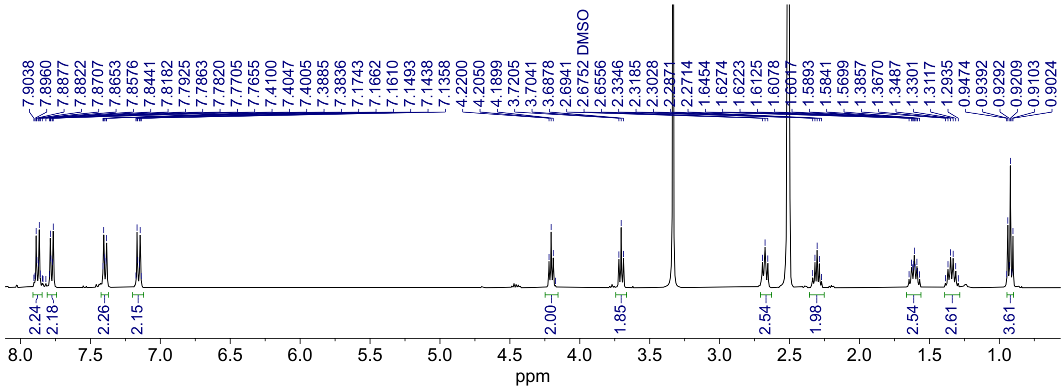

Figure 7.9: ^{1}H-NMR spectrum of SC4-Azo 1 in methanol-d4. DMSO peak observable at 2.5 ppm and methanol peak at 3.3 ppm.

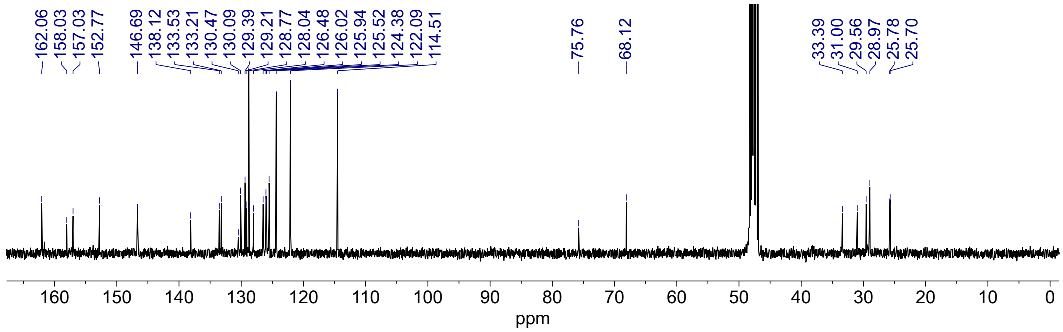

Figure 7.10: ^{13}C-NMR spectrum of SC4-Azo 1 in methanol-d4.

powder. This was then dissolved in a small quantity of water and further purified by RP-18 chromatography, with the product being eluted with 10% acetonitrile and 90% water. After evaporation of the solvent, 277 mg of final product was obtained, corresponding to a yield of 18%.

^{1}H NMR (400 MHz, Methanol-d4) δ (ppm) 7.88 (d, J = 8.7 Hz, 2H, H7), 7.79 (d, J = 8.0 Hz, 2H, H6), 7.62 (s, 2H, H15), 7.56 (d, J = 2.2 Hz, 2H, H16/H17), 7.40 (s, 2H, H16/H17), 7.34 (d, J = 8.1 Hz, 2H, H5), 7.33 (s, 2H, H14), 7.19 (d, J = 8.6 Hz, 2H, H8), 4.63 (d, J = 12.4 Hz, 2H, H12 axial), 4.60 (t, J = 14.3 Hz, 2H, H9), 4.38 (d, J = 13.2 Hz, 2H, H13 axial), 4.06 (t, J = 5.5 Hz, 1H), 3.37 (d, J = 15.0 Hz, 2H, H13 equatorial), 3.34 (d, J = 31.1 Hz, 2H, H12 equatorial), 2.71 (t, J = 7.7 Hz, 2H, H4), 2.45 (d, J = 8.6 Hz, 2H, H10), 1.68 (p, J = 7.5 Hz, 2H, H3), 1.42 (h, J = 7.5 Hz, 2H, H2), 0.99 (t, J = 7.3 Hz, 3H, H1).

^{13}C NMR (101 MHz, Methanol-d4) δ (ppm) 161.78, 157.01, 151.02, 146.79, 145.65, 133.58, 133.26, 129.38, 129.09, 128.72, 128.09, 126.47, 126.02, 125.50, 124.19, 122.14, 114.69, 65.23, 35.08, 33.39, 30.92, 29.63, 21.98, 12.86.

HR-MS (ESI - negative mode) m/z: calculated for ($C_{47}H_{45}N_2O_{17}S_4$) [M^{4-} + $3H^{+}$]$^{-}$: 1037.1606; found, 1037.1591.

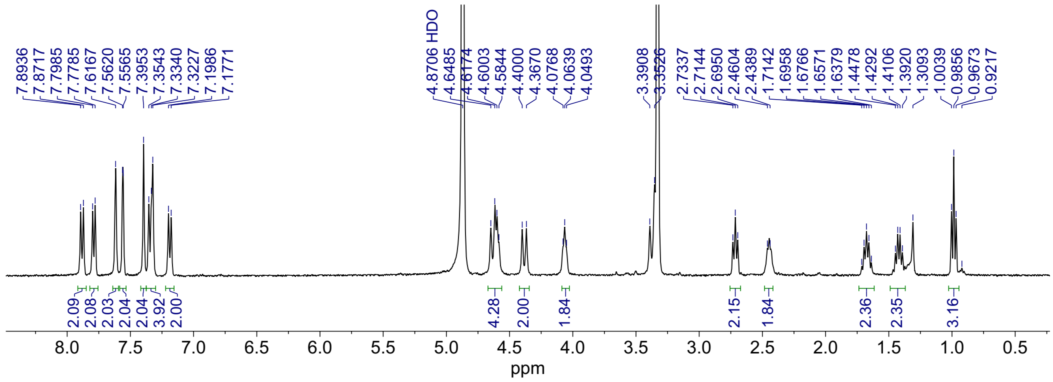

Figure 7.11: ^{1}H-NMR spectrum of SC4-Azo 2 in methanol-d4. HDO peak observable at 4.9 ppm and methanol peak at 3.3 ppm.

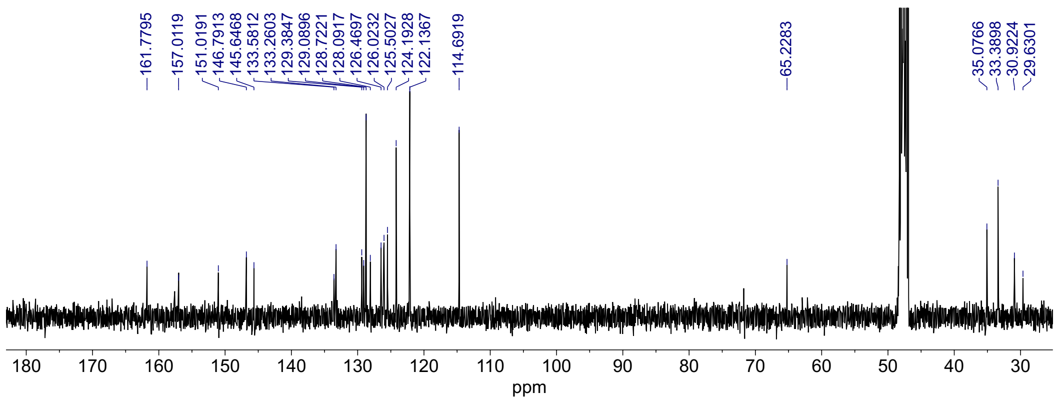

Figure 7.12: ^{13}C-NMR spectrum of SC4-Azo 2 in methanol-d4.

7.2.3 DASPI Dyes

The general procedure for synthesis of Et-DASPI and Jd-DASPI was based in the protocol by Wang *et al.* and was done with the addition of N-methylpyridinium with the respective aldehyde, obtained commercially, in the presence of catalytic amounts of piperidine.[304] Me-DASPI was obtained commercially.

Et-DASPI: ^{1}H-NMR (400 MHz, D_2O) δ 8.32 (d, J = 6.7 Hz, 2H), 7.80 (d, J = 6.7 Hz, 2H), 7.66 (d, J = 16.1 Hz, 1H), 7.56 (d, J = 8.9 Hz, 2H), 6.99 (d, J = 16.1 Hz, 1H), 6.82 (d, J = 8.8 Hz, 2H), 4.11 (s, 3H), 3.38 (J = 7.0 Hz, 4H), 1.09 (t, J = 7.1 Hz, 6H).

Jd-DASPI: ^{1}H-NMR (400 MHz, D_2O) δ 8.29 (d, J = 6.7 Hz, 2H), 7.76 (d, J = 6.6 Hz, 2H), 7.56 (d, J = 16.0 Hz, 1H), 7.16 (s, 2H), 6.93 (d, J = 16.0 Hz, 1H), 4.10 (s, 3H), 3.20 – 3.13 (4H), 2.69 (t, J = 6.4 Hz, 4H), 1.87 (p, J = 6.1 Hz, 4H).

7.2.4 Ditopic Receptor

As schematized in Chapter 3, Figure 3.18, several attempts at functionalization of CB7 were attempted, with variable success. The reactions reported in the corresponding section are

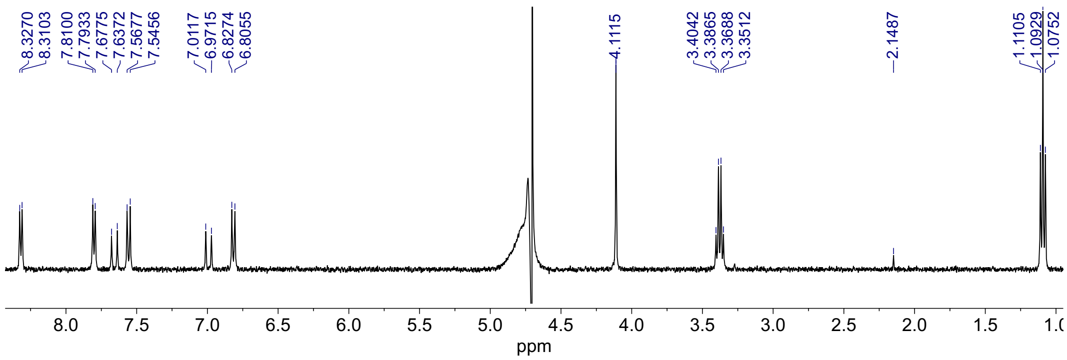

Figure 7.13: ^{1}H-NMR spectrum of Et-DASPI in D_2O. HDO peak observable at 4.7 ppm and acetone residual peak at 2.15 ppm.

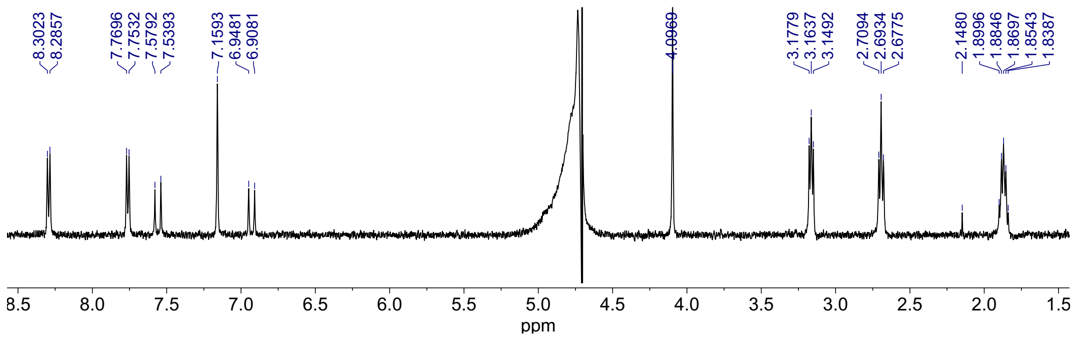

Figure 7.14: ^{1}H-NMR spectrum of Jd-DASPI in D_2O. HDO peak observable at 4.7 ppm and acetone residual peak at 2.15 ppm..

described here in further detail.

7.2.4.1 CB7-OH

The synthesis protocol of CB7-OH was done as reported by Dong *et al.* by chemical oxidation of CB7 using $(NH_4)_2S_2O_8$ and Na_2SO_4.[238] Different batches of CB7-OH were prepared but for each 1 g of CB7 (0.86 mmol) approximately 1.4 equivalents of each of the other reactants were used (in this example 1.2 mmol). The different reagents were dissolved in water and heated at 65 °C for 18 hours. The mixture was filtered to removed excess insoluble $(NH_4)_2S_2O_8$ and the remainder of the supernatant was evaporated and separated using a polymeric CHP20P resin and water as eluent. Fractions were recovered and analyzed for berberine emission enhancement - these fractions were then analyzed by ESI-MS with the guest cystamine, to confirm the degree of hydroxylation of each fraction. Fractions which presented the expected mass spectroscopy fragments were recovered and solvent was evaporated and then the resulting powder was dried under vaccum. Yields of reaction varied for each batch but remained between 7 and 11%. NMR spectrum of one of the CB7-OH fractions can be found in Chapter 3, Section 3.3 in Figure 3.19.

7.2.4.2 CB7-propargyl

Synthesis of CB7-propargyl was done according to the procedure used in the work by Zhang *et al.*[305] 20 mg of CB7-OH (0.17 mmol) were dissolved in 1.5 mL of dry DMSO and, under N_2 atmosphere, 25 eq. of NaH were added slowly over a course of 30 min. 700 μL of propargyl bromide (6.2 mmol) were added at 0 °C and left with continuous stirring at room temperature for 18 h. Due to the high salt concentration, purification procedures were not successful with only a small fraction of CB7-propargyl detected by ESI-MS at 685.3 m/z (expected 684.7, Figure 7.15).

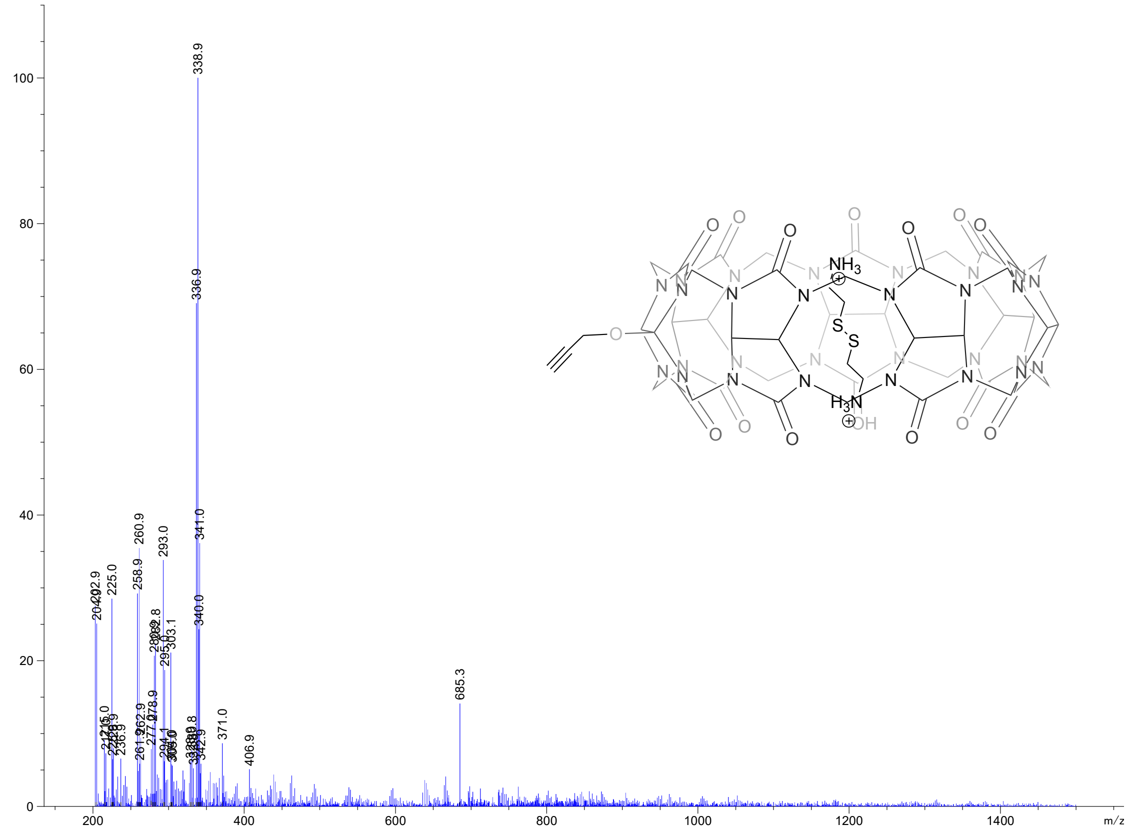

Figure 7.15: ESI-MS spectrum of the CB7-propargyl reaction mixture in the presence of cystamine. Structure of the CB7-propargyl:cystamine complex in inset.

7.2.4.3 Superacid Mediated Synthesis of CB7-COOH and CB7-Br

Superacid mediated synthesis of CB7-COOH and CB7-Br was done based on the previously described protocol developed by Kim and coworkers.[239]

20 mg CB7-OH was dissolved in methanosulfonic acid (670 μL) and added to 300 equivalents of the correspondant reagent dissolved in the same acid (300 μL). The two methanosulfonic acid samples were added together dropwise in an ice bath and 240 μL of triflic acid was added dropwise over ice to the previous sample and this reaction mixture was agitated at 50 °C for 5 hours. After the reaction, the mixture was mixed with 6 mL of cold water and precipitated with excess acetone. The fine powder was centrifuged out

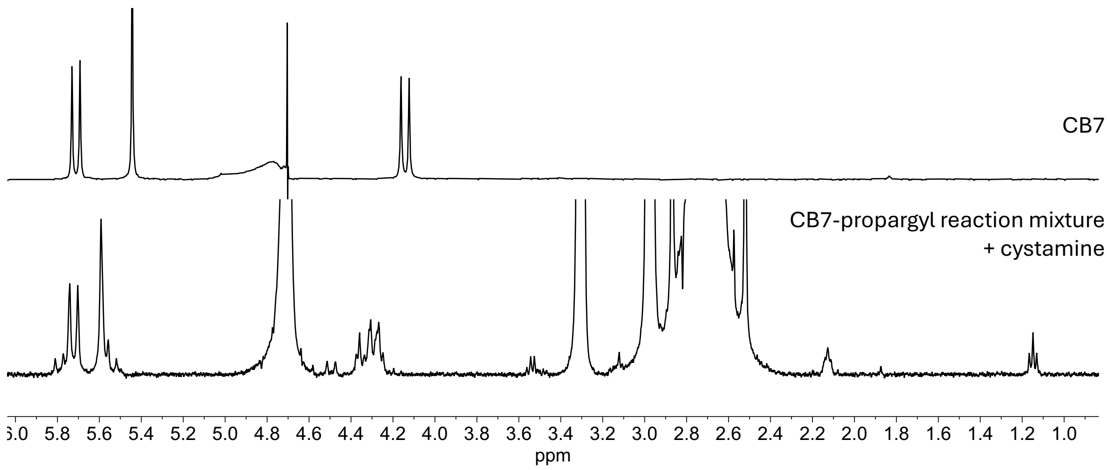

Figure 7.16: ^{1}H-NMR spectra of CB7 (top) and CB7-propargyl reaction mixture with an excess of the guest cystamine (bottom) in D_2O.

of solution and the recovered product was dried under vaccum overnight. All reactants used and specific conditions for each reaction is presented in Appendix B.3. The ^{1}H-NMR spectrum of the product for the reaction with 3-bromopropionitrile can be found in Chapter 3, Section 3.3, in Figure 3.20, and the product for the reaction with cyanoacetic acid is presented below and appears to be consistent with the literature.[239]

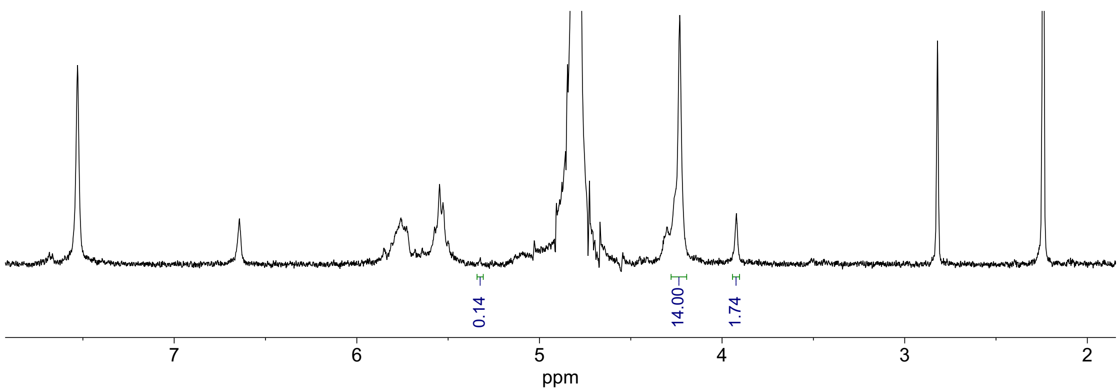

Figure 7.17: ^{1}H-NMR spectra of CB7-COOH in D_2O with integrals of protons associated with CB7-OH at 5.32 ppm (< 0.14H) and the protons that are believed to correspond to the equatorial bridge protons of the modified CB7 unit at 4.23 ppm (14H) and the CB7-COOH functional group -CH_2- group at 3.92 ppm ($\approx$ 2H). This integration allows to estimate the yield to be $\approx$ 86%.

7.2.4.4 CB7-N_3

5 mg of CB7-Br (3.8 μmol) and 2.5 mg of NaN_3 (38 μmol) were dissolved in D_2O and added to an NMR tube. This tube was heated at 80 °C for 48 hours and ^{1}H-NMR spectra were taken at different intervals to ascertain the progress of the reaction until equilibrium was

reached. ^{1}H-NMR spectrum of the final solution is presented in 3, Section 3.3, in Figure 3.20, however, to confirm the conversion to the CB7-N_3 species further characterization by NMR and HR-MS is still needed.

7.3 Liposome preparation and characterization

Liposomes were prepared by different methods according to the size of the vesicles.

For large unilamellar vesicles (LUV) the thin-film hydration method was used for obtention of the vesicles and extrusion through differently sized membranes was done in order to nanosize them. 1 mL of a 10 mg/ml solution of lipid, in this case L-α-phosphatidylcholine (Egg, Chicken), EYPC, obtained from Avanti Polar Lipids (reference no. 840051), was added to a round bottom flask and carefully rotated and evaporated under N_2 stream to obtain a thin film of lipid. This was dried under vacuum for a minimum of 1 hour and 1 mL of the solution to encapsulate - either phosphate buffer (PB) 5 mM pH 7.4 or 50 mM carboxyfluorescein (CF) in this same buffer - was added and mixed at 40 °C for 30 min. After mixing, 10 freeze-thaw cycles were done to improve encapsulation and unilamellarity of the vesicles. Extrusion through 100 or 200 nm membrane was done, 23 times for each sample, maintaining the temperature at 40 °C. For the liposomes prepared only with buffer solution, the obtained turbid solution was ready to use and was examined by DLS to determine the average size of the liposomes in solution. For liposomes with encapsulated CF, the extrusion step was followed by a size-exclusion column with Sephadex G-25 (V = 37 mL), eluted with PB 5 mM pH 7.4, originating two fractions, one with high turbity, containing LUV$\supset$CF, and a transparent, highly fluorescent one containing the excess of non-encapsulated CF.

Giant unilamellar vesicles (GUV) were obtained through the solvent evaporation method.[306] A solution of 1.5 mg/ml of EYPC in chloroform was prepared and 500 μL of this solution was added to 100 μL of methanol and 3.5 mL of PB 5 mM pH 7.4 in a round-bottom flask. This immiscible mixture was then slowly evaporated over the course of 30 min at 40 °C, on a rotary evaporator, with slow decreases of pressure to ensure the slow evaporation of the organic phase. Once no evaporation was observed at 100 mbar, the sample was left to evaporate an additional 5 min. originating a high turbidity solution with only one phase. This technique yielded mostly polydisperse samples with several GUV observable under the microscope, with a variable size that appeared to range between 1 to 100 μm, as shown in Section 5.2.

7.4 Oil in Water (O/W) emulsion preparation

Polydisperse O/W emulsions were obtained by addition of a small aliquot of organic solvent, either O-DCB or diethylbenzene, to a solution of the given surfactant at the wanted concentration and vortexed for 5 to 10 seconds or until a stable dispersion was observed.

Monodisperse droplets were made by microfluidic fabrication, using a Dolomite Microfluidics microfluidic system with two Mitos P pressure pumps to control continuous phase and disperse phase flow (disperse phase injected at 500 mbar and continuous phase at 2000 mbar) into a Telos 2 Reagent Chip (50 μm).[249,251,307] The disperse phase varied in contents but corresponded to the organic O-DCB phase with the necessary reagents in each droplet stock and the continuous phase corresponded to the SC4-4C surfactant solution at 0.37 wt%.

7.5 NMR spectroscopy experiments

7.5.1 Structural Characterization of Synthesized Molecules and Supramolecular Complexes in D_2O and other deuterated solvents

^{1}H-NMR resonances of each compound were assigned at 298 K, unless stated otherwise, using standard ^{1}H-COSY, ^{1}H-ROESY (300 ms mixing time) and, when necessary, 2D ^{1}H,^{13}C-HSQC experiments, with natural abuncancy ^{13}C.

Complexation experiments were done in D_2O and ^{1}H-NMR resonances of each compound in solution were assigned using the same experiments mentioned above and the assigned spectra of each free species. If necessary, different ratios of the different elements of the complexes were used to clarify specific ressonances. Ratio used in each experiment is indicated in the respective spectrum.

7.5.2 Structural Characterization of Peptide Supramolecular Complexes in H_2O/D_2O

^{1}H-NMR resonances of the peptides were assigned at 298 K using standard ^{1}H-TOCSY (80 ms mixing time), ^{1}H-ROESY (150 ms mixing time) and 2D ^{1}H,^{13}C-HSQC experiments, with natural abuncancy ^{13}C. Spectra of peptides and the respective complexes were made in H_2O/D_2O 90%/10% mixture, with PB 5 mM pH 7.4, with water supression, in order to observe the chemical shifts of labile protons, like those of amide, guanidinium and amine groups.

The titration assays presented in Chapter 2, that aided in both attribution of peptide chemical shifts and in clarifying the stoichiometry of the complexes, were done by preparation of two different samples, both with a fixed concentration of peptide, with 3 equivalents of the host SC4 added to one of them, to be used as titrant. The solution with excess SC4 was used to obtain the NMR spectrum at 3 eq. of host and every other concentration below that. For the high equivalent samples presented with R_4, those were prepared in batch, or by direct addition of a concentrated SC4 solution. All solutions were prepared with a H_2O/D_2O 90%/10% mixture, in PB 5 mM pH 7.4.

7.5.3 Quantification by ^{1}H-NMR spectroscopy

Both methods of quantification by ^{1}H-NMR use an internal reference with a well defined concentration in order to quantify the sample of unknown quantity by a comparative method. The reference chosen for this effect was maleic acid, seeing as it presents a single singlet at a 6.3 ppm chemical shift, corresponding to the alkene symmetric protons.

7.5.3.1 Quantification of Peptide Samples with Coaxial Tube

The method used for the quantification of oligoarginines was done in collaboration with Dr. Ana Sofia Ferreira and based on the recent paper by Ogura and Wakayama.[308]

In order to not add contaminants to peptide stocks that could interfere with future experiments, the reference for this method is added in an inner tube, the coaxial tube, which will contain the reference in the same solvent as the sample. The relation between the concentration of this reference, C_R, and that of the peptide sample, C_S, is dependent on the ratio between respective peak integrals, I_R and I_S, and ratio of respective number of protons that said peak corresponds to, H_R and H_S, and volume of analyzed sample (Equation 7.1).

$$C_S = \frac{I_S}{I_R} \cdot \frac{H_R}{H_S} \cdot \frac{V_R}{V_S} \cdot C_R \tag{7.1}$$

Unlike when working with an internal reference in the same sample as the compound to quantify, where $V_R = V_S$ (μL), the effective volume analyzed by the NMR equipment in the coaxial and outer tubes are unknown, so it was necessary to obtain these values experimentally. For this a reference of Potassium Hydrogen Phthalate of a known concentration was used in the outer tube, yielding a V_R/V_S of 0.0977 for this coaxial and outer tube pair, which were used for all quantifications. NMR spectra for quantification were done with an increased relaxation delay (above 10 seconds) due to maleic acid's higher T_1 value and the unknown values for the peptides.

7.5.3.2 Quantification of lipids in liposome samples

This method uses the protocol reported by Hennig and coworkers, where a small amount (50-175 μL) of the aqueous LUV stock after gel filtration is mixed with a chloroform-methanol mixture in order to completely solubilize the lipids in the LUV solution.[309] Depending on the concentration of lipids and the volume added of stock LUV different mixtures of chloroform and methanol were used, but in general 100 μL of MeOD and 430 μL of $CDCl_3$ were used. In this case, a small volume of a concentrated maleic acid solution was directly added to this mixture, vortexed, and ^{1}H-NMR were obtained with a T_1 above 5 seconds. All solvents used were deuterated with the exception of the LUV stocks.

7.6 Characterization Techniques and protocol

7.6.1 Direct titrations

Direct titrations were done by direct addition of small aliquots of a stock solution of the titrant species to a solution of the titrated compound at a fixed concentration (specific details are referenced in the figure of each direct titration). To avoid dilution effects, the same concentration of titrated species was added to the titrant stock solution.

Assays with hosts that can lead to aggregation phenomena, i.e. SC4-nPy (Section 4.1), the direct titrations followed by optical techniques were done in batch to avoid kinetic effects of aggregation influencing quantitative data.

ITC experiments varied the presence of host or guest as titrant, depending on solubility limitations or baseline issues, however, the elements present in the ITC cell and syringe are indicated in each figure and experiment presented. Baselines were obtained for the higher concentration titrations due to interferance by heat of dilution of the syringe sample in the measurement. Baselines were obtained by titrating the same concentration of titrant in the syringe with only the solvent or buffer in the cell. ITC experiments where aggregation occured were not done due to the thermodynamic contribution of the aggregation process to the heat variation of the binding. For hygroscopic peptides with aromatic amino acids, the molar extinction coefficient (ε) of the amino acids were used to quantify the prepared solutions ($\varepsilon_{278nm}^{Trp}$ = 5580 $M^{-1}cm^{-1}$, $\varepsilon_{280nm}^{Tyr}$ = 1490 $M^{-1}cm^{-1}$ and $\varepsilon_{258nm}^{Phe}$ = 195 $M^{-1}cm^{-1}$).[310]

The model used for fitting of the experimental data was the equal binding sites model present in the software provided by Malvern Panalytical, with calculation of the number binding of sites (n) and full thermal characterization.

7.6.2 Binding assays of heteroternary complexes

Binding assays shown in Section 3.2 were done as explained above, with the distinction of the heteroternary complex assembly, where both CB7 and dye concentrations were fixed and BB was added directly to the preformed complex. Fitting of the data was done by considering all affinity constants, previously obtained in other direct titration experiments. The calculation of the ternary binding constant was based on the information present in the Annex I, Section I.2.1.1.

7.6.3 Competitive Assays

Competitive assays were done in the presence of the chosen dye and host at a fixed concentration so that the complex exceeds a molar fraction of 0.9. Competitive assays with species that lead to aggregation were done at lower concentration and lower complex fractions, to avoid this phenomenon interfering with the binding event. Aliquots of the competitor are then added sequentially until a plateau is reached in the experiment or, for lower affinity pairs, until only low variations of signal can be observed. Correction for dilution were done accordingly to the initial volume of the sample and aliquot volume.

Dye-host pairs, affinities of these complexes and concentrations used are reported in the respective sections and figures.

7.6.4 Competitive Assays with heteroternary complexes

Competitive assays done with the heteroternary dual-host system were done in a similar fashion to the normal competitive assays, however, the molar fractions of the species were optimized through prediction by the scripts present in Annex I, Section I.2.2, in order to be in a semiquenched state, where addition of CB7 competitor could lead to further quenching and addition of BB competitor would lead to further enhancement. The corresponding concentrations of the species are presented in the respective Figures with the UV-vis and Fluorescence spectroscopy assays.

7.6.5 Principal Component Analysis

Samples for Principal Component Analysis (PCA) were prepared in batch in plastic cuvettes and emission measurements were analyzed by fluorescence spectroscopy with excitation at 347 nm. Triplicate samples were prepared for each peptide and for each of the sensors and the data used for the calculation of the principal components is presented in the caption of each figure. The calculation and figure preparation was done with Python 3.9 and the python libraries Pandas and Numpy for data wrangling, sklearn.decomposition for the PCA, matplotlib for plotting. The script used is presented in the Annex I.2.3.

7.6.6 Dye-Efflux Assays

For the measurement of both SC4-Azo 1 and 2 and SC4-4Py effectiveness as counterion activators of polyarginine transport, dye efflux assays were executed at several counterion activator concentrations, while maintaining the concentration of peptide and LUV fixed as indicated in the respective figures. For the dye efflux assays, CF emission was followed throughout the assay, with consecutive additions of the elements of the solution - the initial solution presented only the vesicles at a fixed concentration. A counterion activator aliquot is then added according to the concentration to be tested and the emission is measured to confirm that CF remains encapsulated; some counterion activators can act as detergents at sufficient concentrations. Finally, the peptide in question is added and fluorescence spectra are measured until the emission stabilizes and a maximum of release is reached. If the counterion activator has the capacity to activate the transport, CF should be co-transported to the exterior of the liposome with the influx of the counterion-peptide complex. Finally, Triton X-100 is added to the solution to dissolve the vesicles and obtain the maximum amount of CF that could be released from the liposomes and emit in the outside medium. EC_{50} and Y_{max} values were calculated from the values of corrected emission at the plateau that is reached, according to previously reported assays.

The light-modulation offered by the novel counterion activators SC4-Azo 1 and 2 was tested by performing dye efflux assays as previously described, with the addition of an interval in the measurement where the solution was irradiated at 500 nm.

7.6.7 Critical Aggregation Concentration

Critical aggregation concentration (CAC) for SC4-nPy sensors both when free in solution and in the presence of different analytes was calculated by the pyrene aggregate emission onset. For all samples the measurements were determined by preparation of batch samples at different concentrations, with the sensor-peptide complex CAC calculation being done at a fixed ratio of sensor to guest, which is indicated in the respective figure.

7.6.8 Surface Tension Measurement

Surfactant samples were prepared at 0.025 wt% in a 4 mL quartz cuvette and surface tension was measured in a Ramé-Hart Model 500 Advanced Goniometer/Tensiometer, by measurement of the contact angle of a pendant drop of O-DCB after 10 min of stabilization in the respective surfactant solution. Each experiment was repeated three times, for three different O-DCB droplets, maintaining the volume of the droplet as consistent as possible across triplicates.

7.6.9 Chemiluminescence assays

Chemiluminescence assays were done with bis(2,4,6-trichlorophenyl)oxalate (TCPO) (1.7 mM) and the dye 9,10-(diphenylethynyl)anthracene (0.11 mM) in the presence of the triethylsilane protected peroxide, $(TES)_2$-peroxide (10 mM). These assays were first tested in glass vials in O-DCB, by addition of the several necessary chemiluminescence components, with the exception of the catalyst for peroxide deprotection. The mixture was stirred continuously and the addition of 10 mM of the respective deprotection catalyst (Table 4.2 in Section 4.2) was done while filming the flask with a phone camera for initial fluorescence detection.

Assays in droplets were done by preparation of two distinct O/W emulsion batches: the first was prepared with the chemiluminescence reaction mixture, at the same concentrations as referred above, without deprotection catalyst, in the organic phase and 0.037 wt% SC4-4C in the aqueous phase and a separate O/W emulsion was prepared only with the deprotection catalyst in O-DCB and 0.037 wt% SC4-4C in the aqueous phase.

Detection of chemiluminescence was tested for the stable droplets in cell culture chambers with a mounted glass coverslip, by adding 600 μL of bidistilled water and an equal volume of each batch of emulsions to the bottom of the chamber. The droplet coalescence was induced by addition of an excess amount of ArgOMe, and emission was detected by fluorescence spectroscopy with an optical fiber mount, located directly above the cell culture chamber with the emulsion mixture.

7.6.10 Epoxidation induced by droplet coalescence assays

Epoxidation assays in droplets were done in a similar manner to those of the CL reaction, with the initial tests done in O-DCB and then later the components mCPBA and DPH being added to different monodisperse emulsion batches, at 5 and 0.1 mM, respectively, both prepared in an aqueous 0.037 wt% SC4-4C solution. DPH epoxidation by mCPBA in droplets was done by adding 5 μL of each droplet batch to 600 μL of bidistilled water in the cell culture chambers with a mounted coverslip and emission was detected by fluorescence spectroscopy with an optical fiber mount set-up. Spectra were obtained immediately after addition of the mCPBA batch to the DPH droplets, when the peptide solution was added and 1 hour after addition of the SC4-4C guest to evaluate the extent of epoxidation.

7.6.11 Microscopy and Biological Assays

7.6.11.1 Cell Microscopy

Cell microscopy assays were performed by PhD student Yeray Folgar-Cameán, at Montenegro Lab, CIQUS, Santiago de Compostela University, Spain.

HeLa (cervix adenocarcinoma cells) cell line was obtained from ATCC and cultured in Dulbecco's Modified Eagle's Medium (Dulbecco's Modified Eagle Medium (DMEM); 4500 mg/L glucose, L-glutamine, sodium pyruvate, and sodium bicarbonate) supplemented with 10% fetal bovine serum (FBS) and 1% Penicillin-Streptomycin-Glutamine Mix (Fisher) (complete DMEM). They were maintained at 37 °C, 5% CO_2, and 95% humidity in an INCO 108 incubator (Memmert).

HeLa cells were seeded the day before at 100,000 cells/mL (100 μL/well of a 96-well plate). Calixarenes *E*-2 and *Z*-2 (10, 50, 100, and 250 nM) and TAMRA-R_8 (3 μM) samples were diluted in DMEM stock and added to the cells (50 μL/well) for 25 min at 37 °C, 5% CO_2. Before imaging, cells were treated with 1 μM Hoechst 33342 for 20 minutes to stain nuclei. Afterwards, cell culture media was removed, cells were washed with PBS, and 50 μL of complete DMEM without phenol red were added. Cells were immediately imaged using the 60× oil objective of a Dragonfly spinning disc confocal microscope mounted on a Nikon Eclipse Ti-E and equipped with an Andor Zyla 4.2 PLUS sCMOS digital camera. Fluorescence of Hoechst was excited with the 405 nm laser and the emission was detected at 450/50 nm; for the TAMRA fluorescence, an excitation of 561 nm was used while the emission was detected at 620/60 nm. Images were processed using ImageJ software (v1.52b).

7.6.11.2 GUV Microscopy

Samples for miscroscopy of Giant Unilamellar Vesicles (GUV) were prepared with the stock solution of EYPC-GUV at 300 μM, with addition of 30 μM of the sensor SC4-4Py. Different concentrations of peptide were added as indicated in the presented figures with microsocopy results. A small aliquot of each solution was deposited in glass slides equiped with SecureSeal™Imaging Spacers with 9 mm of diameter and 0.12 mm of depth in order not to disturb the GUV structures, and covered with coverslips. Images were obtained immediately after preparation of the slides and after several minutes to hours after to analyze the kinetic stability of the SC4-4Py-peptide structures in the vesicle membrane. Both 10x objective and 20x and 60× oil objectives were used for imaging, on a Dragonfly spinning disc confocal microscope mounted on a Nikon Eclipse Ti-E and equipped with an Andor Zyla 4.2 PLUS sCMOS digital camera, using the epifluorescence mode due to limitation of confocal setup in terms of excitation wavelength (> 400 nm). The SC4-4Py was excited with the DAPI longpass filter set with excitation at 365 nm and emission detection from 413 nm. Images were processed using ImageJ software (v1.52b).

7.6.11.3 Double Emulsion Microscopy

Microscopy samples were prepared directly in cell culture chambers with a mounted glass coverslip, by adding 600 μL of MilliQ water so as to cover the coverslip completely. The double emulsion preparation is added slowly with a micropipette in order to create an even distribution of droplets in the bottom of the chamber. Bright-field images were obtained in an inverted microscope at different magnifications and fluorescence microscopy images were obtained in a Zeiss Axiovert 200 inverted widefield fluorescence microscope equipped with a Zeiss AxioCam HRc camera, by using the DAPI channel filter set for excitation and emission detection.

7.6.12 Biological Assays

All biological assays were performed by PhD student Yeray Folgar-Carmeán, at Montenegro Lab, CIQUS, Santiago de Compostela University, Spain.

Flow cytometry assays were done with HeLa cells, seeded the day before at 100,000 cells/mL (100 μL/well of a 96-well plate). Calixarenes *E*-2 and *Z*-2 (10, 50, 100, and 250 nM) and TAMRA-R_8 (3 μM) samples were diluted in DMEM stock and added to the cells (50 μL/well) for 25 min at 37 °C, 5% CO_2. Immediately after incubation, cells were detached by replacing samples with 100 μL of Trypsin-EDTA for 10 min at 37 °C, 5% CO_2. Once cells were in suspension, trypsin was neutralized by the addition of 100 μL PBS containing 2% FBS and 5 mM EDTA. TAMRA fluorescence was excited at 532 nm (green laser) and measured on a Guava easyCyte BG HT collecting the emission at 583/26nm (Yellow-G channel), using InCyte v3.2 (GuavaSoft, Millipore). Cells with typical FSC and SSC parameters were selected and the mean fluorescence intensity was calculated for each sample. Each condition was measured in quadruplicate. Data analysis was performed with the InCyte software included in GuavaSoft 3.2 (Millipore).

Cell viability assays were done with HeLa cells as well, prepared in the same conditions as the previous assay. Cells were then incubated with calixarene *E*-2 or *Z*-2 samples diluted in DMEM stock (0.01, 0.05, 0.1, 0.15, 0.25, 0.5, 0.75, 1, 2.5, 5, 7.5, 10, 15, 20, 40, 60, 80 and 100 μM, 50 μL/well) for 24 hours. Afterwards, samples were removed and replaced with 100

μL of fresh complete DMEM supplemented with 0.5 mg/mL MTT. Cells were incubated for 2 hours before carefully removing the supernatant and dissolving the formazan crystals with DMSO (100 μL/well). The absorbance at 570 nm was measured with a plate reader (Tecan Infinite F200Pro) and the data normalized to the value of untreated cells (100% viability), after blank subtraction (cells previously treated with Triton X-100). Each condition was measured in triplicate. Curve fitting was performed with GraphPad Prism 6 software (v6.01) using a 4-parameters logistic model.

8

Work Dissemination

8.1 Publications

Joana N. Martins, Beatriz Raimundo, Alicia Rioboo, Yeray Folgar-Cameán, Javier Montenegro, and Nuno Basílio. "Photoswitchable Calixarene Activators for Controlled Peptide Transport across Lipid Membranes" *Journal of the American Chemical Society*, 2023, 145 (24), 13126-13133, DOI: 10.1021/jacs.3c01829

8.2 Oral and Poster Communications

8.2.1 Oral Communications

8.2.1.1 National Conferences

- "Supramolecular Sensors for Biologically Relevant Analytes", presented on the 29th of March of 2021, at 14º Encontro Nacional de Química Física, 14ENQF (Online)

- "Detecting two distinct analytes with a single dye: A ternary host:guest complex with orthogonal recognition units", presented on the 4th of April of 2023, at 15º Encontro Nacional de Química Física, 15ENQF (Online)

- "Novel Photo-Responsive Calixarenes for the Control of the Transport of Hydrophilic Peptides Across Synthetic and Cellular Membranes", presented on the 24th of July of 2023, at the XXVIII Encontro Nacional da Sociedade Portuguesa de Química, Aveiro, Portugal

8.2.1.2 International Conferences

- "Light-Controlled Counterion Activation of the Transport of Arginine-Rich Peptides Across Synthetic Phospholipidic Membranes", presented on the 11th of July of 2022, at RICI IX - Iberian Meeting on Colloids and Interfaces, Santiago de Compostela, Spain

- "A three-component self-assembled chemosensor for the detection of two distinct analytes using a single dye", presented on the 7th of June of 2023, at Affinity 2023, Lisbon, Portugal
- "Dual-emission sensing systems in phospholipidic artificial membranes", presented on the 24th of June of 2024, at RICI X - Iberian Meeting on Colloids and Interfaces, Coimbra, Portugal
- "Novel Photo-Responsive Calixarenes for the Control of the Transport of Hydrophilic Peptides Across Synthetic and Cellular Membranes", presented on the 10th of July of 2024, at the 9th EuChemS Chemistry Congress (ECC9), Dublin, Ireland
- "p-Sulfonatocalix[4]arene-based ratiometric array for sensing of cationic peptides in solution and different platforms", presented on the 27th of February of 2025, at the XIX Iberian Peptide Meeting (EPI 2025), Santiago de Compostela, Spain.

8.2.2 Poster communications

- "Supramolecular Ratiometric Sensors for Polycationic Peptides", presented at the 24th PhotoIUPAC, between the 17th and 22nd of July of 2022, Amsterdam, The Netherlands

Bibliography

1. Lourenço, J. M. *The NOVAthesis LaTeX Template User's Manual* NOVA University Lisbon (2021). `https://github.com/joaomlourenco/novathesis/raw/main/template.pdf` (cit. on p. i).
2. Lehn, J.-M. Supramolecular Chemistry: Receptors, Catalysts, and Carriers. *Science* **227,** 849–856 (4689 1985) (cit. on pp. 1, 4, 26, 93).
3. Cram, D. J. The Design of Molecular Hosts, Guests, and Their Complexes. *Science* **240,** 760–767 (4853 1988) (cit. on pp. 1, 4, 26).
4. Pedersen, C. J. The Discovery of Crown Ethers. *Science* **241,** 536–540 (4865 1988) (cit. on pp. 1, 26).
5. Rücker, A. W. XXII.–On the range of molecular forces. *Journal of the Chemical Society, Transactions* **53,** 222–262 (1888) (cit. on p. 1).
6. Lehn, J.-M. in *Supramolecular Chemistry: Concepts and Perspectives* 1–9 (VCH, 1995) (cit. on pp. 1, 2, 4, 17).
7. Tu, Y. *et al.* Mimicking the Cell: Bio-inspired functions of supramolecular assemblies. *Chemical Reviews* **116,** 2023–2078 (4 2016) (cit. on pp. 1, 17, 26–28, 93, 111).
8. Chen, H. & Stoddart, J. F. From molecular to supramolecular electronics. *Nature Reviews Materials* **6,** 804–828 (9 2021) (cit. on p. 1).
9. Selinger, A. J. & Hof, F. Adaptive Supramolecular Networks: Emergent Sensing from Complex Systems. *Angewandte Chemie - International Edition* **62,** 1–5 (2023) (cit. on pp. 1, 2, 24, 62).
10. Krämer, J. *et al.* Molecular Probes, Chemosensors, and Nanosensors for Optical Detection of Biorelevant Molecules and Ions in Aqueous Media and Biofluids. *Chemical Reviews* **122,** 3459–3636 (2022) (cit. on pp. 1, 20, 21, 114).
11. Zhang, Y. *et al.* Design Principles of Nanosensors for Multiplex Detection of Contaminants in Food. *Small* **21** (26 2025) (cit. on p. 1).

12. Tenchov, R., Bird, R., Curtze, A. E. & Zhou, Q. Lipid Nanoparticles – From Liposomes to mRNA Vaccine Delivery, a Landscape of Research Diversity and Advancement. *ACS Nano* **15,** 16982–17015 (11 2021) (cit. on p. 1).

13. Milane, L. & Amiji, M. Clinical approval of nanotechnology-based SARS-CoV-2 mRNA vaccines: impact on translational nanomedicine. *Drug Delivery and Translational Research* **11,** 1309–1315 (4 2021) (cit. on pp. 1, 26, 93).

14. Tan, C. S., Barrio, J. D., Liu, J. & Scherman, O. A. Supramolecular polymer networks based on cucurbit[8]uril host-guest interactions as aqueous photo-rheological fluids. *Polymer Chemistry* **6,** 7652–7657 (44 2015) (cit. on pp. 1, 18, 20, 75).

15. Bastings, M. M. *et al.* A fast pH-switchable and self-healing supramolecular hydrogel carrier for guided, local catheter injection in the infarcted myocardium. *Advanced Healthcare Materials* **3,** 70–78 (1 2014) (cit. on p. 1).

16. Aebersold, R. *et al.* How many human proteoforms are there? *Nature Chemical Biology* **14,** 206–214 (3 2018) (cit. on p. 2).

17. Dun, S. V., Ottmann, C., Milroy, L. G. & Brunsveld, L. Supramolecular Chemistry Targeting Proteins. *Journal of the American Chemical Society* **139,** 13960–13968 (40 2017) (cit. on p. 2).

18. Chen, J. *et al.* Sensing Base Modifications in Non-Canonically Folded DNA with an Optimized Host: Guest Sensing Array. *ACS Sensors* **7,** 2164–2169 (8 2022) (cit. on pp. 2, 12).

19. Zhong, C. *et al.* Cucurbit[n]uril-Immobilized Sensor Arrays for Indicator-Displacement Assays of Small Bioactive Metabolites. *ACS Applied Nano Materials* **4,** 4676–4687 (5 2021) (cit. on pp. 2, 22, 48).

20. Hu, X.-Y. *et al.* A heteromultivalent host–guest sensor array for cell recognition and discrimination. *Chemical Communications* **58,** 13198–13201 (95 2022) (cit. on p. 2).

21. Atkins, P. & Paula, J. D. in *Physical Chemistry* 8th ed., 620–651 (Oxford University Press, 2006) (cit. on p. 3).

22. König, B. Molecular Recognition. The principle and recent chemical examples. *Journal für Praktische Chemie/Chemiker-Zeitung* **337,** 339–346 (1 1995) (cit. on pp. 3, 4).

23. Atkins, P. & Paula, J. D. in *Physical Chemistry* 8th ed., 362–403 (Oxford University Press, 2006) (cit. on p. 3).

24. Fischer, E. Einfluss der Configuration auf die Wirkung der Enzyme. *Berichte der deutschen chemischen Gesellschaft* **27,** 2985–2993 (1894) (cit. on p. 4).

25. Frieden, E. Non-covalent interactions: Key to biological flexibility and specificity. *Journal of Chemical Education* **52,** 754 (12 1975) (cit. on p. 4).

26. Cram, D. J. & Cram, J. M. Host-Guest Chemistry. *Science* **183,** 803–809 (4127 1974) (cit. on p. 4).

27. Beatty, M. A. & Hof, F. Host-guest binding in water, salty water, and biofluids: General lessons for synthetic, bio-targeted molecular recognition. *Chemical Society Reviews* **50,** 4812–4832 (8 2021) (cit. on pp. 4, 5, 48).

28. Kubik, S. When Molecules Meet in Water-Recent Contributions of Supramolecular Chemistry to the Understanding of Molecular Recognition Processes in Water. *ChemistryOpen* **11** (4 2022) (cit. on pp. 4, 13, 26).

29. Biedermann, F., Nau, W. M. & Schneider, H.-J. The Hydrophobic Effect Revisited-Studies with Supramolecular Complexes Imply High-Energy Water as a Noncovalent Driving Force. *Angewandte Chemie – International Edition* **53,** 11158–11171 (42 2014) (cit. on pp. 4, 13).

30. Pinalli, R., Pedrini, A. & Dalcanale, E. Biochemical sensing with macrocyclic receptors. *Chemical Society Reviews* **47,** 7006–7026 (18 2018) (cit. on pp. 4, 12).

31. Shetty, D., Khedkar, J. K., Park, K. M. & Kim, K. Can we beat the biotin–avidin pair?: cucurbit[7]uril-based ultrahigh affinity host–guest complexes and their applications. *Chemical Society Reviews* **44,** 8747–8761 (23 2015) (cit. on p. 4).

32. Martins, J. N., Lima, J. C. & Basílio, N. Selective Recognition of Amino Acids and Peptides by Small Supramolecular Receptors. *Molecules* **26,** 106 (1 2020) (cit. on pp. 4, 5, 16).

33. Chen, X. Y., Chen, H. & Fraser Stoddart, J. The Story of the Little Blue Box: A Tribute to Siegfried Hünig. *Angewandte Chemie – International Edition* **62** (1 2023) (cit. on pp. 5, 10, 37).

34. Odell, B. *et al.* Cyclobis(paraquat-p-phenylene). A Tetracationic Multipurpose Receptor. *Angewandte Chemie - International Edition* **27,** 1547–1550 (1988) (cit. on pp. 5, 10, 62).

35. Crowley, P. B. Protein-Calixarene Complexation: From Recognition to Assembly. *Accounts of Chemical Research* **55,** 2019–2032 (15 2022) (cit. on pp. 5, 6, 8, 35).

36. Shaurya, A. *et al.* An easily accessible, lower rim substituted calix[4]arene selectively binds: N, N -dimethyllysine. *Organic and Biomolecular Chemistry* **19,** 4691–4696 (21 2021) (cit. on pp. 5, 95).

37. Huang, C. *et al.* Cellular Uptake of Cell-Penetrating Peptides Activated by Amphiphilic p-Sulfonatocalix[4]arenes. *Chemistry – A European Journal* **30** (2024) (cit. on pp. 5, 29, 103).

38. Gutsche, C. D. & Muthukrishnan, R. Calixarenes. 1. Analysis of the product mixtures produced by the base-catalyzed condensation of formaldehyde with para-substituted phenols. *The Journal of Organic Chemistry* **43,** 4905–4906 (25 1978) (cit. on p. 5).

39. Shinkai, S., Mori, S., Koreishi, H., Tsubaki, T. & Manabe, O. Hexasulfonated calix[6]arene derivatives: a new class of catalysts, surfactants, and host molecules. *Journal of the American Chemical Society* **108,** 2409–2416 (9 1986) (cit. on pp. 5, 83, 85).

40. Gutsche, C. D. & Nam, K. C. Calixarenes. 22. Synthesis, properties, and metal complexation of aminocalixarenes. *Journal of the American Chemical Society* **110,** 6153–6162 (18 1988) (cit. on p. 5).

41. Gutsche, C. D. & Bauer, L. J. The Conformational Properties of Calix[4]arenes, Calix[6]arenes, Calix[8]arenes, and Oxacalixarenes. *Journal of the American Chemical Society* **107,** 6052–6059 (21 1985) (cit. on pp. 5, 6, 49).

42. Giuliani, M., Morbioli, I., Sansone, F. & Casnati, A. Moulding calixarenes for biomacromolecule targeting. *Chemical Communications* **51,** 14140–14159 (75 2015) (cit. on pp. 6, 49).

43. Shinkai, S., Araki, K., Kubota, M., Arimura, T. & Matsuda, T. Ion template effects on the conformation of water-soluble calixarenes. *The Journal of Organic Chemistry* **56,** 295–300 (1 1991) (cit. on p. 6).

44. Souchon, V., Leray, I. & Valeur, B. Selective detection of cesium by a water-soluble fluorescent molecular sensor based on a calix[4]arene-bis(crown-6-ether). *Chemical Communications,* 4224–4226 (40 2006) (cit. on pp. 6, 7).

45. Garcia-Rio, L., Basílio, N. & Francisco, V. Counterion effect on sulfonatocalix[n]arene recognition. *Pure and Applied Chemistry* **92,** 25–37 (1 2020) (cit. on pp. 6, 7).

46. Lehn, J. M. *et al.* Binding of acetylcholine and other quaternary ammonium cations by sulfonated calixarenes. Crystal structure of a [choline-tetrasulfonated calix[4]arene] complex. *Supramolecular Chemistry* **5,** 97–103 (2 1995) (cit. on pp. 6, 7).

47. Douteau-Guével, N., Coleman, A. W., Morel, J.-p. & Morel-Desrosiers, N. Complexation of basic amino acids by water-soluble calixarene sulphonates as a study of the possiblemechanisms of recognition of calixarene sulphonates by proteins. *Journal of Physical Organic Chemistry* **11,** 693–696 (10 1998) (cit. on pp. 6, 7, 41).

48. Pires, A. S., Muñoz, K. D., de Freitas, V., Basílio, N. & Cruz, L. Host-Guest Chemosensor Ensembles based on Water-Soluble Sulfonated Calix[n]arenes and a Pyranoflavylium Dye for the Optical Detection of Biogenic Amines. *Journal of Agricultural and Food Chemistry* **72,** 3719–3729 (7 2024) (cit. on pp. 6, 22, 48).

49. Bernardo, A. R. *et al.* Host–guest complexation at the electrode/solution interface: the inclusion of an amphiphilic viologen guest by an amphiphilic calix[6]arene host. *Chemical Communications,* 529–530 (4 1994) (cit. on p. 6).

50. Guo, D.-s., Wang, L.-h. & Liu, Y. Highly Effective Binding of Methyl Viologen Dication and Its Radical Cation by p -Sulfonatocalix[4,5]arenes. *The Journal of Organic Chemistry* **72,** 7775–7778 (20 2007) (cit. on p. 6).

51. Dsouza, R. N., Pischel, U. & Nau, W. M. Fluorescent dyes and their supramolecular host/guest complexes with macrocycles in aqueous solution. *Chemical Reviews* **111,** 7941–7980 (12 2011) (cit. on pp. 6, 21, 69).

52. Guthrie, J. P. Hydrolysis of esters of oxy acids: pKa values for strong acids; Brønsted relationship for attack of water at methyl; free energies of hydrolysis of esters of oxy acids; and a linear relationship between free energy of hydrolysis and pK a holding over a range of 20pK units. *Canadian Journal of Chemistry* **56,** 2342–2354 (17 1978) (cit. on p. 6).

53. Hermans, J., Leach, S. J. & Scheraga, H. A. Thermodynamic Data from Difference Spectra. 1,2 II. Hydrogen Bonding in Salicylic Acid and its Implications for Proteins. *Journal of the American Chemical Society* **85,** 1390–1395 (10 1963) (cit. on p. 6).

54. Morel, J. P. & Morel-Desrosiers, N. Binding of monovalent metal cations by the p-sulfonatocalix[4]arene: Experimental evidence for cation-π interactions in water. *Organic and Biomolecular Chemistry* **4,** 462–465 (3 2006) (cit. on p. 6).

55. Beshara, C. S., Jones, C. E., Daze, K. D., Lilgert, B. J. & Hof, F. A simple calixarene recognizes post-translationally methylated lysine. *ChemBioChem* **11,** 63–66 (1 2010) (cit. on pp. 7, 41).

56. Douteau-Guével, N., Coleman, A. W., Morel, J.-P. & Morel-Desrosiers, N. Complexation of the basic amino acids lysine and arginine by three sulfonatocalix[n]arenes (n = 4, 6 and 8) in water: microcalorimetric determination of the Gibbs energies, enthalpies and entropies of complexation. *Journal of the Chemical Society, Perkin Transactions 2,* 629–634 (3 1999) (cit. on pp. 7, 41).

57. Hof, F. Host-guest chemistry that directly targets lysine methylation: Synthetic host molecules as alternatives to bio-reagents. *Chemical Communications* **52,** 10093–10108 (66 2016) (cit. on p. 7).

58. Warmerdam, Z. *et al.* Binding Methylarginines and Methyllysines as Free Amino Acids: A Comparative Study of Multiple Host Classes. *ChemBioChem* **23,** e202100502 (2 2022) (cit. on p. 7).

59. Douteau-Guével, N., Perret, F., Coleman, A. W., Morela, J. P. & Morel-Desrosiers, N. Binding of dipeptides and tripeptides containing lysine or arginine by p-sulfonatocalixarenes in water: NMR and microcalorimetric studies. *Journal of the Chemical Society, Perkin Transactions 2,* 524–532 (3 2002) (cit. on pp. 7, 41).

60. Ghale, G. *et al.* Chemosensing ensembles for monitoring biomembrane transport in real time. *Angewandte Chemie - International Edition* **53,** 2762–2765 (10 2014) (cit. on pp. 7, 26, 31, 37, 41).

61. Perret, F. *et al.* Anionic fullerenes, calixarenes, coronenes, and pyrenes as activators of oligo/polyarginines in model membranes and live cells. *Journal of the American Chemical Society* **127,** 1114–1115 (4 2005) (cit. on pp. 7, 41, 94, 95, 99, 101).

62. McGovern, R. E., McCarthy, A. A. & Crowley, P. B. Protein assembly mediated by sulfonatocalix[4]arene. *Chemical Communications* **50,** 10412–10415 (72 2014) (cit. on p. 8).

63. Mallon, M., Dutt, S., Schrader, T. & Crowley, P. B. Protein Camouflage: Supramolecular Anion Recognition by Ubiquitin. *ChemBioChem* **17,** 774–783 (8 2016) (cit. on p. 8).

64. Kolusheva, S., Zadmard, R., Schrader, T. & Jelinek, R. Color fingerprinting of proteins by calixarenes embedded in lipid/polydiacetylene vesicles. *Journal of the American Chemical Society* **128,** 13592–13598 (41 2006) (cit. on p. 8).

65. Alex, J. M. *et al.* Phosphonated Calixarene as a "molecular Glue" for Protein Crystallization. *Crystal Growth and Design* **18,** 2467–2473 (4 2018) (cit. on p. 8).

66. Zheng, Z. *et al.* Guanidinocalix[5]arene for sensitive fluorescence detection and magnetic removal of perfluorinated pollutants. *Nature Communications* **10** (1 2019) (cit. on p. 9).

67. Wang, H. Y. *et al.* Non-invasive and Sensitive Fluorescence Detection of Phenylpyruvic Acid via a Guanidinomethyl-modified Calixarene. *Analysis and Sensing* **4** (2 2024) (cit. on p. 9).

68. Zheng, Z. *et al.* Ultrasensitive and specific fluorescence detection of a cancer biomarker: Via nanomolar binding to a guanidinium-modified calixarene. *Chemical Science* **9,** 2087–2091 (8 2018) (cit. on p. 9).

69. Sansone, F. *et al.* DNA condensation and cell transfection properties of guanidinium calixarenes: Dependence on macrocycle lipophilicity, size, and conformation. *Journal of the American Chemical Society* **128,** 14528–14536 (45 2006) (cit. on p. 9).

70. Bagnacani, V. *et al.* Arginine clustering on calix[4]arene macrocycles for improved cell penetration and DNA delivery. *Nature Communications* **4** (2013) (cit. on p. 9).

71. Rispoli, F. *et al.* Clustering Zwitterionic Amino Acids at the Upper Rim of Cone Calix[4]arene Triggers the Selective Recognition of Gram-Negative Bacterial Envelope. *Small Structures* **6** (6 2025) (cit. on p. 9).

72. Geng, W. C. *et al.* A Noncovalent Fluorescence Turn-on Strategy for Hypoxia Imaging. *Angewandte Chemie - International Edition* **58,** 2377–2381 (8 2019) (cit. on pp. 9, 19).

73. Karci, F., Şener, I. & Deligöz, H. Azocalixarenes. 1: Synthesis, characterization and investigation of the absorption spectra of substituted azocalix[4]arenes. *Dyes and Pigments* **59,** 53–61 (1 2003) (cit. on p. 10).

74. Yue, Y. X. *et al.* Azocalixarenes: a scaffold of universal excipients with high efficiency. *Science China Chemistry* **67,** 1697–1706 (5 2024) (cit. on p. 10).

75. Hou, X. *et al.* Single-Molecule Macrocyclic Carrier Overcomes the Direct Transmembrane of Medium-Sized Cargoes. *Journal of the American Chemical Society* **147,** 20919–20929 (24 2025) (cit. on pp. 10, 18, 19, 103).

76. Goodnow, T. T., Reddington, M. V., Stoddart, J. F. & Kaifer, A. E. Cyclobis(paraquat-p-phenylene): A Novel Synthetic Receptor for Amino Acids with Electron-Rich Aromatic Moieties. *Journal of the American Chemical Society* **113,** 4335–4337 (1991) (cit. on pp. 10, 37, 38, 40, 62).

77. Bernardo, A. R., Stoddart, J. F. & Kaifer, A. E. Cyclobis(paraquat-p-phenylene) as a Synthetic Receptor for Electron-Rich Aromatic Compounds: Electrochemical and Spectroscopic Studies of Neurotransmitter Binding. *Journal of the American Chemical Society* **114,** 10624–10631 (1992) (cit. on pp. 10, 37).

78. Bria, M. *et al.* An investigation of the complexation properties of cyclobis(paraquat-p-phenylene) in water. *Tetrahedron Letters* **48,** 301–304 (2007) (cit. on pp. 10, 56).

79. Trabolsi, A. *et al.* Radically enhanced molecular recognition. *Nature Chemistry* **2,** 42–49 (1 2010) (cit. on p. 10).

80. Ogoshi, T., Kanai, S., Fujinami, S., Yamagishi, T.-a. & Nakamoto, Y. para -Bridged Symmetrical Pillar[5]arenes: Their Lewis Acid Catalyzed Synthesis and Host–Guest Property. *Journal of the American Chemical Society* **130,** 5022–5023 (15 2008) (cit. on p. 10).

81. Ogoshi, T., Hashizume, M., Yamagishi, T. A. & Nakamoto, Y. Synthesis, conformational and host-guest properties of water-soluble pillar[5]arene. *Chemical Communications* **46,** 3708–3710 (21 2010) (cit. on p. 10).

82. Moran, J. R., Karbach, S. & Cram, D. J. Cavitands: Synthetic Molecular Vessels. *Journal of the American Chemical Society* **104,** 5826–5828 (7 1982) (cit. on p. 12).

83. Hof, F., Trembleau, L., Ullrich, E. C. & Rebek, J. Acetylcholine recognition by a deep, biomimetic pocket. *Angewandte Chemie - International Edition* **42,** 3150–3153 (27 2003) (cit. on p. 12).

84. Hooley, R. J., Biros, S. M. & Rebek, J. Normal hydrocarbons tumble rapidly in a deep, water-soluble cavitand. *Chemical Communications,* 509–510 (5 2006) (cit. on p. 12).

85. Hua, B., Shao, L., Zhang, Z., Sun, J. & Yang, J. Pillar[6]arene/acridine orange host–guest complexes as colorimetric and fluorescence sensors for choline compounds and further application in monitoring enzymatic reactions. *Sensors and Actuators B: Chemical* **255,** 1430–1435 (2018) (cit. on p. 12).

86. Li, C. *et al.* Molecular selective binding of basic amino acids by a water-soluble pillar[5]arene. *Chemical Communications* **49,** 1924–1926. ISSN: 13597345 (19 2013) (cit. on p. 12).

87. Shu, X., Xu, K., Hou, D. & Li, C. Molecular Recognition of Water-soluble Pillar[n]arenes Towards Biomolecules and Drugs. *Israel Journal of Chemistry* **58,** 1194–1204 (11 2018) (cit. on p. 12).

88. Pinalli, R., Suman, M. & Dalcanale, E. Cavitands at Work: From Molecular Recognition to Supramolecular Sensors. *European Journal of Organic Chemistry,* 451–462 (3 2004) (cit. on p. 12).

89. Liu, Y. *et al.* Protein recognition by a self-assembled deep cavitand monolayer on a gold substrate. *Langmuir* **28,** 1391–1398 (2 2012) (cit. on p. 12).

90. Lian, R. *et al.* Self-Aggregative Recognition and Extraction of Perfluorooctanesulfonate with Flexible Cationic Water-Soluble Deep Cavitands. *Journal of the American Chemical Society* (2025) (cit. on pp. 12, 24).

91. Liu, Y. *et al.* Site-Selective Sensing of Histone Methylation Enzyme Activity via an Arrayed Supramolecular Tandem Assay. *Journal of the American Chemical Society* **139,** 10964–10967 (32 2017) (cit. on pp. 12, 24).

92. Pinalli, R. *et al.* The Origin of Selectivity in the Complexation of N-Methyl Amino Acids by Tetraphosphonate Cavitands. *Journal of the American Chemical Society* **138,** 8569–8580 (27 2016) (cit. on p. 12).

93. Gill, A. D. *et al.* Sensing of citrulline modifications in histone peptides by deep cavitand hosts. *Chemical Communications* **55,** 13259–13262 (88 2019) (cit. on p. 12).

94. Chen, J. *et al.* Supramolecular Host:Guest Arrays Site-Selectively Recognize Peptide Phosphorylation and Kinase Activity. *Journal of the American Chemical Society* **147,** 841–850 (1 2025) (cit. on p. 12).

95. Behrend, R., Meyer, E. & Rusche, F. I. Ueber Condensationsproducte aus Glycoluril und Formaldehyd. *Justus Liebigs Annalen der Chemie* **339,** 1–37 (1 1905) (cit. on p. 13).

96. Freeman, W. A., Mock, W. L. & Shih, N. Y. Cucurbituril. *Journal of the American Chemical Society* **103,** 7367–7368 (24 1981) (cit. on p. 13).

97. Rekharsky, M. V. *et al.* A synthetic host-guest system achieves avidin-biotin affinity by overcoming enthalpy–entropy compensation. *Proceedings of the National Academy of Sciences* **104,** 20737–20742 (52 2007) (cit. on p. 13).

98. Moghaddam, S. *et al.* New ultrahigh affinity host-guest complexes of cucurbit[7]uril with bicyclo[2.2.2]octane and adamantane guests: Thermodynamic analysis and evaluation of M2 affinity calculations. *Journal of the American Chemical Society* **133,** 3570–3581 (10 2011) (cit. on p. 13).

99. Sinn, S., Spuling, E., Bräse, S. & Biedermann, F. Rational design and implementation of a cucurbit[8]uril-based indicator-displacement assay for application in blood serum. *Chemical Science* **10,** 6584–6593 (27 2019) (cit. on pp. 13, 22, 48).

100. Montes-Navajas, P. & Garcia, H. Complexes of basic tricyclic dyes in their acid and basic forms with cucurbit[7]uril: Determination of pKa and association constants in the ground and singlet excited state. *Journal of Photochemistry and Photobiology A: Chemistry* **204,** 97–101 (2-3 2009) (cit. on p. 13).

101. Hirani, Z. *et al.* Molecular Recognition of Methionine-Terminated Peptides by Cucurbit[8]uril. *Journal of the American Chemical Society* **140,** 12263–12269 (38 2018) (cit. on p. 14).

102. Rekharsky, M. V., Ko, Y. H., Selvapalam, N., Kim, K. & Inoue, Y. Complexation Thermodynamics of Cucurbit[6]uril with Aliphatic Alcohols, Amines, and Diamines. *Supramolecular Chemistry* **19,** 39–46 (1-2 2007) (cit. on p. 14).

103. Das, D., Assaf, K. I. & Nau, W. M. Applications of Cucurbiturils in Medicinal Chemistry and Chemical Biology. *Frontiers in Chemistry* **7,** 1–23 (2019) (cit. on pp. 14, 62).

104. Ganapati, S. *et al.* Molecular Containers Bind Drugs of Abuse in Vitro and Reverse the Hyperlocomotive Effect of Methamphetamine in Rats. *ChemBioChem* **18,** 1583–1588 (16 2017) (cit. on p. 14).

105. Lazar, A. I. *et al.* Nanomolar Binding of Steroids to Cucurbit[n]urils: Selectivity and Applications. *Journal of the American Chemical Society* **138,** 13022–13029 (39 2016) (cit. on pp. 14, 62).

106. Zhang, S. *et al.* Binding affinities of cucurbit[n]urils with cations. *Chemical Communications* **55,** 14131–14134 (94 2019) (cit. on p. 14).

107. Uzunova, V. D., Cullinane, C., Brix, K., Nau, W. M. & Day, A. I. Toxicity of cucurbit[7]uril and cucurbit[8]uril: An exploratory in vitro and in vivo study. *Organic and Biomolecular Chemistry* **8,** 2037–2042 (9 2010) (cit. on p. 14).

108. Isobe, H., Sato, S. & Nakamura, E. Synthesis of Disubstituted Cucurbit[6]uril and Its Rotaxane Derivative. *Organic Letters* **4,** 1287–1289 (8 2002) (cit. on p. 15).

109. Jon, S. Y. *et al.* Facile synthesis of cucurbit[n]uril derivatives via direct functionalization: Expanding utilization of cucurbit[n]uril. *Journal of the American Chemical Society* **125,** 10186–10187 (34 2003) (cit. on pp. 15, 69).

110. Isaacs, L. *et al.* The inverted cucurbit[n]uril family. *Journal of the American Chemical Society* **127,** 18000–18001 (51 2005) (cit. on p. 15).

111. Lagona, J., Fettinger, J. C. & Isaacs, L. Cucurbit[n]uril analogues: Synthetic and mechanistic studies. *Journal of Organic Chemistry* **70,** 10381–10392 (25 2005) (cit. on p. 15).

112. Cao, L. & Isaacs, L. Daisy Chain Assembly Formed from a Cucurbit[6]uril Derivative. *Organic Letters* **14,** 3072–3075 (12 2012) (cit. on p. 15).

113. Vinciguerra, B., Zavalij, P. Y. & Isaacs, L. Synthesis and Recognition Properties of Cucurbit[8]uril Derivatives. *Organic Letters* **17,** 5068–5071 (20 2015) (cit. on p. 15).

114. Bockus, A. T. *et al.* Cucurbit[7]uril-Tetramethylrhodamine Conjugate for Direct Sensing and Cellular Imaging. *Journal of the American Chemical Society* **138,** 16549–16552 (50 2016) (cit. on pp. 15, 22).

115. Takisawa, N., Shirahama, K. & Tanaka, I. Interactions of amphiphilic drugs with alpha-, beta-, and gamma-cyclodextrins. *Colloid & Polymer Science* **271,** 499–506 (5 1993) (cit. on pp. 15, 16).

116. Ma, D. *et al.* Acyclic cucurbit[n]uril-type molecular containers bind neuromuscular blocking agents in vitro and reverse neuromuscular block in vivo. *Angewandte Chemie - International Edition* **51,** 11358–11362 (45 2012) (cit. on pp. 15–17).

117. Schrader, T., Bitan, G. & Klärner, F. G. Molecular tweezers for lysine and arginine-powerful inhibitors of pathologic protein aggregation. *Chemical Communications* **52,** 11318–11334 (76 2016) (cit. on pp. 15–17).

118. Buschmann, H. J., Schollmeyer, E. & Mutihac, L. The formation of amino acid and dipeptide complexes with α-cyclodextrin and cucurbit[6]uril in aqueous solutions studied by titration calorimetry. *Thermochimica Acta* **399,** 203–208 (1-2 2003) (cit. on p. 16).

119. Bekos, E. J., Gardella, J. A. & Bright, F. V. The binding of free oligopeptides to cyclodextrins: The role of the tyrosine group. *Journal of Inclusion Phenomena and Molecular Recognition in Chemistry* **26,** 185–195 (4 1996) (cit. on p. 16).

120. Cameron, K. S. *et al.* Modified γ-cyclodextrins and their rocuronium complexes. *Organic Letters* **4,** 3403–3406 (20 2002) (cit. on p. 16).

121. Loftsson, T., Brewster, M. E. & Másson, M. Role of cyclodextrins in improving oral drug delivery. *American Journal of Drug Delivery* **2,** 261–275 (4 2004) (cit. on p. 16).

122. Yin, H., Bardelang, D. & Wang, R. Macrocycles and Related Hosts as Supramolecular Antidotes. *Trends in Chemistry* **3,** 1–4 (1 2021) (cit. on p. 16).

123. Iizuka, K., Takezawa, H. & Fujita, M. Template and Solid-State-Assisted Assembly of an M9L6 Expanded Coordination Cage for Medium-Sized Molecule Encapsulation. *Journal of the American Chemical Society* **146,** 32311–32316 (47 2024) (cit. on p. 16).

124. Fujita, M., Tominaga, M., Hori, A. & Therrien, B. Coordination Assemblies from a Pd(II)-Cornered Square Complex. *Accounts of Chemical Research* **38,** 369–378 (4 2005) (cit. on p. 16).

125. Tashiro, S. *et al.* Sequence-Selective Recognition of Peptides within the Single Binding Pocket of a Self-Assembled Coordination Cage. *Journal of the American Chemical Society* **127,** 4546–4547 (13 2005) (cit. on p. 16).

126. Takezawa, H., Murase, T., Resnati, G., Metrangolo, P. & Fujita, M. Recognition of polyfluorinated compounds through self-aggregation in a cavity. *Journal of the American Chemical Society* **136,** 1786–1788 (5 2014) (cit. on p. 16).

127. Ndendjio, S. A. Z. & Isaacs, L. Molecular recognition properties of acyclic cucurbiturils toward amino acids, peptides, and a protein. *Supramolecular Chemistry* **31,** 432–441 (7 2019) (cit. on p. 17).

128. Meiners, A. *et al.* Specific inhibition of the Survivin–CRM1 interaction by peptide-modified molecular tweezers. *Nature Communications* **12** (1 2021) (cit. on p. 17).

129. Lehn, J.-M. Toward Self-Organization and Complex Matter. *Science* **295,** 2400–2403 (5564 2002) (cit. on p. 17).

130. Karsenti, E. Self-organization in cell biology: a brief history. *Nature Reviews Molecular Cell Biology* **9,** 255–262 (3 2008) (cit. on p. 17).

131. Wang, K., Guo, D. S., Wang, X. & Liu, Y. Multistimuli responsive supramolecular vesicles based on the recognition of p-sulfonatocalixarene and its controllable release of doxorubicin. *ACS Nano* **5,** 2880–2894 (4 2011) (cit. on pp. 18, 20).

132. Jiang, R. *et al.* Vesicle-Encapsulated Chemosensing Ensembles Allow Monitoring of Transmembrane Uptake Coupled with Enzymatic Reactions. *Angewandte Chemie - International Edition* **64** (13 2025) (cit. on pp. 18, 31, 32, 111).

133. Tootoonchi, M. H., Sharma, G., Calles, J., Prabhakar, R. & Kaifer, A. E. Cooperative Self-Assembly of a Quaternary Complex Formed by Two Cucurbit[7]uril Hosts, Cyclobis(paraquat-p-phenylene), and a “Designer” Guest. *Angewandte Chemie - International Edition* **55,** 11507–11511 (2016) (cit. on pp. 18, 55).

134. Shen, J., Ren, C. & Zeng, H. Membrane-Active Molecular Machines. *Accounts of Chemical Research* **55,** 1148–1159 (8 2022) (cit. on pp. 18, 94).

135. Cui, Y. H. *et al.* Pillar[5]arene pseudo[1]rotaxane-based redox-responsive supramolecular vesicles for controlled drug release. *Materials Chemistry Frontiers* **3,** 1427–1432 (7 2019) (cit. on p. 18).

136. Baroncini, M., Silvi, S. & Credi, A. Photo- And Redox-Driven Artificial Molecular Motors. *Chemical Reviews* **120,** 200–268 (1 2020) (cit. on pp. 18, 20, 94).

137. Basílio, N. & Pischel, U. Drug Delivery by Controlling a Supramolecular Host-Guest Assembly with a Reversible Photoswitch. *Chemistry - A European Journal* **22,** 15208–15211 (43 2016) (cit. on pp. 18, 19).

138. Ferreira, P. *et al.* A Visible–Near-Infrared Light-Responsive Host–Guest Pair with Nanomolar Affinity in Water. *Chemistry - A European Journal* **25,** 3477–3482 (14 2019) (cit. on pp. 18, 19).

139. Máximo, P. *et al.* Photomodulation of ultrastable host-guest complexes in water and their application in light-controlled steroid release. *Organic Chemistry Frontiers* **9,** 4238–4249 (16 2022) (cit. on pp. 18, 19).

140. Pan, Y. C., Hu, X. Y. & Guo, D. S. Biomedical Applications of Calixarenes: State of the Art and Perspectives. *Angewandte Chemie - International Edition* **60,** 2768–2794 (6 2021) (cit. on pp. 18, 20).

141. Koumura, N., Zijlstra, R. W. J., van Delden, R. A., Harada, N. & Feringa, B. L. Light-driven monodirectional molecular rotor. *Nature* **401,** 152–155 (6749 1999) (cit. on pp. 18, 20).

142. Zhang, Z. *et al.* Macrocyclic-Amphiphile-Based Self-Assembled Nanoparticles for Ratiometric Delivery of Therapeutic Combinations to Tumors. *Advanced Materials* **33** (12 2021) (cit. on p. 18).

143. Langton, M. J. Engineering of stimuli-responsive lipid-bilayer membranes using supramolecular systems. *Nature Reviews Chemistry* **5,** 46–61 (1 2021) (cit. on pp. 18, 94).

144. Peng, S., Wang, K., Guo, D. S. & Liu, Y. Supramolecular polymeric vesicles formed by p-sulfonatocalix[4]arene and chitosan with multistimuli responses. *Soft Matter* **11,** 290–296 (2 2015) (cit. on p. 20).

145. Cooper, G. M. in *The Cell: A Molecular Approach* 2nd ed., 421–466 (Sinauer Associates, 2000) (cit. on p. 20).

146. Johnson, T. G. & Langton, M. J. Molecular Machines For The Control Of Transmembrane Transport. *Journal of the American Chemical Society* **145,** 27167–27184 (50 2023) (cit. on pp. 20, 29, 30, 103).

147. Brunsveld, L., Folmer, B. J., Meijer, E. W. & Sijbesma, R. P. Supramolecular polymers. *Chemical Reviews* **101,** 4071–4097 (12 2001) (cit. on pp. 20, 75).

148. Appel, E. A. *et al.* Supramolecular cross-linked networks via host-guest complexation with cucurbit[8]uril. *Journal of the American Chemical Society* **132,** 14251–14260 (40 2010) (cit. on pp. 20, 75).

149. Wiskur, S. L., Ait-Haddou, H., Lavigne, J. J. & Anslyn, E. V. Teaching Old Indicators New Tricks. *Accounts of Chemical Research* **34,** 963–972 (12 2001) (cit. on pp. 21, 22, 48).

150. Silva, A. P. D., Moody, T. S. & Wright, G. D. Fluorescent PET (Photoinduced Electron Transfer) sensors as potent analytical tools. *Analyst* **134,** 2385–2393 (12 2009) (cit. on p. 21).

151. Daly, B., Ling, J. & Silva, A. P. D. Current developments in fluorescent PET (photoinduced electron transfer) sensors and switches. *Chemical Society Reviews* **44,** 4203–4211 (13 2015) (cit. on p. 21).

152. Sedgwick, A. C. *et al.* Indicator displacement assays (IDAs): The past, present and future. *Chemical Society Reviews* **50,** 9–38 (1 2021) (cit. on pp. 21, 22, 48).

153. Li, M. *et al.* Cucurbit[7]uril-conjugated dyes as live cell imaging probes: Investigation on their cellular uptake and excretion pathways. *Organic and Biomolecular Chemistry* **17,** 6215–6220 (25 2019) (cit. on p. 22).

154. Alnajjar, M. A. & Hennig, A. Fluorescence Turn-ON Displacement Assays with Cucurbit[7]uril–Thiophenylpyridinium Complexes as Host–Dye Reporter Pairs. *Organic Letters* **26,** 9126–9131 (42 2024) (cit. on pp. 22, 48).

155. Jia, T. *et al.* Azocalixarene-Based Supramolecular System for the Detection of Paraquat via an Improved Indicator Displacement Assay. *Journal of Agricultural and Food Chemistry* **70,** 15981–15989 (50 2022) (cit. on pp. 22, 48).

156. Guo, D. S., Uzunova, V. D., Su, X., Liu, Y. & Nau, W. M. Operational calixarene-based fluorescent sensing systems for choline and acetylcholine and their application to enzymatic reactions. *Chemical Science* **2,** 1722–1734 (9 2011) (cit. on pp. 22, 26, 31, 48, 96).

157. Chen, J. *et al.* Selective Molecular Recognition and Indicator Displacement Sensing of Neurotransmitters in Cellular Environments. *ACS Sensors* **8,** 3195–3204 (8 2023) (cit. on pp. 22, 26, 28, 29).

158. Liu, X., Smith, D. G. & Jolliffe, K. A. Are two better than one? Comparing intermolecular and intramolecular indicator displacement assays in pyrophosphate sensors. *Chemical Communications* **52,** 8463–8466 (54 2016) (cit. on p. 22).

159. Zwicker, V. E. *et al.* A Fluorogenic Probe for Cell Surface Phosphatidylserine Using an Intramolecular Indicator Displacement Sensing Mechanism. *Angewandte Chemie - International Edition* **58,** 3087–3091 (10 2019) (cit. on pp. 22, 23).

160. Zheng, Z., Geng, W. C., Gao, J., Mu, Y. J. & Guo, D. S. Differential calixarene receptors create patterns that discriminate glycosaminoglycans. *Organic Chemistry Frontiers* **5,** 2685–2691 (18 2018) (cit. on p. 23).

161. Maity, D. *et al.* A Selective Cucurbit[8]uril-Peptide Beacon Ensemble for the Ratiometric Fluorescence Detection of Peptides. *Chemistry – A European Journal* **25,** 13088–13093 (57 2019) (cit. on pp. 23, 48).

162. Zhang, S., Assaf, K. I., Huang, C., Hennig, A. & Nau, W. M. Ratiometric DNA sensing with a host–guest FRET pair. *Chemical Communications* **55,** 671–674 (5 2019) (cit. on pp. 23, 48).

163. Jia, T. *et al.* FRET-Based Host-Guest Supramolecular Probe for On-Site and Broad-Spectrum Detection of Pyrethroids in the Environment. *Journal of Agricultural and Food Chemistry* **72,** 3773–3782 (7 2024) (cit. on pp. 23, 48).

164. Tian, J.-H., Zheng, Z., Pan, Y.-C., Wang, Y. & Guo, D.-S. Macrocycle-based differential sensing: Design strategies and applications. *Responsive Materials* **3.** ISSN: 2834-8966 (1 2025) (cit. on pp. 23, 24, 48).

165. Selinger, A. & Hof, F. *Function from complexity: chemical systems that achieve sensing using host-type molecules and complex equilibria* 2025. `https://chemrxiv.org/engage/chemrxiv/article-details/688bd207728bf9025e60bd0b` (cit. on pp. 23, 24, 48).

166. Minaker, S. A., Daze, K. D., Ma, M. C. F. & Hof, F. Antibody-Free Reading of the Histone Code Using a Simple Chemical Sensor Array. *Journal of the American Chemical Society* **134,** 11674–11680 (28 2012) (cit. on p. 24).

167. Selinger, A. J. *et al.* Mixed host co-assembled systems for broad-scope analyte sensing. *Chemical Science* **15,** 12388–12397 (31 2024) (cit. on pp. 24, 25).

168. Chen, J. *et al.* Selective discrimination and classification of G-quadruplex structures with a host-guest sensing array. *Nature Chemistry* **13,** 488–495 (5 2021) (cit. on p. 24).

169. Chen, J. *et al.* Supramolecular Host:Guest Arrays Site-Selectively Recognize Peptide Phosphorylation and Kinase Activity. *Journal of the American Chemical Society* **147,** 841–850 (1 2025) (cit. on p. 24).

170. Tian, J. H. *et al.* A facile way to construct sensor array library via supramolecular chemistry for discriminating complex systems. *Nature Communications* **13,** 1–12 (1 2022) (cit. on pp. 24, 25).

171. Yeates, T. O. & Padilla, J. E. Designing supramolecular protein assemblies. *Current Opinion in Structural Biology* **12,** 464–470 (4 2002) (cit. on p. 26).

172. Alberts, B. *et al.* in *Molecular Biology of the Cell* (ed Science, G.) 4th ed. (2002) (cit. on pp. 26, 28, 93).

173. Huang, H. *et al.* The investigation of mRNA vaccines formulated in liposomes administrated in multiple routes against SARS-CoV-2. *Journal of Controlled Release* **335,** 449–456 (2021) (cit. on pp. 26, 93).

174. Schwendener, R. A. Liposomes as vaccine delivery systems: A review of the recent advances. *Therapeutic Advances in Vaccines* **2,** 159–182 (6 2014) (cit. on pp. 26, 93).

175. Mattia, E. & Otto, S. Supramolecular systems chemistry. *Nature Nanotechnology* **10,** 111–119 (2 2015) (cit. on pp. 26–28).

176. Chen, H., Huang, Z., Wu, H., Xu, J. F. & Zhang, X. Supramolecular Polymerization Controlled through Kinetic Trapping. *Angewandte Chemie - International Edition* **56,** 16575–16578 (52 2017) (cit. on pp. 26, 70).

177. Liu, B. *et al.* Out-of-Equilibrium Self-Replication Allows Selection for Dynamic Kinetic Stability in a System of Competing Replicators. *Angewandte Chemie - International Edition* **61** (18 2022) (cit. on p. 26).

178. Pei, D. & Buyanova, M. Overcoming Endosomal Entrapment in Drug Delivery. *Bioconjugate Chemistry* **30,** 273–283 (2019) (cit. on p. 28).

179. Nishihara, M. *et al.* Arginine magic with new counterions up the sleeve. *Organic & Biomolecular Chemistry* **3,** 1659 (9 2005) (cit. on pp. 29, 94, 95, 99, 101).

180. Peng, S. *et al.* Phosphorylation-Responsive Membrane Transport of Peptides. *Angewandte Chemie - International Edition* **56,** 15742–15745 (2017) (cit. on pp. 29, 94, 95, 100).

181. Zhang, D. Y. *et al.* Structurally screening calixarenes as peptide transport activators. *Chemical Communications* **57,** 12627–12630 (94 2021) (cit. on pp. 29, 94, 100).

182. Pan, Y.-C. *et al.* An Amphiphilic Sulfonatocalix[5]arene as an Activator for Membrane Transport of Lysine-rich Peptides and Proteins. *Angewandte Chemie - International Edition* **60,** 1875–1882 (2021) (cit. on pp. 29, 94).

183. Jog, P. V. & Gin, M. S. A light-gated synthetic ion channel. *Organic Letters* **10,** 3693–3696 (17 2008) (cit. on pp. 29, 30).

184. Choi, Y. R. *et al.* Azobenzene-based chloride transporters with light-controllable activities. *Chemical Communications* **50,** 15305–15308 (97 2014) (cit. on pp. 29, 30, 94).

185. Johnson, T. G., Sadeghi-Kelishadi, A. & Langton, M. J. A Photo-responsive Transmembrane Anion Transporter Relay. *Journal of the American Chemical Society* **144,** 10455–10461 (23 2022) (cit. on pp. 29–31, 94).

186. Ghosh, S. & Isaacs, L. Biological catalysis regulated by cucurbit[7]uril molecular containers. *Journal of the American Chemical Society* **132,** 4445–4454 (12 2010) (cit. on p. 32).

187. Salvio, R. *et al.* Upper Rim Bifunctional cone-Calix[4]arenes Based on a Ligated Metal Ion and a Guanidinium Unit as DNAase and RNAase Mimics. *Journal of Organic Chemistry* **81,** 4728–4735 (11 2016) (cit. on pp. 32, 33, 111).

188. Basílio, N., Pessêgo, M., Acuña, A. & García-Río, L. Sulfonatocalixarene Counterion Exchange Binding Model in Action: Metal-Ion Catalysis Through Host-Guest Complexation. *ChemCatChem* **11,** 5397–5404 (21 2019) (cit. on pp. 32, 33).

189. Chernikova, E. Y., Berdnikova, D. V., Peregudov, A. S., Fedorova, O. A. & Fedorov, Y. V. Encapsulation-Controlled Photoisomerization of a Styryl Derivative: Stereoselective Formation of the Anti Z-Isomer in the Cucurbit[7]uril Cavity. *ChemPhysChem* **21,** 442–449 (5 2020) (cit. on pp. 32, 33).

190. Tehrani, F. N. *et al.* Supramolecular Catalysis of a Catalysis-Resistant Diels-Alder Reaction: Almost Theoretical Acceleration of Cyclopentadiene Dimerization inside Cucurbit[7]uril. *ACS Catalysis* **12,** 2261–2269 (4 2022) (cit. on pp. 32, 33).

191. Colaço, M. *et al.* Diazocines as Guests of Cucurbituril Macrocycles: Light-Responsive Binding and Supramolecular Catalysis of Thermal Isomerization. *Journal of the American Chemical Society* **147,** 734–745 (1 2025) (cit. on pp. 32–34).

192. Isom, D. G., Castañeda, C. A., Cannon, B. R. & E., B. G.-M. Large shifts in pKa values of lysine residues buried inside a protein. *Proceedings of the National Academy of Sciences* **108,** 5260–5265 (13 2011) (cit. on p. 32).

193. Bakirci, H., Koner, A. L., Schwarzlose, T. & Nau, W. M. Analysis of host-assisted guest protonation exemplified for p-sulfonatocalix[4]arene-towards enzyme-mimetic pKa shifts. *Chemistry - A European Journal* **12,** 4799–4807 (18 2006) (cit. on pp. 32, 111).

194. Ghosh, I. & Nau, W. M. The strategic use of supramolecular pKa shifts to enhance the bioavailability of drugs. *Advanced Drug Delivery Reviews* **64,** 764–783 (9 2012) (cit. on p. 32).

195. Casnati, A. & Salvio, R. An equal terms comparison of the proficiency of artificial phosphodiesterases by using simple models of RNA or DNA as benchmarks–the takeaway to design next generation supramolecular catalysts. *Coordination Chemistry Reviews* **531** (2025) (cit. on p. 33).

196. Assaf, K. I. & Nau, W. M. Cucurbiturils: from synthesis to high-affinity binding and catalysis. *Chemical Society Reviews* **44,** 394–418 (2 2015) (cit. on pp. 33, 34).

197. Mock, W. L., Irra, T. A., Wepsiec, J. P. & Manimaran, T. L. Cycloaddition induced by cucurbituril. A case of Pauling principle catalysis. *The Journal of Organic Chemistry* **48,** 3619–3620 (20 1983) (cit. on p. 33).

198. Carlqvist, P. & Maseras, F. A theoretical analysis of a classic example of supramolecular catalysis. *Chemical Communications,* 748–750 (7 2007) (cit. on p. 33).

199. Finbloom, J. A., Han, K., Slack, C. C., Furst, A. L. & Francis, M. B. Cucurbit[6]uril-Promoted Click Chemistry for Protein Modification. *Journal of the American Chemical Society* **139,** 9691–9697 (28 2017) (cit. on pp. 33, 34).

200. Uhlenheuer, D. A., Petkau, K. & Brunsveld, L. Combining supramolecular chemistry with biology. *Chemical Society Reviews* **39,** 2817–2826 (8 2010) (cit. on p. 35).

201. Bier, D. *et al.* The Molecular Tweezer CLR01 Stabilizes a Disordered Protein-Protein Interface. *Journal of the American Chemical Society* **139,** 16256–16263 (45 2017) (cit. on p. 35).

202. Guillory, X. *et al.* Supramolecular Enhancement of a Natural 14-3-3 Protein Ligand. *Journal of the American Chemical Society* **143,** 13495–13500 (34 2021) (cit. on p. 35).

203. Flood, R. J., Cerofolini, L., Fragai, M. & Crowley, P. B. Multivalent Calixarene Complexation of a Designed Pentameric Lectin. *Biomacromolecules* **25,** 1303–1309 (2 2024) (cit. on p. 35).

204. Ramberg, K. O., Engilberge, S., Skorek, T. & Crowley, P. B. Facile Fabrication of Protein-Macrocycle Frameworks. *Journal of the American Chemical Society* **143,** 1896–1907 (4 2021) (cit. on p. 35).

205. Mummidivarapu, V. V., Rennie, M. L., Doolan, A. M. & Crowley, P. B. Noncovalent PEGylation via Sulfonatocalix[4]arene-A Crystallographic Proof. *Bioconjugate Chemistry* **29,** 3999–4003 (12 2018) (cit. on p. 35).

206. Dang, D. T., Schill, J. & Brunsveld, L. Cucurbit[8]uril-mediated protein homotetramerization. *Chemical Science* **3,** 2679–2684 (9 2012) (cit. on p. 36).

207. Guagnini, F., Engilberge, S., Ramberg, K. O., Pérez, J. & Crowley, P. B. Engineered assembly of a protein-cucurbituril biohybrid. *Chemical Communications* **56,** 360–363 (3 2020) (cit. on p. 36).

208. Ramberg, K. O. *et al.* Segregated Protein-Cucurbit[7]uril Crystalline Architectures via Modulatory Peptide Tectons. *Chemistry - A European Journal* **27,** 14619–14627 (59 2021) (cit. on p. 36).

209. Biedermann, F. & Scherman, O. A. Cucurbit[8]uril mediated donor-acceptor ternary complexes: A model system for studying charge-transfer interactions. *Journal of Physical Chemistry B* **116,** 2842–2849 (2012) (cit. on p. 38).

210. Baharfar, M., Hillier, A. C. & Mao, G. Charge-Transfer Complexes: Fundamentals and Advances in Catalysis, Sensing, and Optoelectronic Applications. *Advanced Materials* **36** (42 2024) (cit. on p. 38).

211. Close, D. M. Calculated vertical ionization energies of the common α-amino acids in the gas phase and in solution. *Journal of Physical Chemistry A* **115,** 2900–2912 (13 2011) (cit. on p. 40).

212. Li, X., Li, N. & Zhao, L. The reactive activities of natural amino acids: key principles of peptide-templated Au cluster synthesis. *Science Bulletin* **61,** 1732–1738 (22 2016) (cit. on p. 40).

213. Biedermann, F., Vendruscolo, M., Scherman, O. A., De Simone, A. & Nau, W. M. Cucurbit[8]uril and blue-box: High-energy water release overwhelms electrostatic interactions. *Journal of the American Chemical Society* **135,** 14879–14888 (2013) (cit. on pp. 40, 111).

214. Thakuria, R., Nath, N. K. & Saha, B. K. The Nature and Applications of π-π Interactions: A Perspective. *Crystal Growth and Design* **19,** 523–528 (2 2019) (cit. on p. 40).

215. Martins, J. N. *et al.* Photoswitchable Calixarene Activators for Controlled Peptide Transport across Lipid Membranes. *Journal of the American Chemical Society* **145,** 13126–13133 (24 2023) (cit. on pp. 41, 43, 52, 93, 117).

216. Richarz, R. & Wüthrich, K. Carbon-13 NMR chemical shifts of the common amino acid residues measured in aqueous solutions of the linear tetrapeptides H-Gly-Gly-X- L- Ala-OH. *Biopolymers* **17,** 2133–2141 (9 1978) (cit. on p. 44).

217. Rule, G. S. & Hitchens, T. K. in *Fundamentals of Protein NMR Spectroscopy* 1–27 (Springer-Verlag, 2003) (cit. on pp. 44, 182).

218. Webb, J. L. in *Enzyme and Metabolic Inhibitors* 1st ed., 1–12 (Academic Press, 1963) (cit. on p. 47).

219. Cui, Q. & Karplus, M. Allostery and cooperativity revisited. *Protein Science* **17,** 1295–1307 (8 2008) (cit. on p. 47).

220. Shen, Z. *et al.* Design of SARS-CoV-2 PLpro Inhibitors for COVID-19 Antiviral Therapy Leveraging Binding Cooperativity. *Journal of Medicinal Chemistry* **65,** 2940–2955 (4 2022) (cit. on p. 47).

221. Palma, G. Z. D., Angelini, A. A. R., Vitali, V., Flecha, F. L. G. & Alleva, K. Cooperativity in regulation of membrane protein function: phenomenological analysis of the effects of pH and phospholipids. *Biophysical Reviews* **15,** 721–731 (4 2023) (cit. on p. 47).

222. Shinkai, S., Araki, K., Grootenhuis, P. D. J. & Reinhoudt, D. N. pKa determination of water-soluble calix[4]arenes. *Journal of the Chemical Society, Perkin Transactions 2,* 1883 (12 1991) (cit. on p. 49).

223. Bates, R. G., Siegel, G. L. & Acree, S. F. The Second Dissociation Constant of p-phenolsulfonic acid and pH values of phenolsulfonate chloride buffers from 0 to 60 °C. *Journal of Research of the N.ational Bureau of Standards* **31,** 205–223 (1943) (cit. on p. 49).

224. Kleckner, I. R. & Foster, M. P. An introduction to NMR-based approaches for measuring protein dynamics. *Biochimica et Biophysica Acta - Proteins and Proteomics* **1814,** 942–968 (8 2011) (cit. on p. 51).

225. Shimoyama, D. & Haino, T. Entropy-Driven Cooperativity in the Guest Binding of an Octaphosphonate Bis-cavitand. *Chemistry - A European Journal* **26,** 3074–3079 (14 2020) (cit. on p. 55).

226. Kaifer, A. E. Portal Effects on the Stability of Cucurbituril Complexes. *Israel Journal of Chemistry* **58,** 244–249 (2018) (cit. on p. 55).

227. Sun, S. *et al.* Interaction of a hemicyanine dye and its derivative with DNA and cucurbit[7]uril. *New Journal of Chemistry* **38,** 3600–3605 (2014) (cit. on pp. 56, 58).

228. Chen, X. Y., Chen, H. & Fraser Stoddart, J. The Story of the Little Blue Box: A Tribute to Siegfried Hünig. *Angewandte Chemie - International Edition* **62** (2023) (cit. on p. 56).

229. Raimundo, B. *Fluorescent Chemosensor Ensemble For The Detection of Benzodiazepines In Aqueous Media* MA thesis (NOVA School of Science and Technology, 2023) (cit. on pp. 56, 197).

230. Clayden, J., Greevs, N. & Warren, S. in *Organic Chemistry* 2nd ed., 181–208 (Oxford University Press, 2012) (cit. on p. 58).

231. Guo, D. S., Wang, K. & Liu, Y. Selective binding behaviors of p-sulfonatocalixarenes in aqueous solution. *Journal of Inclusion Phenomena and Macrocyclic Chemistry* **62,** 1–21 (1-2 2008) (cit. on p. 58).

232. Dube, S., Satish, S. & Rawtani, D. Aptasensors in environmental forensics: Tracking the silent killers. *WIREs Forensic Science* **5,** 1–14 (2023) (cit. on pp. 61, 62).

233. Puckowski, A. *et al.* Bioaccumulation and analytics of pharmaceutical residues in the environment: A review. *Journal of Pharmaceutical and Biomedical Analysis* **127,** 232–255 (2016) (cit. on p. 61).

234. Zenker, A., Cicero, M. R., Prestinaci, F., Bottoni, P. & Carere, M. Bioaccumulation and biomagnification potential of pharmaceuticals with a focus to the aquatic environment. *Journal of Environmental Management* **133,** 378–387 (2014) (cit. on p. 61).

235. S, D. L., B, V. G. & Murali, V. From prescription to pollution: The ecological consequences of NSAIDs in aquatic ecosystems. *Toxicology Reports* **13,** 1–9 (2024) (cit. on p. 61).

236. Hawkins, D. M. The Problem of Overfitting. *Journal of Chemical Information and Computer Sciences* **44,** 1–12 (1 2004) (cit. on p. 67).

237. Ayhan, M. M. *et al.* Comprehensive Synthesis of Monohydroxy-Cucurbit[n]urils (n = 5, 6, 7, 8): High Purity and High Conversions. *Journal of the American Chemical Society* **137,** 10238–10245 (2015) (cit. on pp. 69, 71).

238. Dong, N. *et al.* Synthesis and Binding Properties of Monohydroxycucurbit[7]uril: A Key Derivative for the Functionalization of Cucurbituril Hosts. *Journal of Organic Chemistry* **83,** 5467–5473 (2018) (cit. on pp. 69, 126).

239. Ghosh, S. K. *et al.* Superacid-Mediated Functionalization of Hydroxylated Cucurbit[n]urils. *Journal of the American Chemical Society* **141,** 17503–17506 (2019) (cit. on pp. 70, 71, 127, 128).

240. Zhang, H. *et al.* Aggregate Science: From Structures to Properties. *Advanced Materials* **32,** 2001457–2001457 (36 2020) (cit. on p. 75).

241. Lehn, J. M. in *Supramolecular Chemistry: Concepts and Perspectives* 81–87 (VCH, 1995). ISBN: 3-527-29312-4 (cit. on p. 75).

242. Basílio, N. & Garcia-Rio, L. Calixarene-based surfactants: Conformational-dependent solvation shells for the alkyl chains. *ChemPhysChem* **13,** 2368–2376 (9 2012) (cit. on pp. 78, 83, 85).

243. Zana, R. Dimeric and oligomeric surfactants. Behavior at interfaces and in aqueous solution: a review. *Advances in Colloid and Interface Science* **97,** 205–253 (1-3 2002) (cit. on p. 78).

244. Zana, R., Levy, H., Papoutsi, D. & Beinert, G. Micellization of Two Triquaternary Ammonium Surfactants in Aqueous Solution. *Langmuir* **11,** 3694–3698 (10 1995) (cit. on p. 78).

245. Esumi, K., Taguma, K. & Koide, Y. Aqueous Properties of Multichain Quaternary Cationic Surfactants. *Langmuir* **12,** 4039–4041 (16 1996) (cit. on p. 78).

246. McClements, D. J. Crystals and crystallization in oil-in-water emulsions: Implications for emulsion-based delivery systems. *Advances in Colloid and Interface Science* **174,** 1–30 (2012) (cit. on p. 83).

247. Roland, I., Piel, G., Delattre, L. & Evrard, B. Systematic characterization of oil-in-water emulsions for formulation design. *International Journal of Pharmaceutics* **263,** 85–94. ISSN: 03785173 (1-2 2003) (cit. on p. 83).

248. Zolfaghari, R., Fakhru'l-Razi, A., Abdullah, L. C., Elnashaie, S. S. & Pendashteh, A. Demulsification techniques of water-in-oil and oil-in-water emulsions in petroleum industry. *Separation and Purification Technology* **170,** 377–407 (2016) (cit. on p. 83).

249. Zarzar, L. D. *et al.* Dynamically reconfigurable complex emulsions via tunable interfacial tensions. *Nature* **518,** 520–524 (2015) (cit. on pp. 83, 85, 130).

250. He, Y., Savagatrup, S., Zarzar, L. D. & Swager, T. M. Interfacial Polymerization on Dynamic Complex Colloids: Creating Stabilized Janus Droplets. *ACS Applied Materials and Interfaces* **9,** 7804–7811 (2017) (cit. on p. 83).

251. Nisisako, T. Recent advances in microfluidic production of Janus droplets and particles. *Current Opinion in Colloid and Interface Science* **25,** 1–12 (2016) (cit. on pp. 85, 130).

252. Español, E. S. & Villamil, M. M. Calixarenes: Generalities and their role in improving the solubility, biocompatibility, stability, bioavailability, detection, and transport of biomolecules. *Biomolecules* **9** (2019) (cit. on p. 85).

253. Delahaije, R. J., Sagis, L. M. & Yang, J. Impact of Particle Sedimentation in Pendant Drop Tensiometry. *Langmuir* **38,** 10183–10191 (33 2022) (cit. on p. 86).

254. Rauhut, M. M. *et al.* Chemiluminescence from reactions of electronegatively substituted aryl oxalates with hydrogen peroxide and fluorescent compounds. *Journal of the American Chemical Society* **89,** 6515–6522 (1967) (cit. on p. 87).

255. Silva, S. M. *et al.* Kinetic studies on the peroxyoxalate chemiluminescence reaction: Determination of the cyclization rate constant. *Luminescence* **17,** 313–320 (5 2002) (cit. on p. 87).

256. Imaizumi, N., Hayakawa, K., Miyazaki, M. & Imai, K. Stability of bis(2,4,6-trichlorophenyl) oxalate in high-performance liquid chromatography for chemiluminescence detection. *The Analyst* **114,** 161 (2 1989) (cit. on p. 87).

257. Rodriguez, E. B. & Rodriguez-Amaya, D. B. Formation of apocarotenals and epoxycarotenoids from β-carotene by chemical reactions and by autoxidation in model systems and processed foods. *Food Chemistry* **101,** 563–572 (2007) (cit. on p. 87).

258. Kim, C., Traylor, T. G. & Perrin, C. L. MCPBA Epoxidation of Alkenes: Reinvestigation of Correlation between Rate and Ionization Potential. *Journal of the American Chemical Society* **120,** 9513–9516 (1998) (cit. on p. 87).

259. Cooper, G. M. *The Cell: A Molecular Approach* 8th ed. (Oxford University Press, pp. 45– 80, 2019) (cit. on p. 94).

260. Barboiu, M. Encapsulation versus Self-Aggregation toward Highly Selective Artificial K+ Channels. *Accounts of Chemical Research* **51,** 2711–2718 (11 2018) (cit. on p. 94).

261. Riccardis, F. D., Izzo, I., Montesarchio, D. & Tecilla, P. Ion transport through lipid bilayers by synthetic ionophores: Modulation of activity and selectivity. *Accounts of Chemical Research* **46,** 2781–2790 (12 2013) (cit. on p. 94).

262. Chen, J.-Y. & Hou, J.-L. Controllable synthetic ion channels. *Organic Chemistry Frontiers* **5,** 1728–1736 (2018) (cit. on p. 94).

263. Davis, A. P., Sheppard, D. N. & Smith, B. D. Development of synthetic membrane transporters for anions. *Chemical Society Reviews* **36,** 348–357 (2 2007) (cit. on p. 94).

264. Montenegro, J., Ghadiri, M. R. & Granja, J. R. Ion channel models based on self-assembling cyclic peptide nanotubes. *Accounts of Chemical Research* **46,** 2955–2965 (12 2013) (cit. on p. 94).

265. Gasparini, G., Bang, E. K., Montenegro, J. & Matile, S. Cellular uptake: lessons from supramolecular organic chemistry. *Chemical Communications* **51,** 10389–10402 (2015) (cit. on p. 94).

266. Gale, P. A., Davis, J. T. & Quesada, R. Anion transport and supramolecular medicinal chemistry. *Chemical Society Reviews* **46,** 2497–2519 (9 2017) (cit. on p. 94).

267. Matile, S., Jentzsch, A. V., Montenegro, J. & Fin, A. Recent synthetic transport systems. *Chemical Society Reviews* **40,** 2453–2474 (5 2011) (cit. on p. 94).

268. Gokel, G. W. & Negin, S. Synthetic ion channels: From pores to biological applications. *Accounts of Chemical Research* **46,** 2824–2833 (12 2013) (cit. on p. 94).

269. Qu, D. H., Wang, Q. C., Zhang, Q. W., Ma, X. & Tian, H. Photoresponsive Host-Guest Functional Systems. *Chemical Reviews* **115,** 7543–7588 (15 2015) (cit. on p. 94).

270. Wezenberg, S. J. *et al.* Photomodulation of Transmembrane Transport and Potential by Stiff-Stilbene Based Bis(thio)ureas. *Journal of the American Chemical Society* **144,** 331–338 (1 2022) (cit. on p. 94).

271. Wang, W. Z. *et al.* Light-Driven Molecular Motors Boost the Selective Transport of Alkali Metal Ions through Phospholipid Bilayers. *Journal of the American Chemical Society* **143,** 15653–15660 (38 2021) (cit. on p. 94).

272. Wang, C. *et al.* A Light-Operated Molecular Cable Car for Gated Ion Transport. *Angewandte Chemie - International Edition* **60,** 14836–14840 (27 2021) (cit. on p. 94).

273. Salunke, S. B., Malla, J. A. & Talukdar, P. Phototriggered Release of a Transmembrane Chloride Carrier from an o -Nitrobenzyl-Linked Procarrier. *Angewandte Chemie* **131,** 5408–5412 (16 2019) (cit. on p. 94).

274. Ahmad, M., Metya, S., Das, A. & Talukdar, P. A Sandwich Azobenzene-Diamide Dimer for Photoregulated Chloride Transport. *Chemistry - A European Journal* **26,** 8703–8708 (40 2020) (cit. on p. 94).

275. Kerckhoffs, A. & Langton, M. J. Reversible photo-control over transmembrane anion transport using visible-light responsive supramolecular carriers. *Chemical Science* **11,** 6325–6331 (24 2020) (cit. on p. 94).

276. Liu, T. *et al.* Light-controlled ion channels formed by amphiphilic small molecules regulate ion conduction via cis-trans photoisomerization. *Chemical Communications* **49,** 10311–10313 (87 2013) (cit. on p. 94).

277. García-López, V. *et al.* Molecular machines open cell membranes. *Nature* **548,** 567–572 (7669 2017) (cit. on p. 94).

278. Barba-Bon, A. *et al.* Boron clusters as broadband membrane carriers. *Nature* **603,** 637–642 (2022) (cit. on p. 94).

279. Sakai, N. & Matile, S. Anion-Mediated Transfer of Polyarginine across Liquid and Bilayer Membranes. *Journal of the American Chemical Society* **125,** 14348–14356 (47 2003) (cit. on pp. 94, 99).

280. Sakai, N., Takeuchi, T., Futaki, S. & Matile, S. Direct observation of anion-mediated translocation of fluorescent oligoarginine carriers into and across bulk liquid and anionic bilayer membranes. *ChemBioChem* **6,** 114–122 (1 2005) (cit. on p. 94).

281. Montenegro, J. & Matile, S. Anionic activators for differential sensing with cell-penetrating peptides. *Chemistry - An Asian Journal* **6,** 681–689 (2 2011) (cit. on pp. 94, 95).

282. Takeuchi, T., Montenegro, J., Hennig, A. & Stefan, M. Pattern generation with synthetic sensing systems in lipid bilayer membranes. *Chemical Science* **2,** 303–307 (2 2011) (cit. on p. 94).

283. Fischer, P. M. Cellular uptake mechanisms and potential therapeutic utility of peptidic cell delivery vectors: Progress 2001-2006. *Medicinal Research Reviews* **27,** 755–795 (6 2007) (cit. on pp. 94, 101).

284. Chuard, N. *et al.* Activation of Cell-Penetrating Peptides with Ionpair-π Interactions and Fluorophiles. *Journal of the American Chemical Society* **138,** 11264–11271 (35 2016) (cit. on pp. 95, 101).

285. Szymański, W., Beierle, J. M., Kistemaker, H. A., Velema, W. A. & Feringa, B. L. Reversible photocontrol of biological systems by the incorporation of molecular photoswitches. *Chemical Reviews* **113,** 6114–6178 (8 2013) (cit. on p. 95).

286. Beharry, A. A. & Woolley, G. A. Azobenzene photoswitches for biomolecules. *Chemical Society Reviews* **40,** 4422–4437 (8 2011) (cit. on p. 95).

287. Basilio, N., García-Río, L. & Martín-Pastor, M. Counterion Binding in Solutions of p-Sulfonatocalix[4]arene. *The Journal of Physical Chemistry B* **114,** 7201–7206 (21 2010) (cit. on pp. 95, 118, 121).

288. Böhmer, V. Calixarenes, Macrocycles with (Almost) Unlimited Possibilities. *Angewandte Chemie – International Edition* **34,** 713–745 (7 1995) (cit. on p. 95).

289. Bandara, H. M. & Burdette, S. C. Photoisomerization in different classes of azobenzene. *Chemical Society Reviews* **41,** 1809–1825 (5 2012) (cit. on p. 95).

290. Walrant, A. *et al.* Different membrane behaviour and cellular uptake of three basic arginine-rich peptides. *Biochimica et Biophysica Acta - Biomembranes* **1808,** 382–393 (1 2011) (cit. on p. 96).

291. Lou, J., Schuster, J. A., Barrera, F. N. & Best, M. D. ATP-Responsive Liposomes via Screening of Lipid Switches Designed to Undergo Conformational Changes upon Binding Phosphorylated Metabolites. *Journal of the American Chemical Society* **144,** 3746–3756 (8 2022) (cit. on pp. 96, 101).

292. Barba-Bon, A. *et al.* Fluorescence Monitoring of Peptide Transport Pathways into Large and Giant Vesicles by Supramolecular Host-Dye Reporter Pairs. *Journal of the American Chemical Society* **141,** 20137–20145 (2019) (cit. on pp. 96, 99).

293. Priegue, J. M. *et al.* In Situ Functionalized Polymers for siRNA Delivery. *Angewandte Chemie - International Edition* **55,** 7492–7495 (26 2016) (cit. on p. 101).

294. Bos, J. E., Siegler, M. A. & Wezenberg, S. J. Activity Control of a Synthetic Transporter by Photodynamic Modulation of Membrane Mobility and Incorporation. *Journal of the American Chemical Society* **146,** 31085–31093 (45 2024) (cit. on p. 103).

295. Yang, L. *et al.* Macrocyclic membranes: from liquid to solid state. *Chemical Society Reviews* (2025) (cit. on p. 103).

296. Malik, S. A. & Madhavan, N. H+/X- Co-Transport Driven by Azobenzene Containing Aromatic Amides. *ChemPhotoChem* **8** (12 2024) (cit. on p. 103).

297. Johnson, T. G., Sadeghi-Kelishadi, A. & Langton, M. J. Length dependent reversible off-on activation of photo-switchable relay anion transporters. *Chemical Communications* **60,** 7160–7163 (56 2024) (cit. on p. 103).

298. Zhang, T.-H. *et al.* Engineering the novel azobenzene-based molecular photoswitches for suppressing bacterial infection through dynamic regulation of biofilm formation. *Pest Management Science* **81,** 585–598 (2 2025) (cit. on p. 103).

299. Kalyanasundaram, K. & Thomas, J. K. Environmental Effects on Vibronic Band Intensities in Pyrene Monomer Fluorescence and Their Application in Studies of Micellar Systems. *Journal of the American Chemical Society* **99,** 2039–2044 (7 1977) (cit. on p. 104).

300. Hopp, M. T. *et al.* Heme Determination and Quantification Methods and Their Suitability for Practical Applications and Everyday Use. *Analytical Chemistry* **92,** 9429–9440 (2020) (cit. on p. 114).

301. Chu, Y. L., Cheng, C. C., Chen, Y. P., Yen, Y. C. & Chang, F. C. A new supramolecular POSS electroluminescent material. *Journal of Materials Chemistry* **22,** 9285–9292 (18 2012) (cit. on p. 118).

302. Tkachenko, I. M. *et al.* Design, synthesis and photoisomerization behavior of novel azobenzene-based dyes containing different alkyl chains and isolation groups. *Tetrahedron Letters* **57,** 5505–5510 (49 2016) (cit. on p. 121).

303. Haiying, L. & Zhongfan, L. A convenient synthesis of novel mercapto-ended azobenzene derivatives. *Synthetic Communications* **28,** 3779–3785 (20 1998) (cit. on p. 121).

304. Wang, X. M. *et al.* Two-photon pumped lasing stilbene-type chromophores containing various terminal donor groups: Relationship between lasing efficiency and intramolecular charge transfer. *Journal of Materials Chemistry* **10,** 2698–2703 (12 2000) (cit. on p. 125).

305. Zhang, S. *Synthesis of Mono-Functionalized Cucurbit[n]urils and Exploration of their Applications* PhD thesis (Jacobs University, 2019), 27–46 (cit. on p. 127).

306. Moscho, A., Orwar, O., Chiu, D. T., Modi, B. P. & Zare, R. N. Rapid preparation of giant unilamellar vesicles. *Proceedings of the National Academy of Sciences* **93,** 11443–11447 (21 1996) (cit. on p. 129).

307. Li, J. *et al.* Janus Emulsion Biosensors for Anti-SARS-CoV-2 Spike Antibody. *ACS Central Science* **7,** 1166–1175 (7 2021) (cit. on p. 130).

308. Ogura, T. & Wakayama, M. Coaxial-Tube Quantitative Nuclear Magnetic Resonance for Various Solutions Using SI-Traceable Concentration References. *Analytical Chemistry* **96,** 11657–11665 (2024) (cit. on p. 131).

309. Hein, R., Uzundal, C. B. & Hennig, A. Simple and rapid quantification of phospholipids for supramolecular membrane transport assays. *Organic and Biomolecular Chemistry* **14,** 2182–2185 (2016) (cit. on p. 131).

310. Fasman, G. D. *Handbook of Biochemistry and Molecular Biology* 3rd ed., 183–203 (CRC Press, 1976) (cit. on p. 132).

311. Doreleijers, J. F. *et al.* BioMagResBank database with sets of experimental NMR constraints corresponding to the structures of over 1400 biomolecules deposited in the Protein Data Bank. *Journal of Biomolecular NMR* **26,** 139–146 (2 2003) (cit. on p. 182).

312. Henderson, L. J. Concerning the Relationship Between the Strength of Acids and their Capacity to Preserve Neutrality. *American Journal of Physiology-Legacy Content* **21,** 173–179 (2 1908) (cit. on p. 196).

313. Miller, S. N. *The Dynamics of Newton' s Method on Cubic Polynomials* PhD thesis (Marshall University, 2006), 11–12 (cit. on pp. 276, 277).

A

Supplementary Information for Chapter 2

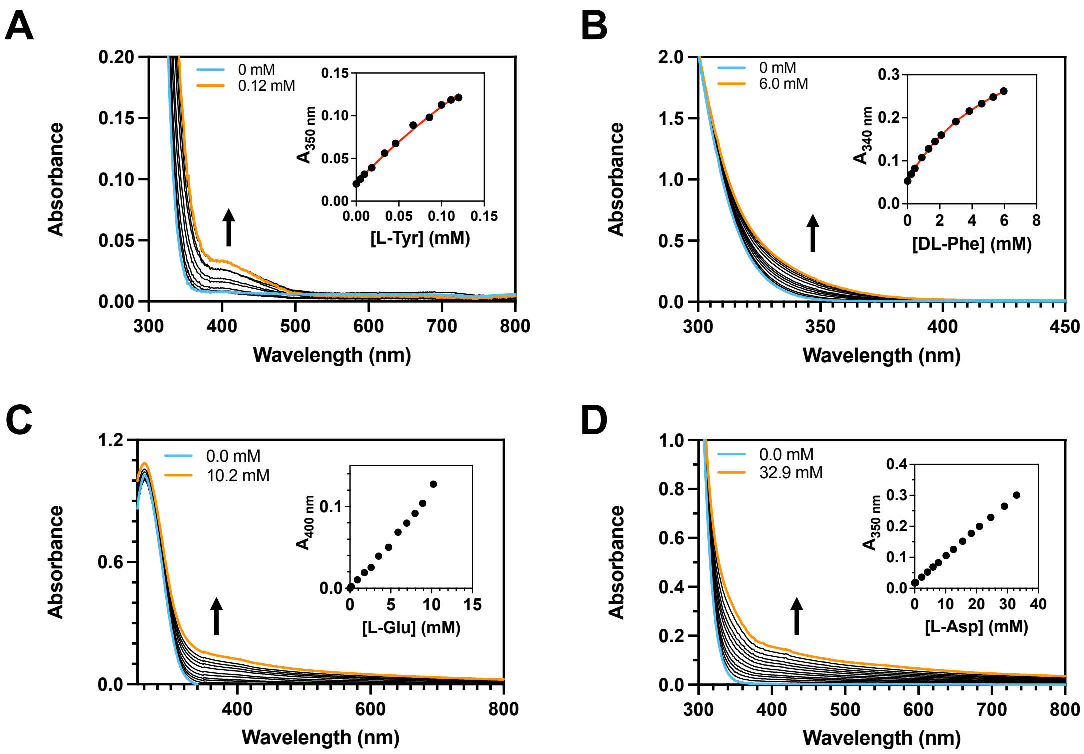

Figure A.1: Direct titrations of BB (0.2 mM) with **A.** L-Tyr, **B.** DL-Phe, **C.** L-Glu and **D.** L-Asp, followed by UV-vis spectroscopy, by the appearance of the respective CT band or increase of baseline. Variation of absorbance at a fixed λ is shown in inset.

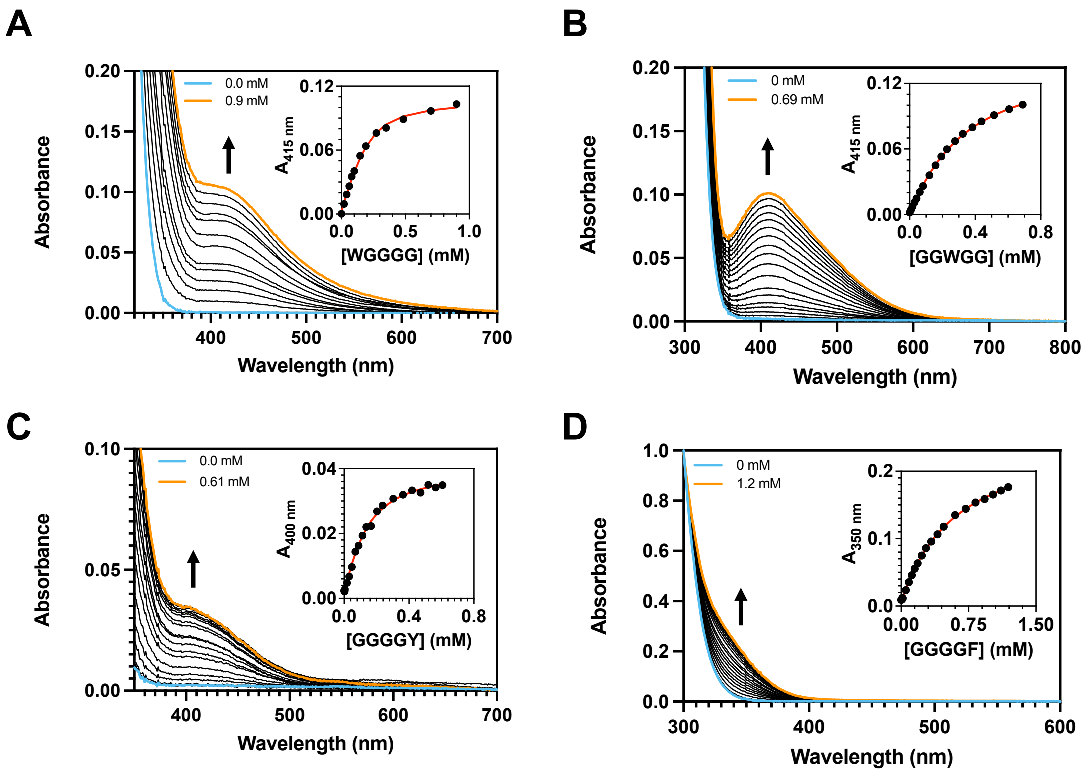

Figure A.2: Direct titrations of BB (0.2 mM) with **A.** WGGGG, **B.** GGWGG, **C.** GGGGY and **D.** GGGGF, followed by UV-vis spectroscopy, by the appearance of the respective CT band or increase of baseline. Variation of absorbance at a fixed λ_{CT} for A to C is shown in inset and respective fitting in red.

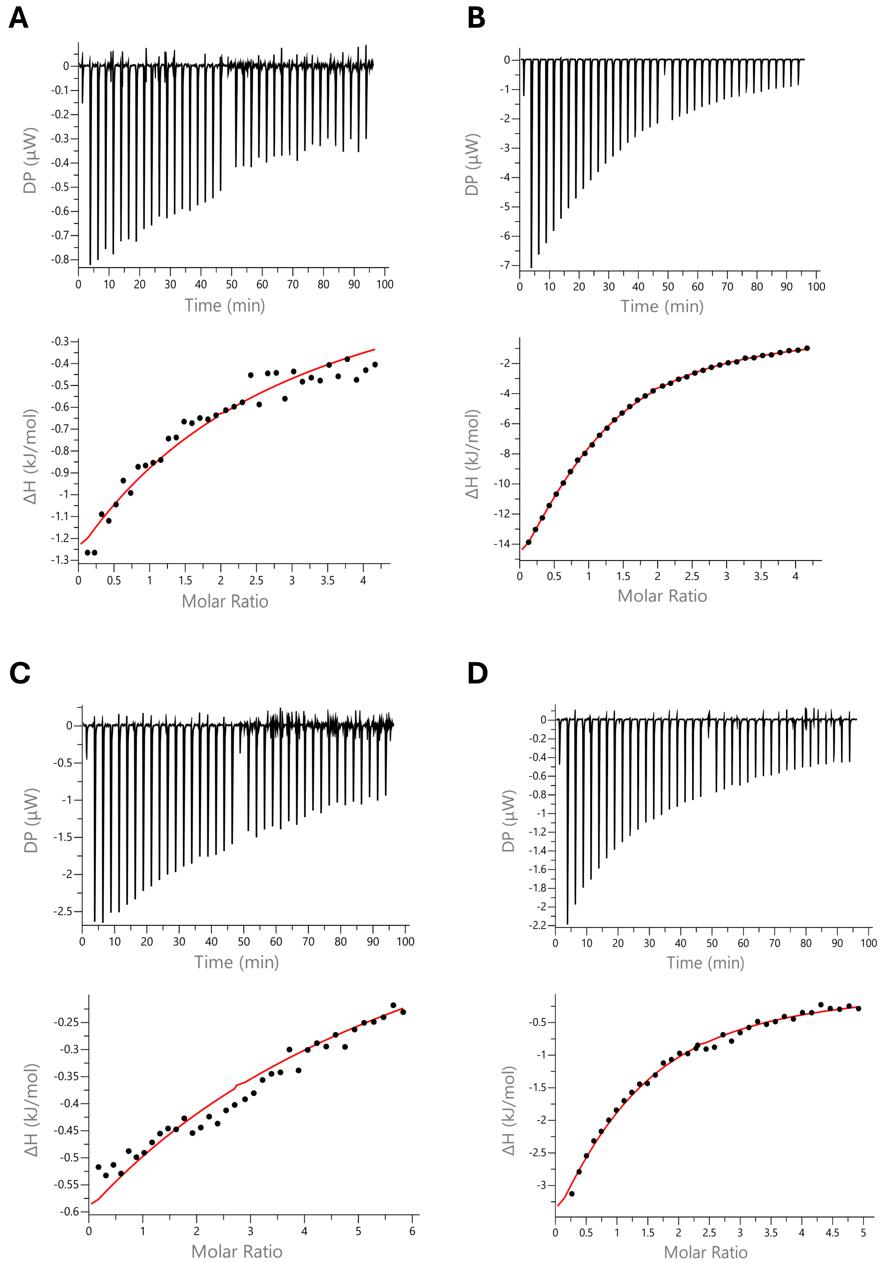

Figure A.3: ITC isotherms of titration of **A.** BB (0.7 mM) with L-Tyr, **B.** GGGGY (0.25 mM) with BB, **C.** BB (1 mM) with DL-Phe and **D.** GGGGF (0.25 mM) with BB, obtained at 25°C. Number of sites obtained for the binding of BB to GGGGY was 0.78 ± 0.04 and GGGGF was 0.87 ± 0.09, while number of sites for the amino acids binding to BB was not obtained due to lack of full isotherm curve.

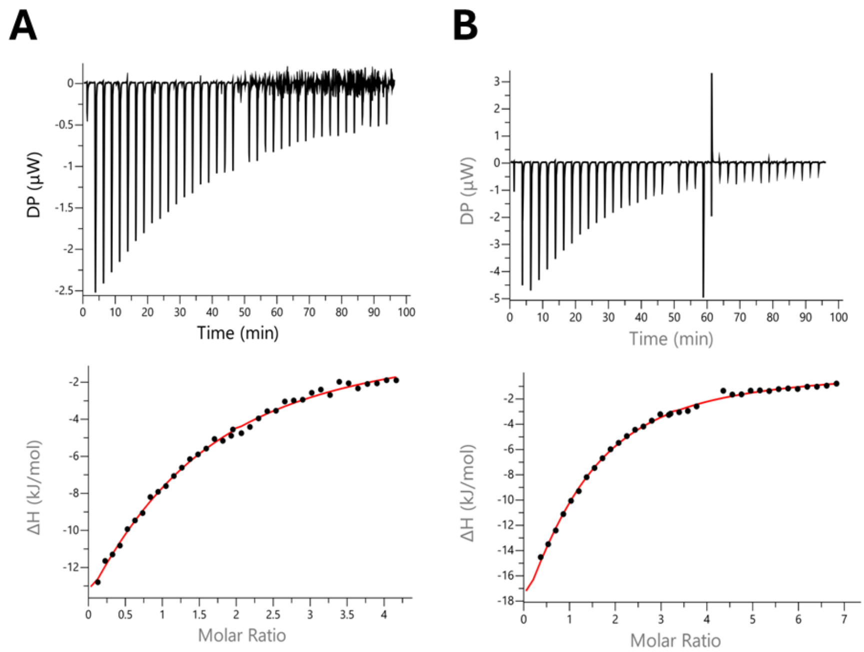

Figure A.4: ITC isotherms of titration of **A.** GGWGG (0.1 mM) and **B.** WGGGG (0.1 mM) with BB, obtained at 25°C. Number of sites obtained for the binding of BB to GGWGG was 1.14 ± 0.12 and WGGGG was 1.29 ± 0.08.

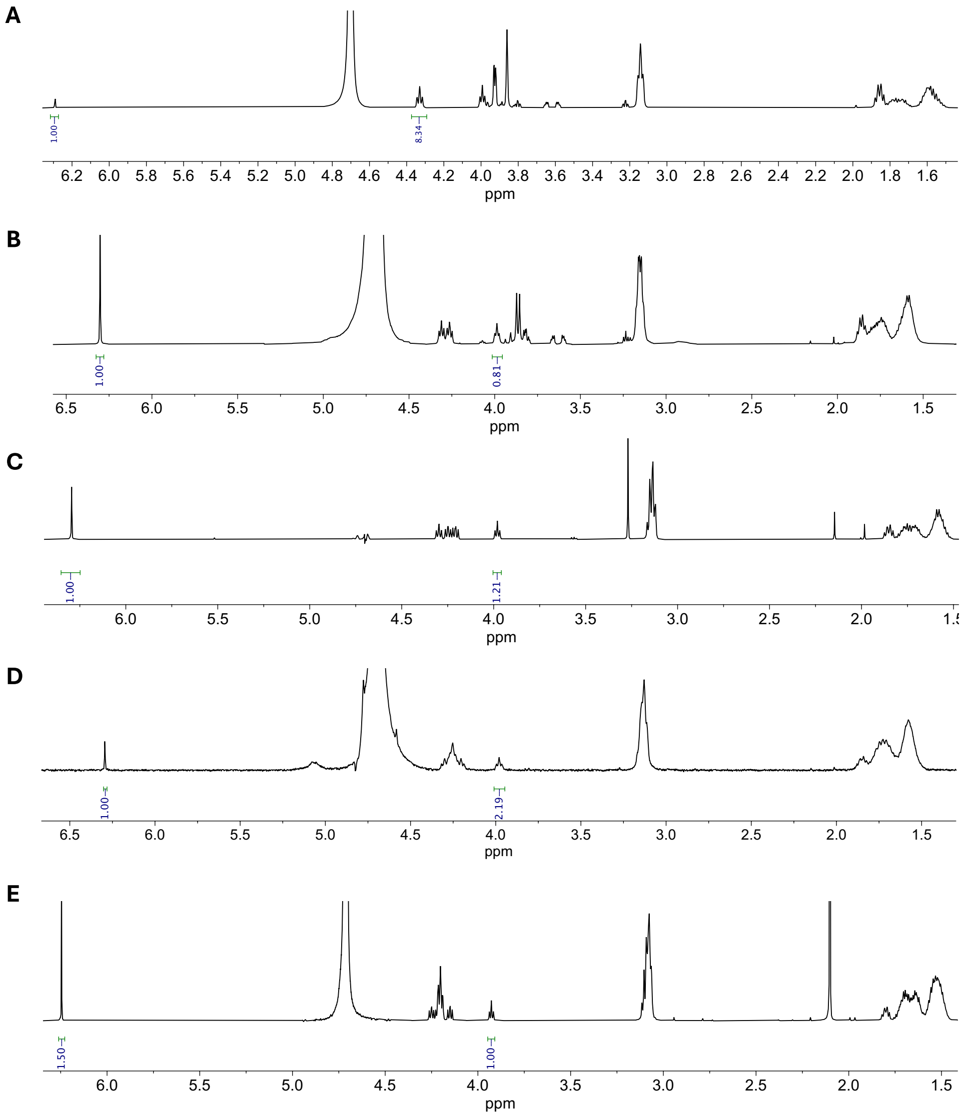

Figure A.5: ^{1}H-NMR spectra of the peptides **A.** R_2G_2, **B.** R_3G, **C.** R_4, **D.** R_6 and **E.** R_8, in D_2O, in the presence of maleic acid, 3.53 mM, in a coaxial tube. The integrals presented are of the reference and peptides H_α proton in each sample, which were used for sample quantification.

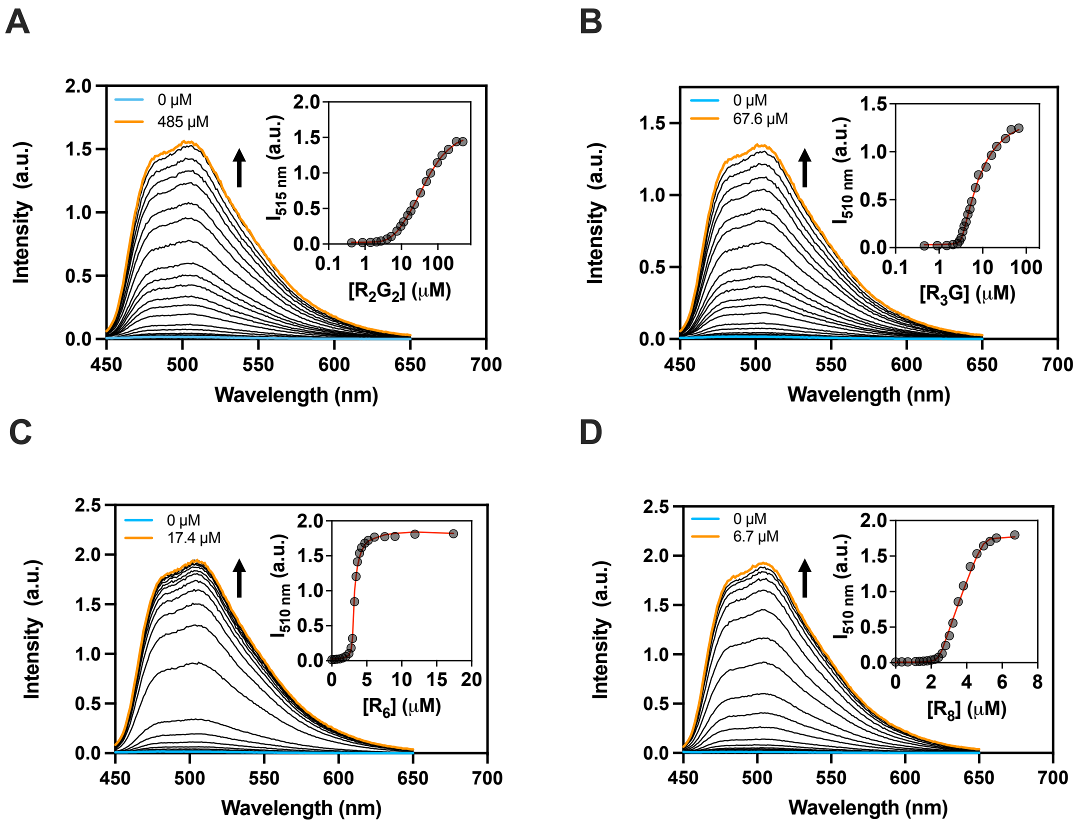

Figure A.6: Indicator displacement assays (IDA) done with the SC4-LCG pair for quantification of the oligoarginines **A.** R_2G_2, **B.** R_3G, **C.** R_6 and **D.** R_8, followed by fluorescence spectroscopy (λ_{exc} = 369 nm). LCG and SC4 concentrations were fixed at 0.1 and 3.3 μM for all peptides except R_8 where the concentration of SC4 was fixed at 5 μM. Insets show the fitting of the data with A and B using the 1:1 competitive model, with concentration of peptide in logarithmic scale for better observation of emission enhancement onset and C. and D. using the 2:1 host:guest competitive model.

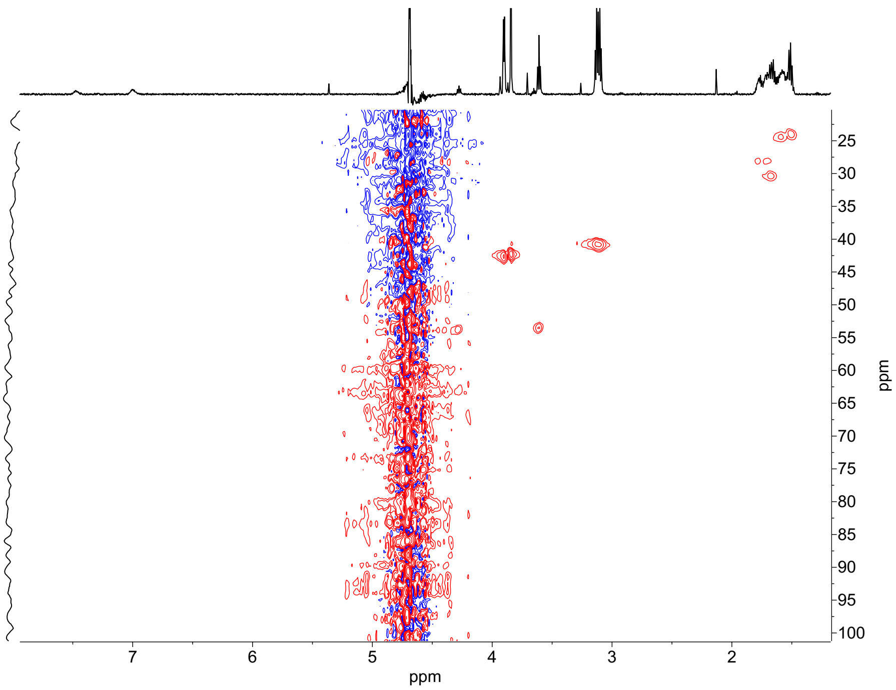

Figure A.7: ^{1}H-^{13}C-HSQC NMR spectrum of the peptide R_2G_2 (0.22 mM), obtained with natural abundancy ^{13}C, done in 10% D_2O:90% H_2O.

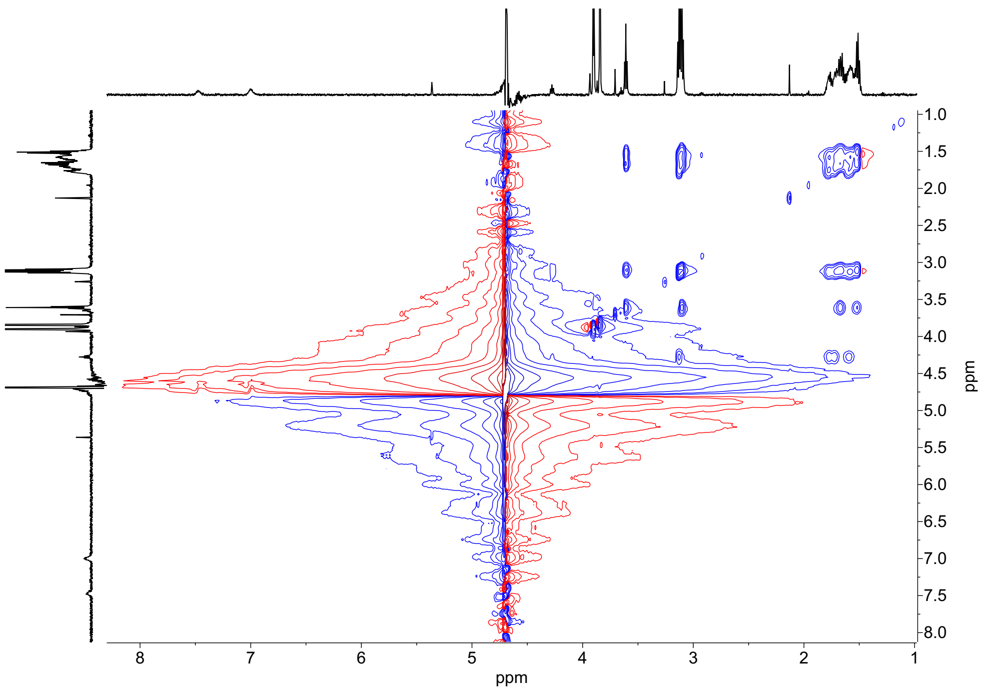

Figure A.8: ^{1}H-TOCSY NMR spectrum of the peptide R_2G_2 (0.22 mM), done in 10% D_2O:90% H_2O.

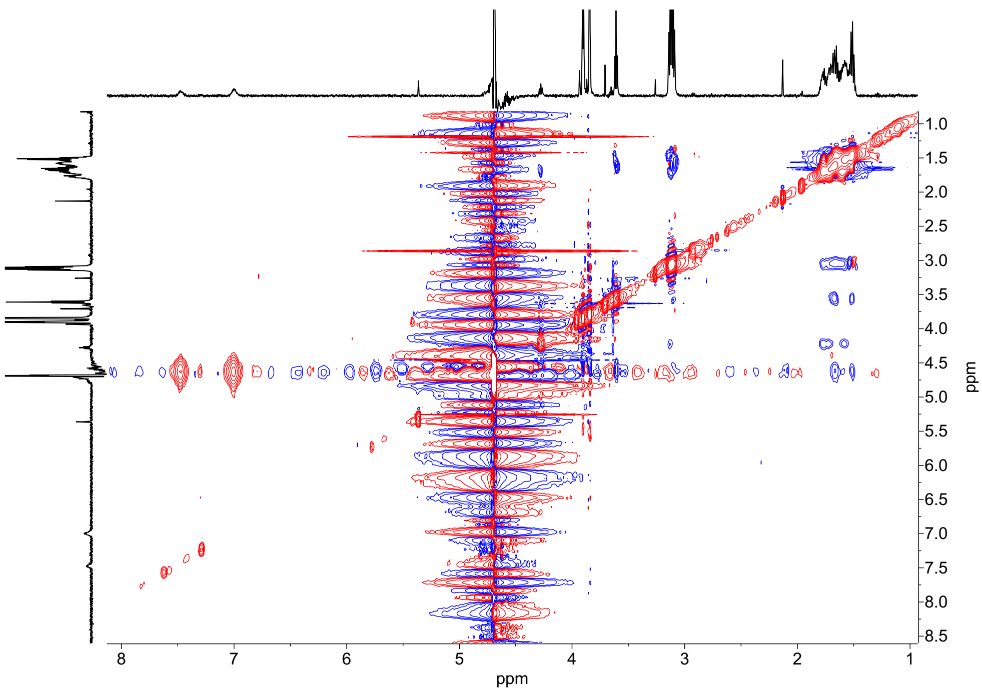

Figure A.9: ^{1}H-ROESY NMR spectrum of the peptide R_2G_2 (0.22 mM), done in 10% D_2O:90% H_2O.

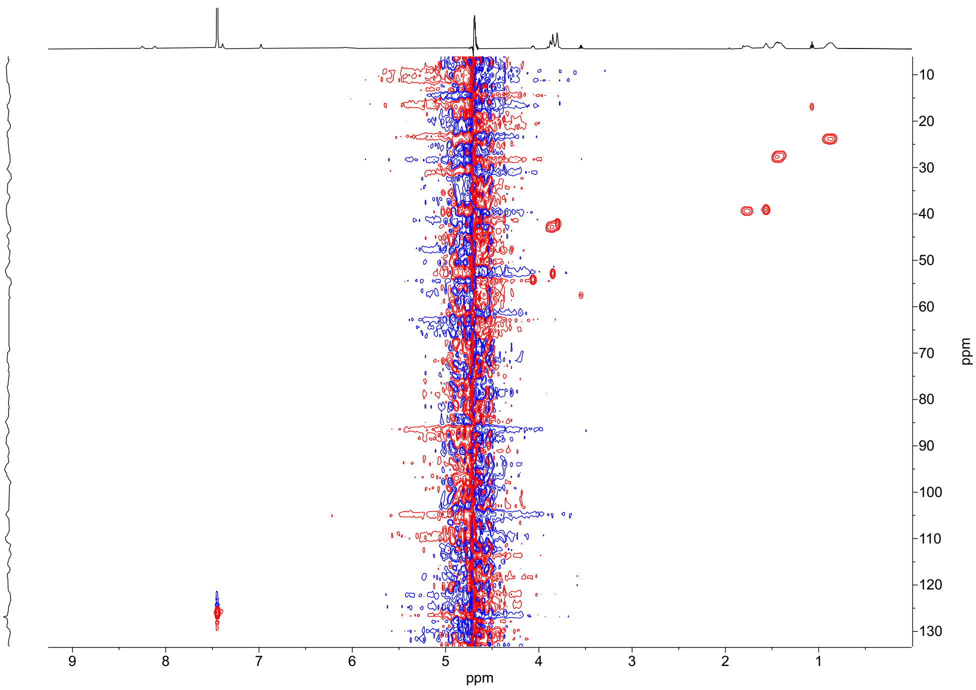

Figure A.10: ^{1}H-^{13}C-HSQC NMR spectrum of the peptide R_2G_2 (0.22 mM) with 1.5 equivalents of SC4, obtained with natural abundancy ^{13}C. The spectrum was done in 10% D_2O:90% H_2O and the signals observed at 1.1 and 3.6 ppm in the proton chemical shifts correspond to a contamination with ethanol.

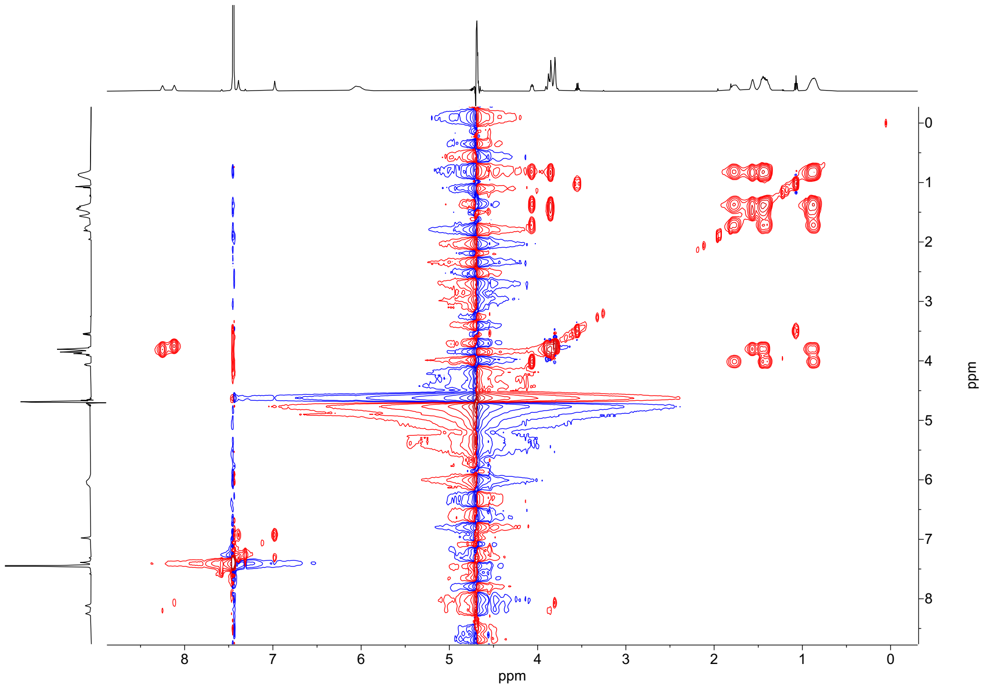

Figure A.11: ^{1}H-TOCSY NMR spectrum of the peptide R_2G_2 (0.22 mM) with 1.5 equivalents of SC4. The spectrum was done in 10% D_2O:90% H_2O and the signals observed at 1.1 and 3.6 ppm correspond to a contamination with ethanol.

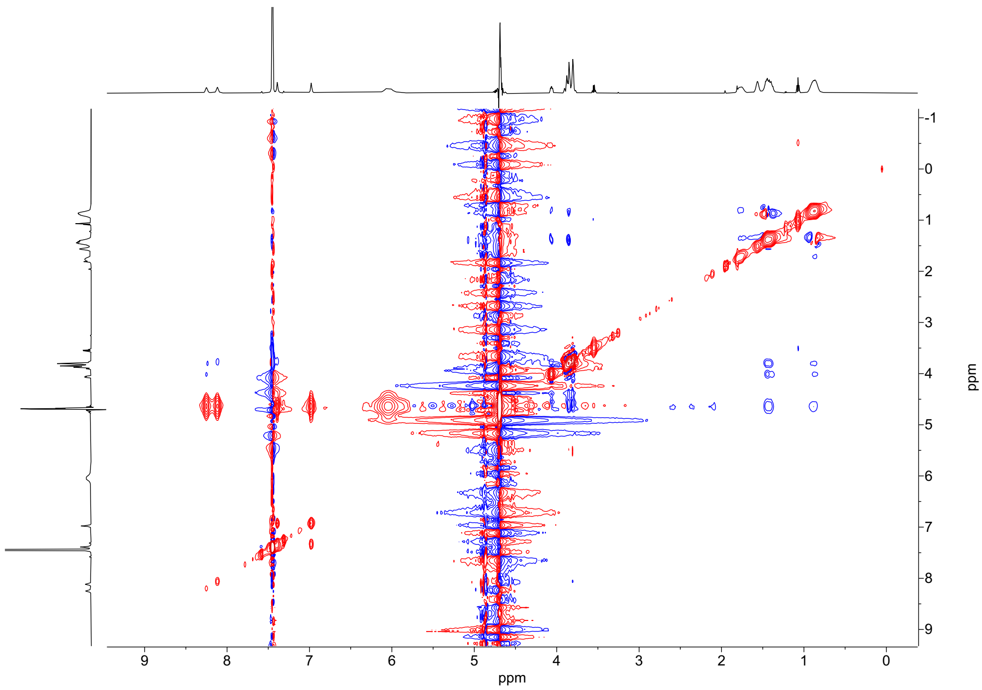

Figure A.12: ^{1}H-ROESY NMR spectrum of the peptide R_2G_2 (0.22 mM) with 1.5 equivalents of SC4. The spectrum was done in 10% D_2O:90% H_2O and the signals observed at 1.1 and 3.6 ppm correspond to a contamination with ethanol.

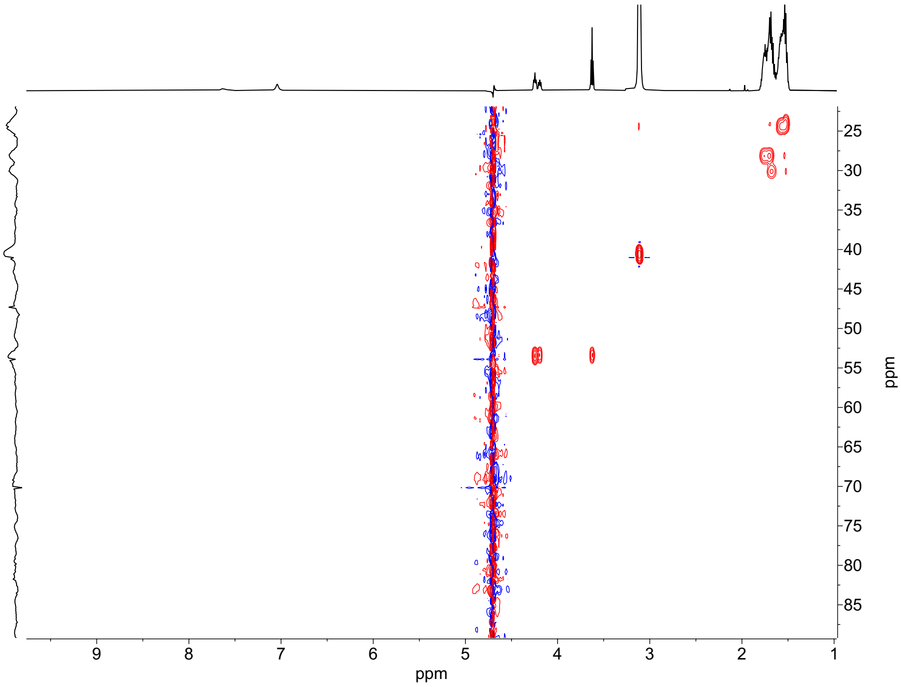

Figure A.13: ^{1}H-^{13}C-HSQC NMR spectrum of the peptide R_4 (0.59 mM), obtained with natural abundancy ^{13}C. The spectrum was done in 10% D_2O:90% H_2O.

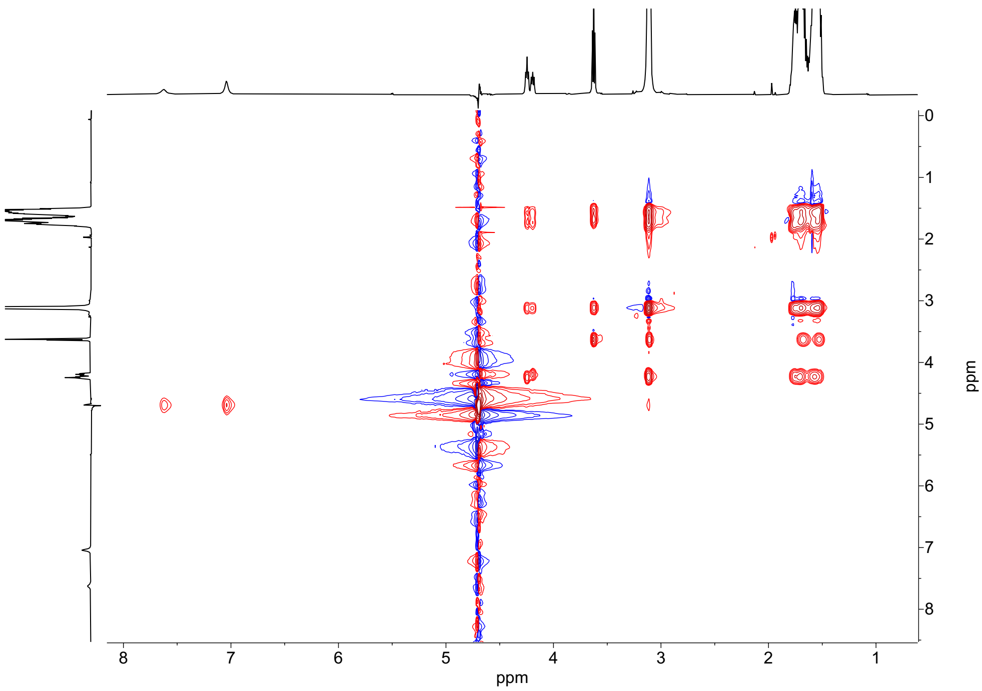

Figure A.14: ^{1}H-TOCSY NMR spectrum of the peptide R_4 (0.59 mM), done in 10% D_2O:90% H_2O.

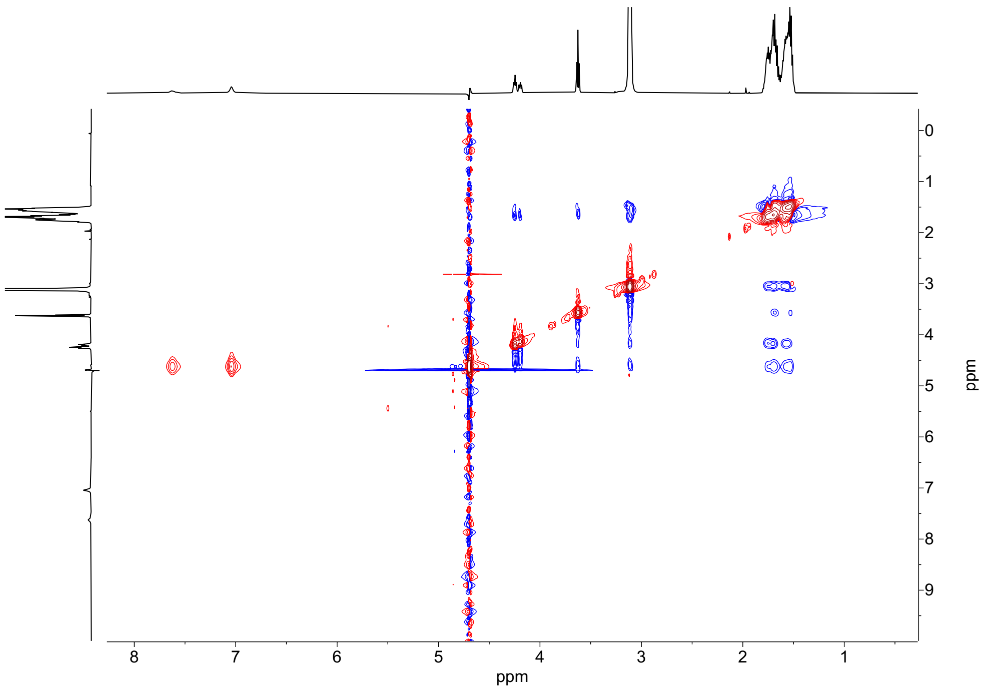

Figure A.15: ^{1}H-ROESY NMR spectrum of the peptide R_4 (0.59 mM), done in 10% D_2O:90% H_2O.

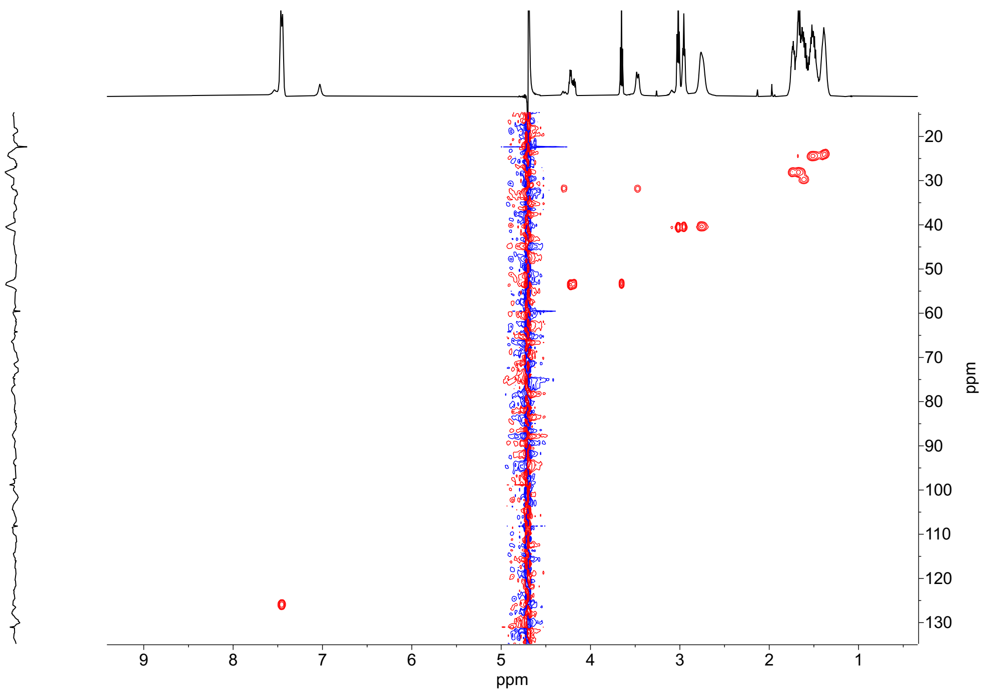

Figure A.16: ^{1}H-^{13}C-HSQC NMR spectrum of the peptide R_4 (0.59 mM) with 0.35 equivalents of SC4, obtained with natural abundancy ^{13}C. The spectrum was done in 10% D_2O:90% H_2O.

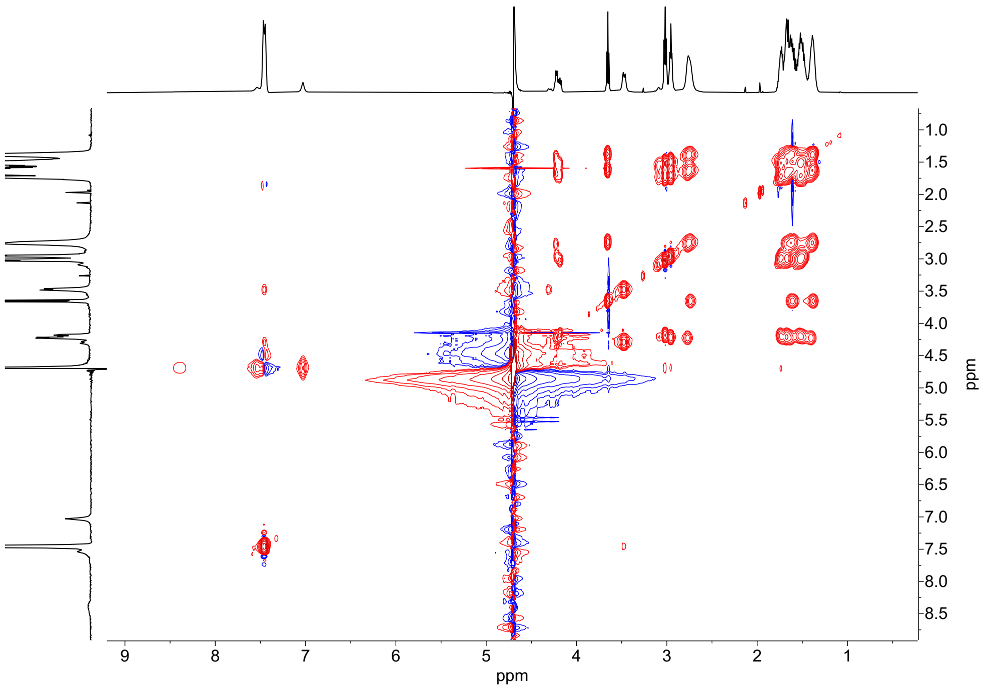

Figure A.17: ^{1}H-TOCSY NMR spectrum of the peptide R_4 (0.59 mM) with 0.35 equivalents of SC4. The spectrum was done in 10% D_2O:90% H_2O.

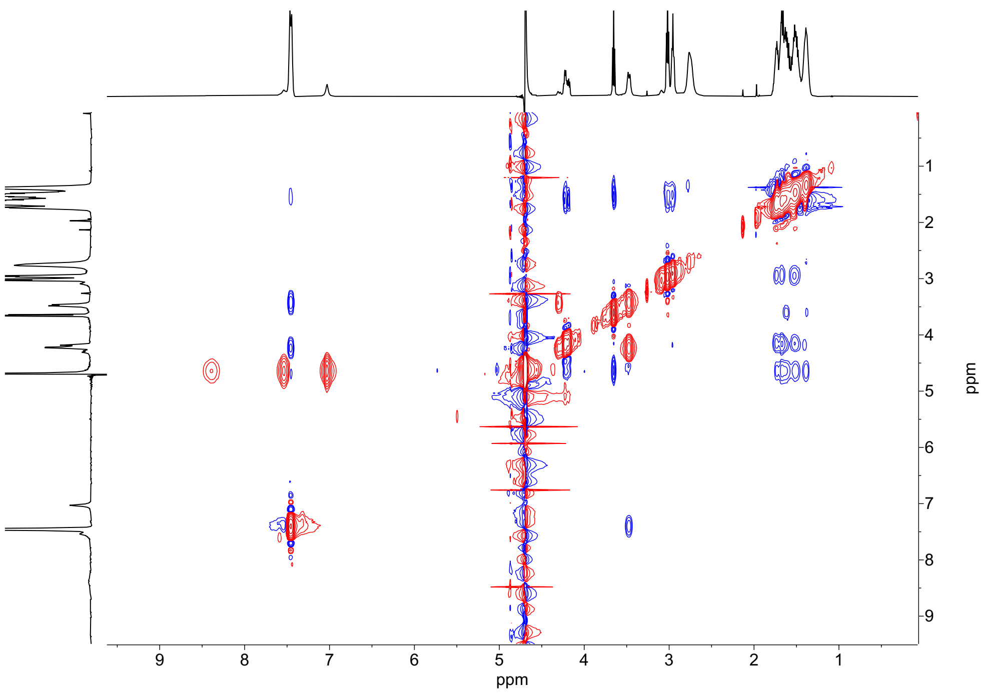

Figure A.18: ^{1}H-ROESY NMR spectrum of the peptide R_4 (0.59 mM) with 0.35 equivalents of SC4. The spectrum was done in 10% D_2O:90% H_2O.

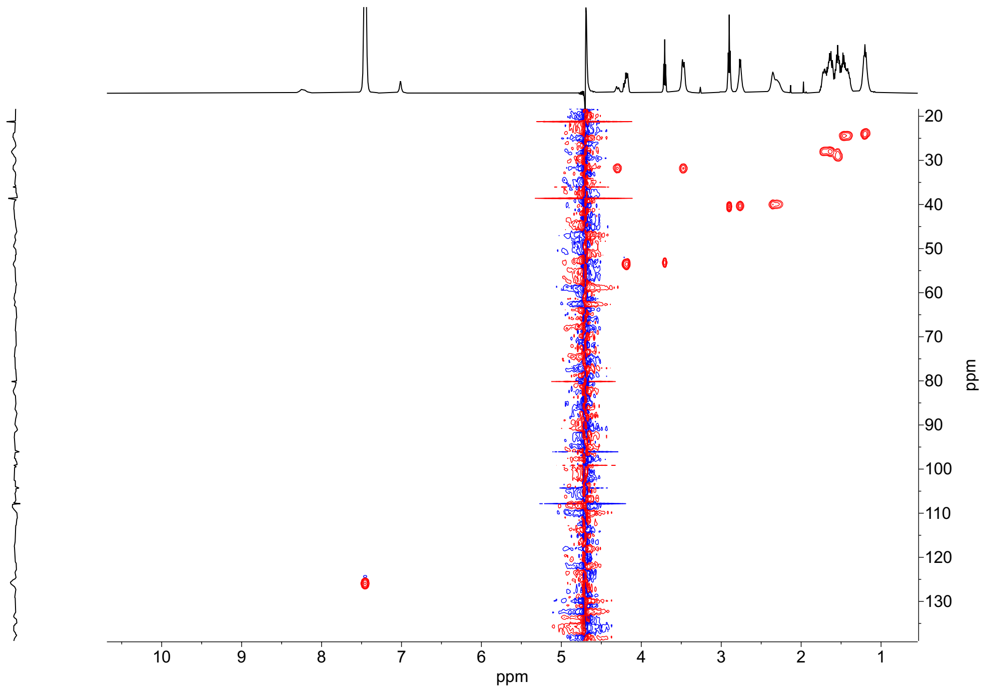

Figure A.19: ^{1}H-^{13}C-HSQC NMR spectrum of the peptide R_4 (0.59 mM) with 0.8 equivalents of SC4, obtained with natural abundancy ^{13}C. The spectrum was done in 10% D_2O:90% H_2O.

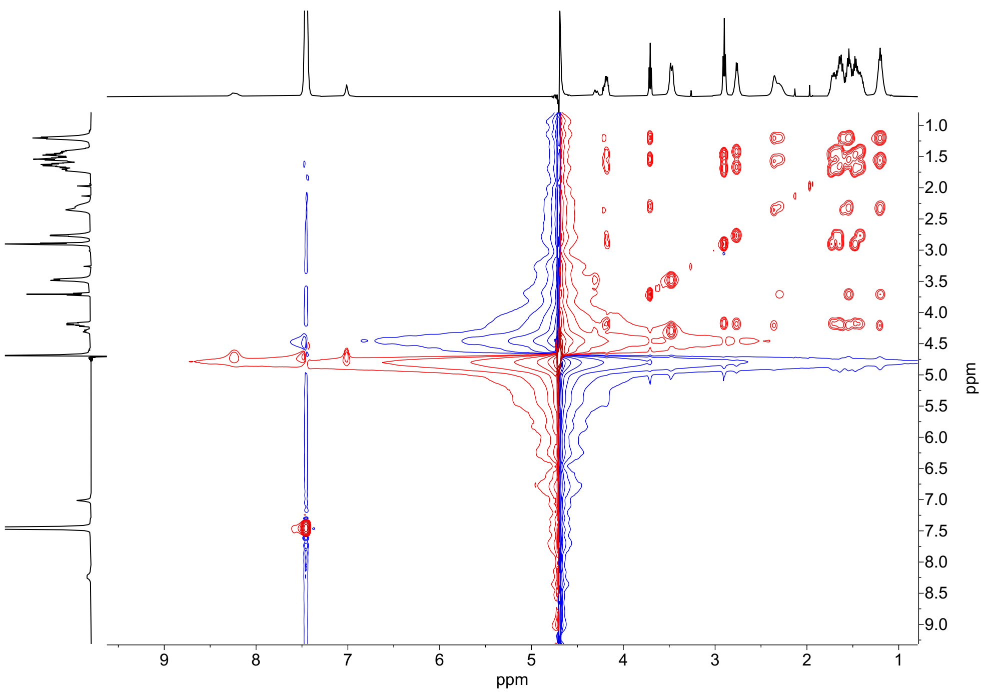

Figure A.20: ^{1}H-TOCSY NMR spectrum of the peptide R_4 (0.59 mM) with 0.8 equivalents of SC4. The spectrum was done in 10% D_2O:90% H_2O.

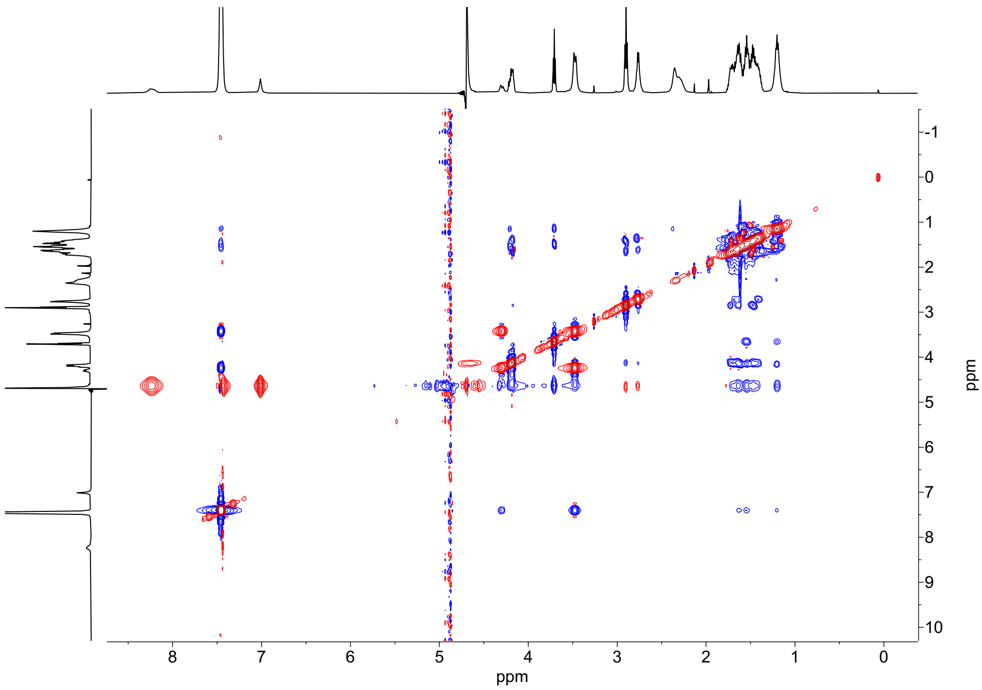

Figure A.21: ^{1}H-ROESY NMR spectrum of the peptide R_4 (0.59 mM) with 0.8 equivalents of SC4. The spectrum was done in 10% D_2O:90% H_2O.

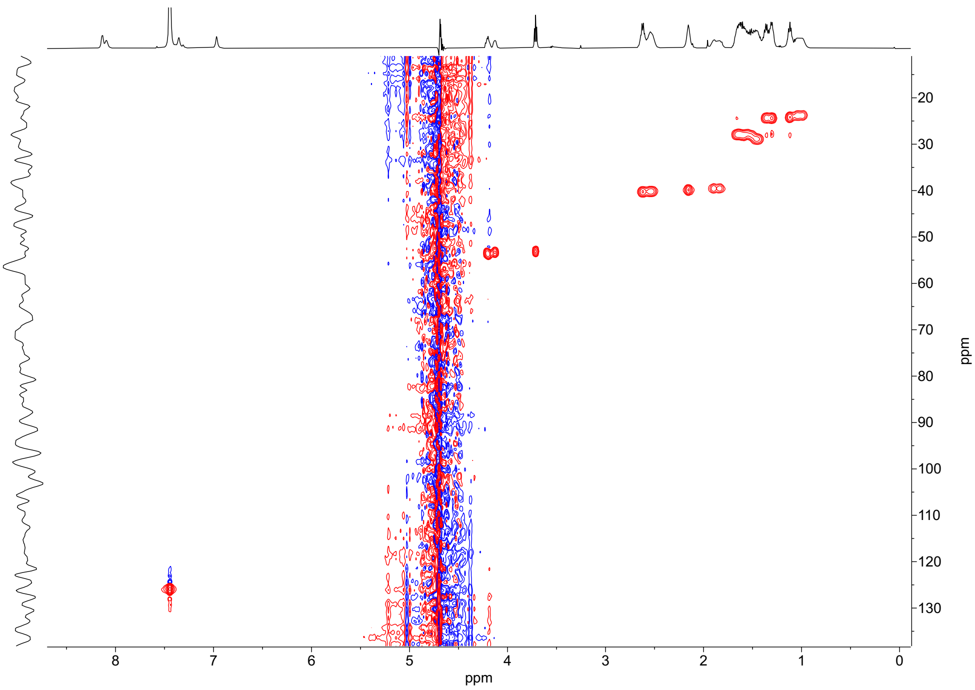

Figure A.22: ^{1}H-^{13}C-HSQC NMR spectrum of the peptide R_4 (0.59 mM) with 1.5 equivalents of SC4, obtained with natural abundancy ^{13}C. The spectrum was done in 10% D_2O:90% H_2O.

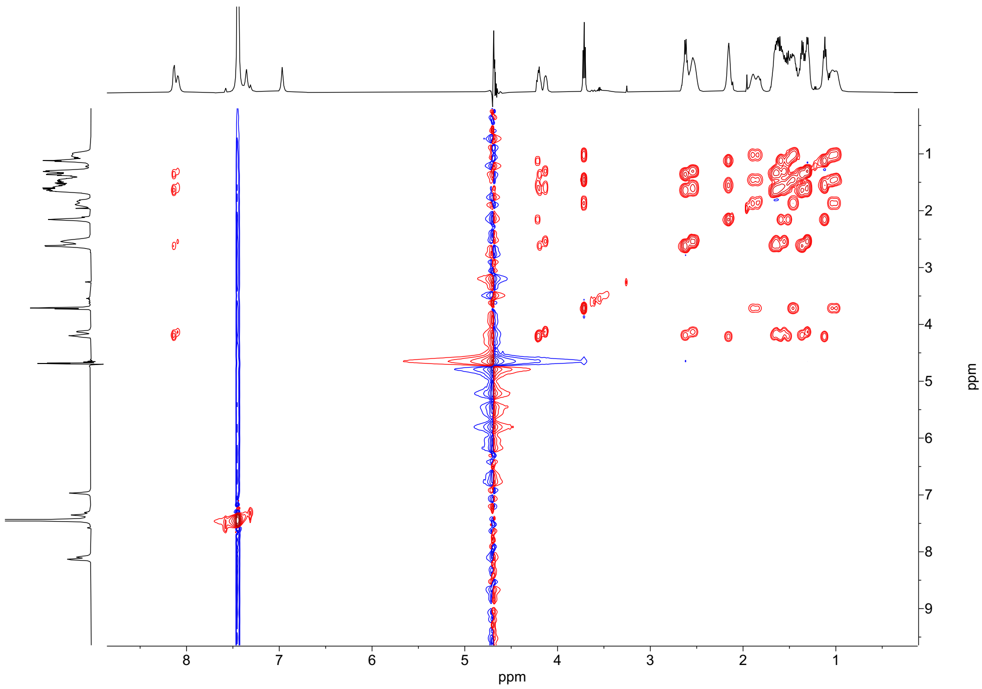

Figure A.23: ^{1}H-TOCSY NMR spectrum of the peptide R_4 (0.59 mM) with 1.5 equivalents of SC4. The spectrum was done in 10% D_2O:90% H_2O.

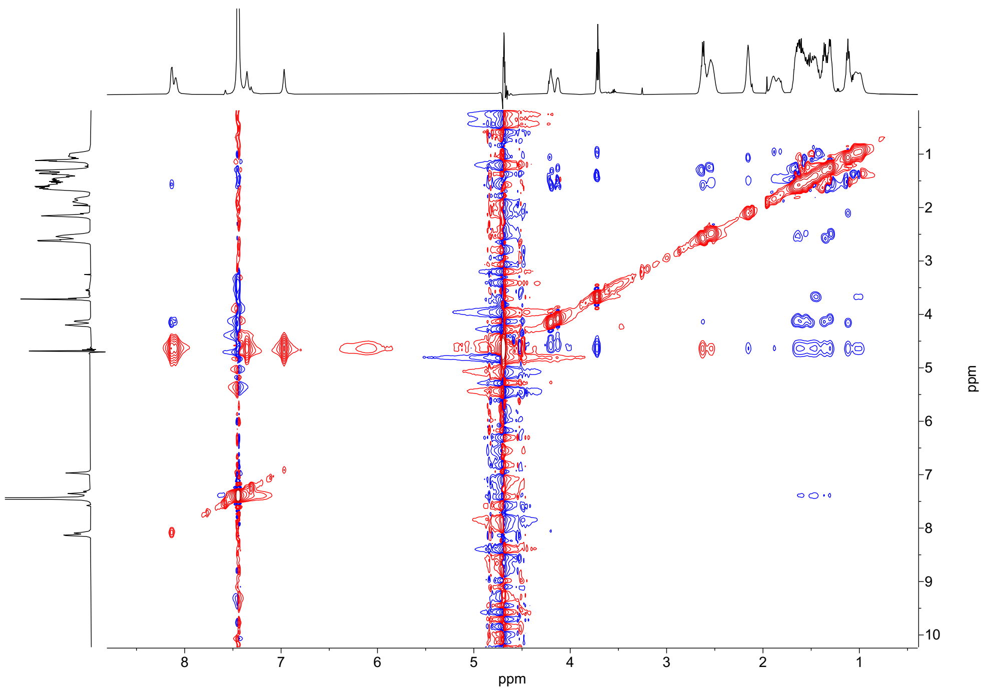

Figure A.24: ^{1}H-ROESY NMR spectrum of the peptide R_4 (0.59 mM) with 1.5 equivalents of SC4. The spectrum was done in 10% D_2O:90% H_2O.

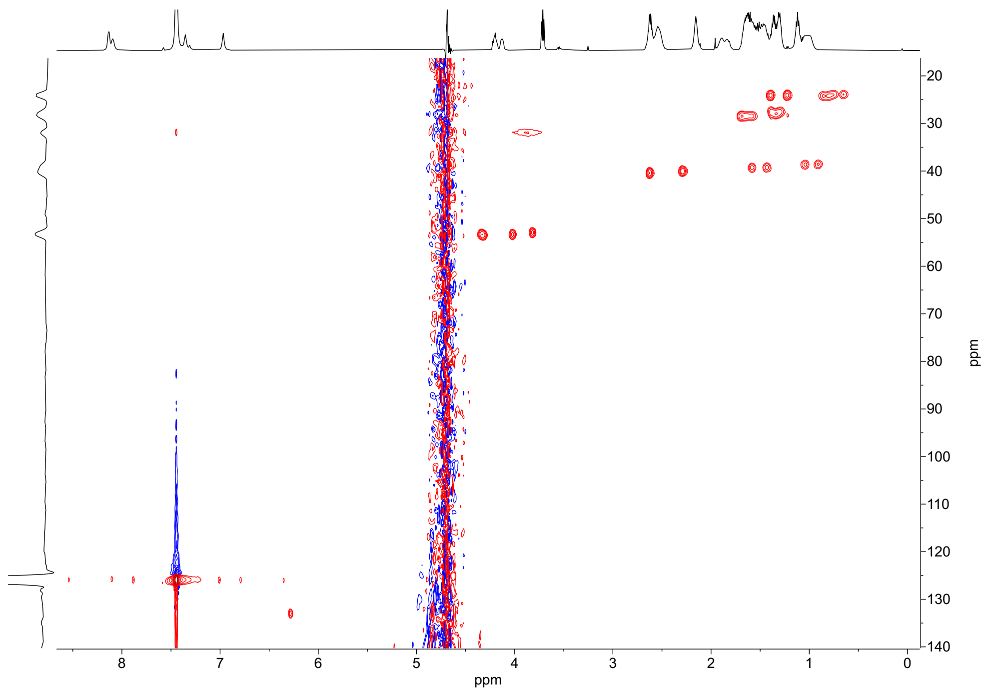

Figure A.25: ^{1}H-^{13}C-HSQC NMR spectrum of the peptide R_4 (0.59 mM) with 10 equivalents of SC4, obtained with natural abundancy ^{13}C. The spectrum was done in 10% D_2O:90% H_2O.

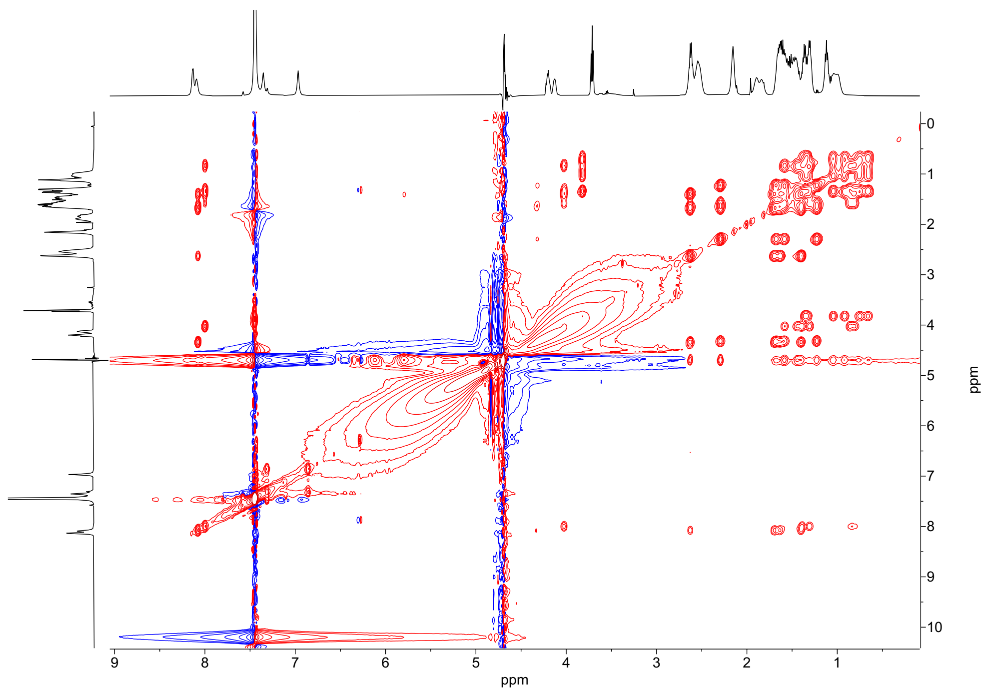

Figure A.26: ^{1}H-TOCSY NMR spectrum of the peptide R_4 (0.59 mM) with 10 equivalents of SC4. The spectrum was done in 10% D_2O:90% H_2O. Baseline correction was not fully successful due to interferance from broad free SC4 chemical shifts near the solvent peak.

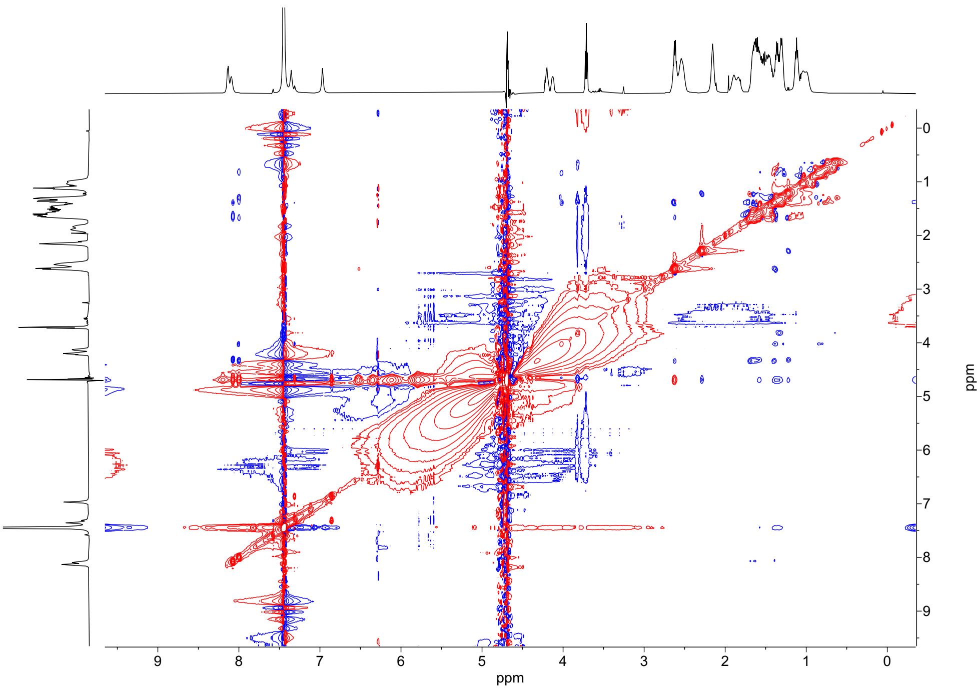

Figure A.27: ^{1}H-ROESY NMR spectrum of the peptide R_4 (0.59 mM) with 10 equivalents of SC4. The spectrum was done in 10% D_2O:90% H_2O. Baseline correction was not fully successful due to interferance from broad free SC4 chemical shifts near the solvent peak.

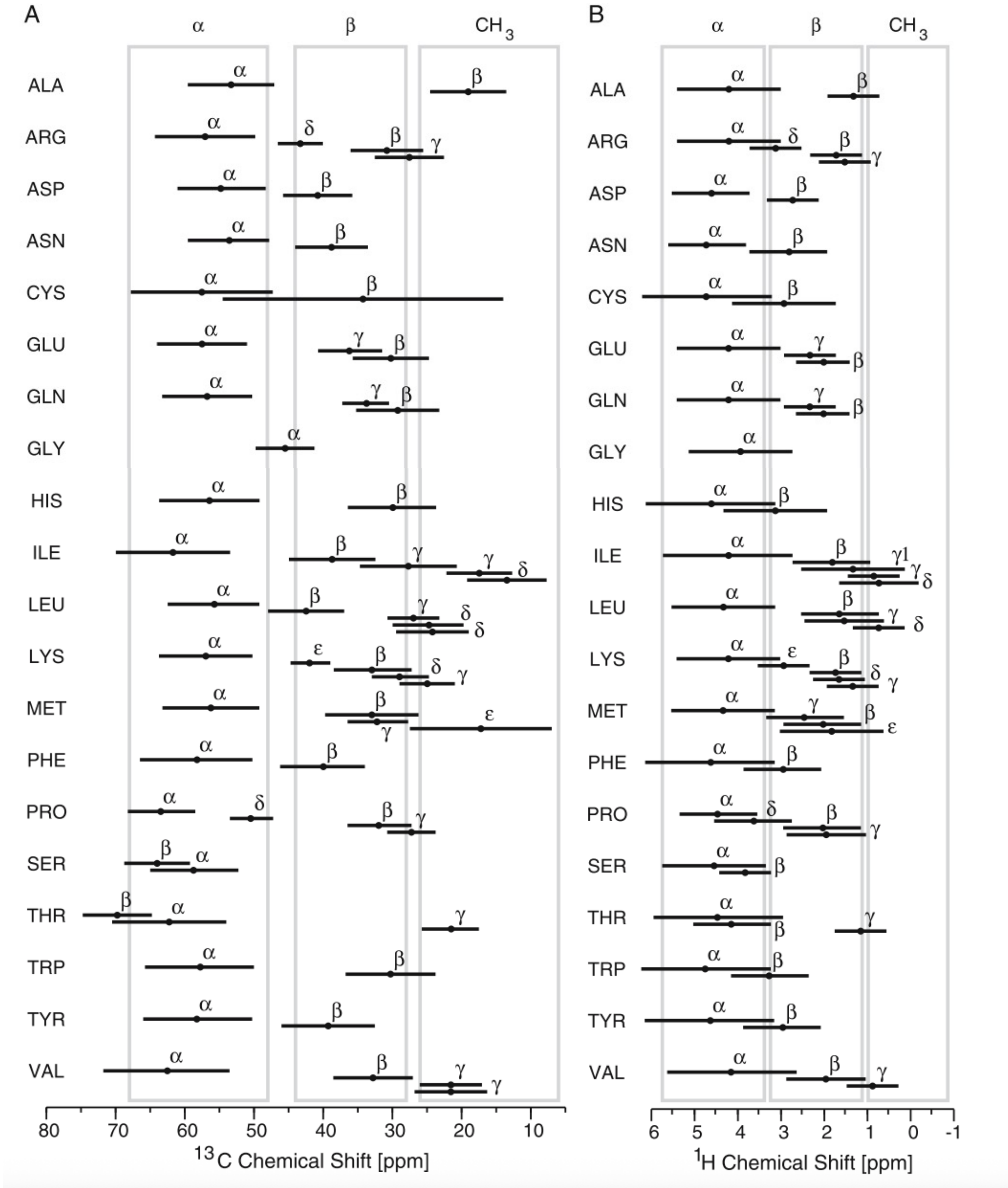

Figure A.28: The distribution of observed carbon (A, left) and proton (B, right) chemical shifts in proteins. The solid circles mark the average chemical shift. The solid lines indicate $\pm 3\delta$; 95% of the observed chemical shifts fall within this range. The gray boxes indicate nominal chemical shift ranges for α, β, and methyl atoms. In the case of carbon shifts, these ranges separate the atom types quite well. Note that there are a few exceptions, for example, the β-carbons of serine and threonin fall in the α-region and the α-carbon of Gly can fall in the β-carbon region. Data from the BioMagResBank database of chemical shifts.[311] Reproduced with permission from Rule, G. S., and Hitchens, T. K. (2003). *NMR Spectroscopy. In Fundamentals of Protein NMR Spectroscopy* (pp. 1–27). Springer-Verlag. Copyright 2003 Springer Nature.[217]

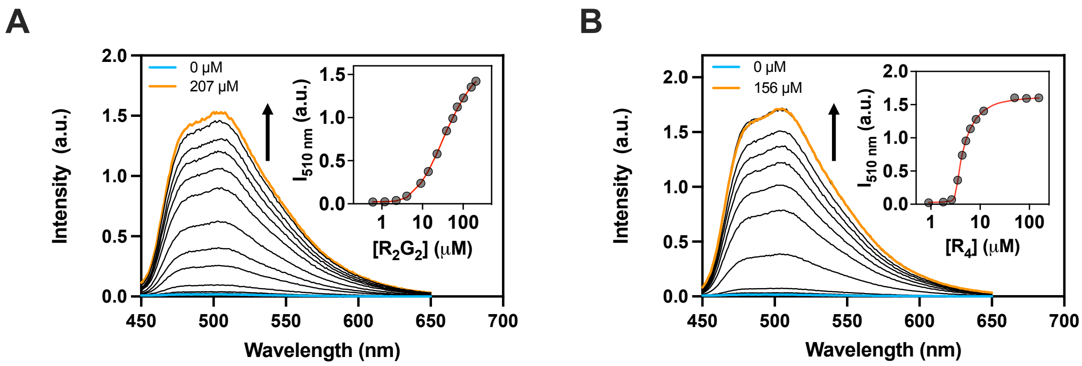

Figure A.29: Indicator displacement assays done with the SC4-LCG (3 and 0.1 μM, respectively) pair, followed by fluorescence spectroscopy (λ_{exc} = 369 nm) for quantification of the oligoarginines **A.** R_2G_2 and **B.** R_4 samples, used for NMR spectroscopy studies, yielding 0.22 mM and 0.59 mM.

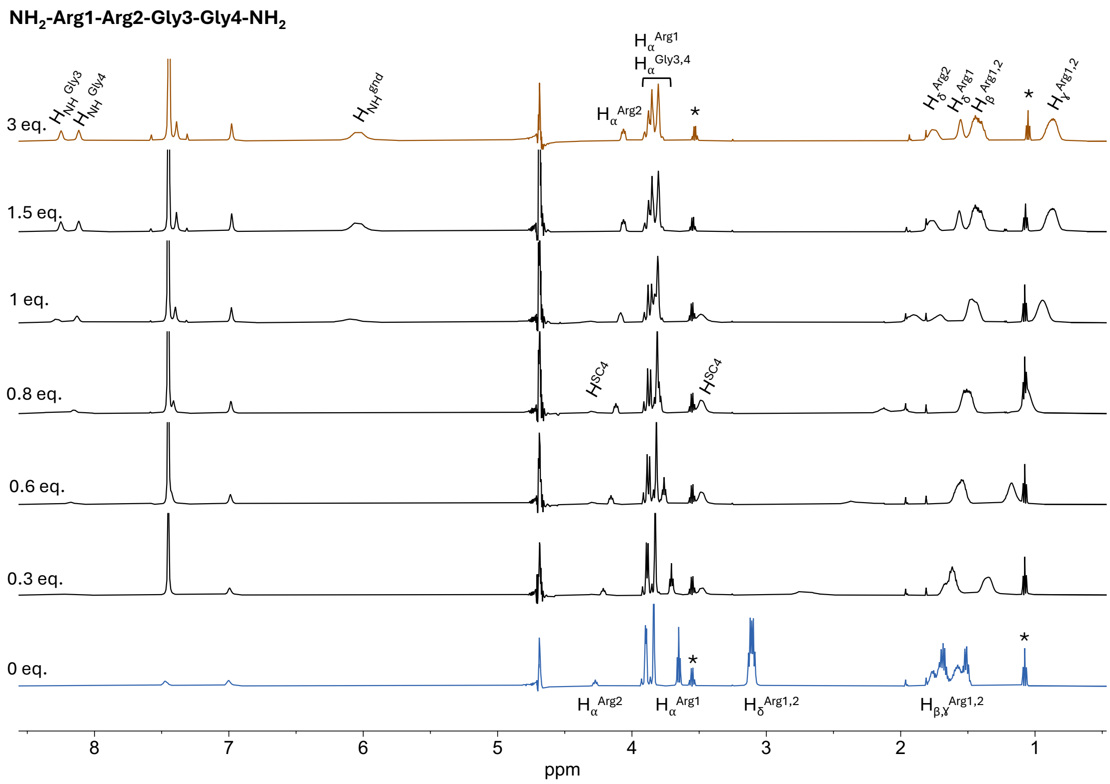

Figure A.30: Titration of peptide R_2G_2 (0.22 mM, quantified by LCG-SC4 IDA, Figure A.29) with SC4 followed by ^{1}H-NMR spectroscopy.

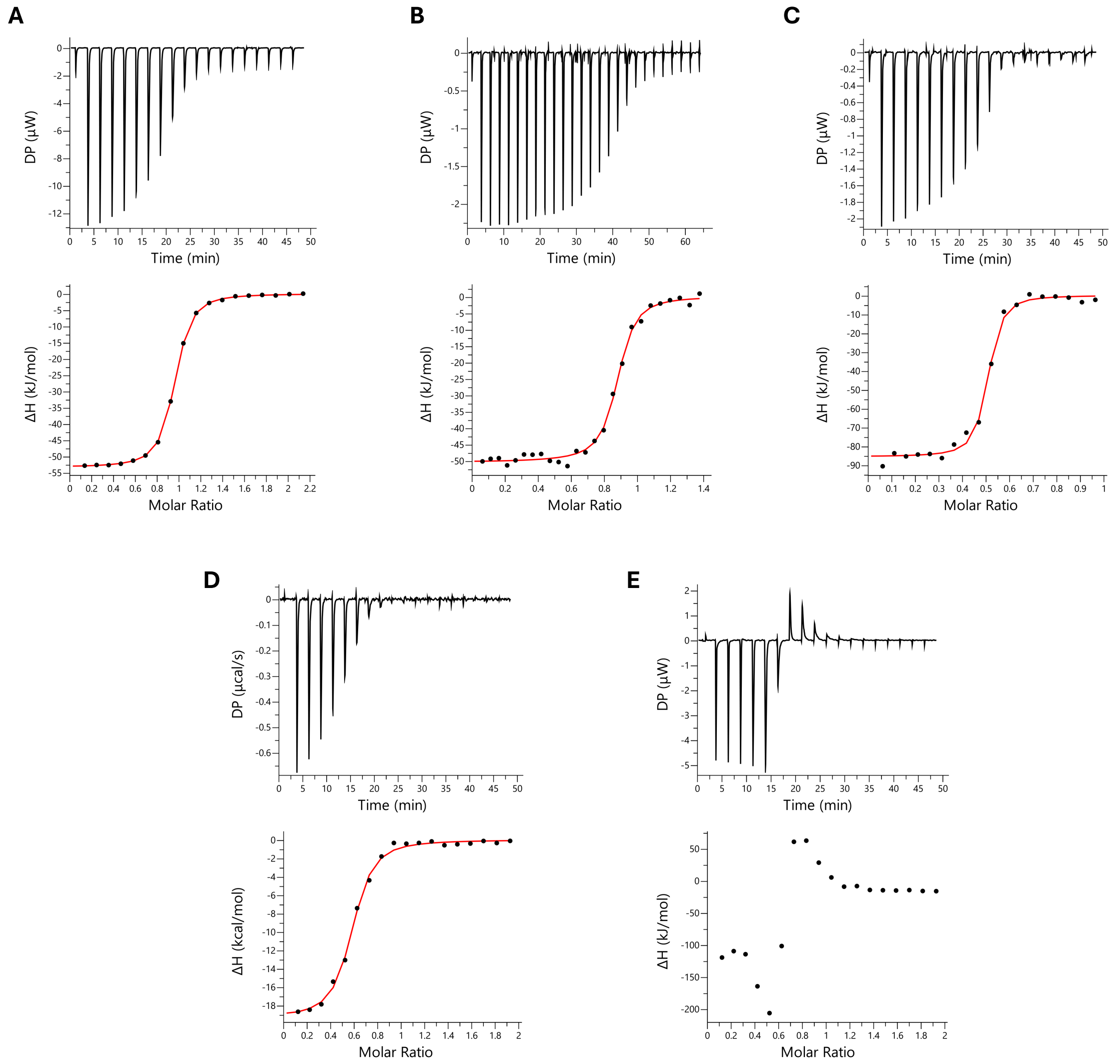

Figure A.31: ITC isotherms of the titrations of host SC4 with the different oligoarginines, at 25°C: **A.** R_2G_2 (100 μM SC4 and 1.14 mM peptide), **B.** R_3G (35 μM SC4 and 175 μM peptide), **C.** R_4 (20 μM SC4 and 200 μM peptide), **D.** R_6 (20 μM SC4 and 200 μM peptide), **E.** R_8 (20 μM SC4 and 200 μM peptide).

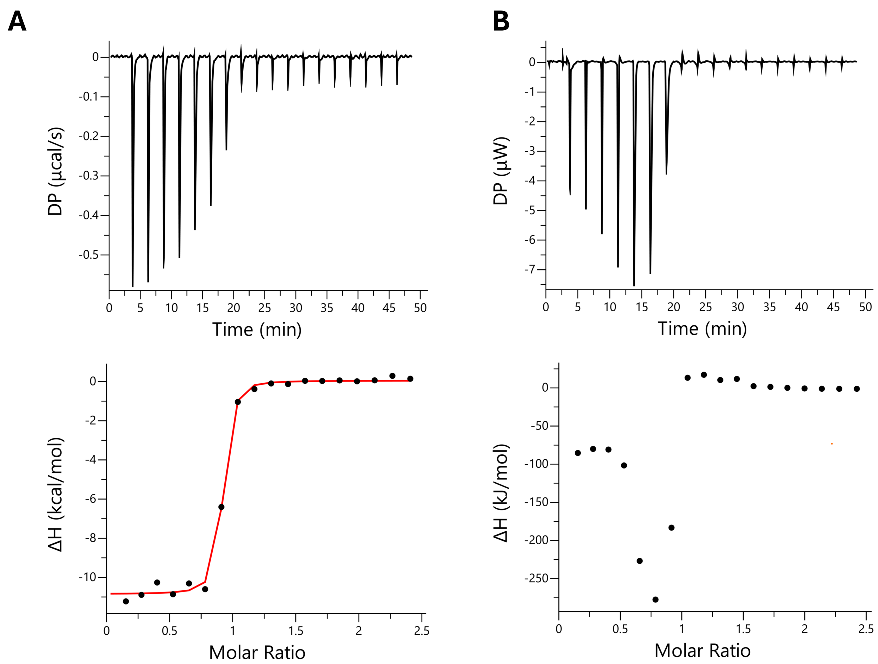

Figure A.32: ITC isotherms of the titrations of **A.** R_4 (20 μM) and **B.** R_8 (16 μM) with the host SC4 (200 μM), at 25°C.

B

Supplementary Information for Chapter 3

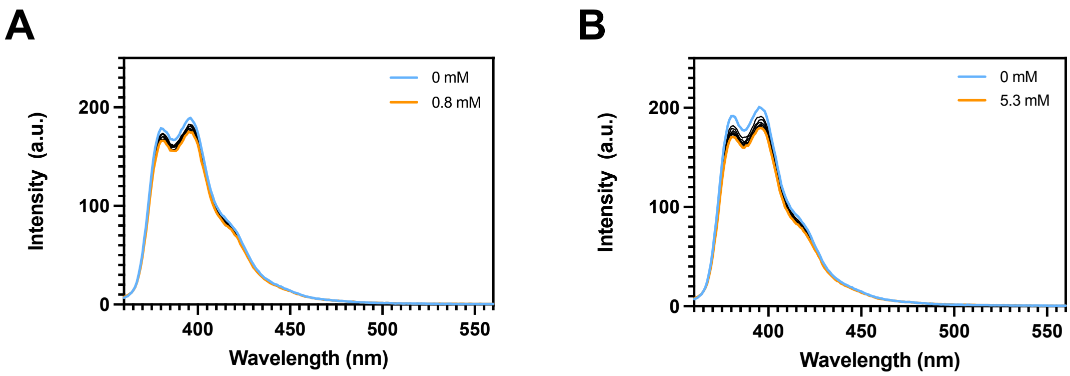

Figure B.1: Direct titration of SC4-4Py with the sodium salts of the counterions of the several analytes studied: **A.** NaI; **B.** NaCl, followed by fluorescence spectroscopy (λ_{exc} = 340 nm). No significant quenching of pyrene emission was observed.

Table B.1: Stern-Volmer constants (K_{SV} / M^{-1}) of Lucigenin (LCG) quenching by the counterions of the several analytes studied.

Analyte	**Counterion**	**K_{SV} / M^{-1}**
L-Arginine	Cl^-	300
Choline	Cl^-	290
Acetylcholine	Cl^-	350
Putrescine	2 Cl^-	690
DM-DABCO	I^-	540

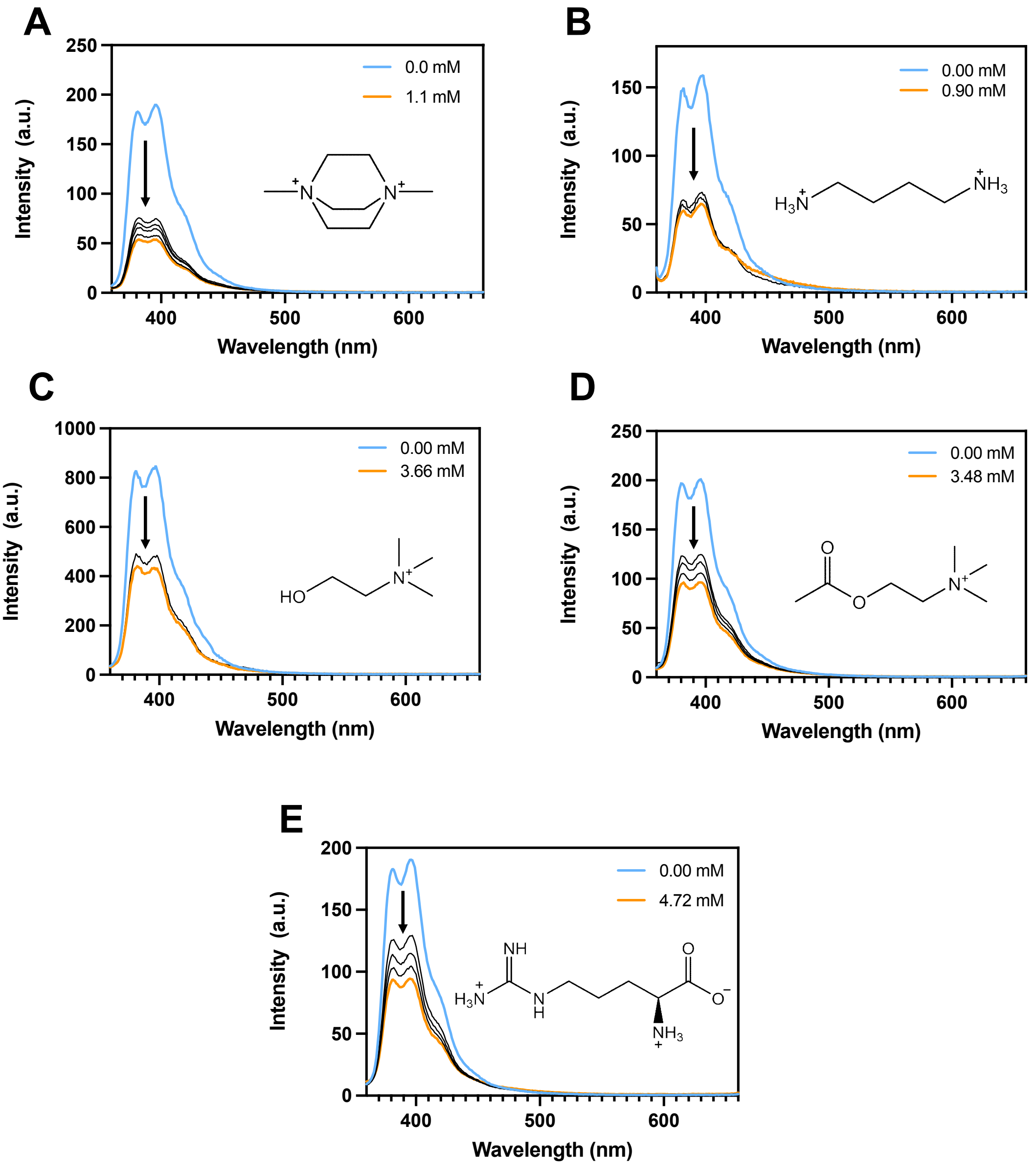

Figure B.2: Fluorescence spectra (λ_{exc} = 340 nm) of SC4-4Py (2 μM) with an excess of the different analytes studied: **A.** DM-DABCO; **B.** Putrescine; **C.** Choline; **D.** Acetylcholine and **E.** L-Arginine. No aggregation was detected for any of the analytes in the concentration used in the displacement assays, even though Putrescine does show potential pre-aggregates near 500 equivalents, by the slight increase in emission at ≈ 460 nm.

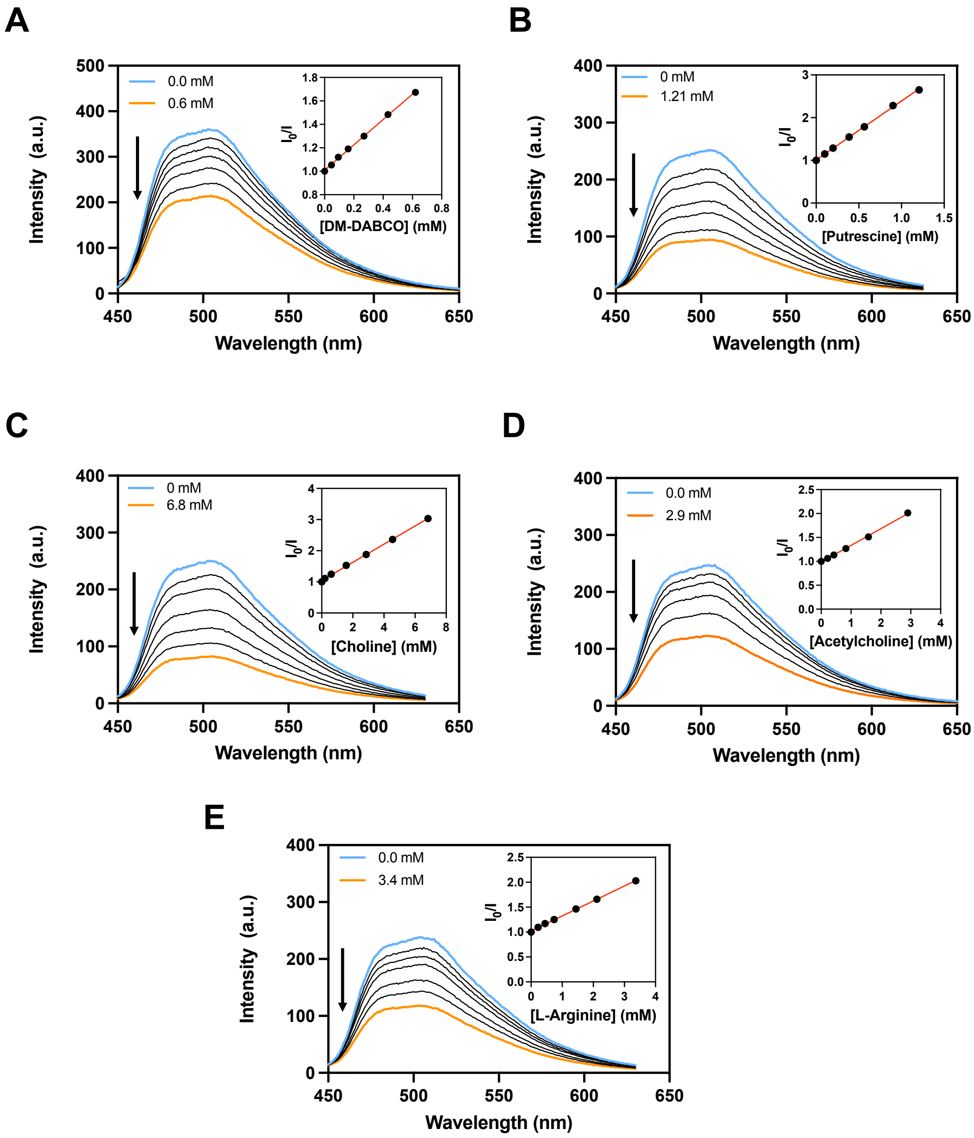

Figure B.3: Direct titrations of LCG (0.5 μM) with the different analytes studied: **A.** DM-DABCO; **B.** Putrescine; **C.** Choline; **D.** Acetylcholine and **E.** L-Arginine, followed by fluorescence spectroscopy (λ_{exc} = 340 nm). These analytes have the anionic counterions of Iodine for DM-DABCO and Chloride for the remainder analytes and the concentration of the quencher species was adjusted according to stoichiometry of counterions. All Stern-Volmer (SV) linearizations are presented in the insets and the K_{SV} obtained by fitting of the data to this linearization are presented in Table B.1.

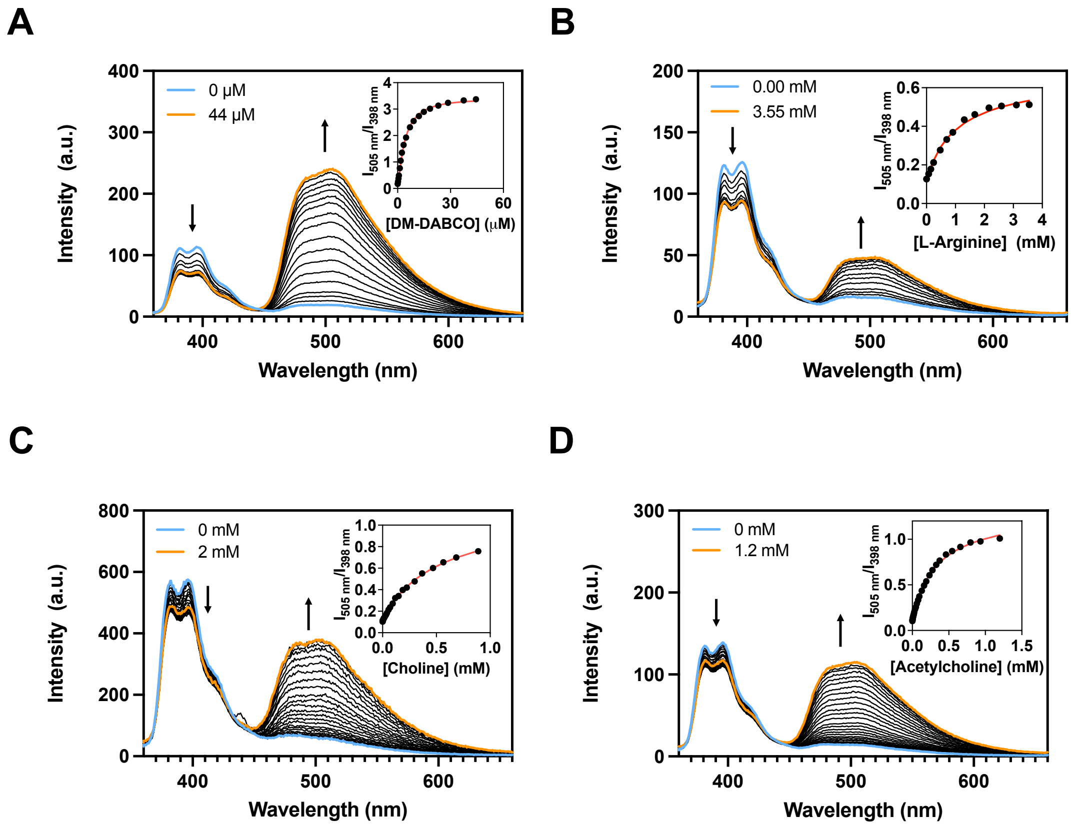

Figure B.4: Ratiometric IDA of **A.** DM-DABCO, **B.** L-Arginine, **C.** Choline and **D.** Acetylcholine with the system SC4-4Py-LCG. The fitting of the ratio between LCG emission, at 505 nm, and SC4-4Py emission, at 398 nm (λ_{exc} = 340 nm), can be found in the insets and respective affinity constants obtained for each guest in Table 3.1

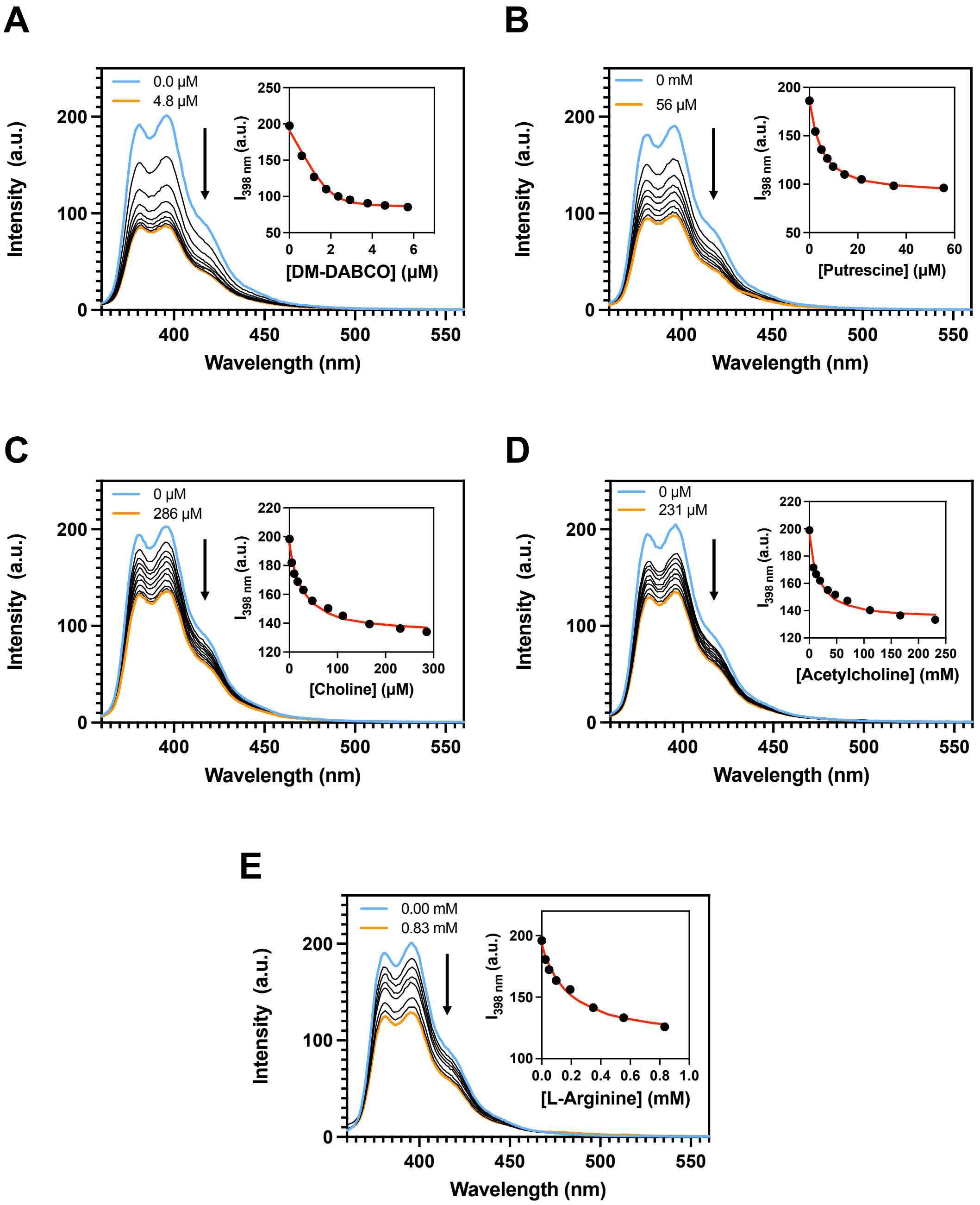

Figure B.5: Direct titration of SC4-4Py (2 μM) with the analytes studied: **A.** DM-DABCO, **B.** Putrescine, **C.** Choline, **D.** Acetylcholine and **E.** L-Arginine, followed by fluorescence spectroscopy (λ_{exc} = 340 nm).

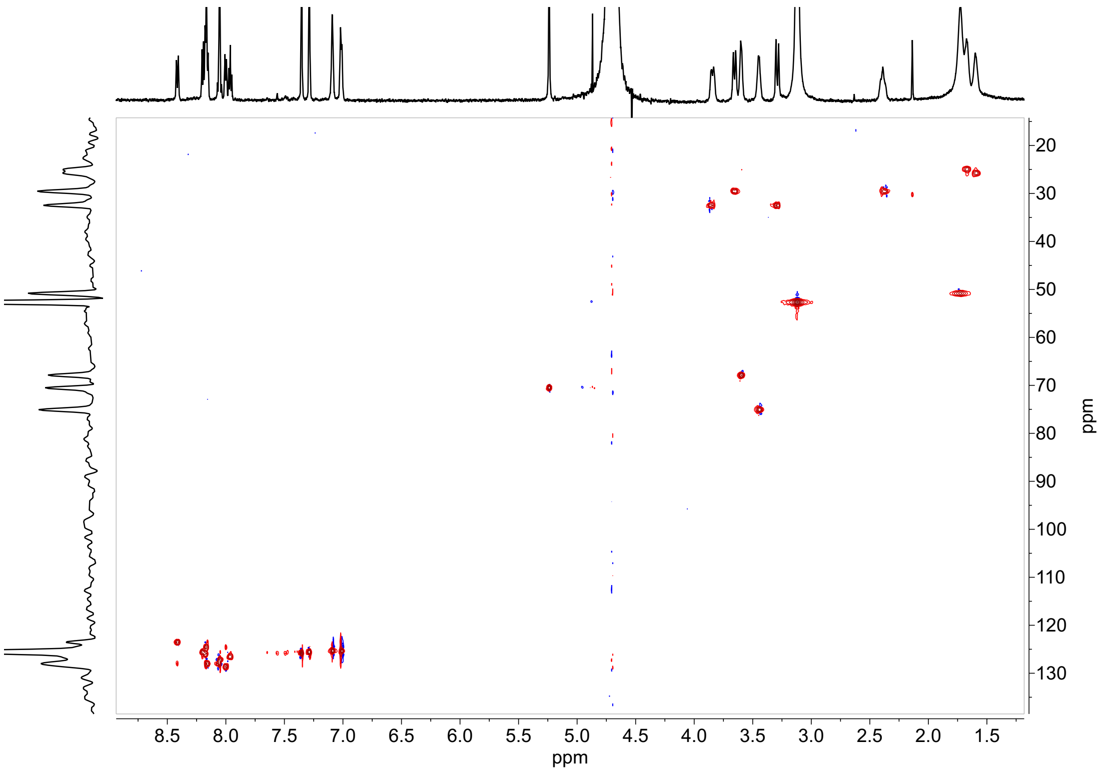

Figure B.6: ^{1}H-^{13}C-HSQC NMR spectrum of SC4-4Py (0.5 mM) and DM-DABCO (0.67 mM) in D_2O pD 7.

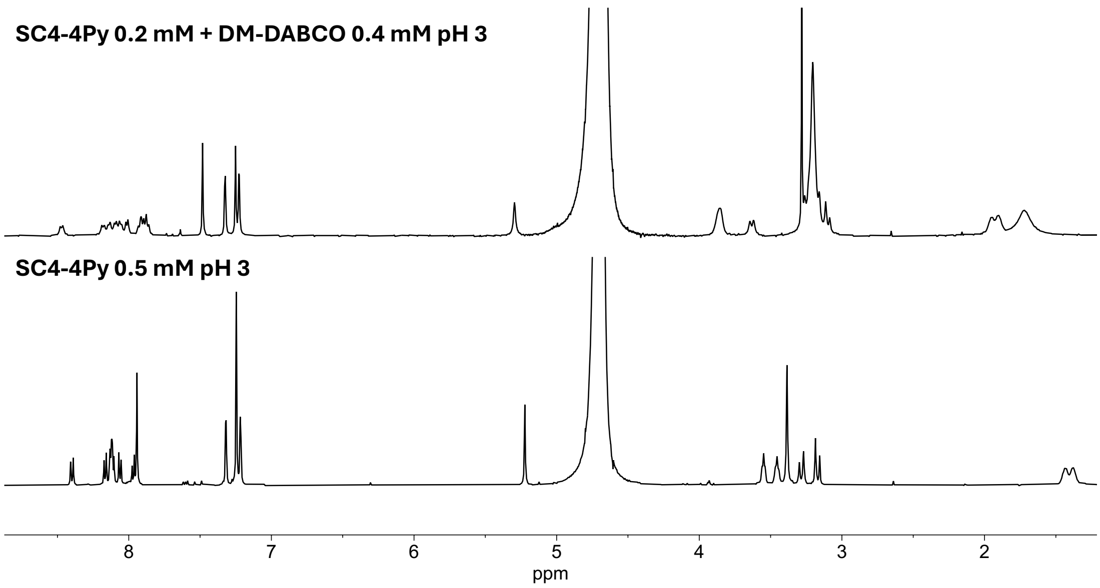

Figure B.7: ^{1}H-NMR spectra of SC4-4Py (0.5 mM) and SC4-4Py-DM-DABCO complex (0.2 and 0.4 mM, respectively) in D_2O pD 3.

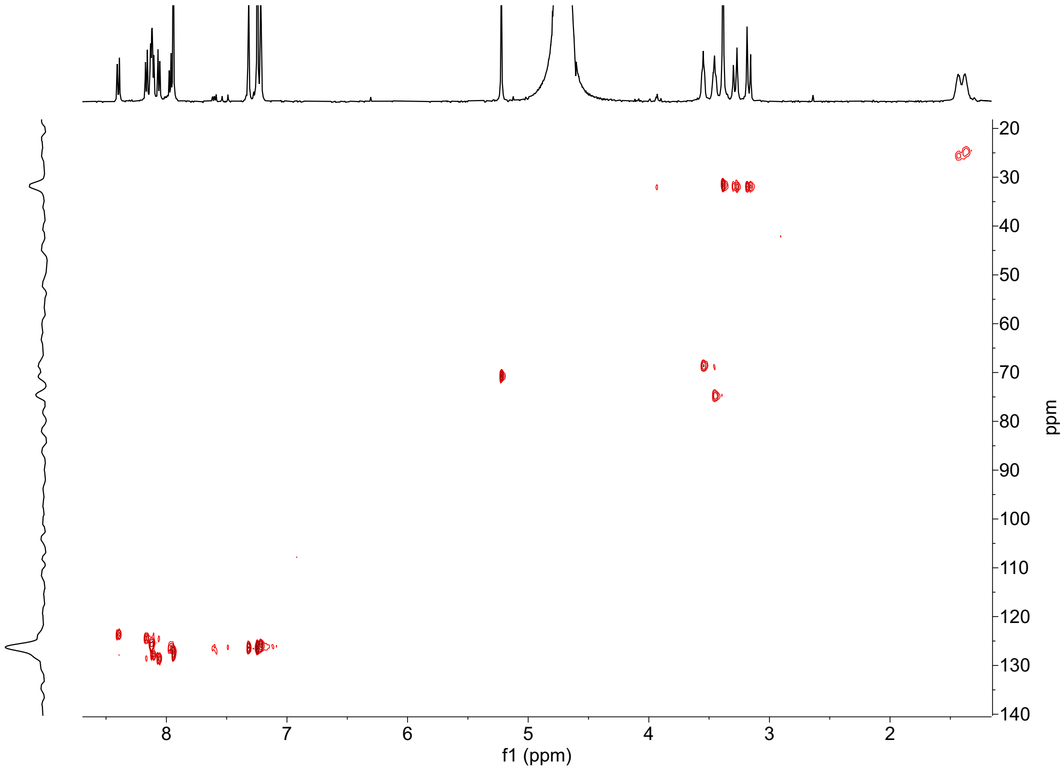

Figure B.8: ^{1}H-^{13}C-HSQC NMR spectrum of SC4-4Py (0.5 mM) in D_2O at pD 3.

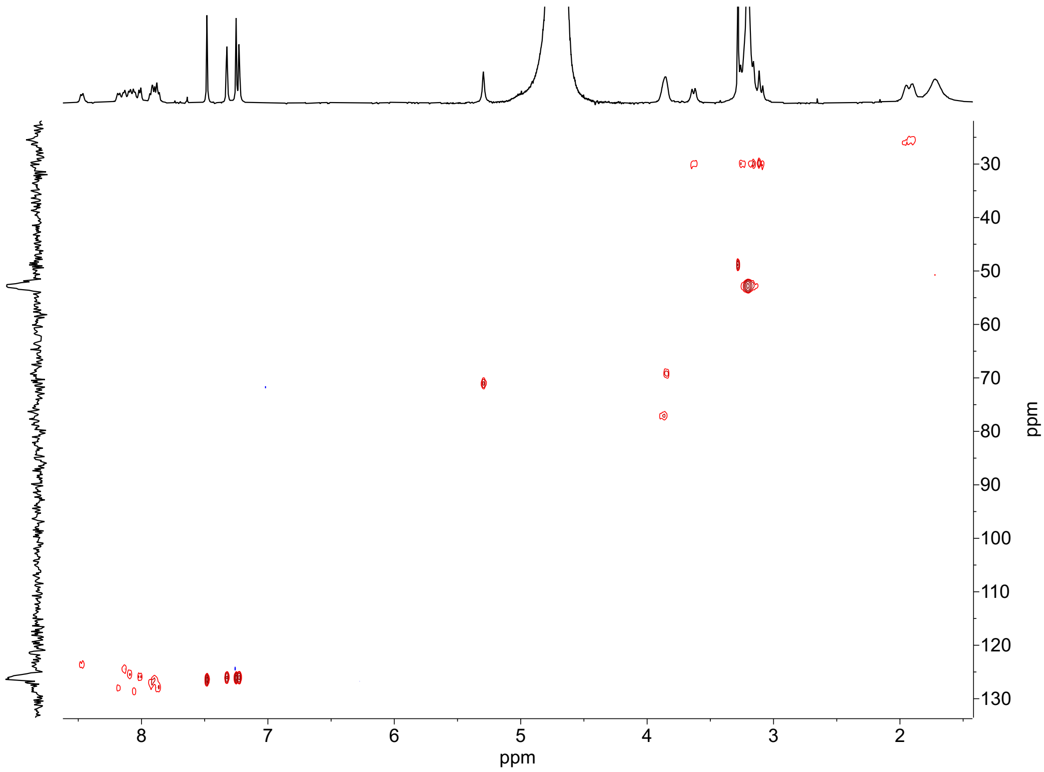

Figure B.9: ^{1}H-^{13}C-HSQC NMR spectrum of SC4-4Py-DM-DABCO complex (0.2 and 0.4 mM, respectively) in D_2O at pD 3.

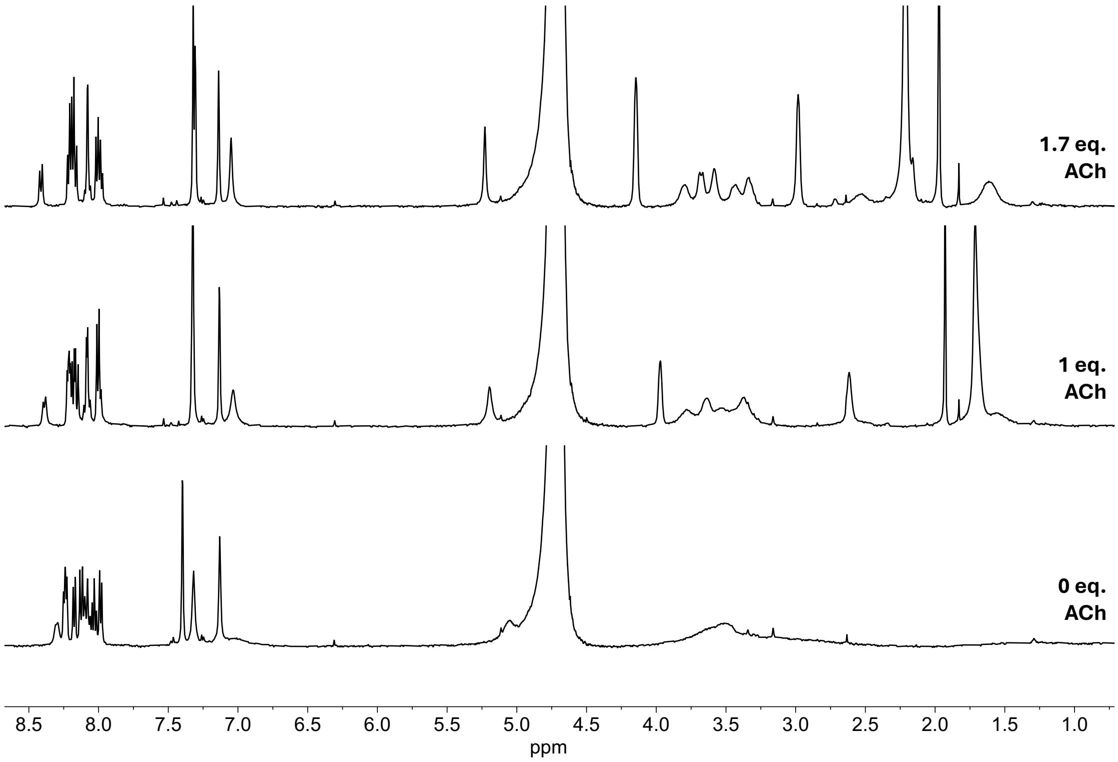

Figure B.10: ^{1}H-NMR spectra of SC4-4Py (0.5 mM) in the absence of Acetylcholine (ACh) and in the presence of 1 and 1.7 equivalents of this analyte in D_2O at pD 7.

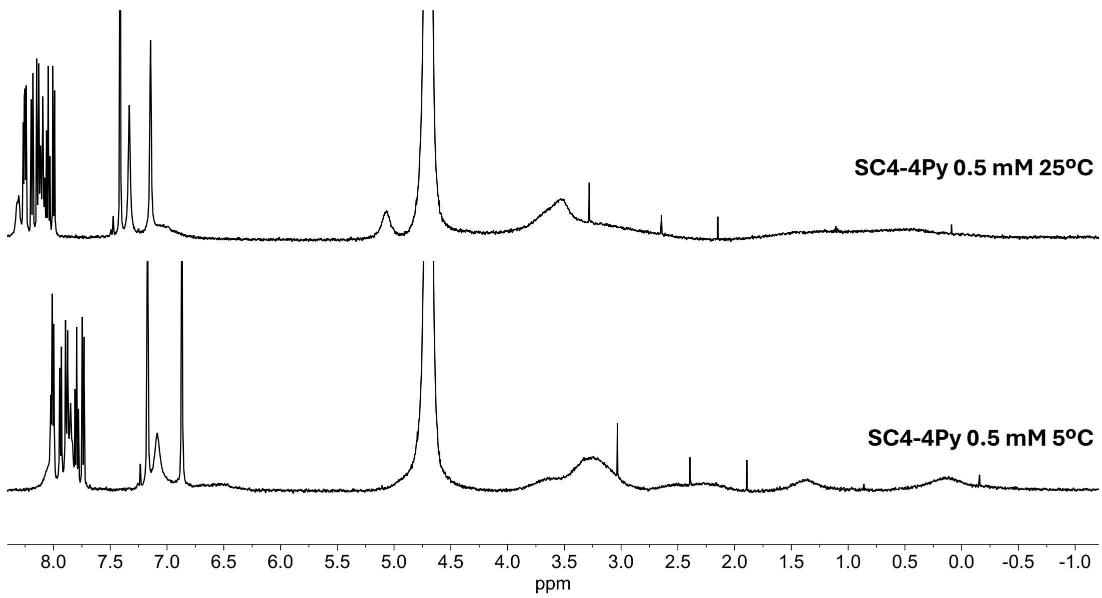

Figure B.11: ^{1}H-NMR spectra of SC4-4Py (0.5 mM) at 25 and 5℃ in D_2O at pD 7, with slight sharpening of SC4 chemical shifts particularly noticeable between 0 and 4 ppm.

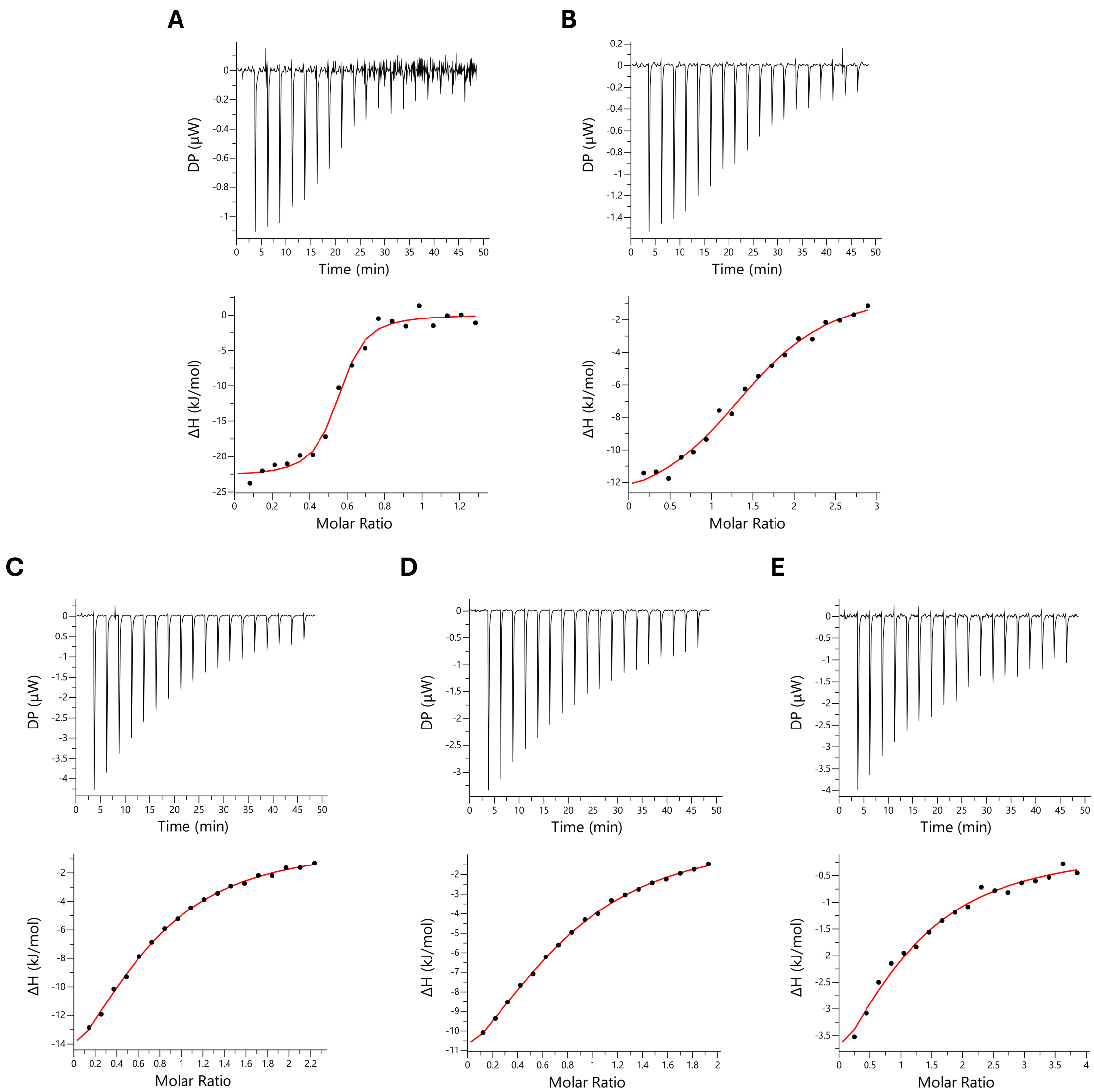

Figure B.12: ITC isotherms of the titration of SC4-4Py with **A.** DM-DABCO, **B.** Putrescine, **C.** Acetylcholine, **D.** Choline and **E.** L-Arginine. Concentration of SC4-4Py was fixed at **A.** 30, **B.** 40, **C.** and **D.** 150 and **E.** 200 μM, obtained at 25°C. The number of sites obtained for each titration was of **A.** 0.66, **B.** 1.52, **C.** 0.65 and **D.** 0.74. To be able to fit the Arg data the number of sites needed to be fixed at 1. The deviations from 1:1 binding appear to be caused by small errors in concentration of analyte stock solutions due to their highly higroscopic nature. Only Putrescine showed a deviation to this trend, likely due to the difficult manipulation of this compound, so errors in measuring mass are likely the cause of this difference.

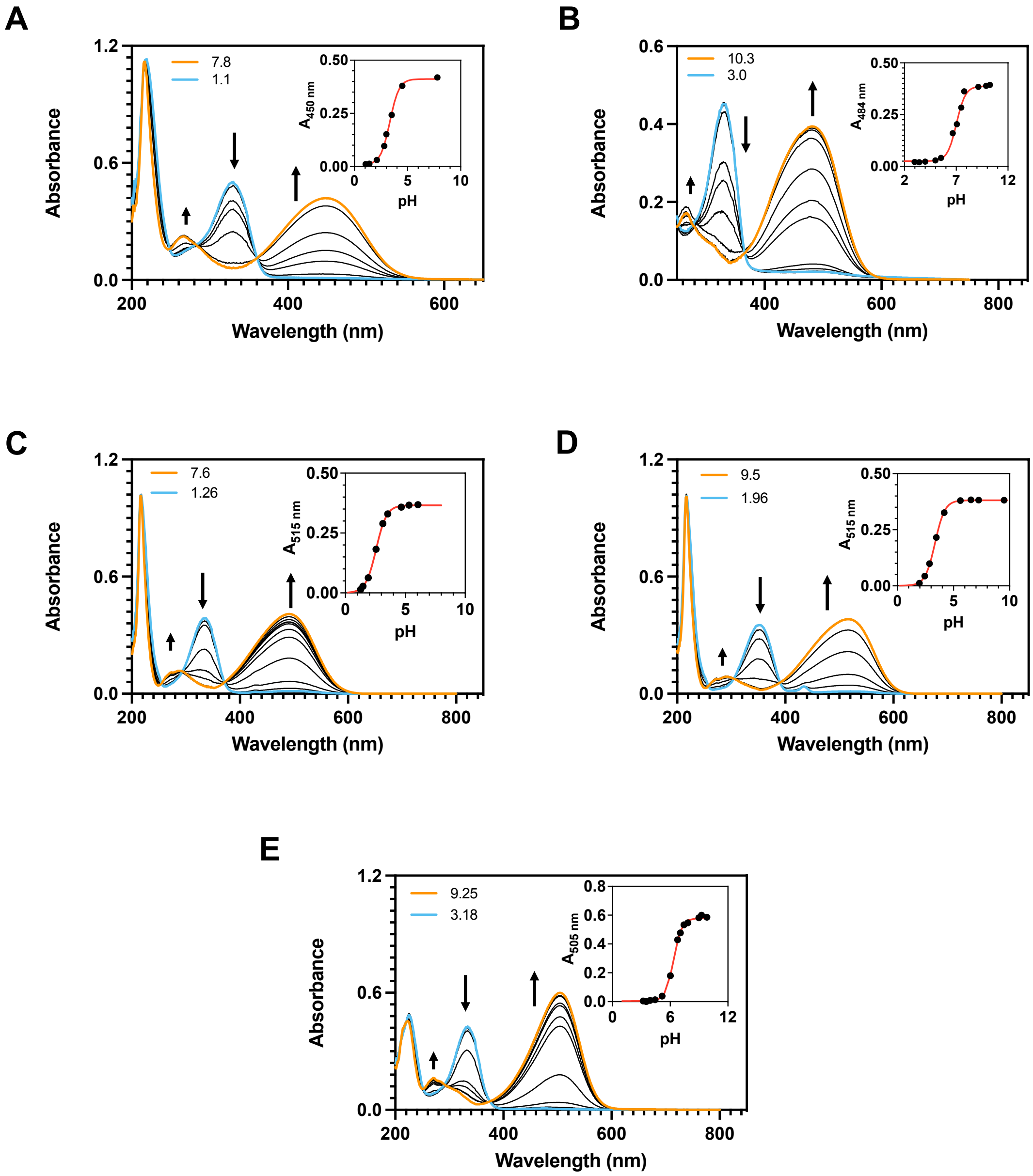

Figure B.13: UV-Visible spectroscopy of the dyes at different pH, in the presence and absence of CB7: **A.** Me-DASPI , **B.** Me-DASPI-CB7, **C.** Jd-DASPI , **D.** Jd-DASPI-CB7 and **E.** Et-DASPI-CB7, with respective fitting to the Henderson–Hasselbalch equation using the λ_{max} of absorption for each dye and dye-CB7 pair, for the lowest energy absorption band of the mono-cationic dye species.[312]

Table B.2: pK_a values of the different DASPI dyes and respective CB7-DASPI complexes. The pK_a shift between bound and unbound dyes is also presented, with a maximum of 3.69 for the dye with dimethylamine and 0.79 with julolidine in the aniline moiety.

Dye	**pK_a**		**pK_a shift**
	Free Dye	**CB7:Dye**	
Me-DASPI	3.33	7.02	3.69
Et-DASPI	4.28[229]	6.36	2.08
Jd-DASPI	2.56	3.35	0.79

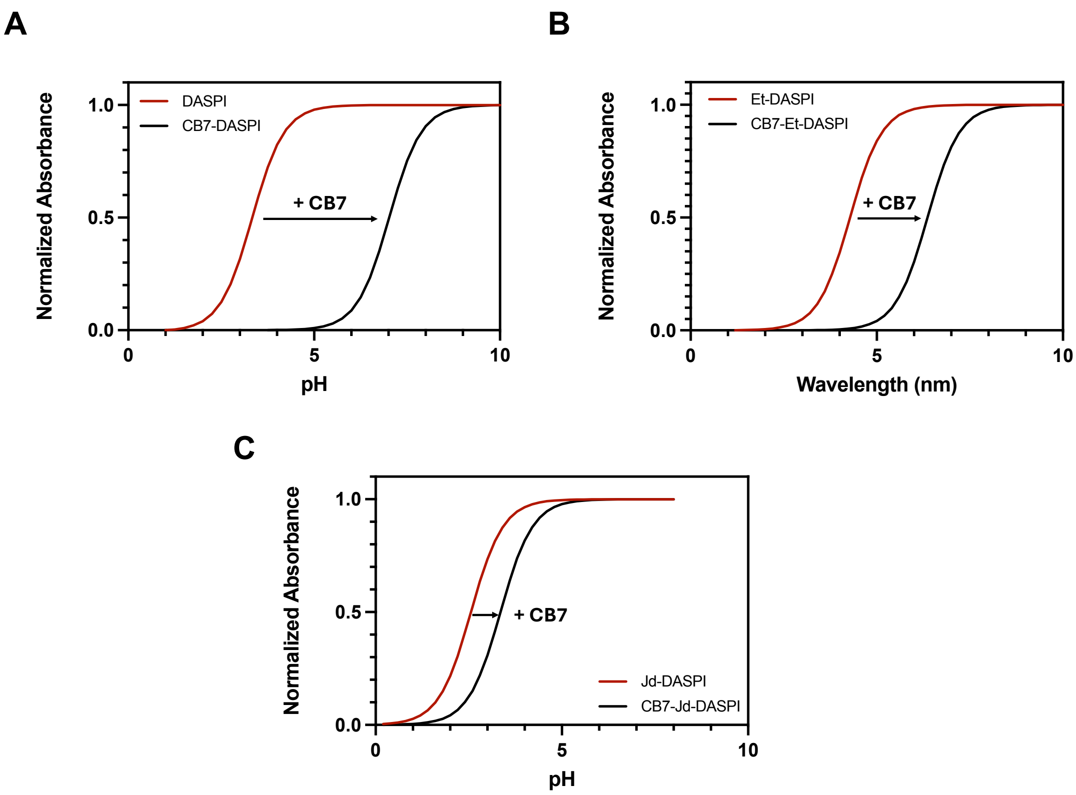

Figure B.14: pK_a comparison between the free dyes, **A.** Me-DASPI, **B.** Et-DASPI and **C.** Jd-DASPI and respective complex with CB7.

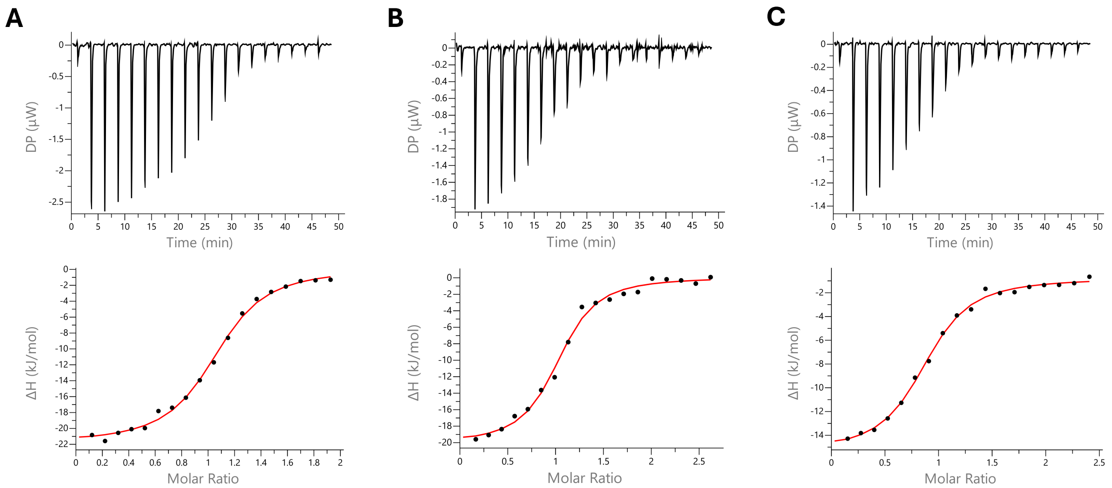

Figure B.15: ITC isotherms for the binding of the dyes (50 μM) **A.** Me-DASPI, **B.** Et-DASPI and **C.** Jd-DASPI with the host CB7 (in syringe, 500 μM), at 25°C.

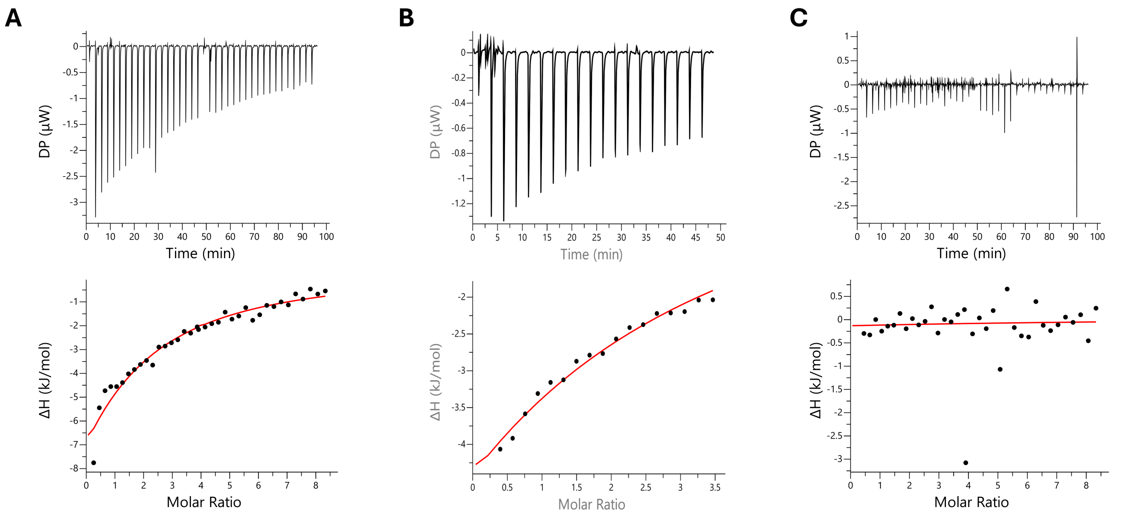

Figure B.16: ITC isotherms for the binding of the dyes **A.** Me-DASPI, **B.** Et-DASPI and **C.** Jd-DASPI with the host BB, at 25°C. For Me and Jd-DASPI the concentration was fixed at 100 μM for the dyes and 2 mM for BB while for Et-DASPI the dye was added, in the syringe, at 2 mM, to BB in the cell at 100 μM.

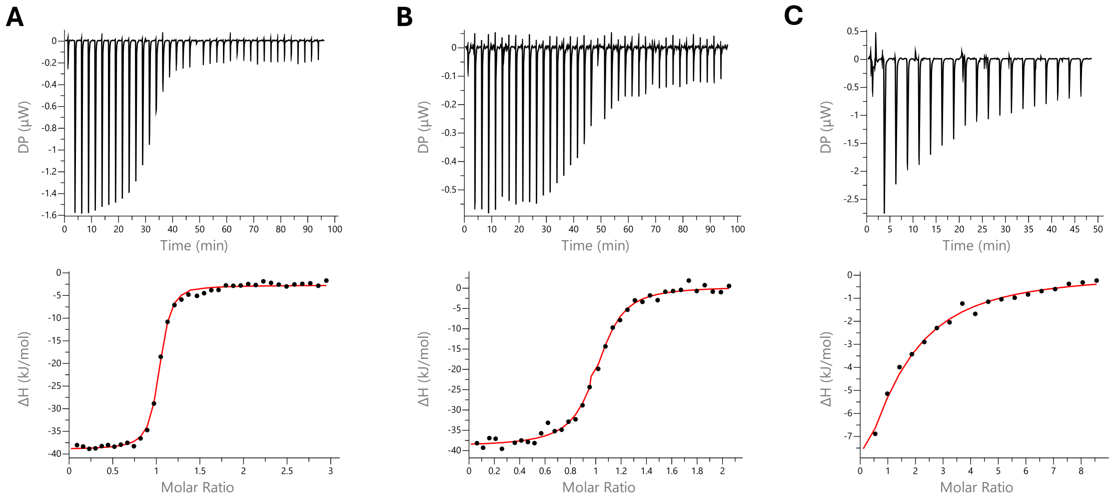

Figure B.17: ITC isotherms for the binding of BB to the 1:1 CB7 complexes with the dyes **A.** Me-DASPI (25 μM of CB7 and dye), **B.** Et-DASPI (15 μM of CB7 and dye) and **C.** Jd-DASPI (50 μM of CB7 and dye) with the host BB, at 25°C. This host was added in the syring with concentrations of A. 500 μM, B. 60 μM and C. 2 mM.

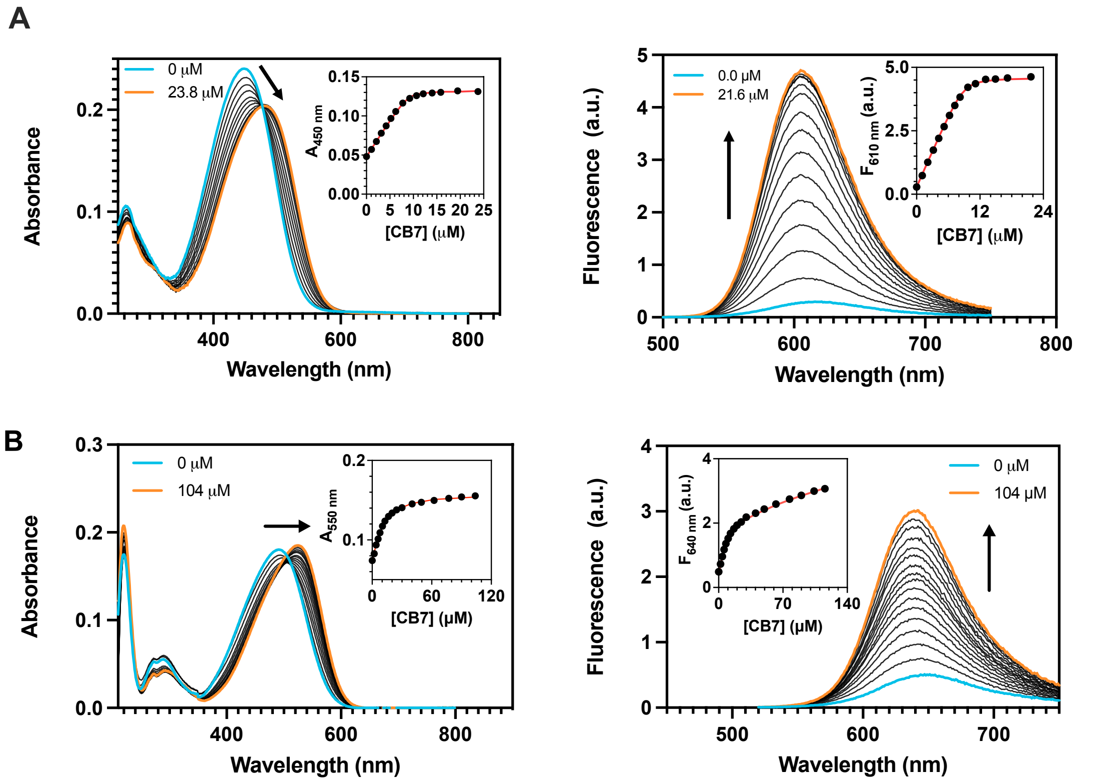

Figure B.18: **A.** Titration of the Me-DASPI with CB7 followed by UV-vis (left) and fluorescence spectroscopies (right, λ_{exc} = 517 nm). The concentration of dye was fixed at 9 μM for both techniques. **B.** Titration of Jd-DASPI with CB7 followed by UV-vis (left) and fluorescence spectroscopies (right, λ_{exc} = 505 nm). The concentration of dye was fixed at 7.6 μM, for both UV-vis and fluorescence spectroscopy studies. Fitting of the experimental data was done using the 1 to 1 model for Me-DASPI and using the 2 to 1 model for Jd-DASPI (see Annex I) and can be found in inset.

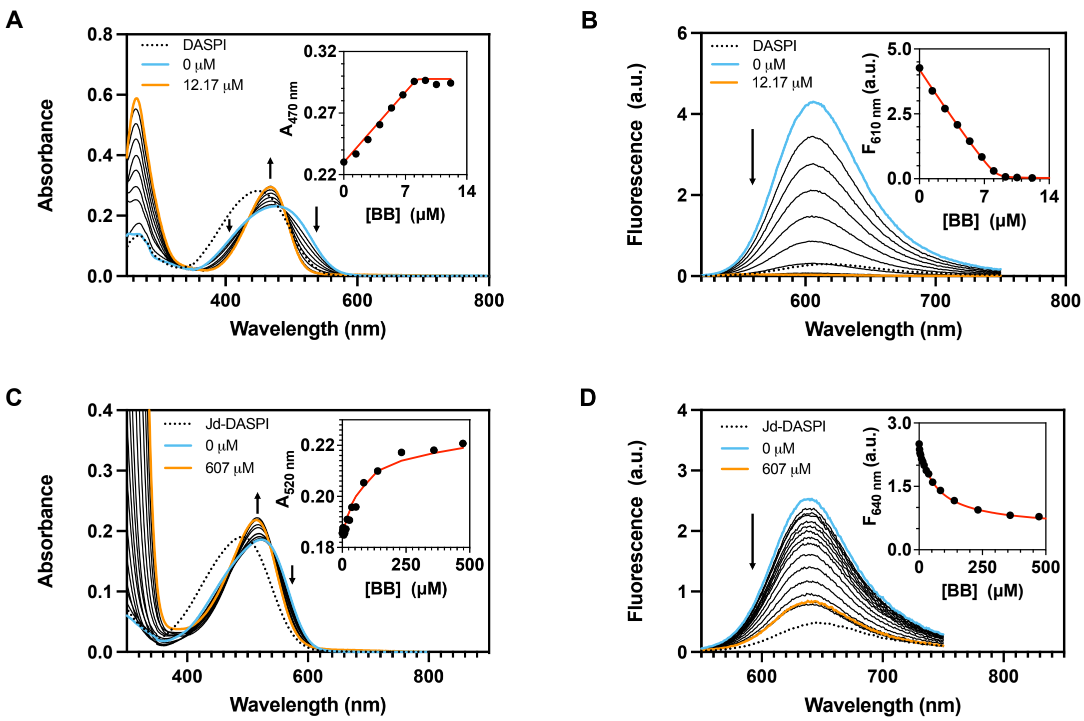

Figure B.19: Titration of the Me-DASPI-CB7 complex with BB followed by **A.** UV-vis and **B.** fluorescence spectroscopies (λ_{exc} = 468 nm). The concentration of dye and CB7 were fixed at, respectively, 8.3 μM and 15 μM, for both techniques. Titration of Jd-DASPI-CB7 complex with BB followed by **C.** UV-vis and **D.** fluorescence spectroscopies (λ_{exc} = 530 nm). The concentration of dye and CB7 were fixed at, respectively, 7.6 and 45.6 μM, for UV-vis studies and at 8 and 48 μM for fluorescence assays. Fitting of the experimental data to each of the ternary complex model presented in Annex I can be found in inset.

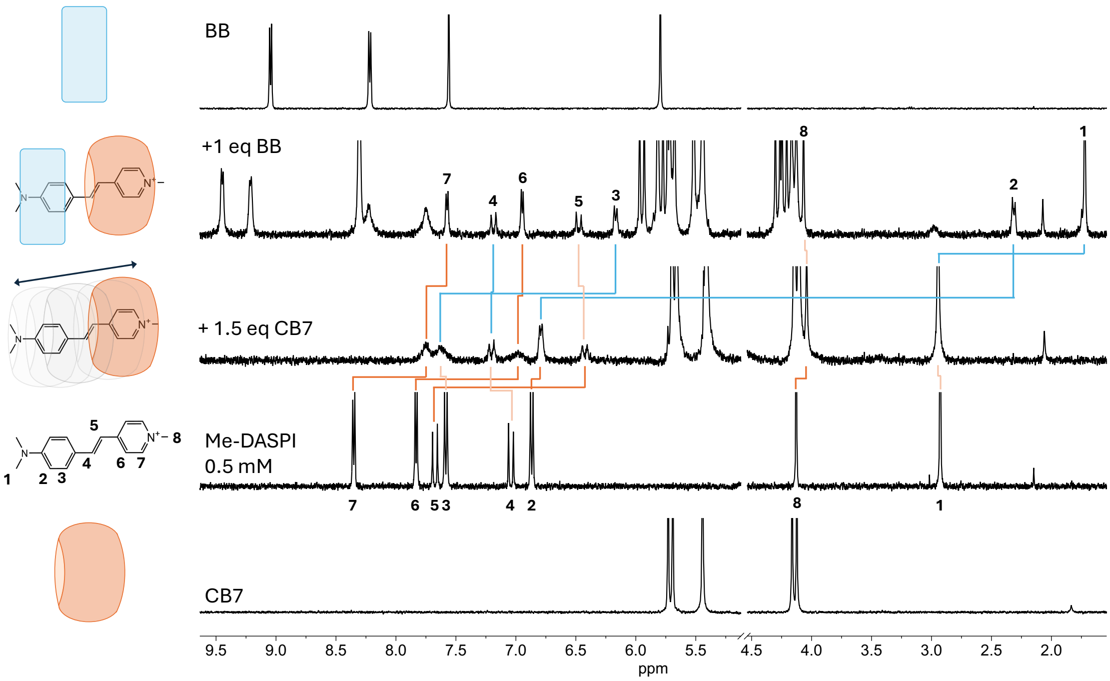

Figure B.20: ^{1}H-NMR spectra of CB7, Me-DASPI, of the CB7-Me-DASPI and CB7-Me-DASPI-BB complexes and BB in D_2O pD 8 and respective expected structures based on the assigned Me-DASPI proton chemical shifts. Arrow on the CB7-Me-DASPI suggested structure represents the mobility of CB7 on the dye, due to the signal broadening at 1.5 and lower equivalents of the host, which os a common behaviour for these types of complexes. Assignment of free dye was done comparatively, with aid of previously reported ^{1}H-NMR spectrum, while the 1:1 and 1:1:1 complex assignment was done by analysis of 2D experiments COSY and ROESY, presented in the appendixes B.22 through B.25.

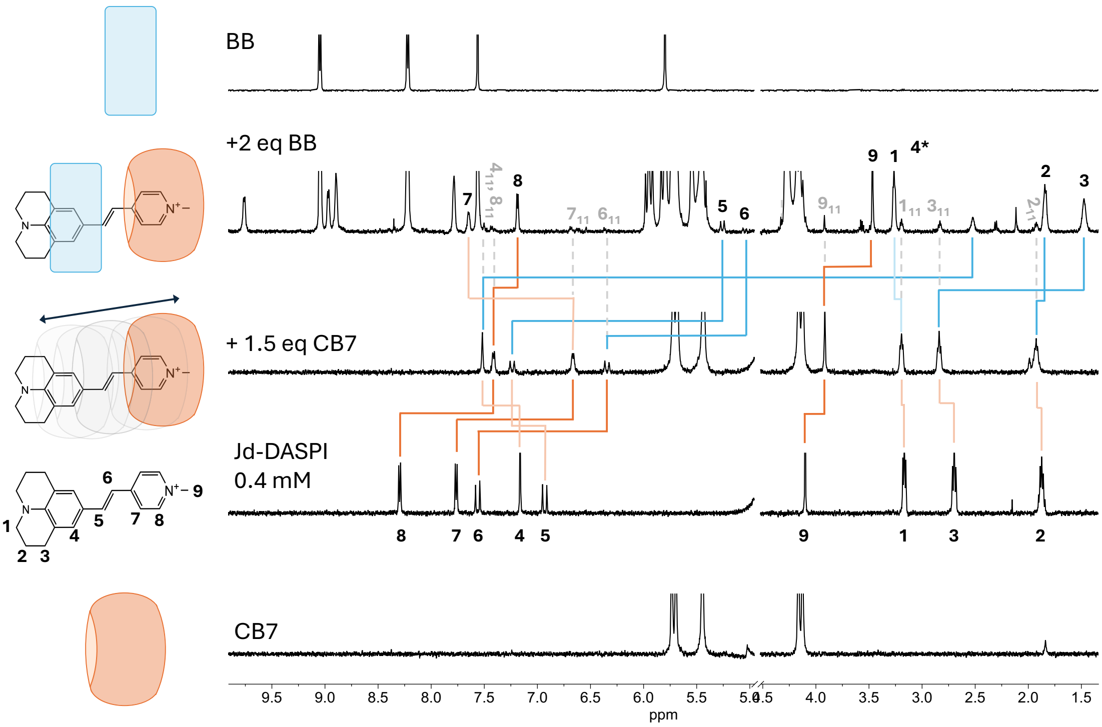

Figure B.21: ^{1}H-NMR spectra of CB7, Jd-DASPI, CB7-Jd-DASPI and CB7-Jd-DASPI-BB complexes and BB in D_2O pD 8 and respective expected structures based on the assigned Jd-DASPI proton chemical shifts. Arrow on the CB7-Jd-DASPI suggested structure represents the mobility of CB7 on the dye, due to the signal broadening at 1.5 and lower equivalents of the host. Addition of excess BB (2 eq.) leads to an equilibrium between ternary and binary complex, with the unaffected binary complex - CB7-Jd-DASPI - chemical shifts represented by dashed lines and labels in grey. Assignment of free dye was done comparatively, with aid of previously reported ^{1}H-NMR spectrum, while the 1:1 and 1:1:1 complex assignment was done by analysis of 2D experiments COSY and ROESY, presented in the appendixes B.30 through B.33.

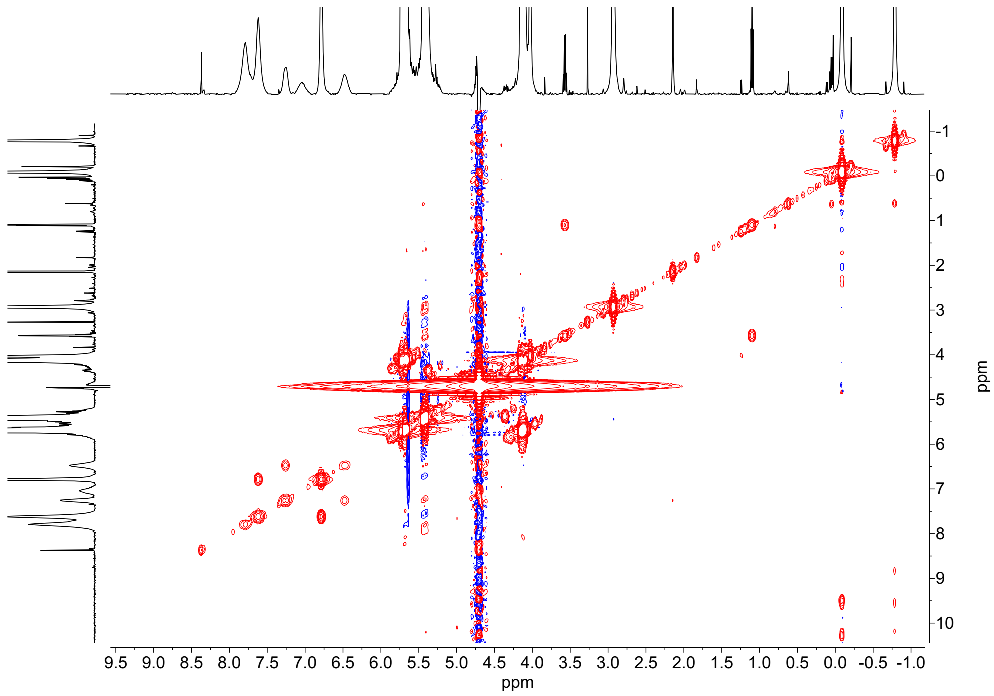

Figure B.22: ^{1}H-COSY NMR spectrum of Me-DASPI-CB7 complex with 0.5 mM of dye and 1.5 equivalents of CB7, in D_2O.

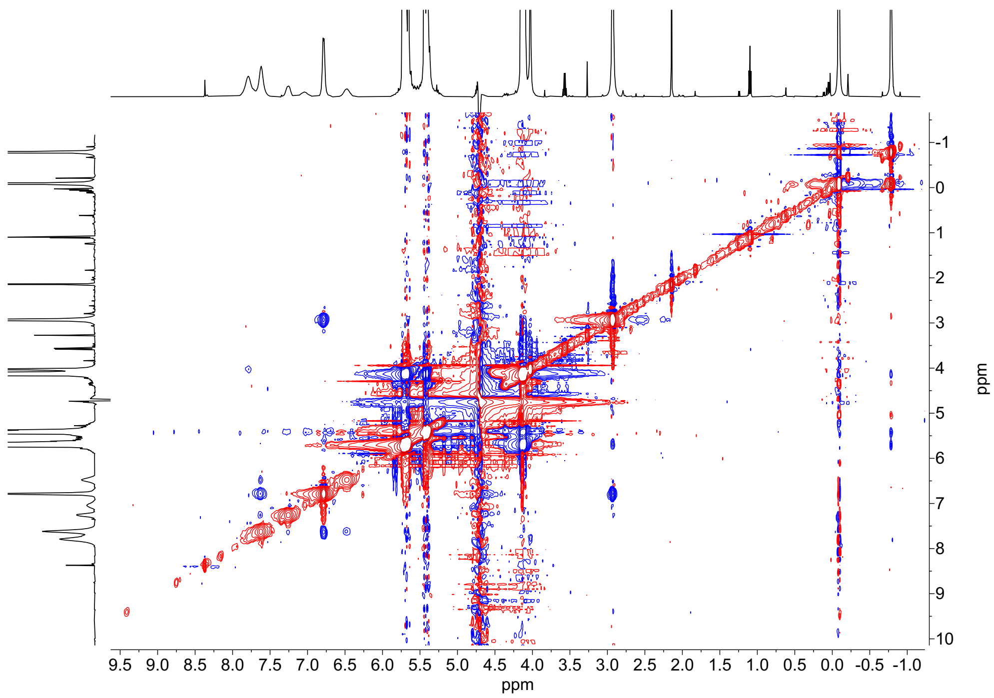

Figure B.23: ^{1}H-ROESY NMR spectrum of Me-DASPI-CB7 complex with 0.5 mM of dye and 1.5 equivalents of CB7, in D_2O.

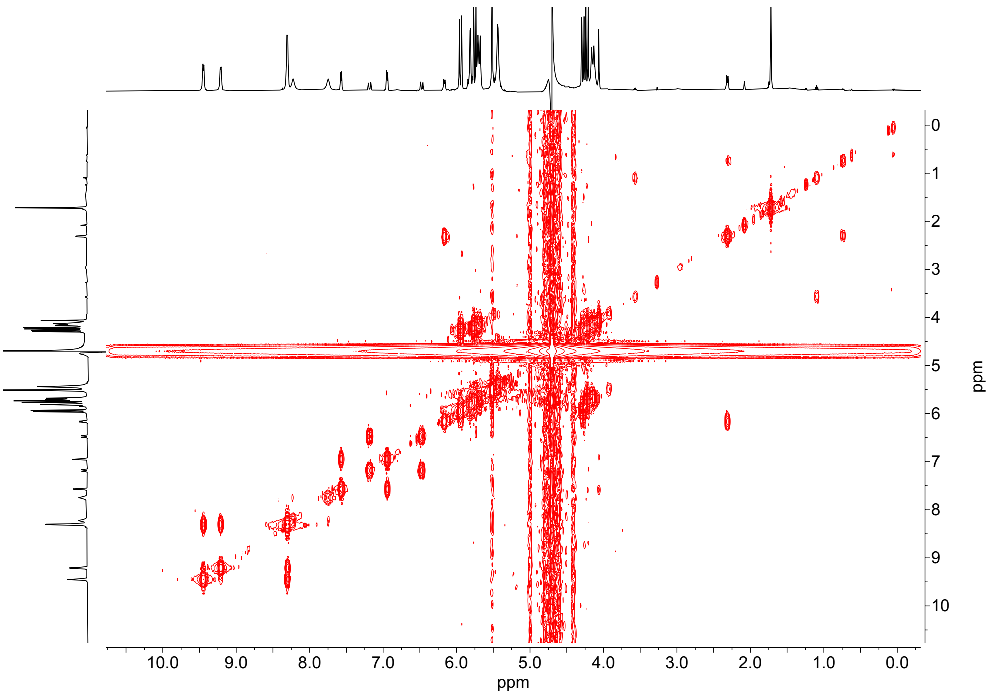

Figure B.24: [1]H-COSY NMR spectrum of Me-DASPI-CB7-BB complex with 0.5 mM of dye and 1.5 and 1 equivalents of CB7 and BB, respectively, in D_2O.

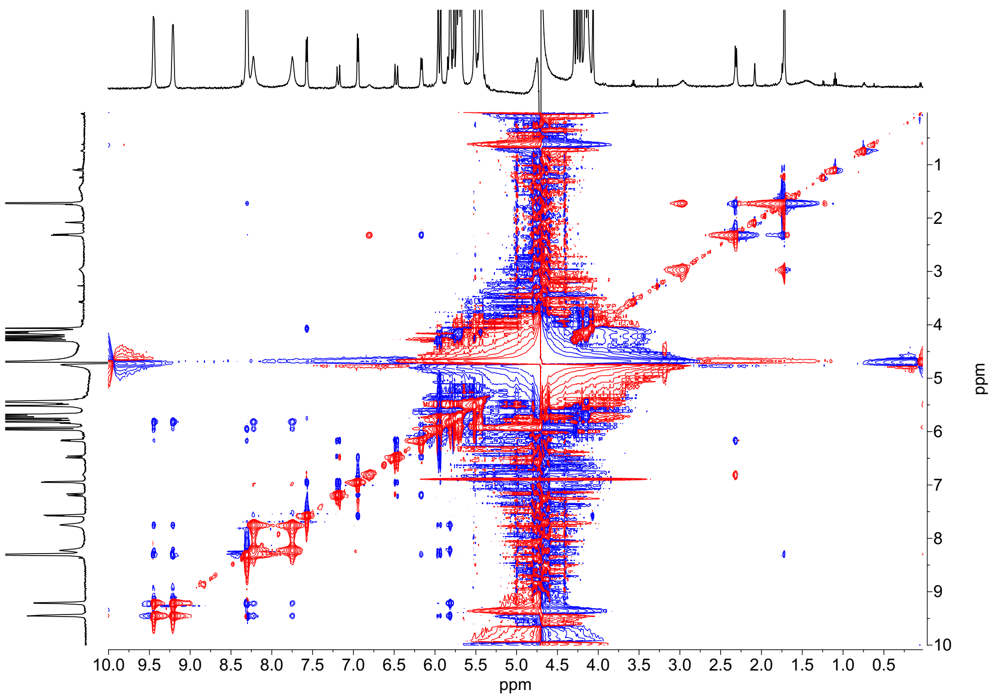

Figure B.25: [1]H-ROESY NMR spectrum of Me-DASPI-CB7-BB complex with 0.5 mM of dye and 1.5 and 1 equivalents of CB7 and BB, respectively, in D_2O.

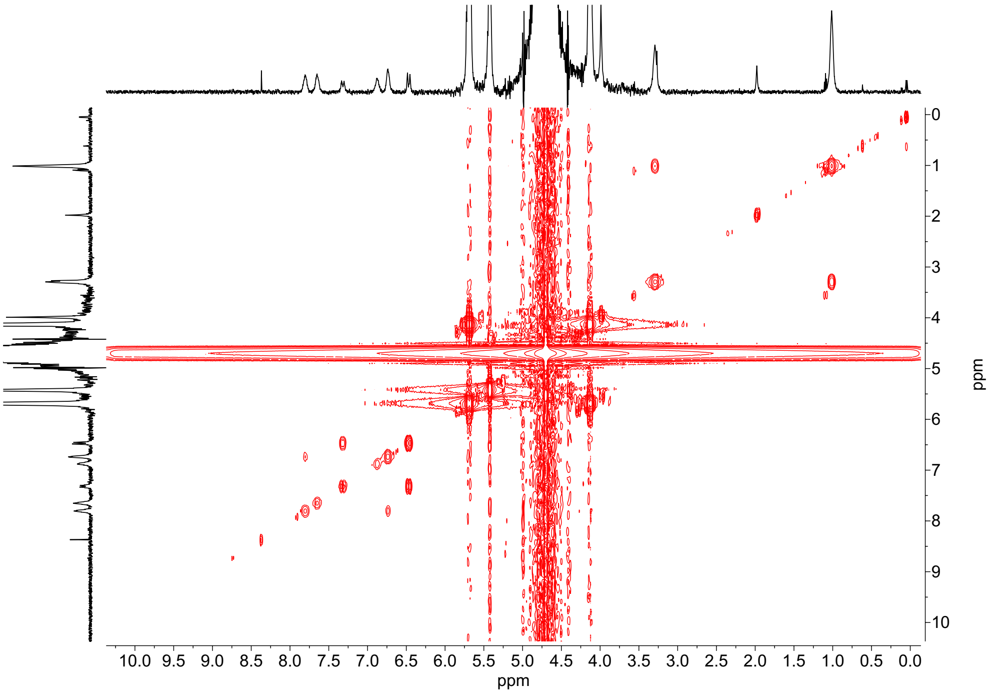

Figure B.26: [1]H-COSY NMR spectrum of Et-DASPI-CB7 complex with 0.5 mM of dye and 1.5 equivalents of CB7, in D_2O

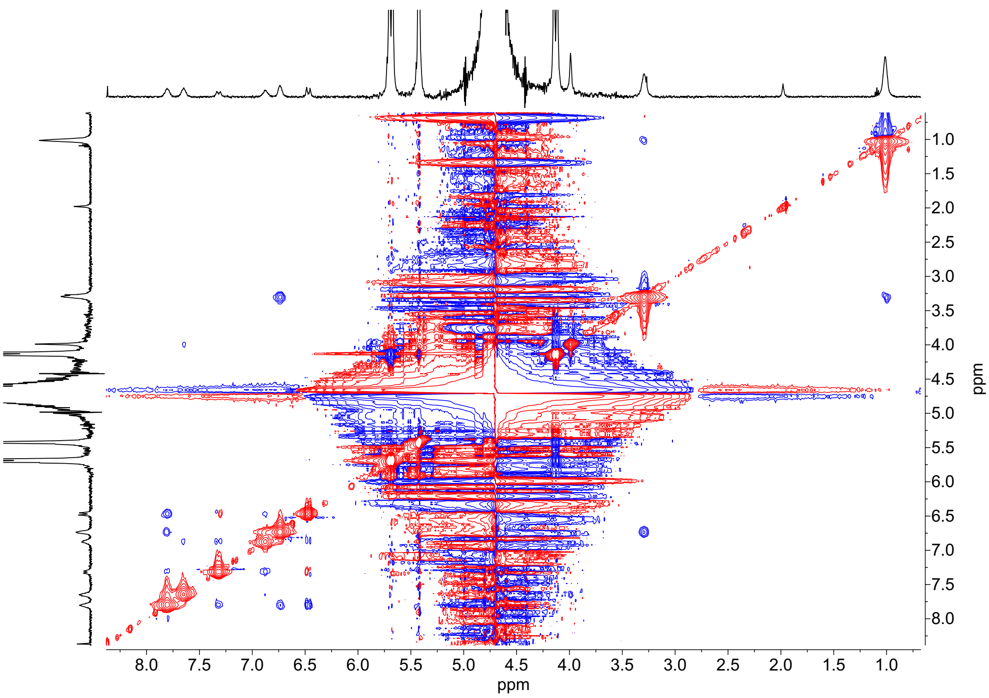

Figure B.27: [1]H-ROESY NMR spectrum of Et-DASPI-CB7 complex with 0.5 mM of dye and 1.5 equivalents of CB7, in D_2O.

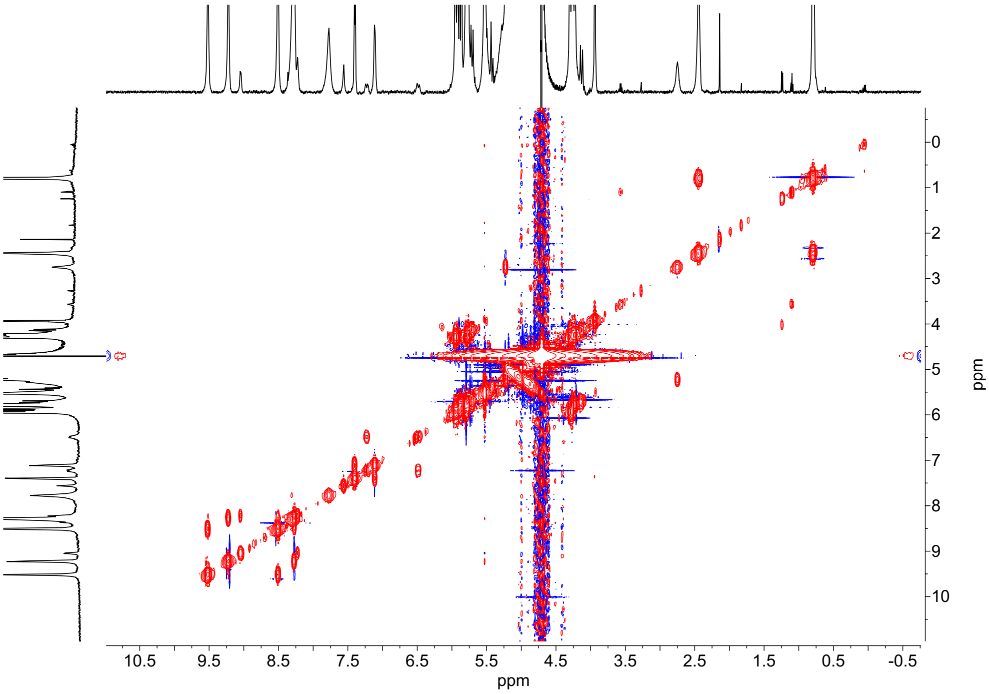

Figure B.28: [1]H-COSY NMR spectrum of Et-DASPI-CB7-BB complex with 0.5 mM of dye and 1.5 and 1 equivalents of CB7 and BB, respectively, in D_2O.

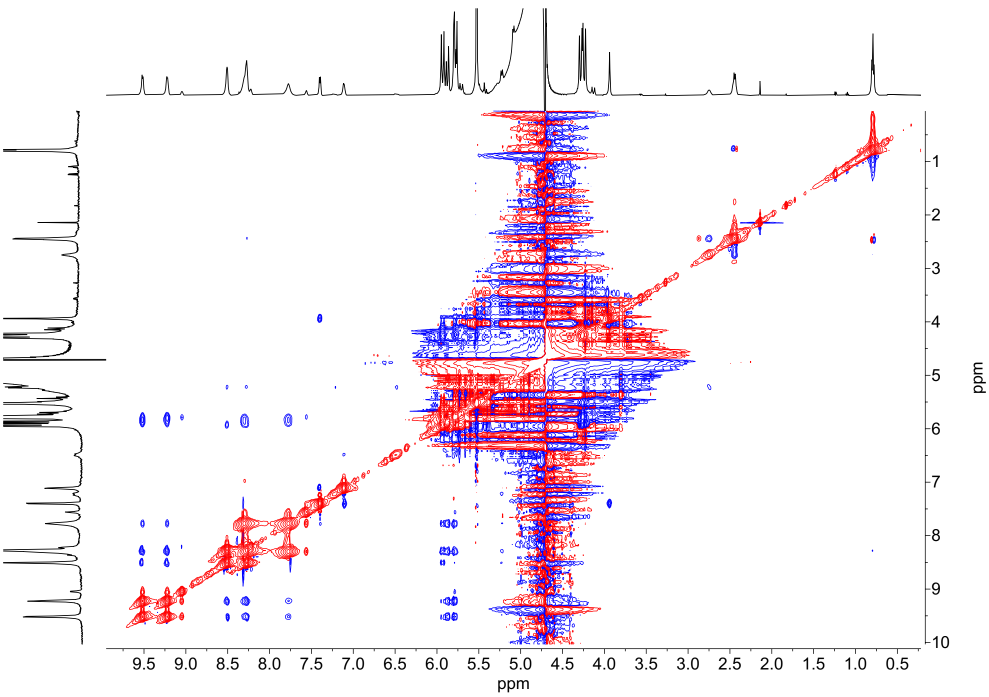

Figure B.29: [1]H-ROESY NMR spectrum of Et-DASPI-CB7-BB complex with 0.5 mM of dye and 1.5 and 1 equivalents of CB7 and BB, respectively, in D_2O.

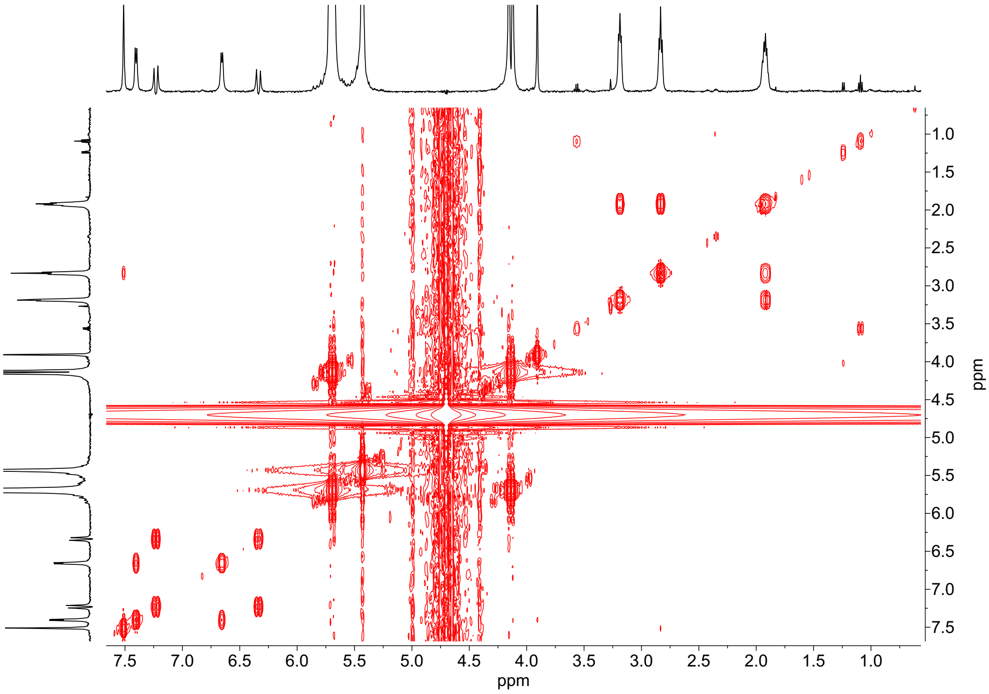

Figure B.30: ¹H-COSY NMR spectrum of Jd-DASPI-CB7 complex with 0.4 mM of dye and 1.5 equivalents of CB7, in D_2O

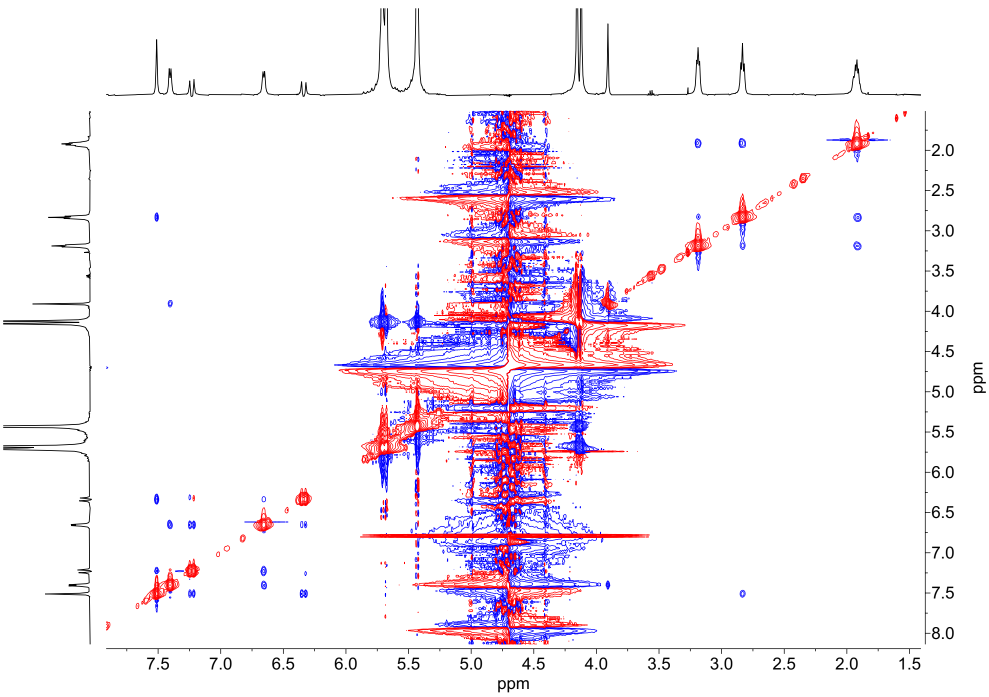

Figure B.31: ¹H-ROESY NMR spectrum of Jd-DASPI-CB7 complex with 0.4 mM of dye and 1.5 equivalents of CB7, in D_2O

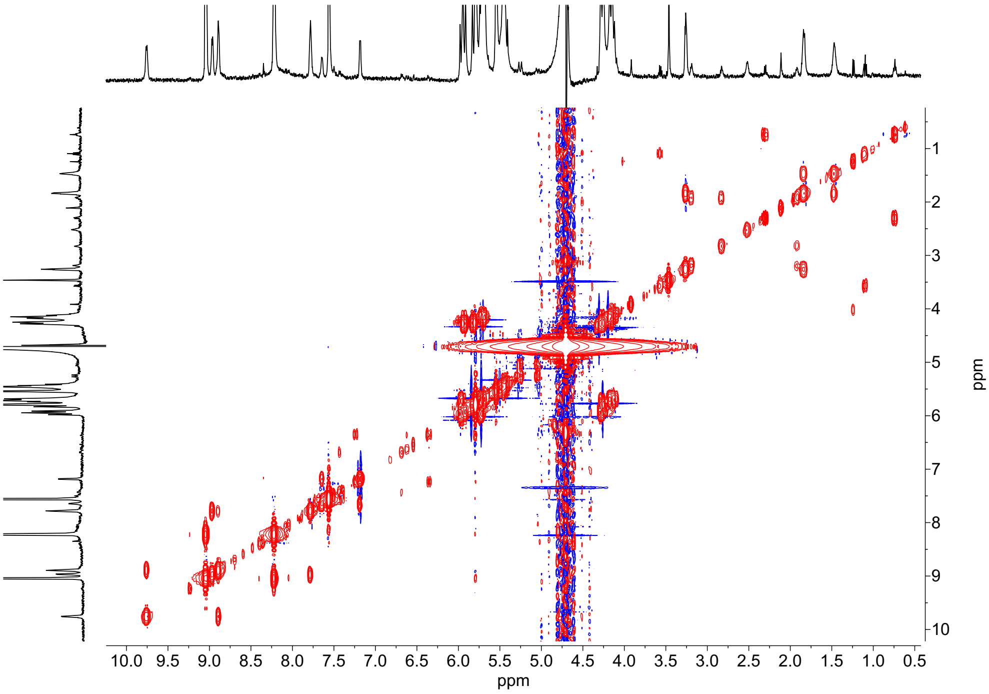

Figure B.32: ^{1}H-COSY NMR spectrum of Jd-DASPI-CB7-BB complex with 0.4 mM of dye and 1.5 and 2 equivalents of CB7 and BB, respectively, in D_2O.

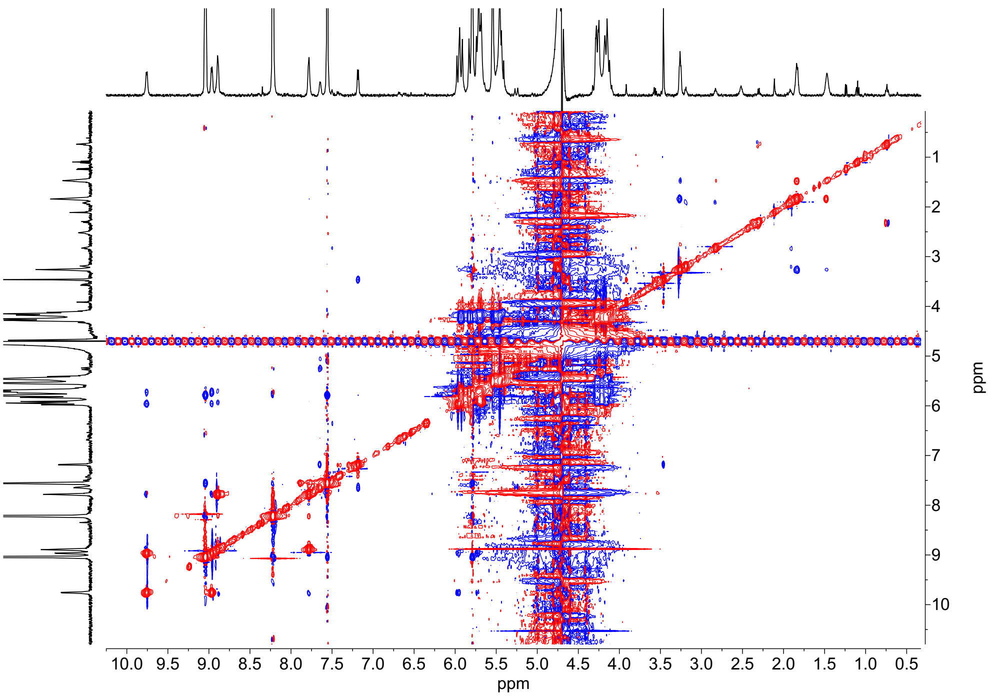

Figure B.33: ^{1}H-ROESY NMR spectrum of Jd-DASPI-CB7-BB complex with 0.4 mM of dye and 1.5 and 2 equivalents of CB7 and BB, respectively, in D_2O.

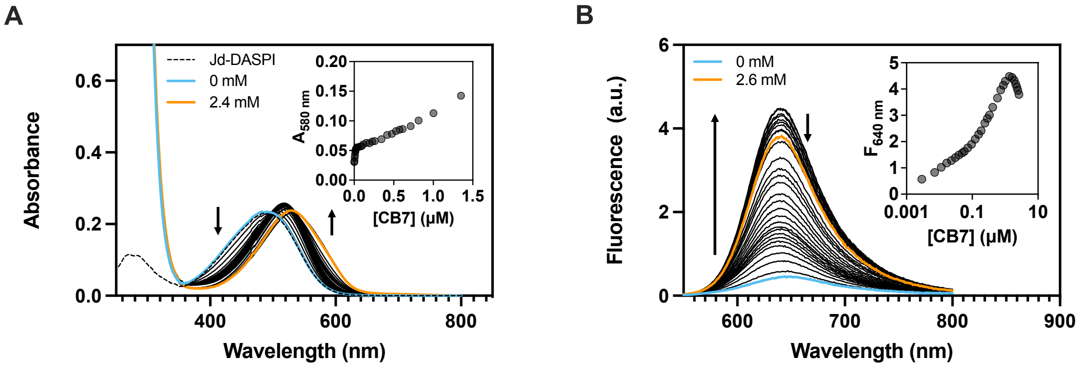

Figure B.34: Titration of a Jd-DASPI-BB mixture (100 μM BB and 10 μM Jd-DASPI) with CB7 up to an excess of this host, followed by **A.** UV-vis and **B.** fluorescence spectroscopies (λ_{exc} = 530 nm). Variation at a fixed wavelength can be found in inset. Fitting of this data to the 2:1:1 model was not possible, likely due to other processes occurring simultaneously that shift the species distribution or their photophysical properties, e.g. aggregation or precipitation.

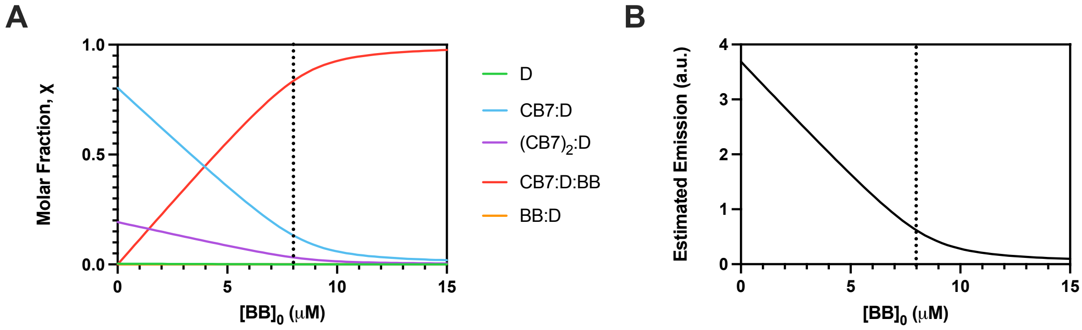

Figure B.35: **A.** Molar fractions of the species Et-DASPI (8.6 μM), CB7 (25 μM) and BB in solution at varying initial BB concentrations. **B.** Estimated emission based on the molar fractions presented in A. The dotted line in both graphs represents the chosen concentration of BB in order to obtain the maximum of CB7:Et-DASPI:BB fraction while allow for both quenching and enhancement if either of the hosts is displaced.

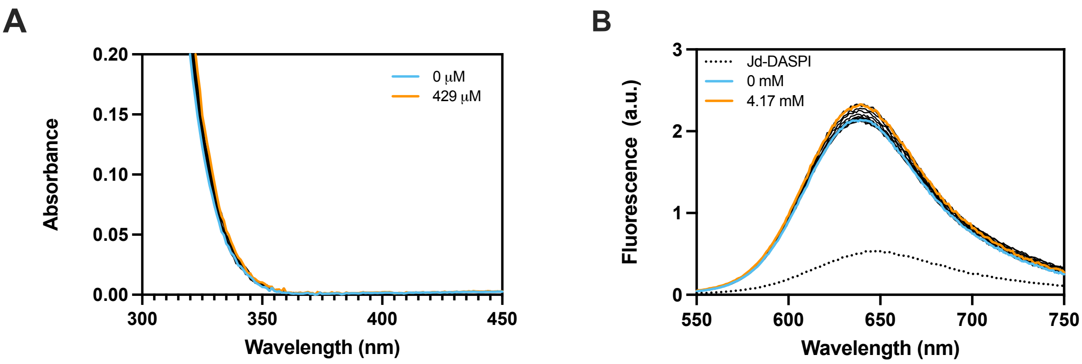

Figure B.36: **A.** Direct titration of BB with Nandrolone, followed by UV-vis spectroscopy and **B.** displacement of Jd-DASPI (8.6 μM) from CB7 (25 μM) with the analyte Naproxen followed by fluorescence spectroscopy (λ_{exc} = 530 nm).

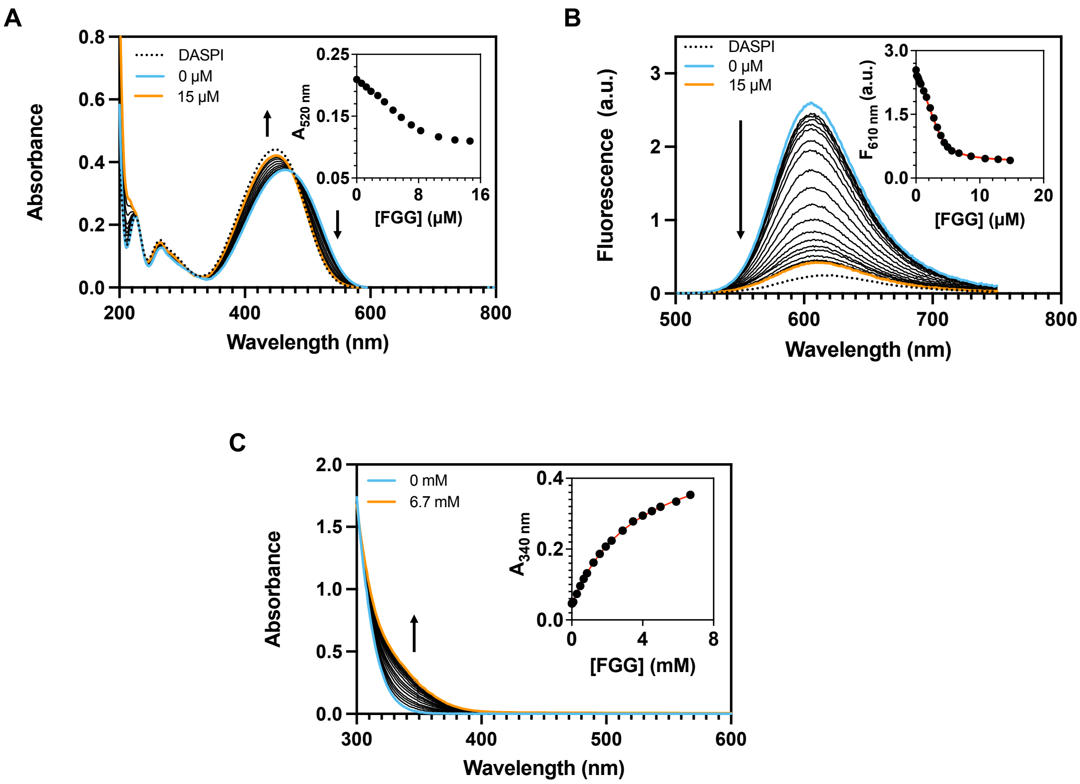

Figure B.37: Displacement of Me-DASPI from CB7 with FGG, followed by **A.** UV-vis and **B.** fluorescence spectroscopies (λ_{exc} = 468 nm). Concentration of Me-DASPI and CB7 was fixed at 15 μM for UV-Vis assays and 6 and 7.5 μM, respectively, for the fluorescence assays. **C.** Direct titration of BB (150 μM) with FGG, followed by UV-vis spectroscopy.

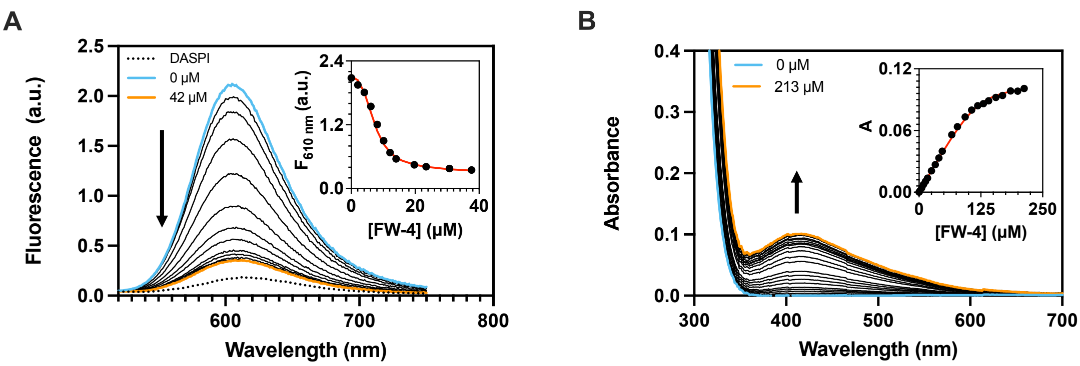

Figure B.38: **A.** Displacement of Me-DASPI (4.7 μM) from CB7 (9.5 μM) with FGGW, followed by fluorescence spectroscopies (λ_{exc} = 468 nm). **C.** Direct titration of BB (150 μM) with FGGW, followed by UV-vis spectroscopy. Appearance of CT band centered at 415 nm confirms binding at the C-terminal Trp.

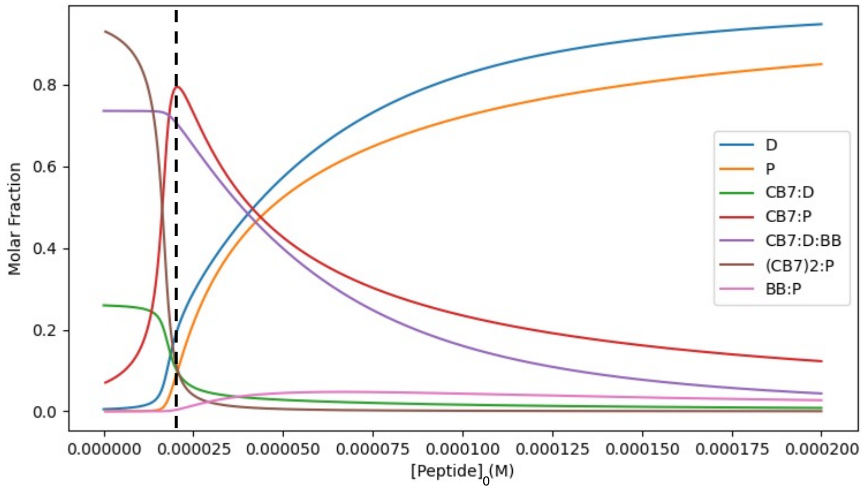

Figure B.39: Molar fractions of species in a predicted ternary displacement with Et-DASPI and the two hosts and competitor FGGW, using concentrations used in the assay shown in Figure 3.15. Dashed line shows concentration at which there is a sharp decrease in the molar fraction of $(CB7)_2$:Peptide complex, which indicates that at concentrations above $\approx$ 20 μM, BB should be free to bind to the peptide C-terminal.

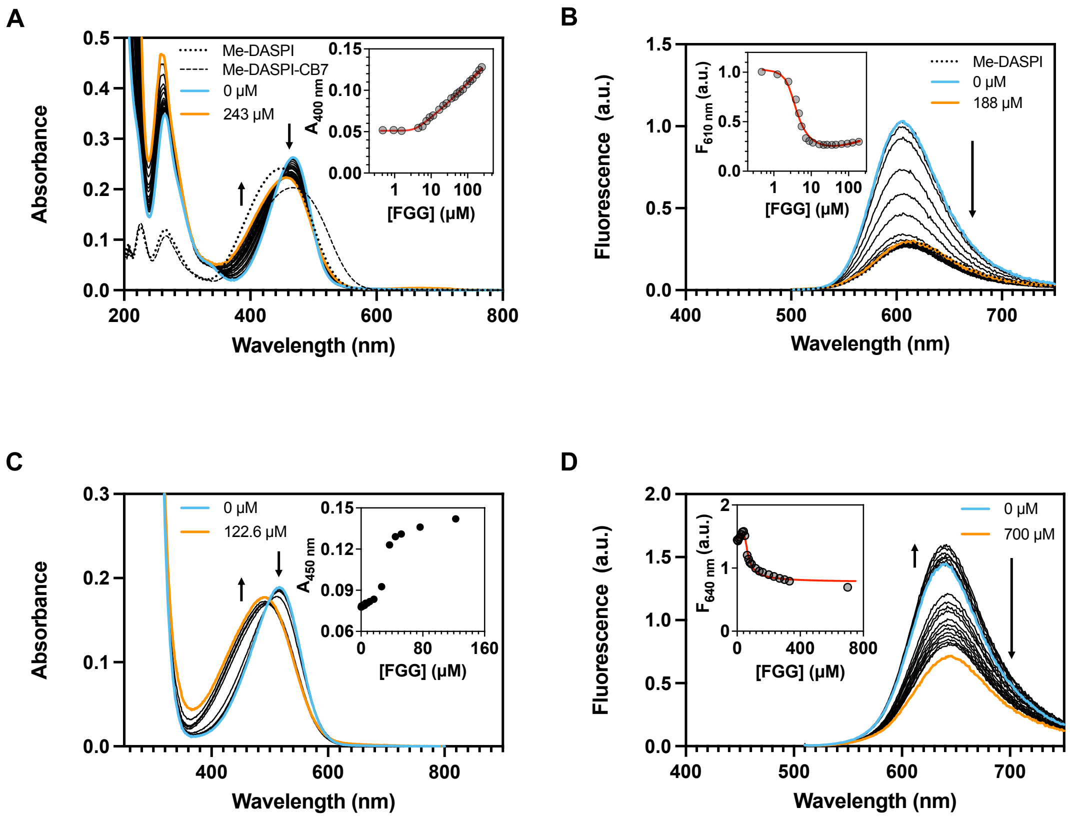

Figure B.40: Ternary complex displacement with Me-DASPI, with the peptide FGG, followed by **A.** UV-vis and **B.** fluorescence spectroscopies (λ_{exc} = 468 nm). Concentration of the hosts, BB and CB7, and Me-DASPI were fixed at 6, 10 and 7.8 μM for both assays. Ternary complex displacement with Jd-DASPI, with the same peptide, followed by **C.** UV-vis and **D.** fluorescence spectroscopies (λ_{exc} = 470 nm). For these assays, the concentrations of BB, CB7 and Jd-DASPI were fixed at 50, 60 and 7.5 μM, respectively. Insets in A., B. and D. show fitting of the spectroscopical data at a fixed wavelength with the ternary complex competitive model presented in Annex I.

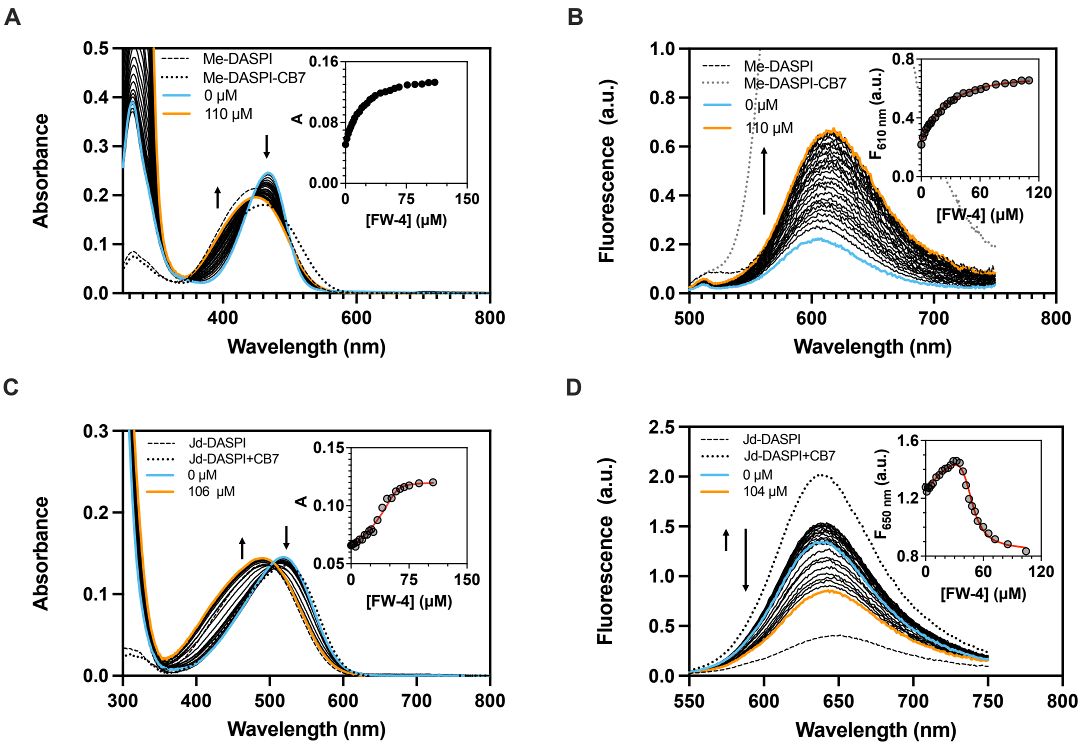

Figure B.41: Ternary complex displacement with Me-DASPI, with the peptide FGGW, followed by **A.** UV-vis and **B.** fluorescence spectroscopies (λ_{exc} = 468 nm). Concentration of the hosts, BB and CB7, and Me-DASPI were fixed at 8, 8.2 and 7 μM for both assays. Ternary complex displacement with Jd-DASPI, with the same peptide, followed by **C.** UV-vis and **D.** fluorescence spectroscopies (λ_{exc} = 470 nm). For these assays, the concentrations of BB, CB7 and Jd-DASPI were fixed at 50, 60 and 8 μM, respectively. Insets in B., C. and D. show fitting of the spectroscopical data at a fixed wavelength with the ternary complex competitive model presented in Annex I.

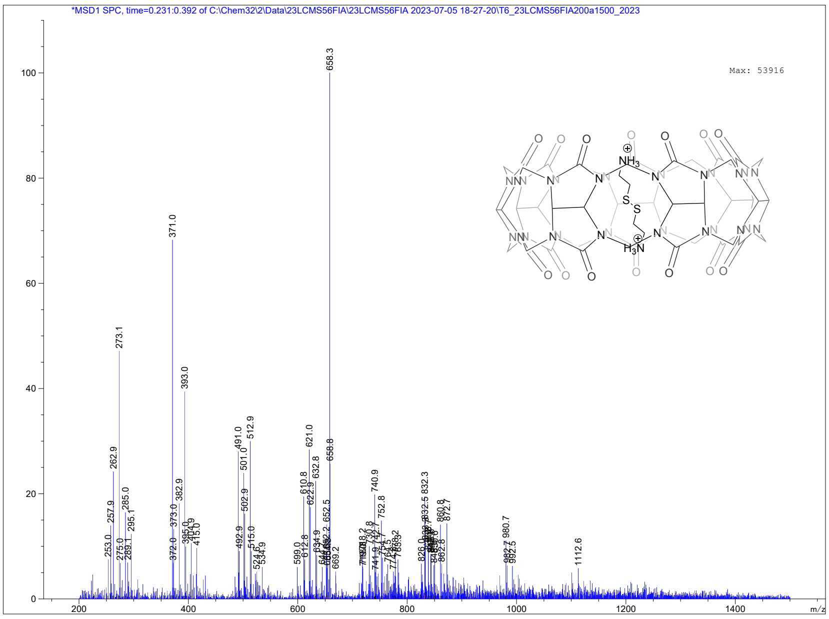

Figure B.42: ESI-MS spectrum of fraction 6 of CB7 chemical oxidation reaction, corresponding to the fraction with a majority of CB7, in the presence of Cys, found at 658.3 m/z. Structure of the Cys and CB7 complex can be found in inset.

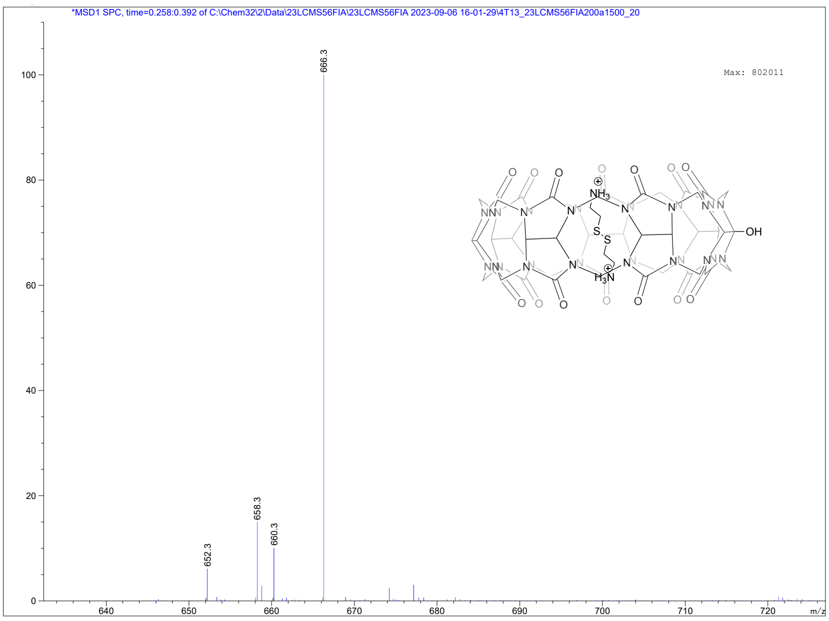

Figure B.43: ESI-MS spectrum of fraction 13 of CB7 chemical oxidation reaction, corresponding to the fraction with a majority of CB7-OH, in the presence of Cys, found at 666.3 m/z. Structure of the Cys and CB7-OH complex can be found in inset.

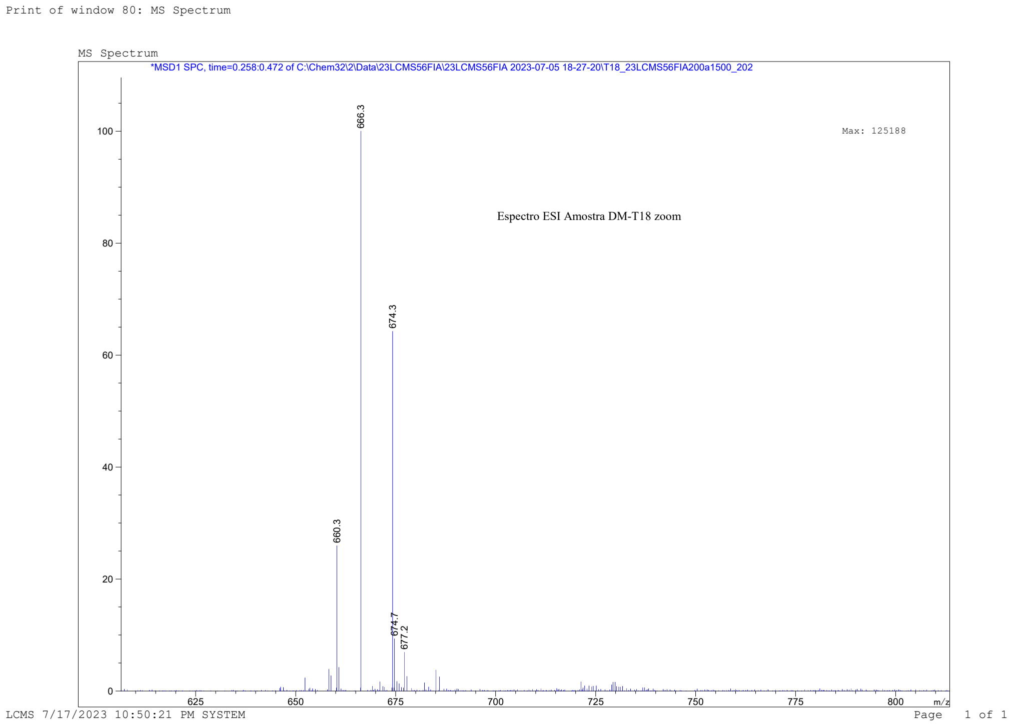

Figure B.44: ESI-MS spectrum of fraction 17 of CB7 chemical oxidation reaction, corresponding to the fraction with a mixture of CB7-OH and CB7-OH_2, in the presence of Cys, found at 666.3 and 674.3 m/z.

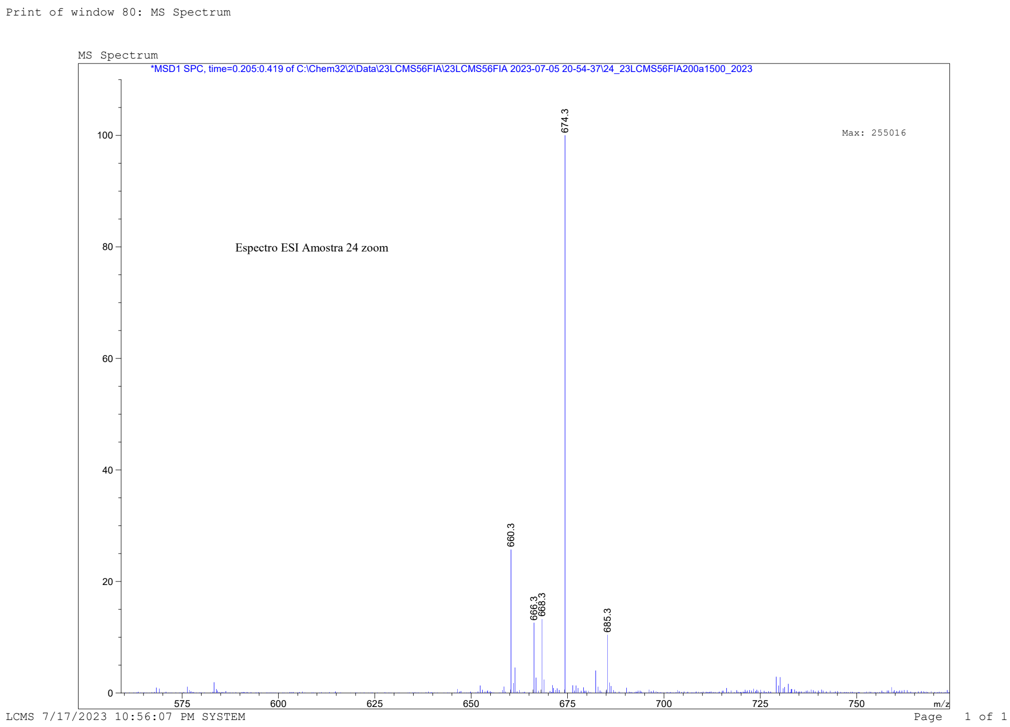

Figure B.45: ESI-MS spectrum of fraction 24 of CB7 chemical oxidation reaction, corresponding to the fraction with a majority of CB7-OH_2, in the presence of Cys, found at 674.3 m/z.

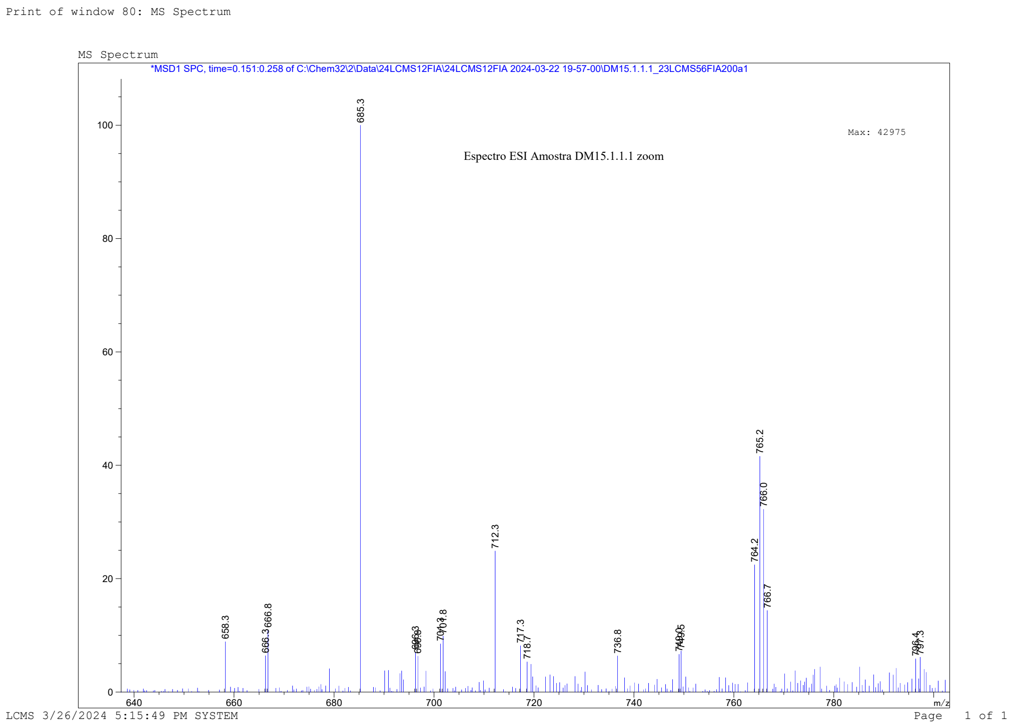

Figure B.46: ESI-MS spectrum of the reaction mixture after work-up of the reaction of CB7-OH with propargyl alcohol in the presence of NaH, in the presence of Cys. It appears to present a majority of CB7-propargyl (m/z expected at 684.7 and found at 685.3).

Table B.3: List of substitution reactions done by the superacid carbocation formation method, reagents used and respective quantities used, in relation to CB7-OH quantity, and final yield obtained.

Reaction Code	Reagent Structure	Equivalents added	Yield
CB7-C$^+$.1	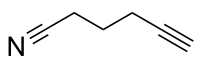	100 eq.	-
CB7-C$^+$.2	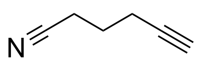 + Molecular Sieves	100 eq.	-
CB7-C$^+$.3	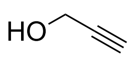	300 eq.	-
CB7-C$^+$.4	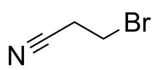	300 eq.	Quantitative
CB7-C$^+$.5	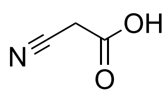	300 eq.	~ 86%

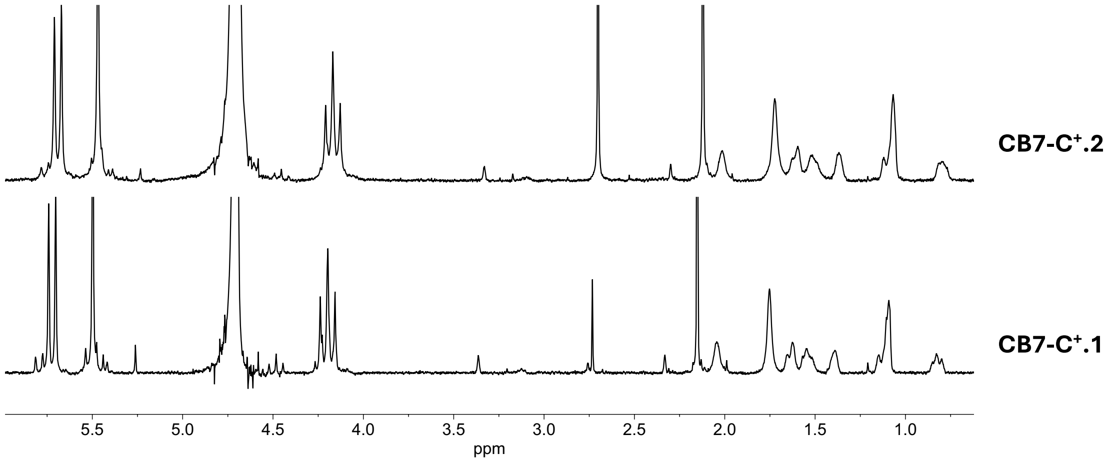

Figure B.47: ^{1}H-NMR spectra of the reaction mixtures of reactions CB7-C$^+$.1 and 2 after work-up procedure, done in D_2O in the presence of 1-adamantamine, for solubilization purposes. These test assays were done with CB7:CB7-OH mixture was used in this reaction, so it is expected that CB7 proton integration should be higher. Consumption of CB7-OH is shown by reduction of the integration from 0.78 to 0.34 of the characteristic proton signal presented by this reagent (5.26 ppm) when compared to the CB7 signal at 4.19 ppm, which was normalized to 20. On the other hand, the lack of appearance of the aliphatic protons added by the monofunctionalization indicate that it is unlikely that the reaction has occurred.

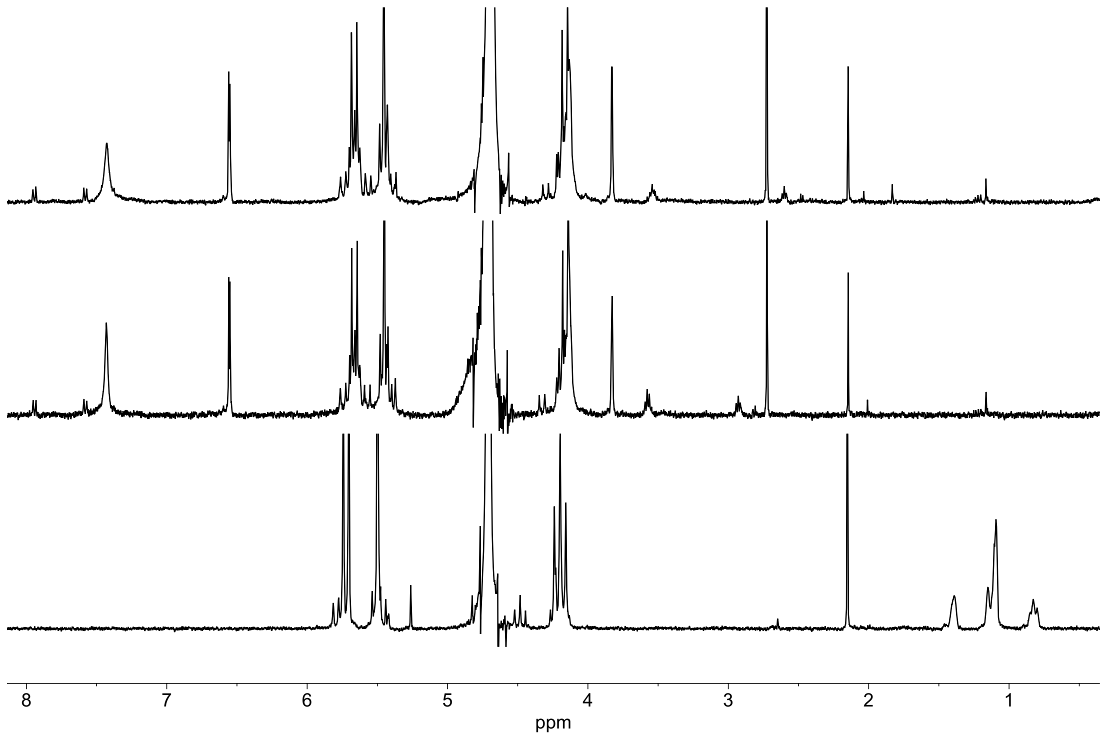

Figure B.48: Full ^{1}H-NMR spectra of the products CB7-OH (bottom), CB7-Br (middle) and CB7-N_3 (top) in D_2O in the presence of 1-adamantamine for CB7-OH and p-Xylylenediamine for the remaining two.

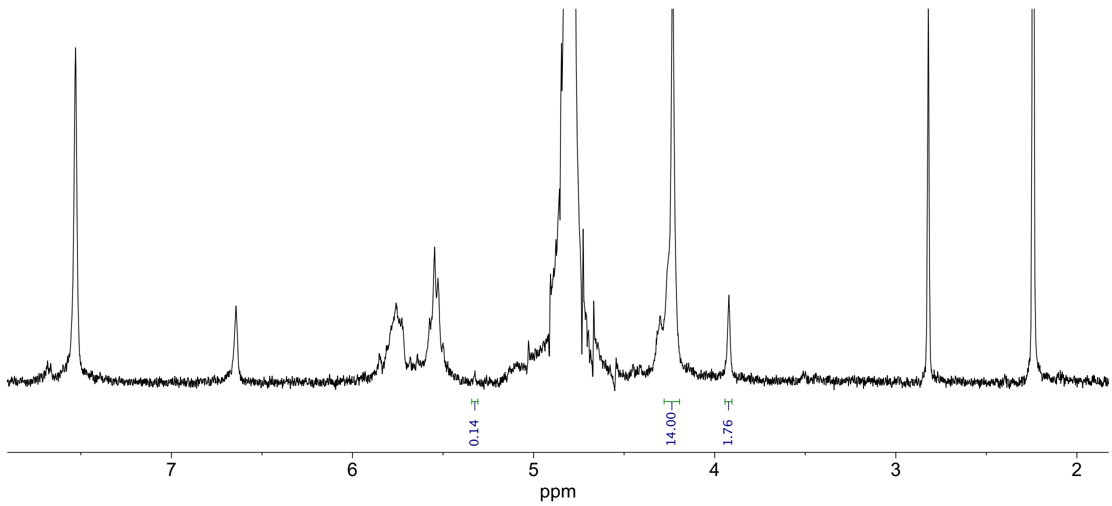

Figure B.49: [1]H-NMR spectra of the product of the superacid substitution reaction of CB7-OH with 4-cyanoacetic acid (CB7-C^+.5) in D_2O pD 10.

C

Supplementary Information for Chapter 4

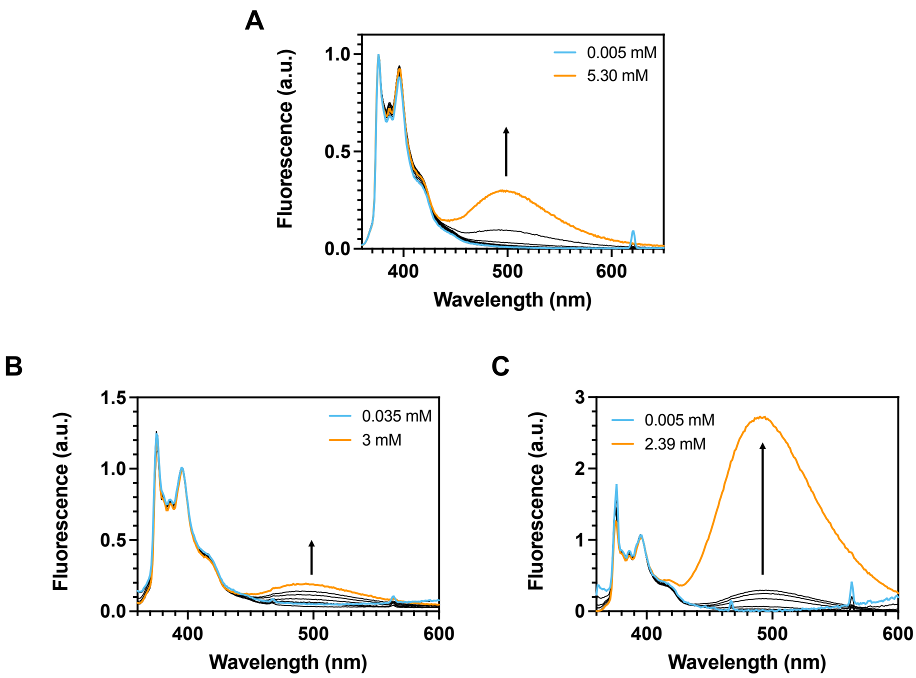

Figure C.1: Emission spectra of the SC4-nPy sensors, **A.** SC4-4Py, **B.** SC4-6Py, **C.** SC4-8Py, at increasing concentrations. Emission normalized at **A.** 376 nm and **B.**, **C.** at 396 nm (λ_{exc} = 347 nm).

Table C.1: Critical Aggregation concentration (CAC / μM) of the sensors in the presence of 2 equivalents of peptide. For larger peptides the CAC falls below the limit of detection for these molecules, using fluorescence spectroscopy.

Peptide	**[SC4-4Py] / μM**	**[SC4-6Py] / μM**	**[SC4-8Py] / μM**
R_2G_2	-	-	11.80
R_3G	8.25	2.79	0.87
R_4	1.72	0.51	0.16
R_6	0.19	< 0.02	< 0.01
R_8	< 0.01	< 0.01	< 0.01

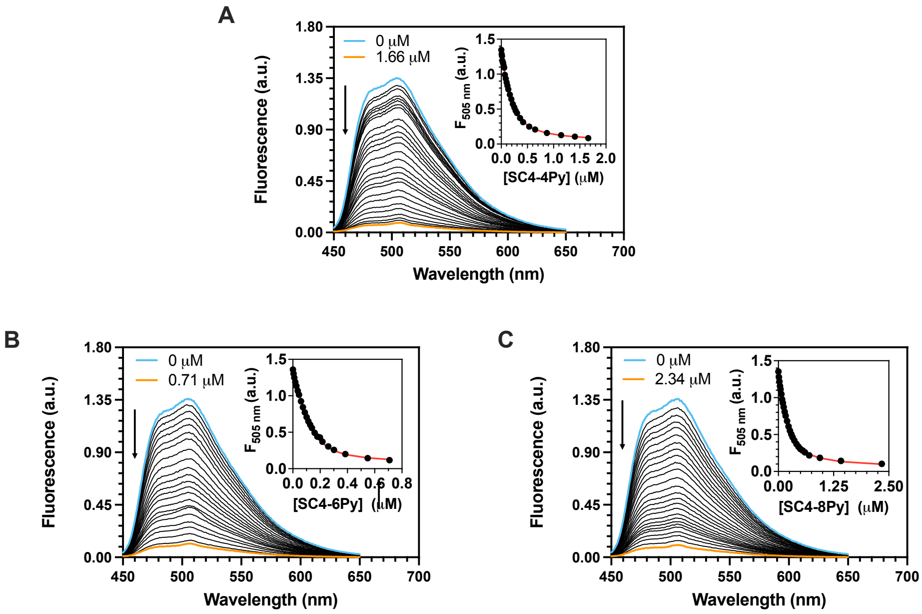

Figure C.2: Direct titrations of the indicator, LCG, for the IDA with **A.** SC4-4Py, **B.** SC4-6Py and **C.** SC4-8Py, followed by fluorescence spectroscopy ($\lambda_{exc} = 369$ nm). LCG concentration was fixed at 0.17 and 0.2 μM, respectively.

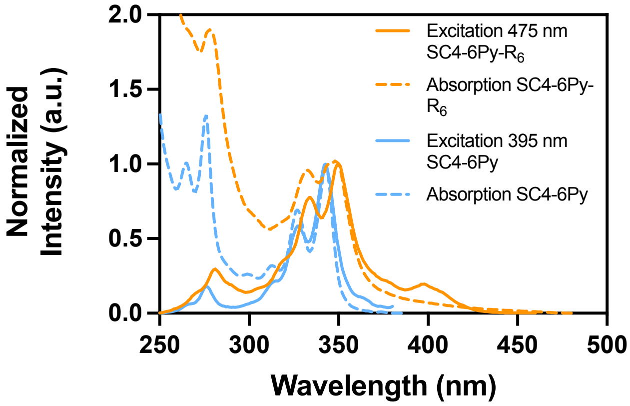

Figure C.3: Excitation spectra (full line) and absorbance spectra (dashed line) of SC4-6Py in the absence (blue) and in the presence of R_6 (orange) with the emission maximum fixed at 395 and 475 nm, respectively. SC4-6Py concentration for the monomer absorption and excitation spectra was 6 μM and 0.5 equivalents of peptide were added to the solution to obtain the aggregate spectra.

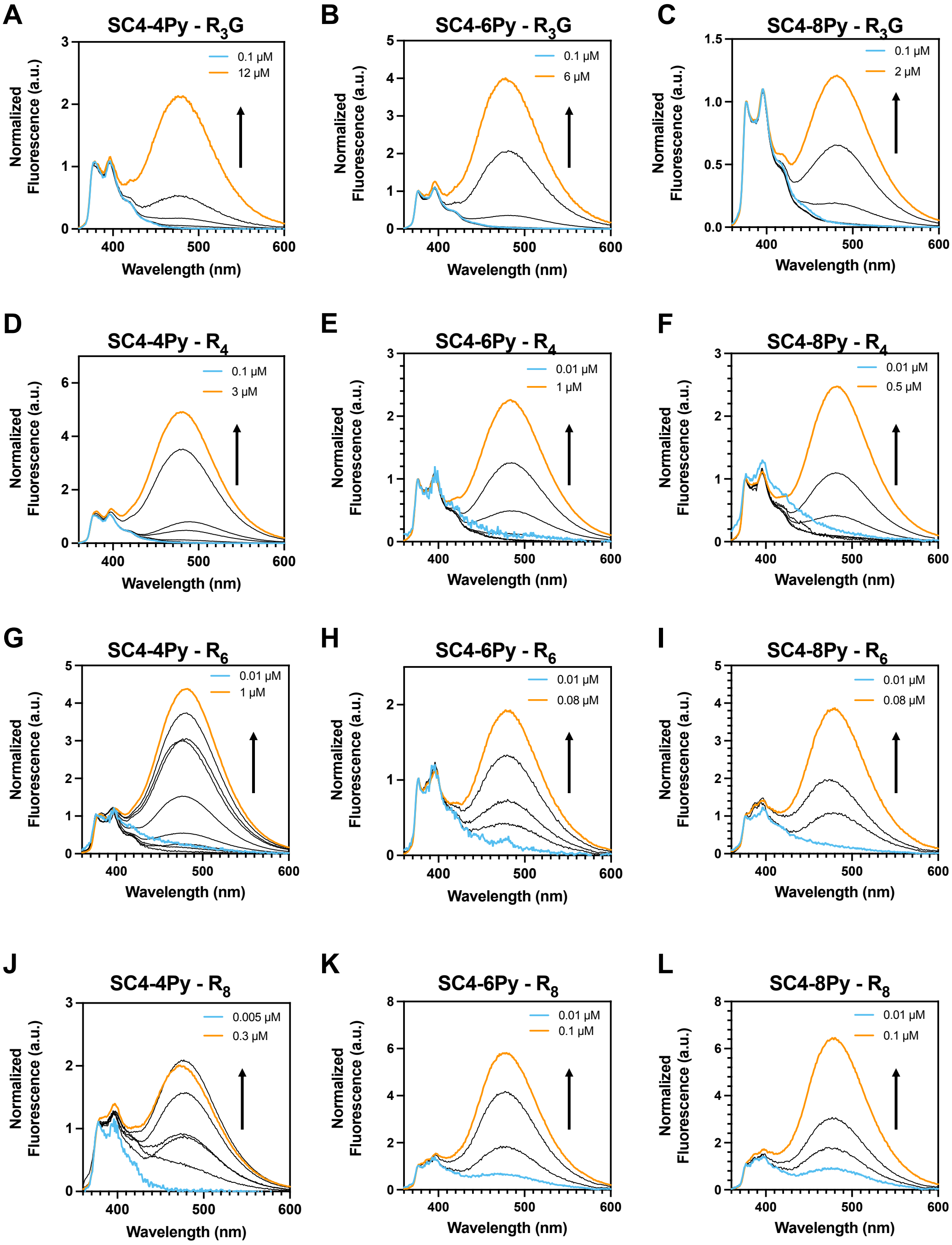

Figure C.4: Fluorescence spectra (λ_{exc} = 347 nm), normalized for the fluorescence at 366 nm, of the SC4-nPy:peptide complexes at different concentrations, maintaining a ratio of 1:2 of sensor to peptide. The concentration presented corresponds to the sensor concentration. Complexes of **A.**, **B.**, **C.** R_3G, **D.**, **E.**, **F.** R_4, **G.**, **H.**, **I.** R_6 and **J.**, **K.**, **L.** R_8, with SC4-4Py, SC4-6Py and SC4-8Py, respectively.

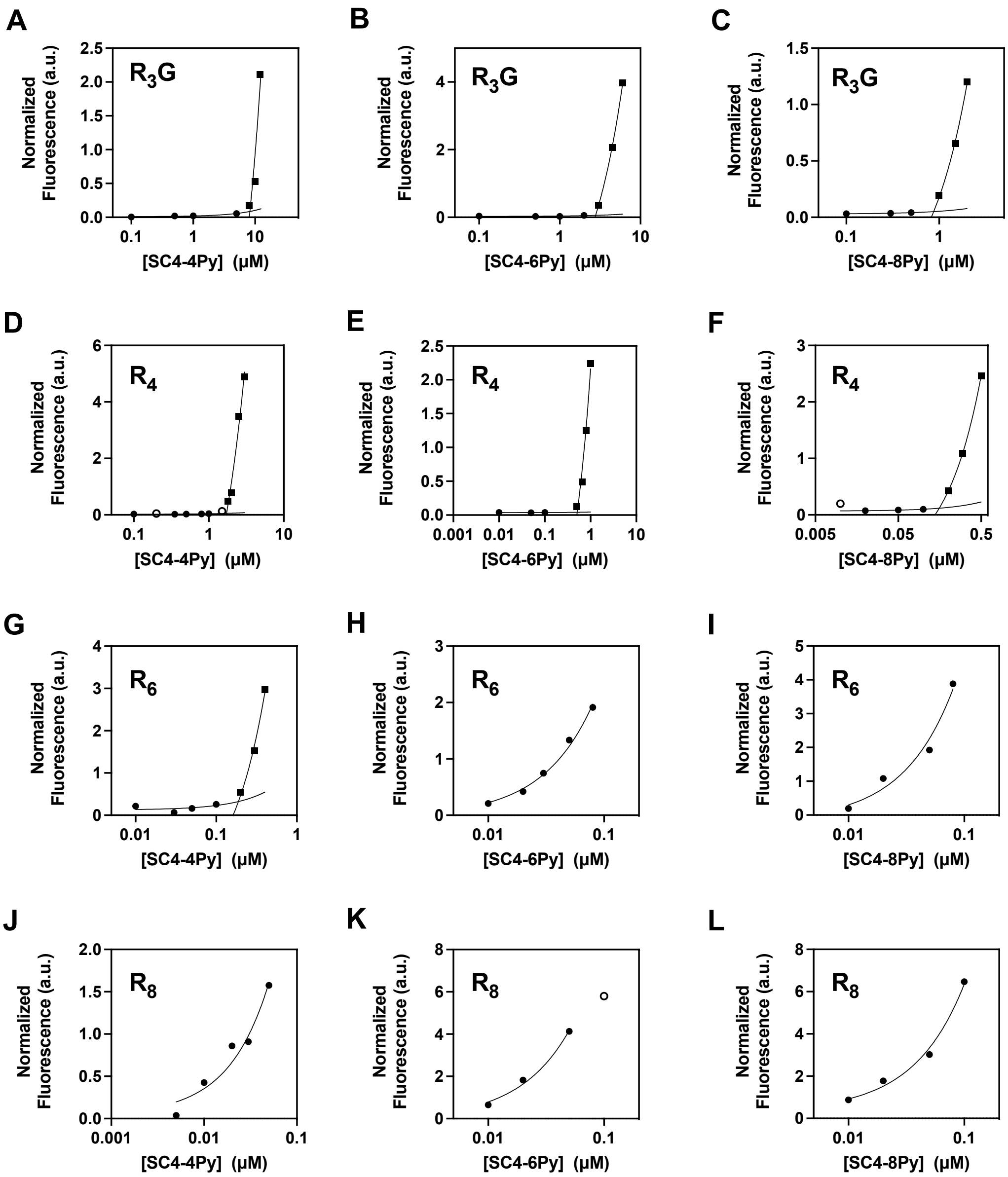

Figure C.5: Fluorescence at 480 nm, normalized for the fluorescence at 366 nm, of the SC4-nPy:peptide complexes at different concentrations, maintaining a ratio of 1:2 of sensor to peptide. The concentration presented corresponds to the sensor concentration, presented in a logarithmic scale. Complexes of **A.**, **B.**, **C.** R_3G, **D.**, **E.**, **F.** R_4, **G.**, **H.**, **I.** R_6 and **J.**, **K.**, **L.** R_8, with SC4-4Py, SC4-6Py and SC4-8Py, respectively.

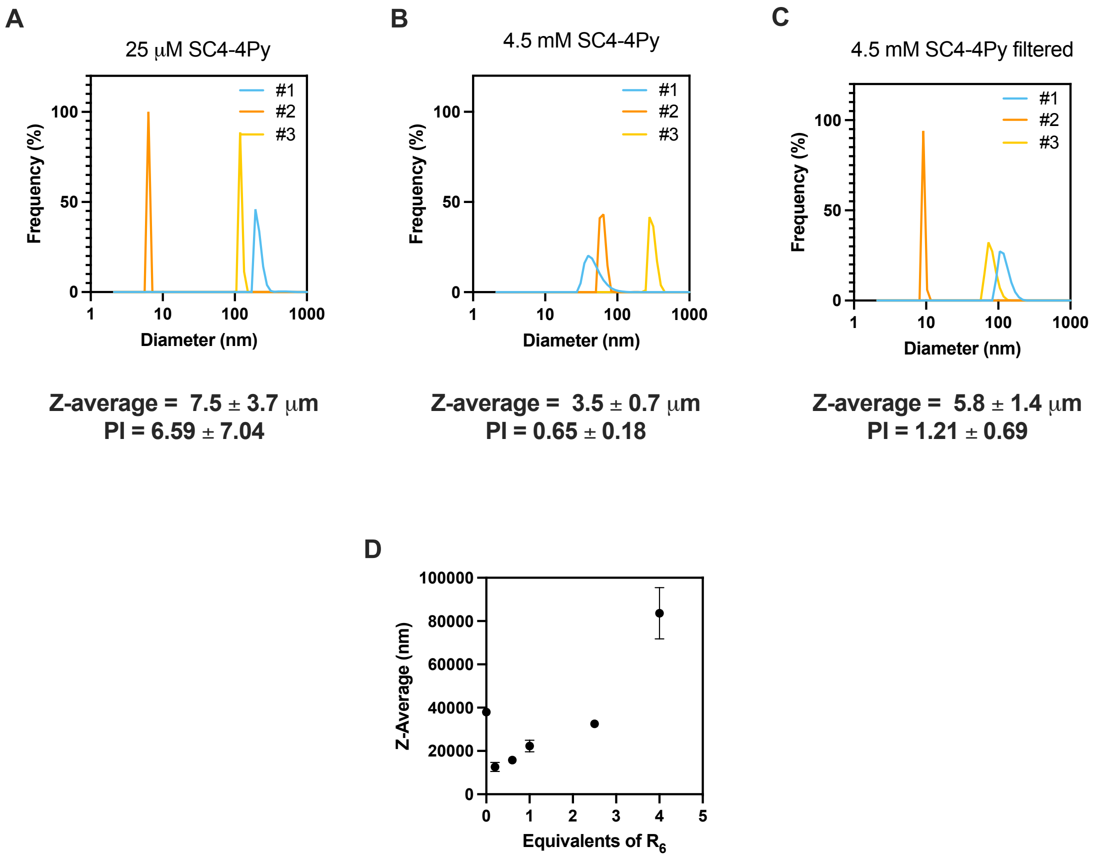

Figure C.6: Dynamic Light Scattering experiments of SC4-4Py in PB 5 mM pH 7.4 **A.** below CAC, at 25 μM and above CAC **B.** before and **C.** after filtration, at 4.5 mM. Filtration was done with 0.45 μm polypropylene syringe filter. Average of Z-average obtained from the triplicates presented is indicated below the respective graph with the average polydispersitivity index. **D.** Z-average of SC4-4Py (1 μM) in the presence of different concentration of guest, R_6.

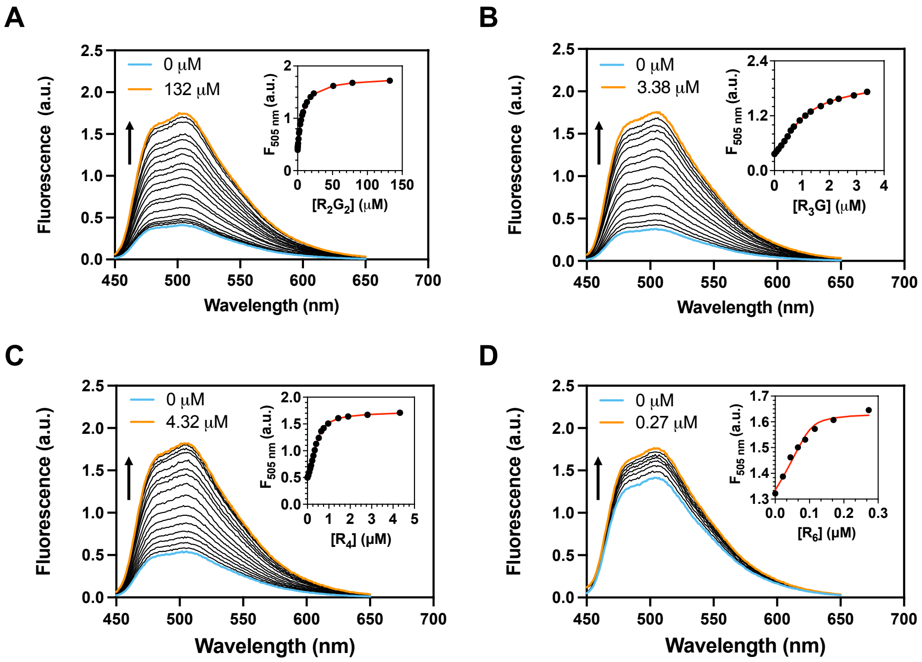

Figure C.7: Fluorescence spectra of the displacement assays done with LCG and the receptor SC4-4Py (λ_{exc} = 369 nm). Concentration of Lucigenin was fixed at 0.1 μM and SC4-4Py concentration at **A.** 0.46, **B.** 0.50, **C.** 0.40 and **D.** 0.10 μM for R_2G_2, R_3G, R_4 and R_6 displacement assays, respectively.

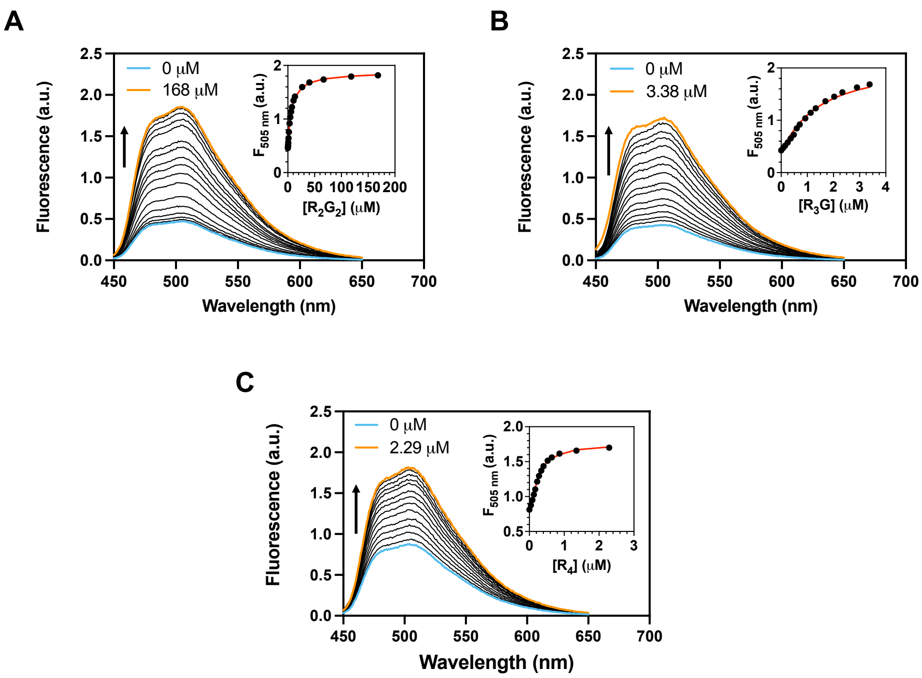

Figure C.8: Fluorescence spectra of the displacement assays done with LCG and the receptor SC4-6Py (λ_{exc} = 369 nm). Concentration of Lucigenin was fixed at 0.1 μM and SC4-6Py concentration at **A.** 0.31, **B.** 0.32 and **C.** 0.20 μM for R_2G_2, R_3G and R_4 displacement assays, respectively.

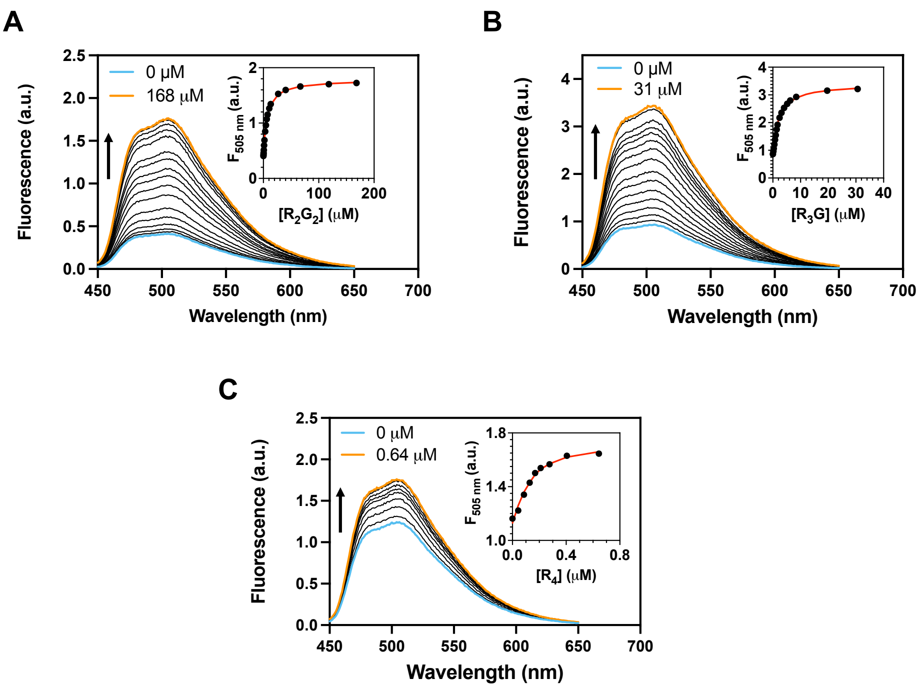

Figure C.9: Fluorescence spectra of the displacement assays done with LCG and the receptor SC4-8Py (λ_{exc} = 369 nm). Concentration of Lucigenin was fixed at 0.1 μM and SC4-8Py concentration at **A.** 0.46, **B.** 0.20 and **C.** 0.10 μM for R_2G_2, R_3G and R_4 displacement assays, respectively.

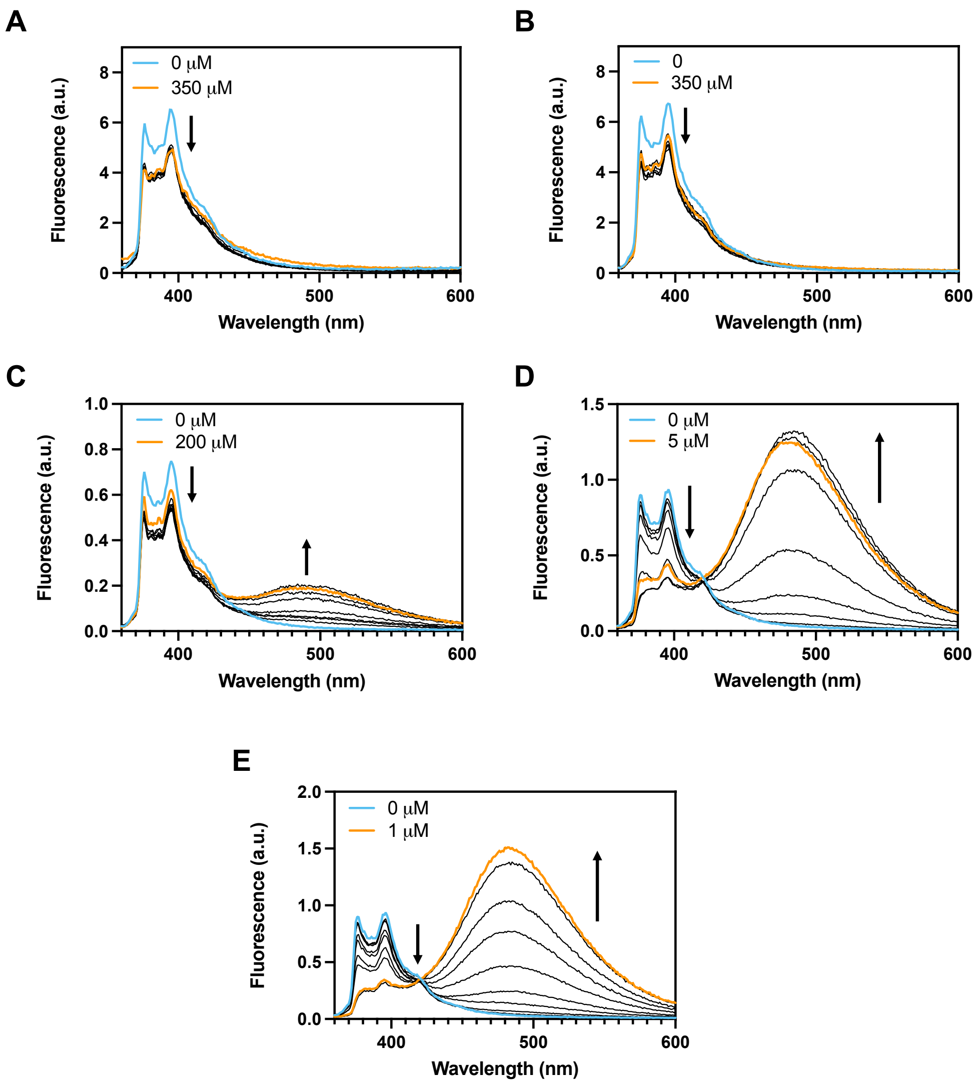

Figure C.10: Direct titrations, followed by fluorescence spectroscopy (λ_{exc} = 347 nm), of the selected oligoarginines, **A.** R_2G_2, **B.** R_3G, **C.** R_4, **D.** R_6 and **E.** R_8, with pyrene sensor, SC4-4Py (1 μM).

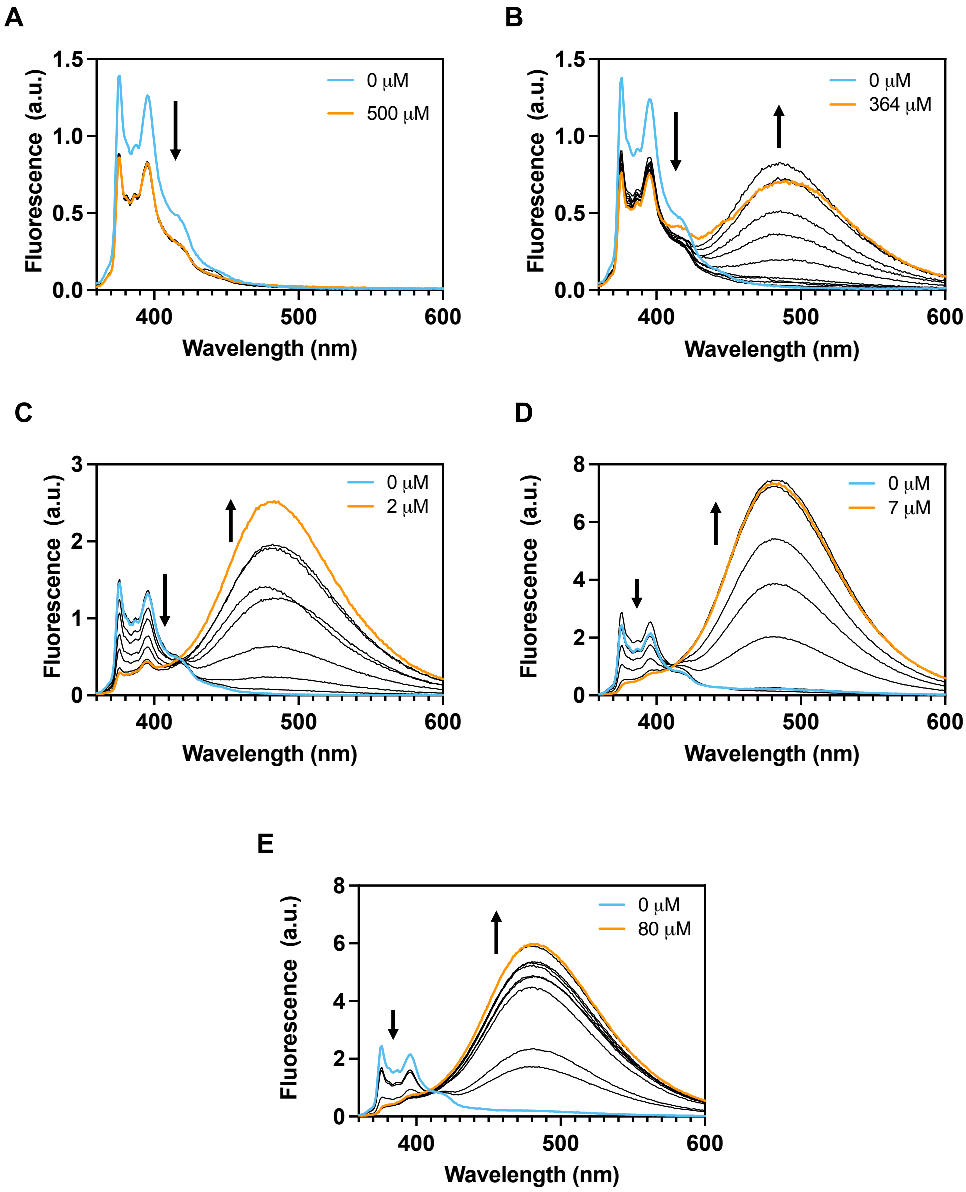

Figure C.11: Direct titrations, followed by fluorescence spectroscopy (λ_{exc} = 347 nm), of the selected oligoarginines, **A.** R_2G_2, **B.** R_3G, **C.** R_4, **D.** R_6 and **E.** R_8, with pyrene sensor, SC4-6Py (1 μM).

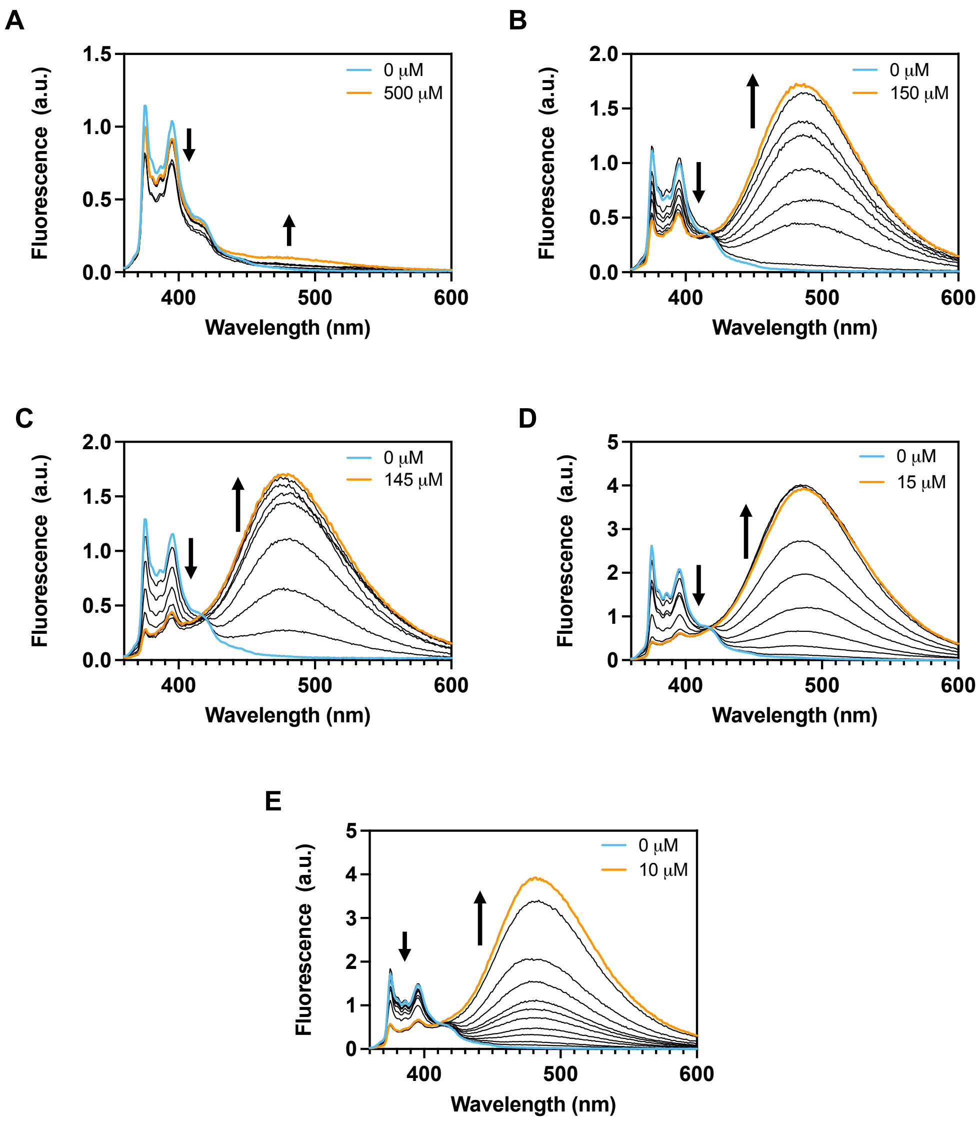

Figure C.12: Direct titrations, followed by fluorescence spectroscopy (λ_{exc} = 347 nm), of the selected oligoarginines, **A.** R_2G_2, **B.** R_3G, **C.** R_4, **D.** R_6 and **E.** R_8, with pyrene sensor, SC4-8Py (1 μM).

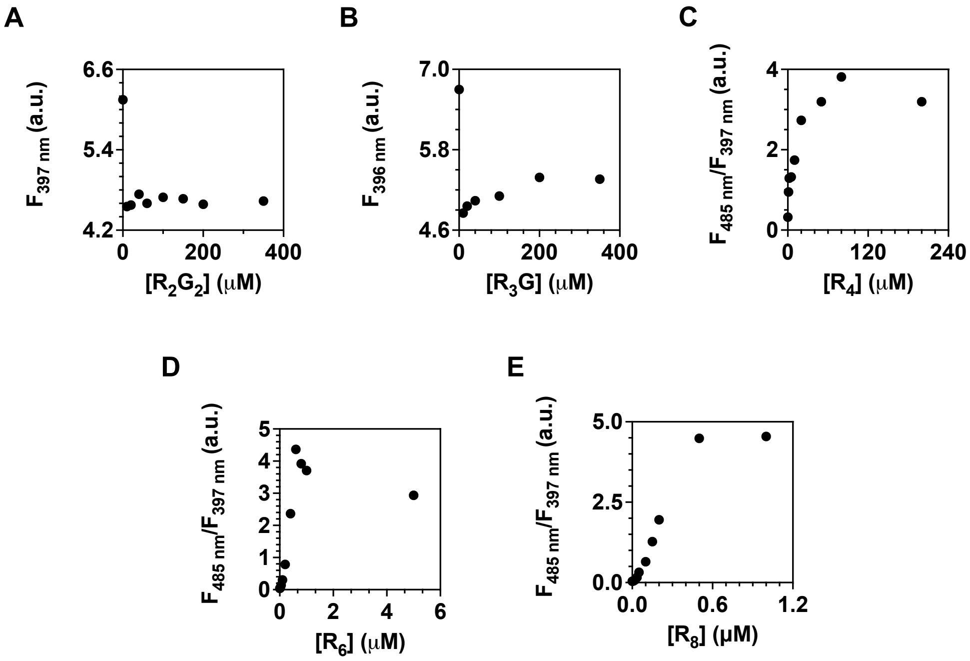

Figure C.13: Emission variation of SC4-4Py in the presence of increasing concentration of **A.** R_2G_2 and **B.** R_3G at 396 nm and ratio of monomer (396 nm) and aggregate emission (486 nm) in the presence of **C.** R_4, **D.** R_6 and **E.** R_8.

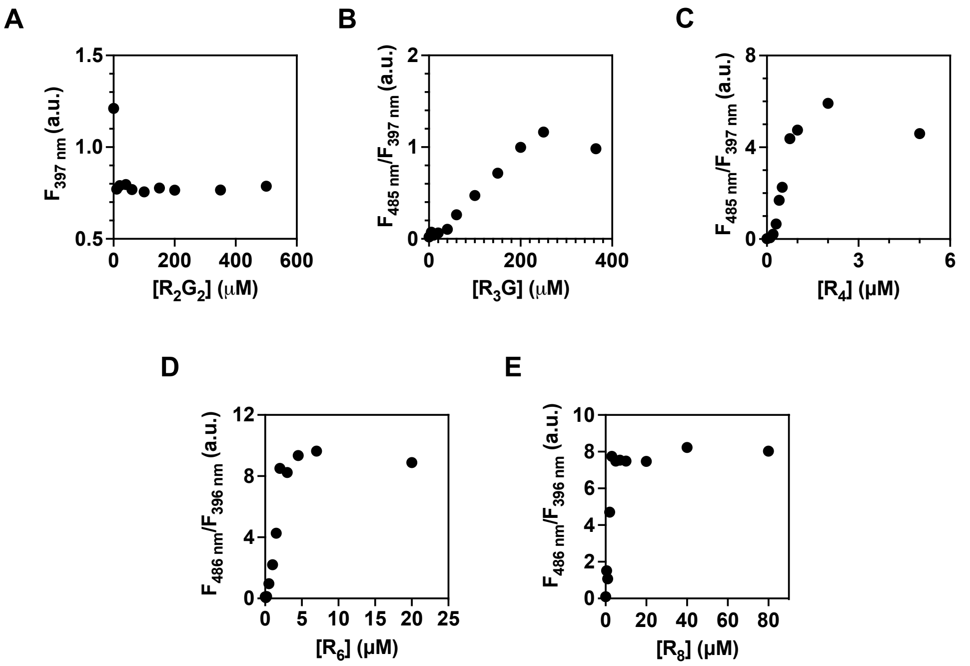

Figure C.14: Emission variation of SC4-6Py in the presence of increasing concentration of **A.** R_2G_2 at 397 nm and ratio of monomer (397 nm) and aggregate emission (486 nm) in the presence of **B.** R_3G, **C.** R_4, **D.** R_6 and **E.** R_8.

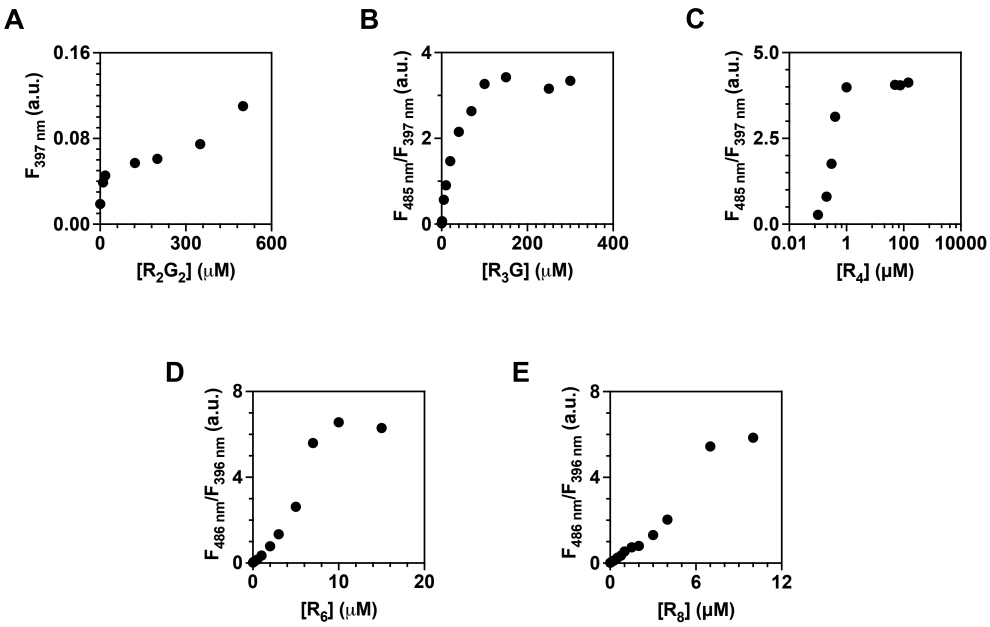

Figure C.15: Emission variation of SC4-8Py in the presence of increasing concentration of **A.** R_2G_2 at 397 nm and ratio of monomer (397 nm) and aggregate emission (486 nm) in the presence of **B.** R_3G, **C.** R_4, **D.** R_6 and **E.** R_8.

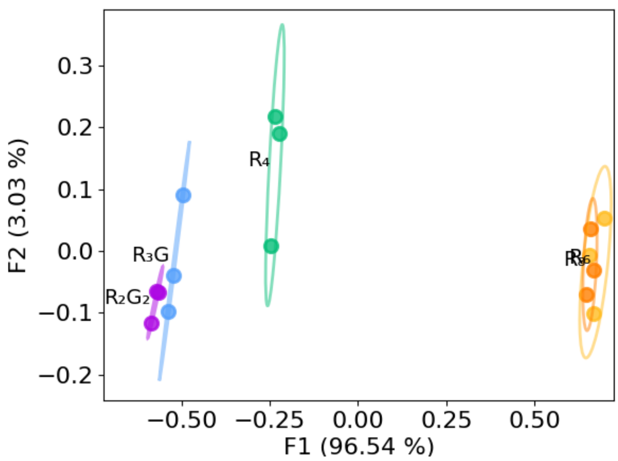

Figure C.16: Principal component analysis (PCA) of of the emission of the three SC4-nPy sensors (5 μM) in the presence of 10 μM of each peptide, following only the quenching of monomer emission. The data used consisted of the data at three different wavelengths (λ = 366, 376 and 384 nm), and using triplicate samples of each of the peptides. The ellipses correspond to 95% confidence intervals for each group of peptide samples. While distinction of some of the peptides is possible, for larger oligoarginines differentiation is quickly lost when the ratiometric signal is not used.

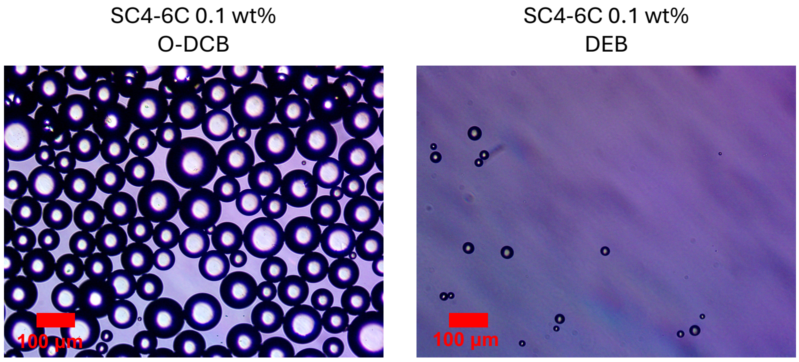

Figure C.17: Comparison of obtained O/W emulsions in SC4-6C 0.1 wt% with the two organic solvents, o-dichlorobenzene (O-DCB) and diethylbenzene (DEB), captured by optical microscopy.

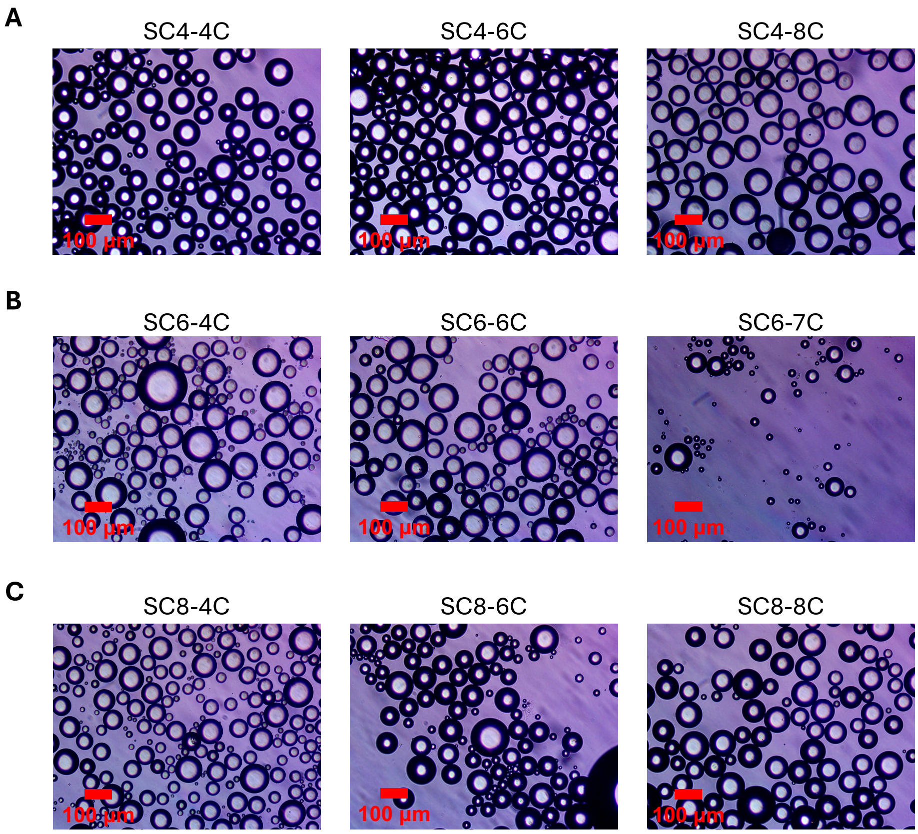

Figure C.18: Optical microscope images of obtained polydispersed droplets in 0.1 wt% solution of the surfactants, SCn-mC, with the hosts **A.** SC4, **B.** SC6 and **C.** SC8. SC6-7C, due to solubility limitations (< 1 mg/mL), droplets were obtained in a saturated solution.

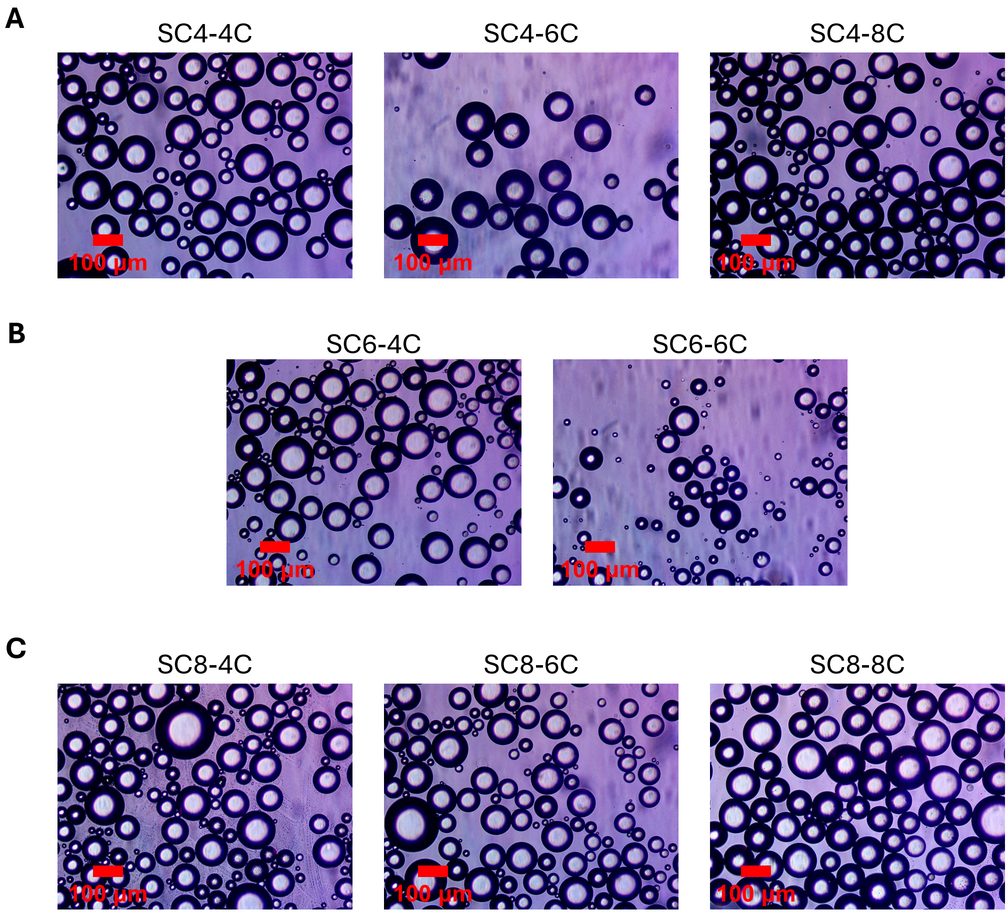

Figure C.19: Optical microscope images of obtained polydispersed droplets in 0.05 wt% solution of the surfactants, SCn-mC, with the hosts **A.** SC4, **B.** SC6 and **C.** SC8.

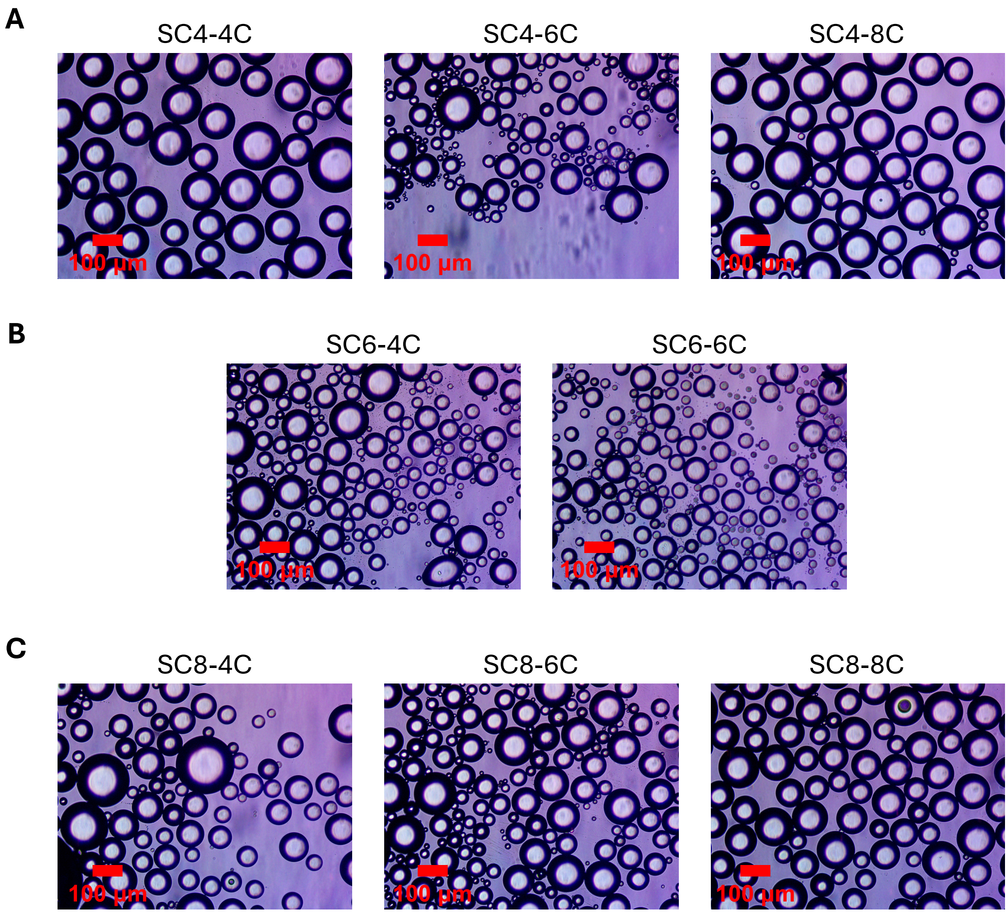

Figure C.20: Optical microscope images of obtained polydispersed droplets in 0.025 wt% solution of the surfactants, SCn-mC, with the hosts **A.** SC4, **B.** SC6 and **C.** SC8.

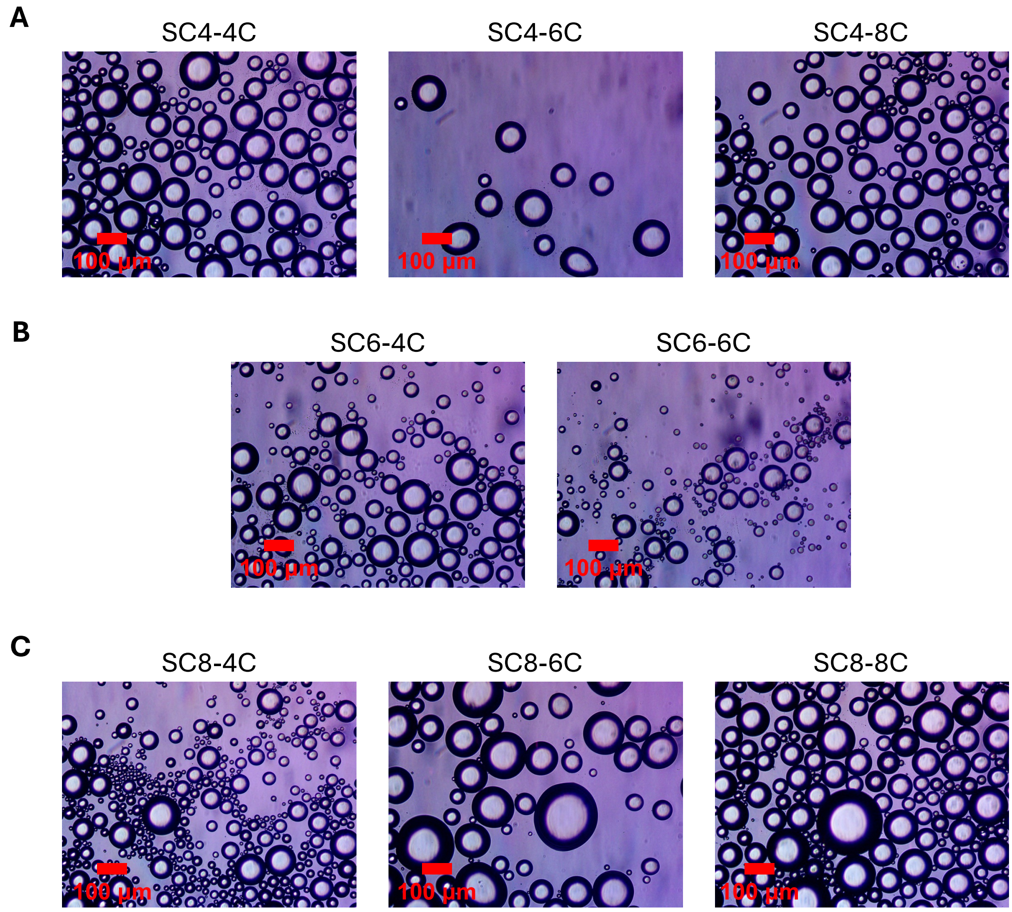

Figure C.21: Optical microscope images of obtained polydispersed droplets in 0.0125 wt% solution of the surfactants, SCn-mC, with the hosts **A.** SC4, **B.** SC6 and **C.** SC8.

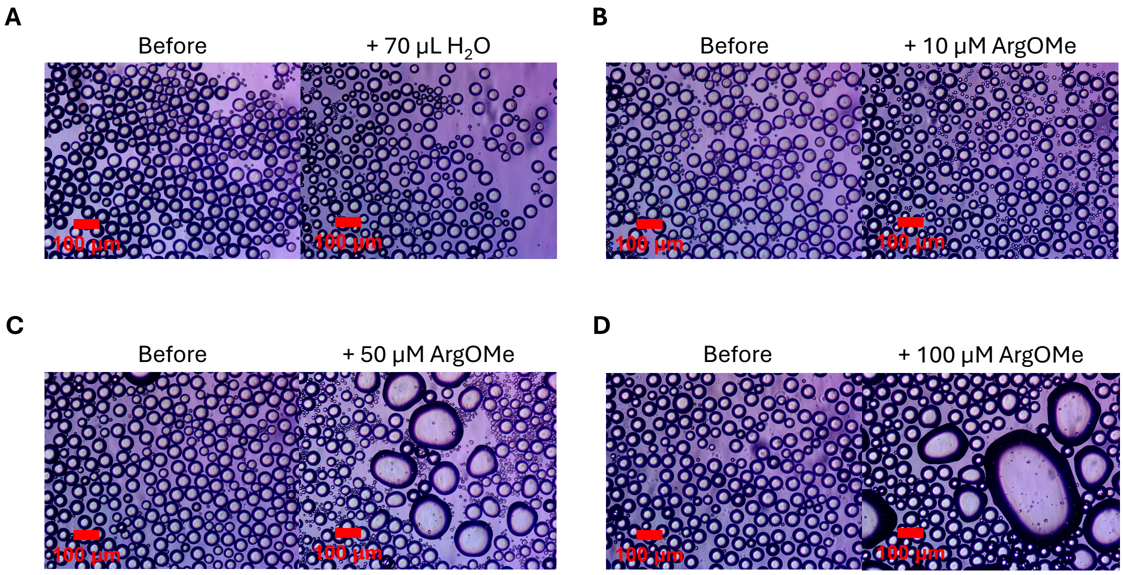

Figure C.22: Optical microscopy images of O/W O-DCB monodisperse droplets prepared in SC4-4C 0.037 wt% before and after addition of **A.** 70 μL of H_2O, **B.** 10 μM, **C.** 50 μM and **D.** 100 μM of ArgOMe.

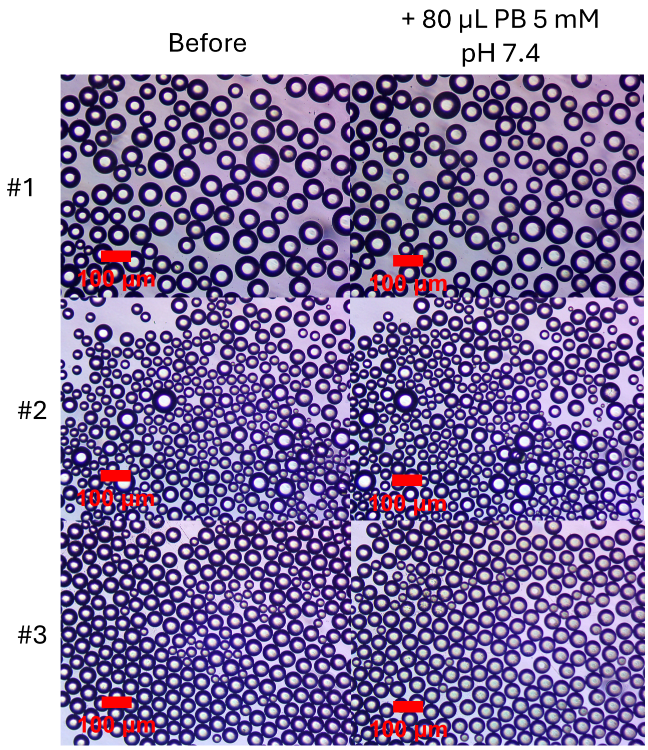

Figure C.23: Optical microscopy images of triplicates of O/W O-DCB monodisperse droplets prepared in SC4-4C 0.037 wt% before and after addition of PB 5 mM pH 7.4.

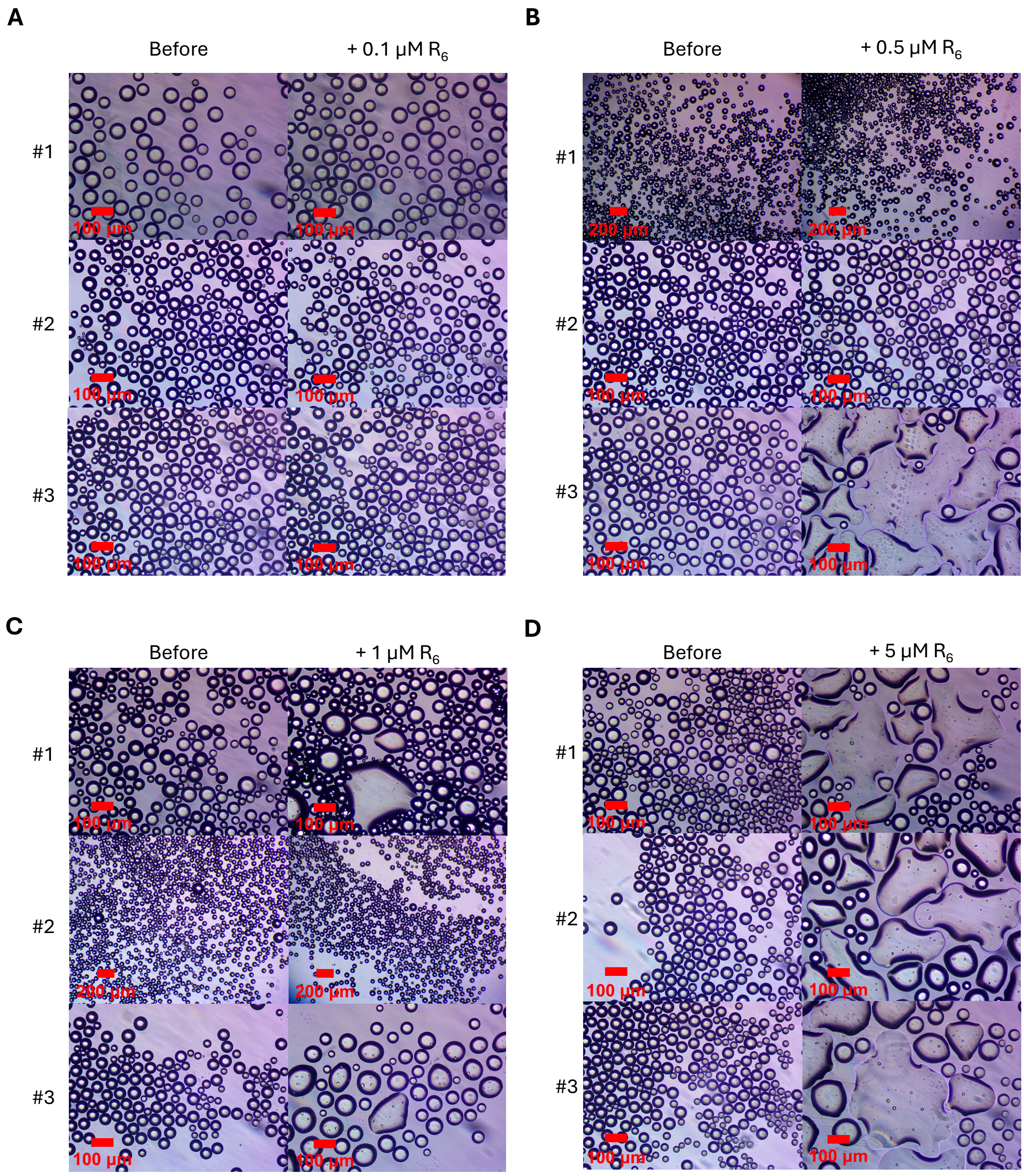

Figure C.24: Optical microscopy images of triplicates of O/W O-DCB monodisperse droplets prepared in SC4-4C 0.037 wt% before and after addition of **A.** 0.1 μM, **B.** 0.5 μM, **C.** 1 μM and **D.** 5 μM of peptide R_6.

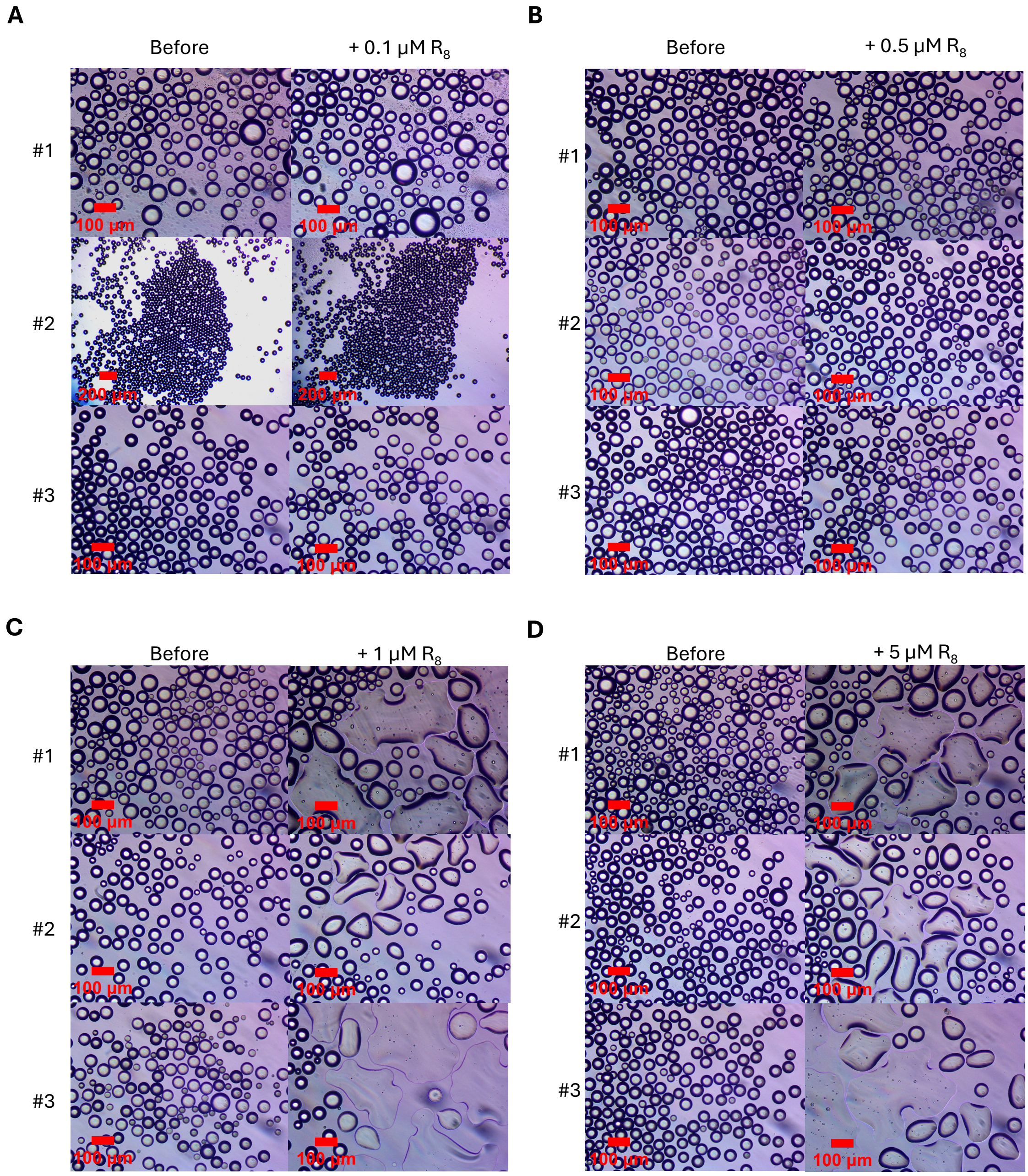

Figure C.25: Optical microscopy images of triplicates of O/W O-DCB monodisperse droplets prepared in SC4-4C 0.037 wt% before and after addition of **A.** 0.1 μM, **B.** 0.5 μM, **C.** 1 μM and **D.** 5 μM of peptide R_8.

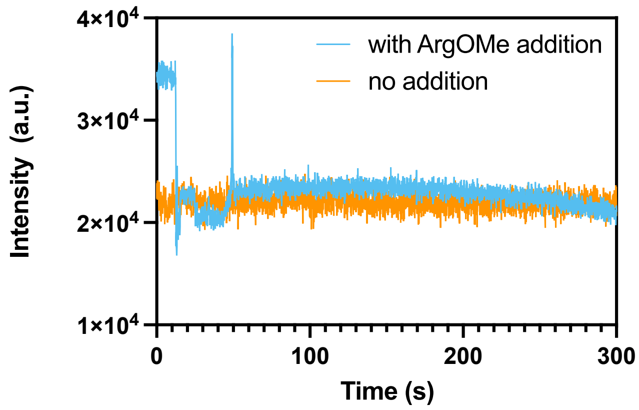

Figure C.26: Variation of emission of chemiluminescence reactants droplet samples with time and with addition of guest ArgOMe, leading to coalescence, (λ_{exc} = 350 nm) followed at 420 nm. A mix of polydisperse droplet batches with chemiluminescence reactants in one batch and the catalyst for deprotection of the TES-protected peroxide, DBU, in a distinct batch. The decrease in emission intensity for the ArgOMe addition was most likely caused by initial stray light from the experimental setup as well as disturbance of droplets upon aliquot addition.

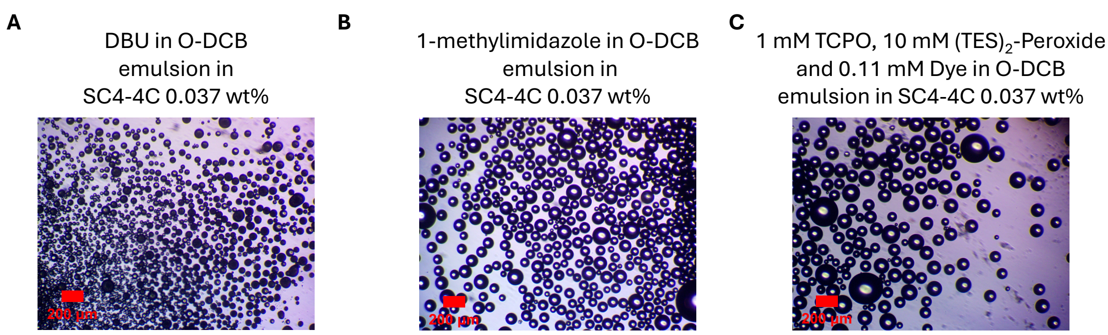

Figure C.27: Optical microscopy images of O/W polydisperse droplets of **A.** 10 mM DBU, **B.** 10 mM 1-methylimidazole and **C.** CL reagents, 1 mM TCPO, 10 mM protect peroxide and 0.11 mM of dye in O-DCB prepared in SC4-4C 0.037 wt% aqueous solution.

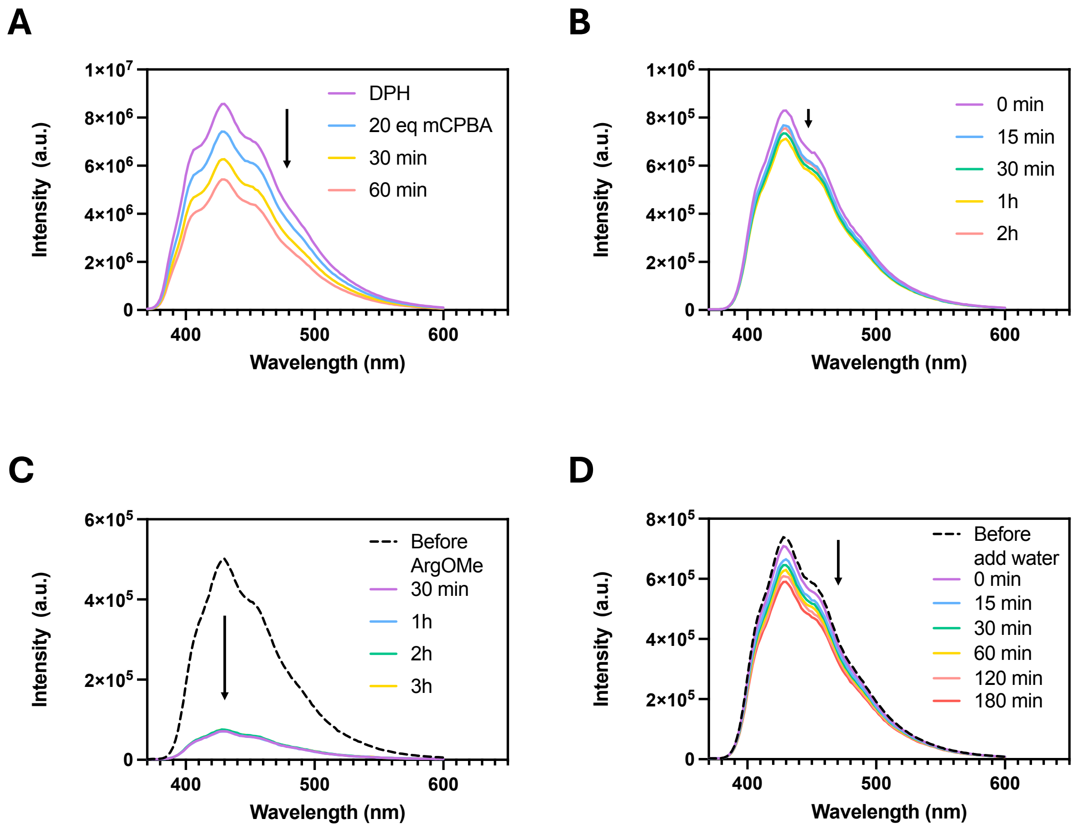

Figure C.28: Fluorescence spectroscopy (λ_{exc} = 350 nm) control experiments for epoxidation reaction in organic phase and in polydisperse droplets. **A.** DPH emission quenching in O-DCB in the presence of excess of mCPBA, imediately after addition and 30 and 60 min after addition. **B.** Fluorescence spectra over time of a mix of two polydisperse droplet batches with DPH and mCPBA in the organic phase. **C.** Fluorescence spectra of DPH polydisperse droplets before and at different times after addition of ArgOMe. **D.** Fluorescence spectra over time of a mix of two polydisperse droplet batches with DPH and mCPBA in the organic phase with addition of water, in the same volume that was added of the guest in C.

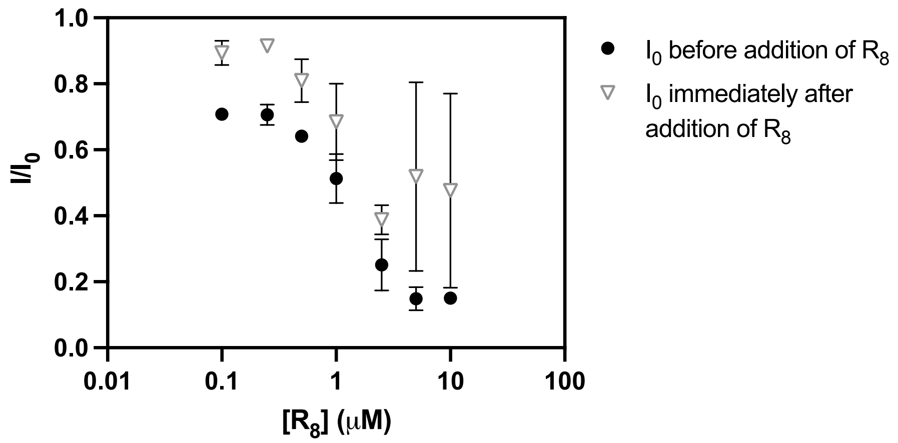

Figure C.29: Variation of emission ratio with the increase of peptide, R_8, concentration. 5 μL of each droplet batch were mixed before analyte addition. The black circles correspond to the emission normalization using the emission before addition of guest as I_0 and the inverted lined triangles correspond to the emission normalization using the emission immediately after addition of guest as I_0. The trend appears to be consistent, however the second method of normalization has a much higher error associated with it, most likely due to the slight time variations on how long after guest addition that emission spectrum was obtained.

D

Supplementary Information for Chapter 5

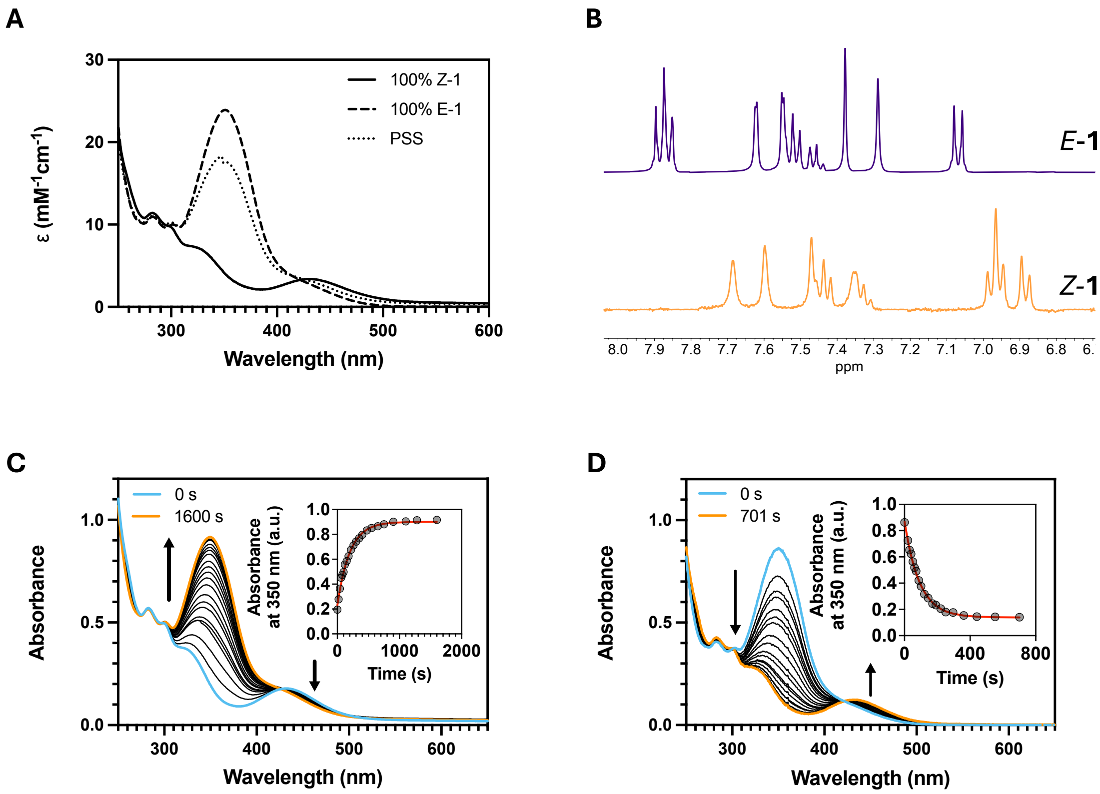

Figure D.1: **A.** Absorbance spectra of both *E* and *Z* isomers of 1 and the photostationary state (PSS; 70:30 *E*:*Z*) obtained after irradiation at 500 nm. **B.** Partial ^{1}H-NMR (in CD_3OD) spectra of the aromatic region of 1 at the dark-adapted state (*E* isomer) and at 366 nm (*Z* isomer). **C.** $Z \rightarrow E$ and **D.** $E \rightarrow Z$ photoisomerization of 1 followed by UV-vis spectroscopy upon irradiation at 500 and 366 nm, respectively.

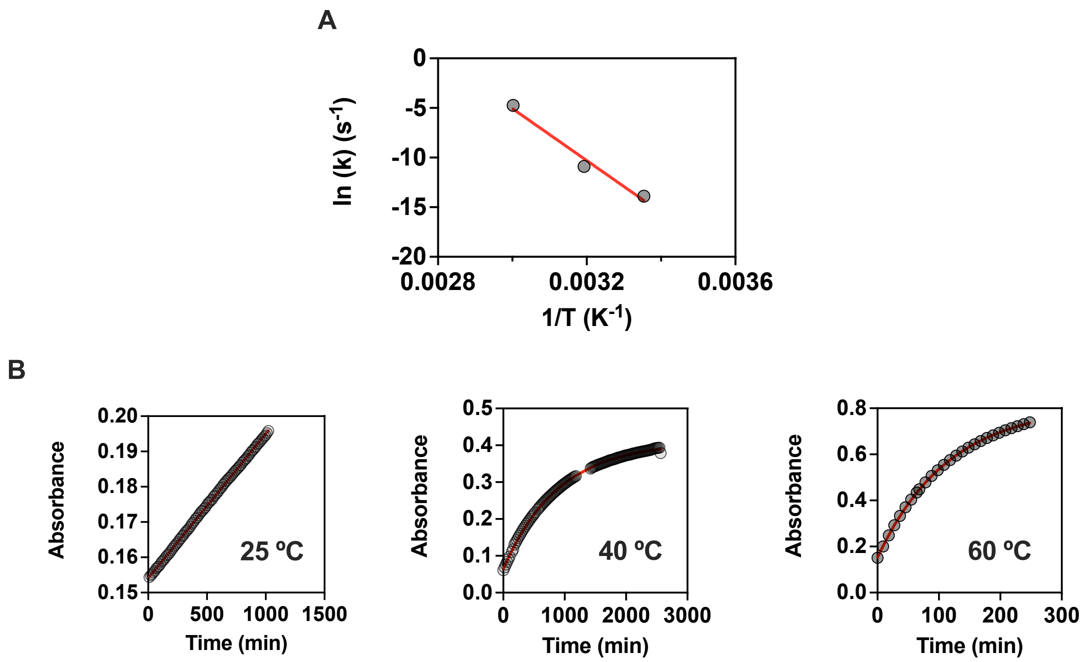

Figure D.2: **A.** Linearization of the rate constant of *Z*-1 thermal conversion to the *E* isomer, in function of the temperature. **B.** Thermal conversion of *Z*-1 to *E*-1 at different temperatures, used for the calculation of the activation energy of the thermal isomerization. The rate constants calculated for the conversion at 25, 40 and 60 °C were of 1.03×10^{-6}, 1.87×10^{-5} and 8.68×10^{-3} s^{-1}, respectively.

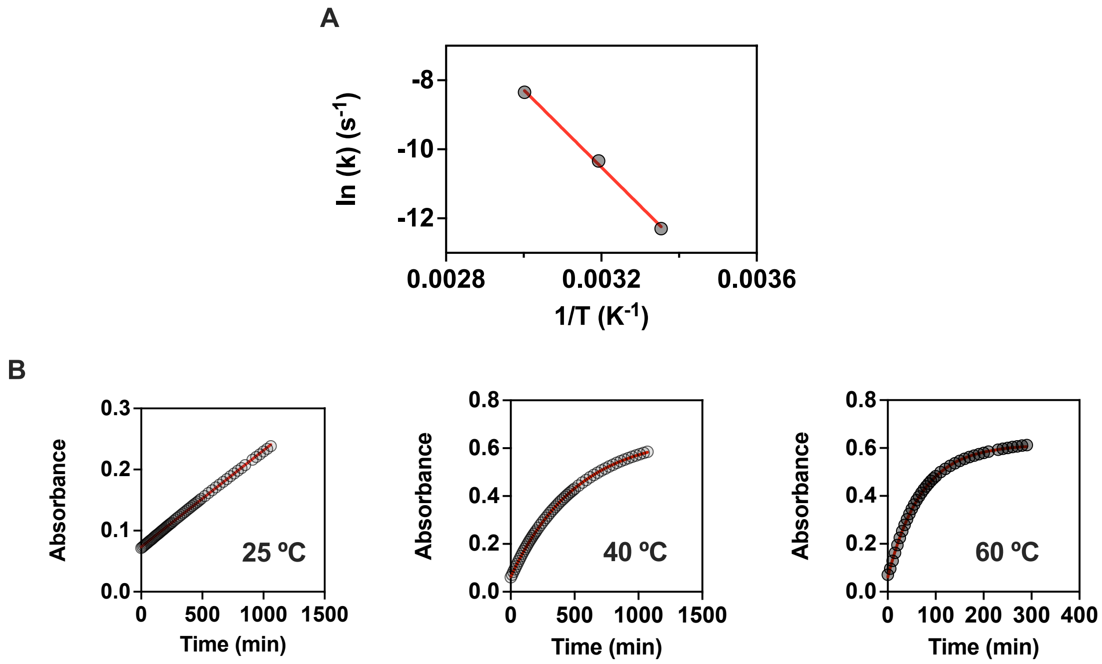

Figure D.3: **A.** Linearization of the rate constant of *Z*-2 thermal conversion to the *E* isomer, in function of the temperature. **B.** Thermal conversion of *Z*-2 to *E*-2 at different temperatures, used for the calculation of the activation energy of the thermal isomerization. The rate constants calculated for the conversion at 25, 40 and 60 °C were of 4.55×10^{-6}, 3.24×10^{-5} and 2.37×10^{-4} s^{-1}, respectively.

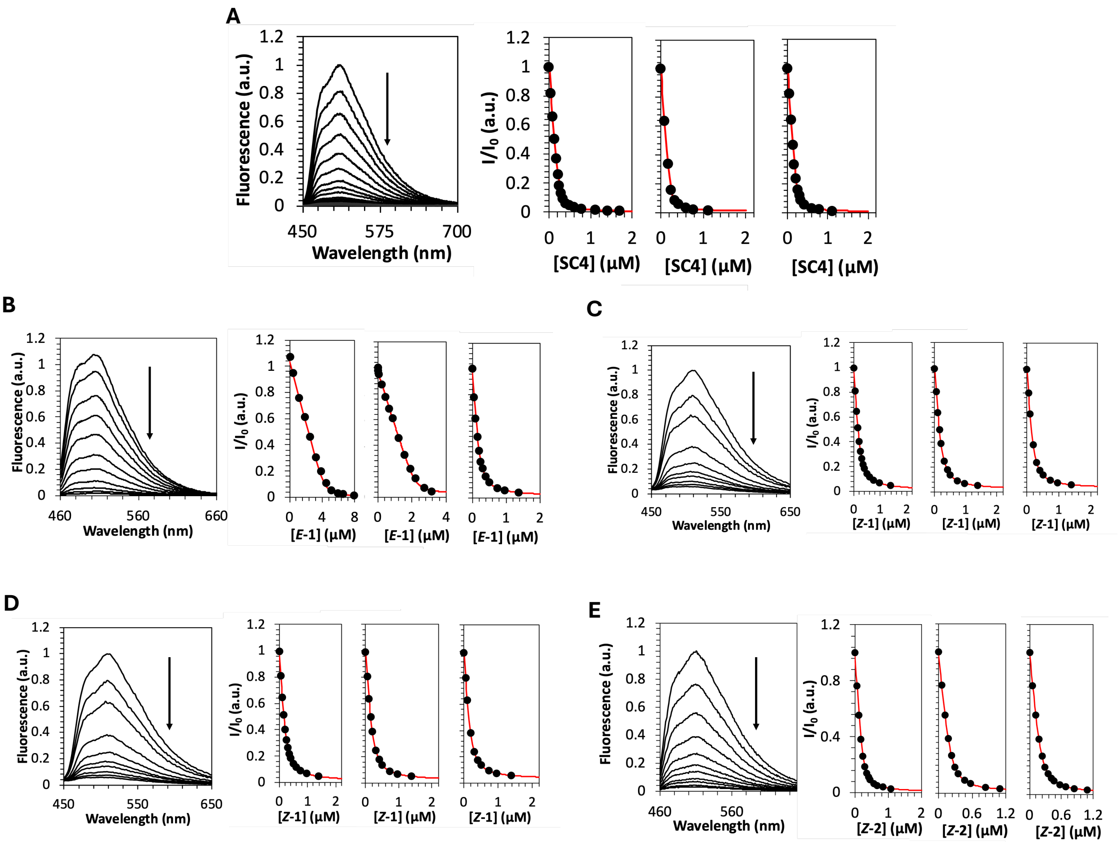

Figure D.4: Fluorescence titration of the lucigenin dye with increasing concentrations of **A.** SC4, **B.** *E*-1, **C.** *Z*-1, **D.** *E*-2 and **E.** *Z*-2 in water (5 mM phosphate buffer pH 7.3, λ_{exc} = 369 nm). LCG concentration was fixed 0.2 μM in all experiments, except for the first *E*-1 and *E*-2 titrations where [LCG] = 4.8 and 1.5 μM, respectively. All titrations were performed three times.

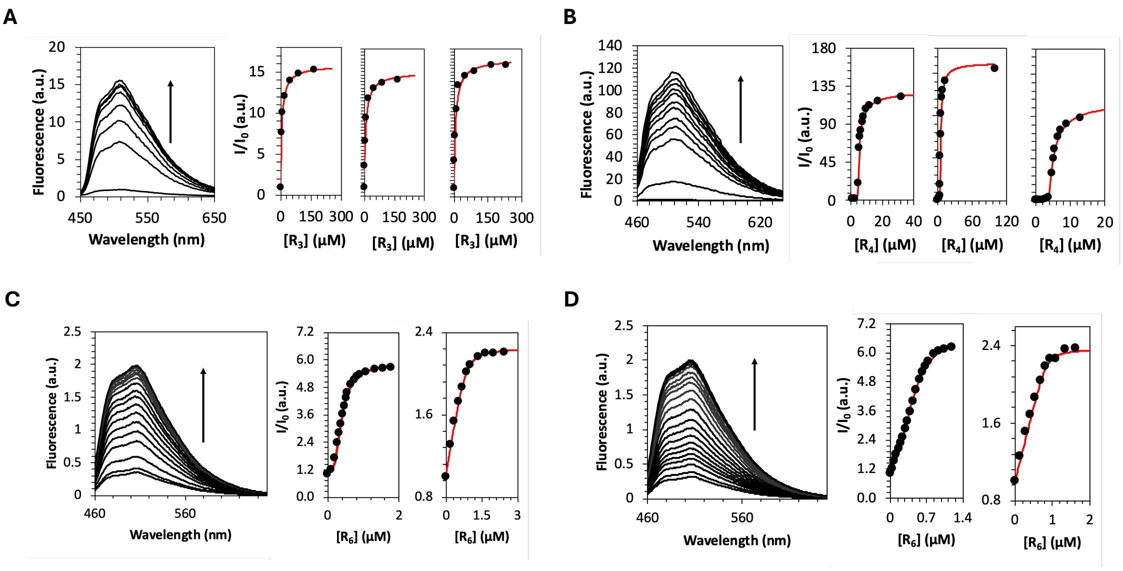

Figure D.5: Indicator displacement assay of the several oligoarginines **A.** R_3 **B.** R_4 **C.** R_6 and **D.** R_8, using SC4:LCG as the reporter pair (5 mM phosphate buffer pH 7.3, λ_{exc} = 369 nm). LCG and SC4 concentrations were fixed at **A.** 0.22 and 0.50 μM, for all three replicates, **B.** 0.22 and 4.7 μM for the first titration and 0.22 and 4.3 μM for the remaining two replicates, **C.** 0.22 and 0.45 μM and 1.1 and 0.85 μM and **D.** 0.28 and 0.43 μM and 1.1 and 0.85 μM, respectively, from left to right.

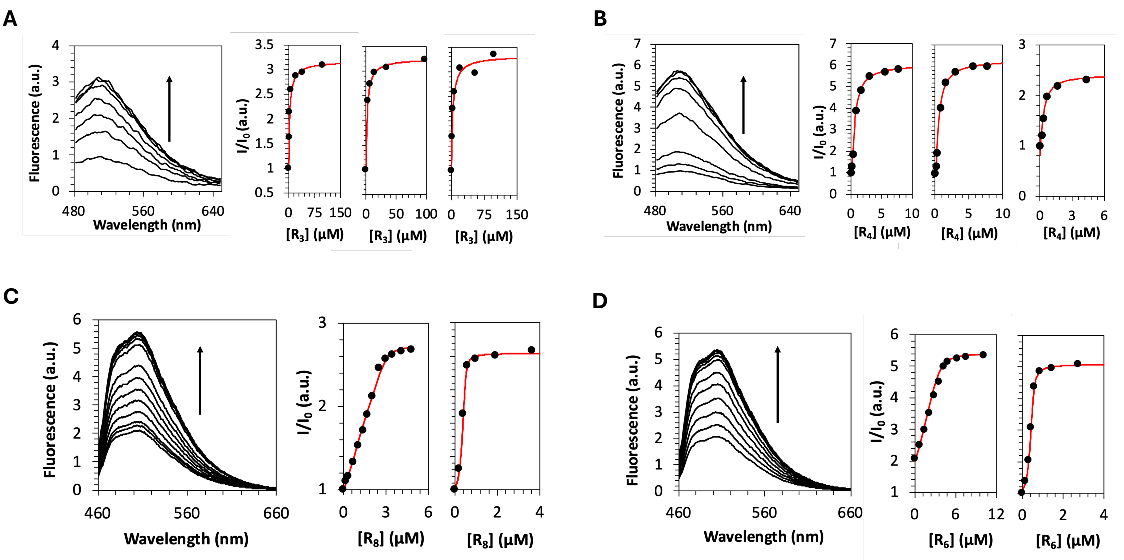

Figure D.6: Indicator displacement assay of the several oligoarginines **A.** R_3 **B.** R_4 **C.** R_6 and **D.** R_8, using *E*-1:LCG as the reporter pair (5 mM phosphate buffer pH 7.3, λ_{exc} = 369 nm). LCG and *E*-1 concentrations were fixed at **A.** 0.11 and 0.25 μM, for all three replicates, **B.** 0.22 and 0.5 μM, for the first two titrations and 0.22 and 0.23 μM for the remaining replicate, **C.** 4.0 and 3.8 μM and 0.22 and 0.5 μM, **D.** 4 and 3 μM and 0.22 and 0.5 μM, respectively, from left to right.

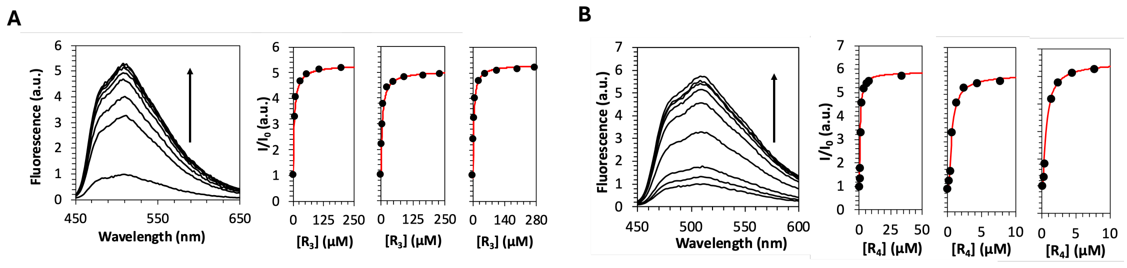

Figure D.7: Indicator displacement assay of the several oligoarginines **A.** R_3 **B.** R_4, using *Z*-1:LCG as the reporter pair (5 mM phosphate buffer pH 7.3, λ_{exc} = 369 nm). LCG and *Z*-1 concentrations were fixed at 0.22 and 0.5 μM, respectively, for all experiments.

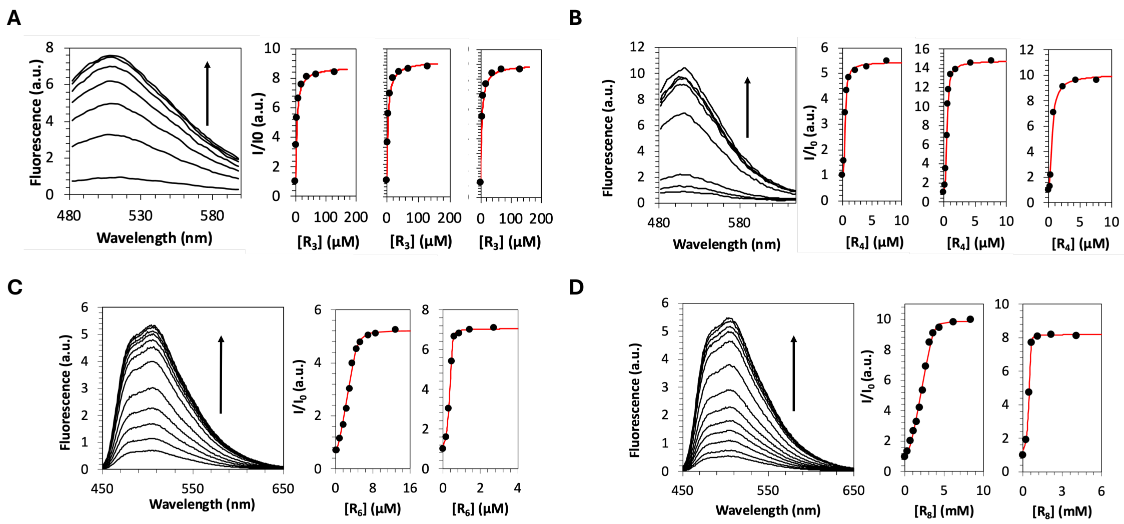

Figure D.8: Indicator displacement assay of the several oligoarginines **A.** R_3 **B.** R_4 **C.** R_6 and **D.** R_8, using *E*-2:LCG as the reporter pair (5 mM phosphate buffer pH 7.3, λ_{exc} = 369 nm). LCG and *E*-2 concentrations were fixed at **A.** 0.2 and 0.6 μM, for the first two experiments and 0.22 and 0.6 μM, for the remaining replicate, **B.** 0.22 and 0.5 μM, 0.22 and 0.58 μM and 0.22 and 0.55 μM, **C.** 4.0 and 4.3 μM and 0.22 and 0.5 μM, **D.** 3.6 and 4.3 μM and 0.22 and 0.6 μM, respectively, from left to right.

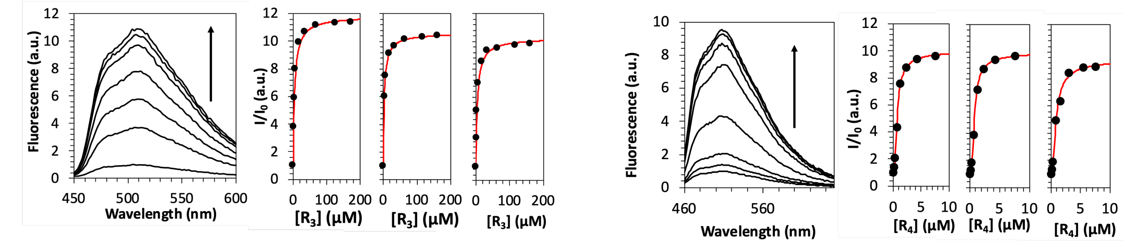

Figure D.9: Indicator displacement assay of the several oligoarginines **A.** R_3 **B.** R_4, using *Z*-2:LCG as the reporter pair (5 mM phosphate buffer pH 7.3, λ_{exc} = 369 nm). LCG and *Z*-2 concentrations were fixed at **A.** 0.22 and 0.5 μM for all three replicates and **B.** 0.22 and 0.66 μM, 0.22 and 0.72 μM and 0.22 and 0.77 μM, respectively, from left to right.

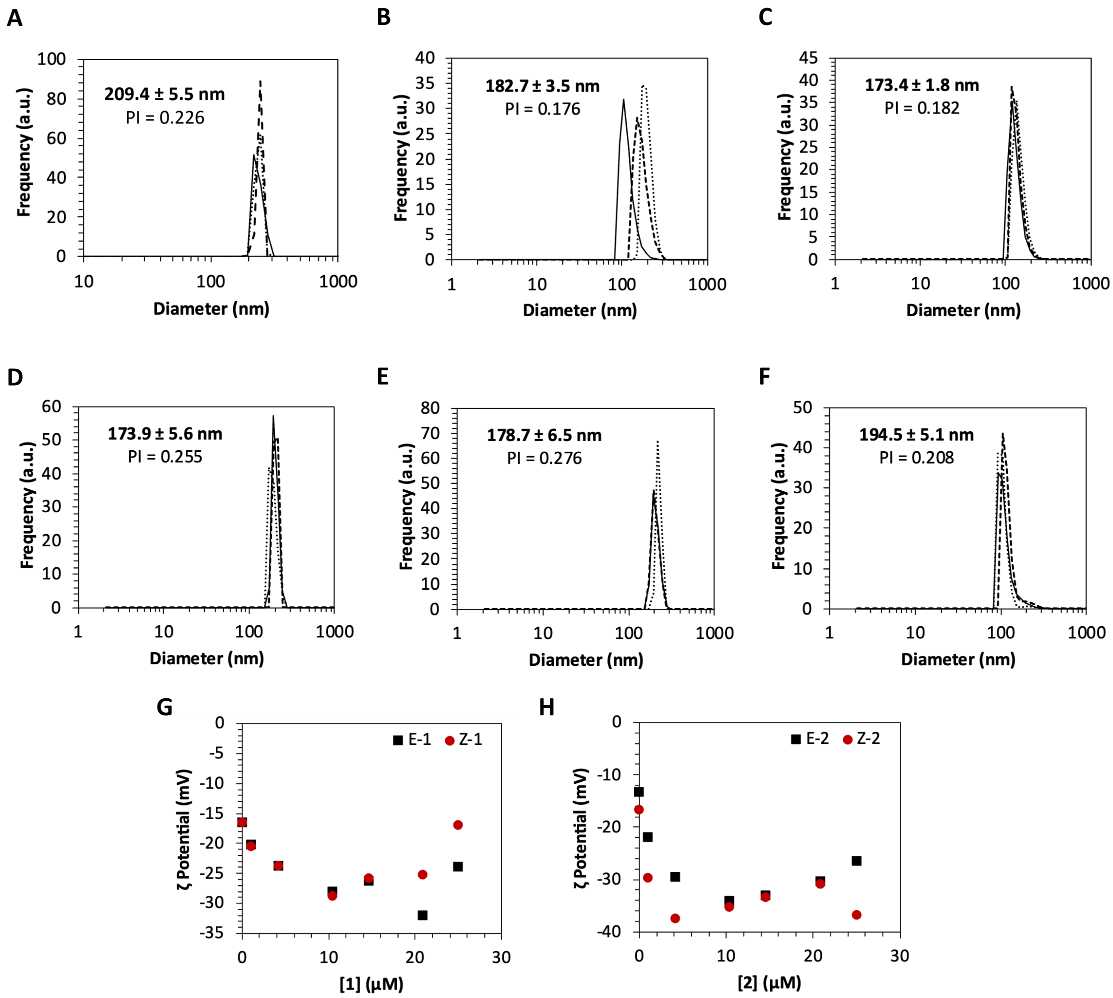

Figure D.10: **A.** to **F.** correspond to the average size distribution of the EYPC-LUV with CF, synthesized for dye-efflux and lightactivated release assays and respective Z-Average diameter: **A.** in the absence of peptide and counterion activator, in the presence of **B.** R_6, **C.** *E*-2, **D.** *Z*-2, **E.** R_6 - *E*-2 and **F.** R_6 - *Z*-2. These assays were done in the same conditions as in the following fluorescence assays, with 15 μM of EYPC-LUV$\supset$CF, 200 nM of counterion activator 2 and 4 μM of peptide. ζ-potential of the EYPC-LUV, at 260 μM, in the presence of increasing concentrations of both *E* and *Z* isomers of **G.** 1 and **H.** 2. The decrease in ζ-potential indicates that upon addition of 1 and 2 to a LUV mixture, these incorporate into the liposome membrane.

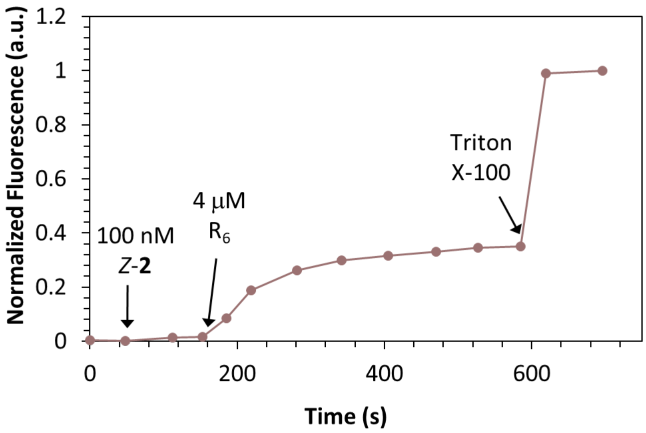

Figure D.11: Example of release assay kinetics with addition of each element marked in the graph. The EYPC-LUV⊃CF concentration was maintained at 15 μM throughout these assays, with 50 mM concentration of CF inside the liposomes. The addition of the peptide initiates the transport activation and in the end of the assay, the measurement is normalized by the addition of Triton X-100, which destroys the vesicles and leads to the maximum of CF emission (λ_{em} = 520 nm, λ_{exc} = 490 nm).

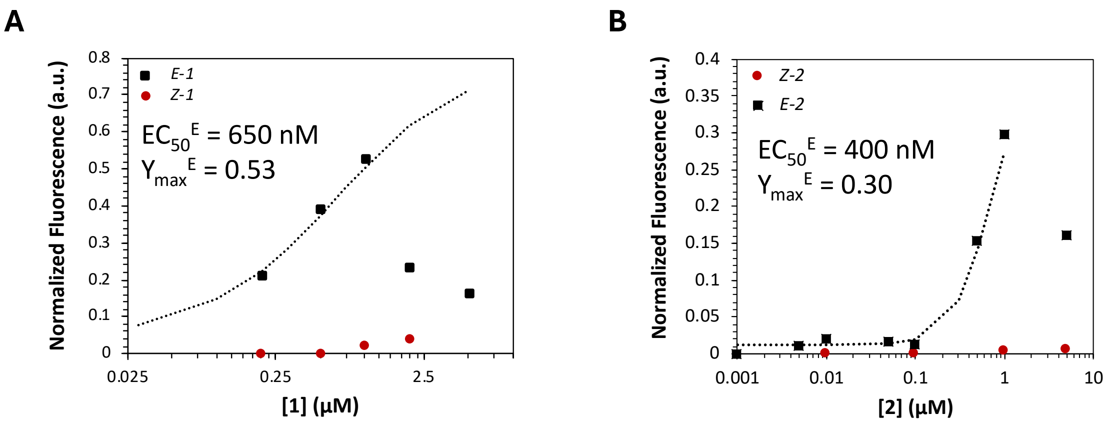

Figure D.12: Dose-response curves of the activation of release of Carboxyfluorescein by the two calix-azo activators, **A.** 1 and **B.** 2, in the presence of the peptide R_4 (5 μM). The EYPC-LUV⊃CF concentration was maintained at 15 μM throughout these assays, with 50 mM concentration of CF inside the liposomes. The efficient concentration at 50% release (EC_{50}) and maximum release of each of the activators' isomers (*E* and *Z* represented by black squares and red circles, respectively) is presented, as well as the respective fitted curves for the trans isomer; no considerable activation was observed for the *Z* isomers of both 1 and 2.

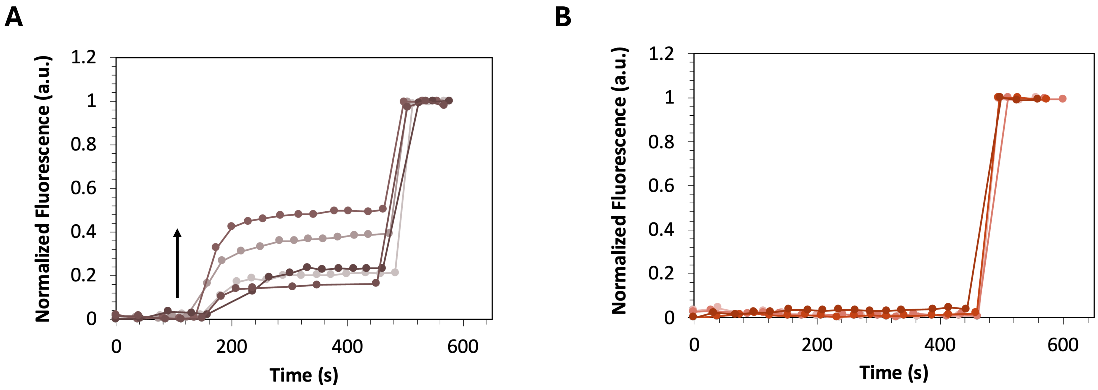

Figure D.13: Release assay kinetics for each **A.** *E* and **B.** *Z*-1 concentration represented in the dose response curves in Figure D.12, in the presence of 5 μM of the peptide R_4 (λ_{em} = 520 nm, λ_{exc} = 490 nm). At approximately 80 s, the counterion activator is added, while the peptide is added at 140 s, which corresponds to the marked increase in emission, observed in A. For *Z*-1, no activation was observed in the presence of this peptide. The measurement is normalized with the addition of a small aliquot of Triton X-100 after stabilization of release of CF by the 1-R_4 complex, to obtain the maximum emission of CF possible.

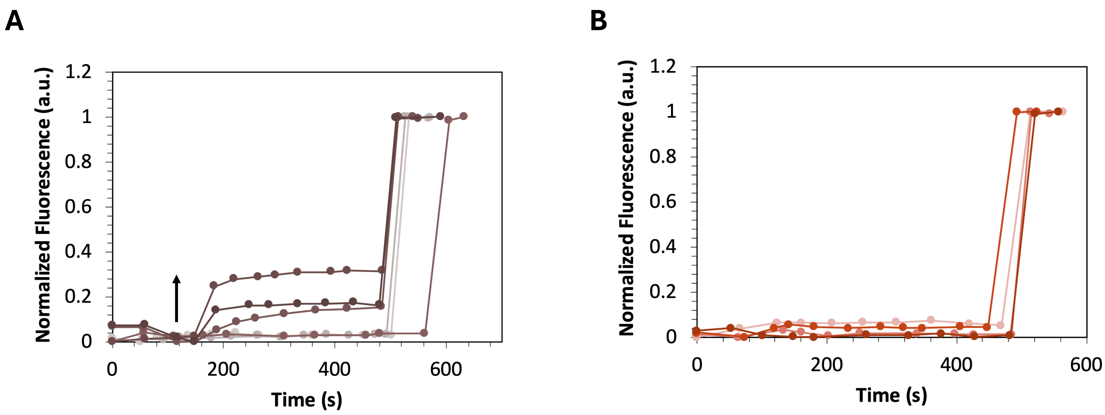

Figure D.14: Release assay kinetics for each **A.** *E* and **B.** *Z*-2 concentration represented in the dose response curves in Figure D.12, in the presence of 5 μM of the peptide R_4 (λ_{em} = 520 nm, λ_{exc} = 490 nm). At approximately 80 s, the counterion activator is added, while the peptide is added at 140 s, which corresponds to the marked increase in emission, observed in A. For *Z*-2, no activation was observed in the presence of this peptide. The measurement is normalized with the addition of a small aliquot of Triton X-100 after stabilization of release of CF by the 2-R_4 complex, to obtain the maximum emission of CF possible.

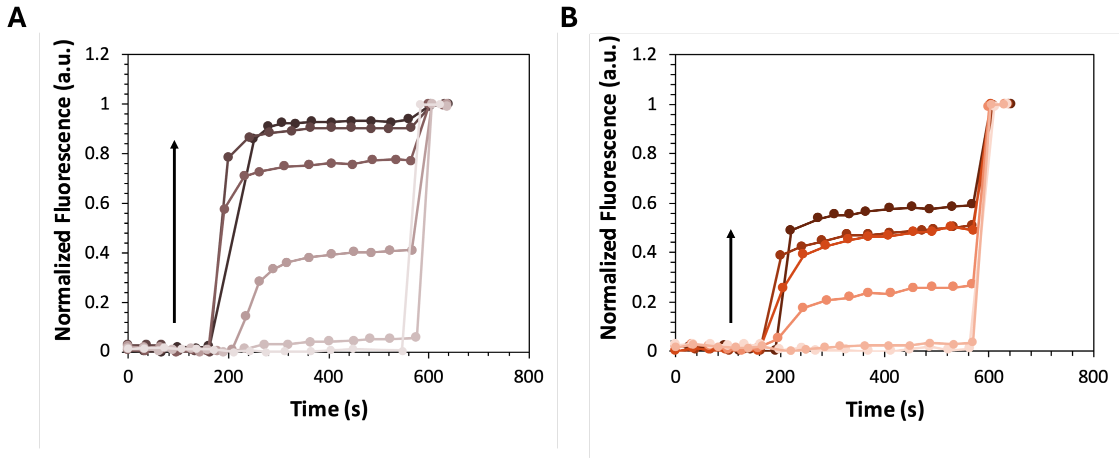

Figure D.15: Release assay kinetics for each **A.** *E* and **B.** *Z*-1 concentration represented in the dose response curves in Figure 5.4, in the presence of 4 μM of the peptide R_6 (λ_{em} = 520 nm, λ_{exc} = 490 nm). At approximately 80 s, the counterion activator is added, while the peptide is added at 140 s, which corresponds to the marked increase in emission, observed in both A and B. The measurement is normalized with the addition of a small aliquot of Triton X-100 after stabilization of release of CF by the 1-R_6 complex, to obtain the maximum emission of CF possible.

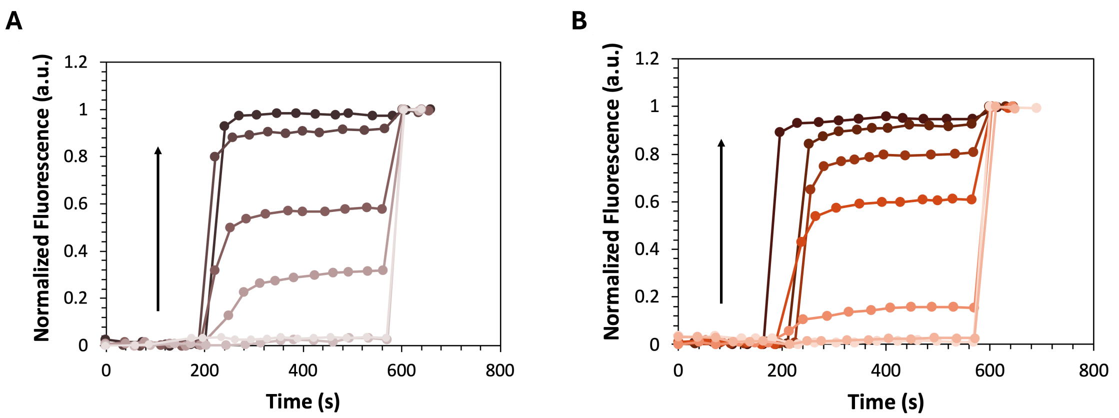

Figure D.16: Release assay kinetics for each **A.** *E* and **B.** *Z*-2 concentration represented in the dose response curves in Figure 5.4, in the presence of 4 μM of the peptide R_6 (λ_{em} = 520 nm, λ_{exc} = 490 nm). At approximately 80 s, the counterion activator is added, while the peptide is added at 140 s, which corresponds to the marked increase in emission, observed in both A and B. The measurement is normalized with the addition of a small aliquot of Triton X-100 after stabilization of release of CF by the 2-R_6 complex, to obtain the maximum emission of CF possible.

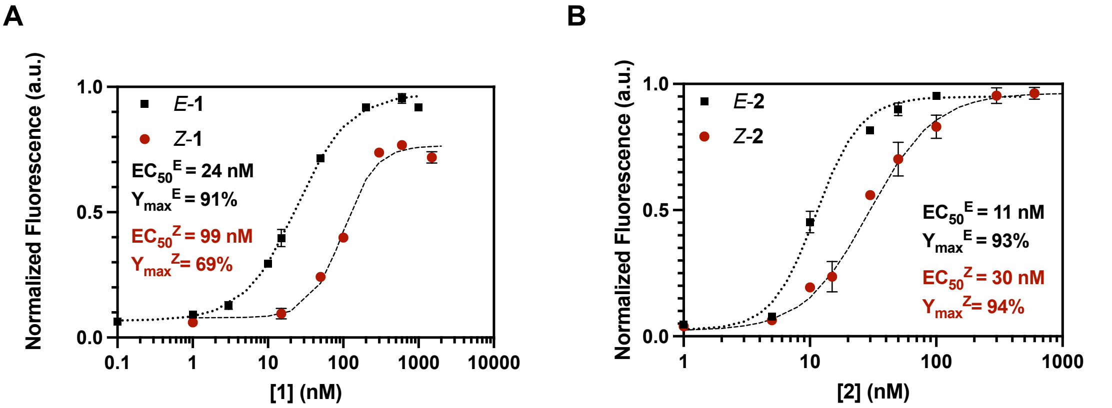

Figure D.17: Dose-response curves of the activation of release of Carboxyfluorescein by the two calix-azo activators, **A.** 1 and **B.** 2, in the presence of the peptide R_8 (4 μM). The EYPC-LUV⊃CF concentration was maintained at 15 μM throughout these assays, with 50 mM concentration of CF inside the liposomes. The efficient concentration at 50% release (EC_{50}) and maximum release of each of the activators' isomers (*E* and *Z* represented by black squares and red circles, respectively) is presented, as well as the respective fitted curves.

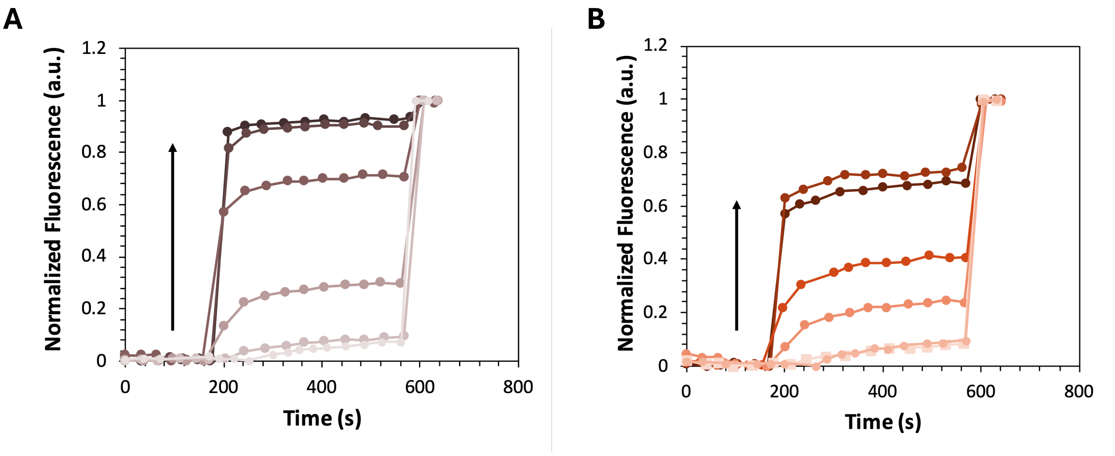

Figure D.18: Release assay kinetics for each **A.** *E* and **B.** *Z*-1 concentration represented in the dose response curves in Figure D.17, in the presence of 4 μM of the peptide R_8 (λ_{em} = 520 nm, λ_{exc} = 490 nm). At approximately 80 s, the counterion activator is added, while the peptide is added at 140 s, which corresponds to the marked increase in emission, observed in both A and B. The measurement is normalized with the addition of a small aliquot of Triton X-100 after stabilization of release of CF by the 1-R_8 complex, to obtain the maximum emission of CF possible.

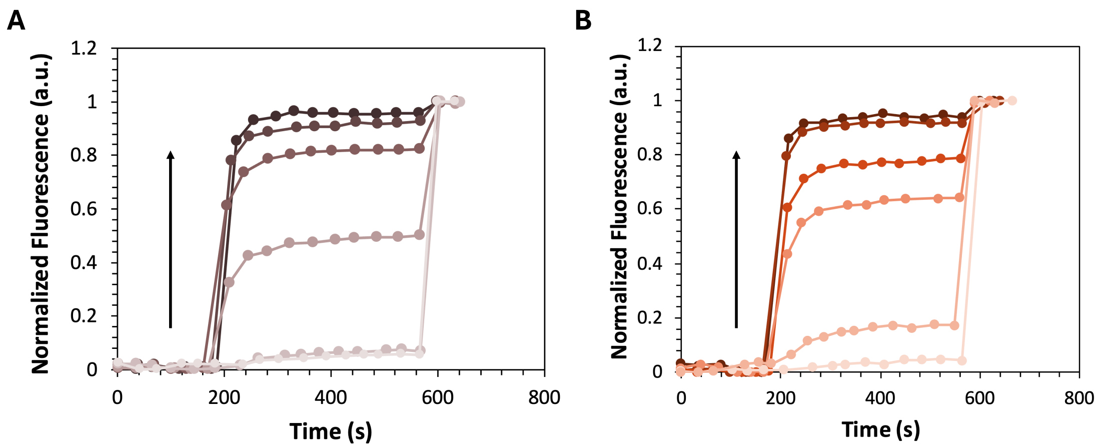

Figure D.19: Release assay kinetics for each **A.** *E* and **B.** *Z*-2 concentration represented in the dose response curves in Figure D.17, in the presence of 4 μM of the peptide R_8 (λ_{em} = 520 nm, λ_{exc} = 490 nm). At approximately 80 s, the counterion activator is added, while the peptide is added at 140 s, which corresponds to the marked increase in emission, observed in both A and B. The measurement is normalized with the addition of a small aliquot of Triton X-100 after stabilization of release of CF by the 2-R_8 complex, to obtain the maximum emission of CF possible.

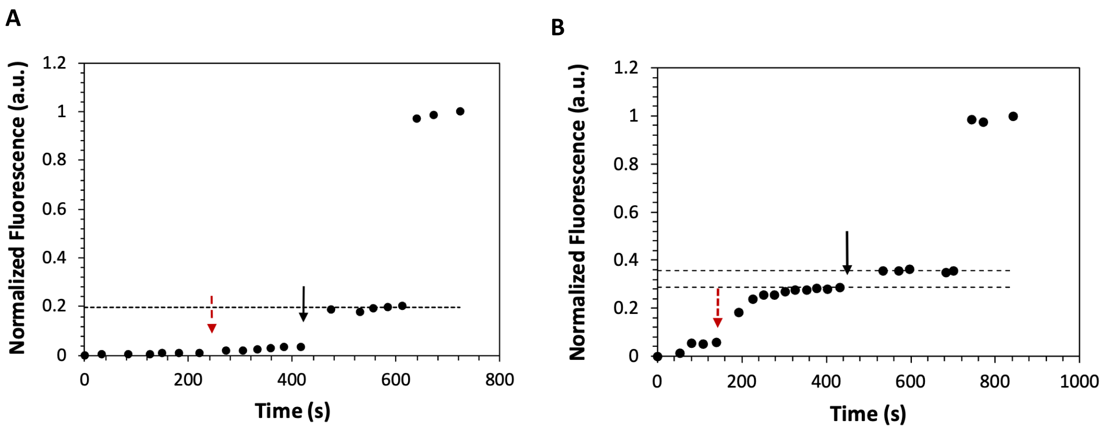

Figure D.20: Light-modulated dye efflux assays done with the peptide **A.** R_6, 4 μM , and **B.** R_8, 5 μM , with a fixed concentration of *Z*-1 of 0.20 μM for both assays. 40 μM of EYPC-LUV and 20 μM EYPC-LUV⊃CF (50 mM of CF) were used in the first assay and 30 μM of EYPC-LUV and 7 μM EYPC-LUV⊃CF (50 mM of CF) were used in the latter. The assay was performed in the same way as the dye release assays (addition of the peptide marked with a red dashed arrow) with an additional irradiation step for an interval of 30 to 40 min (marked with a black arrow), leading to an increase in release of 15% for the peptide R_6 and only 7% for the peptide R_8.

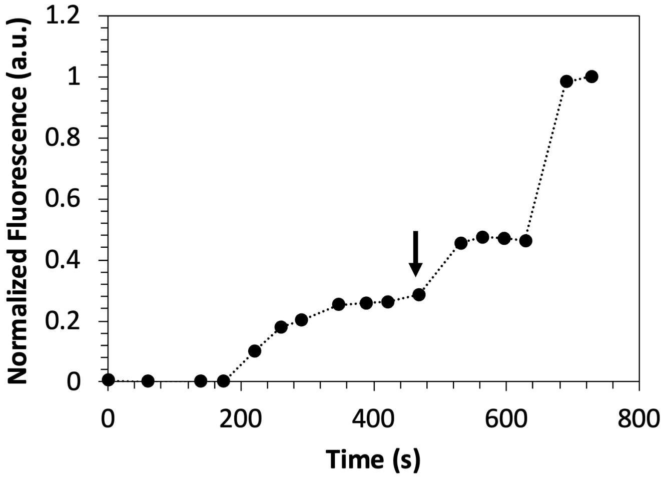

Figure D.21: Light-modulated dye efflux assay done with the peptide R_8, 4 μM, with a fixed concentration of Z-2 of 16 nM (λ_{em} = 520 nm, λ_{exc} = 490 nm). 15 μM of EYPC-LUV⊃CF (50 mM of CF) were used and the light activation step was done with a single 25 min irradiation cycle at 500 nm (marked with a black arrow). The increase of release obtained was of 14%.

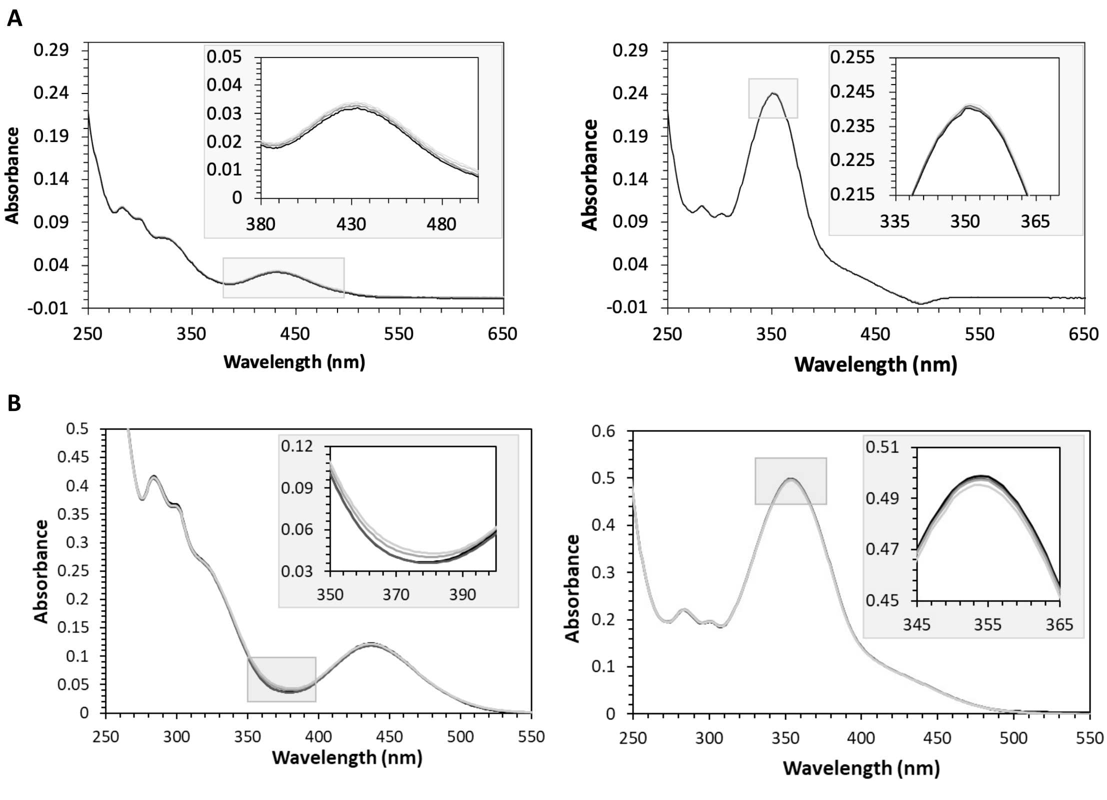

Figure D.22: Absorption spectra of Z and E- **A.** 1 and **B.** 2 in the presence of EYPC-LUV⊃CF (lipid concentration at 12 μM and CF concentration of 50 mM inside the LUV), after irradiation in the fluorimeter, used for previous experiments – excitation slits fixed at 0.5 nm, window of measurement of 100 nm and integration time of 0.1 s. Black spectrum corresponds to the initial absorption spectrum and light grey to the spectrum after 25 spectra done in the fluorimeter in the acquisition settings described.

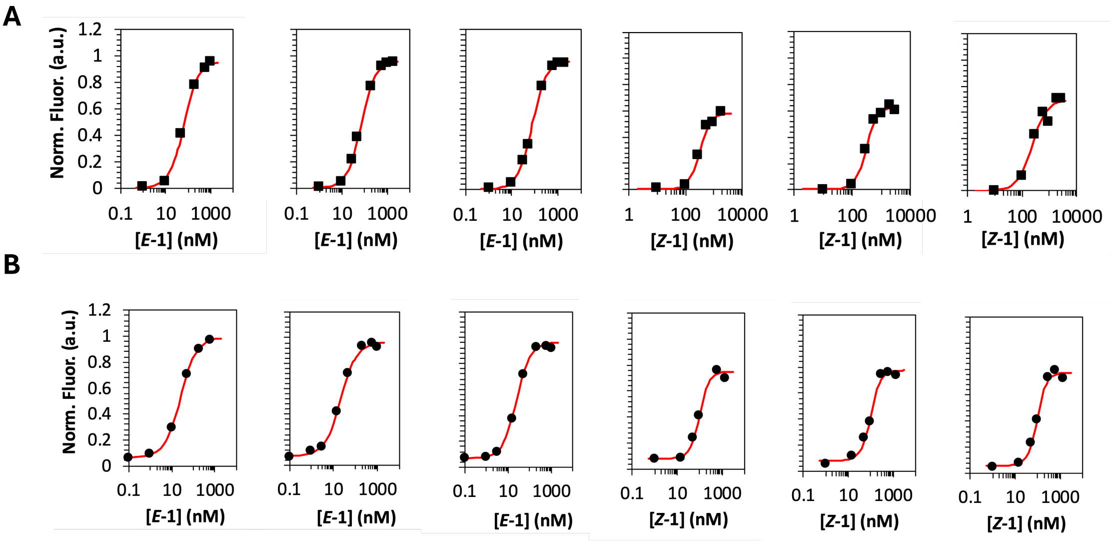

Figure D.23: Triplicates of the dose-response curves for the peptides **A.** R_6 and **B.** R_8, with both isomers of the activator 1. LUV concentration was fixed at 15 μM with 50 mM of CF encapsulated and peptide concentration was fixed at 4 μM.

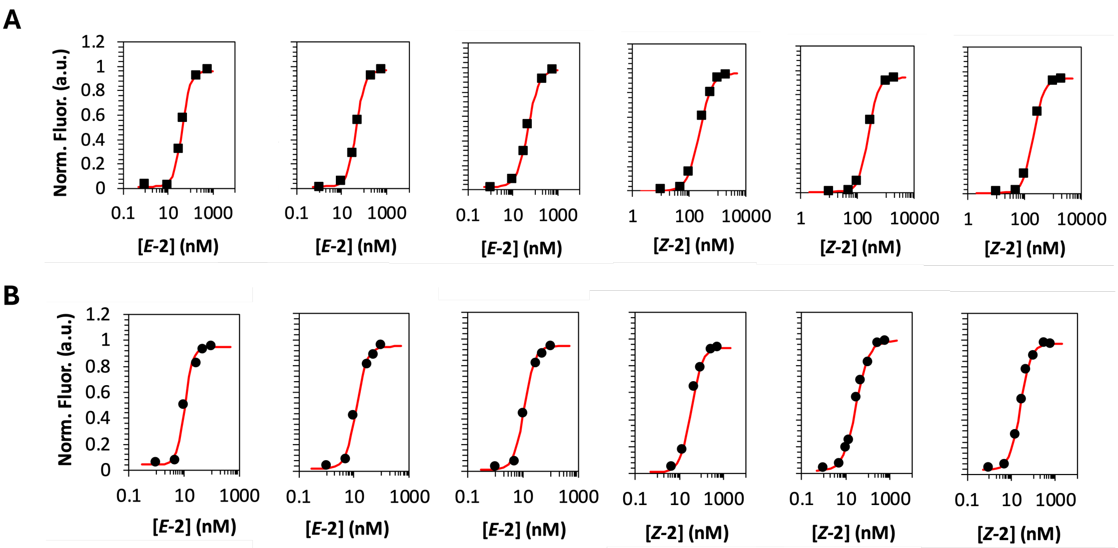

Figure D.24: Triplicates of the dose-response curves for the peptides **A.** R_6 and **B.** R_8, with both isomers of the activator 2. LUV concentration was fixed at 15 μM with 50 mM of CF encapsulated and peptide concentration was fixed at 4 μM.

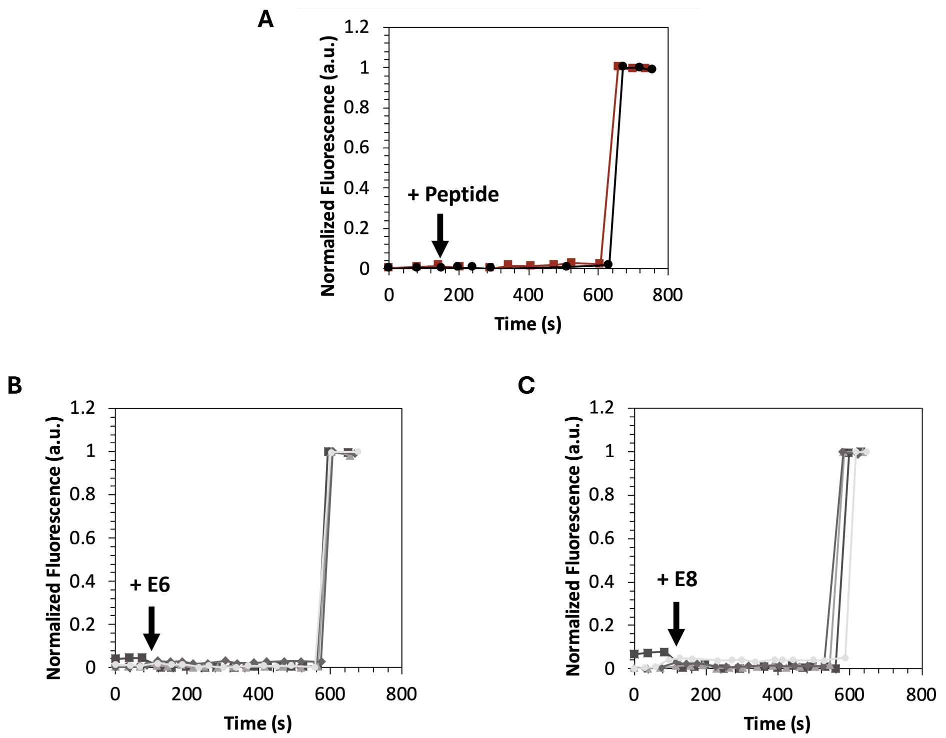

Figure D.25: Dye release assay control experiments (λ_{em} = 520 nm, λ_{exc} = 490 nm). **A.** Addition of both R_6 (black circles) and R_8 (red squares) at 4 μM to LUV solutions (15 μM of lipid, with 50 mM CF encapsulated) did not activate the transport of CF to the outside of the liposomes. **B.** and **C.** show the addition of anionic peptides that do not interact with the calixarene unit (E_6 and E_8, respectively) to a LUV (15 μM of lipid, with 50 mM CF encapsulated) and calixarene activator solution (*E*-2 from 10 nM to 100 μM, from light to dark, respectively).

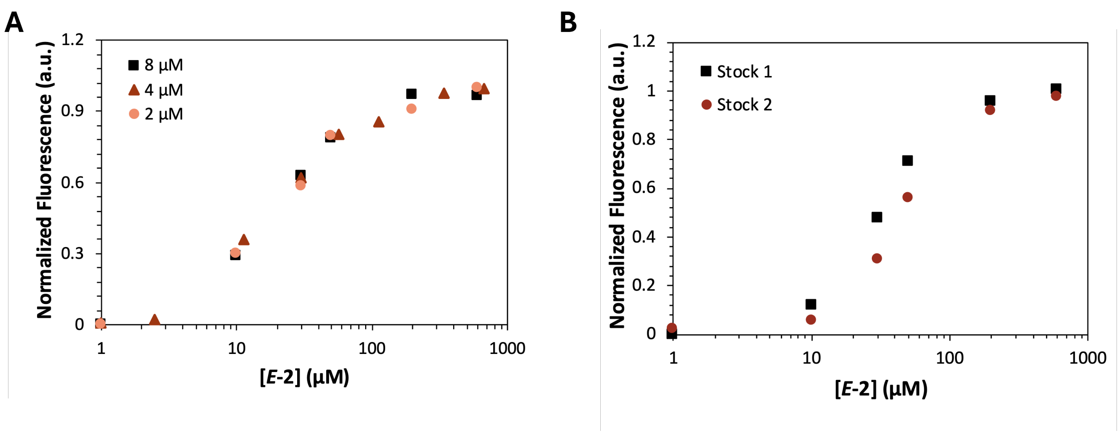

Figure D.26: Dose response curves of the activation of release of CF by the calixarene activator 2 in the presence of **A.** different concentrations of peptide, R_6, and **B.** different LUV stocks at 15 μM lipid concentration in each stock.

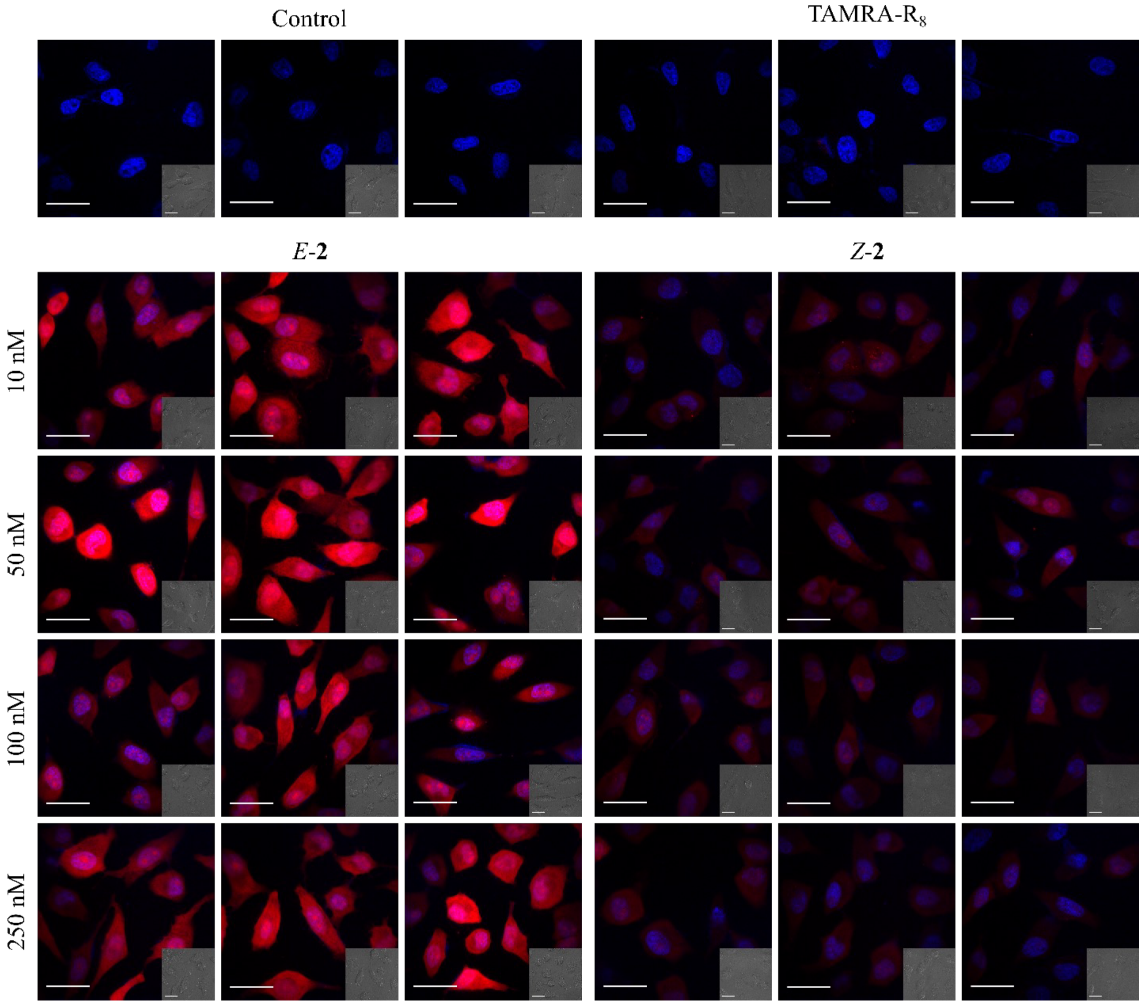

Figure D.27: Confocal microscopy images of TAMRA-R_8 (in red) cellular uptake enhanced by *E*-2 and *Z*-2. HeLa cells were incubated with TAMRA-R_8 (3 μM) in the absence (top row, right panel) or presence of several *E*-2 and *Z*-2 concentrations (10, 50, 100 and 250 nM) in DMEM stock for 25 min. Afterwards, nuclei were counterstained with Hoechst (in blue). Hoechst has been adjusted to similar intensities. Differential interference contrast (DIC) images in insets. Three representative images are presented for each condition. Scale bars, 50 μm.

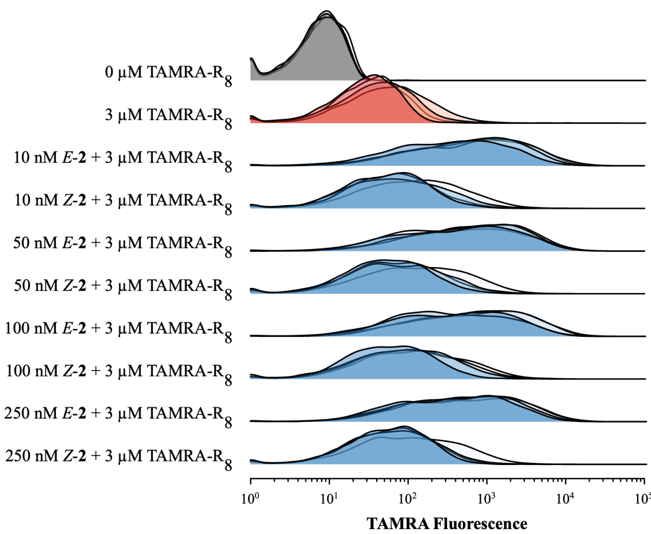

		R1	R2	R3	R4
	Control	9.10	8.51	8.23	8.19
	TAMRA-R$_8$	48.16	101.30	82.67	39.25
***E*-2**	**10 nM**	1509.30	1625.74	1279.15	856.91
	50 nM	1144.89	1480.93	1347.63	1117.65
	100 nM	1569.76	1510.04	934.77	960.32
	250 nM	1249.76	1252.16	1041.01	849.96
***Z*-2**	**10 nM**	119.15	160.44	94.49	83.65
	50 nM	137.94	155.80	99.42	80.02
	100 nM	229.26	181.69	107.07	73.67
	250 nM	108.17	120.96	89.64	79.71

Figure D.28: Flow cytometry results of TAMRA-R$_8$ cellular uptake enhanced by *E*-2 and *Z*-2. HeLa cells were incubated with TAMRA-R$_8$ (3 μM) in the absence or presence of several *E*-2 and *Z*-2 concentrations (10, 50, 100 and 250 nM) in DMEM stock for 25 min. Afterwards, cells were trypsinized and analyzed by flow cytometry. Left, normalized histograms showing TAMRA fluorescence from four replicates (curves in different colour tones) per sample. Right, TAMRA mean fluorescence intensity values for each sample and replicate (R1-R4).

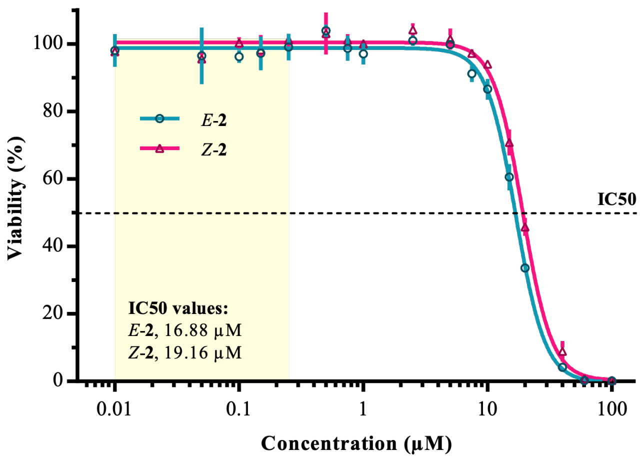

y = y₀+(ymax-y₀)/(1+(x/IC50)^n)				
	E-2		*Z*-2	
	Value	Error	Value	Error
y_0	-0.364	1.179	0.274	1.342
y_{max}	98.780	0.630	100.400	0.659
IC50	16.880	0.324	19.160	0.428
n	3.650	0.259	3.691	0.306
R^2	0.998	NA	0.998	NA

Figure D.29: MTT viability assay at increasing concentrations of *E*-2 and *Z*-2. HeLa cells were incubated with the samples in DMEM stock for 24 hours before the MTT addition. Curve fitting was performed with GraphPad Prism 6 software (v6.01) using a 4-parameters logistic model (right table). In yellow, region of concentrations employed in the delivery assays. Half Maximal Inhibitory Concentrations (IC_{50}): $IC_{50}^{E-2} = 16.88\mu M$; $IC_{50}^{Z-2} = 19.16\mu M$.

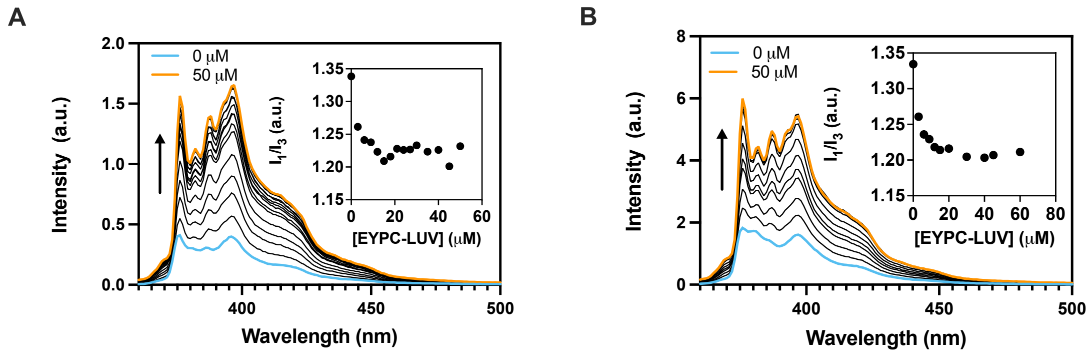

Figure D.30: Dependence of the fluorescent intensity of **A.** SC4-6Py (3.27 μM) and **B.** SC4-8Py (3.25 μM) upon the addition of egg yolk phosphatidylcholine liposome (λ_{exc} = 343 nm), EYPC-LUV (0 – 50 μM). The inset shows the ratio between the intensity of the first band (at 376 nm) and the third band (at 386 nm) at different LUV concentrations.

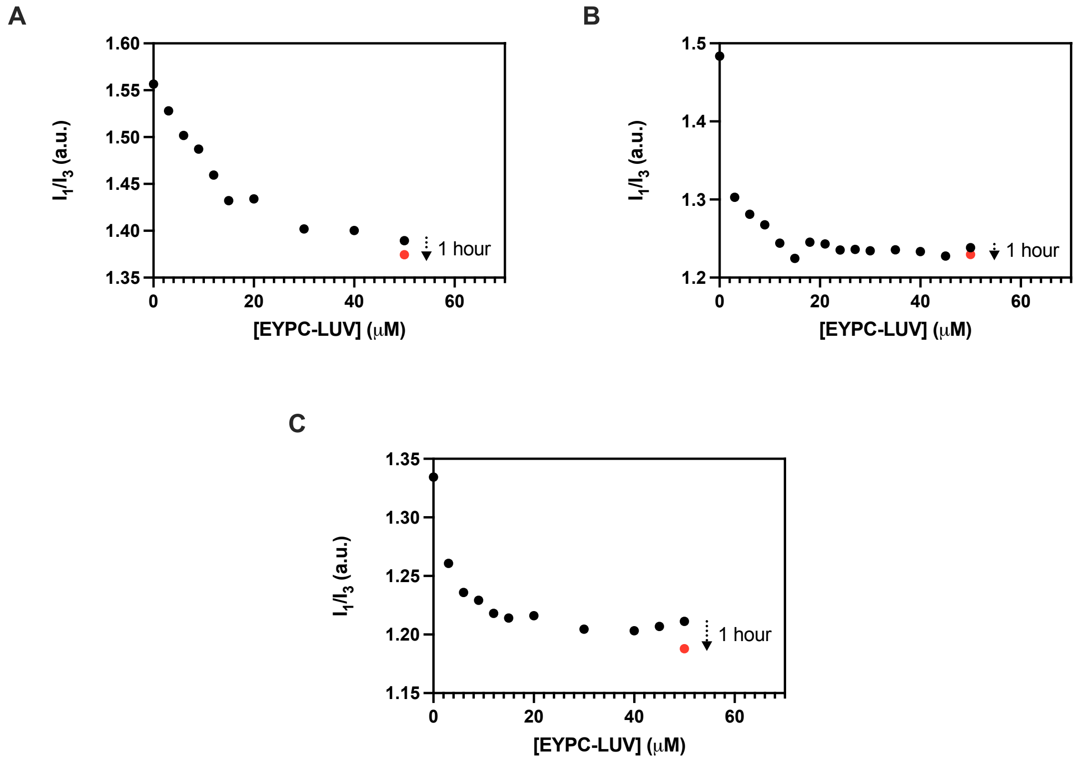

Figure D.31: Ratio of I_1 and I_3 bands of **A.** SC4-4Py (5.75 μM), **B.** SC4-6Py (3.27 μM) and **C.** SC4-8Py (3.25 μM) upon the addition of liposome (0 – 50 μM). The red point shows the change of the ratio after 1 hour at 50 μM of liposome.

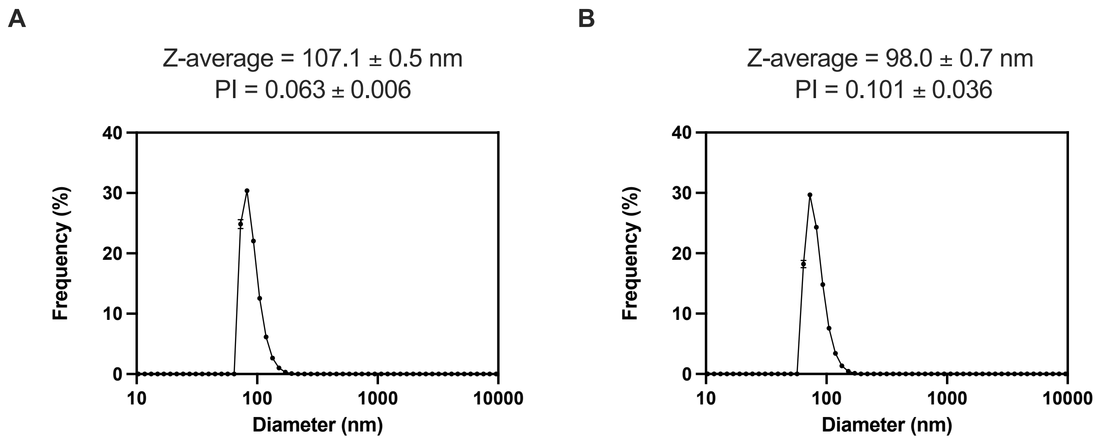

Figure D.32: Average size distribution of the EYPC-LUV, synthesized for ζ-potential studies with SC4-4Py **A.** in the absence of SC4-4Py and **B.** in the presence of excess of this sensor (70 μM). Respective Z-Average diameter and polydispersivity index with standard deviations are presented above the respective sample.

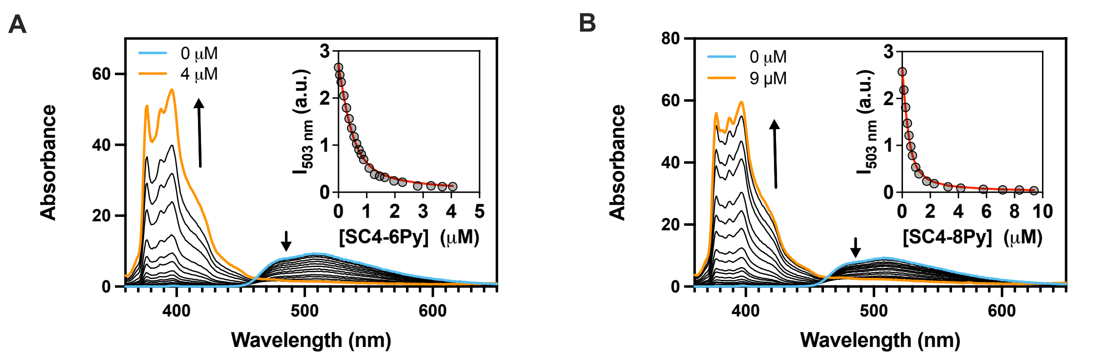

Figure D.33: Titration of LCG (0.5 μM) with **A.** SC4-6Py and **B.** SC4-8Py in the presence of EYPC-LUVs (200 μM), followed by fluorescence spectroscopy (λ_{exc} = 340 nm). Fitting of emission data at 503 nm can be found in the inset.

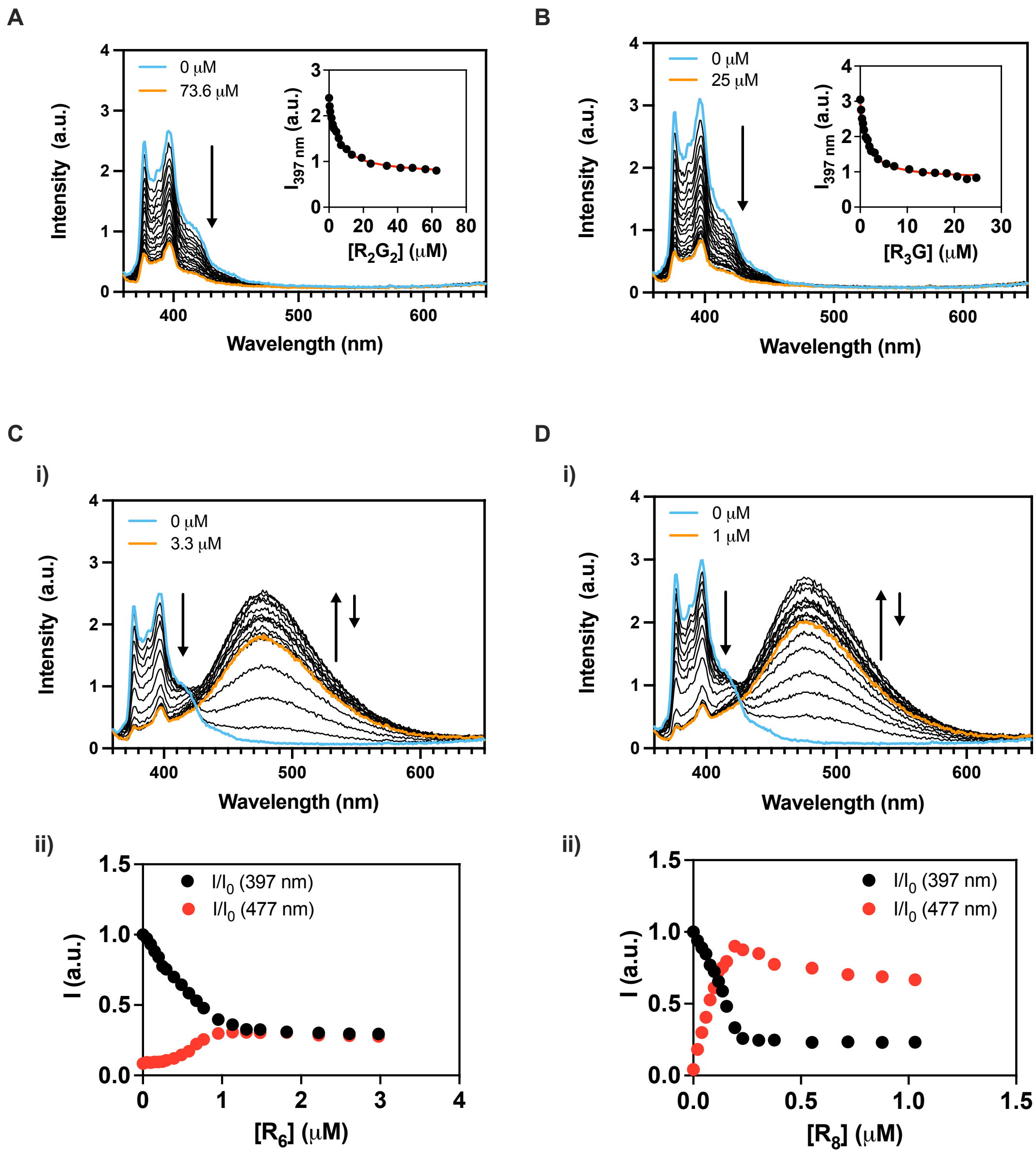

Figure D.34: Direct titration of SC4-4Py (0.7 μM) incorporated into EYPC-LUVs (7 μM) with the peptides **A.** R_2G_2, **B.** R_3G, **C.** R_6 and **D.** R_8, followed by fluorescence spectroscopy (λ_{exc} = 347 nm). Respective fitting can be found in inset for A and B and variation at 397 and 477 nm can be found in ii) for C and D.

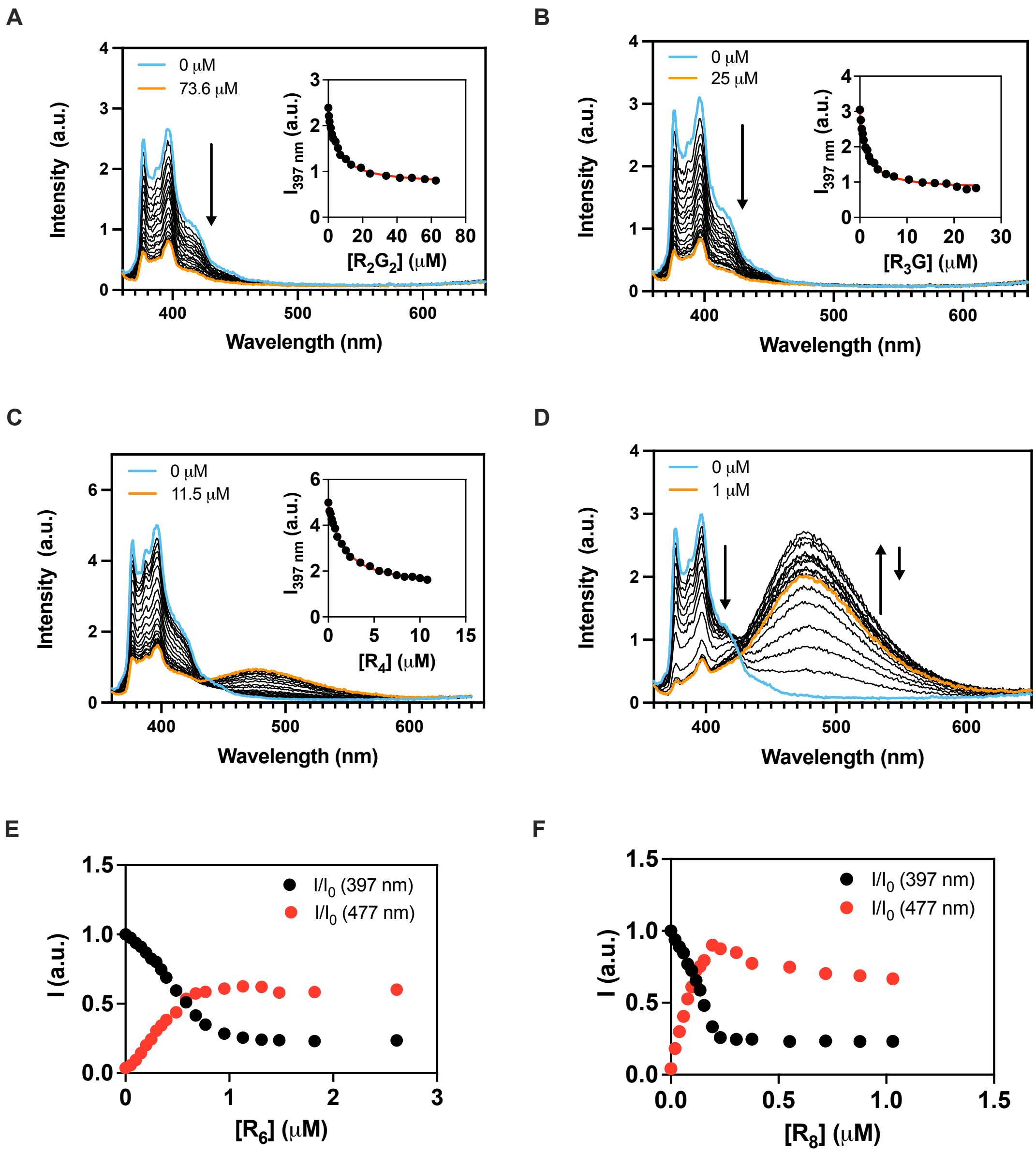

Figure D.35: Direct titration of SC4-6Py (0.7 μM) incorporated into EYPC-LUVs (7 μM) with the peptides **A.** R_2G_2, **B.** R_3G, **C.** R_4 and **D.** R_8, followed by fluorescence spectroscopy (λ_{exc} = 347 nm). Respective fitting can be found in inset for A, B and C and variation at 397 and 477 nm can be found in **E.** for R_6 and **F.** for R_8.

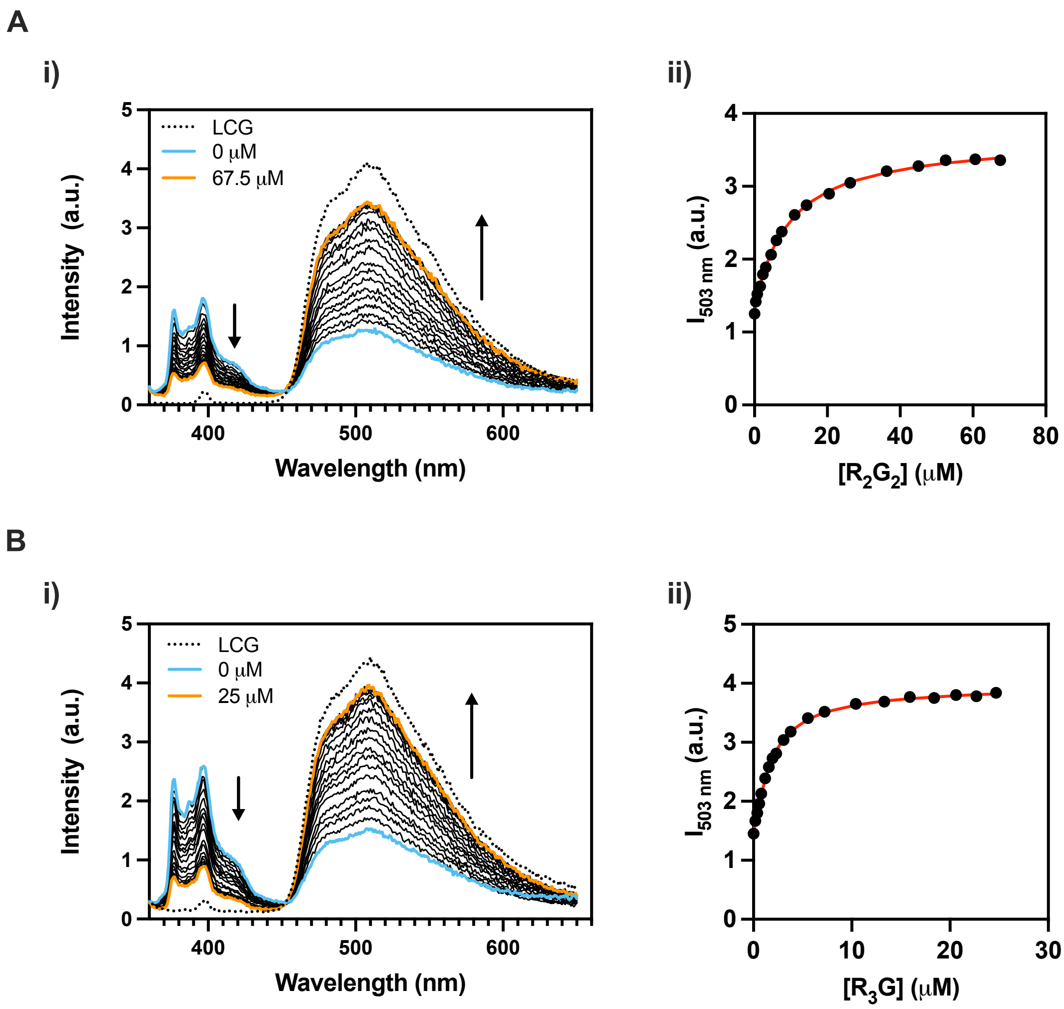

Figure D.36: IDA of the LCG-SC4-4Py pair (0.2 and 0.7 μM, respectively) inserted in EYPC-LUV (7 μM) with the guests **A.** R_2G_2 and **B.** R_3G and respective fitting of the experimental data in ii). All studies were done in PB 5 mM pH 7.4 (λ_{exc} = 340 nm).

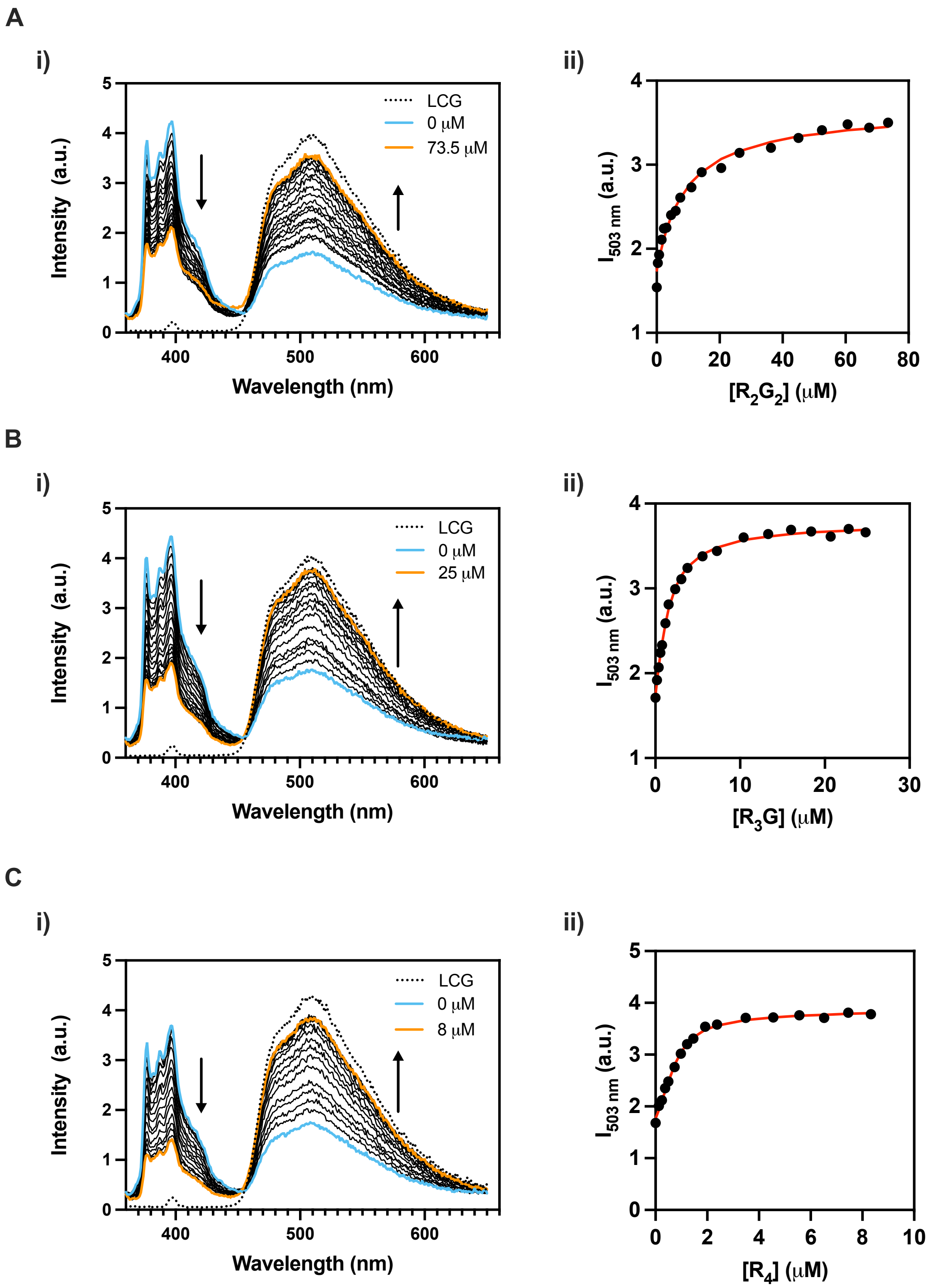

Figure D.37: IDA of the LCG-SC4-6Py pair (0.2 and 0.7 μM, respectively) inserted in EYPC-LUV (7 μM) with the guests **A.** R_2G_2, **B.** R_3G and **C.** R_4 and respective fitting of the experimental data in ii). All studies were done in PB 5 mM pH 7.4 (λ_{exc} = 340 nm).

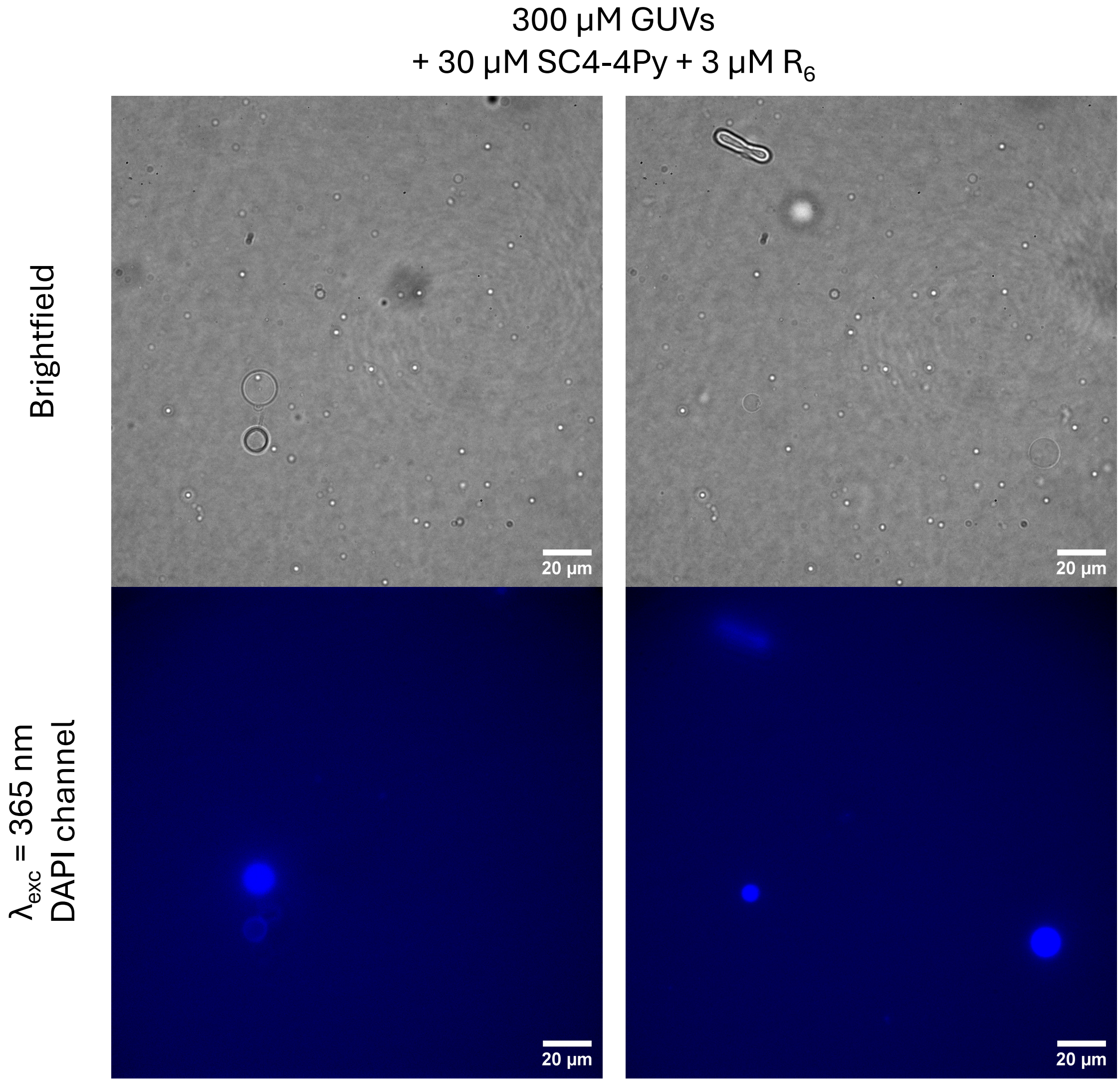

Figure D.38: Fluorescence microscopy images of EYPC-GUVs, in PB 5 mM pH 7.4, obtained in the confocal microscope in epifluorescence mode in the presence of only SC4-4Py and in the presence of the sensor and 3 μM of the peptide R_6, with the brighfield image and respective SC4-4Py emission (λ_{exc} = 365 nm) detected in the DAPI channel.

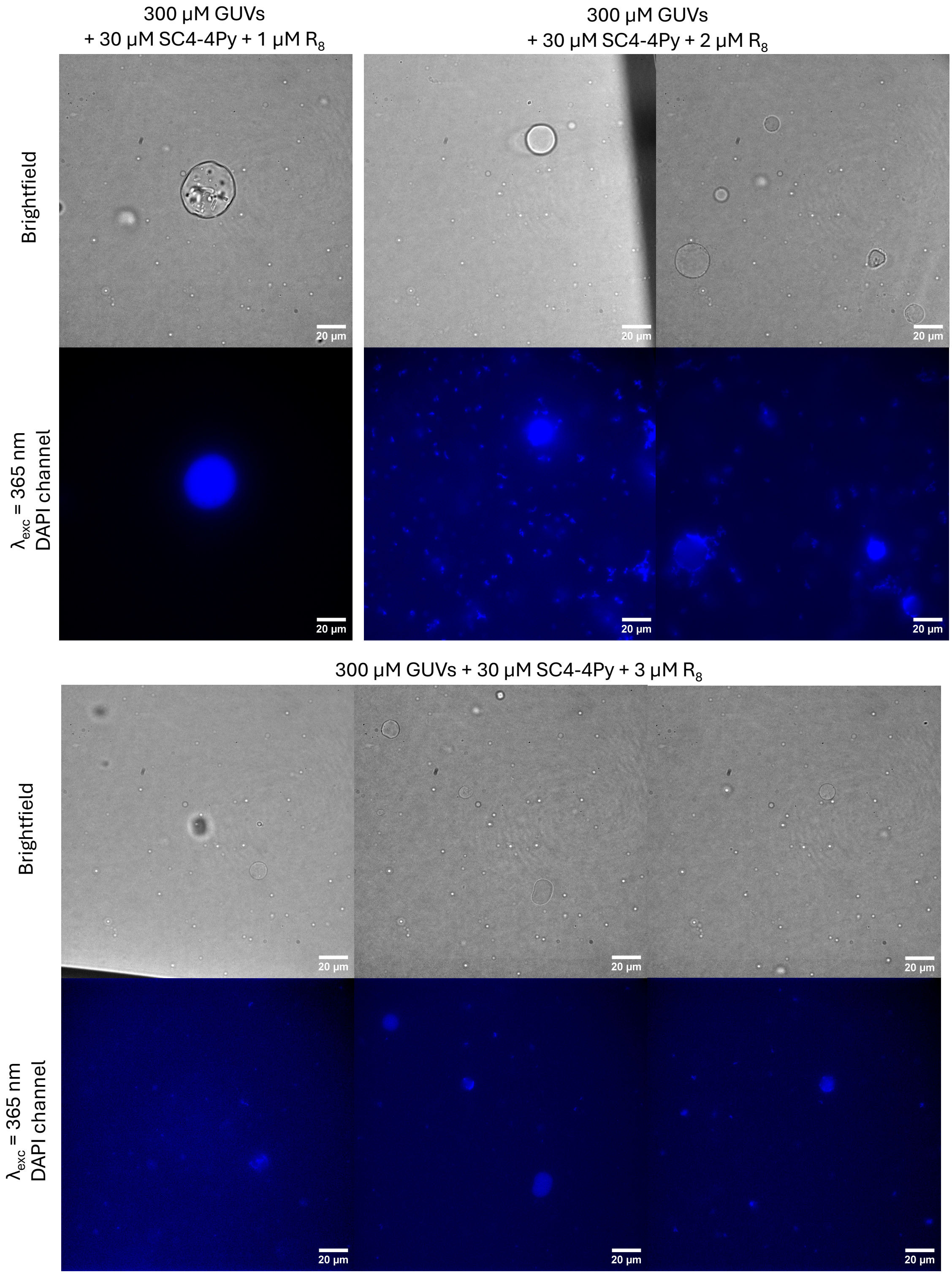

Figure D.39: Additional fluorescence microscopy images of EYPC-GUVs, in PB 5 mM pH 7.4, obtained in the confocal microscope in epifluorescence mode in the presence of only SC4-4Py and in the presence of the sensor and 1, 2 and 3 μM of the peptide R_8, with the brighfield image and respective SC4-4Py emission (λ_{exc} = 365 nm) detected in the DAPI channel.

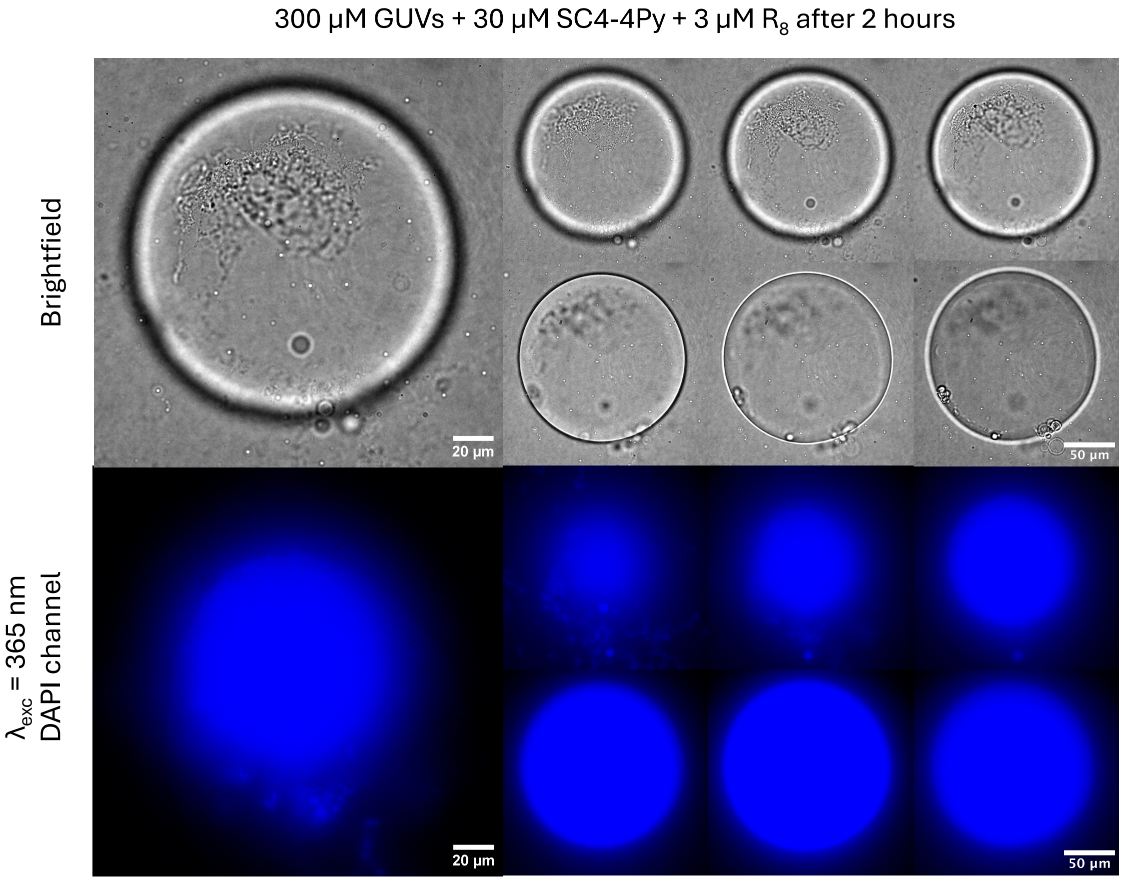

Figure D.40: Fluorescence microscopy images of EYPC-GUVs obtained in the confocal microscope in epifluorescence mode in the presence of only SC4-4Py and 3 μM of R_8 after 2 hours of incubation and respective z-stacks at different heights, for both brightfield and DAPI channel (λ_{exc} = 365 nm). While not clear in the emission images, in the brightfield different irregular structures can be found following the curvature of the membrane of the vesicle.

E

Supplementary Information for Chapter 7

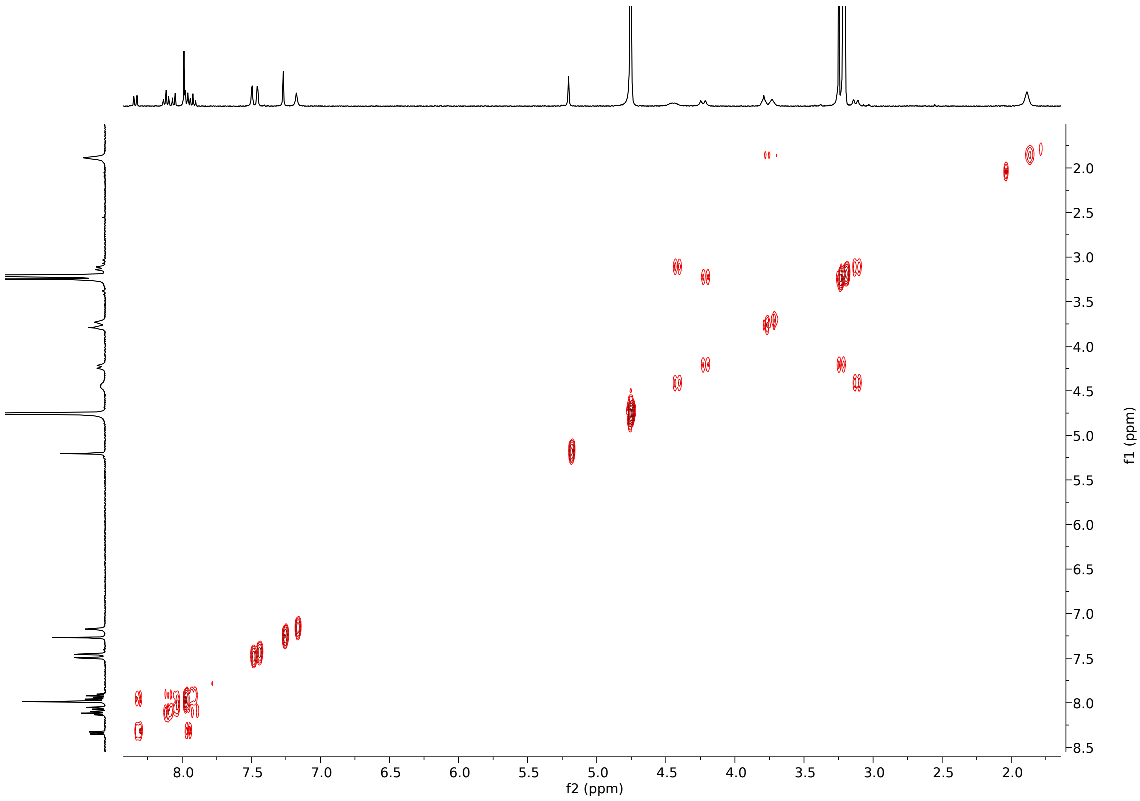

Figure E.1: [1]H-COSY NMR spectrum of SC4-4Py in methanol-d4.

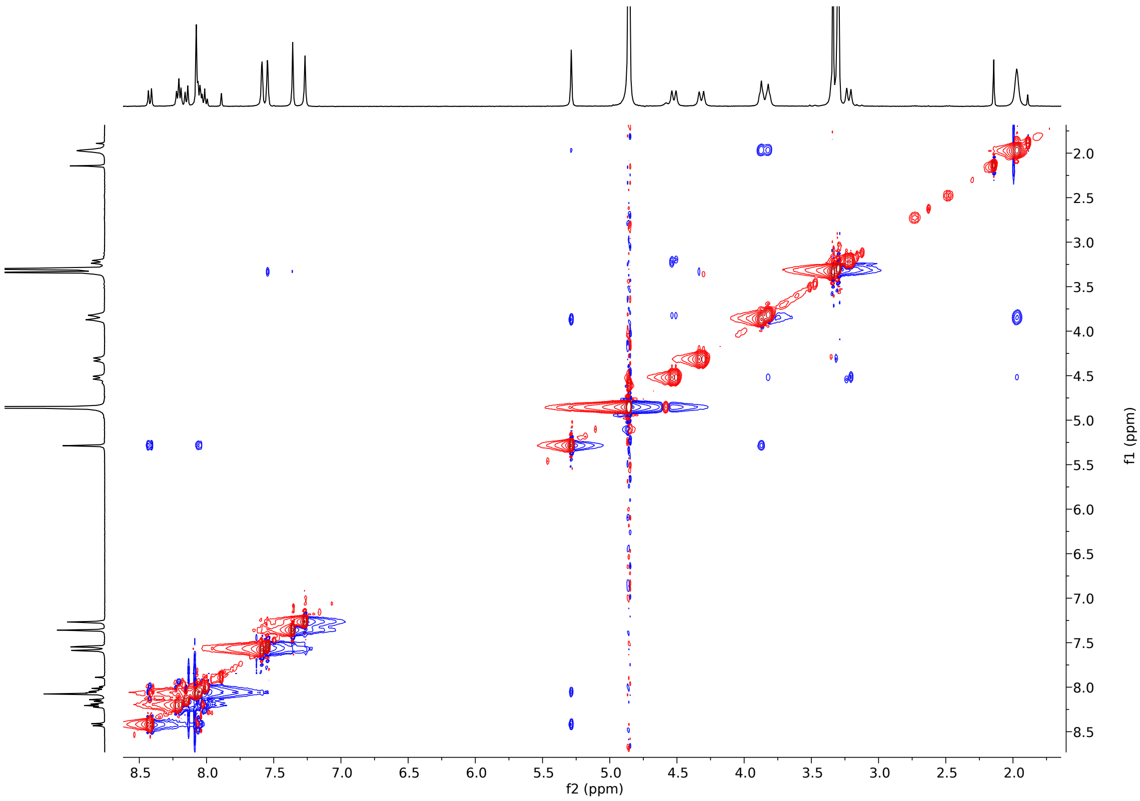

Figure E.2: ^{1}H-ROESY NMR spectrum of SC4-4Py in methanol-d4.

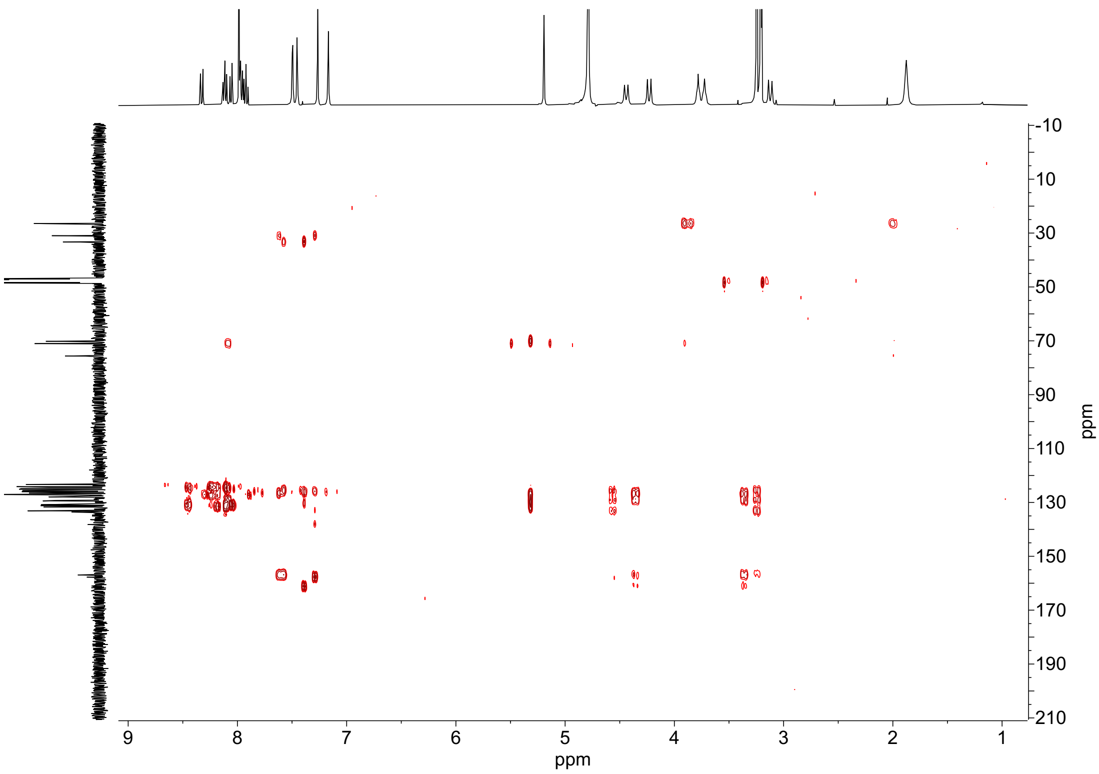

Figure E.3: ^{1}H,^{13}C-Heteronuclear Multiple Bond Correlation (HMBC) NMR spectrum of SC4-4Py in methanol-d4.

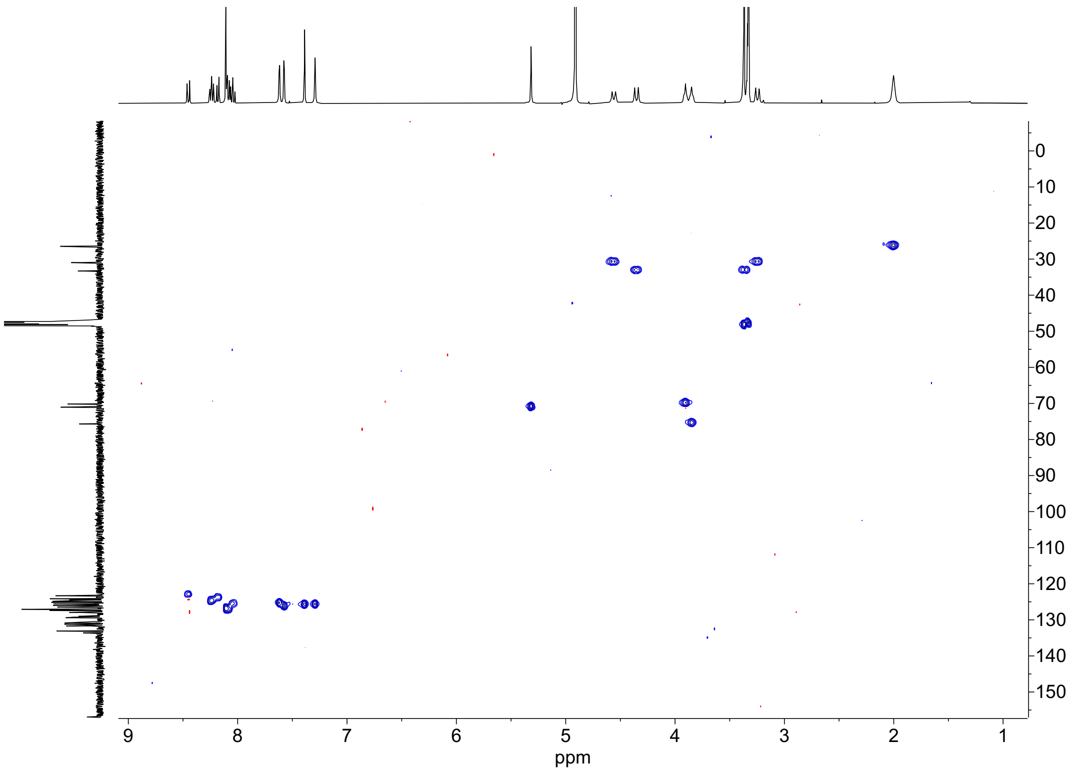

Figure E.4: $^{1}H,^{13}C$-HSQC NMR spectrum of SC4-4Py in methanol-d4.

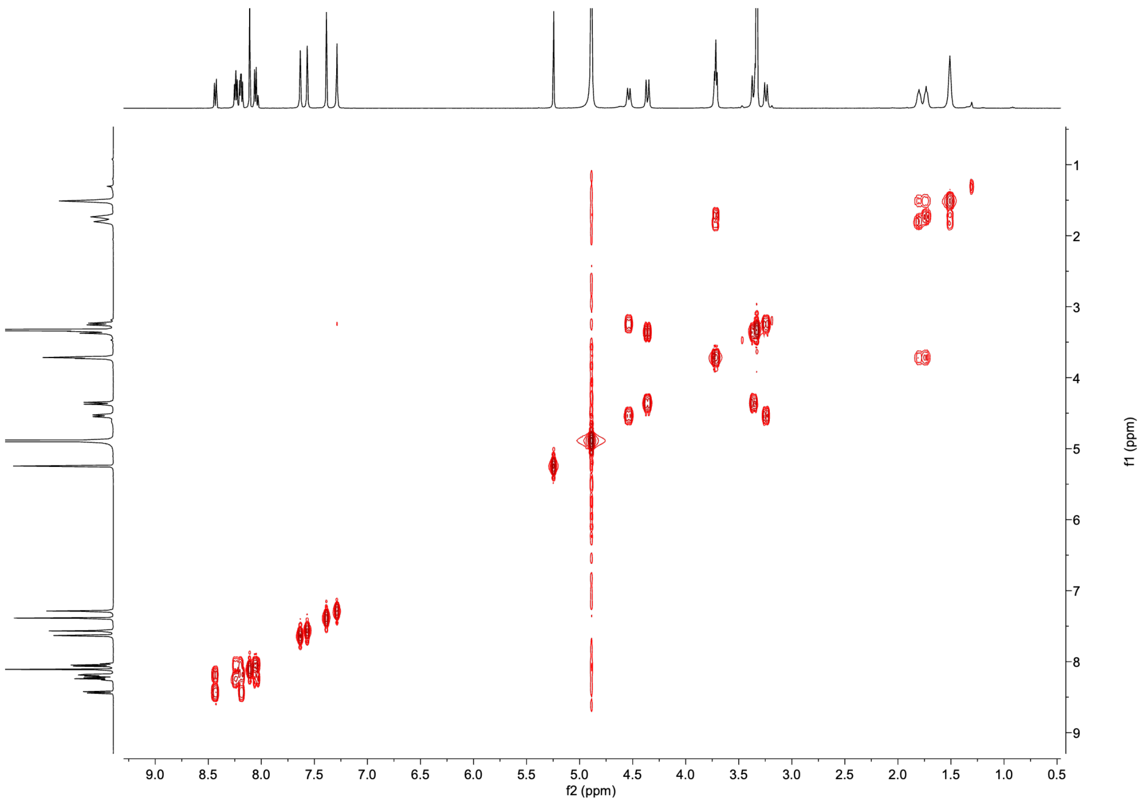

Figure E.5: ^{1}H-COSY NMR spectrum of SC4-6Py in methanol-d4.

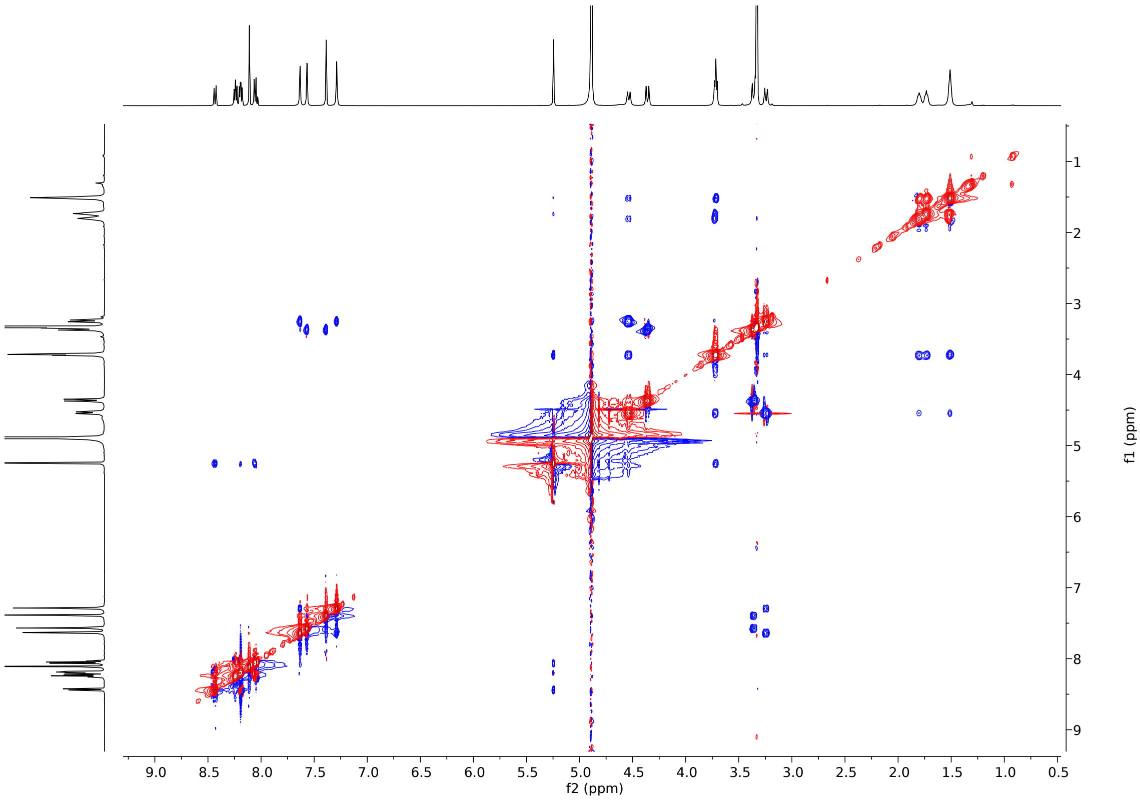

Figure E.6: ^{1}H-ROESY NMR spectrum of SC4-6Py in methanol-d4.

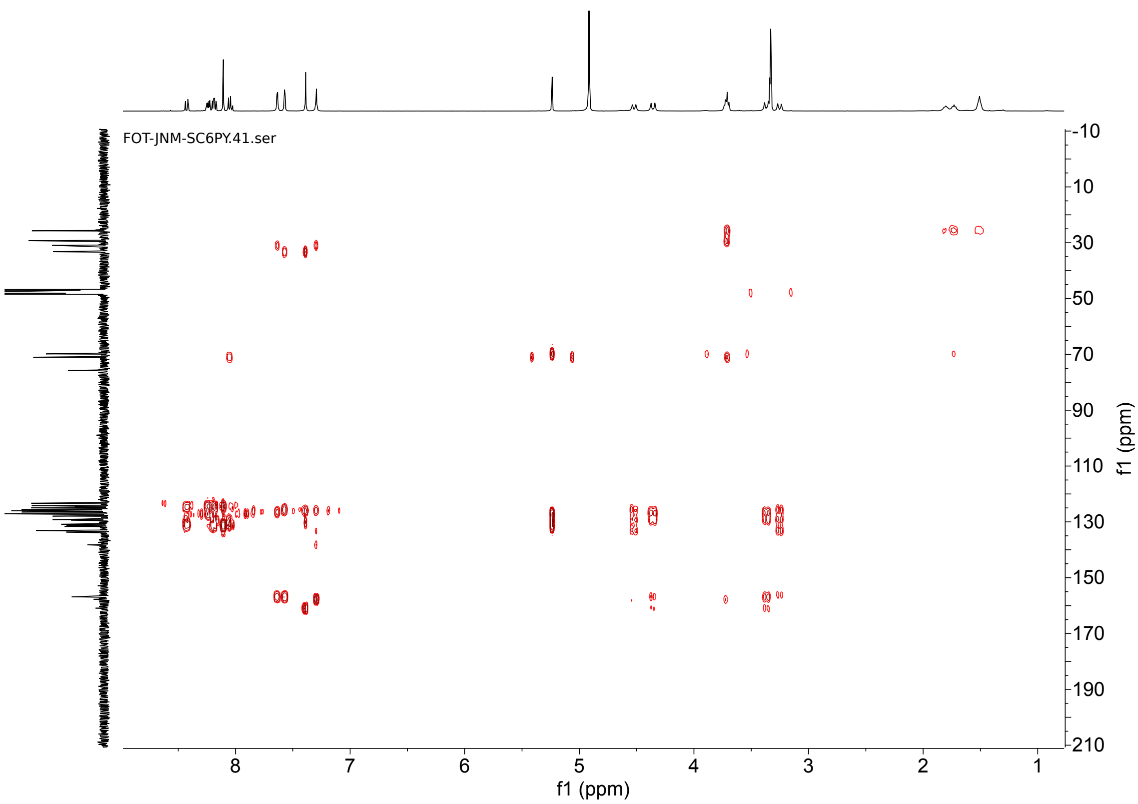

Figure E.7: ^{1}H,^{13}C-HMBC NMR spectrum of SC4-6Py in methanol-d4.

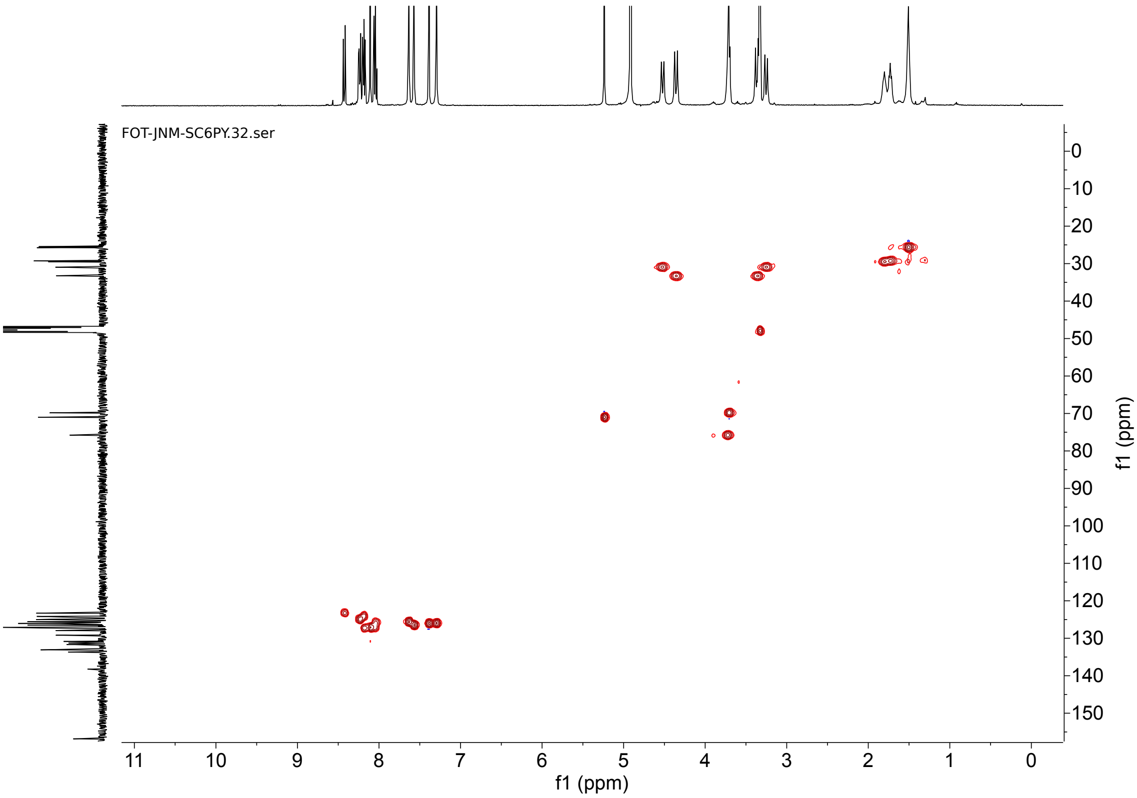

Figure E.8: $^{1}H,^{13}C$-HSQC NMR spectrum of SC4-6Py in methanol-d4.

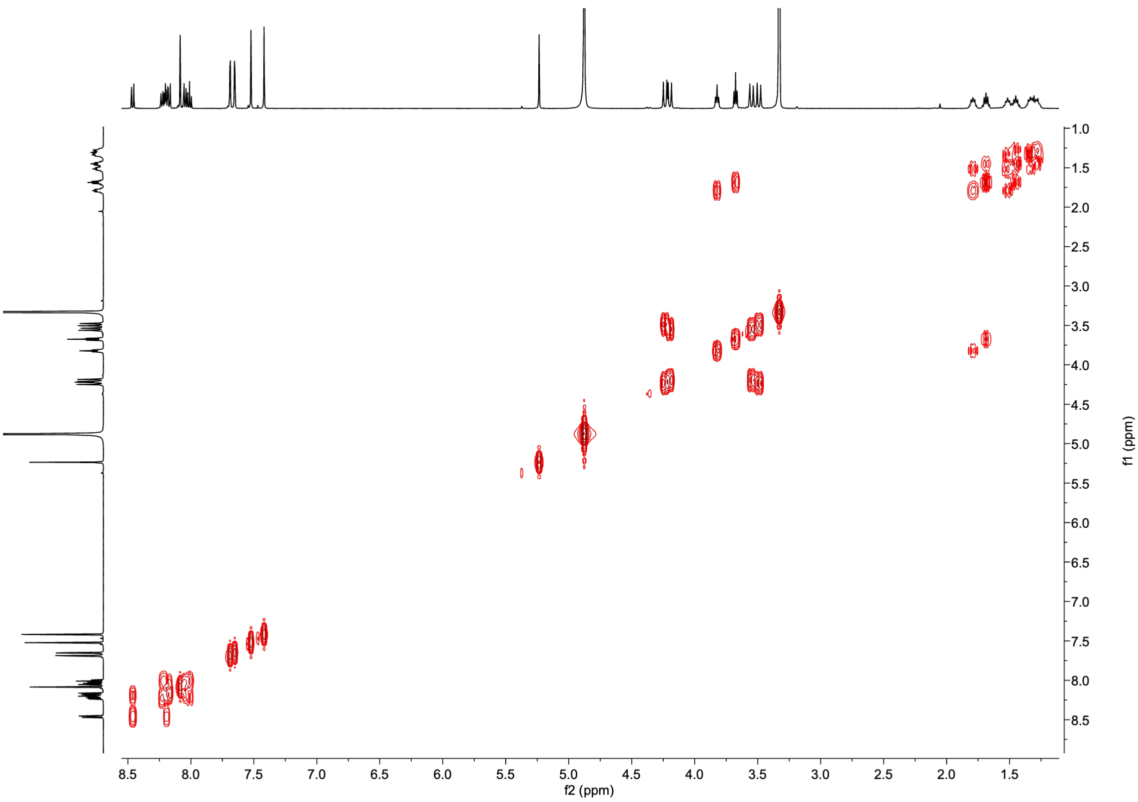

Figure E.9: ^{1}H-COSY NMR spectrum of SC4-8Py in methanol-d4.

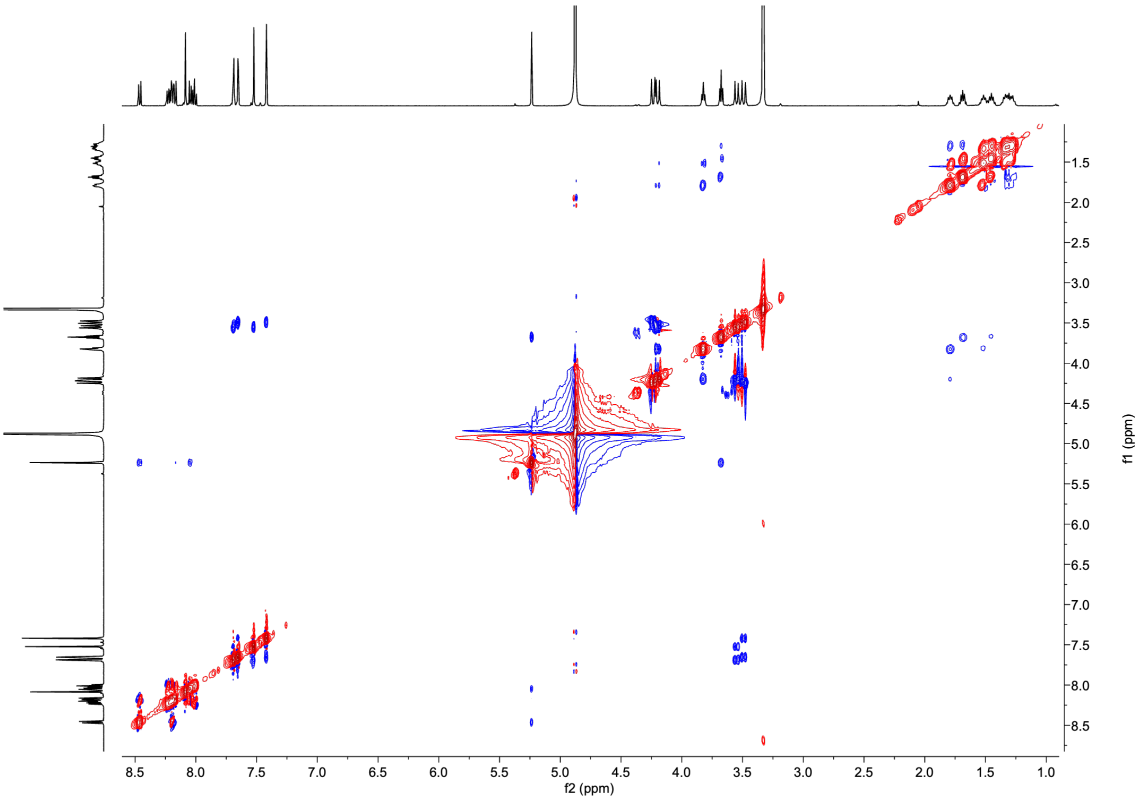

Figure E.10: ^{1}H-ROESY NMR spectrum of SC4-8Py in methanol-d4.

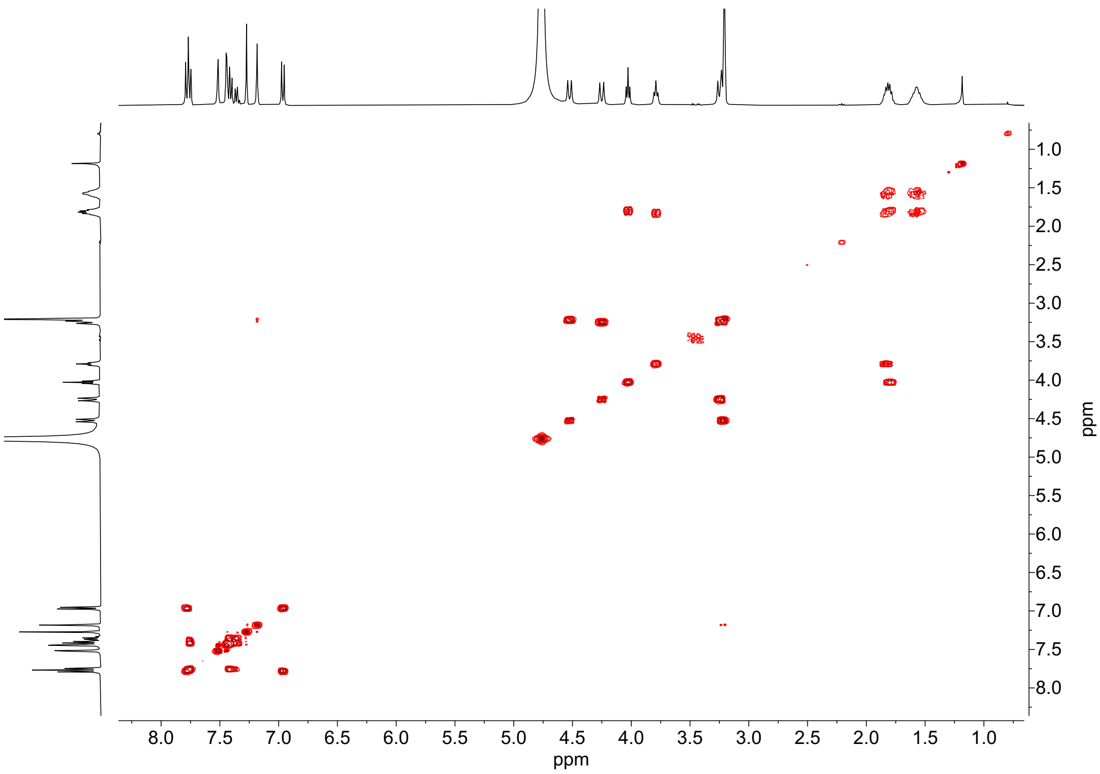

Figure E.11: ^{1}H-COSY NMR spectrum of SC4-Azo 1 in methanol-d4.

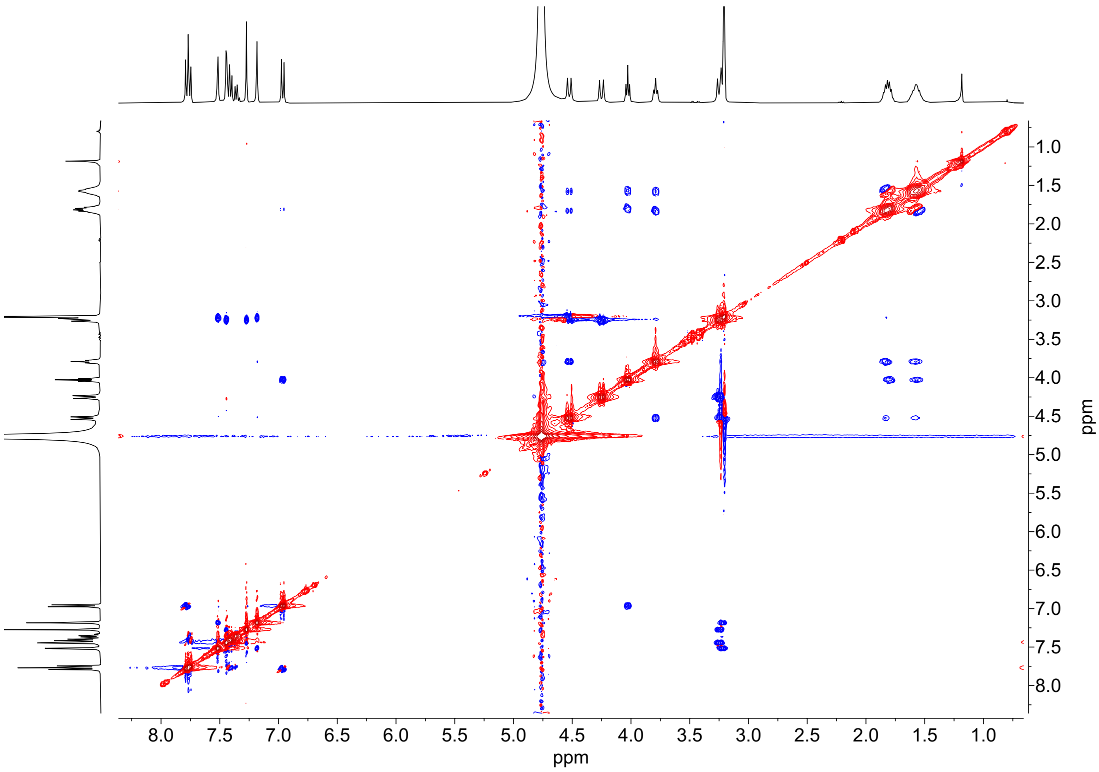

Figure E.12: [1]H-ROESY NMR spectrum of SC4-Azo 1 in methanol-d4.

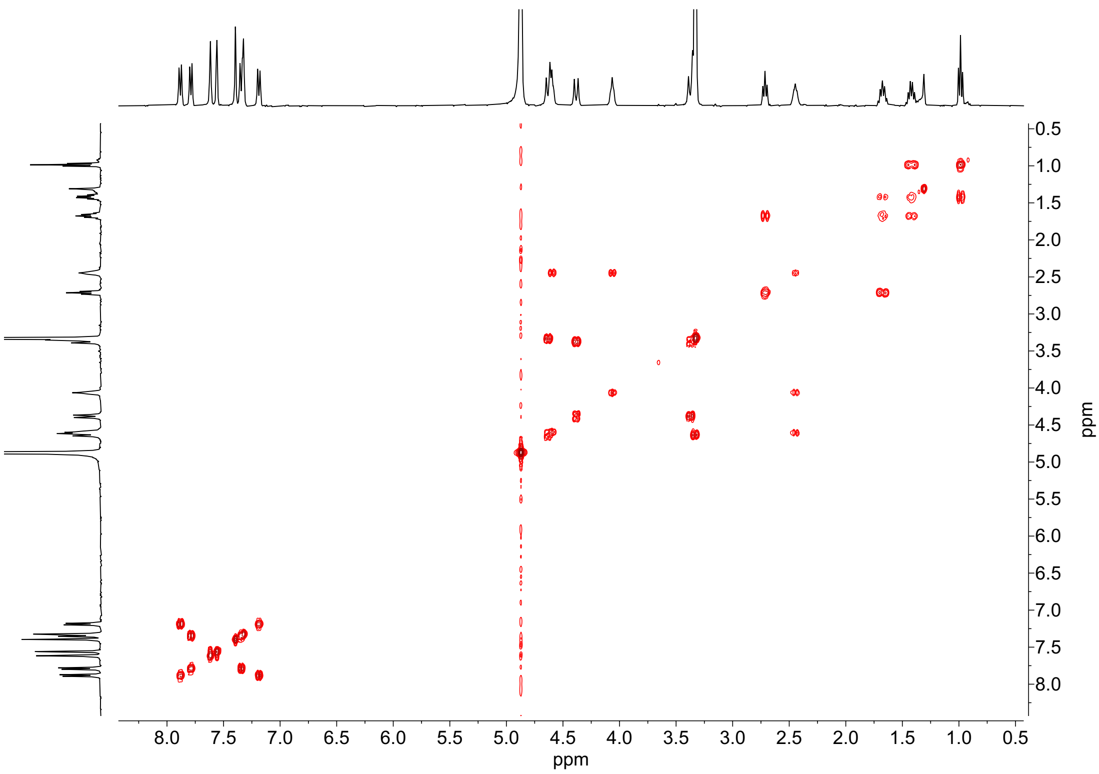

Figure E.13: [1]H-COSY NMR spectrum of SC4-Azo 2 in methanol-d4.

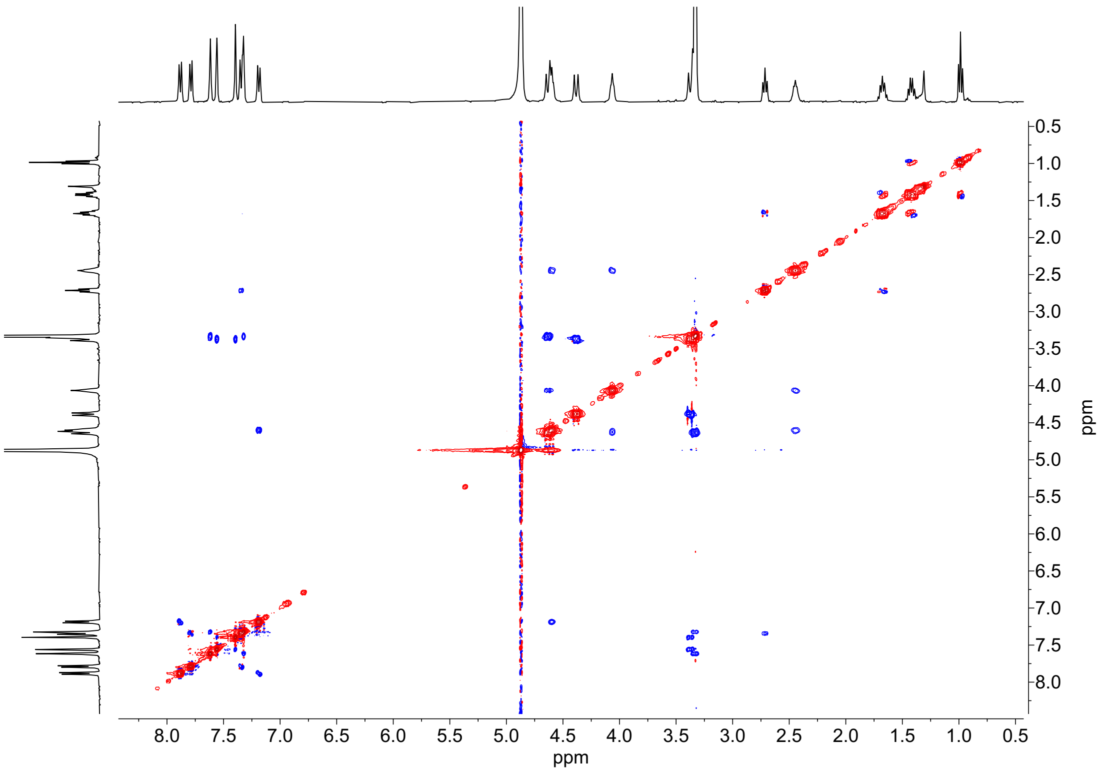

Figure E.14: ^{1}H-ROESY NMR spectrum of SC4-Azo 2 in methanol-d4.

I

Binding Affinity Models for Affinity Calculation and Predictions

I.1 Formulas and Deductions

The calculation of binding affinities between different species can be done through the relation between affinity constants and mass equilibria of the species if the kinetics of the process are fast enough. This Annex describes the formulas and deductions used for fitting of data obtained through physical characterization of the supramolecular systems studied, which allowed the obtention of the molar fractions of species in solution. Both for emission and absorption data, the total intensity can be obtained through the weighted sum of all of the individual species emission, using the values of molar fractions. In the NMR spectroscopy experiments, the systems studied presented fast exchange between species, which allowed the use of a similar relation, in this case with the observed chemical shift corresponding to the weighted average between the initial and final species, e.g. the free and bound guest, like shown in Chapter 2.

Quenching of Lucigenin (LCG) emission in Chapter 2 was accounted into the fitting of the data and is described in Section I.1.7.

I.1.1 1 to 1 Binding Model

Considering the two species, host (H) and guest (G), we have the following binding equilibrium:

$$H + G \rightleftharpoons HG$$

,described by the affinity constant K_a (M^{-1}):

$$K_a = \frac{[HG]}{[H][G]} \tag{I.1}$$

Rearranging the mass equilibrium equation, it is possible to express guest concentration at equilibrium, [G], using the initial concentration of both species, $[G]_0$ and $[H]_0$, host concentration at equilibrium, [H], and K_a of this binding event:

$$\begin{cases} [H]_0 = [H] + [HG] \\ [G]_0 = [G] + [HG] \end{cases} \Leftrightarrow \begin{cases} [H] = [H] + [HG] \\ [G] = \frac{[G]_0}{1+K_a[H]} \end{cases}$$

, originating a quadratic equation, presented below, that can be easily solved using common data treatment tools and the least squares optimization method:

$$a[H]^2 + b[H] + c = 0 \tag{I.2}$$

$$\begin{aligned} a &= K_a \\ b &= 1 + K_a[G]_0 - K_a[H]_0 \\ c &= -[H]_0 \end{aligned}$$

I.1.2 2 to 1 Binding Model

In this model, it is assumed that two guests bind to one host, but for 2 to 1 binding events where two hosts bind two different sites in a guest, the same expressions can be used, by only switching the host for the guest in the expressions. With this in mind the equilibriums in this situation are the following:

$$\begin{aligned} H + G &\rightleftharpoons HG \\ HG + G &\rightleftharpoons HG_2 \end{aligned}$$

, described by the affinity constants K_{11} (M^{-1}), identical to K_a in equation I.1, and K_{21} (M^{-1}) for the second binding event, which can also be expressed in function of K_{11}:

$$K_{21} = \frac{[HG_2]}{[HG][G]} \Leftrightarrow K_{21} = \frac{[HG_2]}{K_{11}[H][G]^2} \tag{I.3}$$

When looking to the mass equilibrium equations, it is necessary to account for concentration of all the species involved in the second binding process as well:

$$\begin{cases} [H]_0 = [H] + [HG] + [HG_2] \\ [G]_0 = [G] + [HG] + 2[HG_2] \end{cases} \Leftrightarrow \begin{cases} [H] = \frac{[H]_0}{1+K_{11}[G]+K_{11}K_{21}[G]^2} \\ [G]_0 = [G] + [HG] + 2[HG_2] \end{cases}$$

, originating a cubic equation, presented below, that can be solved using Newton's iterative method:[313]

$$a[G]^3 + b[G]^2 + c[G] + d = 0 \tag{I.4}$$

$$\begin{aligned} a &= K_{11}K_{21} \\ b &= 2K_{11}K_{21}[H]_0 - K_{11}K_{21}[G]_0 + K_{11} \\ c &= K_{11}[H]_0 - K_{11}[G]_0 + 1 \\ d &= -[G]_0 \end{aligned}$$

I.1.3 1 to 1 Competitive Model

For competitive assays, as is the case of Indicator Displacement Assays (IDA), the model needs to take into account both affinity of host towards the indicator (I) and the guest that is competing for the same binding site (G). The binding events between the different species can be expressed by the following equilibria:

$$H + G \rightleftharpoons HG$$
$$H + I \rightleftharpoons HI$$

, described by the affinity constants K_{HG} and K_{HI} (M^{-1}) which described the binding of the guest, G, and of the indicator, I, to the host, H, respectively. These can be expressed in the following expressions:

$$K_{HG} = \frac{[HG]}{[H][G]} \tag{I.5}$$

$$K_{HI} = \frac{[HI]}{[H][I]} \tag{I.6}$$

, where [H], [G], [I], [HG] and [HI] (M) are the concentrations of host, guest, indicator and host-guest and host-indicator complexes in equilibrium, respectively. The mass equilibrium of all the species can be described through these equations:

$$\begin{cases} [H]_0 = [H] + [HG] + [HI] \\ [G]_0 = [G] + [HG] \\ [I]_0 = [I] + [HI] \end{cases} \Leftrightarrow \begin{cases} [H]_0 = [H] + K_{HG}[H][G] + K_{HI}[H][I] \\ [G] = \frac{[G]_0}{1+K_{HG}[H]} \\ [I] = \frac{[I]_0}{1+K_{HI}[H]} \end{cases}$$

, where $[H]_0$, $[G]_0$ and $[I]_0$ (M) are the total concentration of each species in solution. Replacing both I and G concentrations in equilibrium, [I] and [G] (M), with the expressions based on the affinity constants a cubic expression is reached, that can be solved using the Newton's iterative method, as well:[313]

$$a[H]^3 + b[H]^2 + c[H] + d = 0 \tag{I.7}$$

$$\begin{aligned} a &= K_{HG}K_{HI} \\ b &= K_{HI} + K_{HG} - K_{HI}K_{HG}[H]_0 + K_{HI}K_{HG}[G]_0 + K_{HI}K_{HG}[I]_0 \\ c &= 1 - K_{HI}[H]_0 - K_{HG}[H]_0 + K_{HG}[G]_0 + K_{HI}[G]_0 \\ d &= -[H]_0 \end{aligned}$$

For hosts which can bind to several identical binding sites in one larger guest but bind solely to one indicator molecule, this expression can be easily adapted by adaptation of the general association constant for the guest:

$$\begin{aligned} nH + G &\rightleftharpoons H_nG \\ K_{H_nG} &= \frac{[H_nG]}{[H]^n[G]} \end{aligned} \tag{I.8}$$

, where n represents the number of binding sites for the host, and alters the final cubic expression slightly to:

$$\begin{aligned} a &= K_{H_nG}K_{HI} \\ b &= K_{HI} + K_{H_nG} - K_{HI}K_{H_nG}[H]_0 + K_{HI}K_{H_nG}[G]_0 + nK_{HI}K_{H_nG}[I]_0 \\ c &= 1 - K_{HI}[H]_0 - K_{H_nG}[H]_0 + K_{H_nG}[G]_0 + nK_{HI}[C]_0 \\ d &= -[H]_0 \end{aligned}$$

I.1.4 2 to 1 Competitive Model

If the two binding sites for a host on a given guest are not equal, which is often the case due to various interfering factors, like steric hindrance and electrostatic repulsion between host molecules, the expression presented above needs to be changed slightly and the binding of the first and second host need to be considered separately. Most of the system is identical to the 1 to 1 competitive model but we have the added 2 to 1 process:

$$\begin{aligned} &H + G \rightleftharpoons HG \\ &HG + H \rightleftharpoons H_2G \\ &H + I \rightleftharpoons HI \end{aligned}$$

, with the affinity of the binding of the second host molecule and H_2G complex formation being expressed by K_{H_2G} (M^{-1}):

$$K_{H_2G} = \frac{[H_2G]}{[HG][H]} = \frac{[H_2G]}{K_{HG}[G][H]^2} \tag{I.9}$$

Transposing this to the mass equilibrium, this originate the following system of three equations:

$$\begin{cases} [H]_0 = [H] + [HG] + [HI] + 2[H_2G] \\ [G]_0 = [G] + [HG] + [H_2G] \\ [I]_0 = [I] + [HI] \end{cases}$$

Due to the added complexity of the system, the equations were all equaled to 0, as presented below:

$$\begin{cases} [H] + K_{HG}[G][H] + K_{HI}[H][I] + 2K_{H_2G}K_{HG}[G][H]^2 - [H]_0 = 0 \\ [G] + K_{HG}[G][H] + K_{H_2G}K_{HG}[G][H]^2 - [G]_0 = 0 \\ [I] + K_{HI}[I][H] - [I]_0 = 0 \end{cases} \tag{I.10}$$

, and the roots of the equations were obtained through root finding algorithms for non-linear functions, based on matricial calculation. The methodology and Python 3 scripts used for optimization of the roots of more complex equation systems can be found in Section I.2.

I.1.5 Ternary Binding Model

The heteroternary system presented in Section 3.2 is a complex system that can be described by the equilibria presented in Figure 3.8. Using the same nomenclature for clarity, this system presents two different hosts, BB and CB7, and a dye, D, and is described as:

$$\begin{aligned}
&CB7 + D \rightleftharpoons CB7 : D\\
&CB7 : D + CB7 \rightleftharpoons (CB7)_2 : D\\
&BB + D \rightleftharpoons BB : D\\
&BB + CB7 \rightleftharpoons CB7 : BB\\
&CB7 : D + BB \rightleftharpoons CB7 : D : BB\\
&CB7 : D : BB + CB7 \rightleftharpoons (CB7)_2 : D : BB
\end{aligned}$$

The affinities (M^{-1}) of this system can be described as:

$$K_{11} = \frac{[CB7 : D]}{[CB7][D]} \tag{I.11}$$

$$K_{21} = \frac{[(CB7)_2 : D]}{[CB7 : D][CB7]} = \frac{[(CB7)_2 : D]}{K_{11}[CB7]^2[D]} \tag{I.12}$$

$$K'_{11} = \frac{[BB : D]}{[BB][D]} \tag{I.13}$$

$$K_{CB7:BB} = \frac{[CB7 : BB]}{[CB7][BB]} \tag{I.14}$$

$$K_{111} = \frac{[CB7 : D : BB]}{[CB7 : D][BB]} = \frac{[CB7 : D : BB]}{K_{11}[CB7][D][BB]} \tag{I.15}$$

$$K_{211} = \frac{[(CB7)_2 : D : BB]}{[CB7 : D : BB][CB7]} = \frac{[(CB7)_2 : D : BB]}{K_{11}K_{111}[CB7]^2[D][BB]} \tag{I.16}$$

Expressing the mass equilibrium equations considering the previous affinity constants and equaling them to 0, the system of equations presented in Equation I.19 can be obtained. Much like the 2 to 1 competitive model, the solution to this non-linear system of equations can be obtained through optimization algorithms that are used in the scripts presented in Section I.2.

I.1.6 Ternary Competitive Model

The ternary competitive model is very similar to the previous one but adds the equilibriums of both hosts with the competitor that is added, the guest, G, and the respective affinity constants of binding to both CB7 and BB:

$$CB7 + G \rightleftharpoons CB7 : G$$

$$BB + G \rightleftharpoons BB : G$$

$$K_{CB7:G} = \frac{[CB7 : G]}{[CB7][G]} \tag{I.17}$$

$$K_{BB:G} = \frac{[BB : G]}{[BB][G]} \tag{I.18}$$

Adding these equilibria to the system of equations obtained for the previous system, the system of 4 equations presented in Equation I.20 is obtained:

Mass equilibrium equations for the ternary system:

$$\begin{cases} [CB7]_0 = [CB7] + [CB7:D] + 2[(CB7)_2:D] + [CB7:BB] + [CB7:D:BB] + 2[(CB7)_2:D:BB] \\ [BB]_0 = [BB] + [BB:D] + [CB7:BB] + [CB7:D:BB] + [(CB7)_2:D:BB] \\ [D]_0 = [D] + [CB7:D] + [(CB7)_2:D] + [BB:D] + [CB7:D:BB] + [(CB7)_2:D:BB] \end{cases} \Leftrightarrow$$

$$\begin{cases} [CB7] + K_{11}[CB7][D] + 2K_{21}[CB7]^2[D] + K_{CB7:BB}[CB7][BB] + K_{11}K_{111}[CB7][D][BB] + 2K_{11}K_{111}K_{211}[CB7]^2[D][BB] - [CB7]_0 = 0 \\ [BB] + K'_{11}[BB][D] + K_{CB7:BB}[CB7][BB] + K_{11}K_{111}[CB7][D][BB] + K_{11}K_{111}K_{211}[CB7]^2[D][BB] - [BB]_0 = 0 \\ [D] + K_{11}[CB7][D] + K_{21}[CB7]^2[D] + K'_{11}[BB][D] + K_{11}K_{111}[CB7][D][BB] + K_{11}K_{111}K_{211}[CB7]^2[D][BB] - [D]_0 = 0 \end{cases} \tag{I.19}$$

Mass equilibrium equations for the ternary competitive system:

$$\begin{cases} [CB7]_0 = [CB7] + [CB7:D] + 2[(CB7)_2:D] + [CB7:BB] + [CB7:D:BB] + 2[(CB7)_2:D:BB] + [CB7:G] \\ [BB]_0 = [BB] + [BB:D] + [CB7:BB] + [CB7:D:BB] + [(CB7)_2:D:BB] + [BB:G] \\ [D]_0 = [D] + [CB7:D] + [(CB7)_2:D] + [BB:D] + [CB7:D:BB] + [(CB7)_2:D:BB] \\ [G]_0 = [G] + [CB7:G] + [BB:G] \end{cases} \Leftrightarrow$$

$$\begin{cases} [CB7] + K_{11}[CB7][D] + 2K_{21}[CB7]^2[D] + K_{CB7:BB}[CB7][BB] + K_{11}K_{111}[CB7][D][BB] + 2K_{11}K_{111}K_{211}[CB7]^2[D][BB] + \\ +K_{CB7:G}[CB7][G] - [CB7]_0 = 0 \\ [BB] + K'_{11}[BB][D] + K_{CB7:BB}[CB7][BB] + K_{11}K_{111}[CB7][D][BB] + K_{11}K_{111}K_{211}[CB7]^2[D][BB] + K_{BB:G}[BB][G] - [BB]_0 = 0 \\ [D] + K_{11}[CB7][D] + K_{21}[CB7]^2[D] + K'_{11}[BB][D] + K_{11}K_{111}[CB7][D][BB] + K_{11}K_{111}K_{211}[CB7]^2[D][BB] - [D]_0 = 0 \\ [G] + K_{CB7:G}[CB7][G] + K_{BB:G}[BB][G] - [G]_0 = 0 \end{cases} \tag{I.20}$$

I.1.7 Lucigenin quenching

The total intensity of fluorescence of a sample is given by:

$$F_T = \sum X_n F_n \tag{I.21}$$

, where n corresponds to a given emissive species in solution, F_n and X_n to the intensity of emission at a given wavelength and molar fraction of the species n and F_T to the total emission of the sample at the same wavelength. In the case of LCG samples, it was assumed that the anion did not have any further effect on the quenching of the complexed LCG, seeing as this species is in an already quenched state. For a given quencher, Q, we have the Stern-Volmer equation:

$$\frac{F_0}{F} = 1 + K_{SV}[Q] \Leftrightarrow F = \frac{F_0}{1 + K_{SV}[Q]} \tag{I.22}$$

, where F corresponds to the final fluorescence after quenching, F_0 the emission in the absence of quencher, [Q] to the quencher concentration in the sample, in M, and K_{SV} to the Stern-Volmer constant (M_{-1}). The value of calculated F_{LCG} was corrected for the expected emission in the presence of the correspondent quencher concentration for each point of the fitting and this was the value considered in the final fitting.

I.2 Python 3 Script for Affinity Constant Calculation, Species Molar Fractions and Principal Component Analysis (PCA)

Although root obtention can be done through matricial calculation as well in Microsoft Excel, with the "Solver" tool, the ternary complex formation and displacement of hosts from this complex by different guests, was also done with the functionalities from Python and the libraries SciPy, Pandas and NumPy.

These Python 3 scripts were developed both for the fitting of spectroscopical data for the CB7:dye:BB system presented in Chapter 3, Section 3.2, applicable for both UV-vis and Fluorescence spectroscopy data, for prediction of the species distribution in solution if we vary the concentration of one of the species and fix all others. The first allowed the determination of the affinity constants of the guests for both CB7 and BB, showing the quantitative analysis possible with such a host displacement assay, while the latter helped determine the ideal concentration of CB7, BB and dye at which to do said displacements.

Additionally, it is also presented the script written for principal component analysis (PCA) of the results for the library of oligoarginines studied in Chapter 4, Section 4.1, with the family of sensors SC4-nPy.

I.2.1 Scripts for fitting of spectroscopical data

These scripts were developed in 2022 and 2023 with Python version 3.9.6. All files with the exception of data files which are exemplified herein can be found in the repository present in the GitHub page in the following link:

https://github.com/JoanaNMartins/BindingAssays.

I.2.1.1 Script 1 - CB7_Dye_addBB_fit.py

The first script for fitting of spectroscopical data refers to the titration of a previously formed CB7-Dye complex with increasing concentrations of BB. The affinity constants designation is associated with the respective equilibrium in the script. Concentrations of the species in the assay, as well as initial guesses for the affinity towards both hosts and fluorescence values of all the species, should be changed, in the header section of the script to the conditions used in the assay. The minimum and maximum values can be found at the end of the script, under min_values and max_values and numerical values should be inserted as bounds for the optimization. Each value corresponds to the same list position as in the guesses list above them.

Having inputed these values, the script should be ran in the desired python Integrated Development Environment (IDE) software used and a window will open requesting a file to be opened. This file should be a .csv file with only two columns, the firts should only have the numerical values of BB concentration added, in M, and the second should be the corrected fluorescence values at the chosen wavelength, for eventual dilution correction, as presented in Figure I.1.

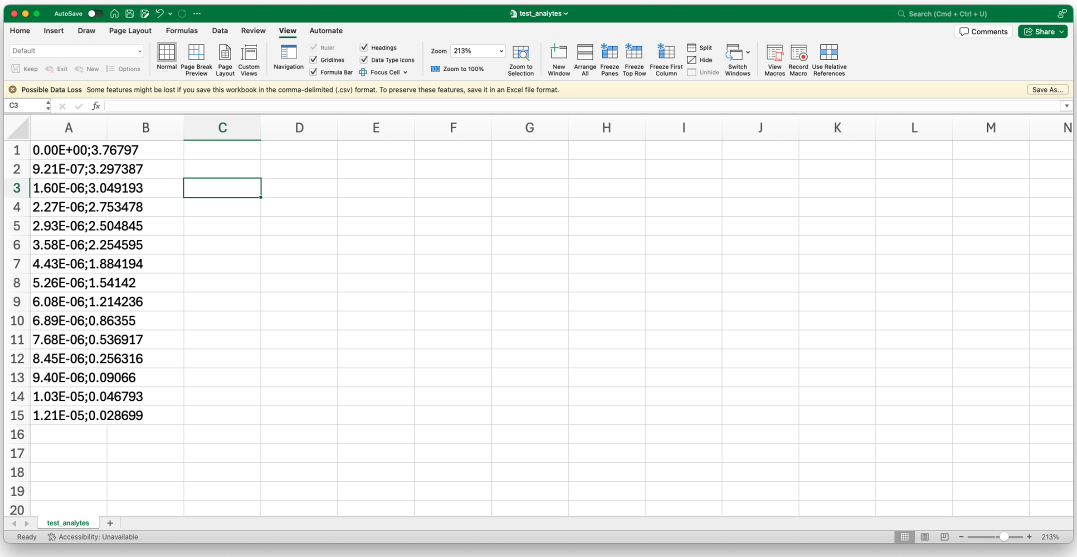

Figure I.1: Example .csv file for the input of concentration and emission values for fitting.

The output will include a Microsoft Excel file with values of concentrations and molar ratio of the species in equilibrium as well as the calculated emission value, while the results of affinity values and emission value for each species will be given in the terminal.

The .csv file with concentrations should be separated with ";", otherwise change the separator in line 266 to the corresponding separator in your .csv file. If the optimization is taking too long it is advised that the error associated with the fitting be lowered from 1 x 10^{-17} or another value that can be considered acceptable for your set of data. This script in particular takes a few minutes to present a solution; future scripts will aim at improving the time the calculation takes to run by use of different root finding algorithms.

Listing I.1: Script 1 - Ternary complex fitting

```
from scipy import optimize
import pandas as pd
import numpy as np
import matplotlib.pyplot as plt

from tkinter import Tk
from tkinter.filedialog import askopenfilename


''' This file applies to a system with 4 species, with the following
  behaviour:

G + CB7 -> CB7:G              (K11)
CB7:G + CB7 - > (CB7)2:G      (K21)
G + BB -> BB:G                (KBB_G)
CB7 + BB -> CB7:BB            (KBB_CB7)
CB7:G + BB -> CB7:G:BB        (K111)
```

```
CB7:G:BB + CB7 -> (CB7)2:G:BB (K211)

Instead of the calculation, this file aims to do the fitting to a set of experimental data

'''

# Concentrations of the species in the assay
CB7_0 = np.float64(5e-5)
G_0 = np.float64(4.2e-6)

# Known Affinity constants in M-1
K11 = np.float64(9e5)
K21 = np.float64(1e4)
KBB_G = np.float64(1e3)
KBB_CB7 = np.float64(1e3)

# Affinity guesses:
K111_guess = np.float64(1e5)
K211_guess = np.float64(1e4)

# Fluorescence guesses:
FD = 0.3
F11 = 4
F21 = 8
F111 = 0.05
F211 = 0.1


def eq(vars, bb_0, k):
  # Can change name, but the vars and a_0 must be maintained
  # and consistent with jac
  k11, k21, kbb_g, kbb_cb7, k111, k211 = k
  bb, cb7, g = vars

  cb7_g = k11 * cb7 * g
  cb7_2_g = k21 * k11 * cb7 ** 2 * g
  bb_g = kbb_g * g * bb
  cb7_bb = kbb_cb7 * bb * cb7
  cb7_g_bb = k111 * k11 * cb7 * g * bb
  cb7_2_g_bb = k211 * k111 * k11 * cb7 **2 * g * bb

  f_bb = bb + bb_g + cb7_bb + cb7_g_bb + cb7_2_g_bb - bb_0
  f_cb7 = cb7 + cb7_g + cb7_bb + 2 * cb7_2_g + cb7_g_bb + 2 * cb7_2_g_bb - CB7_0
  f_g = g + cb7_g + cb7_2_g + bb_g + cb7_g_bb + cb7_2_g_bb - G_0

  return [f_bb,
          f_cb7,
          f_g]
```

```


def jac(vars, bb_0, k):

  k11, k21, kbb_g, kbb_cb7, k111, k211 = k

  bb, cb7, g = vars

  cb7_g = k11 * cb7 * g
  cb7_2_g = k21 * k11 * cb7 ** 2 * g
  bb_g = kbb_g * g * bb
  cb7_bb = kbb_cb7 * bb * cb7
  cb7_g_bb = k111 * k11 * cb7 * g * bb
  cb7_2_g_bb = k211 * k111 * k11 * cb7 **2 * g * bb

  # 1st line for the jacobian - derivates of the BB function (in function of
   BB, CB7, G and A, respectively)
  fp_bb_bb = 1 + kbb_g * g + kbb_cb7 * cb7 + k111 * k11 * cb7 * g + k211 *
  k111 * k11 * cb7 **2 *g
  fp_bb_cb7 = bb + bb_g + kbb_cb7 * bb + k111 * k11 * bb * g + 2 * k211 *
  k111 * k11 * cb7 * bb * g
  fp_bb_g = bb + kbb_g * bb + cb7_bb + k111 * k11 * cb7 * bb + k211 * k111 *
   k11 * cb7 **2 * bb

  # 2nd line for the jacobian - derivates of the CB7 function
  fp_cb7_bb = cb7 + cb7_g + kbb_cb7 * cb7 + 2 * cb7_2_g + k111 * k11 * cb7 *
   g + 2 * k211 * k111 * k11 * cb7 **2 *g
  fp_cb7_cb7 = 1 + k11 * g + kbb_cb7 * bb + 4 * k21 * k11 * cb7 * g + k111 *
   k11 * bb * g + 4 * k211 * k111 * k11 * cb7 * bb *g
  fp_cb7_g =  cb7 + k11 * cb7 + cb7_bb + 2 * k21 * k11 * cb7 **2 + k111 *
  k11 * bb * cb7 + 2 * k211 * k111 * k11 * cb7 **2 * bb

  # 3rd line for the jacobian - derivatives of the G function
  fp_g_bb = g + cb7_g + cb7_2_g + kbb_g * g + k111 * k11 * cb7 * g + k211 *
  k111 * k11 * cb7 **2 * g
  fp_g_cb7 = g + k11 * g + 2* k21 * k11 * g * cb7 + bb_g + k111 * k11 * bb *
   g + 2 * k211 * k111 * k11 * cb7 * bb * g
  fp_g_g = 1 + k11 * cb7 + k21 * k11 * cb7**2 + kbb_g * bb + k111 * k11 * bb
   * cb7 + k211 * k111 * k11 * cb7 **2 * bb

  return np.array([[fp_bb_bb, fp_bb_cb7, fp_bb_g],
                   [fp_cb7_bb, fp_cb7_cb7, fp_cb7_g],
                   [fp_g_bb, fp_g_cb7, fp_g_g]])


def try_solution(bb_max, k, trials, error, eq, jac):

  for i in range(trials):
    initial_guess = [np.random.uniform(0, bb_max),
                     np.random.uniform(0, CB7_0), np.random.uniform(0, G_0)]
```

```

  sol = optimize.root(eq, jac=jac, args=(bb_max, k), x0=initial_guess)

  if 0 <= sol.x[0] <= bb_max and 0 <= sol.x[1] <= CB7_0 and 0 <= sol.x[2] <= G_0:

    zero = eq(vars=sol.x, bb_0=bb_max, k=k)

    if -error <= zero[0] <= error and -error <= zero[1] <= error and -error <= zero[2] <= error:
      return sol.x
      break


def calc_solution_list(x, trials, k, error, eq, jac):

  k11, k21, kbb_g, kbb_cb7, k111, k211 = k

  values = [[],
            [],
            []]

  for bb_max in x:
    sol = try_solution(bb_max, k, trials=trials, error=error, eq=eq,
                       jac=jac)
    values[0].append(sol[0])
    values[1].append(sol[1])
    values[2].append(sol[2])

return values


def add_concentrations_list(k, values):

  k11, k21, kbb_g, kbb_cb7, k111, k211 = k

  c_11 = list()
  c_21 = list()
  c_111 = list()
  c_211 = list()

  for i in range(len(values[0])):

    c_11.append(k11 * values[1][i] * values[2][i])
    c_21.append(k11 * k21 * values[1][i] ** 2 * values[2][i])
    c_111.append(k11 * k111 * values[1][i] * values[2][i] * values[0][i])
    c_211.append(k11 * k111 * k211 * values[1][i] **2 * values[2][i] * values[0][i])

  values.append(c_11)
```

```
    values.append(c_21)
    values.append(c_111)
    values.append(c_211)

    return values


def add_fractions_list(values):

    x_dye = list()
    x_11 = list()
    x_21 = list()
    x_111 = list()
    x_211 = list()

    for i in range(len(values[0])):
        x_dye.append(values[2][i] / G_0)
        x_11.append(values[3][i] / G_0)
        x_21.append(values[4][i] / G_0)
        x_111.append(values[5][i] / G_0)
        x_211.append(values[6][i] / G_0)

    values.append(x_dye)
    values.append(x_11)
    values.append(x_21)
    values.append(x_111)
    values.append(x_211)

    return values


def add_values_to_df(df, values):
    df["BB"] = values[0]
    df["CB7"] = values[1]
    df["G"] = values[2]
    df["CB7:G"] = values[3]
    df["CB7_2:G"] = values[4]
    df["CB7:G:BB"] = values[5]
    df["CB7_2:G:BB"] = values[6]
    df["X_dye"] = values[7]
    df["X_CB7:G"] = values[8]
    df["X_CB7_2:G"] = values[9]
    df["X_CB7:G:BB"] = values[10]
    df["X_CB7_2:G:BB"] = values[11]


def calc_fluor_df(df, f_optimized):
    fdye, f11, f21, f111, f211 = f_optimized

```

```
  df["F_calc"] = fdye * df["X_dye"] + f11 * df["X_CB7:G"] + f21 * df["
  X_CB7_2:G"] + f111 * df["X_CB7:G:BB"] + f211 * df["X_CB7_2:G:BB"]


def show_graph_fractions(df, concentrations=False):

  if concentrations == True:

    plt.plot(df["BB0"], df["G"], "-", label = "G")
    plt.plot(df["BB0"], df["[CB7:G]"], '-', label = "[CB7:G]")
    plt.plot(df["BB0"], df["[CB7_2:G]"], '-', label= "[CB7_2:G]")
    plt.plot(df["BB0"], df["[CB7:G:BB]"], '-', label = "[CB7:G:BB]")
    plt.plot(df["BB0"], df["[CB7_2:G:BB]"], '-', label = "[CB7_2:G:BB]")
    plt.legend()
    plt.show()

  else:

    plt.plot(df["BB0"], df["X_dye"], '-', label = "Free Dye (G)")
    plt.plot(df["BB0"], df["X_CB7:G"], '-', label = "CB7:G")
    plt.plot(df["BB0"], df["X_CB7_2:G"], '-', label = "CB7_2:G")
    plt.plot(df["BB0"], df["X_CB7:G:BB"], '-', label = "CB7:G:BB")
    plt.plot(df["BB0"], df["X_CB7_2:G:BB"], '-', label = "CB7_2:G:BB")
    plt.legend()
    plt.show()


def show_graph_fluor(df):
  plt.plot(df["BB0"], df["F"], '.', label = "Exp")
  plt.plot(df["BB0"], df["F_calc"], '-', label = "Calc")
  plt.xscale('log')
  plt.legend()
  plt.show()

def fluor_calc(x, k111, k211,
  fg, f11, f21, f111, f211):

  k = (K11, K21, KBB_G, KBB_CB7, k111, k211)

  values = calc_solution_list(x, trials=int(1e6), k=k, error=1e-17, eq=eq,
  jac=jac)

  if len(values[-1]) != len(x):
    print("The optimization was not successful")
  else:
    add_concentrations_list(k, values)
    add_fractions_list(values)
```

```
    return fg * np.array(values[7]) + f11 * np.array(values[8]) + f21 * np.array(values[9]) + f111 * np.array(values[10]) + f211 * np.array(values[11])



if __name__ == "__main__":

    # A file with two columns needs to be entered,
    # only with the values, with concentration in the first
    # and experimental values of fluorescence in the second

    guesses = [K111_guess, K211_guess, FD, F11, F21, F111, F211]
    min_values = [1e3, 1e3, 0, 1, 5, 0, 0]
    max_values = [1e7, 1e6, 3, 10, 20, 1, 1]

    Tk().withdraw()
    fileName = askopenfilename()
    dataTable = pd.read_csv(fileName, header=None, sep=";")
    dataTable.rename(columns = {0 : "BB0", 1: "F"}, inplace=True)
    dataTable.dropna(inplace=True)

    parameters, covariance = optimize.curve_fit(fluor_calc, dataTable["BB0"],
                                                dataTable["F"], p0=guesses,
                                                bounds=(min_values, max_values))

    k = [K11, K21, KBB_G, KBB_CB7]
    k.append(parameters[0])
    k.append(parameters[1])

    f_optimized = parameters[2::1]

    values = calc_solution_list(dataTable["BB0"], trials=int(1e5), k=k,
                                error=1e-17, eq=eq, jac=jac)

    if len(values[-1]) != len(dataTable["BB0"]):
      print("The optimization was not successful")
    else:
      add_concentrations_list(k, values)
      add_fractions_list(values)
      add_values_to_df(dataTable, values)
      calc_fluor_df(dataTable, f_optimized=f_optimized)
      show_graph_fluor(dataTable)
      print(f"Values of k:{k}\n Values of fluor:{f_optimized}")
```

I.2.1.2 Script 2 - CB7_Dye_BB_A_fit_KA.py

This script needs the same type of file but with the data of the competitive assay with concentration of guest and spectroscopical data in columns 1 and 2, respectively. The same limitations and way of operating apply as with Script 1. Separator chnage can be done in line 291.

Listing I.2: Script 2 - Competitive Assay with ternary complex fitting

```
1  from scipy import optimize
2  import pandas as pd
3  import numpy as np
4  import matplotlib.pyplot as plt
5
6  from tkinter import Tk
7  from tkinter.filedialog import askopenfilename
8
9
10 ''' This file applies to a system with 4 species, with the following
     behaviour:
11
12 G + CB7 -> CB7:G                (K11)
13 CB7:G + CB7 - > (CB7)2:G        (K21)
14 G + BB -> BB:G                  (KBB_G)
15 CB7 + BB -> CB7:BB              (KBB_CB7)
16 CB7:G + BB -> CB7:G:BB          (K111)
17 CB7:G:BB + CB7 -> (CB7)2:G:BB   (K211)
18 CB7 + A -> CB7:A                (KA)
19 BB + A -> BB:A                  (KBB_A)
20
21 Instead of the calculation, this file aims to do the fitting to a set of
     experimental data
22
23 '''
24
25 # Concentrations of the species in the assay
26 CB7_0 = np.float64(2.5e-5)
27 G_0 = np.float64(8e-6)
28 BB_0 = np.float64(6e-6)
29
30 # Known Affinity constants in M-1
31 K111 = np.float64(9.5e6)
32 K211 = np.float64(1)
33
34 K11 = np.float64(1e6)
35 K21 = np.float64(1)
36 KBB_G = np.float64(1e3)
37 KBB_CB7 = np.float64(1e3)
38
39 # Affinity guesses:
40 KA_guess = np.float64(1e7)
41 KBB_A_guess = np.float64(1e5)
42
43 # Fluorescence guesses:
44 FD = 0.5
```

```
F11 = 2
F21 = 5
F111 = 0.35
F211 = 0.01


def eq(vars, a_0, k):
  # Can change name, but the vars and a_0 must be maintained
  # and consistent with jac
  k11, k21, k111, k211, kbb_g, kbb_cb7, kbb_a, ka = k
  bb, cb7, g, a = vars

  cb7_g = k11 * cb7 * g
  cb7_2_g = k21 * k11 * cb7 ** 2 * g
  bb_g = kbb_g * g * bb
  cb7_bb = kbb_cb7 * bb * cb7
  cb7_g_bb = k111 * k11 * cb7 * g * bb
  cb7_2_g_bb = k211 * k111 * k11 * cb7 **2 * g * bb
  cb7_a = ka * cb7 * a
  bb_a = kbb_a * bb * a

  f_bb = bb + bb_g + cb7_bb + cb7_g_bb + cb7_2_g_bb + bb_a - BB_0
  f_cb7 = cb7 + cb7_g + cb7_bb + 2 * cb7_2_g + cb7_g_bb + 2 * cb7_2_g_bb +
 cb7_a - CB7_0
  f_g = g + cb7_g + cb7_2_g + bb_g + cb7_g_bb + cb7_2_g_bb - G_0
  f_a = a + cb7_a + bb_a - a_0

  return [f_bb,
          f_cb7,
          f_g,
          f_a]


def jac(vars, a_0, k):

  k11, k21, k111, k211, kbb_g, kbb_cb7, kbb_a, ka = k

  bb, cb7, g, a = vars

  cb7_g = k11 * cb7 * g
  cb7_2_g = k21 * k11 * cb7 ** 2 * g
  bb_g = kbb_g * g * bb
  cb7_bb = kbb_cb7 * bb * cb7
  cb7_a = ka * cb7 * a
  bb_a = kbb_a * bb * a
  cb7_g_bb = k111 * k11 * cb7 * g * bb
  cb7_2_g_bb = k211 * k111 * k11 * cb7 **2 * g * bb

  # 1st line for the jacobian - derivates of the BB function (in function of
   BB, CB7, G and A, respectively)
```

```
    fp_bb_bb = 1 + kbb_g * g + kbb_cb7 * cb7 + k111 * k11 * cb7 * g + k211 * k111 * k11 * cb7 **2 *g + kbb_a * a
    fp_bb_cb7 = bb + bb_g + kbb_cb7 * bb + k111 * k11 * bb * g + 2 * k211 * k111 * k11 * cb7 * bb * g + bb_a
    fp_bb_g = bb + kbb_g * bb + cb7_bb + k111 * k11 * cb7 * bb + k211 * k111 * k11 * cb7 **2 * bb + bb_a
    fp_bb_a = bb + bb_g + cb7_bb + cb7_g_bb + cb7_2_g_bb + kbb_a * bb

    # 2nd line for the jacobian - derivates of the CB7 function
    fp_cb7_bb = cb7 + cb7_g + kbb_cb7 * cb7 + 2 * cb7_2_g + k111 * k11 * cb7 * g + 2 * k211 * k111 * k11 * cb7 **2 *g + cb7_a
    fp_cb7_cb7 = 1 + k11 * g + kbb_cb7 * bb + 4 * k21 * k11 * cb7 * g + k111 * k11 * bb * g + 4 * k211 * k111 * k11 * cb7 * bb *g + ka * a
    fp_cb7_g =  cb7 + k11 * cb7 + cb7_bb + 2 * k21 * k11 * cb7 **2 + k111 * k11 * bb * cb7 + 2 * k211 * k111 * k11 * cb7 **2 * bb + cb7_a
    fp_cb7_a = cb7 + cb7_g + 2 * cb7_2_g + cb7_bb + cb7_g_bb + 2 * cb7_2_g_bb + ka * cb7

    # 3rd line for the jacobian - derivatives of the G function
    fp_g_bb = g + cb7_g + cb7_2_g + kbb_g * g + k111 * k11 * cb7 * g + k211 * k111 * k11 * cb7 **2 * g
    fp_g_cb7 = g + k11 * g + 2* k21 * k11 * g * cb7 + bb_g + k111 * k11 * bb * g + 2 * k211 * k111 * k11 * cb7 * bb * g
    fp_g_g = 1 + k11 * cb7 + k21 * k11 * cb7**2 + kbb_g * bb + k111 * k11 * bb * cb7 + k211 * k111 * k11 * cb7 **2 * bb
    fp_g_a = g + cb7_g + cb7_2_g + bb_g + cb7_g_bb + cb7_2_g_bb

    # 4th line for the jacobian - derivatives of the A function
    fp_a_bb = a + cb7_a + kbb_a * a
    fp_a_cb7 = a + ka * a + bb_a
    fp_a_g = a + cb7_a + bb_a
    fp_a_a = 1 + ka * cb7 + kbb_a * bb

    return np.array([[fp_bb_bb, fp_bb_cb7, fp_bb_g, fp_bb_a],
                     [fp_cb7_bb, fp_cb7_cb7, fp_cb7_g, fp_cb7_a],
                     [fp_g_bb, fp_g_cb7, fp_g_g, fp_g_a],
                     [fp_a_bb, fp_a_cb7, fp_a_g, fp_a_a]])


def try_solution(a_max, k, trials, error, eq, jac):

    for i in range(trials):
        initial_guess = [np.random.uniform(0, BB_0),
                         np.random.uniform(0, CB7_0),
                         np.random.uniform(0, G_0),
                         np.random.uniform(0, a_max)]

        sol = optimize.root(eq, jac=jac, args=(a_max, k), x0=initial_guess)

```

```
  if 0 <= sol.x[0] <= BB_0 and 0 <= sol.x[1] <= CB7_0 and 0 <= sol.x[2] <= G_0 and 0 <= sol.x[3] <= a_max:

    zero = eq(vars=sol.x, a_0=a_max, k=k)

    if -error <= zero[0] <= error and -error <= zero[1] <= error and -error <= zero[2] <= error and -error <= zero[3] <= error:
      return sol.x
      break


def calc_solution_list(x, trials, k, error, eq, jac):

  k11, k21, k111, k211, kbb_g, kbb_cb7, kbb_a, ka = k

  values = [[],
            [],
            [],
            []]

  for a_max in x:
    sol = try_solution(a_max, k, trials=trials, error=error, eq=eq, jac=jac)
    values[0].append(sol[0])
    values[1].append(sol[1])
    values[2].append(sol[2])
    values[3].append(sol[3])

  return values


def add_concentrations_list(k, values):

  k11, k21, k111, k211, kbb_g, kbb_cb7, kbb_a, ka = k

  c_11 = list()
  c_21 = list()
  c_111 = list()
  c_211 = list()

  for i in range(len(values[0])):

    c_11.append(k11 * values[1][i] * values[2][i])
    c_21.append(k11 * k21 * values[1][i] ** 2 * values[2][i])
    c_111.append(k11 * k111 * values[1][i] * values[2][i] * values[0][i])
    c_211.append(k11 * k111 * k211 * values[1][i] **2 * values[2][i] * values[0][i])

  values.append(c_11)
  values.append(c_21)
  values.append(c_111)
```

```
    values.append(c_211)

    return values


def add_fractions_list(values):

    x_dye = list()
    x_11 = list()
    x_21 = list()
    x_111 = list()
    x_211 = list()

    for i in range(len(values[0])):
        x_dye.append(values[2][i] / G_0)
        x_11.append(values[4][i] / G_0)
        x_21.append(values[5][i] / G_0)
        x_111.append(values[6][i] / G_0)
        x_211.append(values[7][i] / G_0)

    values.append(x_dye)
    values.append(x_11)
    values.append(x_21)
    values.append(x_111)
    values.append(x_211)

    return values


def add_values_to_df(df, values):
    df["BB"] = values[0]
    df["CB7"] = values[1]
    df["G"] = values[2]
    df["A"] = values[3]
    df["CB7:G"] = values[4]
    df["CB7_2:G"] = values[5]
    df["CB7:G:BB"] = values[6]
    df["CB7_2:G:BB"] = values[7]
    df["X_dye"] = values[8]
    df["X_CB7:G"] = values[9]
    df["X_CB7_2:G"] = values[10]
    df["X_CB7:G:BB"] = values[11]
    df["X_CB7_2:G:BB"] = values[12]


def calc_fluor_df(df, f_optimized):
    fdye, f11, f21, f111, f211 = f_optimized

    df["F_calc"] = fdye * df["X_dye"] + f11 * df["X_CB7:G"] + f21 * df["
   X_CB7_2:G"] + f111 * df["X_CB7:G:BB"] + f211 * df["X_CB7_2:G:BB"]
```

```


def show_graph_fractions(df, concentrations=False):

  if concentrations == True:

    plt.plot(df["A0"], df["G"], "-", label = "G")
    plt.plot(df["A0"], df["[CB7:G]"], '-', label = "[CB7:G]")
    plt.plot(df["A0"], df["[CB7_2:G]"], '-', label= "[CB7_2:G]")
    plt.plot(df["A0"], df["[CB7:G:BB]"], '-', label = "[CB7:G:BB]")
    plt.plot(df["A0"], df["[CB7_2:G:BB]"], '-', label = "[CB7_2:G:BB]")
    plt.legend()
    plt.show()

  else:

    plt.plot(df["A0"], df["X_dye"], '-', label = "Free Dye (G)")
    plt.plot(df["A0"], df["X_CB7:G"], '-', label = "CB7:G")
    plt.plot(df["A0"], df["X_CB7_2:G"], '-', label = "CB7_2:G")
    plt.plot(df["A0"], df["X_CB7:G:BB"], '-', label = "CB7:G:BB")
    plt.plot(df["A0"], df["X_CB7_2:G:BB"], '-', label = "CB7_2:G:BB")
    plt.legend()
    plt.show()


def show_graph_fluor(df):
  plt.plot(df["A0"], df["F"], '.', label = "Exp")
  plt.plot(df["A0"], df["F_calc"], '-', label = "Calc")
  "plt.xscale('log')"
  plt.legend()
  plt.show()


def fluor_calc(x, kbb_a, ka,
  fg, f11, f21, f111, f211):

  k = (K11, K21, K111, K211, KBB_G, KBB_CB7, kbb_a, ka)

  values = calc_solution_list(x, trials=int(1e6), k=k, error=1e-19,
                              eq=eq, jac=jac)

  if len(values[-1]) != len(x):
    print("The optimization was not successful")
  else:
    add_concentrations_list(k, values)
    add_fractions_list(values)


```

```
    return fg * np.array(values[8]) + f11 * np.array(values[9]) + f21 * np.
    array(values[10]) + f111 * np.array(values[11]) + f211 * np.array(values
    [12])



if __name__ == "__main__":

    # A file with two columns needs to be entered,
    # only with the values, with concentration in the first
    # and experimental values of fluorescence in the second

    guesses = [KBB_A_guess, KA_guess, FD, F11, F21, F111, F211]
    min_values = [1, 1e3, 0, 1, 1, 0, 0]
    max_values = [1e6, 1e9, 3, 10, 20, 1, 1]

    Tk().withdraw()
    fileName = askopenfilename()
    dataTable = pd.read_csv(fileName, header=None, sep=";")
    print(dataTable)
    dataTable.rename(columns = {0 : "A0", 1: "F"}, inplace=True)
    dataTable.dropna(inplace=True)

    parameters, covariance = optimize.curve_fit(fluor_calc, dataTable["A0"],
                                                dataTable["F"], p0=guesses,
                                                bounds=(min_values, max_values))

    k = [K11, K21, K111, K211, KBB_G, KBB_CB7]
    k.append(parameters[0])
    k.append(parameters[1])

    f_optimized = parameters[2::1]

    values = calc_solution_list(dataTable["A0"], trials=int(1e6), k=k,
                                error=1e-19, eq=eq, jac=jac)

    if len(values[-1]) != len(dataTable["A0"]):
        print("The optimization was not successful")
    else:
        add_concentrations_list(k, values)
        add_fractions_list(values)
        add_values_to_df(dataTable, values)
        calc_fluor_df(dataTable, f_optimized=f_optimized)
        show_graph_fluor(dataTable)
        print(f"Values of k:{k}\n Values of fluor:{f_optimized}")
        dataTable.to_excel(r"prediction_data.xlsx",
        sheet_name="Dye_name")
```

I.2.2 Scripts for prediction of species distribution in ternary systems

These scripts were done to predict the species distribution in the ternary systems with CB7-Dye-BB and to predict the conditions at which to do competitive assays with this system.

I.2.2.1 Script 3 - CB7_Dye_BB_root_rngGuess.py

This script allows the prediction of ternary species distribution for a given set of initial CB7 and dye concentration, and variable BB concentrations. This could be easily adapted to predict that same variation but for addition of one of the other elements. If the concentrations will be given in an interval, these limits can be set in the script and no file needs to be inputed, as it is in the script below. Alternatively, if there is the need to known the molar fractions at more specific BB concentrations, then a file like the one presented in Figure I.2 should be inputed, with the concentrations in M, by commenting out line 51 of the code and reinserting the lines 6-8 and 42-47 by removing the comment marker ''' that enclose them. The prediction data will be generated in a plot with the molar fractions in relation to the BB concentrations and the numeric values will be saved in the "prediction_data.xlsx" file.

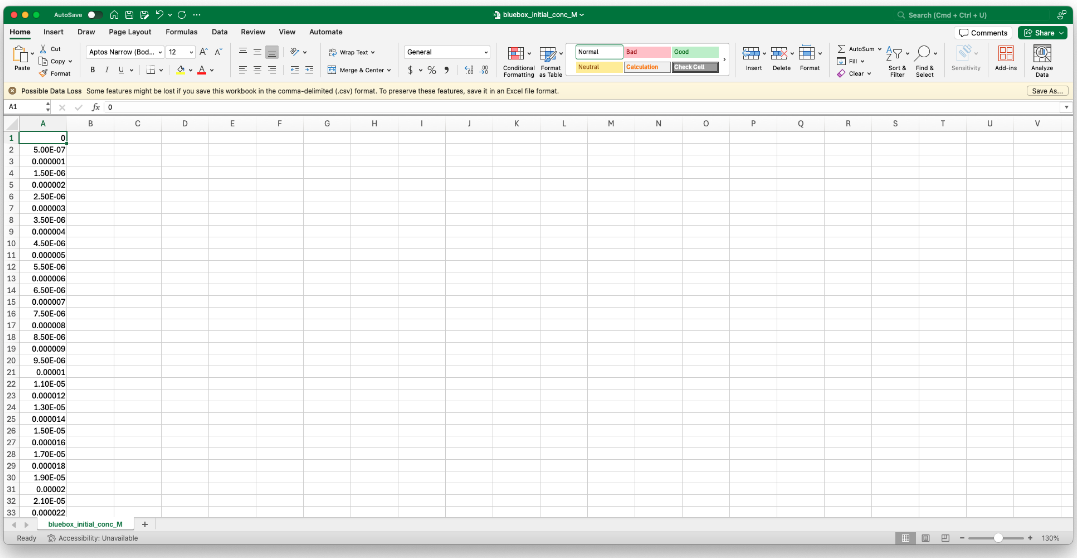

	A
1	0
2	5.00E-07
3	0.000001
4	1.50E-06
5	0.000002
6	2.50E-06
7	0.000003
8	3.50E-06
9	0.000004
10	4.50E-06
11	0.000005
12	5.50E-06
13	0.000006
14	6.50E-06
15	0.000007
16	7.50E-06
17	0.000008
18	8.50E-06
19	0.000009
20	9.50E-06
21	0.00001
22	1.10E-05
23	0.000012
24	1.30E-05
25	0.000014
26	1.50E-05
27	0.000016
28	1.70E-05
29	0.000018
30	1.90E-05
31	0.00002
32	2.10E-05
33	0.000022

Figure I.2: Example .csv file for the input of concentration values for fitting.

Listing I.3: Script 3 - Ternary complex molar fraction prediction

```
1  from scipy import optimize
2  import pandas as pd
3  import numpy as np
4  import matplotlib.pyplot as plt
5
6  ''' #uncomment to use the file as input for concentration
```

```
from tkinter import Tk
from tkinter.filedialog import askopenfilename
'''



''' This file applies to a system with 3 species, with the following behaviour:

G + CB7 -> CB7:G               (K11)
CB7:G + CB7 - > (CB7)2:G       (K21)
G + BB -> BB:G                 (KBB_G)
CB7 + BB -> CB7:BB             (KBB_CB7)
CB7:G + BB -> CB7:G:BB         (K111)
CB7:G:BB + CB7 -> (CB7)2:G:BB (K211)

BB initial concentration is what varies and the species distribution will be expressed in relation to that
BB concentrations will be given in .csv file and the initial concentrations of CB7 and G in the system
will be used as initial guesses for the equilibrium concentrations

'''

CB7_0 = np.float64(25e-5) # Concentrations in M, in caps because they're constants
G_0 = np.float64(8.6e-6)
BB = np.float64(15e-6)

K111 = np.float64(9.5e6)
K211 = np.float64(0)

K11 = np.float64(1e6) # Affinity constants in M-1
K21 = np.float64(1e3)
KBB_G = np.float64(1e3)
KBB_CB7 = np.float64(1e3)



''' # To take the [BB] out of a faile comment this in and comment line 51 out

Tk().withdraw()
fileName = askopenfilename()
dataTable = pd.read_csv(fileName, header=None, sep=";")
dataTable.rename(columns = {0 : "[BB]0"}, inplace=True)
'''



dataTable = pd.DataFrame(np.linspace(0, BB, 60), columns=["[BB]0"])
```

```

values_bb = list()
values_cb7 = list()
values_g = list()

def equations(vars, bb_0):

  bb, cb7, g = vars

  cb7_g = K11 * cb7 * g
  cb7_2_g = K21 * K11 * cb7 ** 2 * g
  bb_g = KBB_G * g * bb
  cb7_bb = KBB_CB7 * bb * cb7
  cb7_g_bb = K111 * K11 * cb7 * g * bb
  cb7_2_g_bb = K211 * K111 * K11 * cb7 **2 * g * bb

  f_bb = bb + bb_g + cb7_bb + cb7_g_bb + cb7_2_g_bb - bb_0
  f_cb7 = cb7 + cb7_g + cb7_bb + 2 * cb7_2_g + cb7_g_bb + 2 * cb7_2_g_bb -
 CB7_0
  f_g = g + cb7_g + cb7_2_g + bb_g + cb7_g_bb + cb7_2_g_bb - G_0

  return [f_bb,
          f_cb7,
          f_g]


def jac(vars, bb_0):

  bb, cb7, g = vars

  cb7_g = K11 * cb7 * g
  cb7_2_g = K21 * K11 * cb7 ** 2 * g
  bb_g = KBB_G * g * bb
  cb7_bb = KBB_CB7 * bb * cb7

  # 1st line for the jacobian - derivates in function of BB
  fp_bb_bb = 1 + KBB_G * g + KBB_CB7 * cb7 + K111 * K11 * cb7 * g + K211 *
 K111 * K11 * cb7 **2 *g
  fp_bb_cb7 = bb + bb_g + KBB_CB7 * bb + K111 * K11 * bb * g + 2 * K211 *
 K111 * K11 * cb7 * bb * g
  fp_bb_g = bb + KBB_G * bb + cb7_bb + K111 * K11 * cb7 * bb + K211 * K111 *
 K11 * cb7 **2 * bb

  # 2nd line for the jacobian - derivates in function of CB7
  fp_cb7_bb = cb7 + cb7_g + KBB_CB7 * cb7 + 2 * cb7_2_g + K111 * K11 * cb7 *
 g + 2 * K211 * K111 * K11 * cb7 **2 *g
  fp_cb7_cb7 = 1 + K11 * g + KBB_CB7 * bb + 4 * K21 * K11 * cb7 * g + K111 *
 K11 * bb * g + 4 * K211 * K111 * K11 * cb7 * bb *g
  fp_cb7_g =  cb7 + K11 * cb7 + cb7_bb + 2 * K21 * K11 * cb7 **2 + K111 *
 K11 * bb * cb7 + 2 * K211 * K111 * K11 * cb7 **2 * bb
```

```

  # 3rd line for the jacobian - derivatives in function of G
  fp_g_bb = g + cb7_g + cb7_2_g + KBB_G * g + K111 * K11 * cb7 * g + K211 * K111 * K11 * cb7 **2 * g
  fp_g_cb7 = g + K11 * g + 2* K21 * K11 * g * cb7 + bb_g + K111 * K11 * bb * g + 2 * K211 * K111 * K11 * cb7 * bb * g
  fp_g_g = 1 + K11 * cb7 + K21 * K11 * cb7**2 + KBB_G * bb + K111 * K11 * bb * cb7 + K211 * K111 * K11 * cb7 **2 * bb

  return np.array([[fp_bb_bb, fp_bb_cb7, fp_bb_g],
                  [fp_cb7_bb, fp_cb7_cb7, fp_cb7_g],
                  [fp_g_bb, fp_g_cb7, fp_g_g]])


num_trials = int(1e6)
error = 1e-15

for bb_max in dataTable["[BB]0"]:
  for i in range(num_trials):
    initial_guess = [np.random.uniform(0, bb_max),
    np.random.uniform(0, CB7_0),
    np.random.uniform(0, G_0)]

sol = optimize.root(equations, jac=jac, args=bb_max, x0=initial_guess)

if 0 <= sol.x[0] <= bb_max and 0 <= sol.x[1] <= CB7_0 and 0 <= sol.x[2] <= G_0:

  zero = equations(vars=sol.x, bb_0=bb_max)

if -error <= zero[0] <= error and -error <= zero[1] <= error and -error <= zero[2] <= error:
  values_bb.append(np.float64(sol.x[0]))
  values_cb7.append(np.float64(sol.x[1]))
  values_g.append(np.float64(sol.x[2]))
  break

if len(values_bb) != len(dataTable["[BB]0"]):
  print("The optimization was not successful")
else:
  dataTable["BB"] = values_bb
  dataTable["CB7"] = values_cb7
  dataTable["G"] = values_g


dataTable["[CB7:G]"] = K11 * dataTable["CB7"] * dataTable["G"]
dataTable["[CB7_2:G]"] = K21 * K11 * dataTable["CB7"] ** 2 * dataTable["G"]
dataTable["[CB7:G:BB]"] = K11 * K111 * dataTable["CB7"] * dataTable["G"] * dataTable["BB"]
```

```
dataTable["[CB7_2:G:BB]"] = K11 * K111 * K211 * dataTable["CB7"] **2 *
  dataTable["G"] * dataTable["BB"]
dataTable["[BB:G]"] = KBB_G * dataTable["BB"] * dataTable["G"]

dataTable["X_G"] = dataTable["G"] / G_0
dataTable["X_CB7:G"] = dataTable["[CB7:G]"] / G_0
dataTable["X_CB7_2:G"] = dataTable["[CB7_2:G]"] / G_0
dataTable["X_CB7:G:BB"] = dataTable["[CB7:G:BB]"] / G_0
dataTable["X_CB7_2:G:BB"] = dataTable["[CB7_2:G:BB]"] / G_0
dataTable["X_BB_G"] = dataTable["[BB:G]"] / G_0

plt.plot(dataTable["[BB]0"], dataTable["X_G"], "-", label = "G")
plt.plot(dataTable["[BB]0"], dataTable["X_CB7:G"], '-', label = "CB7:G")
plt.plot(dataTable["[BB]0"], dataTable["X_CB7_2:G"], '-', label = "(CB7)2:G"
  )
plt.plot(dataTable["[BB]0"], dataTable["X_CB7:G:BB"], '-', label = "CB7:G:BB
  ")
plt.plot(dataTable["[BB]0"], dataTable["X_CB7_2:G:BB"], '-', label = "(CB7)
  2:G:BB")
plt.plot(dataTable["[BB]0"], dataTable["X_BB_G"], '-', label = "BB:G")
plt.xlabel("[BB] (M)")
plt.ylabel("Molar Fraction")
plt.legend()
plt.show()

dataTable.to_excel(r"prediction_data.xlsx",
sheet_name="Dye_Name")
```

I.2.2.2 Script 4 - CB7_Dye_BB_A2binding_sites.py

For prediction of species in solution for the host displacement system in the presence of a guest that presents binding sites for both CB7 and BB, the following script was written. The script considers the binding of CB7 to two sites on the guest peptide and BB to one of these binding sites and, while the predictions made did not consider the binding of BB to the CB7:peptide complex because no binding affinity is know at this point, this can be considered by simply changing this value from 0 to the calculated value in M^{-1}. Otherwise, this script functions in the same manner as the previous script.

Listing I.4: Script 4 - Host displacement assay with binding sites for both hosts prediction

```
from scipy import optimize
import pandas as pd
import numpy as np
import matplotlib.pyplot as plt

''' #uncomment to use the file as input for concentration
from tkinter import Tk
from tkinter.filedialog import askopenfilename
'''
```

```


''' This file applies to a system with 4 species, with the following
  behaviour:

D + CB7 -> CB7:D               (KD11)
CB7:D + CB7 - > (CB7)2:D       (KD21)
D + BB -> BB:D                 (KBB_D)
CB7 + BB -> CB7:BB             (KBB_CB7)
CB7:D + BB -> CB7:D:BB         (KD111)
CB7:D:BB + CB7 -> (CB7)2:D:BB  (KD211)

CB7 + P -> CB7:P               (KP11)
BB + P -> BB:P                 (KBB_P)
CB7:P + CB7 -> (CB7)2:P        (KP21)
CB7:P + BB -> CB7:P:BB         (KP111)
CB7:P:BB + CB7 -> (CB7)2:P:BB  (KP211)

'''

CB7_0 = np.float64(25e-6) # Concentrations in M, in caps because they're
  constants
D_0 = np.float64(8e-6)
BB_0 = np.float64(6e-6)
P = np.float64(20e-5)

KD11 = np.float64(3e6)
KD21 = np.float64(0)

KBB_D = np.float64(1e3)
KBB_CB7 = np.float64(1e3)

KD111 = np.float64(2.5e7) # Affinity constants in M-1
KD211 = np.float64(0)

KP111 = np.float64(0)
KP211 = np.float64(0)

KP11 = np.float64(5e7)
KP21 = np.float64(8e5)
KBB_P = np.float64(1.5e5)

# Para tirar valores de [BB] ou [A] dum ficheiro

'''Tk().withdraw()
fileName = askopenfilename()
dataTable = pd.read_csv(fileName, header=None, sep=";")

rows, columns = dataTable.shape

```

```
'''
dataTable = pd.DataFrame(np.linspace(0, P, 400), columns=["P0"])
rows, columns = dataTable.shape

'''

if columns == 2:
  dataTable.rename(columns = {0 : "P0", 1: "Fd"}, inplace=True)

  dataTable["BB_0"] = np.float64(BB_0 / dataTable["Fd"])
  dataTable["CB7_0"] = np.float64(CB7_0 / dataTable["Fd"])
  dataTable["D_0"] = np.float64(D_0 / dataTable["Fd"])

elif columns == 1:
  dataTable.rename(columns = {0 : "P0"}, inplace=True)

  dataTable["BB_0"] = np.float64(BB_0)
  dataTable["CB7_0"] = np.float64(CB7_0)
  dataTable["D_0"] = np.float64(D_0)

'''

dataTable["BB_0"] = np.float64(BB_0)
dataTable["CB7_0"] = np.float64(CB7_0)
dataTable["D_0"] = np.float64(D_0)

values_bb = list()
values_cb7 = list()
values_d = list()
values_p = list()

def equations(vars, p_0, bb_0, cb7_0, d_0):

  bb, cb7, d, p = vars

  cb7_d = KD11 * cb7 * d
  cb7_2_d = KD21 * KD11 * cb7 ** 2 * d
  bb_d = KBB_D * d * bb
  cb7_bb = KBB_CB7 * bb * cb7
  cb7_d_bb = KD111 * KD11 * cb7 * d * bb
  cb7_2_d_bb = KD211 * KD111 * KD11 * cb7 **2 * d * bb
  cb7_p = KP11 * cb7 * p
  bb_p = KBB_P * bb * p
  cb7_p_cb7 = KP21 * KP11 * cb7**2 * p
  cb7_p_bb = KP111 * KP11 * cb7 * bb * p
  cb7_2_p_bb = KP211 * KP111 * KP11 * cb7**2 * p * bb


  f_bb = bb + bb_d + cb7_bb + cb7_d_bb + cb7_2_d_bb + bb_p + cb7_p_bb +
  cb7_2_p_bb - bb_0
```

```
    f_cb7 = cb7 + cb7_d + cb7_bb + 2 * cb7_2_d + cb7_d_bb + 2 * cb7_2_d_bb + cb7_p + cb7_p_bb + cb7_2_p_bb + cb7_p_cb7 - cb7_0
    f_d = d + cb7_d + cb7_2_d + bb_d + cb7_d_bb + cb7_2_d_bb - d_0
    f_p = p + cb7_p + bb_p + cb7_p_cb7 + cb7_p_bb + cb7_2_p_bb - p_0

    return [f_bb,
            f_cb7,
            f_d,
            f_p]


def jac(vars, p_0, bb_0, cb7_0, d_0):

    bb, cb7, d, p = vars

    cb7_d = KD11 * cb7 * d
    cb7_2_d = KD21 * KD11 * cb7 ** 2 * d
    bb_d = KBB_D * d * bb
    cb7_bb = KBB_CB7 * bb * cb7
    cb7_p = KP11 * cb7 * p
    cb7_p_cb7 = KP21 * KP11 * cb7**2 * p
    bb_p = KBB_P * bb * p
    cb7_d_bb = KD111 * KD11 * cb7 * d * bb
    cb7_2_d_bb = KD211 * KD111 * KD11 * cb7 **2 * d * bb
    cb7_p_bb = KP111 * KP11 * cb7 * bb * p
    cb7_2_p_bb = KP211 * KP111 * KP11 * cb7**2 * p * bb

    # 1st line for the jacobian - derivates of the BB function (in function of BB, CB7, G and A, respectively)
    fp_bb_bb = 1 + KBB_D * d + KBB_CB7 * cb7 + KD111 * KD11 * cb7 * d + KD211 * KD111 * KD11 * cb7 **2 *d + KBB_P * p + KP111 * KP11 * cb7 * p + KP211 * KP111 * KP11 * cb7**2 * p
    fp_bb_cb7 = bb + bb_d + KBB_CB7 * bb + KD111 * KD11 * bb * d + 2 * KD211 * KD111 * KD11 * cb7 * bb * d + bb_p + KP111 * KP11 * bb * p + 2 * KP211 * KP111 * KP11 * cb7 * bb * p
    fp_bb_d = bb + KBB_D * bb + cb7_bb + KD111 * KD11 * cb7 * bb + KD211 * KD111 * KD11 * cb7 **2 * bb + bb_p + cb7_p_bb + cb7_2_p_bb
    fp_bb_p = bb + bb_d + cb7_bb + cb7_d_bb + cb7_2_d_bb + KBB_P * bb +  KP111 * KP11 * bb * cb7 + KP211 * KP111 * KP11 * cb7**2 * bb

    # 2nd line for the jacobian - derivates of the CB7 function
    fp_cb7_bb = cb7 + cb7_d + KBB_CB7 * cb7 + 2 * cb7_2_d + KD111 * KD11 * cb7 * d + 2 * KD211 * KD111 * KD11 * cb7 **2 *d + cb7_p + KP111 * KP11 * cb7 * p + 2 * KP211 * KP111 * KP11 * cb7**2 * p + cb7_p_cb7
    fp_cb7_cb7 = 1 + KD11 * d + KBB_CB7 * bb + 4 * KD21 * KD11 * cb7 * d + KD111 * KD11 * bb * d + 4 * KD211 * KD111 * KD11 * cb7 * bb *d + KP11 * p + KP111 * KP11 * bb * p + 4 * KP211 * KP111 * KP11 * cb7* p * bb + 4 * KP21 * KP11 * cb7 * p
```

```
  fp_cb7_d =  cb7 + KD11 * cb7 + cb7_bb + 2 * KD21 * KD11 * cb7 **2 + KD111 * KD11 * bb * cb7 + 2 * KD211 * KD111 * KD11 * cb7 **2 * bb + cb7_p + cb7_p_bb + cb7_p_cb7 + cb7_2_p_bb
  fp_cb7_p = cb7 + cb7_d + 2 * cb7_2_d + cb7_bb + cb7_d_bb + 2 * cb7_2_d_bb + KP11 * cb7 + KP111 * KP11 * bb * cb7 + 2 * KP21 * KP11 * cb7**2 + 2 * KP211 * KP111 * KP11 * cb7**2 * bb

  # 3rd line for the jacobian - derivatives of the G function
  fp_d_bb = d + cb7_d + cb7_2_d + KBB_D * d + KD111 * KD11 * cb7 * d + KD211 * KD111 * KD11 * cb7 **2 * d
  fp_d_cb7 = d + KD11 * d + 2* KD21 * KD11 * d * cb7 + bb_d + KD111 * KD11 * bb * d + 2 * KD211 * KD111 * KD11 * cb7 * bb * d
  fp_d_d = 1 + KD11 * cb7 + KD21 * KD11 * cb7**2 + KBB_D * bb + KD111 * KD11 * bb * cb7 + KD211 * KD111 * KD11 * cb7 **2 * bb
  fp_d_p = d + cb7_d + cb7_2_d + bb_d + cb7_d_bb + cb7_2_d_bb

  # 4th line for the jacobian - derivatives of the A function
  fp_p_bb = p + cb7_p + KBB_P * p + KP111 * KP11 * cb7 * p + cb7_p_cb7 + KP211 * KP111 * KP11 * cb7**2 * p
  fp_p_cb7 = p + KP11 * p + bb_p + KP111 * KP11 * bb * p + 2 * KP21 * KP11 * cb7 * p + 2 * KP211 * KP111 * KP11 * cb7 * p * bb
  fp_p_d = p + cb7_p + bb_p + cb7_p_bb + cb7_p_cb7 + cb7_2_p_bb
  fp_p_p = 1 + KP11 * cb7 + KBB_P * bb + KP111 * KP11 * bb * cb7 + KP21 * KP11 * cb7**2 + KP211 * KP111 * KP11 * cb7**2 * bb

  return np.array([[fp_bb_bb, fp_bb_cb7, fp_bb_d, fp_bb_p],
                  [fp_cb7_bb, fp_cb7_cb7, fp_cb7_d, fp_cb7_p],
                  [fp_d_bb, fp_d_cb7, fp_d_d, fp_d_p],
                  [fp_p_bb, fp_p_cb7, fp_p_d, fp_p_p]])


num_trials = int(1e6)
error = 1e-17

for tuple in dataTable.itertuples(index=False):
  if columns == 2:
    p_max, fd, bb_0, cb7_0, d_0 = tuple
  elif columns == 1:
    p_max, bb_0, cb7_0, d_0 = tuple

for i in range(num_trials):
  initial_guess = [np.random.uniform(0, bb_0), np.random.uniform(0, cb7_0),
np.random.uniform(0, d_0), np.random.uniform(0, p_max)]

  sol = optimize.root(equations, jac=jac, args=(p_max, bb_0, cb7_0, d_0), x0=initial_guess)

  if 0 <= sol.x[0] <= bb_0 and 0 <= sol.x[1] <= cb7_0 and 0 <= sol.x[2] <= d_0 and 0 <= sol.x[3] <= p_max:

```

```
        zero = equations(vars=sol.x, p_0=p_max, cb7_0 = cb7_0, bb_0 = bb_0, d_0=
    d_0)

      if -error <= zero[0] <= error and -error <= zero[1] <= error and -error <=
     zero[2] <= error and -error <= zero[3] <= error:
        values_bb.append(np.float64(sol.x[0]))
        values_cb7.append(np.float64(sol.x[1]))
        values_d.append(np.float64(sol.x[2]))
        values_p.append(np.float64(sol.x[3]))
        break


  if len(values_p) != len(dataTable["P0"]):
    print("The optimization was not successful")
  else:
    dataTable["BB"] = values_bb
    dataTable["CB7"] = values_cb7
    dataTable["D"] = values_d
    dataTable["P"] = values_p

  dataTable["[CB7:P]"] = KP11 * dataTable["CB7"] * dataTable["P"]
  dataTable["[CB7:D]"] = KD11 * dataTable["CB7"] * dataTable["D"]
  dataTable["[CB7_2:D]"] = KD11 * KD21 * dataTable["CB7"] ** 2 * dataTable["D"
    ]
  dataTable["[CB7:D:BB]"] = KD11 * KD111 * dataTable["CB7"] * dataTable["D"] *
     dataTable["BB"]
  dataTable["[CB7_2:D:BB]"] = KD11 * KD111 * KD211 * dataTable["CB7"] **2 *
    dataTable["D"] * dataTable["BB"]
  dataTable["[CB7:P_2]"] = KP21 * KP11 * dataTable["CB7"] ** 2 * dataTable["P"
    ]
  dataTable["[BB:P]"] = KBB_P * dataTable["BB"] * dataTable["P"]

  dataTable["X_D"] = dataTable["D"] / dataTable["D_0"]
  dataTable["X_CB7:D"] = dataTable["[CB7:D]"] / dataTable["D_0"]
  dataTable["X_CB7:D:BB"] = dataTable["[CB7:D:BB]"] / dataTable["D_0"]
  dataTable["X_P"] = dataTable["P"] / dataTable["P0"]
  dataTable["X_CB7:P"] = dataTable["[CB7:P]"] / dataTable["P0"]
  dataTable["X_CB7:P2"] = dataTable["[CB7:P_2]"] / dataTable["P0"]
  dataTable["X_BB:P"] = dataTable["[BB:P]"] / dataTable["P0"]


  plt.plot(dataTable["P0"], dataTable["X_D"], "-", label = "D")
  plt.plot(dataTable["P0"], dataTable["X_P"], "-", label = "P")
  plt.plot(dataTable["P0"], dataTable["X_CB7:D"], '-', label = "CB7:D")
  plt.plot(dataTable["P0"], dataTable["X_CB7:P"], '-', label = "CB7:P")
  plt.plot(dataTable["P0"], dataTable["X_CB7:D:BB"], '-', label = "CB7:D:BB")
  plt.plot(dataTable["P0"], dataTable["X_CB7:P2"], '-', label = "(CB7)2:P")
  plt.plot(dataTable["P0"], dataTable["X_BB:P"], '-', label = "BB:P")
  plt.xlabel("[Peptide] (M)")
  plt.ylabel("Molar Fraction")
```

```
plt.legend()
plt.show()

dataTable.to_excel(r"C:\\Users\\joana\\Documents\\Programming\\BindingAssays
  \\BindingAssays\\Dev\\ExampleData\\prediction_data.xlsx",
sheet_name="Dye")
```

I.2.3 Scripts for Principal Component Analysis of Array Data

For data treatment for PCA, the data should be organized with the label for the different groups of guests to categorize and discriminate in the first column, with the triplicate done separate in three groups with all guests, and the different data sets at the emission wavelengths to analyze for the different sensors should be presented in each new column following that, with each line being the data for one measurement of one peptide for a given sensor and wavelength combination. The example of the data used for obtention of the PCA presented in Chapter 4, Section 4.1, can be found in Figure I.3. The output will be generated in a plot which will be shown in a *matplotlib* window and should be adjusted and saved as desired. No additional files were used for this calculation but these can be found in the repository in this link: https://github.com/JoanaNMartins/PCA/tree/main. The following script refers to the contents of the "PCA_test.py" file.

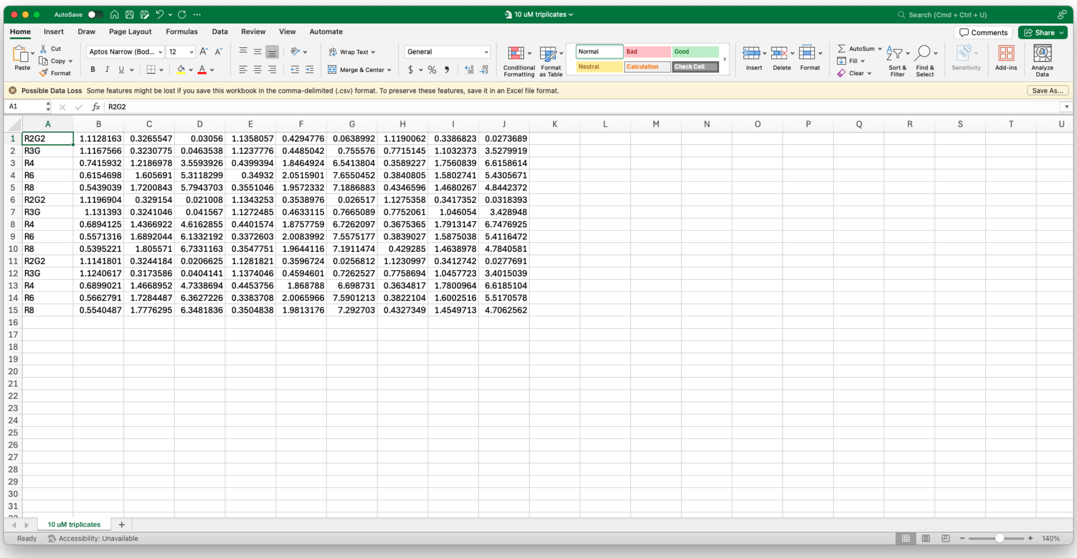

	A	B	C	D	E	F	G	H	I	J
1	R2G2	1.1128163	0.3265547	0.03056	1.1358057	0.4294776	0.0638992	1.1190062	0.3386823	0.0273689
2	R3G	1.1167566	0.3230775	0.0463538	1.1237776	0.4485042	0.755576	0.7715145	1.1032373	3.5279919
3	R4	0.7415932	1.2186978	3.5593926	0.4399394	1.8464924	6.5413804	0.3589227	1.7560839	6.6158614
4	R6	0.6154698	1.605691	5.3118299	0.34932	2.0515901	7.6550452	0.3840805	1.5802741	5.4305671
5	R8	0.5439039	1.7200843	5.7943703	0.3551046	1.9572332	7.1886883	0.4346596	1.4680267	4.8442372
6	R2G2	1.1196904	0.329154	0.021008	1.1343253	0.3538976	0.026517	1.1275358	0.3417352	0.0318393
7	R3G	1.131393	0.3241046	0.041567	1.1272485	0.4633115	0.7665089	0.7752061	1.046054	3.428948
8	R4	0.6894125	1.4366922	4.6162855	0.4401574	1.8757759	6.7262097	0.3675365	1.7913147	6.7476925
9	R6	0.5571316	1.6892044	6.1332192	0.3372603	2.0083992	7.5575177	0.3839027	1.5875038	5.4116472
10	R8	0.5395221	1.805571	6.7331163	0.3547751	1.9644116	7.1911474	0.429285	1.4638978	4.7840581
11	R2G2	1.1141801	0.3244184	0.0206625	1.1281821	0.3596724	0.0256812	1.1230997	0.3412742	0.0277691
12	R3G	1.1240617	0.3173586	0.0404141	1.1374046	0.4594601	0.7262527	0.7758694	1.0457723	3.4015039
13	R4	0.6899021	1.4668952	4.7338694	0.4453756	1.868788	6.698731	0.3634817	1.7800964	6.6185104
14	R6	0.5662791	1.7284487	6.3627226	0.3383708	2.0065966	7.5901213	0.3822104	1.6002516	5.5170578
15	R8	0.5540487	1.7776295	6.3481836	0.3504838	1.9813176	7.292703	0.4327349	1.4549713	4.7062562

Figure I.3: Example .csv file for the input of values of emission at different wavelengths and for triplicate samples of peptides at a fixed concentration. First column presents the name of the category for PCA to group together, while B through D corresponds for the emission values for SC4-4Py at 376, 420 and 480 nm, E to G corresponds for the emission values for SC4-6Py for the same wavelengths, and H to J corresponds to SC4-8Py emissions.

Listing I.5: Script 5 - Principal Component Assay

```python
import matplotlib.pyplot as plt
import matplotlib
import numpy as np
from sklearn.decomposition import PCA
from tkinter import Tk
from tkinter.filedialog import askopenfilename
import pandas as pd
from matplotlib.patches import Ellipse

Tk().withdraw()
fileName = askopenfilename()
df = pd.read_csv(fileName, header=None, sep=";")
df.dropna(inplace=True)
labels = df[0]
df = df.drop(labels=0, axis=1)

pca = PCA(n_components=2)
number_of_reps = 3

X_pca = pd.DataFrame(pca.fit(df).transform(df), columns = ["PC1", "PC2"])
X_pca["labels"] = labels

unique_labels = X_pca["labels"].unique()

plt.figure()
colors = ["navy", "turquoise", "purple", "darkorange", "pink"]
lw = 2

matplotlib.rcParams.update({'font.size': 16})

for name, color in zip(unique_labels, colors):
  category_data = X_pca[X_pca["labels"] == name]
  plt.scatter(category_data["PC1"], category_data["PC2"],
              s=80, alpha=0.8, lw=lw,
              label=name, color=color)

# Plot 95% confidence ellipses
for label, color in zip(unique_labels, colors):
  group_data = X_pca[X_pca["labels"] == label]
  cov_matrix = np.cov(group_data[["PC1", "PC2"]].T)
  lambda_, v = np.linalg.eig(cov_matrix)
  lambda_ = np.sqrt(lambda_)
  ell = Ellipse(xy=(np.mean(group_data["PC1"]),
                  np.mean(group_data["PC2"])),
                  width=lambda_[0] * 2 * 2, height=lambda_[1] * 2 * 2,
                  angle=np.rad2deg(np.arccos(v[0, 0])),
                  alpha=0.5, color=color, lw=lw)
  ell.set_facecolor('none')
  plt.gca().add_patch(ell)
```

```
    # Annotate ellipse with label
    plt.annotate(label, xy=(np.mean(group_data["PC1"]),
                            np.mean(group_data["PC2"])), xytext=(-10, 10),
                            textcoords='offset points', ha='right',
                            va='top', fontsize=14, color='black')


plt.xlabel(f"F1 ({round(pca.explained_variance_ratio_[0], 4) * 100:.2f} %)")
plt.ylabel(f"F2 ({round(pca.explained_variance_ratio_[1], 4) * 100:.2f} %)")

plt.show()
```

2025 Supramolecular Strategies for the Sensing and Transport of Peptides Joana N. Martins

UNIVERSIDADE NOVA DE LISBOA